MSc Eng Wiktoria Lipińska

Institute of Fluid-Flow Machinery Polish Academy of Sciences

Fabrication of gold, copper and titanium nanostructures obtained during thermal processing and their characteristics

Doctoral dissertation
Institute of Fluid-Flow Machinery Polish Academy of Sciences

Supervisor:
PhD DSc Eng Katarzyna Siuzdak Professor of IMP PAN

Gdańsk, *December 2023*

Acknowledgments

I would like to sincerely express my gratitude to Professor Katarzyna Siuzdak
for providing me the opportunity to learn and grow as a scientist.
Thank you for sharing your knowledge and experience.

Thanks to PhD DSc Katarzyna Grochowska , PhD DSc Eng Jacek Ryl Prof GUT,
PhD DSc Eng Jakub Karczewski Prof GUT, Msc Eng Adrian Olejnik,
PhD Eng Zuzanna Bielan, PhD DSc Eng Agnieszka Witkowska Prof GUT
for the assistance in measurements and valuable contribution in manuscripts preparation.

I am grateful for the opportunity to work with Professor Elisabeth Lojou
during my internship, at French National Centre for Scientific Research in Marseille.
Thank you for your time and scientific discussions.

Last but not least, thanks to Kamil, my parents Izabela and Marcin,
family and friends for support, and filling my life with happiness.

This dissertation was supported by

Preludium-18 project titled: “Ordered mosaic of the bimetallic Au-Cu nanoparticles onto the conductive substrate – fabrication and properties” financed by National Science Centre in Poland, project no. 2019/35/N/ST5/02604.

Solaris National Synchrotron Radiation Centre proposal titled: “The effect of atmosphere on AuCu structure properties during rapid thermal treatment” 212011

This work has been carried out in Laboratory of Functional Materials,
Centre for Plasma and Laser Engineering, Institute of Fluid-Flow Machinery PAS

Table of contents

1. Abstract

The PhD dissertation concerns the development of the fabrication procedure of bimetallic AuCu nanoparticles obtained on nanostructured titanium and titanium dioxide platform. Such electrodes act as material photoelectrochemically active under visible light illumination water splitting and alcohol oxidation processes finding future application in solar cells and fuel cells production. The materials were fabricated using electrochemical anodization of Ti foil, chemical etching, thin AuCu alloy, Au, Cu layers deposition in various configurations and thicknesses by means of magnetron sputtering as well as using rapid and gradual thermal treatment. The fabrication process of gold, copper and titanium nanostructures was optimized, especially the impact of different temperatures, rates, time and atmosphere (air, vacuum, argon and hydrogen) during thermal treatment on materials performance was investigated. Detailed characterization of morphology, optical and structural properties as well as electrochemical and photoelectrochemical activity in the presence of solar light simulator illumination was carried out. Based on experimental data correlation between size, shape, structure and chemical composition of gold and copper nanoparticles and their optical and electrochemical properties was determined. The theoretical part of this study discusses gold nanoparticles, discrete band states in nanoparticles, surface plasmon resonance, the p-type and n-type semiconductors on the example of copper oxides and titanium dioxide, doping of semiconductors by introduction of additional energy levels into their structure and mechanism of charge transfer at the p-n junction. Furthermore, detailed description of methods used for fabrication and then material characterization is presented and enriched with literature data on examples of materials discussed in thesis. The main result shown in this PhD thesis is the development of fabrication procedure of ordered Ti nanodimples and TiO_2 nanotubes platforms modified by AuCu nanoparticles which are characterized by increased absorption in visible light as well as enhanced photoactivity and catalytic activity. The data described here can contribute in fabrication of new functional nanomaterials active in processes of converting solar energy into electricity as well as more efficient solar and fuel cells in industry.

2. Streszczenie

Praca doktorska dotyczy opracowania metody otrzymywania bimetalicznych nanocząstek AuCu na nanostrukturyzowanym podłożu tytanu i ditlenku tytanu jako materiałów elektrodowych umożliwiających zastosowanie w urządzeniach do fotogeneracji prądu w świetle widzialnym, rozkładu wody do tlenu i wodoru oraz procesach utleniania alkoholi wykorzystywanych w ogniwach paliwowych. Materiały otrzymano z wykorzystaniem procesu anodyzacji elektrochemicznej foli tytanowej, trawienia chemicznego, rozpylania magnetronowego cienkich warstw stopu AuCu, Au, Cu w różnych konfiguracjach i o różnych grubościach oraz gwałtownej i stopniowej obróbki termicznej. Przeprowadzono optymalizację procesu wytwarzania nanostruktur złota, miedzi i tytanu, w szczególności wpływu obróbki termicznej na właściwości materiału poprzez zmianę takich parametrów jak temperatura, czas, szybkość nagrzewania oraz środowisko, w którym odbywało się wygrzewanie elektrod (powietrze, próżnia, argon, wodór). Wykonano szczegółową charakterystykę morfologii, właściwości optycznych i strukturalnych jak również aktywności elektrochemicznej i fotoelektrochemicznej w obecności światła symulującego światło słoneczne. Na podstawie danych eksperymentalnych określono korelacje pomiędzy wielkością, kształtem, strukturą i składem chemicznym nanocząstek złota i miedzi, a ich właściwościami optycznymi oraz elektrochemicznymi. W części teoretycznej opisano nanocząstki złota, dyskretne stany energetyczne w nanocząstkach, powierzchniowy rezonans plazmonowy, półprzewodnik typu p i n na przykładzie tlenków miedzi i ditlenku tytanu, wprowadzanie dodatkowych poziomów energetycznych do półprzewodnika poprzez jego domieszkowanie oraz mechanizm przeniesienia ładunku na złączu p-n. Ponadto, przedstawiono szczegółowy opis metod wytwarzania, a następnie metod użytych do charakterystyki materiałów, który został wzbogacony danymi literaturowymi dotyczącymi przykładów materiałów opisywanych w rozprawie. Rezultatem przeprowadzonych badań jest otrzymanie uporządkowanych struktur nanodołków Ti oraz nanorurek TiO_2 pokrytych bimetalicznymi nanocząstkami AuCu charakteryzującymi się zwiększoną absorpcją w świetle widzialnym, wzrostem fotoaktywności oraz aktywności katalitycznej. Zagadnienia opisane w rozprawie mogą przyczynić się do stworzenia nowych materiałów funkcjonalnych aktywnych w procesach konwersji energii słonecznej na elektryczną oraz efektywniejszych ogniw słonecznych i paliwowych w produkcji przemysłowej.

3. List of abbreviations

A – absorbance

AFM – atomic force microscopy

c – concentration of absorbing species

C – capacitance

C_{dl} – double layer capacitance

C_{ext} – extinction cross section

C_{sca} – scattering cross section

C_{abs} – absorption cross section

CE – counter electrode

CPE – constant phase element

CB – conduction band

CSD – chemical solvent deposition

CV – cyclic voltammetry

CVD – chemical vapour deposition

d – spacing of the crystal layers
– thickness of layer

D – diffusion coefficient

E – potential

E(t) – potential at time t

EDX – energy dispersive X-ray spectroscopy

E_a – anodic peak potential

E_c – cathodic peak potential

E_g – energy band gap

E_F – position of Fermi level

E_B – binding energy of electron

E_k – kinetic energy of photon

EIS – electrochemical impedance spectroscopy

EXAFS – X-ray absorption fine structure

EEC – electrical equivalent circuit

F – Faraday constant

FIB – focused ion beam

FTO – fluorine-doped tin oxide

HER – hydrogen evolution reaction

h – Planck's constant

i – current

IPCE – incident photon-to-electron conversion efficiency

ITO – indium-doped tin oxide

i_a – anodic peak current

i_c – cathodic peak current

I_0 – intensity of incident light

I – intensity of transmitted light

j – photocurrent

$j_{(dark)}$ – current density registered without light illumination

$j_{(vis)}$ - current density registered under visible light illumination

l – optical path length

LSPR – localized surface plasmon resonance

LV – linear voltammetry

MF – muffle furnace

n – diffraction order
– number of electrons transferred in the reaction
– constant phase element exponent

N_e – number of photogenerated electrons

N_p – number of photoelectrons from incident light

NPs – nanoparticles

OER – oxygen evolution reaction

P – incident light power density

PVD – physical vapour deposition

R – resistance
– universal gas constant

R_{ct} – charge transfer resistance

R_e – electrolyte resistance

RE – reference electrode

RTA – rapid thermal annealing

SEM – scanning electron microscopy

SPR – surface plasmon resonance

t – time

T – temperature

TEM – transmission electron microscopy

TiNDs – titanium nanodimples

TiO_2NTs – titanium dioxide nanotubes

Q – quasi-capacitance

Q_e – extinction efficiency coefficient

Q_a – adsorption efficiency coefficient

Q_s – scattering efficiency coefficient

W_{Or} – Warburg coefficient

WE – working electrode

VB – valence band

XAS – X-ray absorption spectroscopy

XANES – X-ray absorption near-edge structure

XRD – X-ray diffractometry

XPS – X-ray photoelectron spectroscopy

Z – impedance

ΔE – peak-to-peak separation potential

ε – molar absorption coefficient

$\mathcal{E}_1$ – dielectric constant of NP

$\mathcal{E}_m$ – dielectric constant of medium

λ – wavelength

ν – photon frequency

ω – frequency

ϕ – work function

φ – phase shift

θ – angle between incident ray and the scatter plane

Ψ_n – Riccati-Bessel function

ξ_n – Riccati-Bessel function

4. Introduction

4.1. Functional nanomaterials

Humans have always had a deep curiosity with electricity. Therefore, various extraordinary inventions came to light and were implemented in order to increase the quality of life. In this work, a lot of attention will be dedicated to electrical energy technology, especially solar energy. It is well established that the Sun's radiation can be used to generate electricity. Sun can be regarded as a renewable and clean energy source because it does not produce pollutants in contrast to carbon and oil sources. Electricity, solar energy and the Sun are all connected in terms of fundamental physical interactions. The latter was actually worshiped in ancient times. In the beginning the Sun was treated as a god. Ra in ancient Egypt, Helios and Apollo in Greek mythology are a few of the well-known gods of Sun. It can be claimed that religion was first including the god and goodness of the Sun. After many years scientists began to believe in the potential of the Sun, thanks to which generating electricity from that source was explored. Taking the above into account, first and foremost it seems reasonable to believe that this PhD thesis provides new insight and knowledge. After many pages the subject of new nanomaterials active towards energy conversion processes and future application of nanomaterials in industry will be well versed.

With the rapid growth of technology, constructions and devices and whole machines often become miniaturized. Because of that, the field of engineering nanomaterials is building in strength. The miniaturization process ensures less consumption of materials which are needed for their production. An added benefit includes less space being required for their production and storage, which ultimately reduces costs. Miniaturization of elements is akin with maximization of benefits in the production engineering process. Reducing the size of elements while increasing their effectiveness and functionality is possible thanks to the development of modern technologies, in particular nanotechnology that in recent years provides us a lot of benefits: long lasting batteries, high contrast emitting devices or highly sensitive detectors. Fabrication and analysis of new nanomaterials provide information of their structure and unique properties that can be utilized in the construction of electrical components and devices at nanoscale. Regarding energy conversion, nanomaterials are used for example in solar cells, water splitting devices as well as fuel cells. They are synthesised in various shapes such as nanoparticles (NPs), nanotubes, nanosheets, nanowires, nanoframes, or in the form of alloys and composites, where nanoalloys are composed of two or more metals, and nanocomposites are fabricated by mixtures of polymers[1]. In the literature it is possible to find many research related to application of

nanomaterials which are being invented to replace currently used macromaterials in the industry as more efficient ones. Crystalline Si-solar cells with the power conversion efficiency (PCEs) of 26.7 % have been the main photovoltaic technology for several years[2]. In recent papers, one of the most extensively developed solar cells are perovskites and modified perovskites which can be competitive with silicone material because of high PCEs (in many reports over 24 %)[3]. One of the example for the modification of solar cells is implementation of TiO_2 nanoparticles to perovskite solar cell as the electron transfer layer in order to reduce charge transfer resistance, restrain recombination process and improve the stability[4]. Furthermore, in the case of water splitting process, Pt-based and Ir-based electrocatalysts used for hydrogen evolution and oxygen evolution reaction respectively, are coupled with additional compounds as Ir-Cu nanoframes[5], Pt-Cu nanoparticles[6] and graphene oxide (Pt, Pd, Au) composite[7]. Doping by other metals can reduce the overpotential and increase materials catalytic activity. Moreover, addition of non-noble metal like copper instead the noble one reduces catalyst costs. In the case of alcohol fuel cells, where Pt is commercially used as a catalyst, application of platinum not as a mesh but in the form of nanoparticles that can be deposited on TiO_2 nanotubes results in the reduction of used metal amounts and therefore production costs[8]. Whereas the combination of Pt and Cu as bimetallic catalysts enhances ethanol oxidation in contrast to monometallic Pt via hindering the tendency to Pt-H adsorption at low overpotential[9]. Those examples indicate how nanostructures can be beneficial for technological development.

Nanomaterials are tiny materials with at least one dimension in the range of 1-100 nm. It has been shown, that chemical, physical and mechanical properties of bulk and nano-size materials are different[10]. The difference in the properties between the bulk material and nanomaterial results from the enhanced surface to volume ratio and the quantum confinement[11]. As surface to volume ratio increases more atoms are exposed to the surrounding environment and the material becomes more chemically active (Figure 1a). In the case of quantum confinement, reducing the size of materials results in squeezing electrons into space smaller than they prefer within nanoparticles with smaller dimensions than in bulk (Figure 1b). Bigger size of nanoparticles are assigned to weaker confinement and decrease of the bandgap energy, whereas, smaller NPs give stronger confinement and increase of the bandgap energy (Figure 1c)[11,12]. Furthermore, with decreasing nanoparticle dimension discrete bands start to appear. Such phenomenon has significant influence on electrical and optical properties of nanomaterials. It should be also highlighted that the band gap energy depends on the material type such as metal or semiconductor.

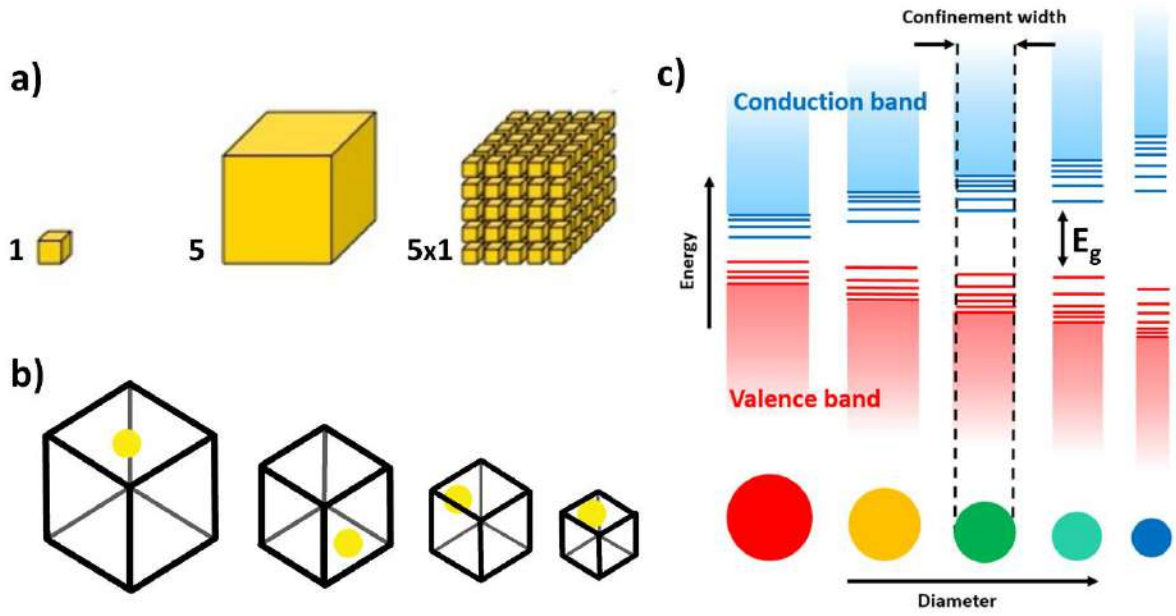

Figure 1. a) Visualisation of materials with various surface area and b, c) schematic representation of quantum confinement effect (dots are assigned to nanoparticles, E_g – energy band gap)[12].

In the case of nanoparticles, size, shape, structure and homogeneity of NPs as well as platform where nanoparticles are deposited on have significant influence on above mentioned properties since those features play the great role in the contact between the material and the outer environment. Therefore, the fabrication procedure and the facile control of its parameters are crucial for their properties and further applications. The synthesis methods for nanoparticles can be divided into top-down and bottom-up approaches (Figure 2)[13]. In top-down approach the bulk material is decomposed into smaller fragments using typically physical methods like chemical vapour deposition, physical vapour deposition, lithography and laser ablation. The bottom-up technique is based on the assembling of single atoms and molecules into larger nanostructures. For this purpose, different chemical methods are utilized, for example reduction and oxidation, hydrothermal process, bioreduction, sol-gel process and electrochemical deposition. Nanoparticles which are planned to be applied as a material active towards photocurrent generation or water splitting process should be anchored on the conductive substrate acting as a charge collector. In the case of colloid nanoparticles this process can be realised by direct adsorption of the nanoparticle onto the functionalized surface, spin-coating or electrospraying of the nanoparticles slurry on the substrate[14,15]. Whereas, for NPs fabricated via chemical or physical vapour deposition process, support material must be used already during their fabrication process.

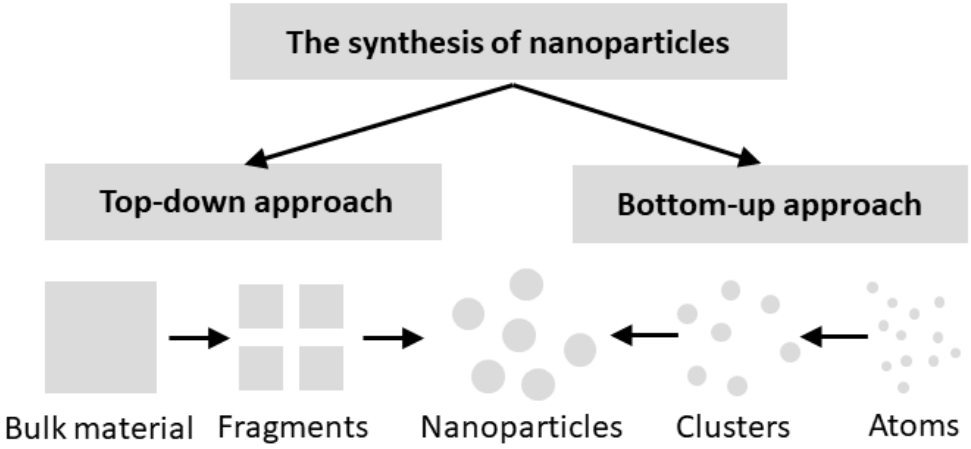

Figure 2. The two different approaches for nanomaterials synthesis.

Metal nanoparticles are widely explored in the field of optics, electronic, catalysis and biochemistry[16]. In the case of noble metal, gold NPs are one of the most extensively studied. First and foremost, Au NPs are characterized by the good stability and electrical conductivity. Moreover, gold nanoparticles are non-toxic, biocompatible and easy to functionalize by chemical or biological compounds[17]. Au NPs absorb light in the visible light range, exhibit surface plasmon resonance and enhance light-matter interactions thus they can generate and transport charges[18]. This is a positive correlation between light absorption and electron-hole pair generation. Surface plasmon resonance is an optical phenomenon in which incident electromagnetic field strongly interacts with free electrons originating from the conduction band[19]. The conduction band electrons excited by light illumination collectively oscillate with incident electromagnetic field and when photon frequency correlates with frequency of free electrons the resonance conditions are achieved[20]. In the case of the planar metal surface the incident electromagnetic radiation activates surface plasmon resonance, SPR, where light propagates along bulk surface. Whereas for spherical metallic surfaces upon light illumination when wavelength of light is greater than dimension of the nanoparticle, incident electromagnetic field activates localized surface plasmon resonance, LSPR[21]. The enhanced surface to volume ratio as well as the possibility to interact with any electromagnetic field due to presence of the free electrons along sphere, result in greater plasmon generation for nanoparticles than planar surface[22]. The plasmon resonance process decays after few femtoseconds. However, during that time it can induce various processes in the plasmonic nanoparticles/semiconductor system[18]. The radiative and the non-radiative decay can be distinguished. The radiative decay is a scattering of light which can be divided into elastic and inelastic ones. In the case of elastic scattering (state (1) in Figure 3) light can be further absorbed by semiconductor platform. In the case of

the non-radiative decay the Landau damping phenomenon (state (2) in Figure 3) or the plasmon induced resonant energy transfer (PIRET) (state (3) in Figure 3) can occur. The scheme of all different plasmon decay processes is presented in Figure 3. The Landau damping is a process of electron-hole pairs generation in plasmonic nanoparticle. In that process hot electrons are scattered inside NP where they undergo elastic collisions and further energy transfer in the form of heat to the environment occurs. The second option is hot electrons injection to semiconductor platform. Another non-radiative decay is the mentioned above PIRET process where energy is transferred to semiconductor through dipole-dipole coupling.

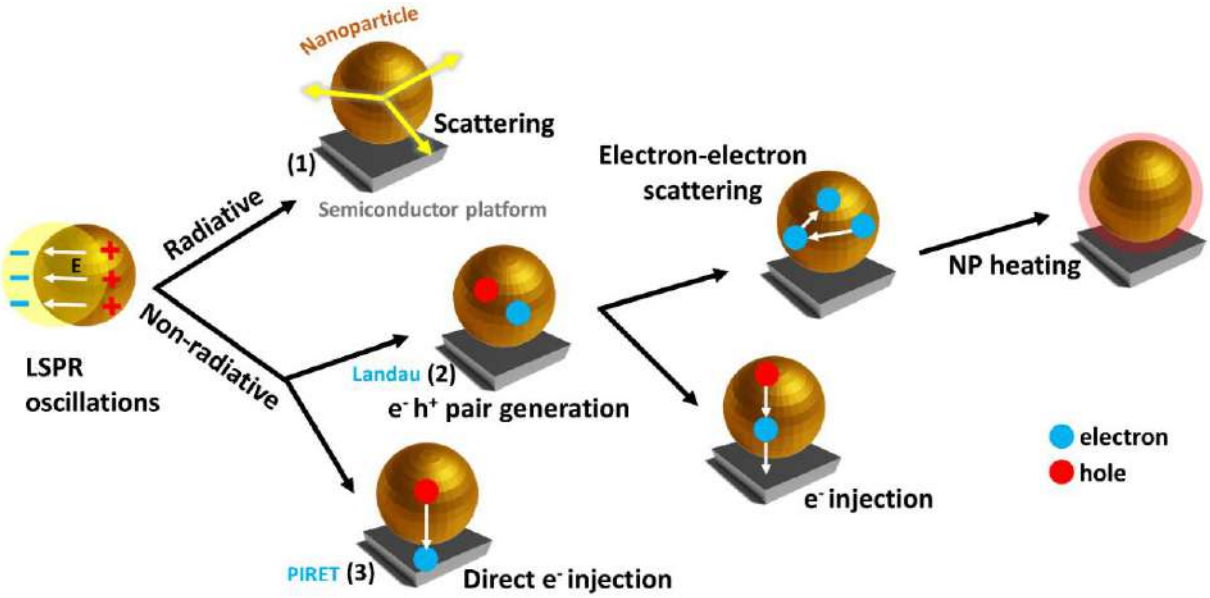

Figure 3. Scheme of different plasmon decay processes[18].

However, it should be added that other factors influence efficiency of light generation for example heat dissipation, reflection and scattering. The maximum absorption peak for Au NPs of 5-50 nm size is located between 520-530 nm[19]. Furthermore, optical properties of Au NPs are strongly affected by their size and shape[23]. The maximum absorbance shifts toward higher values of wavelength with increase of Au NPs size[24]. Whereas, different shape of nanoparticles such as rods, flowers or stars results in the formation of additional bands on the absorbance spectra[25,26]. Spherical NPs are characterized by single peak assigned to dipole resonance, whereas, nanorods have two absorption peaks assigned to transversal and longitudinal dipole LSPR mode[26].

Among other metals, copper is one of the cheapest and the most available. Moreover, bulk Cu is almost as good an electrical conductor as Au. However, copper nanoparticles show a decrease of electrical conductivity associated with Cu oxidation[27]. Copper nanostructures exhibit interesting mechanical properties such as good ductility, malleability and thermal conductivity[28] as well as antibacterial properties[29]. Comparing both metals, copper and gold NPs

are characterized by good absorption in the visible region. The maximum absorption peak for Cu NPs with 20 nm in size is shifted toward higher values in contrast to Au and reaches ca. 580 nm[19]. Nevertheless, the fabrication process of metallic copper nanoparticles as well as their future application are more complicated than of gold due to tendency to oxidation to Cu_2O and CuO in the air atmosphere[30].

In solid state physics, the electrical conductivity of material depends on the effectiveness of electrons flow between valence band (VB) and conduction band (CB). In the case of metal, valence and conduction bands overlap each other (Figure 4a). Electrons in material being a metal are free to move between two bands, whereas, in the case of semiconductors electrons should be excited from VB to CB (Figure 4b). The band gap (E_g) can be defined as the energy difference between top valence band and bottom conduction band[31] as well as the energy which is required to provide for the electron-hole pair generation[32]. The bandgap energy for metals and semiconductors is equal to 0 eV and 1-6 eV, respectively. Electrons can be promoted to the conduction band by the absorption of energy in the form of light or heat[33]. The continuous valence and conduction band in bulk metal starts to separate in metal NPs to discrete states as shown in Figure 1c[34]. The spacing between discrete states and bandgap increases with decrease of nanoparticle size[35]. Metallic NP starts to manifest different electronic structure than bulk metal when its diameter is lower than10 nm (Figure 4c)[36]. In the case of insulator, in which current is unable to flow, the bandgap reaches the values above 6 eV (Figure 4d).

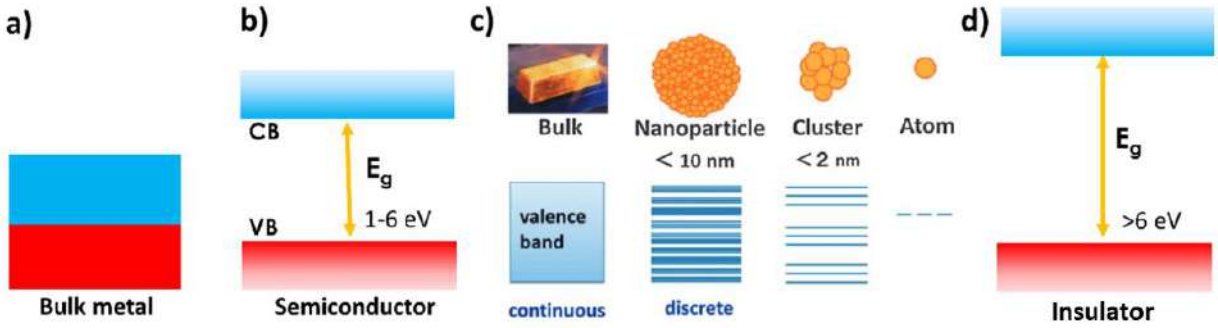

Figure 4. Energy band diagrams for a) bulk metal, b) semiconductor, c) electronic structure of bulk, NP and cluster of metals[36], d) energy band diagram for insulator.

4.2 Semiconductors exhibiting p and n-type conductivity

Semiconductors can be classified based on the position of Fermi level (E_F) which is the energy that corresponds to the equilibrium between the valence and conduction band. When the position of Fermi level is in the middle of energy bandgap, the intrinsic semiconductor can be distinguished (Figure 5a). While n-type and p-type semiconductors are characterized by perturbed carrier concentration where the Fermi level shifts toward CB and VB, respectively (Figure 5b,c)[37]. For example, titanium dioxide and copper oxides are n-type and p-type semiconductors, respectively. Concentration of the majority carriers, holes or electrons, can be changed by doping of the semiconductor. Another classification of semiconductor via bandgap shape can distinguish direct and indirect bandgap transitions. When the maximum of VB and the minimum of CB have the same k-vector (the electron wave vector), the direct transition occurs. If the maximum and minimum of valence and conduction bands are not aligned in $\vec{k}$ the indirect transition takes place.

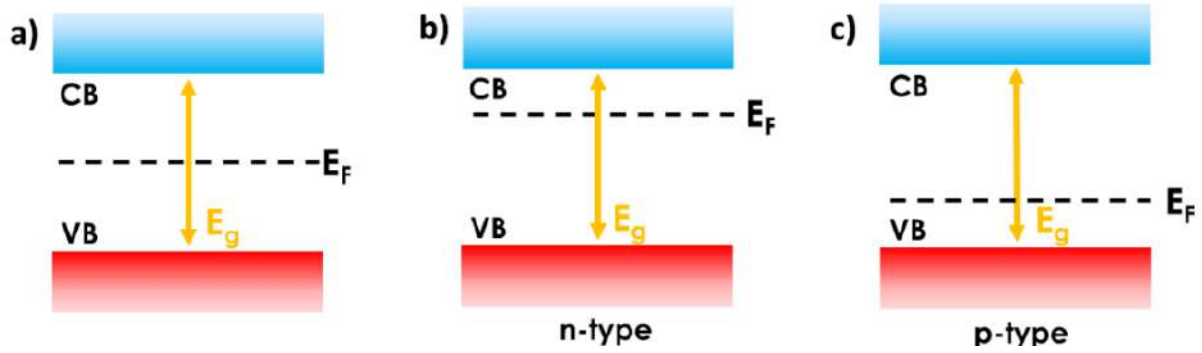

Figure 5. Energy band diagrams for a) intrinsic b) n-type and c) p-type semiconductor.

Titanium dioxide is characterized by the good stability, non-toxicity, low cost and high photoactivity in UV light range[38]. TiO_2 can be found in three crystal forms as anatase, rutile, brookite and such crystalline structure determines its bandgap energy thus light-absorption[39]. TiO_2 has wide bandgap and it is efficient only in UV light. It is well known that UV light covers only 5 % of solar spectrum, therefore various transition metal (Cu, Ni, Cr, Fe), noble metal (Au, Ag, Pt), non-metal (N, S, F) doping, heterojunction construction (CuO/TiO_2), surface modification are developed in order to decrease the bandgap and increase activity in the visible light range[40,41]. Therefore, some surface modifications will be described below.

4.2.1 Doping of titanium dioxide

As it was mentioned above TiO_2 is characterized by wide bandgap of 3.2 eV or 3.0 eV for anatase or rutile[42], respectively. Photoelectrochemical activity can be enhanced by doping of semiconductors[43,37]. Doping is a process of introducing impurities/ metal or non-metal atoms into the semiconductor. It is possible to distinguish two types of doping as shallow and deep doping. Electrons are donor type dopants, whereas, holes are acceptor type dopants. Energy levels of donors and acceptors states are presented in Figure 6. Therefore, TiO_2 can be doped by Cu^{2+} which acts as acceptor dopant and as a consequence narrows TiO_2 bandgap[44,45].

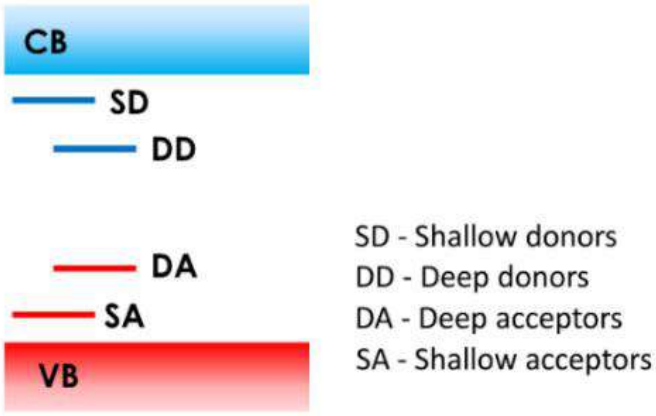

Figure 6. Energy levels of donors and acceptors states in doped semiconductors.

4.2.2 Formation of titania based heterojunction

Furthermore, the modification of TiO_2 by Cu_2O and CuO oxides, characterized by narrower bandgaps of 2.1–2.6 eV and 1.2–1.6 eV respectively, can improve material activity under visible light illumination[46]. The p-n junction can be formed between visible light absorbing p- type copper oxide semiconductor and n-type TiO_2 semiconductor (Figure 7). First of all, it should be mentioned that n-type semiconductor has mostly electrons as charge carriers (donor level), whereas, p-type semiconductor – holes (acceptor level) (Figure 7a). The behaviour of electrons and holes can be visualised as the full sphere (e^-) and the empty sphere (h^+). Charge carriers exist exactly in the opposite direction where electrons are in higher CB and holes in lower VB[47]. When materials are in contact electrons move to p-type semiconductors and holes diffuse to n-type semiconductor (Figure 7b). The space charge region (SPC) which is formed after charge carriers diffusion allows to remain neutral for entire semiconductor[48] (Figure 7c). The p-n junction achieves equilibrium and the Fermi energy becomes the same in both sides of junction. Moving further, when p-n junction is illuminated additional charge carriers are generated. The electron-hole excitation process in the semiconductors can be realized via light

absorption. In this process electron is excited from VB to CB causing hole formation in the VB. Electrons excited by light in p-type semiconductor move to the n-type semiconductor where further together with electrons excited in n-type material are transferred to external circuit and registered by potentiostat-galvanostat (Figure 7d). The position of the p-type CB that is higher comparing to the n-type CB permits transfer of electrons[49].

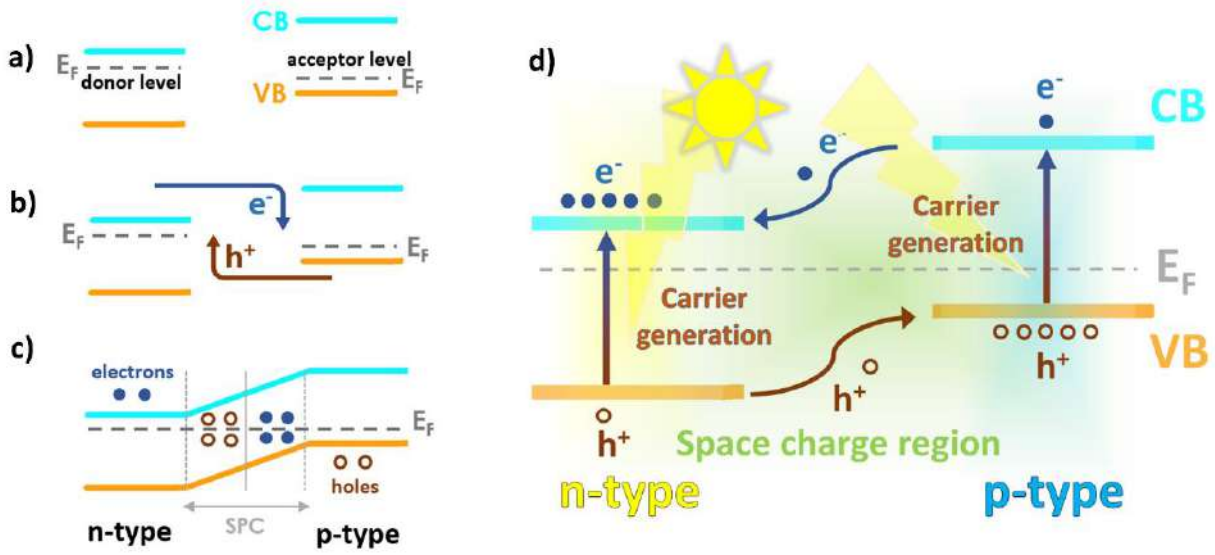

Figure 7. Schematic representation of a) n and p-type semiconductor before contact, b) n and p-type semiconductors in moment of contact, c) p-n junction in equilibrium[50,48] d) band diagram for p-n junction during light illumination[51].

5. Aim and objectives

Bimetallic AuCu nanostructures possess unique optical, electrical and catalytic properties in contrast to monometallic NPs such as broadband absorption in the visible light and surface plasmon resonance. The combination of Au and Cu results in the synergetic effect between two metals as well as improves stability of copper and copper oxides[52]. In order to design photoactive devices which can be applicable in the industry such bimetallic nanostructures need to be deposited on support materials. Nowadays, a lot of research concerns colloid nanoparticles or nanostructures deposited on glass substrates such as ITO (indium tin oxide) or FTO (fluorine-doped tin oxide)[53,54]. However, as was mentioned above colloid nanoparticles cannot be used as photocathodes or photoanodes because of the lack of electrical contact enabling to collect the charge generated during the reaction. In the case of glass substrates high price and easy breakability of such support require careful use and thus can bother some further applications. Furthermore, nanoparticles which are deposited on flat surface can agglomerate. Therefore, in this PhD thesis AuCu nanostructures were deposited on two types of support material such as highly ordered nanodimpled Ti substrate and TiO_2 nanotubes. Ti plate staying a substrate for further synthesis is cheaper than ITO or FTO deposited on glass substrate as well as more flexible. Moreover, TiO_2 which is n-type semiconductor with the bandgap of 3.2 eV and the absorbance band only in UV range can be modified by gold or copper in order to enhance absorbance in the visible light range. Therefore, the interaction between support material and bimetallic AuCu NPs was deeply described. The fabrication process of AuCu nanostructures deposited on Ti/TiO_2 platform was developed and optimized. This procedure included several steps such as electrochemical anodization process of Ti foil, thin AuCu layer magnetron sputtering with different Au, Cu layers sequences and thermal treatment of electrodes in various conditions (temperature, time, heating rate, gas atmosphere). To sum up, the main goal of this PhD thesis is fabrication and characterization of gold, copper, titanium nanostructures considering changes in material morphology, structure, optical properties, electrochemical and photoelectrochemical activity as a result of various processing parameters. Fabricated materials were tested as the photoelectrodes for photocurrent generation, materials active toward oxygen and hydrogen generation as well as alcohol oxidation supported by light illumination.

Above mentioned goals determine the scope of research developed in this PhD thesis:

- Fabrication of ordered Ti nanodimpled platform using electrochemical anodization and chemical etching process as well as modification of such substrates by AuCu layers using magnetron sputtering, and annealing in the muffle furnace or the rapid thermal annealing furnace.
- Fabrication of spaced TiO_2 nanotubes by electrochemical anodization process and modification by AuCu layers using magnetron sputtering as well as further thermal treatment in the rapid thermal annealing furnace.
- The investigation of the impact of the differences between bimetallic AuCu combinations (AuCu alloy, Au and Cu in different layer sequences) and monometallic Au or Cu counterparts on materials properties.
- The effect of various conditions of thermal treatment such as different temperature (from 100 °C to 600 °C), annealing rate (fast or slow), time (short or long) and atmosphere (air, vacuum, argon, hydrogen) of AuCu nanostructures deposited on Ti nanodimples as well as TiO_2 nanotubes on nanomaterials properties.
- The analysis of fabricated AuCu nanostructures obtained on Ti/TiO_2 platform using solid state physics methods: scanning electron microscopy, atomic force microscopy, transmission electron microscopy, X-ray diffractometry, Raman spectroscopy, X-ray photoelectron spectroscopy, X-ray absorption spectroscopy.
- The investigation of optical properties of AuCu–modified Ti/TiO_2 substrates using UV-vis spectroscopy.
- Electrochemical and photoelectrochemical characterization of AuCu nanomosaics obtained on Ti nanodimples and TiO_2 nanotubes using: cyclic voltammetry, linear voltammetry registered in dark as well as under vis and UV-vis light illumination, electrochemical impedance spectroscopy, and measurements of incident photon-to-electron conversion efficiency.
- The analysis of electrochemical and photoelectrochemical activity especially towards oxygen evolution reaction, hydrogen evolution reaction, photocurrent generation and alcohol oxidation assisted by light illumination.

6. Methods

6.1 Nanomaterials fabrication

6.1.1 Electrochemical anodization

6.1.1.1 Titanium dioxide nanotubes

Electrochemical anodization is the process of oxidation of the metallic surface of anode material and formation of oxide layer with increased thickness[55]. The anodization is mostly used for protective corrosion coatings (Figure 8a-c), leading to the formation of continuous oxide layer over the metallic part. However, under particular conditions nanotubular structures can be manufactured on the material surface. Furthermore, anodized aluminium and titanium can also be used for jewellery (Figure 8d). In 1995 Masuda et al.[56] published work concerning ordered metal nanohole arrays of Au and Pt fabricated by noble metal deposition onto anodized porous alumina, injection and polymerization of methyl methacrylate into this structure and removal of alumina by poly (methyl methacrylate). Since that time the high degree nanostructures which can be achieved by anodization process have gained great popularity. It is a wide range of metal oxides which can be formed as self-organized nanostructures during anodization of such substrates as Al, Nb, Ta, Ti, W, Zr, Zn.

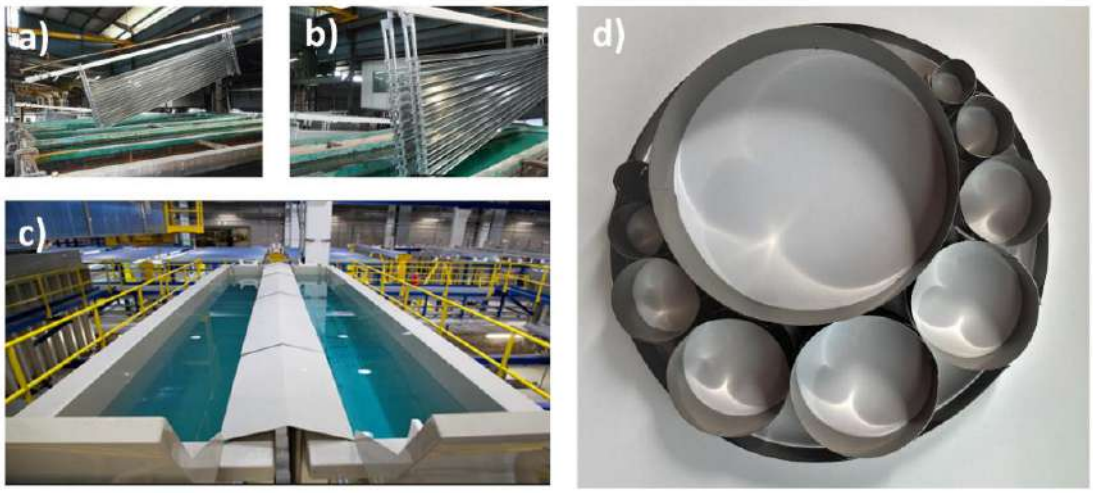

Figure 8. a-c) aluminium anodization baths[57,58] and
d) titania jewellery included in "Cosmos Lem Jewellery" [59].

In the case of Ti, the first layer of ordered titanium dioxide nanotubes have been developed by Assefpour-Dezfuly et al.[60] in 1984 using an electrolyte consisting of chromium trioxide and ammonium fluoride dissolved in distilled water. The schematic diagram of electrochemical anodization cell is presented in Figure 9a. The anodization cell is composed of two electrodes which are connected with power source. The Ti plate acts as an anode while Pt as

a cathode. Any electronic conductor which is inert in electrolyte such as stainless steel, palladium, graphite can take the role of cathode[61]. The electrodes are submerged in electrolyte consisting of water-polyhydroxyalkyl alcohol solution and fluorite ions (F^-) which penetrate and dissolute the anode metal surface. Typically as a source of F^- ions NH_4F and HF are used. Regarding the polyhydroxyalkyl alcohol, glycerine, ethylene or diethylene glycol water solutions are utilized.

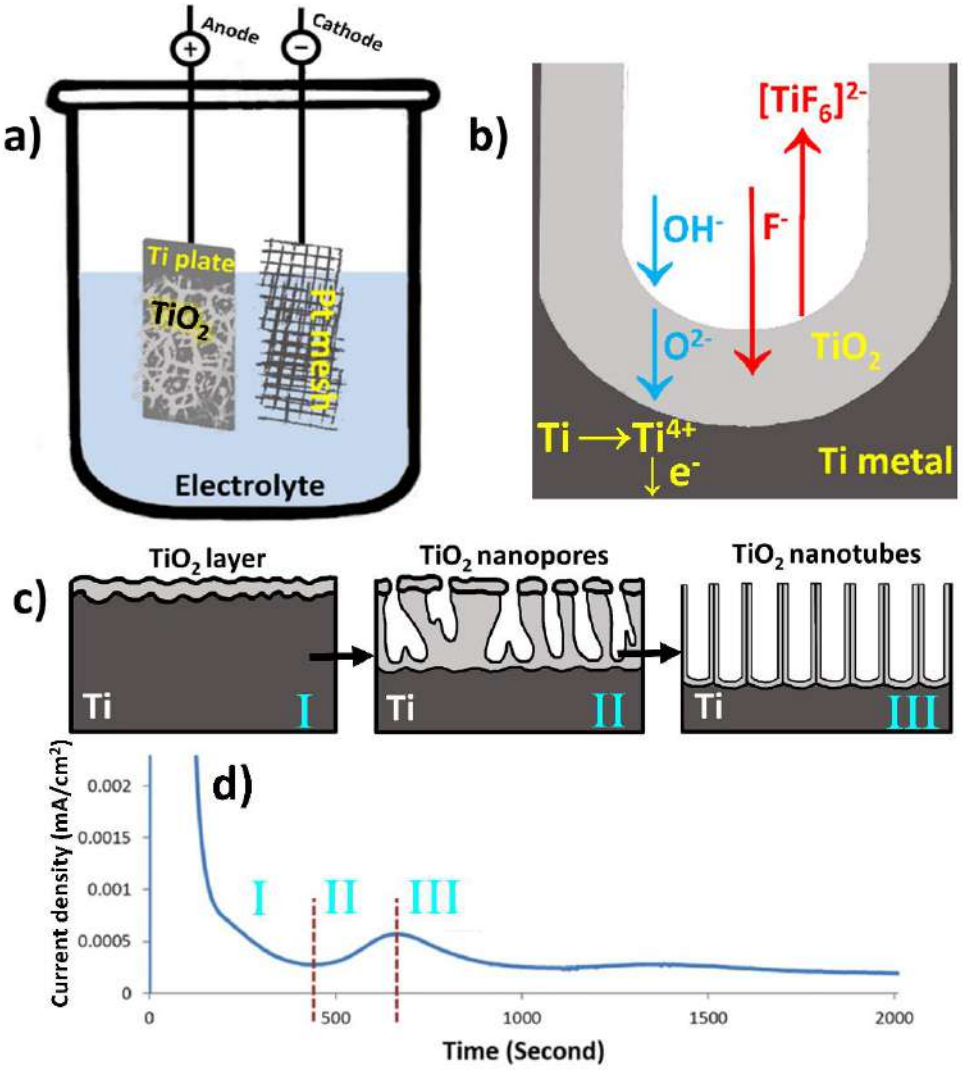

Figure 9. a) Schematic diagram illustrating the anodization cell, b) TiO_2 nanotubes formation mechanism, c) individual steps of nanotubes formation, d) current density vs. time curve in the anodization process[62].

Under applied voltage the anode is positively charged, the anions present in the electrolyte are moving towards the anode, the electrons from the circuit are transferred from anode to cathode and on the surface of electrode reaction occurs. The water oxidation takes place at anode and reduction at cathode according to reactions (1) and (2), respectively:

(1) Anode: $2H_2O \rightarrow O_2 + 4H^+ + 4e^-$

(2) Cathode: $2H_2O + 2e^- \rightarrow H_2 + 2OH^-$

The one proposed reaction mechanism of Ti electrochemical anodization is presented in Figure 9b. The formation of TiO_2 nanotubes is composed of two competitive reactions such as oxide formation by oxygen anions O^{2-} and OH^- (3) as well as dissolution reaction caused by F^- (4) where the oxide formation should be faster than dissolution[63,55].

(3) $Ti + 2H_2O \rightarrow TiO_2 + 4H^+ + 4e^-$

(4) $TiO_2 + 6NH_4F \rightarrow [TiF_6]^{2-} + 6NH_3 + 2H_2O + 2H^+$

At the beginning of the anodization, titanium is oxidized due to the interaction with O^{2-} and OH^- forming titanium dioxide layer. It should be noted that oxygen ions O^{2-} and OH^- on the material/electrolyte interface are formed by water electrolysis. In this stage noted as (I) pores grow randomly on the oxide layer and increase with time. In Figure 9d showing relationship between current and time during anodization the sharp current decrease in stage (I) is caused by the formation of TiO_2 layer that exhibits semiconducting properties with lower conductivity comparing to the initial metallic substrate. Further, in step (II) the O^{2-} penetrates the formed thin film of TiO_2 and interacts with another Ti^{4+} present below the oxide. Simultaneously, Ti^{4+} goes up to titanium oxide/electrolyte interface where is dissolved in the electrolyte. In this stage, pores start to interact and compete with each other. The formation of porous/tree-like nanostructures can be observed. The moment of pores nucleation is assigned to the current increase. In step (III) titania is partially dissoluted by fluoride anions forming $[TiF_6]^{2-}$ that is released to the electrolyte. The plateau current is reached when high ordered TiO_2 nanotubes are formed[64](Figure 9c).

Since from the first anodization process leading to formation of ordered nanostructure, almost 40 years passed, the anodization procedure was upgraded. Therefore, it is possible to distinguish five generation of nanotubes depending on the electrolyte composition (see Table 1)[55,65]. At the beginning the whole process was carried out in water solution where HF was the source of F^- ions (1st generation) and as a result not so uniform tubular layer was obtained. With time, fluoride salts became the source of fluoride ions (2nd generation), and instead of water as a single solvent, organic-water solution was proposed (3rd generation). In 4th generation, not fluoride but other ions, like Cl^- and ClO_4^- are responsible for etching and finally in anodization process included in 5th generation ammonium fluoride became the precursor of F^-.

Table 1. Electrolyte composition for different generation of nanotubes.

Nanotubes generation	Electrolyte composition
1st	hydrogen fluoride (HF) in aqueous electrolyte
2nd	potassium fluoride (KF) and sodium fluoride (NaF) in aqueous electrolyte
3rd	fluoride ions (KF, NaF, NH_4F) in organic electrolytes (dimethyl sulfoxide, formamide, ethanol, ethylene glycol)
4th	hydrochloric acid (HCl), ammonium chloride (NH_4Cl)or perchloric acid ($HClO_4$) in aqueous solution
5th	ammonium fluoride (NH_4F) in glycol electrolyte with water

The SEM images of aligned and spaced TiO_2 nanotubes are presented in Figure 10. Due to the localized stress caused by expansion in volume as well as electrostriction forces titanium oxide becomes the inner-wall of nanotube. Simultaneously, the fluoride rich oxide layer comes to be outer-wall of nanotube. At the beginning TiO_2NTs (titanium dioxide nanotubes) stick together, however in time fluoride rich layer is dissolving. Therefore, the distance between nanotubes increases[66].

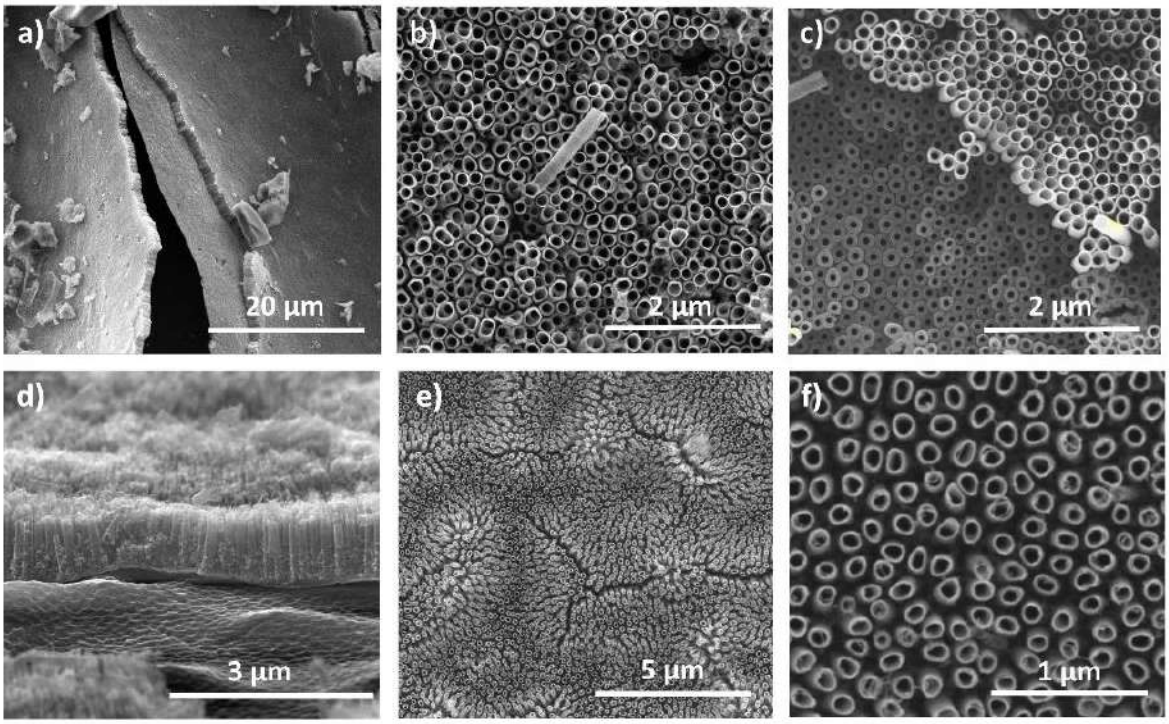

Figure 10. SEM images of a-c) aligned TiO_2NTs and d-f) spaced TiO_2NTs.

Furthermore, voltage, time, temperature and electrolyte composition have an influence on the final morphology of nanotubes. Taking into account spaced TiO_2NTs for voltage, the outer diameter, spacing and length of TiO_2NTs increase with the applied voltage. The SEM images for

nanotubes obtained at 10, 20 and 30 V and the changes of geometrical parameters as a function of applied voltage are shown in Figure 11[67].

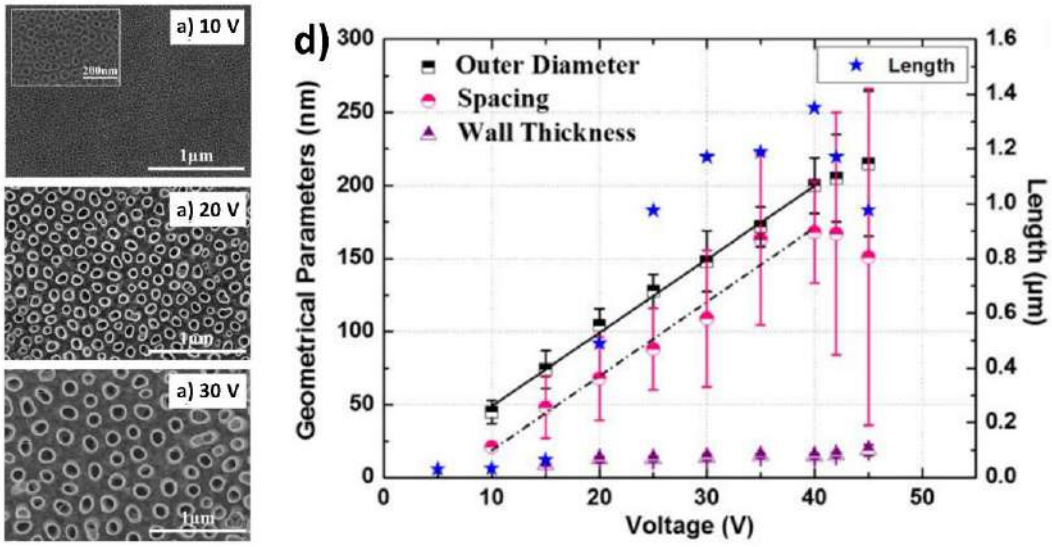

Figure 11. SEM images of spaced TiO_2NTs obtained at a) 10 V, b) 20 V, c) 30 V and d) geometrical parameters such as diameter, spacing, wall thickness and length as a function of applied voltage[67].

In the case of anodization time, the length of TiO_2NTs increases with time due to the thicker titanium dioxide layer growing over whole process (Figure 12b)[68]. However, the process is limited by thickness of Ti foil/Ti layer[69]. According to Regonini et al.[70], after exceeding 1 hour the high ordering of NTs with a length of ca. 3 μm is gradually destroyed and finally can collapse. Taking into account temperature of the electrolyte, with the increase of temperature the diameter and length of nanotubes increase (Figure 12e)[71]. This result can be assigned to the faster rate of the O^{2-} and Ti^{4+} diffusion when the electrolyte is heated.

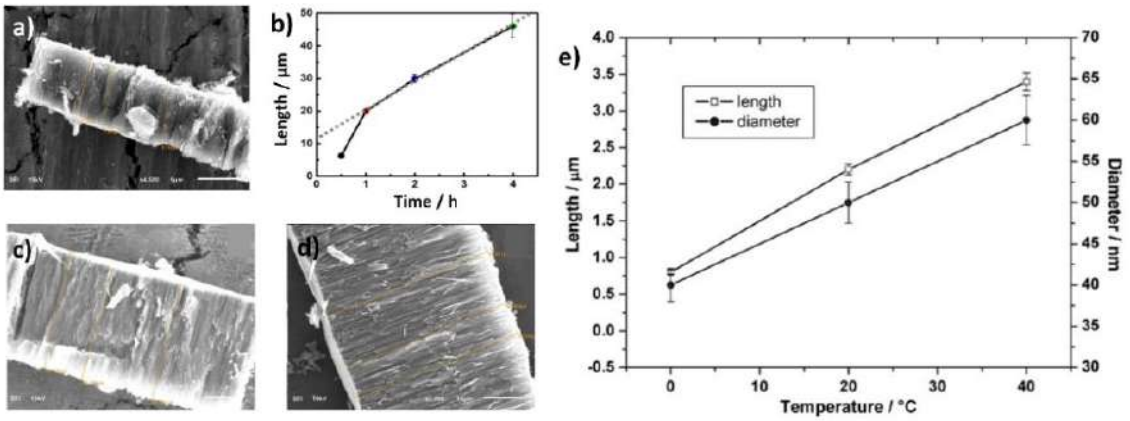

Figure 12. SEM images of TiO_2NTs obtained after a) 30 min, c) 2 hours, d) 4 hours, b) tube length as a function of time[68], d) geometrical parameters (tube diameter and length) as the function of temperature during anodization[71].

Last but not least, one cannot forget about the influence of electrolyte composition. For example a decrease of NTs length can be the effect of the increasing water content in the electrolyte (Figure 13)[72]. When the water content increases, TiO_2 starts to dissolute on the top of nanotubes and too long time can result in they complete removal. Moreover, it should be noted that also the substrate itself plays here important role, namely its shape (rod, wire, mesh or just simple plate) and purity. Summarizing, the manipulation within the various anodization parameters provides the wide range of possible titania morphologies that affect the properties of the material.

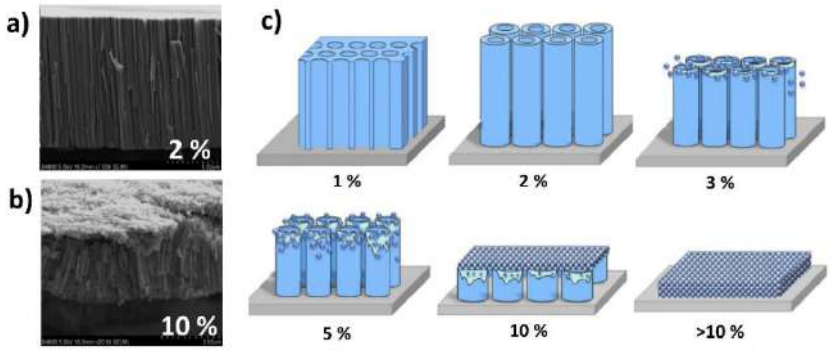

Figure 13. SEM images of TiO_2NTs with a) 2 %, b) 10 % of water content in electrolyte and c) schematic presentation of growth model with various addition of water[72].

Since the material can be directly fabricated onto the stable surface, both on the foil or out of the Ti layer sputtered on the semi-transparent substrate, TiO_2 nanotubes have a wide range of applications such as photocatalytic degradation of organic pollutants, solar cells, electrochromic devices, sensors, especially dye-sensitized solar cells, and biomedical materials (implants, drug delivery platforms)[73]. The electrochemical anodization process of Ti is easily scalable which makes them easier to use in real life not only in scientific laboratories. According to Xiang et al.[74] highly ordered nanomaterials can be formed even on really large substrates to 1 meter length[74]. Nanotubes were fabricated on titanium tube (50, 100, 500 and 1000 mm in length) which was the anode and a stainless steel wire employed as a cathode. The process was carried out in electrolyte composed of NH_4F, ethylene glycol 98 % vol. and deionized water 2 % vol. Stainless wire was inserted inside titanium tube. Ti tube was in the vertical position and its bottom was plugged with silicone cork in order to avoid electrolyte leakage from inside the tube. TiO_2 nanotubes formed inside the tube were immersed in hexane solution which allowed to formation of superhydrophobic surface used in microfluidic devices for drag reduction and increase of heat transfer efficiency. Moreover, any sophisticated equipment or highly controlled atmosphere are not required for the anodization process, only two electrodes, power supply and temperature controlled bath.

6.1.1.2 Titanium nanodimples

For electrochemical applications disc electrodes made from glassy carbon, gold or platinum are mostly used. They consist of the material rod placed inside the Teflon or PEEK cylinder. However, such electrode is typically purchased from some company and because coverage is made from the polymer no thermal treatment can be applied when some other material is deposited on it. Due to that, application of some alternative electrode materials that exhibit metallic behaviour and could be also thermal treated, if needed, are highly desirable. Among others, such requirements are fulfilled by dimpled metallic surfaces.

The first nanoholes/ nanodimpled structures have been fabricated using focused ion beam (FIB) which allows selective removing of material from sample by collisions of low energy ions. Usually gallium is used as a source of metal ions for taking out material from the fabricated sample. Unfortunately, this technique is time-consuming and requires sophisticated and expensive equipment, therefore it is not used for mass-production[75] and cannot be easily adopted by many research teams. Another technique which can be used for nanoholes/ nanodimples fabrications is electron beam lithography (EBL)[76]. In this technique metallic platform is covered by the thin organic film. Then it is scanned by focused electrons beam in order to transfer a pattern into sample surface. The interaction of electrons with polymer change its solubility. Therefore, when material is immersed in solvent the organic film is selectively removed[77]. Such nanostructured platform can be covered by thin metal layer which reproduces the shape of fabricated pattern. However, as in the case of FIB, this technique is expensive and time-consuming. Taking above into account chemical etching of titanium dioxide nanotubes previously fabricated by anodization process seems to be good alternative. Titanium dioxide nanotubes are gently removed out of the substrate and as a result it is covered by the nanodimples (TiNDs). Nanodimples have defined geometry that stays as a unique fingerprint of the bottom of the TiO_2NTs. In order to obtain such a dimpled Ti substrate, Ti overgrown by TiO_2 nanotubes has to be immersed for over 10 h in the diluted oxalic acid solution. Schematic fabrication process is presented in Figure 14. In the end of the process, the foil is covered by the uniformly distributed dimples that can be treated as a nanostructured metallic electrode material.

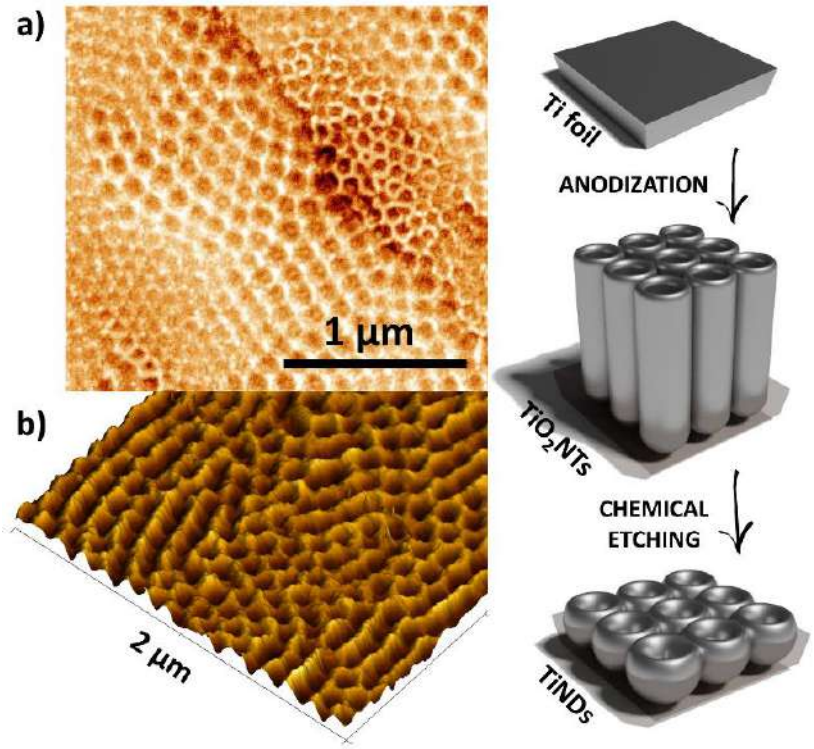

Figure 14. a) SEM and b) AFM image of Ti nanodimples and schematic representation of titanium nanodimples fabrication.

In this work electrochemical anodization process of Ti plates was carried out in multi-anodization setup composed of 8-cells with a thermostatic jacket equipped with software controlled 8-channel electronic amplifier constructed in Laboratory of Functional Materials IMP PAN. I was responsible for the fabrication of TiNDs and TiO_2NTs using electrochemical anodization and chemical etching process.

6.1.2 Magnetron sputtering

Thin metal film deposition is a process involving deposition of thin metal coating mostly on semiconductors in order to alter their properties. Thin films from nanometre to micrometre in thickness can change optical and electrical properties of material as well as perform the protective function of the substrate under the coating. The deposition methods of thin films can be divided into chemical vapour deposition process (CVD) and physical vapour deposition process (PVD) as well as chemical solvent deposition (CSD)[78]. In the case of the PVD, sputtering and thermal evaporation can be distinguished.

In the 19th century the sputtering process was seen as undesired and its results were treated as an impurity[79]. 100 years later, in 1979 Chapin patented the planar magnetron cathode[80]. The scheme of the sputtering system is shown in Figure 16[78]. The sputtering device is composed

of two electrodes: an anode acting as a table for placing the samples and an cathode covered with target being the source of ions. The vacuum chamber is filled with gas, typically Argon. Under applied DC voltage the magnetically enhanced glow discharge is maintained in the chamber. The glow discharge called plasma is ionized gas formed by the applied voltage between the anode and the cathode[81]. The Ar^+ ions are accelerated to the negatively charged target material. Then, the ions are bombarding the target owing to the emission of secondary electrons which are trapped near the target's magnetic and electric fields. These electrons affect locally enhanced ionisation degree of argon molecules which are responsible for ejecting atoms from the target[82]. Those atoms in gas phase are accelerated from target source to the sample where the layer is formed.

It is possible to distinguish three crystal growth modes such as Volmer-Weber mode, Frank-van der Merwe mode and Stranski-Krastanov mode (Figure 15)[83]. In the case of Volmer-Weber mode atoms are stronger bonded to each other than to the surface that leads to formation of clusters or islands. In Frank-van der Merwe mode atoms have stronger interaction with the surface which results in monolayer generation. The third mode, known as Stranski-Krastanov is a combination of Volmer-Weber and Frank-van der Merwe modes. In this case monolayer thick film is covered by nanoislands/nanoclusters on the top of it.

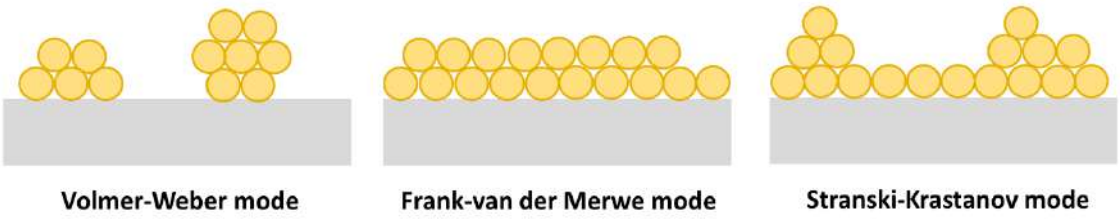

Figure 15. Film growth modes.

The magnetron sputtering technique has application in many fields such as microelectronics (printed circuit boards[84]), sensors (glucose[85], dopamine[86], temperature[87], strain[87]), photovoltaics, photocatalytic systems as well as mechanics and corrosion protection (coating for gas and steam turbines components[88] or jet engines[89]) and it is both applied on the laboratory and technological scale.

It should be highlighted that, magnetron sputtering is eco-friendly technique which does not require toxic solvents in contrast to layers performed in liquid environments. Moreover, application of the high purity target ensures good quality and reproducibility of deposited layers while the whole equipment is not so expensive and does not need big space.

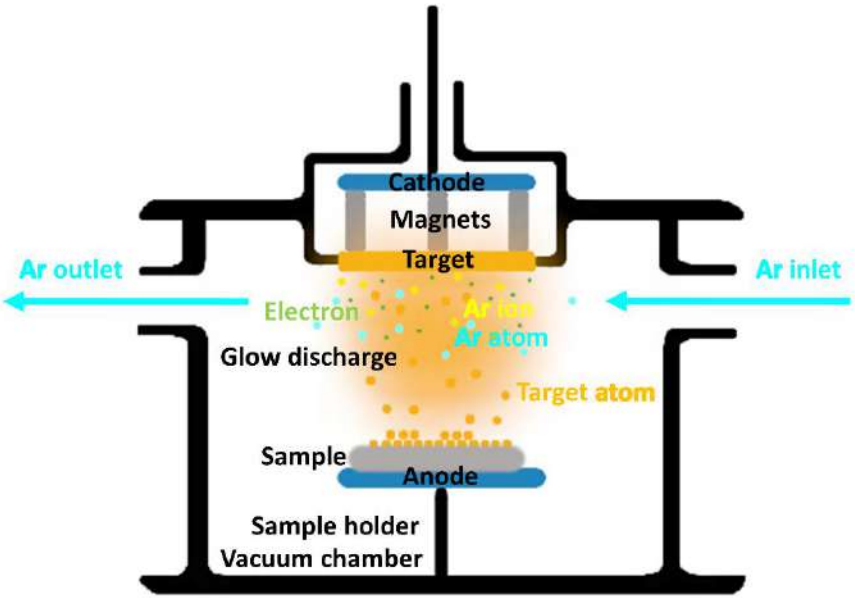

Figure 16. Scheme of the magnetron sputtering process.

In this work magnetron sputtering of Au and Cu layers was carried out using Q150T S system Quorum Technologies. The pure plates of gold (99.99%, Quorum Technologies), copper (99.99%, Quorum Technologies) and gold/copper alloy (Au50/Cu50 at%, Goodfellow) were used as targets. I was responsible for thin Au, Cu, AuCu layers magnetron sputtering.

6.1.3 Thermal treatment

As a result of anodization titanium dioxide in the form of ordered nanotubes is obtained but this material exhibits amorphous phase that is characterized by poor conductivity. Therefore, the electrochemical activity would be hampered. Furthermore, the presence of large number of defects and rapid recombination process of photogenerated electrons and holes lead to low photoactivity of the amorphous phase[90] providing finally also low photoelectrochemical response. Calcination of the as anodized substrates enables phase transition to the crystalline one. This process can be carried out by thermal treatment in furnace. The word furnace comes from French “fornaise” which means “oven”. Over the years, furnaces have been generating heat by wood, coal, fuel and electricity[91]. First electric furnace was developed by Siemens in 1878[92]. There are various types of electric furnaces for example blast, tube, muffle as well as rapid thermal annealing machine and owing to the selected equipment different heat distribution can be ensured.

Muffle furnace is composed of tightly-closed and heated from outside muffle which ensures stable and uniform temperature distribution[91]. The schematic diagram of muffle furnace is presented in Figure 17a. It is mostly front-opened box-type furnace. The temperature

and ramping time can be controlled by software, however, often materials are already placed to the oven preheated to the certain temperature. Then the substrate is exposed to the thermal shock since its temperature is rapidly changed from the room temperature to the one established inside the oven. Thermal insulation is in the form of ceramic muffles made of refractory bricks. The furnace is heated by a metallic wire which can be embedded in a ceramic muffle or mounted inside the chamber commonly up to 1000 – 1200 °C. Muffle furnace can be used for annealing, melting, calcination, oxidation, ashing, stress relieving and hardening.

Rapid thermal annealing is a manufacturing process of materials which provides rapid heating of the material even up to 400 °C/s to high temperatures over 1000 °C using infrared lamp. As was reported by Downey et al.[93] the maximum heating rate can reach up to 400 °C/s for the particular RTA model, namely STEAG AST SHS-3000. The schematic diagram of RTA is presented in Figure 17b. The heat is transferred from lamp through quartz tube to substrate by electromagnetic radiation. The infrared light which is directly absorbed in material is responsible for fast heating rate, whereas, in conventional furnace temperature slowly grows up. RTA can ensure various gas atmospheres as well as gas lines with mixing possibility[94]. The heating process is very short and takes several seconds or minutes (seconds or minutes in RTA vs. hours in conventional furnace).

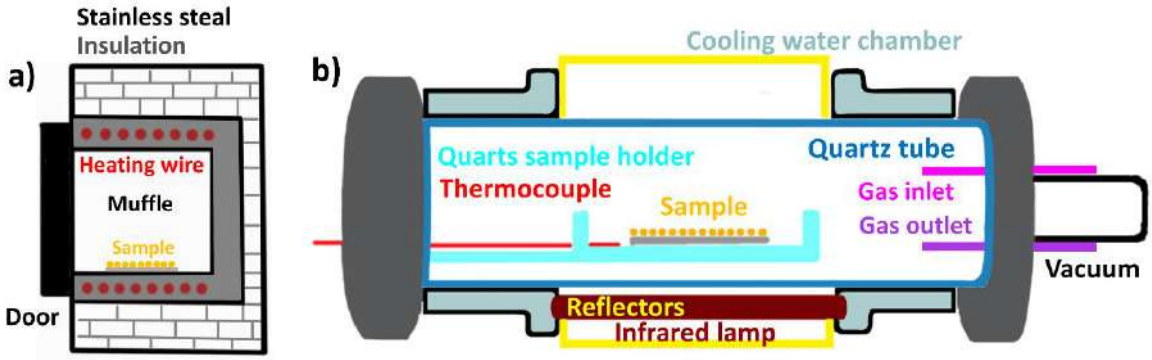

Figure 17. Cross-section of a) muffle furnace, b) rapid thermal annealer.

RTA was used for the first time in the 1970s, for annealed implanted Si wafers in damaged structure which decreased diffusion process in contrast to annealing in the conventional furnace[95]. Along with the development of modern technology and miniaturization of devices, the decrease of diffusion during thermal annealing by RTA becomes more significant, especially for the Si-based metal-oxide semiconductors[96,97]. The RTA is used to reduce transient-enhanced diffusion (TED). TED is a process of enhanced diffusion of dopants in silicon clusters during first thermal treatment. First annealing takes a long time what causes the saturation of

the diffusion process, therefore, during second thermal treatment TED is stopped[98]. In the case of boron-doped silicon the transient-enhanced diffusion is stronger at lower temperatures than at higher, so rapid annealing to optimum temperature reduces the TED effect which occurs in the meantime[99]. Furthermore, RTA process can be beneficial for stabilizing and improving adhesion as well as mechanical properties of low-dielectric isolation layer[95,100].

The rapid thermal annealing can be used for various applications, not only electronic semiconductors device manufacturing but also for solar cells and superalloys. It is well known that crystalline silicon is widely used for photovoltaic cells[101]. Wan et al.[102] compared Si crystallization fabricated by RTA with conventional furnace annealing. Grains size after treatment in RTA is smaller comparing to the case when the thermal annealing is carried out slowly using conventional furnace. Nowadays, not only crystalline silicon, but also TiO_2, especially TiO_2 nanotubes, annealed in RTA are examined toward future application in photovoltaics[103].

Annealing of TiO_2 converts amorphous form of oxide to crystalline anatase or rutile phase depending on the annealing temperature. According to Raza et al.[104] TiO_2 annealed above 300 °C results in anatase phase, whereas, thermal treatment above 500-600 °C can lead to the transition to the rutile phase. Xie et al.[105] investigated photoelectrochemical activity of TiO_2 nanotubes annealed at various temperatures from 300 to 650 °C in the tube furnace in the air atmosphere (Figure 18a). The current increases with increasing temperature which can be assigned to formation of anatase phase and the highest photocurrent was obtained for TiO_2 nanotubes annealed at 450 °C. Above 450 °C the photocurrent decreases. Annealing causes decrease of amorphous domains which act as a recombination centre causing decrease of photocurrent. Furthermore, thermal treatment can lead to the formation of shallow and deep surface states on TiO_2 surface which increase photoelectrochemical activity of materials, however when temperature is too high, their density decreases. The annealing process of titanium dioxide can be also performed in different atmospheres. According to Jiang et al.[106] hydrogenation of TiO_2 carried out in tube furnace filled with hydrogen leads to formation of oxygen vacancy and leads to 3 times higher photocurrent enhancement in comparison to the pristine material (Figure 18b).

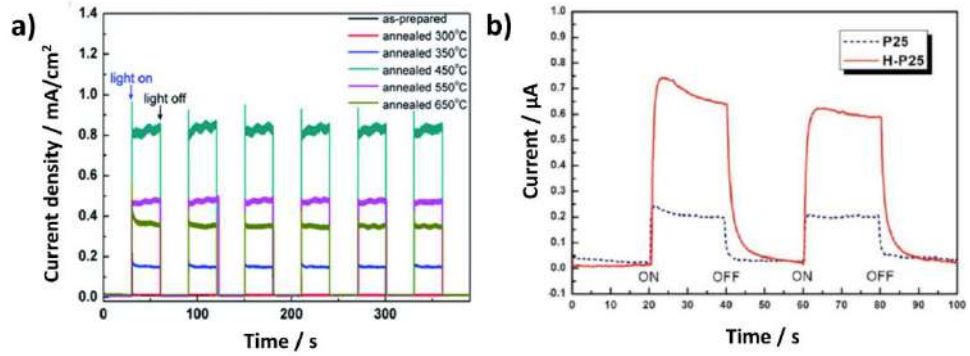

Figure 18. a) Chronoamperometry curves under UV-vis light for TiO_2 nanotubes annealed in various temperatures (tube furnace)[105] b) Chronoamperometry curves under UV light for pristine (P25) and hydrogenated TiO_2 (H-P25)[106].

It can be assumed that, annealing in hydrogen atmosphere leads to formation of oxygen vacancies, inserted surface disorder, improves absorption in visible range and narrowed bandgap. Mohajernia et al.[107] described the influence of reduction treatment in Ar/H_2 atmosphere on photoelectrochemical activity of TiO_2 nanotubes annealed via rapid thermal annealer. As can be seen in Figure 19a after thermal treatment in Ar/H_2 atmosphere the material turns black. Furthermore, based on the SEM and TEM measurements the increase in porosity of titanium dioxide nanostructures was confirmed. Reduction treatment increases absorption of light in visible range as well as photoelectrochemical activity where the maximum effect in terms of photoresponse was obtained for samples annealed at 550 °C (Figure 19b,c). It was investigated that the photocurrent enhancement can be explained not only by increase of absorbance but also enhancement in conductivity caused by formation of both oxygen vacancy and Ti^{3+} cations.

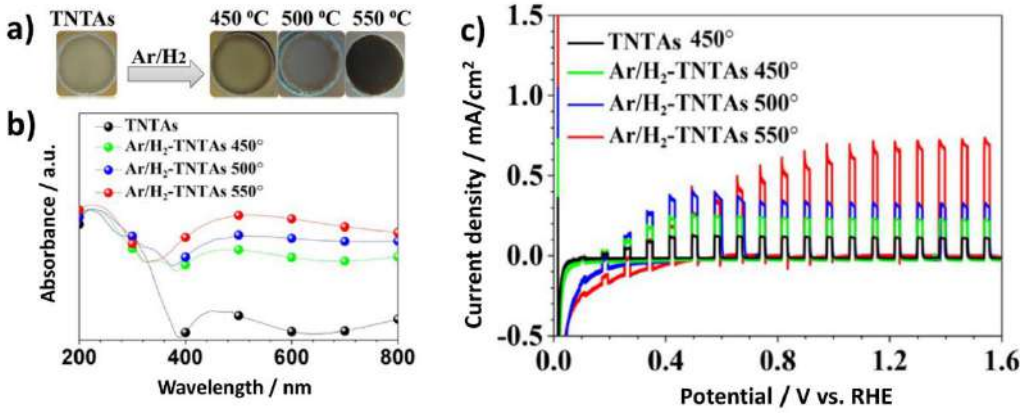

Figure 19. a) Optical images, b) absorbance spectra and c) linear voltammetry curves under standard solar irradiation spectrum (AM1.5) for TiO_2 nanotubes annealed in air at 450 °C (TNTAs) and TiO_2 nanotubes annealed in argon/ hydrogen atmosphere at 450 °C, 500 °C and 550 °C using rapid thermal annealer[107].

In this work samples were annealed in muffle furnace Neotherm and Rapid Thermal Annealing furnace MILA 5000 P-N. The RTA was financed by National Science Centre in Poland via Preludium-18 project no. 2019/35/N/ST5/02604. I was responsible for thermal treatment of materials in the muffle and rapid thermal annealer furnace.

6.2 Techniques used for morphology inspection

6.2.1 Scanning Electron Microscopy

Because fabricated materials exhibit at least one dimension in nanometre range optical microscopy cannot be used for their detailed surface investigation due to the wave nature of light. Owing to the fact that light diffraction occurs around small objects, it becomes impossible to observe details significantly smaller than the wavelength of the incident light. The Abbe limit is the diffraction-limited resolution of optical system which depends on the wavelength and numerical aperture of lenses. Therefore to get information about the geometric parameters of the fabricated materials scanning electron microscopy technique, atomic force microscopy and transmission electron microscopy are utilized frequently.

First scanning electron microscope (SEM) was invented by Knoll and Ruska in 1931[108]. This device overcame the diffraction barrier present in optical microscopes. Nowadays, electron microscopes are treated as a basic equipment in many institutes where research on nanomaterial scale is undertaken.

The scanning electron microscopy is used for the morphology investigation from micrometre to nanometre scale on two-dimensional images. SEM technique is sometimes considered as three-dimensional imaging because of the intense contrast and sense of depth in pictures. The microscope can record the image with magnification from 10 to 1 000 000 times and instrumental resolution of 1–5 nm[109]. It uses beam of high-energy electrons which interact with the material surface where electrons are emitted from the top of the sample surface. Electrons reveal information about morphology as well as chemical structure and crystallinity. The SEM operates in the range of energy from 1 to 20 keV. The most common electron source is a heated tungsten filament. The electron beam is focused on the sample using electromagnetic lenses. As a result of the electron-matter interaction secondary electrons (used for imaging materials), backscattered electrons (used for imaging materials, whereas, electron backscattered diffraction determine crystal structures), Auger electrons, photons (characteristic X-rays used for chemical structure analysis), visible light (cathodoluminescence) and heat are produced at different depth of sample (Figure 20a). Emitted electrons are analysed by detectors and after processing the detailed image of the material morphology is displayed.

The main components of the scanning electron microscope are: electron gun (cathode), anode, aperture, electromagnetic lenses, scanning coils, secondary electron detector, backscattered electron detector, stage, chamber, vacuum system and computer (Figure 20b).

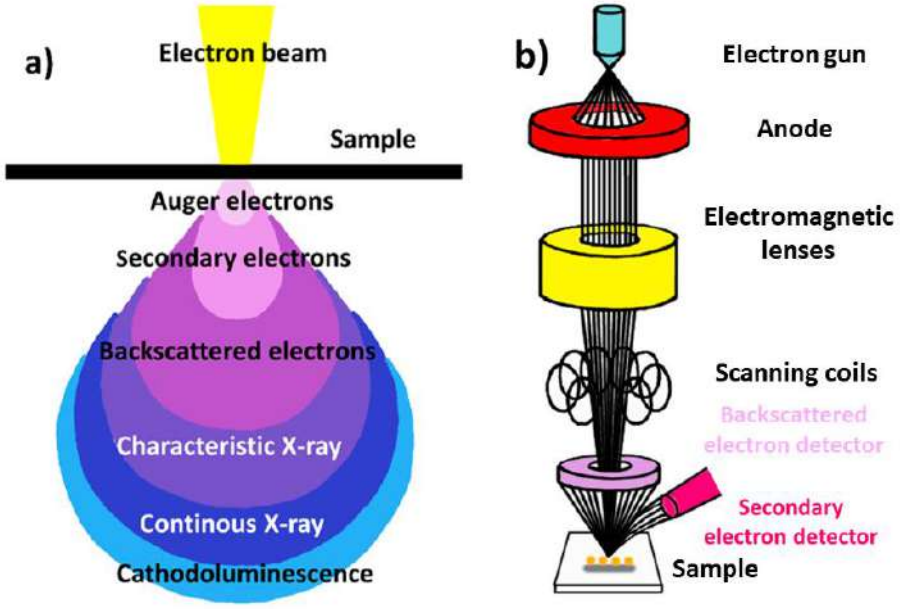

Figure 20. a) Electron-matter interaction volume and types of produced signals, b) schematic diagram of scanning electron microscope.

SEM images of the samples prepared in this work were registered by scanning electron microscope FEI Quanta FEG250. Measurements were carried out by PhD DSc Eng Jakub Karczewski Prof GUT at Faculty of Applied Physics and Mathematics at Gdańsk University of Technology. Moreover, morphology was investigated using scanning electron microscope Hitachi SU3500 at IMP PAN. I was responsible for measurements carried out at IMP PAN. I performed SEM images analysis.

6.2.2 Atomic Force Microscope

Atomic Force Microscopy (AFM) is a microscopic technique used for investigation of morphology by building the map of height of sample surface[110]. Furthermore, AFM depending on the mode can be used for diagnostics of other material properties i.e. electrical conductivity or hardness. First Scanning Tunnelling Microscope was constructed by Binning and Rohrer in 1982. Four years later the same scientists invented Atomic Force Microscope.

The schematic diagram of AFM is presented in Figure 21a. The sharp tip scans the material surface and successively based on the cantilever deflection, forces such as mechanical contact force, Van der Waals interactions, capillary, electrostatic and chemical forces are detected between the needle tip and the surface[111]. The measurement resolution is strongly

dependent on the radius of the tip and when the tip diameter decreases the measurement accuracy increases. Moreover, if electrical conductivity is important for material diagnostics, tip is covered with conducting material such as gold, iridium or carbon. Different forces between the tip and material cause the mechanical bending of the cantilever being the element where the tip is attached (see Figure 21a). During measurements the laser beam is focused on deflecting cantilever which results in changes in reflection of light. Finally the light goes to photodetector and undergoes analysis. The atomic force microscopy has the ability to explore sample in X, Y and Z axis.

There are various AFM modes including (i) contact, (ii) non-contact and (iii) tapping mode (Figure 21b)[110]. In the case of (i) contact mode, one can consider constant height or constant force option. In the constant height mode, the scanner has constant high, whereas, in constant force mode, the cantilever has constant force. The contact mode is used for hard materials for example metallic or ceramic samples. Polymers and biologic films are rather investigated using non-contact technique.

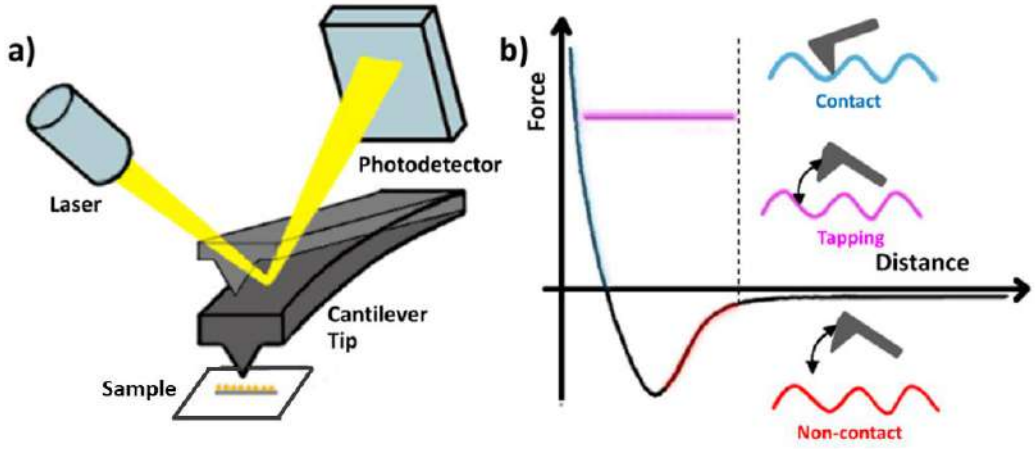

Figure 21. a) Schematic diagram of atomic force microscope, b) different modes of AFM.

AFM images of the samples prepared in this work were recorded by atomic force microscope Nanosurf EasyScan 2 in the contact mode. Measurements were carried out by PhD DSc Eng Jakub Karczewski Prof GUT at Faculty of Applied Physics and Mathematics at Gdańsk University of Technology. I assisted in measurements carried out at Gdańsk University of Technology and performed AFM images analysis.

6.2.3 Transmission Electron Microscope

In order to investigate the nanomaterial in details, namely some specific features occurring locally, other type of electron microscope has to be used, namely transmission electron microscope (TEM). Transmittance is defined as the ratio of the light intensity which passed

through the material to the incident light intensity. The transmission electron microscopy is a microscopic technique used for imaging of materials with the resolution of even 0.1 nm. The TEM uses the beam of electrons and operates in the range of energy from 60 to 150 keV (most often 100 keV) or from 200 keV to 5 MeV (for high voltage electron microscopy)[112]. The microscope can record image with the magnification of 50 000 000 times. The resolution and energy value is ca. 10 times higher than for SEM measurements. TEM is similar to scanning electron microscopy, however, in that case the beam passes through the analysed material. The electron beam is produced using heated tungsten filament. The electron beam is focused on the sample by lenses and passes through it. After passing through the sample, electron beam is magnified by subsequent lenses and finally electrons are analysed by detectors. In the case of sample preparation, it is crucial for TEM images and involves many steps. Samples in the form of liquid suspension are being pipetted on the grid and after solvent evaporation, the material is adsorbed on the grid, whereas, solid samples are cut into very thin lamellas using focused ion beam (FIB) and then mounted on the grid.

TEM images of the samples prepared in this work were recorded by aberration corrected high-resolution transmission electron microscope JEOL ARM 200F. Measurements were carried out by PhD Emerson Coy, Assoc. Prof. AMU at NanoBioMedical Centre at Adam Mickiewicz University. I performed TEM images analysis.

Comparison between SEM, AFM and TEM

The scale of images recorded by different microscopes, namely SEM, AFM and TEM largely overlaps and due to that such techniques often are compared to each other (Figure 22a). As can be seen in Figure 22b the imaging principle differs between SEM or TEM, where electrons are used for morphology analysis, and AFM which exploits atomic forces. In scanning electron microscopy the surface is scanned by electrons, whereas, in transmission electron microscopy electrons are transmitted through the whole volume of the sample. Because of that, TEM allows to explore internal structure of the sample very detailed comparing to SEM or AFM. The preparation of the sample is easier in the case of AFM than SEM or TEM. The AFM measurements can be carried out for conductive as well as insulating materials directly placed on stage and vacuum conditions are not required. The electron microscopies require additional steps in sample preparation such as sputtering of thin metal layers, typically gold, on nonconductive material for further SEM measurements and the formation of lamella or deposition of the small amount of the materials onto the grid analysed via TEM.

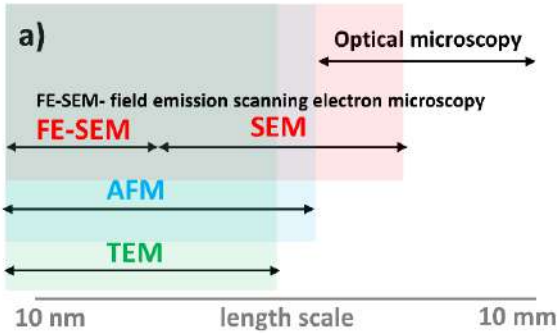

b)

	SEM	AFM	TEM
Imaging principle	electrons	atomic forces	electrons
Resolution	1-5 nm	0.1 nm	0.1 nm
Measurement	two-dimension	three-dimension	two-dimension
Sample type	conductive	conductive or insulating	conductive

Figure 22. a) The length scale of SEM, AFM and TEM, b) comparison of microscopes properties.

6.2.4 Energy dispersive X-ray spectroscopy

Energy dispersive X-ray spectroscopy (EDX) is technique used for identifying elemental composition of sample[113]. In SEM and TEM high-energy electrons interact with atoms on the material surface causing characteristic X-rays emission which allows to perform analysis of elemental composition. When the material is excited by high-energy electrons the core-shell electron is ejected and higher-energy electron fill this place releasing energy. In order to analyse elements, device should be equipped with the energy dispersive detector. Each element has unique electron structure and characteristic peak on emission spectrum. Moreover, EDX can provide the maps of elemental composition for the sample enabling to study uniformity of the different elements distribution.

6.3 Techniques used for optical properties analysis

6.3.1 UV-vis spectroscopy

Light can be absorbed, transmitted, reflected, refracted, diffracted and scattered by the material. The schematic interaction of light with material is presented in Figure 23a. UV-vis spectroscopy is a technique measuring light attenuation after passing light beam through a sample (absorption spectroscopy) or after its reflection (reflectance spectroscopy)[114]. The UV-vis spectroscopy includes measurements typically in the range from ca. 200 nm to 1100 nm covering

ultraviolet (UV), visible (vis) and near-infrared (NIR) regions. During the measurement absorbed UV, vis and NIR light promotes electrons to higher energy states in analysed material.

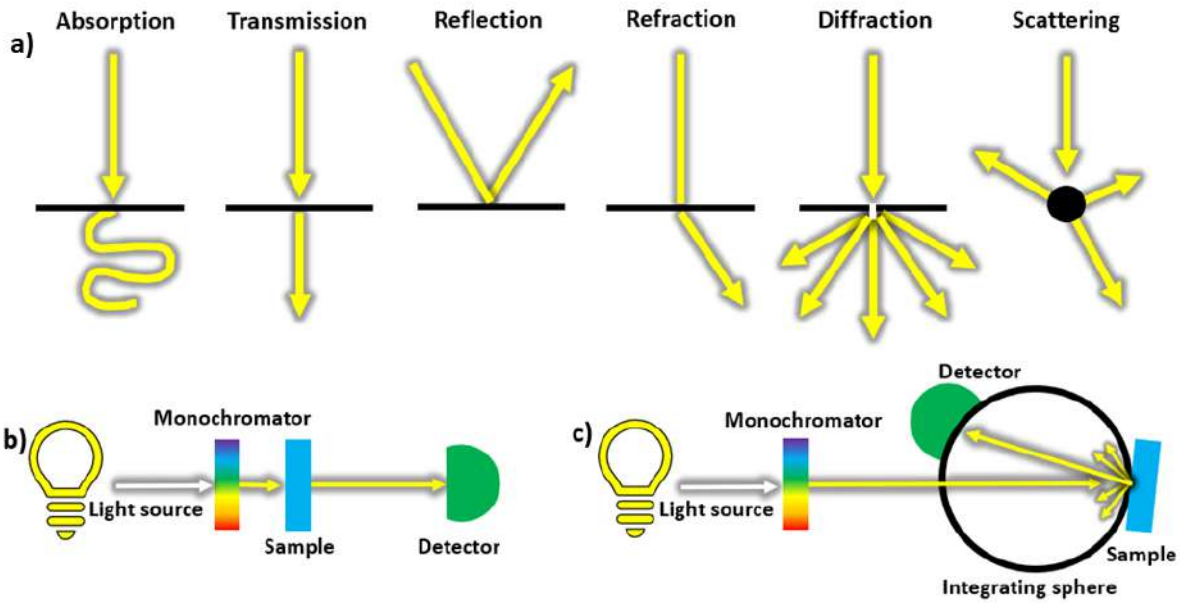

Figure 23. a) Interaction of light with the material, b) absorption and c) reflectance measurement.

The absorbance is defined as the logarithm of ratio of the input light to the intensity of output light (5). In spectroscopy, the Beer-Lambert law is related to the absorption of electromagnetic waves by material which is proportional to the molar absorption coefficient, concentration of absorbing species and optical path length (6). In the case of sample which is in the form of diluted solution, the linear relationship between absorbance and absorber concentration is used. Therefore, the concentration and the type of molecule are taken into account. Light should pass through the solution in order to measure absorbance which is impossible for too high concentrated solutions. Non-transparent samples in the form of solid materials are examined in the reflectance mode.

$$A = \log (I_0/I) \quad (5)$$

$$A = \varepsilon \cdot c \cdot l \quad (6)$$

where

A – absorbance

I_0 – intensity of incident light

I – intensity of transmitted light

ε – molar absorption coefficient / $L \cdot mol^{-1} \cdot cm^{-1}$

c – concentration of absorbing species / $mol \cdot L^{-1}$

l – optical path length / cm

The UV-vis spectroscopy can be used for quantitative determination of species in the sample as well as characterization of optical properties of the material.

The spectrometer has three main components such as light source, monochromator and detector (Figure 23b,c). The UV-vis spectrometer has two light sources such as deuterium and tungsten lamp for generation of UV and visible light, respectively. Additionally, when the integrating sphere is inserted in the UV spectrometer apparatus, the reflectance and scattering measurements of non-transparent materials can be recorded[115]. Typically materials in the form of layers onto the non-transparent substrates or powders are investigated by spectrophotometer arrangement equipped with integrating sphere[116].

The UV-vis spectroscopy can be used to characterize optical properties of metallic nanoparticles[117]. The Mie theory concerning interaction of light with homogenous sphere can be used to estimate the size of nanoparticles. It is a mathematical-physical theory concerning the scattering of electromagnetic wave by sphere and the solution of Maxwell equations[118]. These equations are composed of infinite series of multipole expansion (angle-dependent function) of the polarization of sphere caused by incident wave[119]. Extinction, absorption and scattering are types of interaction of light with matter which are considered in Mie theory (7).

$$(7)\quad Q_e = Q_a + Q_s$$

where

Q_e – extinction efficiency coefficient

Q_a – adsorption efficiency coefficient

Q_s – scattering efficiency coefficient.

Based on the Mie theory the extinction, scattering and absorption can be described by the cross section equations 8, 9 and 10 where a_n and b_n are the Mie coefficients (11, 12).

$$(8)\quad C_{ext} = \frac{2\pi}{|k|^2}\sum_{n=1}^{\infty}(2n+1)\mathrm{Re}[a_n + b_n]$$

$$(9)\quad C_{sca} = \frac{2\pi}{|k|^2}\sum_{n=1}^{\infty}(2n+1)[|a_n|^2 + |b_n|^2]$$

$$(10)\quad C_{abs} = C_{ext} - C_{sca}$$

$$(11)\quad a_n = \frac{m\Psi_n(mx)\Psi'_n(x) - \Psi_n(x)\Psi'_n(mx)}{m\Psi_n(mx)\xi'_n(x) - \xi_n(x)\Psi'_n(mx)}$$

$$(12)\quad b_n = \frac{\Psi_n(mx)\Psi'_n(x) - m\Psi_n(x)\Psi'_n(mx)}{\Psi_n(mx)\xi'_n(x) - m\xi_n(x)\Psi'_n(mx)}$$

where

C_{ext} – extinction cross section

C_{sca} – scattering cross section

C_{abs} – absorption cross section

Ψ_n – Riccati-Bessel function

ξ_n – Riccati-Bessel function

m is the ratio between the refractive index of NP (n_p) and the refractive index of surrounding medium (n_m) described as $m = n_p/n_m$ and x is the ratio between the radius of NP and the light wavelength $x = 2\pi r/\lambda$.

Therefore, the wavelength at which maximum can be observed and the diameter of particle strongly influence the shape of absorption spectra. Furthermore, the interaction between light and particle is dependent on the dielectric constant of the particle and medium. The dielectric constant is the parameter related with the frequency. When the dielectric constant of NP is extremely large at particular frequency, absorption and scattering will be also large. The resonance occurs when:

$$\varepsilon_1 = -2\varepsilon_m \quad (13)$$

where

ε_1 – real part of dielectric constant of NP

ε_m – dielectric constant of medium

UV-vis spectroscopy measurements of samples prepared in this work were carried out using spectrophotometer Lambda 35 Perkin-Elmer equipped with an accessory for reflectance spectra registration (integration sphere). I was responsible for UV-vis spectroscopy measurements and analysis.

6.4 Techniques used for structural properties analysis

6.4.1 X-ray diffractometry

The diffraction pattern occurs when waves go through small slit in the material. Similar phenomenon of X-ray beam passing through crystals was observed by Laue in 1912[120,121]. W. H. Bragg and W. L. Bragg proposed interpretation of Laue's equations in 1913 explaining scattering of X-ray beam by crystal faces.

X-ray diffraction is a technique used for determining the crystallinity and the structure of solid samples. The material is placed between the X-ray tube and detector which move

at various angles in synchronized motion. The CuKα radiation is recommended for structure investigation.The X-rays beam interacts with crystal faces at the incidence angle θ and scatters from crystal faces with the same angle θ[122]. The schematic representation of X-ray diffractometer is shown in Figure 24a. The monochromatic, incident beam falls on the surface of the sample and is scattered by the regularly spaced atoms that are present in crystals. Further, the scattered signals start interfere with each other and they are extinguished (destructive interference) or amplified (constructive interference). The diffraction, that is an effect of constructive interference and subsequent signal amplification, can be described according to Bragg's law (14). The schematic diagram of Bragg diffraction is presented in Figure 24b:

$$n \cdot \lambda = 2d \cdot \sin\theta \quad (14)$$

where

n – diffraction order

λ – wavelength of the X-ray / nm

d – spacing of the crystal layers / Å

θ – angle between incident ray and the scatter plane / degree

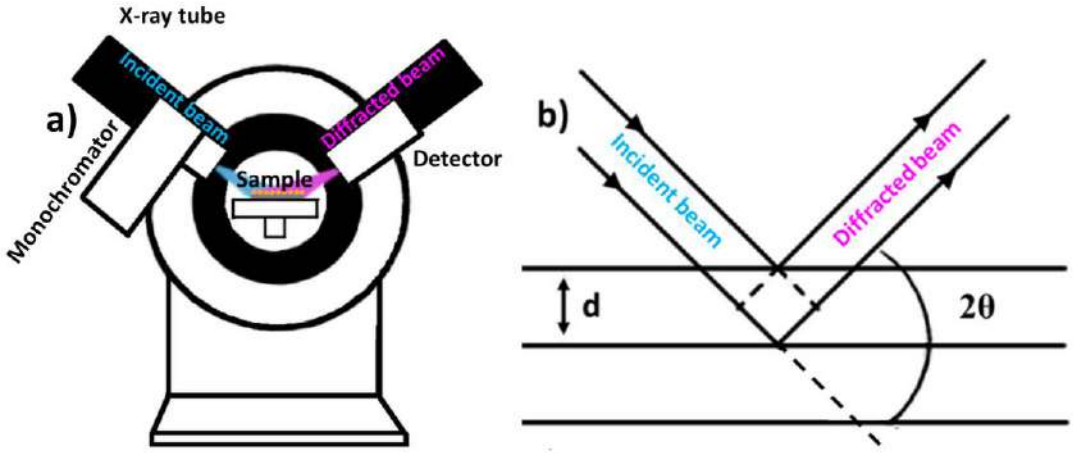

Figure 24. a) Schematic diagram of X-ray diffractometer b) Bragg diffraction.

The XRD diffraction provides information about crystalline structure, orientation parameter, degree of crystallinity as well as crystal defects[123]. The growth of individual grains on the material surface is dependent on grain boundary mobility and driving forces of growth. The structure intends to reduce grain boundary energy as well as decrease of crystal surface energy[124]. Examples of XRD diffraction peaks for the materials described in this dissertation are presented in Table 2.

Table 2. Examples of XRD diffraction peak position for Ti, TiO_2, Cu, Cu_2O, CuO and AuCu.

Compound	2θ / degree	Miller index	Ref.
Ti	34.9	(100)	125,126
Ti	38.3	(002)	125,126
Ti	39.9	(101)	125,126
Ti	52.8	(102)	125,126
Ti	70.4	(103)	125,126
TiO_2 anatase	25.4	(101)	127,128
TiO_2 anatase	48.1	(200)	128
TiO_2 rutile	27.3	(110)	127
TiO_2 rutile	54.2	(211)	127
TiO_2 rutile	56.5	(220)	127
Cu	43.3	(111)	124,129,130
Cu_2O	36.4	(111)	131
CuO	38.9	(111)	132
Au	38.2	(111)	133
AuCu alloy	38.35	(111)	134

XRD measurements for samples prepared in this work were performed using Bruker 2D Phaser diffractometer with CuKα radiation and an XE-T detector. Measurements were carried out by PhD DSc Eng Jakub Karczewski, Assoc. Prof. of GUT at Faculty of Applied Physics and Mathematics at Gdańsk University of Technology. I performed XRD analysis.

6.4.2 Raman spectroscopy

The Raman spectroscopy is a technique which allows to measure vibrational energy modes of investigated material. The sample is illuminated by laser beam and this monochromatic light interacts with molecular vibrations and further scattered photons of a different energy than incident ones are detected and analysed[135]. Three types of scattering such as Rayleigh scattering, anti-Stokes Raman scattering and Stokes Raman scattering can occur when light interacts with molecule (Figure 25). When the energy of incident photons is equal to energy of scattered photons, Rayleigh scattering is present and known as elastic scattering. When the molecule is excited and emits photon that has lower energy than the incident one Stokes Raman scattering occurs, whereas, when molecule loses energy anti-Stokes Raman scattering takes place. Therefore, the Raman scattering is an inelastic scattering.

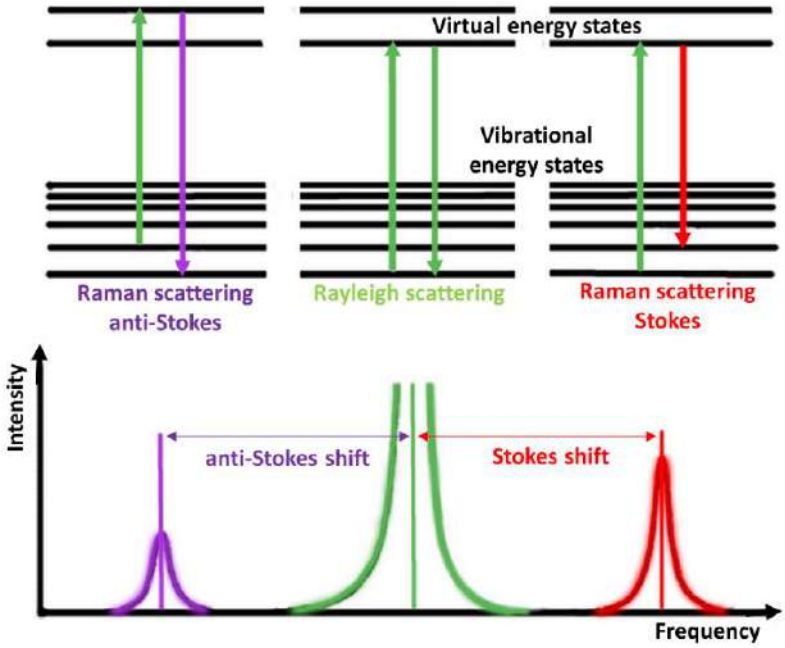

Figure 25. Energy level diagram showing energy states in Raman scattering.

Regarding investigated materials, Raman spectroscopy can be used for detection of various oxides on the material surface. However, it should be noted that the light penetration depth depends on the absorption coefficient and laser wavelength. In the case of TiO_2 anatase phase in most cases it is possible to distinguish five vibrational modes. Three of them are E_g modes associated with stretching of O-Ti-O groups and are located at 149, 199 and 649 cm^{-1}. The other two: B_{1g} and $A_{1g}+B_{1g}$ related to bending vibrations of O-Ti-O groups can be found at 403 and 521 cm^{-1}, respectively[136]. The Raman band positions for copper oxides, gold copper alloy and titanium dioxide are presented in Table 3. Copper and copper oxide atoms are characterized by A_g (296 cm^{-1}) and B_g (346 cm^{-1}, 631 cm^{-1}) vibrational modes[137]. Furthermore, it should be highlighted that not only the creation of new bands but also shifting, broadening and attenuation can be analysed taking into account recorded Raman spectra. For example, the shift in Raman spectra for TiO_2 can be correlated with presence of oxygen vacancy. The band structure for TiO_2 anatase with oxygen vacancy is shown in Figure 26a. Oxygen vacancy states are located in the donor states at 0.8-1.2 eV below CB[138]. The formation of oxygen vacancy leads to surface reconstruction for example changing the local symmetry of Ti by modulating titanium-oxygen bonds[139]. The band shifts towards higher wavenumbers from 149 cm^{-1} to 155 cm^{-1}. According to Pan et al.[138] after deconvolution three bands can be distinguished in that wavenumber range where two of them located at 155 cm^{-1} and 171 cm^{-1} are the new Raman modes (Figure 26b). Furthermore, after thermal treatment of TiO_2 sheets in the form of powder containing oxygen vacancy in the air atmosphere oxygen vacancy disappeared and only one band was present.

Table 3. Raman bands position for copper oxides, titanium dioxide and AuCu alloy.

Compound	Raman shift / cm^{-1}					Ref.
TiO_2 rutile	430 – 450			600 – 610		140,141
TiO_2 anatase	149	199	403	521	646	136
CuO	300		330 - 370	590 – 600		142,143,141
Cu_2O	220		520 - 550	620		142,144,143
AuCu	240 – 270					145,141

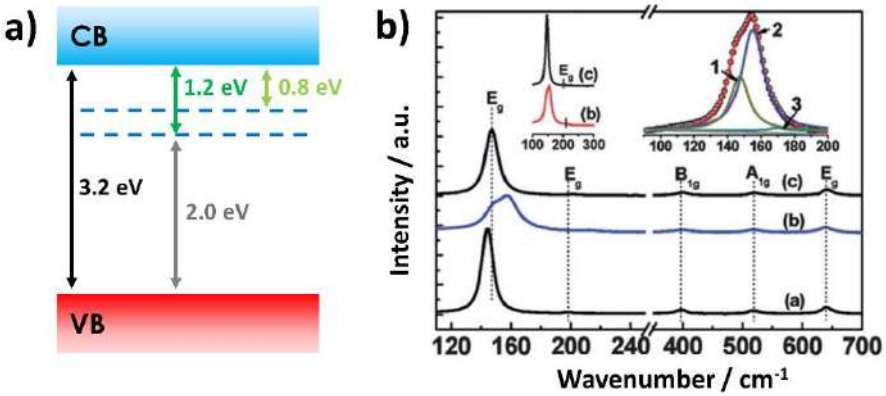

Figure 26. a) Band structure for TiO_2 anatase with oxygen vacancy, b) Raman spectra for (a) the reference anatase TiO_2 (from Aldrich), (b) TiO_2 sheets with oxygen vacancy, (c) TiO_2 sheets[138].

Raman spectra for samples prepared in this work were recorded by means of a confocal micro-Raman spectrometer InVia Renishaw with a material excitation by laser emitting at 514 nm and operated at 50 % of its total power (50 mW) with 3 accumulations. I was responsible for Raman spectroscopy measurements and analysis.

6.4.3 X-ray photoelectron spectroscopy

X-ray photoelectron spectroscopy (XPS) is an analytical technique used for investigation of the chemical nature of elements present at the surface region. This technique takes advantage from the photoelectric effect[146]. Moreover, the technique enables also quantitative elemental analysis at the surface and if Ar^+ etching is applied also the sample composition in deeper parts of the material. The electron emission from the material during light illumination was observed by H. Hertz in 1887, however the formal description was given by A. Einstein in 1905. In order to observe the photoemission, the energy of the photon should be equal or higher than the sum of the kinetic energy (E_k) and the work function (ϕ) (15). The schematic energy levels diagram is shown in Figure 27a[147].

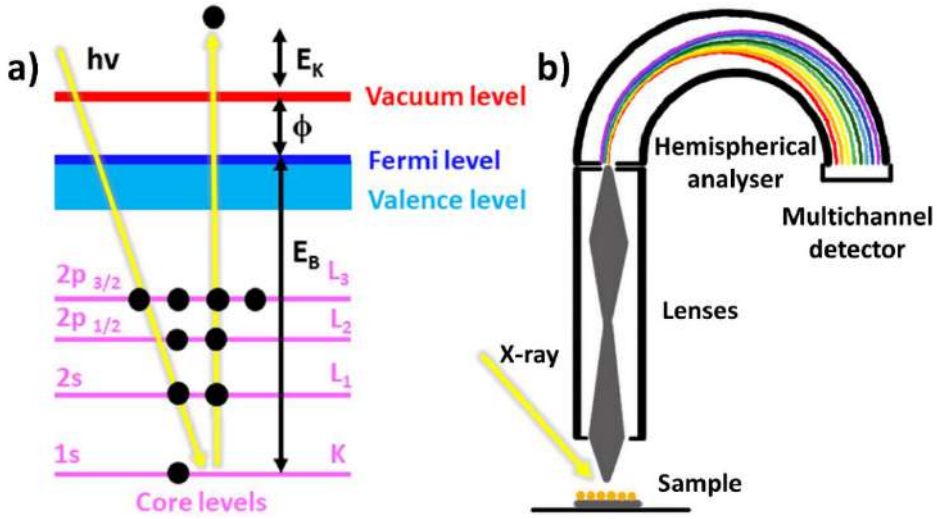

Figure 27. a) Schematic energy levels diagram, b) scheme of XPS instrument.

The work function is a minimum amount of energy required to eject electron from the material surface. If the kinetic energy of photon is equal or higher than the binding energy of electron, then the core electron of atom escapes and emits out of the material (16)[148]:

$$h \cdot \nu = E_k + \phi \quad (15)$$

$$E_B = h \cdot \nu - \phi - E_k \quad (16)$$

where

E_k – kinetic energy of photon / eV

h – Planck's constant ($6.63 \cdot 10^{-34}$ / eV·s)

ν – photon frequency / Hz

ϕ – work function / eV

E_B – binding energy of electron / eV

Investigation of the materials surface is limited to the depth of ca. 10 nm. It should be added that the depth profile can be also obtained using:(i) etching mode with the support of Ar^+ ions, (ii) changing the emission angle or (iii) using various photon energy. However, in the case of the option (i), it should be considered that Ar^+ can interact with atoms and change their oxidations state, thus altering the initial chemical nature of the material.

The X-ray photoelectron spectrometer is composed of X-ray source, aperture, lenses, hemispherical analyser, multi-channel detector. The scheme of XPS instrument is presented in Figure 27b. During XPS measurements the sample is illuminated by soft X-rays (AlKα 1487 eV) or hard X-rays (CrKα 5415 eV)[149]. High-energy radiation causes emission of electrons from the core of the analysed material. When the data are gathered in the form of survey spectra as well as spectra recorded in the binding energy range typical for atoms present in the samples,

e.g. oxygen, titanium, copper, the analysis concerns fitting procedure to find single peaks that are attributed to the particular oxidation state of each element. The characteristic binding energies for titanium, gold and copper are presented in Table 4. Core orbitals, except the s orbitals, can be splitted into two states because of the interaction between unpaired valence and unpaired core-level electrons. Therefore, peaks can be visible in the form of doublet. Doublet is composed of two peaks, that occur due to spin-orbital coupling ($p_{1/2}$, $p_{3/2}$, $d_{3/2}$, $d_{5/2}$, $f_{5/2}$, $f_{7/2}$). These peaks have specific value of area ratio and peak separation dependent on element. During the XPS experiment, it is also possible to record Auger electrons. The Auger effect happens when core electron is removed from its initial place causing the vacancy and then electron from the higher energy level takes this empty place. Energy that is released in that process can be transferred to another electron that is ejected from the atom. Furthermore, because of the energy losses and other physical processes, it is possible to observe some satellite peaks at the high binging energy side.

Table 4. Characteristic binding energy for titanium, gold and copper.

Element oxidation state	Binding energy / eV	Ref.
Ti^0 ($2p_{3/2}$)	453.9	[150]
Ti_2O_3 ($2p_{3/2}$)	457.1	[151]
TiO_2 ($2p_{3/2}$)	458.7	[151]
Au^0 ($4f_{7/2}$)	83.9 - 84.1	[152,153]
Au_2O_3 ($4f_{7/2}$)	85.8	[154,155]
Cu^0 ($2p_{3/2}$)	932.5	[156]
Cu^{1+} ($2p_{3/2}$)	932.7	[157]
Cu^{2+} ($2p_{3/2}$)	933.5 - 934.5	[156,158]

XPS measurements of the samples prepared in this work were carried out using an X-ray photoelectron spectroscope Escalab 250Xi, ThermoFisher Scientific with a monochromatic AlKα source. Measurements and fitting were carried out by PhD DSc Eng Jacek Ryl Prof GUT at Faculty of Applied Physics and Mathematics at Gdańsk University of Technology. I was responsible for XPS analysis.

6.4.4 Methods using synchrotron radiation

The synchrotron is a type of cyclic particle accelerator producing extremely powerful radiation. Synchrotron radiation is used in many advanced measurement techniques with complex device structures. SOLARIS is the only synchrotron in Poland which is located on the Campus of Jagiellonian University in Cracow. In SOLARIS it is possible to carry out research

on 6 different beamlines: PIRX, PHELIX, URANOS, DEMETER, ASTRA, CRYO-EM. In order to perform measurements in SOLARIS, I submitted the application form with the details regarding the planned measurements that was positively considered and I received beam time from 17-22.05.2022 on the Phelix line.

The synchrotron radiation (used by XPS or X-ray absorption spectroscopy) is an electromagnetic radiation emitted by charged particles, typically electrons, which are accelerated by magnetic field. Those high energy electrons travel around a closed-loop path with a speed approaching speed of light emitting X-ray radiation. Synchrotron is composed of electron gun (e-gun), linear particle accelerator (LINAC), booster ring, storage ring, bending magnets, insertion device and beamline (optics and experimental hutch with shutter, slits, monochromator and detector). The scheme of synchrotron is presented in Figure 28. First, electrons are generated by the electron gun cathode and further accelerated to high speed by the linear particle accelerator. In LINAC electrons are accelerated by radio-frequency waves. Then the electrons travel around the booster ring more than one million times where they are accelerated by magnets. With every turn the electrons are faster and faster. When the electrons reach optimal energy (for SOLARIS this energy equals 550 MeV) they are transferred to the storage ring. With a usage of magnets and insertion device (two magnets with opposite magnetic poles) particles obtain speed close to speed of light. Due to that reason storage ring is called the heart of synchrotron. The energy of electrons in the storage ring is higher than in the booster ring reaching in the case of SOLARIS synchrotron 1.5 GeV. The storage ring stores electrons for hours on stable orbit. Moreover, the electrons travel around the ring in a vacuum chamber to prevent particles collisions. Summing up, the charged particles are accelerated in three places such as LINAC, booster as well as storage ring in order to obtain desired electrons speed. The X-ray radiation is directed toward beamlines. There are cabins located around the synchrotron where the beam is splitted from the storage ring to specific stations.

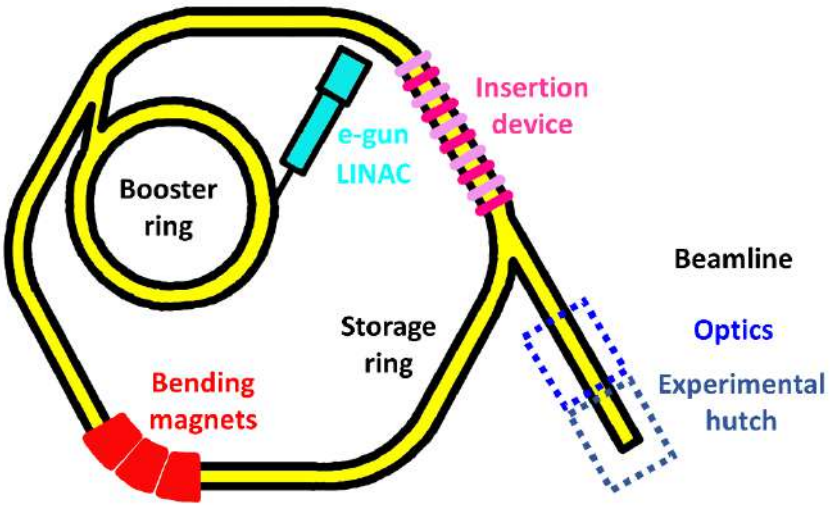

Figure 28. Schematic diagram of synchrotron.

6.4.5 X-ray absorption spectroscopy

X-ray absorption spectroscopy (XAS) is a technique used for the characterization of electronic and structural properties of materials such as oxidation state, site symmetry, and local environment[159]. The absorption of X-rays results in the excitation of core electrons. As typically electrons from 1s or 2p shell are excited. XAS requires a synchrotron radiation source that provides tuneable energy photons to the surface of the material[160]. It should be in here noted that two types of excitation may occur, namely core electron may be transferred to the unoccupied state in the valence band or may be ejected from the absorbing atom as a wave to a continuum (unbound state).

In the recorded XAS spectrum one can distinguish three regions: (i) pre-edge where the X-ray energy is smaller than binding energy, (ii) absorption-edge referred as X-ray absorption near-edge structure (XANES) and (iii) post-edge referred as the extended X-ray absorption fine structure (EXAFS) (Figure 29)[160].

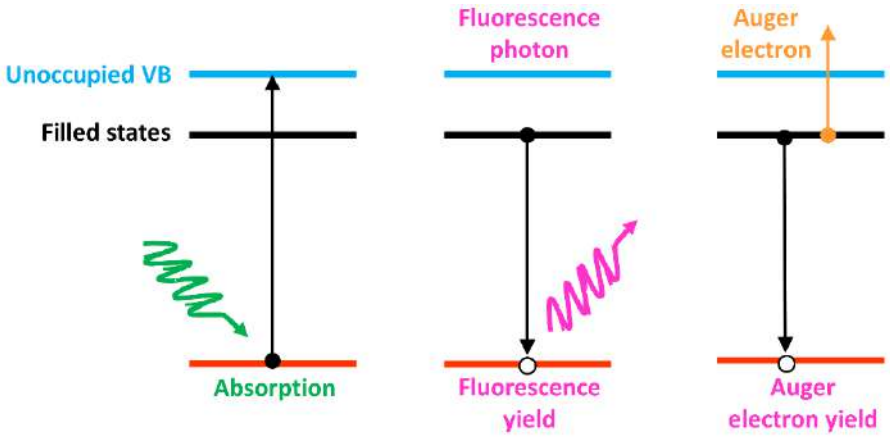

Figure 29. The detection modes of XAS[160].

The registered absorption edge is related to the sudden absorption increase when the X-ray radiation is scanning through the binding energy regime of core-level electrons. In this energy regime the electron transfer to the unoccupied state in the valence band occurs or the photoelectron has just enough energy to be able to escape to the continuum (Figure 29). Usually XANES refers to the region about 10 eV below the absorption edge and 20-50 eV above the edge[161]. It can be used to determine oxidation state and coordination chemistry.

The absorption edges are characteristic for particular electron shells (K, L, M, N)[162]. The schematic representation of X-ray absorption edges is presented in Figure 30a. The L-edge XAS spectrum of TiO_2 is presented in Figure 30b. In the case of TiO_2 the $L_{3\text{-}2}$ edge, excitation of Ti2p electrons to unoccupied d and s states, is in particular of interest because the TiO_2 conduction band is composed of Ti3d states[163], whereas, the valence band is attributed to O2p[164]. The information which can be obtained from the intensity of b_1 and b_2 peaks of the L3-edge is the TiO_2 crystalline phase. If the b_1 peak is more intense than the b_2, the anatase is present. The opposite situation indicates the rutile phase[165]. In the case of copper, taking into account various shapes of L-edge XAS spectra, it is possible to identify Cu^{2+}, Cu^{1+} and Cu^0 (Figure 30c).

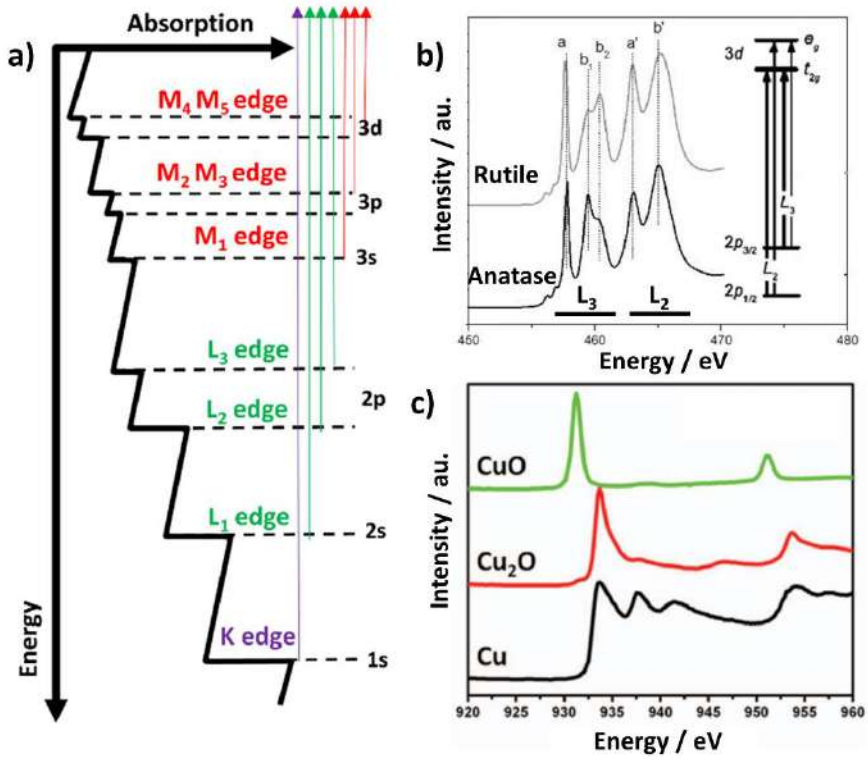

Figure 30. a) Schematic of X-ray absorption edges, b) L-edge XAS spectra of rutile and anatase TiO_2 [163,166], c) L-edge XAS spectra of CuO, Cu_2O and Cu[167].

As it comes to EXAFS part of the XAS spectrum, it corresponds to the oscillating part of the spectrum above the absorption edge. The higher energy of the incident beam may cause

the transfer of electron to the energy continuum and the oscillations correspond to the wave interactions between the ejected photoelectron and electrons surrounding the absorbing atom. The range of EXAFS begins from 50 eV and extends to about 1000 eV above the absorption edge. It can be used to obtain precise information about the local atomic structure.

The measurements presented in the article using synchrotron radiation were performed by me and PhD Eng Zuzanna Bielan at the National Synchrotron Radiation Centre SOLARIS in Cracow (Poland). PHELIX beamline operating at the soft X-ray range was utilized. I was responsible for XPS and XAS analysis.

6.5 Electrochemical and photoelectrochemical activity

Electrochemistry is a field of the physical chemistry concerned with phenomena occurring at the electrode/electrolyte interface. This branch of science is focused on the processes across the electronic conductor and the ionic conductor in the form of electrode and electrolyte respectively, as well as factors which influence on that system (Figure 31)[168].

Figure 31. Schematic representation of reduction and oxidation process.

In the electrode charge is transported by electrons whereas in the electrolyte by movement of ions. It is possible to distinguish two types of reactions, namely reduction and oxidation. In the case of material reduction the electrons flow from electrode to electrolyte, whereas in the material oxidation process from electrolyte to electrode. The electrode reaction rate and current are affected by the mass transfer from electrolyte to electrode, the electron transfer through the electrode, chemical reactions and the electrode surface reactions such as adsorption or desorption processes. The electrode-electrolyte interface can be considered as a capacitor. At particular potential the electrode is charged positively or negatively with respect to the electrolyte with opposite charge. Such charge arrangement is called the electrical double-layer. Three models of the electric double-layer can be distinguished, namely Helmholtz, Gouy–Chapman and Stern model (Figure 32). Helmholtz claimed that all charge in electrode stays at its surface, whereas electrolyte with opposite polarity is separated by short distance from electrode. In the case of Gouy-Chapman model the diffuse layer of charges with capacitance dependent on applied potential and electrolyte concentration is formed on the electrolyte side

of interface. Stern model is a compilation of Helmholtz and Gouy-Chapman models including compact charge layer and diffuse layer.

The information about electrochemical activity of materials can be obtained via various electrochemical techniques such as cyclic and linear voltammetry, chronoamperometry, chronopotentiometry, differential pulse voltammetry, electrochemical impedance spectroscopy and dynamic electrochemical spectroscopy.

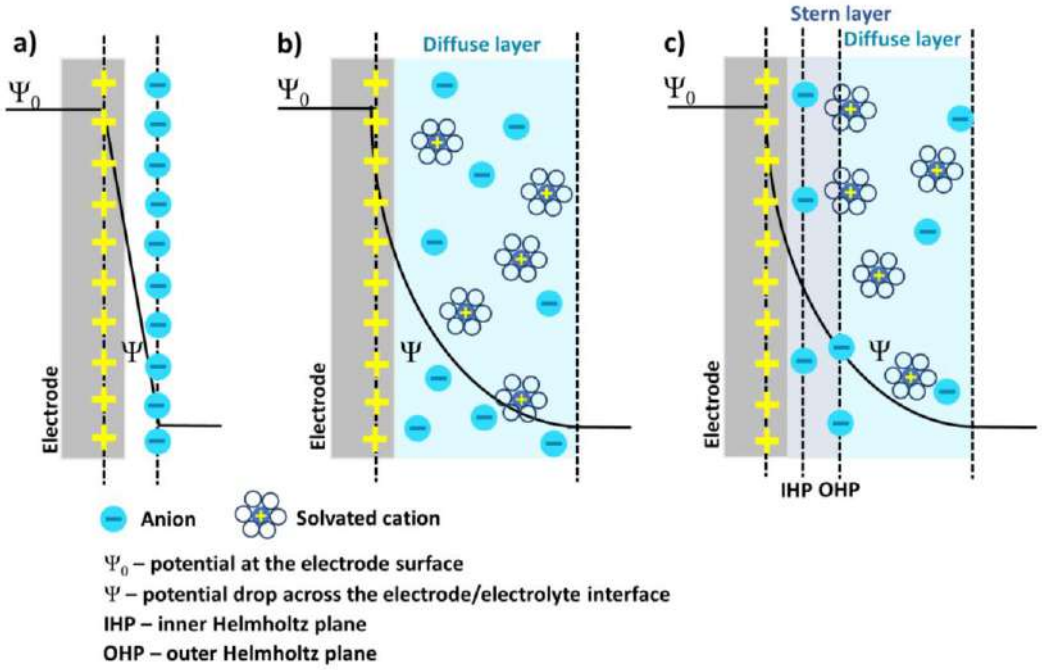

Figure 32. The electrical double-layer a) Helmholtz, b) Gouy-Chapman and c) Stern models[169].

6.5.1 Cyclic voltammetry

Cyclic voltammetry is the most popular electrochemical technique used to study redox reactions, electron transfer kinetics, stability of reaction products, reversibility of a reaction, adsorption-desorption processes, catalytic activity and so on[168]. The cyclic voltammetry measurement is based on changing the potential of working electrode within the specified potential range, scan rate, number of cycles, and measuring the resulting current. The measurements are carried out in three electrode system where the investigated material takes role of working electrode (WE). Remaining two electrodes are the reference electrode (RE) and the counter electrode (CE) (usually Pt mesh) (Figure 33a). The reference electrode is characterized by constant potential which is not dependent on ions dissolved in electrolyte and because of that is the reference point for measurements of WE potential. Typically, when working in aqueous electrolytes following electrode is used: 1) Ag wire covered with silver chloride immersed in the solution of 0.1 M potassium chloride (Ag/AgCl/0.1 M KCl), 2) mercury

sulfate that is Hg-drop of mercury sulfate immersed in the sulfate containing solution such as 0.1 M potassium sulfate (abbreviated MSRE), 3) Pt wire immersed in 1 M hydrogen chloride deareated with hydrogen (abbreviated SHE). The counter electrode provides together with WE electrical circuit over which current flows. All electrodes are placed in the electrochemical cell filled with an electrolyte being the aqueous solution of salt, hydroxide or acid, for example Na_2SO_4, NaOH and PBS (phosphate buffered saline). Depending on the purpose the electrolyte can be deareated or saturated with different gasses. Figure 33b presents typical cyclic voltammogram showing current vs. potential for conducting material, for example platinum or gold immersed in the solution containing ferricyanide/ferrocyanide redox couple. The parameters which describe material activity, namely faradaic reaction related with charge transfer are the anodic and cathodic peak currents (i_p) as well as peak potentials (E_p)[170].

The example of CVs for Pt or Au immersed in the solution of the ferricyanide/ ferrocyanide redox couple is one of the most known and well recognized voltammograms. Platinum and gold are often used for electrocatalytic processes because of their good conductivity which allows fast charge flow through material as well as high stability. However, when material with lower conductivity than Pt or Au is immersed in the electrolyte containing ferricyanide/ferrocyanide redox pair the changes on CVs curves are observed. Reactions occurring on the electrode surface can be reversible, quasi-reversible and irreversible, and their character can be recognized based on the shape of CVs curves (Figure 33c). In the case of reversible process two reactions take place such as oxidation and reduction. The electron transfer is fast which allows to maintain equilibrium at the electrode/electrolyte interface[171]. The reversible reaction can be described in different ways where in the case of electrochemistry the peak-to-peak separation and peak intensity are taken into account. In the reversible reaction the peak-to-peak separation should be relatively small where ΔE should correspond to the value of ca. 57 mV. The equations (17) and (18) describe this dependency[172]. Furthermore, the anodic and cathodic peaks should have the same current intensity.

$$(17)\ \Delta E = (E_a - E_c)$$

$$(18)\ \Delta E = 2.218\ R \cdot T / n \cdot F$$

where

ΔE – peak-to-peak separation potential / V

E_a – anodic potential peak / V

E_c – cathodic potential peak / V

R – universal gas constant (8.314 J / K · mol)

T – temperature / K

n – number of electrons transferred in the reaction

F – Faraday constant ($9.64 \cdot 10^4$ / $C \cdot mol^{-1}$)

However, for the irreversible reaction the electron transfer is slow. In that case, only one reaction occurs, the product of electrochemical reaction does not return to the initial state. Quasi-reversible process is an intermediate process between both and depends on charge-transfer rate as well as mass transport[171]. It should be highlighted that the source of electrons can be a redox pair in electrolyte (as described above) as well as a redox active center in the material. When the electrode material is characterized using cyclic voltammetry, the recorded current is composed of Faraday and capacitive component (Figure 33d). Faradaic current is a result of chemical change in the electrochemical system. The capacitive current depends on the amount of charge which can be stored in the electric double-layer formed at electrode/electrolyte interface.

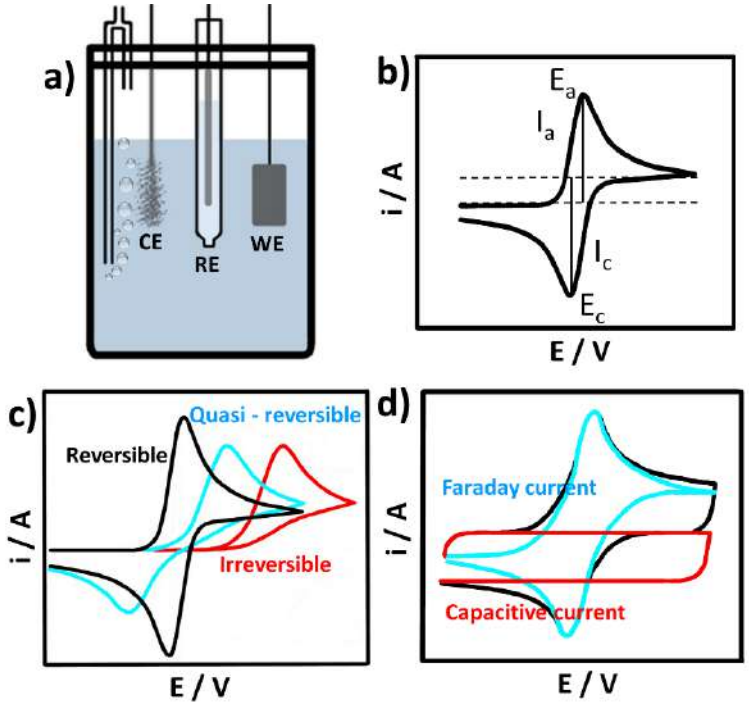

Figure 33. a) The scheme of electrochemical cell, b) the typical cyclic voltammogram, c) the CVs curves showing shape of reversibility/irreversibility of reactions, d) the CV curve presenting contribution of Faradaic and capacitive current.

PhD dissertation concerns gold, copper, titanium, titanium dioxide nanostructures therefore short electrochemical studies for these structures is presented below. Figure 34a. shows cyclic voltammetry for TiO_2 in the form of anatase phase. The CV curve was recorded in 0.1 M NaOH electrolyte. This material exhibits reduction reaction of Ti^{4+} to Ti^{3+} with peak located at ca. -1.3 V vs. Ag/AgCl. The electrochemical activity of gold species such as Au(poly),

Au(100), Au(210) and Au(533) surfaces registered in 0.1 M NaOH solution is presented in Figure 34b[173]. The anodic peak located at ca. +0.3 V vs. Ag/AgCl corresponds to oxidation of metallic gold to Au_2O_3[174]. In the case of reduction peak observed at ca. +0.2 V vs. Ag/AgCl it can be assigned to reduction of gold oxide. Moreover, it can be clearly seen that the shape of oxidation and reduction peaks differs significantly between various gold crystal orientations exposed to the electrolyte interface as a result of specific adsorption of OH^- anions. The electrochemical activity of copper and copper oxides registered in 0.1 M NaOH solution is shown in Figure 34c. First oxidation peak located at 0 V vs. Ag/Ag_2O labelled as A can be assigned to oxidation of Cu to Cu_2O. The second one which can be observed at +0.3 V labelled as B is interpreted as oxidation of Cu/Cu_2O to CuO and $Cu(OH)_2$. During polarization towards the cathodic direction, reduction of Cu^{2+} oxides to Cu^{1+} and Cu^0 is visible (peaks assigned as C and D, respectively). In the case of materials which will be developed in terms of their future application such as photoelectrochemical solar cells, water splitting devices or fuel cells, it is required to obtain stable material which does not dissolve. Therefore, selection of electrolyte and its pH play crucial role. The electrochemical measurements of TiO_2 or Au can be carried out in alkaline, basic and acidic solutions. In the case of Cu alkaline conditions are favourable. The Pourbaix diagram for copper in aqueous media is presented in Figure 35. The copper is passivated and the stable copper oxide is present at surface layer. In acidic solution the dissolution of copper and formation of copper ions in the electrolyte occurs and thus the mass of copper based electrode material changes. Therefore, all electrochemical and photoelectrochemical measurements presented in this PhD thesis were carried out in alkaline electrolytes.

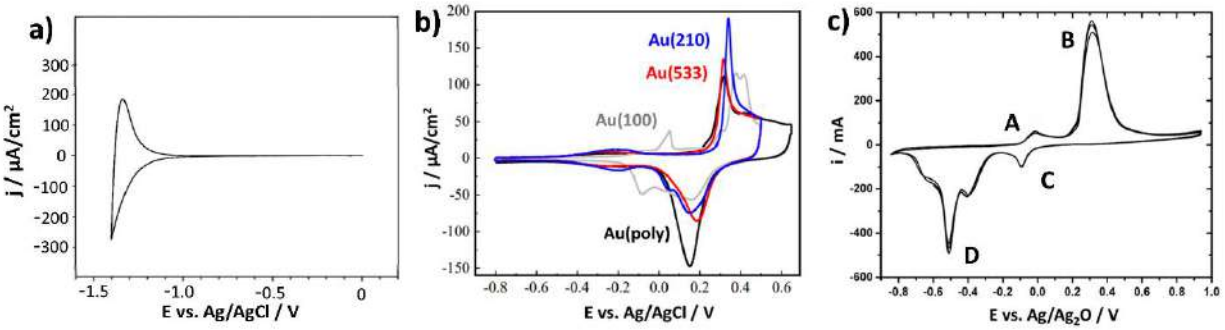

Figure 34. Cyclic voltammetry for a) TiO_2 [175] b) Au(poly), Au(100), Au(210) and Au(533) surfaces[173] and c) polycrystalline copper sample[176] registered in 0.1 M NaOH.

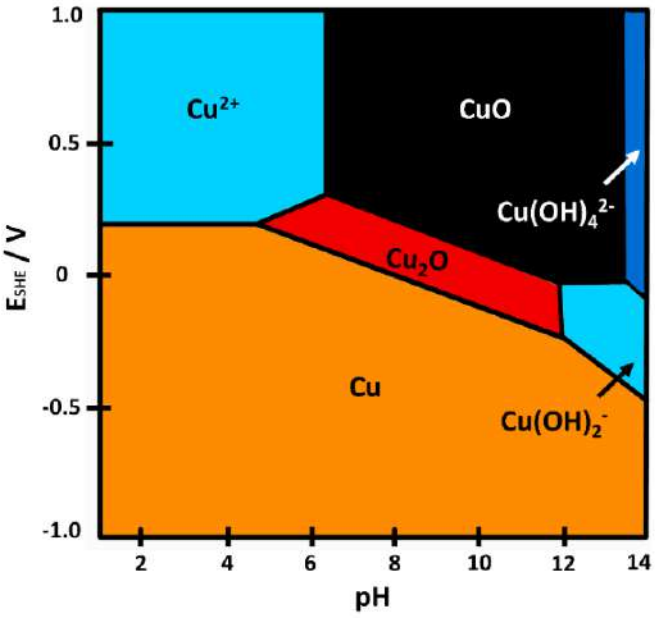

Figure 35. Pourbaix diagram for copper in aqueous media[177].

6.5.2 Linear voltammetry

Linear voltammetry is an electrochemical technique similar to cyclic voltammetry, however, in this case potential is changed from lower to higher potentials or from higher to lower instead of cycling in the selected potential range. Linear voltammetry is one of techniques which can be used to measure the activity towards water splitting process (19)[178]. Water splitting can be realized by performing oxygen evolution reaction (OER) or hydrogen evolution reaction (HER) in which oxygen or hydrogen gas is produced, respectively. The reactions (20) and (21) describe processes which occur in the alkaline solution according to the equations:

$$(19)\ H_2O \rightarrow H_2 + 1/2O_2$$

$$(20)\ 4OH \rightarrow O_2 + 2H_2O + 4e^-$$

$$(21)\ 4H_2O + 4e^- \rightarrow 2H_2 + 4OH^-$$

In order to test activity of the material towards OER it is required to polarize the working electrode from lower to higher potentials, whereas, in the case of HER from higher to lower potentials. The schematic representation of such process is presented in Figure 36. It can be clearly seen that those reactions are characterized by significant increase in current, high slope and gas generation on the electrode surface. Onset potential marked as a dashed line in Figure 36 is the highest or the lowest potential starts to produce hydrogen or oxygen, respectively.

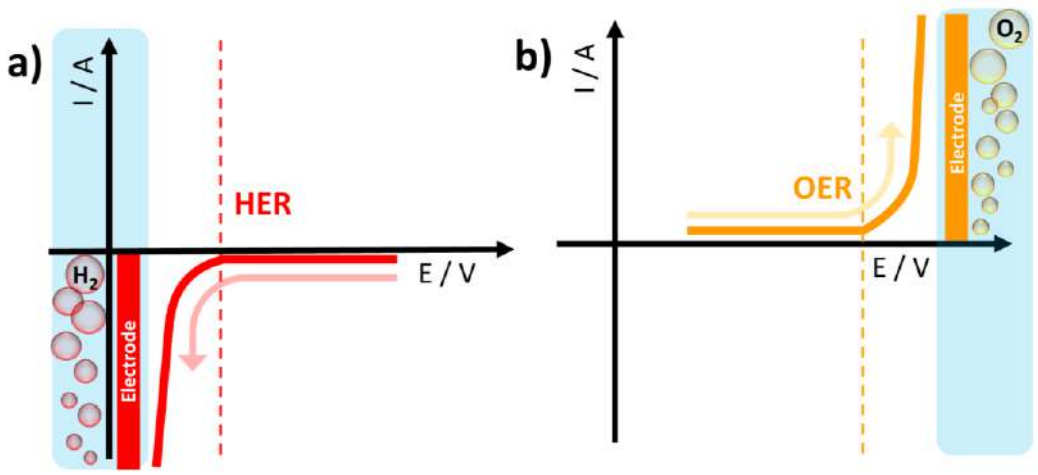

Figure 36. Schematic representation of a) hydrogen and b) oxygen evolution reaction.

Linear voltammetry curves can be recorded in dark but also when the material is exposed to light irradiation in order to explore if incident light can for example support the water splitting process. The electrode can be illuminated by whole spectrum of solar light or only by the selected range, e.g. in the visible light region. The photoelectrochemical measurements are conducted using xenon lamp with AM1.5G filter (global horizontal irradiance spectrum) as a light source with light intensity of 100 mW/cm^2 and the cut-off filter enabling to remove from the spectrum particular wave range (Figure 37).

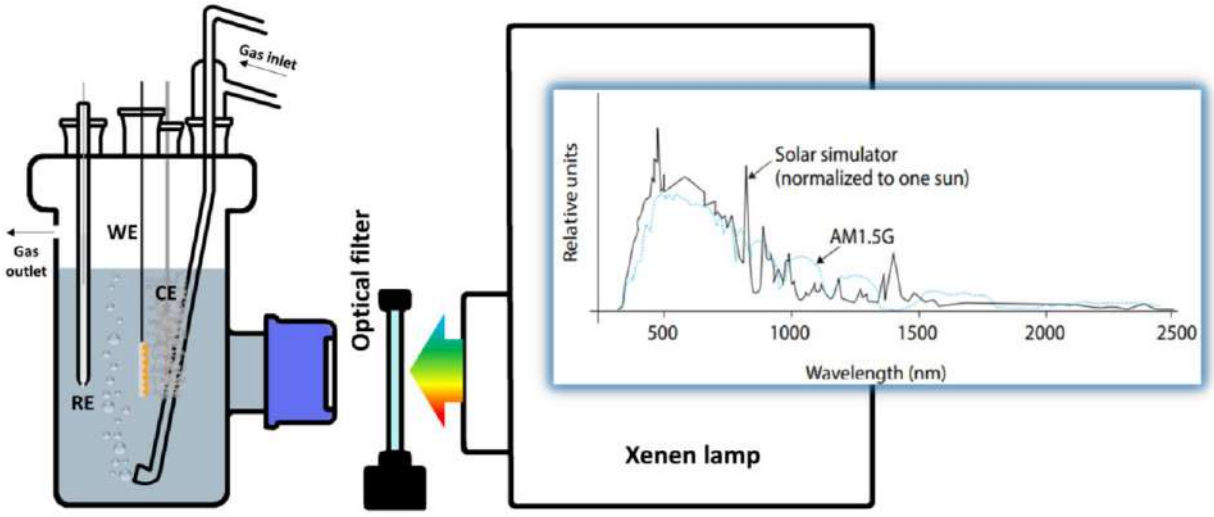

Figure 37. The schematic representation of photoelectrochemical measurements setup.

Electrodes are placed in the electrochemical cell with quartz window which allows the transmission of light from UV to middle infrared. The photocurrent can be measured under chopped dark-light illumination of materials which means that the light is turned on and off in a periodic mode. However, the electrode response can be also tested when first LV is recorded in dark and then under different light conditions. Then the photocurrent is a difference between

the current registered in light and in dark[179]. In order to accurately explore photoanode activity it is required to polarize from lower to higher potentials and from higher to lower for photocathode. The photoanode is the n-type semiconductor for example TiO_2 and the photocathode is the p-type semiconductor such as CuO and Cu_2O[180]. In order to explain the reason behind direction of polarization the flatband potential should be introduced. The flatband potential is potential where depletion layer does not exist. In the case of n-type semiconductor the depletion region is present in the positive potentials from flatband potential (Figure 38a). For p-type depletion region is in the negative potentials to flatband potential (Figure 38d). However, when n-type semiconductor is at negative potentials (Figure 38b) and p-type at positive potentials (Figure 38c) an accumulation region is formed. When semiconductor has accumulation layer it plays similar as metallic electrode under light illumination because of the excess of charges. If there is a depletion region after light illumination the photocurrent can be generated. Additional parameter which can be obtained from voltammogram is the onset potential defining value where the material starts to be photoelectrochemically active. The onset potential is positively shifted towards higher potential than the flatband potential for n-type semiconductors and negatively towards lower potential for p-type semiconductors[181]. The electrode should be polarized in order to provide opposite charges than charges which are present in excess.

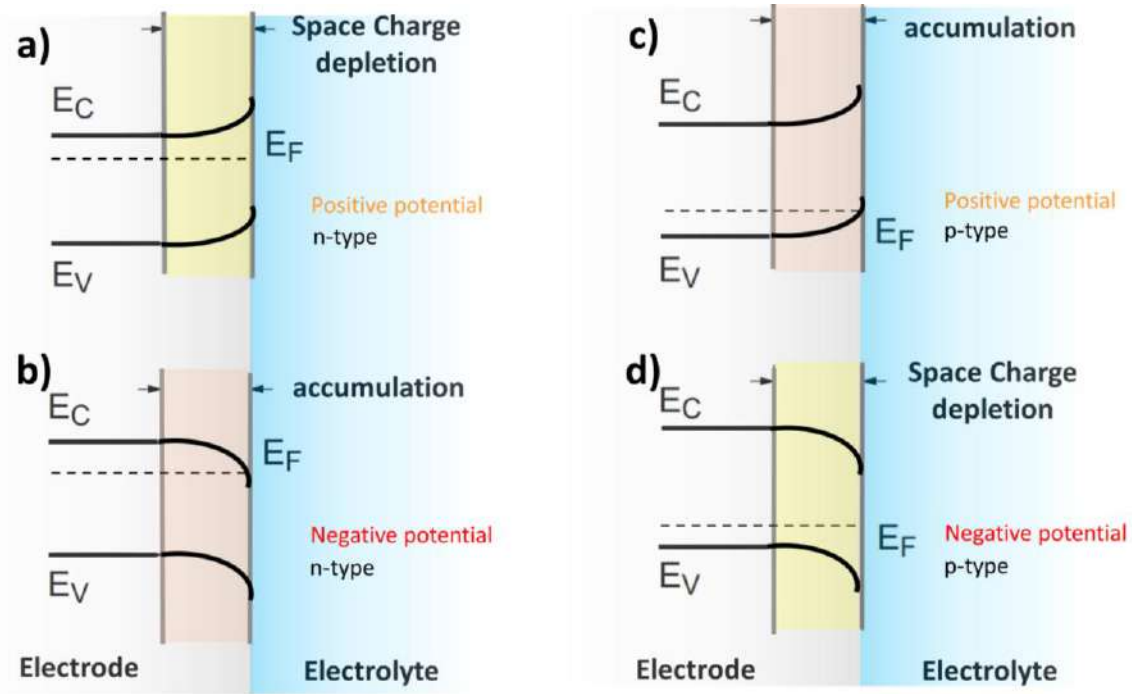

Figure 38. Effect of different applied potentials on a,b) n-type and c,d) p-type semiconductor[182].

6.5.3 Electrochemical impedance spectroscopy

Electrochemical impedance spectroscopy (EIS) is a technique which enables analysis of time-dependent phenomena occurring at the electrode-electrolyte interface[183]. The EIS technique uses the sinusoidal potential excitation signal and the sinusoidal current response at different frequencies during a single measurement (Figure 39a). The current response is at the same frequency as potential excitation but it is shifted in phase. The sinusoidal potential and current are functions of time at defined frequency and amplitude according to equation 22 and 23. Impedance is the AC resistance related to Ohm law (24).

$$(22) \quad E(t) = E_0 \cdot \sin(\omega t)$$

$$(23) \quad I(t) = I_0 \cdot \sin(\omega t + \phi)$$

$$(24) \quad Z(\omega) = E(t) / I(t)$$

where

E(t) – potential at time t / V

I – current / A

t – time / s

ω – frequency / rad · s^{-1}

φ – phase shift / degree

Z – impedance / Ω

The electrochemical impedance spectra mostly can be represented by Nyquist plot as the imaginary part vs. the real part of impedance (Figure 39b). The spectrum is composed of many single points and each of them is registered at different frequency.

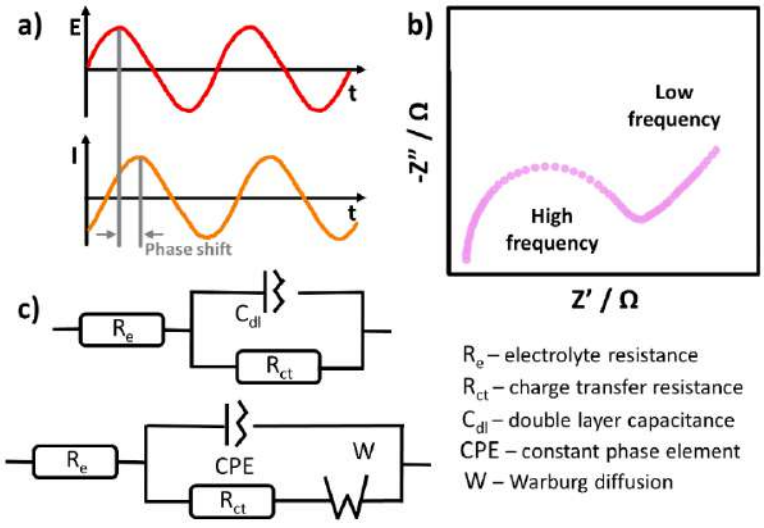

Figure 39. a) The excitation and output signal, b) the example of the EIS spectrum representation in the form of Nyquist plot, c) examples of electrical equivalent circuits [184,185].

In order to analyse EIS data in details it is required to fit the electrical equivalent circuit (EEC) containing different elements like resistor and capacitor that are attributed to the electrode material and electrolyte properties, and processes occurring in the electrochemical setup. Their relations with impedance are represented by equation (25) and (26), respectively.

$$Z_{resistor} = R \quad (25)$$

$$Z_{capacitor} = 1 / j\omega C \quad (26)$$

where

Z – impedance / Ω

R – resistance / Ω

ω – frequency / $rad \cdot s^{-1}$

C – capacitance / F

and j is imaginary unit and is equal to $\sqrt{-1}$.

Equivalent circuit highly supports description of the flow of charge through electrode-electrolyte interface [186].

Two examples of the most known equivalent circuit are presented in Figure 39c. The principal EEC is the Randles circuit model (Figure 39c). It is composed of three elements such as the electrolyte resistance (R_e), the charge transfer resistance (R_{ct}) and the double layer capacitance (C_{dl}). The model describes faradaic reactions as well as nonfaradaic capacitance character. However, for the real electrochemical system Randles model is not enough for proper fitting. Because of that, more elements should be considered to reflect the experimental conditions and describe the analysed system. The pure capacitor (C) is often replaced by constant phase element (CPE) which allows to take into account differences in heterogeneity of materials. Usage of this element is of high importance considering highly porous electrode material that developed surface is much higher than a flat layer. The CPE element can be described by equation (27):

$$CPE = 1 / Q \cdot (j\omega)^n \quad (27)$$

where

CPE – constant phase element

Q – quasi-capacitance / F

n – constant phase element exponent

ω – frequency / $rad \cdot s^{-1}$

and j is imaginary unit and is equal to $\sqrt{-1}$.

The constant phase element exponent is a number between 0 and 1 and describes capacitive behavior as well as heterogeneity of analyzed electrode. If n=0 the impedance becomes pure capacitance, whereas, for n=1 it is assigned to the resistor. Therefore, increase of constant phase element exponent is assigned to decrease of homogeneity.

The Warburg element is employed when additional diffusion processes are involved. The shape of Nyquist plot as straight line with a slope of ca. 45 degree can be assigned to diffusion of ions / reagents through the finite-length layer described by equation (28).

$$(28) \qquad Z_{W_O}(\omega) = \frac{W_{Or}}{\sqrt{\omega}}(1-j)coth\left[W_{Oc}\sqrt{j\omega}\right]$$

where

W_{Or} – Warburg coefficient / $\Omega \cdot cm^2 \cdot s^{-1/2}$

$W_{Oc} = d / D^{0.5}$

d – thickness of layer / cm

D – diffusion coefficient / $cm^2 \cdot s^{-1}$

and j is imaginary unit and is equal to $\sqrt{-1}$.

For example, when an additional compound as methanol, glycol or glycerine is added to the basic 0.1 M NaOH solution and electrode is polarized the positively charged electrode is surrounded by additional cations and anions solvated by NaOH molecules. In that case the mass-transport effect should be taken into account due to additional adsorption layer of alcohol molecules formed on the electrode surface and described as Warburg diffusion element (W) (Figure 38c)[187].

Electrochemical and photoelectrochemical properties of samples prepared in this work were measured using an AutoLab PGStat 302N potentiostat-galvanostat. The xenon lamp (LOT-Quantum Design GmbH) was used as a light source. In the case of measurements recorded under visible light the optical filter was applied (GG420 Schott). The optical filter allowed to cut off wavelengths below 420 nm. The automatic shutter enabled to block and unlock the access to light within the established time, typically 5 seconds. The light intensity of 100 mW/cm^2 was calibrated using the silicon cell (Rera). I was responsible for electrochemical and photoelectrochemical measurements and analysis.

6.5.4 Measurements of incident photon-to-electron conversion efficiency

The incident photon-to-electron conversion efficiency (IPCE) can be defined as ratio of the number of photogenerated electrons to the number of photoelectrons from incident light (equations: 29, 30)[188,189]

$$IPCE = Ne/Np \quad (29)$$

$$IPCE = j \cdot 1240 / P \cdot \lambda \quad (30)$$

where

Ne – number of photogenerated electrons

Np – number of photoelectrons from incident light

j – photocurrent / $A \cdot cm^{-2}$

P – incident light power density / $W \cdot m^{-2}$

λ – wavelength / nm

The IPCE photoelectric spectrometer includes xenon lamp, lamp controller, xenon lamp cooling system, optical fiber, monochromator, filter wheel, electrochemical cell and potentiostat. The schematic representation of IPCE spectrometer is presented in Figure 40. Device is integrated with advanced software which allows to register detailed 3D maps of IPCE vs. wavelength and potential of working electrode. Electrodes are placed in a small cell filled with electrolyte in three-electrode system and equipped with a quartz window. The photocurrent of the sample is measured using chronoamperometry technique for the series of single wavelengths selected from the whole solar spectrum using a monochromator and filter wheel. It should be highlighted that some differences of IPCE values between different laboratories can be noted because light intensity varies from one devices to another[189]. Before measurements it is required to perform calibration process. It is possible to distinguish two types of calibration such as full and partial one. The full calibration refers to measurements of whole light emission spectrum and determination the power of light for each wavelength. Whereas, in the case of partial calibration the power is defined for one selected wavelength and the spectrum is rescaled in respect to this measurement.

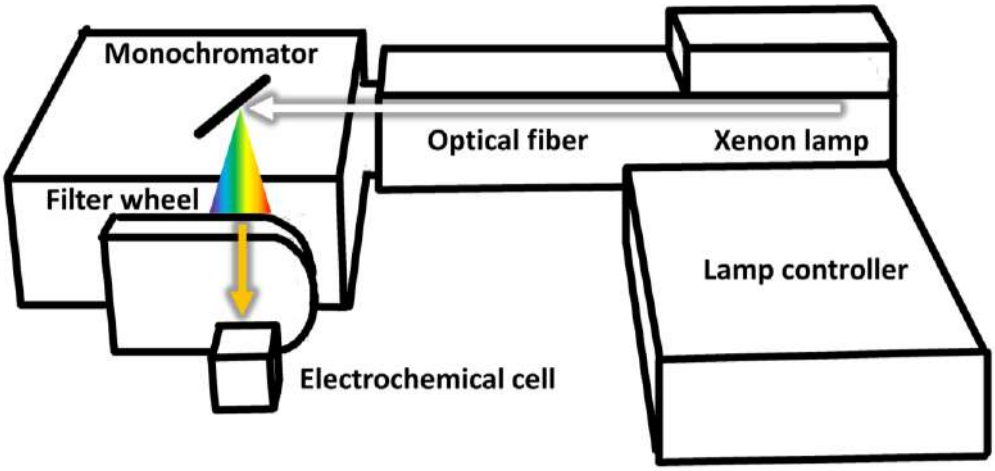

Figure 40. Schematic representation of IPCE photoelectric spectrometer.

The 3D map of the incident photon-to-electron conversion efficiency for samples prepared in this work was registered by photoelectric spectrometer Instytut Fotonowy equipped with Xe lamp 150 W. The light calibrator equipped with photodiode was used to determine light intensity before measurements. I performed IPCE measurements and analysis.

6.6 Density Functional Theory

Density functional theory (DFT) is a quantum chemistry methodology used for calculation of atomic/molecular properties.

DFT calculations were used for determination of absorption spectra, equilibrium atomic orientation on the interface, band structure, projected local density of states spectra of Cu_2O/CuO and Au/Cu_2O/CuO junction. Simulations were carried out by MSc Eng Adrian Olejnik PhD student at Gdansk University of Technology.

7. Results

This PhD thesis is composed of 6 articles which are arranged in a logical sequence. Each subsection contains **brief overview of the article AX** (where X = 1, 2, 3, 4, 5, or 6) with introduction, description of nanomaterial synthesis, optical and structural properties, electrochemical and photoelectrochemical properties and conclusion. Overview includes not only results from articles but also unpublished data which were part of the process during my PhD research. However, those data were crucial for my development as a scientist and can be considered as support for taking further decisions regarding synthesis procedure and material modifications.

A1) W. Lipińska, K. Grochowska, J. Karczewski, J. Ryl, A. Cenian, K. Siuzdak, ***Thermally tuneable optical and electrochemical properties of Au-Cu nanomosaic formed over the host titanium dimples***, Chemical Engineering Journal 399 (2020) 125673 IF=13.0 / 200 points

A2) W. Lipińska, K. Grochowska, J. Karczewski, J. Ryl, K. Siuzdak, ***Temperature-controlled nanomosaics of AuCu bimetallic structure towards smart light management***, Journal of Materials Science: Materials in Electronics 33 (2022) 19385, IF = 2.8 / 70 points

A3) W. Lipińska, A. Olejnik, J. Karczewski, K. Grochowska, K. Siuzdak, ***Annealing Rate as a Crucial Parameter Controlling the Photoelectrochemical Properties of AuCu Mosaic Core-Shell Nanoparticles***, Energy Technology 11 (2023) 2201021 IF= 4.1 / 100 points

A4) W. Lipińska, Z. Bielan, A. Witkowska, J. Karczewski, K. Grochowska, E. Partyka-Jankowska, T. Sobol, M. Szczepanik, K. Siuzdak, ***Insightful studies of AuCu nanostructures deposited on Ti platform: Effect of rapid thermal annealing on photoelectrochemical activity supported by synchrotron radiation studies***, Applied Surface Science 638 (2023) 158048, IF = 6.7 / 140 points

A5) W. Lipińska, K. Grochowska, J. Ryl, J. Karczewski, K. Siuzdak, ***Influence of Annealing Atmospheres on Photoelectrochemical Activity of TiO_2 Nanotubes Modified with AuCu Nanoparticles,*** ACS Applied Materials and Interfaces 13 (2021) 52967, IF = 10.4 / 200 points

A6) W. Lipińska, K. Grochowska, J. Karczewski, E. Coy, K. Siuzdak, ***Electrocatalytic oxidation of methanol, ethylene glycol and glycerine in alkaline media on TiO_2 nanotubes decorated with AuCu nanoparticles for an application in fuel cells,*** Journal of Materials Science 57 (2022) 13345, IF = 4.7 / 100 points

7.1 Influence of annealing in different temperatures of AuCu nanomosaic deposited on Ti nanodimples towards water splitting

Brief overview of the article A1

Introduction

Increasing devastation of the environment induced by fossil fuel consumption push scientists to explore functional materials for renewable energy generation. Furthermore, the efficient usage of resources is of high importance and therefore it can be guaranteed by fabrication of materials at the nano scale size. One of them are nanoparticles ensuring developed surface area and unique optical, electrical and catalytical properties different than of bulk material. Among others, bimetallic AuCu nanoparticles can be proposed as promising ones and can be applied in many fields as for example solar cells[190], oxygen evolution reaction[191], oxygen reduction reaction[192], carbon dioxide reduction[193] and alcohol oxidation processes[194].

Bimetallic AuCu nanostructures (named as 5Au/5Cu and 5Cu/5Au) and monometallic Au (10Au) and Cu (10Cu) counterparts deposited on Ti nanodimples (TiND) were annealed in two different temperatures 450 and 600 °C in the muffle furnace and investigated in terms of morphology, optical, structural and electrochemical properties. In this work, I studied the effect of various annealing temperatures on electrochemical properties especially toward oxygen evolution reaction and hydrogen evolution reaction assisted by light illumination.

Nanomaterial synthesis

The fabrication process of AuCu-decorated Ti electrodes was composed of anodization, chemical etching, magnetron sputtering and annealing in muffle furnace. First of all, Ti plate was cleaned in acetone, ethanol, deionized water, and anodized in two electrode system, where Ti is an anode and Pt is a cathode. The anodization was carried out at voltage of 40 V and temperature of 23 °C, and in the electrolyte containing 0.27 M NH_4F, 1 % vol. water and 99 % vol. ethylene glycol. The process had two stages where first took 2 hours and second one 6 hours. TiO_2 nanotubes which were formed after anodization were chemically etched in the 0.5 % oxalic acid solution. As a result uniformly distributed Ti nanodimples (TiND) were formed on Ti platform. Then nanostructured substrates where covered by thin 5 or 10 nm metal layers (10 nm Au, 10 nm Cu, 5 nm Au / 5 nm Cu, 5 nm Cu / 5 nm Au) using magnetron sputtering machine. Every time the thickness was controlled by quartz crystal microbalance (same device in article A2-A6). At the end materials where thermally treated in muffle furnace (MF) in air atmosphere at 450 °C or 600 °C for 10 minutes. The schematic fabrication process is presented below in the Figure 41.

Figure 41. Schematics of fabrication process of AuCu-decorated nanostructured Ti platform.

Optical and structural properties

To understand the electrochemical and photoelectrochemical properties of the fabricated AuCu materials, it is important to consider the optical and structural properties. The reflectance spectra are shown in Figure 42. The comparison of the reflectance minima for TiND, 10Au, 10Cu, 5Au/5Cu and 5Cu/5Au is presented in Table 5. The reflectance minimum for the TiND electrode annealed at 450 °C is located at 330 nm, whereas, for the TiND thermally treated at 600 °C at 450 nm. The shift towards higher wavelengths is caused by differences in morphology due to higher temperature during annealing where Ti dimples dimension annealed at 450 °C reaches 75.5 ± 5.5 nm and at 600 °C 54.08 ± 8.4 nm. Au, Cu and AuCu-decorated Ti platforms are characterized by different shape of reflectance spectra than pure Ti dimples due to the changes in morphology as well as chemical structure. According to literature for 10 nm gold and copper nanoparticles maxima of absorbance are located at 520 and 580 nm, respectively[195]. In my work 10Au electrode annealed at 600 °C and 10Cu electrode thermally treated at 450 °C with reflectance minima at 510 nm and 580 nm, respectively, overlap those data.

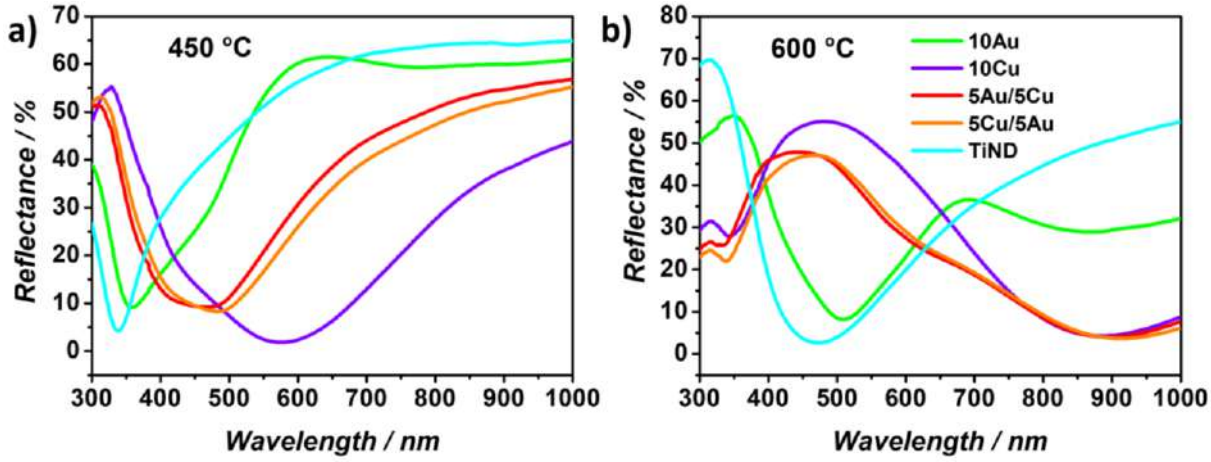

Figure 42. Reflectance spectra for 10Au, 10Cu, 5Au/5Cu, 5Cu/5Au and TiND electrodes thermally treated at a) 450 °C and b) 600 °C.

However, it should be added that interaction of those metals with Ti platform can result in changes of the reflectance spectra shape, because of that for 10Au annealed at 450 °C and 10Cu at 600 °C the contribution to reflectance can come from TiND. Taking into account bimetallic AuCu composition the shapes of spectra for 5Au/5Cu and 5Cu/5Au are almost the same. The reflectance minimum for samples annealed at 450 °C is located at 470 – 480 nm, whereas, for materials annealed at 600 °C at 900 – 910 nm. As observed the absorption band for AuCu electrodes is red shifted compared to 10Au and blue shifted when comparing to 10Cu. Together with the increase of annealing temperature the reflectance band minima shifts towards higher wavelengths.

Table 5. Values of position of the reflectance minimum for materials thermally treated at 450 °C and 600 °C.

Electrode (450 °C)	Position of the reflectance minimum / nm
TiND	330
10Au	360
10Cu	580
5Au/5Cu	470
5Cu/5Au	480

Electrode (600 °C)	Position of the reflectance minimum / nm
TiND	450
10Au	510
10Cu	890
5Au/5Cu	900
5Cu/5Au	910

The XPS measurements determined chemical states of the 5Au/5Cu and 5Cu/5Au electrodes thermally treated at 450 °C (see article A1 Figure 5). The Au4f peak located at 84 eV confirmed presence of metallic Au on the surface[196]. In the case of copper, three separate chemical states of Cu2p 3/2 at 935.0 eV, 933.5 eV and 932.4 eV were assigned to $Cu(OH)_2$ or $CuCO_3$, CuO and AuCu alloy[197]. Furthermore, the Ti2p 3/2 peak located at 458.4 eV was ascribed as Ti_2O_3[198]. The chemical composition of analysed materials supports further electrochemical and photoelectrochemical properties especially significant activity in anodic range associated with presence of AuCu alloy and Cu(II).

Electrochemical and photoelectrochemical properties

Characterization of the electrochemical activity of fabricated samples was carried out using CV and LV in 0.1 M NaOH solution. In the case of materials thermally treated at 450 °C intense faradaic peaks can be observed. Taking into account 10Au electrode the characteristic peaks at +0.3 V and 0 V vs. Ag/AgCl/0.1 M KCl are recognized as oxidation of Au to Au_2O_3 and reduction of Au_2O_3 to Au[199]. In the case of 5Au/5Cu and 5Cu/5Au electrode peaks located at -0.25 V and -0.05 V are identified as oxidation of Cu to Cu_2O and Cu_2O to $CuO/Cu(OH)_2$, respectively[200]. It should be added that the oxidation peaks are less intense than reduction ones

owing to the presence of gold atoms inhibiting oxidation processes. Considering the cathodic regime peaks at +0.05 V and -0.2 V correspond to the reduction of Au_2O_3 to Au and CuO to Cu[201]. Oxygen evolution reaction is initiated at +0.7 V vs. Ag/AgCl/0.1 M KCl, which consequently can be seen on LV curve. The comparison of current density values from linear voltammetry curves registered at +0.8 V as well as at -0.8 V is presented in Table 6. The highest current density at +0.8 V was obtained for bimetallic AuCu material (1.23 mA cm^{-2} for 5Cu/5Au electrode) which was ca. 30 times higher value than for monometallic gold electrode (0.04 mA cm^{-2} for 10Au). The improved activity towards oxygen evolution occurs due to the synergetic effect between gold and copper metals. When electrodes were illuminated by visible light the highest increase between current registered in dark and under vis light at +0.8 V was found for 5Au/5Cu electrode (120 µA cm^{-2}). Furthermore, the value registered at +0.8 V was 15 times higher than for 10Au electrode. As can be seen in the case of AuCu bimetallic nanostructures, OER supported by light illumination increases more significantly if the thin Cu layer is on the top of the electrode surface.

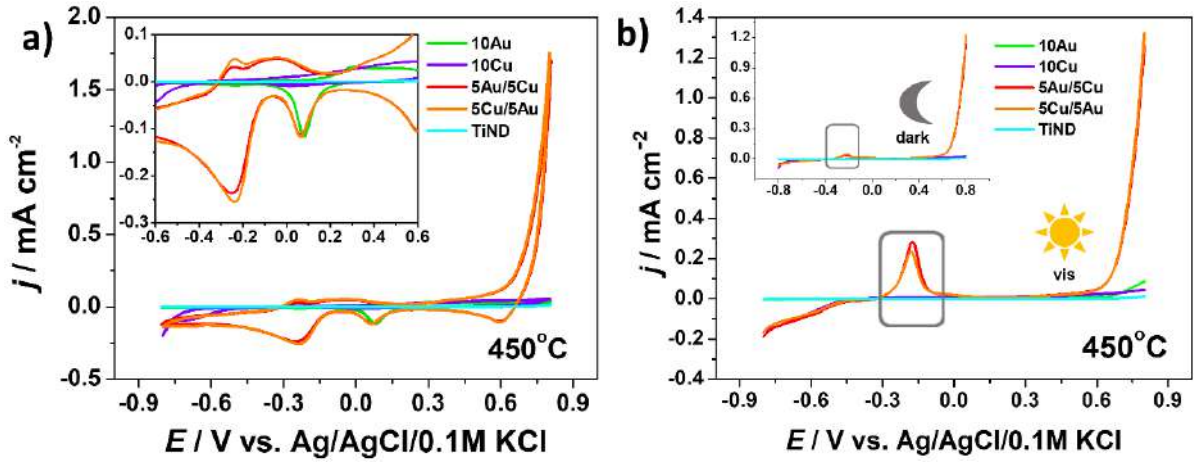

Figure 43. a) Cyclic voltammetry curves and b) linear voltammetry curves for 10Au, 10Cu, 5Au/5Cu, 5Cu/5Au and TiND electrodes annealed at 450 °C in dark and under visible light illumination registered in 0.1 M NaOH.

Table 6. Values of current density registered in dark and under visible light illumination for materials thermally treated at 450 °C.

Electrode	-0.8 V		+0.8 V	
	$j_{(dark)}$ / µA cm^{-2}	$j_{(vis)}$ / µA cm^{-2}	$j_{(dark)}$ / mA cm^{-2}	$j_{(vis)}$ / mA cm^{-2}
TiND	-1.6	-2	0.01	0.01
10Au	-2.5	-4.7	0.04	0.09
10Cu	-90	-160	0.03	0.04
5Au/5Cu	-50	-190	1.14	1.26
5Cu/5Au	-60	-170	1.23	1.32

Electrochemical activity towards CO_2 reduction

It is well known that CO_2 is causing the expand of global warming effect and ocean acidification. Taking into account many literature reports concerning CO_2 reduction reaction and growing level of CO_2 in the atmosphere due to increased consumption of fossil fuels as well as the deforestation, I decided to perform additional measurements on AuCu nanostructures. According to recent literature, gold[202], silver[203], platinum[204] or copper can be used towards electrochemical carbon dioxide reduction reaction. Nevertheless, the combination of two metals can be an interesting alternative, especially when it comes to gold and copper.

The experimental data on electrochemical CO_2 reduction for TiND, 10Au, 10Cu and 5Au/5Cu electrodes annealed at 450 °C is presented below in the Figure 44. Materials were fabricated according to the procedure described in article A1. The CO_2 reduction was determined by linear voltammetry measurements registered in 0.1 M $NaHCO_3$ solution saturated by CO_2. The current density registered at -1 V vs. Ag/AgCl/0.1M KCl for TiND, 10Au, 10Cu and 5Au/5Cu reached 6 μA cm^{-2}, 323 μA cm^{-2}, 78 μA cm^{-2} and 411 μA cm^{-2}, respectively. As can be seen, the synergistic effect caused by Au and Cu manifests as the highest current density for CO_2 reduction at cathodic range in comparison to single metals. The positive effect of AuCu combination was described by Ma et al.[205] and Morales-Guio et al.[206] where bimetallic AuCu nanostructure in the form of core-shell nanoporous $AuCu_3$@Au electrode improves the stability of intermediates and enhances selectivity of C^{2+} products formation. Taking above into account, it can be claimed that AuCu metals open new possibilities toward CO_2 reduction.

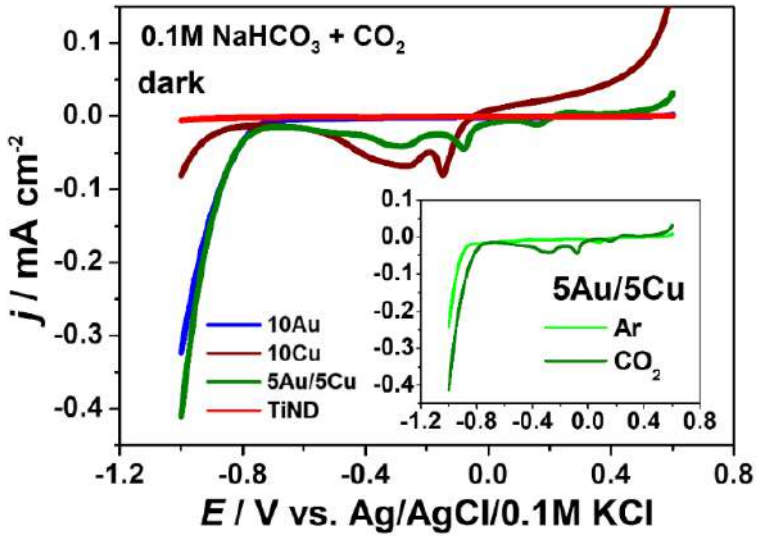

Figure 44. Linear voltammetry curves for TiND, 10Au, 10Cu and 5Au/5Cu electrode annealed at 450 °C in muffle furnace registered in 0.1 M $NaHCO_3$.

Conclusions

In this work, AuCu-nanomosaic on TiND platform fabricated via anodization, chemical etching, magnetron sputtering and thermal treatment in the muffle furnace at 450 °C manifested the best activity towards OER from all of the samples. Taking into account oxygen evolution reaction additionally enhanced by visible light illumination the configuration of 5Au/5Cu exhibited the highest photocurrent enhancement due to the thin copper oxides layer on the top. The bimetallic AuCu nanostructures obtained ca. 30 and 15 times higher current density at +0.8 V in dark and under light illumination than monometallic 10Au electrode. These electrochemical and photoelectrochemical properties can be attributed to the presence of AuCu alloy and Cu (II) species on the electrode surface as well as the absorbance band maximum located at 470 nm.

A1) W. Lipińska, K. Grochowska, J. Karczewski, J. Ryl, A. Cenian, K. Siuzdak, ***Thermally tuneable optical and electrochemical properties of Au-Cu nanomosaic formed over the host titanium dimples***, Chemical Engineering Journal 399 (2020) 125673 IF=13.0 / 200 points mechanical engineering

Chemical Engineering Journal 399 (2020) 125673

Contents lists available at ScienceDirect

Chemical Engineering Journal

journal homepage: www.elsevier.com/locate/cej

Thermally tuneable optical and electrochemical properties of Au-Cu nanomosaic formed over the host titanium dimples

Wiktoria Lipińska[a], Katarzyna Grochowska[a,*], Jakub Karczewski[b], Jacek Ryl[c], Adam Cenian[a], Katarzyna Siuzdak[a]

[a] Centre for Plasma and Laser Engineering, The Szewalski Institute of Fluid-Flow Machinery Polish Academy of Sciences, Fiszera 14 St, 80-231 Gdańsk, Poland
[b] Faculty of Applied Physics and Mathematics, Gdańsk University of Technology, Narutowicza 11/12 St, 80-233 Gdańsk, Poland
[c] Faculty of Chemistry, Gdańsk University of Technology, Narutowicza 11/12 St, 80-233 Gdańsk, Poland

HIGHLIGHTS

- Au-Cu nanomosaic onto titanium dimples formation via facile approach.
- Shift in the absorbance band maximum for the bimetallic materials from 470 nm to 900 nm.
- Combination of Au and Cu metals results in current density almost 15 times higher than for pure Au nanostructures.
- Synergistic effect between the Au and Cu can be achieved via simple thermal treatment of sputtered films.

GRAPHICAL ABSTRACT

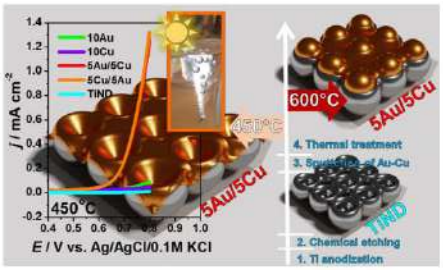

ARTICLE INFO

Keywords:
Au-Cu bimetallic nanostructures
Broad band absorbance
Oxygen evolution reaction
Electrochemical activity
Photoelectrochemical activity

ABSTRACT

Au-Cu nanostructures offer unique optical and catalytic properties unlike the monometallic ones resulting from the specific interaction. Among others, they have the ability to exhibit surface plasmon resonance, electrochemical activity towards the oxygen and hydrogen evolution reaction (OER, HER) as well as improved photoresponse in relation to monometalic but those properties depend highly on the substrate where bimetallic structures are immobilized.

In this work, bimetallic gold-copper mosaics over the conducting structured titanium substrate were fabricated via following steps: anodization of Ti foil, chemical etching of as-formed titania resulting in nanodimpled Ti substrate (TiND), sputtering of thin metal layer (Au, Cu) in various sequences, and finally thermal treatment in furnace at 450 °C or 600 °C. The morphology, optical and structural properties were investigated in details and it was shown that both arrangements of metallic films and thermal conditions strongly affect the morphology and optical features. The XPS results confirmed the presence of gold-copper alloys and copper oxide species. Last but not least, the electrochemical activities were verified in 0.1 M NaOH using cyclic voltammetry and linear voltammetry measurements performed in dark and under visible light illumination. Among all investigated materials in both anodic and cathodic regimes bimetallic 5Au/5Cu sample annealed at 450 °C exhibits the highest response towards OER and HER, respectively. This is further boosted by the light with $\lambda > 420$ nm. Upon exposure to visible light, the current density for 5Au/5Cu and 5Cu/5Au electrodes reached 1.32 mA cm^{-2} and 1.26 mA cm^{-2}, respectively, while in the case of monometallic structures the current was below 10 μA cm^{-2}. Both optical and electrochemical behaviour indicate a strong synergistic effect arising within the bimetallic mosaic formed over the TiND.

* Corresponding author.
E-mail address: kgrochowska@imp.gda.pl (K. Grochowska).

https://doi.org/10.1016/j.cej.2020.125673
Received 20 March 2020; Received in revised form 21 May 2020; Accepted 26 May 2020
Available online 06 June 2020

1. Introduction

Nowadays, the possibilities of fabricating and modifying novel functional materials are widening, due to the rapid development of technology and easier access to the chemical compounds and advanced machines. Nevertheless, taking into account the total production cost, energy consumption as well as waste disposal, special interest is targeted on synthesis methods requiring simple equipment, lowering the usage of precious metals as well as avoiding additional purification steps. Due to the devastation of the environment, both the production of the new nanostructures and their further utilization towards energy conversion and storage should be at the centre of scientists' interest. Realizing the danger of resource depletion, the global warming effect, air pollution and water contamination, the efforts of materials science should be focused on green synthesis methods and efficient usage of resources. Following that, the structures based on metal nanoparticles (NPs) not only reduce material consumption but due to change of their size from the macro to the nano scale they also reveal the unique properties, such as developed surface area, high electric capacitance and conductivity or light absorption in the visible range[1]. Among others, gold nanostructures have been widely explored and successfully applied in organic photovoltaic cells, photocatalysis and electrochemical sensors [2–4]. However, the depletion and rising price of precious metals as well as the safety concerns relating to the use of auric acid [5] force us to find some promising alternative to the monometallic gold structures as well as towards wet chemistry methods. Taking into account those challenges, the reduction of gold consumption in favour of other transition metals, e.g. Ag, Cu, Ni [6–8] as well as the application of physical top-down technique [9] have been proposed as a more environmentally friendly approach.

Following that, the significant growth of interest in the bimetallic Au-Cu nanostructures exhibiting unique optical and catalytical properties is not surprising [10–12]. Those extraordinary optical properties in most cases are related to the surface plasmon resonance (SPR) effect. The SPR is based on the excitation of plasmons, i.e. collective oscillations of free electrons, by light resulting in the enhancement of electromagnetic field arising in the nearest vicinity of the nanoparticles. It should be noted here that optical properties of NPs do not depend only on their chemical composition; but also their dimensions and shape, as well as the surrounding medium, are of high importance. Customarily, gold nanoparticles with dimensions from 5 to 50 nm exhibit absorption peak between 520 and 530 nm [13]. On the other hand, Cu nanoparticles with diameter of 20 nm show the maximum absorption peak at 580 nm[13]. However, when one combines gold and copper together, it is possible to achieve broadband absorption in the visible range [1] and its tuning within the several tens of nm is achievable. For the NPs of 10 nm in diameter surrounded by a medium of 1.4 refractive index, the SPR maxima for Au, Au_3Cu, AuCu, $AuCu_3$, Cu were located at 532 nm, 538 nm, 561 nm, 567 nm, 578 nm, respectively [14]. Apart from the optical features, Au-Cu NPs are characterized by attractive catalytical properties especially towards the electrocatalytic reduction of CO_2 [15] and selective alcohol oxidation [11]. Moreover, reports on the Au/Cu_2O porous heterostructures indicate their higher photoresponse comparing to the pure Cu_2O structure [16] The oxygen evolution reaction (OER), as well as hydrogen evolution reaction (HER) running efficiently at Au-Cu bimetallic structures, were confirmed [17]. Therefore, the Au-Cu NPs can be successfully used in processes dealing with the environmental pollution present in liquid media.

It should be also noted, that the synthesis of Au-Cu bimetallic material not only takes advantage of the lower price of Cu cf Au but also take advantage of the high stability of gold [1]. In such materials, the improved properties of bimetallic structures occur due to the synergistic effect between both metals and this interaction depends on the structure inside the particular Au-Cu NP. The bimetallic nanoparticles can be classified into alloy/intermetallic or core–shell/layer-by-layer structures. In the case of Au-Cu, one can distinguish three different structures of specific stoichiometry such as $AuCu_3$, AuCu and Au_3Cu depending on the composition of individual elements [18]. Analyzing the Au-Cu phase diagram, it can be seen that at 410 °C (1:1 atomic ratio) there is an order–disorder transformation [19] which is related to ordered intermetallic structures or disordered alloy creation. It was found that control of the ordering degree of Au-Cu nanoparticles significantly impacts the electrocatalytic activity [20]. The ordered structures exhibit high catalytic properties towards CO_2 to CO reduction, however the disordered ones enable enhanced hydrogen evolution [20]. Thus, it is very important to control precisely the synthesis procedure of the bimetallic nanoparticles as well as to reveal the electrochemical activity that could be further utilized in the reactions important from the environmental point of view.

In this paper, the synthesis of Au-Cu bimetallic nanomosaics over the textured Ti substrate as well as their morphology, structural, optical, electrochemical and photoelectrochemical characterization are studied. The titanium platform was fabricated via the electrochemical anodization process of Ti foil followed by the selective chemical etching of as formed titania nanotubes. As a result of that process, the ordered titanium nanodimples (TiND) were obtained acting further as host wells. Afterwards, that platform was covered by thin metal layers of Au and Cu in various sequences using the magnetron sputtering technique. In the next stage, the rapid thermal annealing at 450 °C or 600 °C was carried out. For reference, the same procedure was applied to the pristine TiND and TiND with deposited monometallic Cu and Au films. The morphology of materials was investigated by scanning electron microscopy (SEM) and atomic force microscopy (AFM). Fabricated samples were also characterized by X-ray photoelectron spectroscopy (XPS) for the determination of the oxidation states of atoms that form nanomosaics. On the basis of reflectance spectra recorded by UV–vis spectrophotometer the optical properties of nanostructures were analysed. Finally, the electrochemical and photoelectrochemical activities for the series of obtained structures were characterized both in dark and when the electrode was exposed to visible light. The linear voltammetry (LV) and cyclic voltammetry (CV) measurements in 0.1 M NaOH were carried out and significant differences between formed materials were identified. As expected, temperature strongly affects the morphology and properties of the resulting material. Finally, it has been experimentally proven that the synergistic effect between the Au and Cu can be achieved via simple thermal treatment of sputtered gold and copper films.

2. Experimental

2.1. Au-Cu electrode fabrication

Titanium foil (99.7%, Strem), acetone (Protolab), ethanol (96%, Chempur), ammonium fluoride (98%, Chempur), ethylene glycol (99%, Protolab) and oxalic acid dihydrate (99.5%, Sigma-Aldrich) were used for anodization and chemical etching processes of the as-anodized Ti foil. The pure targets of gold (99.99%, Quorum Technologies) and copper (99.99%, Quorum Technologies) were used for thin metal layer deposition.

Firstly, the Ti foil was cut into 2 × 3 cm^2 rectangles and ultrasonically cleaned in acetone, ethanol and deionized water for 10 min in each medium. Immediately, the substrates were used for anodization. That process was conducted in the two-electrode system, where the Ti plate was used as an anode and Pt mesh as a cathode. Both electrodes

were placed against each other 2 cm apart in the cylindrical glass cell. The reactor had a thermostatic jacket for the preservation of a constant temperature of 23 °C during the whole process. The electrodes were immersed in the electrolyte composed of 0.27 M NH_4F dissolved in the mixture composed of 1% vol. deionized water and 99% vol. ethylene glycol. The anodization was carried out in two stages, the first one took 2 h and the second 6 h. At each stage the voltage of 40 V was applied between electrodes. After each anodization formed TiO_2 nanotubes were removed out of the Ti foil by selective chemical etching. This treatment involves the overnight immersion of samples in the 0.5% oxalic acid solution. This way, the titanium substrate covered uniformly by the nanodimples was obtained. Finally, the Ti nanotextured platform was rinsed with deionized water and dried. The obtained nanostructured titanium platform was covered by thin metal layers: 10 nm Au or 10 nm Cu or 5 nm Au and 5 nm Cu in both sequences, namely 5Au/5Cu and 5Cu/5Au using magnetron sputtering machine (Q150T S system, Quorum Technologies). Afterwards, samples were annealed at a temperature of 450 °C or 600 °C for 10 min. Thermal treatment was conducted in air atmosphere. The samples were placed onto the ceramic dish and then transferred to the muffle oven already heated to the established temperature. After processing they were taken out of the oven and left freely to cool down.

2.2. Samples characterization

Investigation of the electrodes morphology was performed using a field emission scanning electron microscope (FEI Quanta FEG250) equipped with an ET secondary detector and with the beam accelerating voltage kept at 10 kV. Additionally, the topography of TiND was studied by an atomic force microscope (AFM) (Nanosurf EasyScan 2). The reflectance spectra of nanostructures were measured by UV–vis spectrophotometer (Lambda 35, Perkin-Elmer) equipped with an accessory for reflectance spectra registration. The reflectance spectra registered with 60 nm/min speed in the wavelength range from 300 to 1000 nm were provided for the whole set of titanium, gold, copper and both types of gold-copper nanostructures.

The chemical nature of fabricated samples was revealed by X-ray photoelectron spectroscope (Escalab 250Xi, ThermoFisher Scientific) with a monochromatic AlKα source. Those measurements were carried out for the selected materials: 10Au, 10Cu, 5Au/5Cu and 5Cu/5Au annealed at 450 °C, because of their prominent photoresponse as will be shown later on. The calibration for XPS spectra was based on the signal attributed to the pure Au metallic state (84.0 eV). The deconvolution of the XPS spectra was performed with Avantage v5.973 software (ThermoFischer Scientific).

The electrochemical and photoelectrochemical studies were conducted using the AutoLab PGStat 302 N potentiostat-galvanostat, in the three-electrode arrangement placed in the cell containing a quartz window. The pristine TiND and modified TiND electrodes were used as the working electrode (WE) whereas Pt mesh was the counter electrode (CE) and Ag/AgCl/0.1 M KCl was the reference electrode (RE). The cyclic voltammetry and linear voltammetry measurements were carried out in deaerated 0.1 M NaOH solution. The polarization curves were recorded from −0.8 V to +0.8 V vs. Ag/AgCl/0.1 M KCl. For CV the scan rate was equal to 50 mV/s whereas for LV to 10 mV/s. In the case of photoelectrochemical tests, the light source was a xenon lamp equipped with filters: AM 1.5 and UV cut-off (GG40, Schott). The irradiation intensity was established to be 100 mW/cm^2 using Si reference cell (Rera). The stability of electrochemical performance was verified by the multicyclic polarization accompanied with the recording of the linear voltammetry scan under visible light irradiation.

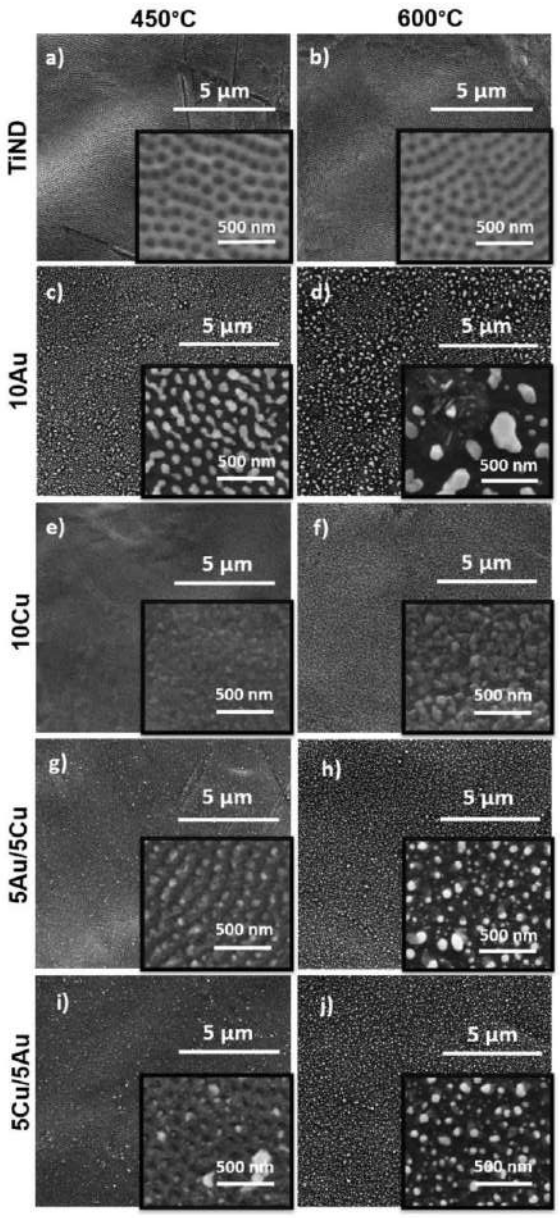

Fig. 1. SEM images of the a) TiND (450 °C), b) TiND (600 °C), c) 10Au (450 °C), d) 10Au (600 °C), e) 10Cu (450 °C), f) 10Cu (600 °C), g) 5Au/5Cu (450 °C), h) 5Au/5Cu (600 °C), i) 5Cu/5Au (450 °C), j) 5Cu/5Au (600 °C). The temperature treatment was indicated in the round brackets.

3. Results and discussion

3.1. Morphology

SEM images of the fabricated samples containing gold, copper and gold-copper metallic species onto titanium nanodimples annealed at 450 °C and 600 °C for 10 min are shown in Fig. 1. As it can be seen, the temperature strongly affects the morphology of materials obtained out of the sputtered thin layers and even the pristine TiND. As given in Fig. 1a and b the annealing at elevated temperature changes the

dimensions of the dimples. The diameter of the bare titanium dimples for the sample annealed at 450 °C was estimated to 75.5 ± 5.5 nm, while for the sample annealed at 600 °C was equal to 54.08 ± 8.4 due to the variety of deformed substructure and changes in the grain size [21]. According to Chen et al., the recrystallization and the significant grain growth take place when the annealing is performed above 500 °C. Moreover, other negative impact of higher temperature treatment is related with the hardness loss attributed to the decrease of dislocation density.

Regarding the case of pure gold, the thermal treatment at 450 °C leads to the formation of a mosaic-like structure composed of Au NPs located in the host titanium dimples as presented in Fig. 1c which is in agreement with our previous works [22,23]. The electrode which has been annealed at the higher temperature of 600 °C is shown in Fig. 1d and is characterized by a higher degree of disorder. As a result, in some areas of the sample bigger gold agglomerates can be found and therefore their size distribution is much wider comparing to the lower temperature conditions. Such phenomenon could be related to the changes of the TiND morphology itself.

SEM images provided in Fig. 1e and f show the copper species formed over the Ti and in both cases, in contrast to gold, no well separated NPs can be revealed. The only difference in material morphology in both temperature regimes is attributable to the grain size. The surface of 10Cu annealed at 450 °C may be regarded as much smoother than 10Cu annealed at 600 °C material where the sharp edges of individual grains can be observed. When SEM images of Au-Cu combinations are analysed, the morphology of the resulting structures can be regarded as a nano-mosaic composed of nanoparticles for the annealing performed under 600 °C while lower temperature did not result in the creation of easily distinguished NPs on the FE SEM image. Nevertheless, when only 450 °C was applied the characteristic dimples are still visible over the Ti substrate as presented in Fig. 1g and i. For the elevated temperature treatment, the whole substrate is almost uniformly covered by NPs but the dimpled nature of the substrate is not seen. This should be related to the changes in the geometrical dimensions of the TiNDs themselves thermally treated in two temperature regimes. The depth of TiND was calculated from AFM images (Fig. 2) and its average value for the material annealed at 450 °C was 11.1 ± 2.3 nm (Fig. 2a), however for samples annealed at 600 °C it was 7.3 ± 2.6 (Fig. 2b). Therefore, a higher temperature makes dimples shallower and in consequence the borders between dimples are less distinctive. For the complete characterization of structure also X-ray diffraction spectra were recorded and are shown (see Fig. S1) and described in the Supplementary Information file.

3.2. Optical properties

The changes in the samples colour is clearly observed by the naked eye (Fig. 3) and since the samples are not transparent the reflectance spectra were recorded (see Fig. 4) to reveal unique optical properties. Regarding the provided digital photographs, one may observe variety of colours from metallic gold for 10Au annealed at 450 °C to intense blue for 5Au/5Cu and 5Cu/5Au bimetallic mosaics formed at 600 °C. For the bare substrate, namely TiND, the colour changes from light yellow to deep orange for 450 °C and 600 °C temperature conditions, respectively. As was reported by Skowroński et al. [24] similar observations regarding the colour impressions were noted for samples composed of titania film over Ti support where the gold tone is observed when the TiO_2 thickness reaches 11 nm and saturated blue in the case of almost 50 nm thick film. Those changes in material colours are in line with the modification of the reflectance shape. When 450 °C was applied, the reflectance minimum for TiND is positioned at 330 nm whereas in the case of 600 °C the reflectance band is broadened and the minimum is shifted to 450 nm. The coloration of the structure results from the interaction of the light and periodical lattice of NDs that allow to describe obtained material as a photonic crystal. According to the morphology analysis, the change of the dimple dimension was observed and in consequence it modulates the position of the reflection band. Similar behaviour was reported by Umh et al. [25] and red shift was noted for Ti platforms composed of the uniformly distributed nanobowls fabricated at different anodization voltage.

When the thin metal films were deposited and then thermally treated, the shape of the reflectance spectra differs significantly due to the changes in the morphology as has been already described and of course depends on the type of deposited metal layer. The reflectance band minima for 10Au, 10Cu, 5Au/5Cu and 5Cu/5Au formed at 450 °C are located at 360 nm, 580 nm, 470 nm and 480 nm, respectively (Fig. 4a). However, for 10Au, 10Cu, 5Au/5Cu and 5Cu/5Au annealed at 600 °C, those minima are situated at ca. 510 nm, 890 nm, 900 nm and 910 nm (Fig. 4b). According to the literature, both when the modelling is applied [14] and for the experimental results [26] the SPR band for 10 nm gold nanoparticles is situated at ca. 520 nm while for copper at ca. 580 nm. Thus, only results for 10Au annealed at 600 °C and Cu annealed at 450 °C overlap those data. Moreover, because copper is an easily oxidized metal the comparison to Cu_2O nanoparticles is here justified. As was reported by Saad et al. [27] and Li et al [28] the absorbance maximum situated at ca. 580 nm results from the exciton formation in Cu_2O. It should be also highlighted that the absorbance spectra significantly depend on the substrate used for NPs immobilization [29] and when the titania is used as a platform for Au nanospheres, the SPR absorbance maximum could be shifted from 400 nm for amorphous substrate up to 554 nm for anatase one. Therefore, we consider that in the case of the fabricated structures herein, especially 10Au (450 °C) and 10Cu (600 °C) the contribution to the reflectance originating from TiND is significant since for the substrate the absorbance maxima is located at 340 and 460 nm, respectively. Additionally, as was reported by Padikkaparambil et al. [30] decoration of the TiO_2 surface with gold led to a change in the intensity

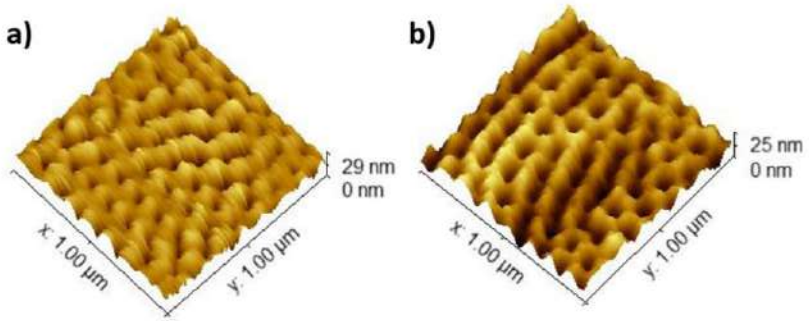

Fig. 2. Topographical AFM 3D image for TiND annealed at a) 450 °C, b) 600 °C.

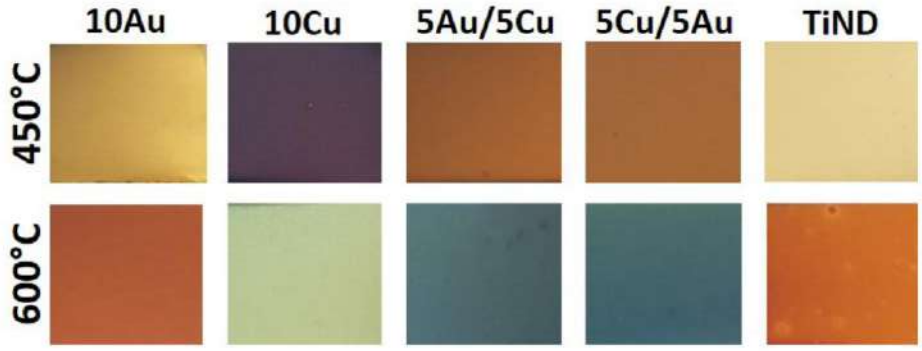

Fig. 3. Images of sample surfaces showing their colour changes due to different annealing temperature.

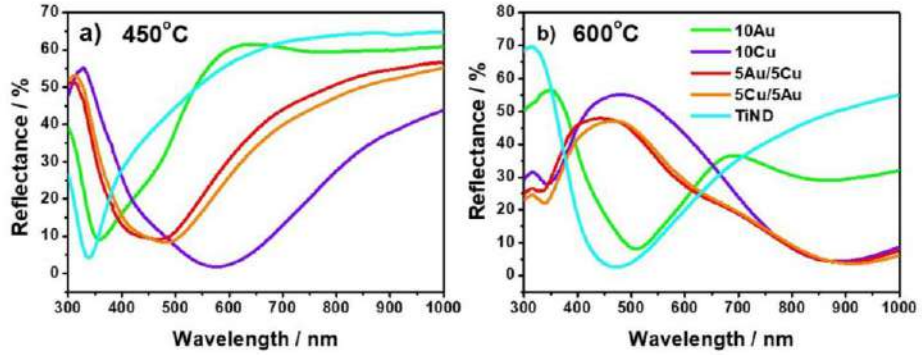

Fig. 4. Reflectance spectra of a) electrodes annealed at 450 °C, b) electrodes annealed at 600 °C.

of the dioxide titanium absorption band. Two absorption maxima around 320–350 nm and 540–570 nm were correlated with different amounts of Au deposited onto TiO_2. In our work, the amount of Au does not change, however, the amount of TiO_2 associated with the change of diameter and depth of nanodimples does, as well as Ti–Au surface interaction, caused by a higher degree of disorder.

Additionally, upon an increase of the annealing temperature the absorbance bands shift towards higher wavelength values by 150 and 310 nm for 10Au and 10Cu, respectively. According to Mohan et al. [31] the absorption band shift from 450 nm to 650 nm for CuO NPs were registered after annealing. However, we would like once again to emphasize the significance of the surface on which CuNPs as well as copper oxides are deposited and its influence on the SPR band location. According to Liu et al. [32] the maximum of absorbance band for CuNPs/FTO was positioned at 350 nm, while Pham et al. [33] showed that the maximum for Cu_2O/TNTs was found at c.a. 300 nm. Moreover, the usage of graphene oxide (GO) as a substrate results in minimum reflectance located at 750 nm for Cu_xO/GO configuration [34] Those experimental findings support the explanation that the big shift of SPR band is determined by the type of platform used for further NPs deposition.

Regarding the bimetallic configurations, it should be highlighted that in both temperature regimes the shape of reflectance spectra for 5Au/5Cu and 5Cu/5Au nanomosaics almost overlaps and the local maxima and minima are positioned nearly at the same wavelengths for particular temperature case. Comparing the profiles of reflectance spectra for both Au-Cu arrangements the minima observed for the samples treated at 450 °C correspond to the local maxima for the materials annealed at 600 °C. For 5Au/5Cu and 5Cu/5Au samples the absorption bands are much wider compared to monometallic substrates but they are blue shifted regarding the band recorded for 10Cu treated at 450 °C and overlap partially (above 750 nm) the spectra of 10Cu when the higher temperature annealing was carried out. It should be noted, that the absorption band for the bimetallic nanomosaic is red shifted compared to the monometallic gold layer treated at the same temperature regimes. This is in accordance with Sinha et al. [35] identifying the formation of single phase Au-Cu alloy as a responsible factor for such change.

Nevertheless, in our opinion the profiles of reflectance spectra for 5Au/5Cu and 5Cu/5Au electrodes manufactured in 450 °C are strongly influenced by the TiND substrate as well as the morphology of the Au-Cu structures. As it has been already mentioned during morphology analysis, the NPs formed at 600 °C are much bigger and well distinguished than if only 450 °C was applied. According to the literature, similar absorbance features were found for AuCu structures within the wide 600–1000 nm waverange [1]. The similar character for Au@Cu_2O reported by Liu et al. [36] and the significant red shift of the absorbance comparing to bare gold structure was explained by the introduction of Cu_2O to the system that is related with the increasing of the effective dielectric constant between the Au core and Cu_2O shell. Summarizing, both the annealing temperature, the composition of metallic layer and the nanotextured morphology of Ti substrate act here as key optical tuning factors.

3.3. Characterization of the chemical nature of samples

The chemical states of gold *Au4f* (Fig. 5a), copper *Cu2p* (Fig. 5b), titanium *Ti2p* (Fig. 5c) and oxygen *O1s* (Fig. 5d) were determined using X-ray photoelectron spectroscopy analysis. The detailed interpretation of all the recorded bands on the basis of the fitting procedure and peak deconvolution is presented below. The obtained results are summarized in Table 1. The high-resolution XPS spectrum for the *Au4f* appears as a

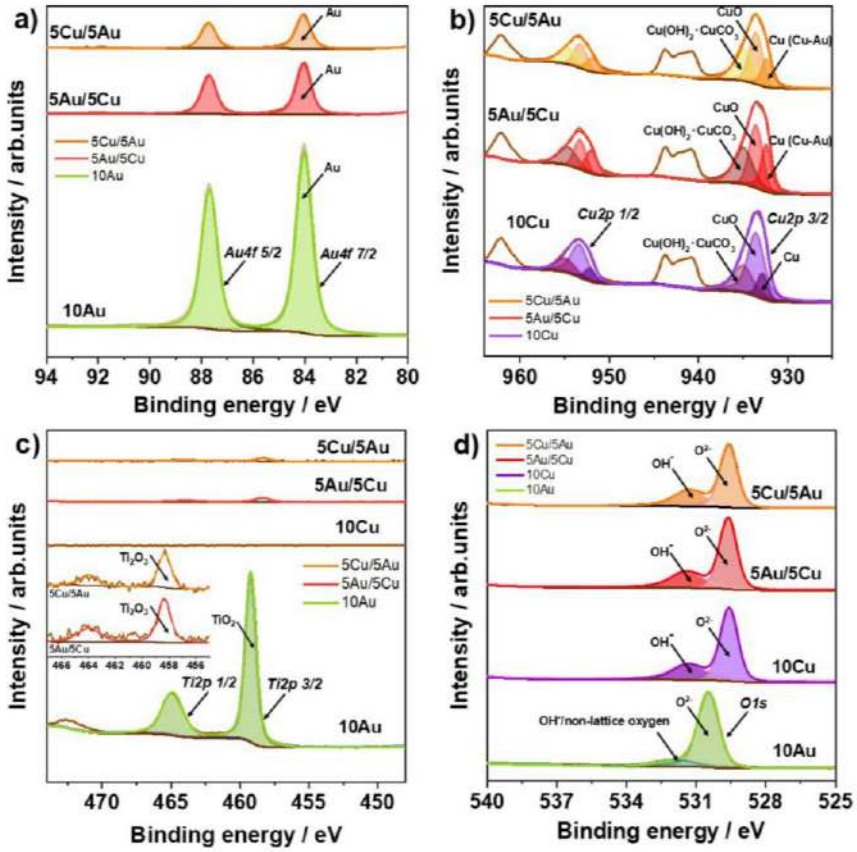

Fig. 5. XPS high resolution spectra registered for 10Au, 10Cu, 5Au/5Cu and 5Cu/5Au samples annealed at 450 °C: a) *Au4f*, b) *Cu2p*, c) *Ti2p* and d) *O1s*.

Table 1
The binding energies (BE) of 10Au, 10Cu, 5Au/5Cu and 5Cu/5Au samples annealed at 450 °C used for XPS analysis.

Peak		Component	BE/eV	At. %	Component	BE/eV	At. %
		10Au			10Cu		
Au4f 7/2		Au	84.0	26.5	–	–	–
Cu2p 3/2		–	–	–	$Cu(OH)_2$ and		
$CuCO_3$	935.0	10.4					
Cu2p 3/2		–	–	–	CuO	933.5	21.6
Cu2p 3/2		–	–	–	Cu	932.8	4.8
Ti2p 3/2		TiO_2	459.2	21.5	–	–	–
O1s		non-lattice oxygen / OH^-	532.0	5.9	OH^-	531.3	19.9
O1s		O^{2-} 5Au/5Cu	530.5	46.1	O^{2-} 5Cu/5Au	529.6	43.3
Au4f 7/2		Au	84.1	7.1	Au	84.1	5.5
Cu2p 3/2		$Cu(OH)_2$ and					
$CuCO_3$	935.0	12.9		Cu $(OH)_2$ and			
$CuCO_3$	935.0	13.4					
Cu2p 3/2		CuO	933.5	13.5	CuO	933.5	13.1
Cu2p 3/2		Cu (Cu-Au)	932.4	8.6	Cu (Cu-Au)	932.3	6.1
Ti2p 3/2		Ti_2O_3	458.4	0.7	Ti_2O_3	458.3	0.6
O1s		OH^-	531.4	19.1	OH^-	531.3	22.1
O1s		O^{2-}	529.6	38.1	O^{2-}	529.6	39.3

peak doublet (Fig. 5a) and confirms the presence of metallic Au (84.0 eV) on the surface [37].

In the case of the high-resolution XPS spectrum for copper, the analysis revealed the diversity of *Cu2p* chemical states. Three separate chemical states were identified and considered for the spectral deconvolution, as shown in Fig. 5b. This element is present primarily as Cu(II) in two various forms: *Cu2p3/2* peak at 935.0 eV present in the energy range characteristic for $Cu(OH)_2$ and/or $CuCO_3$,[38,39] while CuO [40] was confirmed by the signal located at 933.5 eV. The third component arising at 932.8 eV [41] in the case of 10Cu sample was assigned to the metallic Cu with no contributions from other copper oxides [42,43]. Notably, regarding 5Au/5Cu as well as 5Cu/5Au alloys, the location of metallic Cu peak is negatively shifted by 0.4 and 0.5 eV, respectively [42]. The higher binding energy of Cu in the monometallic copper sample than in the bimetallic one is caused by electron transfer from Cu to Au which decreases the electron density within Cu [44]. The dominance of the various Cu(II) species within the analysed spectra is confirmed with satellite feature at approx. 940–945 eV, as well as Cu_{LMM} Auger spectrum, presented in Fig. S2 (Supplementary Information file). In the case of each investigated sample the spectra peaks are present at energy characteristic for Cu(II). This analysis confirms negligible presence or lack of Cu(I) [45].

In the case of titanium, its chemical states vary depending on the investigated material. For 10Au electrode the *Ti2p3/2* peak at 459.2 eV was characterized as TiO_2 which is present at the Au/Ti interface (Fig. 5c). However, for both the 5Au/5Cu and 5Cu/5Au mosaics, the *Ti2p3/2* peak appears negatively shifted by −0.8 eV and confirms the presence of Ti_2O_3 [46] (Fig. 5c). Although, it is worth mentioning that

the Ti share was minor compared to other components since it is covered by gold and copper metal species. Titanium was not detected for the 10Cu electrode, most likely due to the higher thickness of Cu because of the copper oxide formation acting as a TiND cover and the surface character of the XPS analysis.

Last but not least, the detailed analysis of the *O1s* spectrum (Fig. 5d) reveals a similar nature of oxygen species present in 10Cu, 5Au/5Cu and 5Cu/5Au electrodes. The strong peak at 529.6 eV was ascribed to the lattice oxygen in CuO [47] Additionally, peaks located at 531.3 eV were linked to $Cu(OH)_2$ and surface adsorbed OH^- [39]. Unlike other analyses, the main component of *O1s* for 10 Au electrode (Fig. 5d) located at 530.5 eV was ascribed as lattice oxygen derived from titanium dioxide which is exposed to the oxygen rich atmosphere because of Au NPs creation. The second component was characterized as non-lattice oxygen in TiO_2 and hydroxyl species [48].

3.4. Electrochemical performance

The electrochemical activity of the bimetallic nanostructures was characterized using cyclic voltammetry measurements carried out in 0.1 M NaOH solution since gold and especially copper are then stable and do not dissolve, as has been already confirmed by other reports [49–53], and is in agreement with the Pourbaix diagram. The results obtained for bimetallic 5Au/5Cu and 5Cu/5Au structures are shown in Fig. 6 together with gold, copper and titanium nanodimpled samples thermally treated also at 450 °C and 600 °C. Comparing both temperature regimes, the distinctive faradaic activities were observed when the materials were annealed at 450 °C. The anodic peak observed at +0.3 V vs. Ag/AgCl/0.1 M KCl for 10Au electrode corresponds to the formation of Au_2O_3, while at 0 V the reduction of gold oxides is recognized [50] (Fig. 6a). Regarding the 10Cu sample, the signal at −0.7 V is recognized as reduction of Cu(II) to Cu(I) while the other at c.a. + 0.5 V is assigned to the oxidation of Cu(I) to Cu(II) [52]. Comparing the shapes of CV scans for materials annealed at 450 °C, it should be noted that the unique pattern for the bimetallic electrodes was identified. The similar shape of voltamperograms in the potential range below +1.2 V vs. RHE were reported by Liu et al. [15] for Au-Cu films, however in our work much higher current densities were obtained at the anodic limit established here at +0.8 V. For both Au-Cu arrangements barely visible oxidation peaks are present at ca. −0.25 V and −0.05 V and more pronounced signals are observed at ca. −0.20 V, +0.05 V and +0.6 V corresponding to the reduction processes. An analogous set of signals was found for $Au_{50}Cu_{50}$ and $Au_{25}Cu_{75}$ samples and those oxidation peaks were ascribed by Liu et al. [15] to the formation of $Cu(OH)_2$ and then surface part of electrode material exhibits a duplex nature consisting of Cu_2O core and an outer $CuO/Cu(OH)_2$ layer. However, the oxidation processes are less distinctive comparing to the reduction ones indicating that presence of gold atoms inhibits those reactions. It was also confirmed by Passini et al. [54] concluding that such electrochemical activity of copper species present in the bimetallic structure occurs due to their stabilization by gold ones. On the reverse CV scan, the appearance of the reduction peak at −0.2 V could be interpreted as the change from metallic Cu to CuO [55] while at +0.05 V the reduction of gold oxides is demonstrated. In this work, the XPS results confirm the presence of CuO and $Cu(OH)_2$ species as well as the Cu-Au alloy. Therefore, the detailed analysis of XPS spectra supports the proposed interpretation of the signals arising on the CV curve recorded for the bimetallic electrode. Polarizing the working electrode towards anodic limit particularly at +0.7 V vs. Ag/AgCl/0.1 M KCl, the OER is initiated. In this process the molecular oxygen is generated via electrochemical oxidation of hydroxyl ions present in the basic solution: $4OH^- \rightarrow O_2 + 2H_2O + 4e^-$ [56–58]. Such behaviour for other AuCu based structures was not reported in the literature and the electrochemical activity of such kind of electrodes is generally limited to the

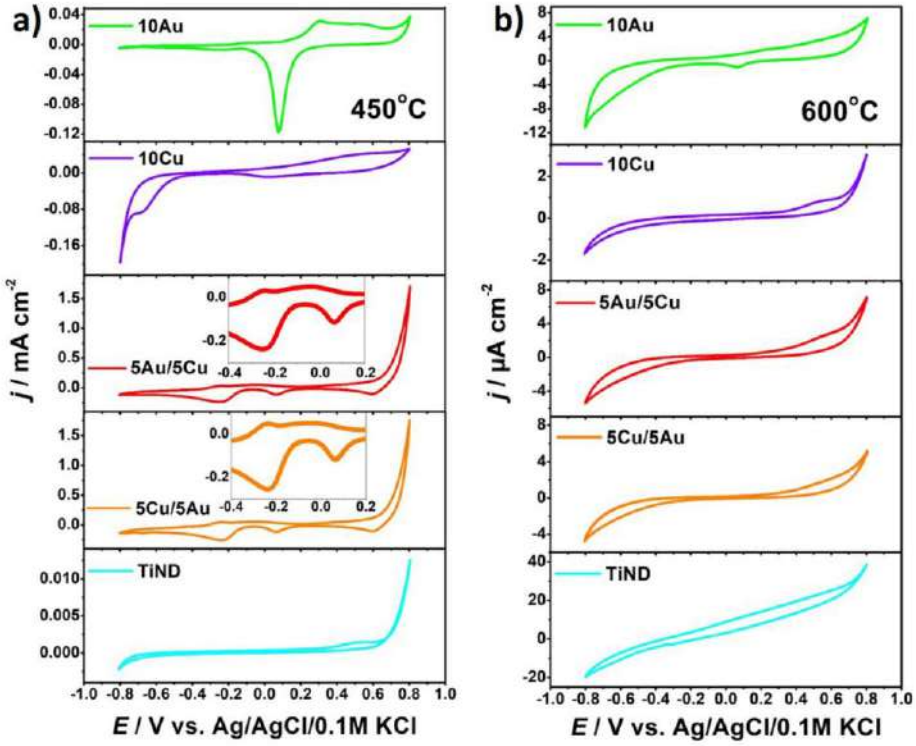

Fig. 6. Cyclic voltammetry curves registered in 0.1 M NaOH at the scan rate of 50 mV/s for samples annealed at a) 450°C and b) 600°C.

cathodic range and reduction processes as reported e.g. by Liu et al. [15], Chen et al. [59] and Wang et al. [60] However, when TiND based materials were annealed at 600 °C (see Fig. 6b) the recorded currents were much lower compared to those treated at 450 °C and almost no faradaic peaks were noticed. Only in the case of pure gold layer some peak current at ca. 0 V ascribed to the reduction of gold oxides was observed [61]. It could be stated that such low electrochemical response results from the formation of highly resistive titania film identified as the rutile phase [62,63]. The significantly diminished activity of both mono- and bimetallic mosaic structures does not favour application of high temperature for the material processing despite morphology inspection indicating the ordered distribution of nanoparticles over the hosted TiNDs.

Additionally, according to Łukaszewski et al. [64] the real surface area of 5Au/5Cu material was estimated basing on the relation between the double layer charging current and the scan rate. As can be observed in Fig. S3, the slope value for 5Au/5Cu is much higher comparing to flat Au disc electrode. The polished Au disc electrode (diameter 2 mm, $s = 0.0314\ cm^2$) acts here as the reference electrode material and since it is ideally flat – the geometric surface area is regarded as an electrochemically active one. Taking above into account and the values of slopes, the real surface area for 5Au/5Cu sample is 10.3 times higher comparing to the flat gold surface that positively impacts onto the overall electrochemical response.

In order to study the photoactivity of the fabricated materials, the linear voltammetry measurements in dark and under visible illumination were carried out (Fig. 7). For the reference samples, namely TiND, 10Au and 10Cu one may observe very low photoresponse (several dozens of $\mu A\ cm^{-2}$) when the thermal annealing was applied at 450 °C (Fig. 8). For the 10Au electrode (Fig. 8a) characteristic oxidation peak at +0.3 V arises at the same intensity in dark and under vis illumination while the photocurrent improvement starts above +0.6 V. However, the signal at +0.8 V might rather correspond to the oxidation of Au(1 1 0) [65] since any gas bubbles were not noticed at the electrode surface. Among other reference materials, for the 10Cu sample the activity towards HER below −0.4 V vs. Ag/AgCl/0.1 M KCl was recognised which is typical for copper-containing electrode materials [66] Under illumination of 10Cu the overpotential increases (Fig. 8b). However, from −0.4 V to the anodic regime the sample exhibits photoanode character [67] but its activity towards effective OER is negligible. The small changes between current density in dark and under electrode illumination for TiND (Fig. 8c) are noticed due to the very thin TiO_2 layer. It is well known that photocurrent is strongly determined by the layer thickness [68,69] thus the presence of a very thin passivation layer of titania does not enable the efficient visible light absorption and photocurrent generation. In all cases of the monometallic materials, namely 10Au, 10Cu and TiND some increase of photocurrent exists but it is much lower than observed for 5Au/5Cu and 5Cu/5Au structures.

To track the difference value, the comparison of current densities recorded at +0.8 V vs. Ag/AgCl/0.1 M KCl in dark and under irradiation were listed in Table 2. As could be observed, the 5Au/5Cu and 5Cu/5Au electrodes annealed at 450 °C showed an impressive increase of both the electrochemical and photoelectrochemical activity in the anodic range above +0.6 V and at cathodic potential values below −0.6 V while at −0.18 V the boosted oxidation process can be distinguished (Fig. 7a).

Taking into account the current density registered for 10Au ($0.04\ mA\ cm^{-2}$), the combination of Au with Cu results in more than a 30 times enhancement ($j = 1.23\ mA\ cm^{-2}$ for 5Cu/5Au) proving the synergising effect arising from the integration between both metals. Following that, the impressive acceleration of the oxygen evolution reaction [58,17] takes place. According to other reports such a feature could be ascribed to the AuCu [17] and CuO [70] activity, as those species have been already confirmed by XPS studies. It should be also underlined that the highest anodic current enhancement was achieved for the 5Au/5Cu electrode and the difference between the current density recorded in dark and under exposure to visible light reaches $120\ \mu A\ cm^{-2}$ whereas for the 5Cu/5Au configuration is lower and equals $90\ \mu A\ cm^{-2}$. This discrepancy results from the better separation of photogenerated charges onto the outer film composed of Cu species [71] in favour of 5Au/5Cu. We would like to highlight here that the formation of both Au/Cu nanomosaics requires only usage of a 5 nm thick copper layer and 5 nm thick gold layer in contrast to other bimetallic nanostructures where even microlong wires [72] or rods [73] are applied indicating high loading of precious metal but first of all usage of auric acid [74,75] Moreover, according to Gong et al. [17] and Pawar et al. [70] the OER onset potential was much higher and equals even +1.7 V vs. RHE (ca. + 1.4 vs. Ag/AgCl/0.1 M KCl) for AuCu branched nanostructures in 0.1 M KOH and +1.6 V vs. RHE (ca. +1.3 vs. Ag/AgCl/0.1 M KCl) for CuO nanosheet in 1 M KOH.

Additionally, the oxidation process significantly enhanced by light took place at the potential of −0.18 V for 5Au/5Cu and 5Cu/5Au. Described electrode behaviour is repeatable as was verified by sequentially registered LV curves while any material detachment out of TiND support was not observed. In dark conditions the current density equals only $35\ \mu A\ cm^{-2}$ and $50\ \mu A\ cm^{-2}$ for 5Au/5Cu and 5Cu/5Au respectively, whereas almost 0.3 and $0.23\ mA\ cm^{-2}$ was reached when the electrode was exposed to the radiation > 420 nm. Similarly, such a distinctive oxidation peak was not observed for pure gold or copper reference materials as well as other gold-copper heterojunctions or metal–metal oxide combinations such as Au-Cu_2O core shell nanowires [71] as well as Au-CuO/n-Si [76], Au-WzCuInS$_2$/ITO [77] ZnO/Au/p-nCu_2O and ZnO/Au/nCu_2O [78] electrodes. However, according to

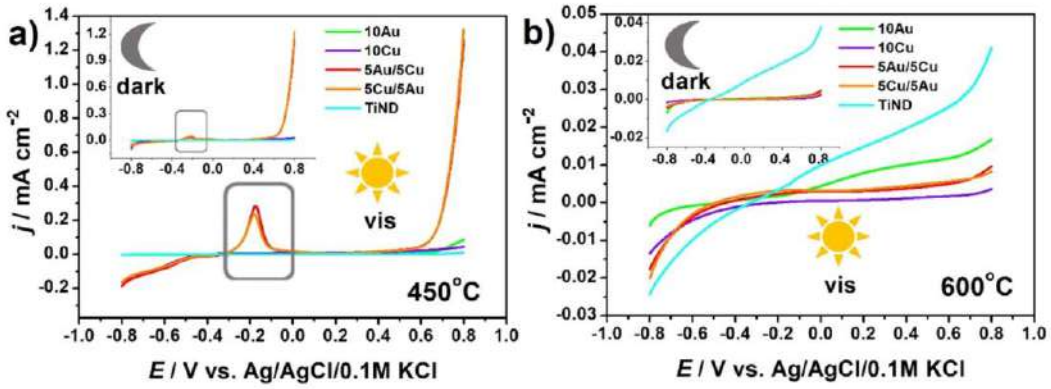

Fig. 7. Linear voltammetry curves registered in 0.1 M NaOH in dark and under visible illumination for samples annealed at a) 450 °C and b) 600 °C.

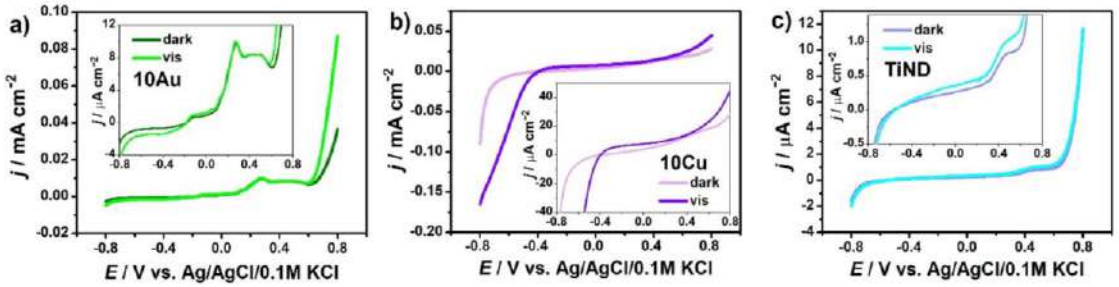

Fig. 8. Linear voltammetry curves registered in 0.1 M NaOH in dark and under visible illumination for samples annealed at 450 °C: a) 10Au, b) 10Cu, c) TiND.

Table 2
The values of current density at +0.8 V vs. Ag/AgCl/0.1 M KCl in dark and under visible light illumination for samples annealed at 450 °C (Fig. 7).

Sample	j (dark)/mA cm^{-2}	Sample	j (vis)/ mA cm^{-2}
10 Au	0.04	10 Au	0.09
10 Cu	0.03	10 Cu	0.04
5Au/5Cu	**1.14**	5Au/5Cu	**1.26**
5Cu/5Au	**1.23**	5Cu/5Au	**1.32**
TiND	0.01	TiND	0.01

Minggu et al. [79] this enhanced process is related to the Cu_2O oxidation ($Cu_2O + 2OH^- \rightarrow 2CuO + H_2O + 2e^-$) and the further current decrease may be related to the peeling of the copper oxide film. Following that, we regard that under irradiation the photogenerated holes are used in the oxidation process of Cu_2O while electrons are transferred via thin titania film towards the metallic substrate and in consequence a substantial current increase is recorded [80]. Since the absorbance spectra for 5Au/5Cu and 5Cu/5Au are very similar, the observed difference between those configurations may result from the various content of Au-Cu alloy species. As has been revealed by XPS inspection, the contribution of Au-Cu is in favour for arrangement where copper film was sputtered onto the gold. According to Sugano et al. [81] the synergistic effect within Au-Cu alloy positively impacts on the oxidation process while as was indicated by Liu et al. [82] copper affects intraband transition and ultimately promotes visible-light activity.

The other unique activity of Au/Cu systems was also recognized in the cathodic potential range. The values of current densities for particular materials treated at 450 °C recorded in dark and under visible irradiation when the electrode was polarized at −0.8 V vs. Ag/AgCl/0.1 M KCl were listed in Table 3 (also see Fig. 9). The cathodic current density for 5Au/5Cu increases from −50 to −190 µA cm^{-2} and for 5Cu/5Au changes from −60 to −170 µA cm^{-2} while for pure gold and bare titania never exceeded a few µA cm^{-2}. However, considering changes in the cathodic range for 10Cu sample similar behaviour to the bimetallic materials was observed and can be assigned to the Cu activity [83] Proposed interpretation is in accordance with the explanation given for other copper containing systems e.g. ZnO/Cu_2O-CuO with embedded Cu(I) and Cu(II) oxides [84] TiO_2/CuO/Cu mesoporous nanofibers [85] and CuNPs on glass carbon or platinum electrodes [83] used for the efficient photocatalytic or catalytic HER evolution. We would like to underline that the achieved enhancement of current in both anodic and cathodic range when the electrode is exposed to visible light is also higher than for other materials of similar composition, e.g. for the Au-Cu alloy deposited onto titanium dioxide nanosheets where the difference between response recorded under light and in dark equals only ca. 10 µA cm^{-2} and the time dependent attenuation of photoactivity was registered [86]. A similar slight increment of photocurrent density was reported by Fu et al. [87] for ZnO@Au@Cu_2O nanotubes and by Xue et al. [88] for the Cu_2O cubes decorated with Au NPs.

It should be also underlined that the most active bimetallic structure 5Au/5Cu annealed at 450 °C exhibits also high stability. The consecutive cyclic voltammetry scans almost overlap while the linear voltammetry curve recorded when the working electrode is exposed to the visible light (see Fig. S4) preserves its shape and corresponds to LV given in Fig. 7a. The continuation of multicyclic dynamic polarization of the material after LV scan also provides the same CV curves confirming resistance towards photocorosion.

Regarding the LV studies carried out for the TiND electrodes annealed at 600 °C, they all exhibit the resistor-like characteristics [89] (Fig. 7b). Moreover, as has been already verified via linear voltammetry measurements, the differences between current densities in dark and under electrode illumination for electrodes annealed at 600 °C were significantly smaller than for those kept at 450 °C. Thus, once again formation of the resistive rutile titania onto the Ti substrate negatively impacts on overall electrode photoresponse.

4. Conclusion

In this work, we proposed formation of the Au-Cu nanomosaic onto titanium dimples via a sequential procedure covering electrochemical oxidation of Ti foil, removal of titania nanotubes layer, sputtering of thin metal layers and finally 10 min. long processing in a furnace heated up to 450 °C or 600 °C. The selective etching of as-grown tubular layer results in the formation of a highly ordered titanium dimpled surface acting as a hosting platform for metal nanostructures. The different temperatures of annealing and various sequence of sputtered Au and Cu metal layers had a great impact on the morphology, optical and electrochemical properties. The treatment at 450 °C of titanium covered by both 5Au/5Cu or 5Cu/5Au compositions preserves the periodic system of nanocaves. However, when 600 °C was applied the gold-copper nanoparticles onto the whole substrate are distributed while Ti dimples are no longer distinguished. The modulation of the optical properties is revealed as a shift in the absorbance band maximum for the bimetallic materials from ca. 470 nm towards up to ca. 900 nm with simultaneous broadening, when low and high temperature annealing was performed. The XPS spectra recorded for Au-Cu based structure confirmed the presence of diverse Cu species, namely Au-Cu alloy, CuO, $Cu(OH)_2$. The activity of all samples was verified in 0.1 M NaOH while

Table 3
The values of current densities at −0.8 V vs. Ag/AgCl/0.1 M KCl in dark and under visible light illumination for samples annealed at 450 °C (Fig. 9a).

Sample	j (dark)/µA cm^{-2}	Sample	j (vis)/µA cm^{-2}
10 Au	−2.5	10 Au	−4.7
10 Cu	−90	10 Cu	−160
5 Au/5 Cu	**−50**	5 Au/5 Cu	**−190**
5 Cu/5 Au	**−60**	5 Cu/5 Au	**−170**
TiND	−1.6	TiND	−2

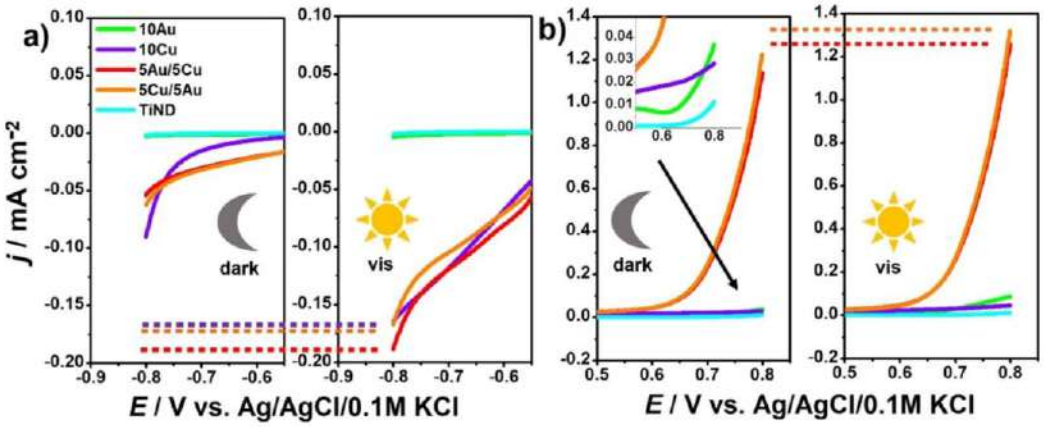

Fig. 9. The selected segments from a) cathodic and b) anodic range of linear voltammetry curves (from Fig. 7a) registered in 0.1 M NaOH in dark and under visible illumination for samples annealed at 450 °C.

the electrode was maintained both in dark and when exposed to visible light, and unique faradaic processes related to the change of the gold and copper oxidation state as well as superior photoresponse of the bimetallic structures were tracked. The electrochemical behaviour of both bimetallic configurations is similar but some noticeable difference in photocurrent enhancement in favour of the 5Au/5Cu sample in both anodic and cathodic limit is observed. The synergistic effect caused by a combination of Au and Cu metals manifests as a current density almost 15 times higher than that recorded for pure gold nanostructures when the electrode is polarized at +0.8 V vs. Ag/AgCl/0.1 M KCl. Summarizing, we presented the unique, combined electrochemical-thermal approach resulting in the formation of stable bimetallic mosaic structure over the nanotextured and elastic Ti foil exhibiting broad band absorbance within the visible range and boosted activity towards oxygen evolution reaction under low polarization conditions.

Declaration of Competing Interest

The authors declare that they have no known competing financial interests or personal relationships that could have appeared to influence the work reported in this paper.

Appendix A. Supplementary data

Supplementary data to this article can be found online at https://doi.org/10.1016/j.cej.2020.125673.

References

[1] C.F. Tan, A.K.S.S. Zin, Z. Chen, C.H. Liow, H.T. Phan, H.R. Tan, G.W. Ho, Inverse stellation of CuAu-ZnO multimetallic-semiconductor nanostartube for plasmon-enhanced photocatalysis, ACS Nano 12 (2018) 4512–4520, https://doi.org/10.1021/acsnano.8b00770.

[2] Z. Kang, X. Yan, Y. Wang, Y. Zhao, Z. Bai, Y. Liu, Y. Zhang, Self-powered photoelectrochemical biosensing platform based on Au NPs@ZnO nanorods array, Nano Res. 9 (2016) 344–352, https://doi.org/10.1007/s12274-015-0913-9.

[3] D.S. Lee, W. Kim, B.G. Cha, J. Kwon, S.J. Kim, M. Kim, J.H. Park, Self-position of Au NPs in perovskite solar cells: optical and electrical contribution, ACS Appl. Mater. Interfaces 8 (2016) 449–454, https://doi.org/10.1021/acsami.5b09365.

[4] S. Xu, L. Guo, Q. Sun, Z.L. Wang, Piezotronic effect enhanced plasmonic photocatalysis by AuNPs/$BaTiO_3$ heterostructures, Adv. Funct. Mater. 29 (2019) 1808737, https://doi.org/10.1002/adfm.201808737.

[5] D. Wen, W. Liu, A.-K. Herrmann, D. Haubold, M. Holzschuh, F. Simon, A. Eychmüller, Simple and sensitive colorimetric detection of dopamine based on assembly of cyclodextrin-modified Au nanoparticles, Small 12 (2016) 2439–2442, https://doi.org/10.1002/smll.201503874.

[6] A. Müller, S. Peglow, M. Karnahl, A. Kruth, H. Junge, V. Brüser, C. Scheu, Morphology, optical properties and photocatalytic activity of photo- and plasma-deposited Au and Au/Ag core/shell nanoparticles on titania layers, Nanomaterials 8 (2018) 502, https://doi.org/10.3390/nano8070502.

[7] J. Ding, X. Li, L. Chen, X. Zhang, X. Tian, Photocatalytic hydrogen production over plasmonic AuCu/$CaIn_2S_4$ composites with different AuCu atomic arrangements, Appl. Catal. B 224 (2018) 322–329, https://doi.org/10.1016/j.apcatb.2017.10.045.

[8] A.L. Strickler, M. Escudero-Escribano, T.F. Jaramillo, Core-shell Au@metal-oxide nanoparticle electrocatalysts for enhanced oxygen evolution, Nano Lett. 17 (2017) 6040–6046, https://doi.org/10.1021/acs.nanolett.7b02357.

[9] L. Chen, X. Wei, X. Zhou, Z. Xie, K. Li, Q. Ruan, Z. Zheng, Large-area patterning of metal nanostructures by dip-pen nanodisplacement lithography for optical applications, Small 13 (2017) 1702003, https://doi.org/10.1002/smll.201702003.

[10] S. Chen, S.V. Jenkins, J. Tao, Y. Zhu, J. Chen, Anisotropic seeded growth of Cu–M (M = Au, Pt, or Pd) bimetallic nanorods with tunable optical and catalytic properties, J. Phys. Chem. C 117 (2013) 8924–8932, https://doi.org/10.1021/jp4013653.

[11] M. Marelli, A. Jouve, A. Villa, R. Psaro, A. Balerna, L. Prati, C. Evangelisti, Hybrid Au/CuO nanoparticles: effect of structural features for selective benzyl alcohol oxidation, J. Phys. Chem. C 123 (2019) 2864–2871, https://doi.org/10.1021/acs.jpcc.8b09449.

[12] F. Du, H. Wang, X. Jin, W. Deng, Ch. Li, Z. Ren, H. Yan, B. Yin, Selective oxidation of 1,2-propanediol to lactic acid over synergistic AuCu/TiO_2 catalysts, Catal. Lett. 149 (2019) 1037–1045, https://doi.org/10.1007/s10562-019-02670-5.

[13] S. Peiris, J. McMurtrie, H.Y. Zhu, Metal nanoparticle photocatalysts: emerging processes for green organic synthesis, Catal. Sci. Technol. 6 (2016) 320–338, https://doi.org/10.1039/C5CY02048D.

[14] Y.H. Su, W.L. Wang, Surface plasmon resonance of Au-Cu bimetallic nanoparticles predicted by a quasi-chemical model, Nanoscale Res. Lett. 8 (2013) 408, https://doi.org/10.1186/1556-276X-8-408.

[15] K. Liu, M. Ma, L. Wu, M. Valenti, D. Cardenas-Morcoso, J.P. Hofmann, J. Bisquert, S. Gimenez, W.A. Smith, Electronic effects determine the selectivity of planar Au–Cu bimetallic thin films for electrochemical CO_2 reduction, ACS Appl. Mater. Interfaces 11 (2019) 16546–16555, https://doi.org/10.1021/acsami.9b01553.

[16] B. Wang, R. Li, Z. Zhang, W. Zhang, X. Yan, X. Wu, R. Zheng, Novel Au/Cu_2O multi-shelled porous heterostructures for enhanced efficiency of photoelectrochemical water splitting, J. Mater. Chem. A 5 (2017) 14415–14421, https://doi.org/10.1039/C7TA02254A.

[17] H. Gong, W. Zhang, F. Li, R. Yang, Enhanced electrocatalytic performance of self-supported AuCuCo for oxygen reduction and evolution reactions, Electrochim. Acta 252 (2017) 261–267, https://doi.org/10.1016/j.electacta.2017.08.194.

[18] Y. Gafner, S. Gafner, L. Redel, I. Zamulin, Dual structural transition in small nanoparticles of Cu-Au alloy, J. Nanopart. Res. 20 (2018) 51, https://doi.org/10.1007/s11051-018-4161-2.

[19] P.P. Fedorov, S.N. Volkov, Au–Cu phase diagram, Rus. J. Inorg. Chem. 61 (2016) 772–775, https://doi.org/10.1134/S0036023616060061.

[20] D. Kim, C. Xie, N. Becknell, Y. Yu, M. Karamad, K. Chan, E.J. Crumlin, J.K. Norskov, P. Yang, Electrochemical activation of CO_2 through atomic ordering transformations of AuCu nanoparticles, J. Am. Chem. Soc. 139 (2017) 8329–8336, https://doi.org/10.1021/jacs.7b03516.

[21] S. Chen, Q. Sun, L. Xiao, J. Sun, Thermal stability of microstructure and mechanical properties of ultrafine-grained pure titanium, In Proceedings 2013ThermalSO.

[22] W. Lipińska, K. Siuzdak, J. Ryl, P. Barski, G. Śliwiński, K. Grochowska, The optimization of enzyme immobilization at Au-Ti nanotextured platform and its impact onto the response towards glucose in neutral media, Mater. Res. Express 6 (2019) 1150e3, https://doi.org/10.1088/2053-1591/ab4fab.

[23] K. Siuzdak, D. Döhler, J. Bachmann, J. Karczewski, K. Grochowska, Light-improved glucose sensing on ordered Au-Ti heterostructure, Optik 206 (2020) 164166, , https://doi.org/10.1016/j.ijleo.2019.164166.

[24] Ł. Skowroński, A.A. Wachowiak, A. Grabowski, Characterization of optical and

microstructural properties of semitransparent TiO2/Ti/glass interference decorative coatings, Appl. Surf. Sci. 388 (2016) 731-470. https://doi.org/10.1016/j.apsusc.2016.05.159.
[25] H.N. Umh, S. Yu, Y.H. Kim, S.Y. Lee, J. Yi, Tuning the structural color of a 2D photonic crystal using a bowl-like nanostructure, ACS Appl. Mater. Interfaces 8 (2016) 15802–15808, https://doi.org/10.1021/acsami.6b03717.
[26] V.V. Malkar, T. Mukherjee, S. Kapoor, Aminopolycarboxylic acids and alginate composite-mediated green synthesis of Au and Ag nanoparticles, J. Nanostruct. Chem. 5 (2015) 1–6, https://doi.org/10.1007/s40097-014-0122-1.
[27] N.A. Saad, M.H. Dar, E. Ramya, S.R.G. Naraharisetty, D. Narayana Rao, Saturable and reverse saturable absorption of a Cu_2O–Ag nanoheterostructure, J. Mater. Sci. 54 (2018) 188–199, https://doi.org/10.1007/s10853-018-2811-5.
[28] R. Li, X. Yan, L. Yu, Z. Zhang, Q. Tang, Y. Pan, The morphology dependence of cuprous oxide and its photocatalytic properties, CrystEngComm 15 (2013) 10049–10058, https://doi.org/10.1039/C3CE41470A.
[29] A. Gołąbiewska, A. Malankowska, M. Jarek, W. Lisowski, G. Nowaczyk, S. Jurga, A. Zaleska-Medynska, The effect of gold shape and size on the properties and visible light-induced photoactivity of Au-TiO_2, Appl. Catal. B 196 (2016) 27–40, https://doi.org/10.1016/j.apcatb.2016.05.013.
[30] S. Padikkaparambil, B. Narayanan, Z. Yaakob, S. Viswanathan, S.M. Tasirin, Au/TiO_2 reusable photocatalysts for dye degradation, Int. J. Photoenergy 2013 (2013) 752605, , https://doi.org/10.1155/2013/752605.
[31] S. Mohan, Y. Singh, D.K. Verma, S.H. Hasan, Synthesis of CuO nanoparticles through green route using Citrus limon juice and its application as nanosorbent for Cr(VI) remediation: process optimization with RSM and ANN-GA based model, Process Saf. Environ. 96 (2015) 156–166, https://doi.org/10.1016/j.psep.2015.05.005.
[32] H. Liu, A. Wang, Q. Sun, T. Wang, H. Zeng, Cu nanoparticles/fluorine-doped tin oxide (FTO) nanocomposites for photocatalytic H_2 evolution under visible light irradiation, Catalysts 7 (2017) 385, https://doi.org/10.3390/catal7120385.
[33] V.V. Pham, D.P. Bui, H.H. Tran, M.T. Cao, T.K. Nguyen, Y.S. Kim, V.H. Le, Photoreduction route for Cu_2O/TiO_2 nanotubes junction for enhanced photocatalytic activity, RSC Adv. 8 (2018) 12420–12427, https://doi.org/10.1039/C8RA01363B.
[34] Y.-H. Chang, C.-M. Wang, Y.-K. Hsu, Y.-H. Pai, J.-Y. Lin, C.-H. Lin, Graphene oxide as the passivation layer for Cu_xO photocatalyst on a plasmonic Au film and the corresponding photoluminescence study, Opt. Express 23 (2015) A1245–A1252, https://doi.org/10.1364/OE.23.0A1245.
[35] S.K. Sinha, C. Srivastava, S. Sampath, K. Chattopadhyay, Tunability of monodispersed intermetallic AuCu nanoparticles through understanding of reaction pathways, RSC Adv. 5 (2015) 4389–4395, https://doi.org/10.1039/C4RA12059K.
[36] C. Liu, H. Dong, N. Wu, Y. Cao, X. Zhang, Plasmonic resonance energy transfer enhanced photodynamic therapy with Au@SiO_2@Cu_2O/perfluorohexane nanocomposites, ACS Appl. Mater. Interfaces 10 (2018) 6991–7002, https://doi.org/10.1021/acsami.8b00112.
[37] M.Z. Hossain, N. Shimizu, Covalent immobilization of gold nanoparticles on graphene, J. Phys. Chem. C 123 (2019) 3512–3516, https://doi.org/10.1021/acs.jpcc.8b09619.
[38] X. Yan, J. Sun, Y. Meng, Experimental insight into the chemical corrosion mechanism of copper with on oil-in-water emulsion solution, RSC Adv. 8 (2018) 9833–9840, https://doi.org/10.1039/C8RA00432C.
[39] H. Park, S.E. Kim, Two-step plasma treatment on copper surface for low temperature Cu thermo-compression bonding, IEEE T. Comp. Pack. Man. 10 (2020) 332–338, https://doi.org/10.1109/TCPMT.2019.2928323.
[40] Y.L. Liu, Y.C. Zhu, L.B. Qu, R. Yang, X.D. Yu, W.W. Zhao, Unique redox Reaction between CuO photocathode and cysteine: insight into the mechanism for cathodic photoelectrochemical bioanalysis, ACS Appl. Bio Mater. 2 (2019) 2703–2707, https://doi.org/10.1021/acsabm.9b00428.
[41] S. Hejazi, S. Mohajernia, Y. Wu, P. Andryskova, G. Zoppellaro, I. Hwang, O. Tomanec, R. Zboril, P. Schmuki, Intrinsic Cu nanoparticle decoration of TiO_2 nanotubes: a platform for efficient noble metal free photocatalytic H_2 production, Electrochem. Commun. 98 (2019) 82–86, https://doi.org/10.1016/j.elecom.2018.11.020.
[42] E. Völker, F.J. Williams, E.J. Calvo, T. Jacob, D.J. Schiffrin, O_2 induced Cu surface segregation in Au–Cu alloys studied by angle resolved XPS and DFT modelling, Phys. Chem. Chem. Phys. 14 (2012) 7448–7455, https://doi.org/10.1039/C2CP40565B.
[43] I. Barroso-Martín, E. Moretti, A. Talon, L. Storaro, E. Rodríguez-Castellón, A. Infantes-Molina, Au and AuCu nanoparticles supported on SBA-15 ordered mesoporous titania-silica as catalysts for methylene blue photodegradation, Materials 11 (2018) 890, https://doi.org/10.3390/ma11060890.
[44] R.J. Chimentao, F. Medina, J.L.G. Fierro, J. Llorca, J.E. Sueiras, Y. Cesteros, P. Salagre, Propene epoxidation by nitrous oxide over Au–Cu/TiO_2 alloy catalysts, J. Mol. Catal. A Chem. 274 (2007) 159–168, https://doi.org/10.1016/j.molcata.2007.05.008.
[45] M.C. Biesinger, Advanced analysis of copper X-ray photoelectron spectra, Surf. Interface Anal. 49 (2017) 1325–1334, https://doi.org/10.1002/sia.6239.
[46] Y. Shi, Y. Zhang, X. Zhang, J. Cai, S. Lin, A non-noble metal oxide Ti_2O_3/rGO composite as efficient and highly stable electrocatalyst for oxygen reduction, Int. J. Hydrog. Energy 44 (2019) 28134–28142, https://doi.org/10.1016/j.ijhydene.2019.09.079.
[47] Y. Wang, M. Zhou, Y. He, Z. Zhou, Z. Sun, In situ loading CuO quantum dots on TiO_2 nanosheets as cocatalyst for improved photocatalytic water splitting, J. Alloys Compd. 813 (2019) 152184, , https://doi.org/10.1016/j.jallcom.2019.152184.
[48] A. Mezni, M.M. Ibrahim, M. El-Kemary, A.A. Shaltout, N.Y. Mostafa, J. Ryl, T. Kumeria, T. Altalhi, M.A. Amin, Cathodically activated Au/TiO_2 nanocomposite synthesized by a new facile solvothermal method: An efficient electrocatalyst with Pt-like activity for hydrogen generation, Electrochim. Acta 290 (2018) 404–418, https://doi.org/10.1016/j.electacta.2018.08.083.
[49] K. Grochowska, J. Ryl, J. Karczewski, G. Śliwiński, A. Cenian, K. Siuzdak, Non-enzymatic flexible glucose sensing platform based on nanostructured TiO_2 – Au composite, J. Electroanal. Chem. 837 (2019) 230–239, https://doi.org/10.1016/j.jelechem.2019.02.040.
[50] N. Shen, H. Xu, W. Zhao, Y. Zhao, X. Zhang, Highly responsive and ultrasensitive non-enzymatic electrochemical glucose sensor based on Au foam, Sensors 19 (2019) 1203, https://doi.org/10.3390/s19051203.
[51] Y. He, G. Wei, J. Lin, M. Sun, Z. Li, Cu and Ni nanoparticles deposited on ITO electrode for nonenzymatic electrochemical carbohydrates sensor applications, Electroanalysis 29 (2017) 965–974, https://doi.org/10.1002/elan.201600606.
[52] L. Zhang, C. Ye, X. Li, Y. Ding, H. Liang, G. Zhao, Y. Wang, A CuNi/C nanosheet array based on a metal–organic framework derivate as a supersensitive non-enzymatic glucose sensor, Nano-Micro Lett. 10 (2018) 28, https://doi.org/10.1007/s40820-017-0178-9.
[53] C. Lu, Z. Li, L. Ren, N. Su, D. Lu, Z. Liu, In situ oxidation of Cu_2O crystal for electrochemical detection of glucose, Sensors 19 (2019) 2926, https://doi.org/10.3390/s19132926.
[54] T. Pasini, M. Piccinini, M. Blosi, R. Bonelli, S. Albonetti, N. Dimitratos, J.A. Lopez-Sanchez, M. Sankar, Q. He, C.J. Kiely, G.J. Hutchings, F. Cavani, Selective oxidation of 5-hydroxymethyl-2-furfural using supported gold–copper nanoparticles, Green Chem. 13 (2011) 2091–2099, https://doi.org/10.1039/C1GC15355B.
[55] S.D. Giri, A. Sarkar, Electrochemical study of bulk and monolayer copper in alkaline solution, J. Electrochem. Soc. 163 (2016) H252, https://doi.org/10.1149/2.0071605jes.
[56] X. Zhang, A. Shan, S. Duan, H. Zhao, R. Wang, W.M. Lau, Au@Co_2P core/shell nanoparticles as a nano-electrocatalyst for enhancing the oxygen evolution reaction, RSC Adv. 9 (2019) 40811–40818, https://doi.org/10.1039/C9RA07535F.
[57] J. Pei, J. Mao, X. Liang, C. Chen, Q. Peng, D. Wang, Y. Li, Ir–Cu nanoframes: one-pot synthesis and efficient electrocatalysts for oxygen evolution reaction, Chem. Commun. 52 (2016) 3793–3796, https://doi.org/10.1039/C6CC00552G.
[58] H. Gong, S. Lu, P. Strasser, R. Yang, Highly efficient AuNi-Cu_2O electrocatalysts for the oxygen reduction and evolution reactions: Important role of interaction between Au and Ni engineered by leaching of Cu_2O, Electrochim. Acta 283 (2018) 1411–1417, https://doi.org/10.1016/j.electacta.2018.07.083.
[59] H. Chen, M. Nishijima, G. Wang, S. Khene, M. Zhu, X. Deng, X. Zhang, W. Wen, Y. Luo, Q. He, The ordered and disordered nano-intermetallic AuCu/C catalysts for the oxygen reduction reaction: The differences of the electrochemical performance, J. Electrochem. Soc. 164 (2017) F1654, https://doi.org/10.1149/2.1331714jes.
[60] G. Wang, L. Xiao, B. Huang, Z. Ren, X. Tang, L. Zhuang, J. Lu, AuCu intermetallic nanoparticles: surfactant-free synthesis and novel electrochemistry, J. Mater. Chem. 22 (2012) 15769–15774, https://doi.org/10.1039/C2JM32264A.
[61] L.D. Burke, J.M. Moran, P.F. Nugent, Cyclic voltammetry responses of metastable gold electrodes in aqueous media, J. Solid State Electrochem. 7 (2003) 529–538, https://doi.org/10.1007/s10008-003-0359-y.
[62] J. Grotberg, A. Hamlekhan, A. Butt, S. Patel, D. Royhman, T. Shokuhfar, C. Sukotjo, C. Takoudis, M.T. Mathew, Thermally oxidized titania nanotubes enhance the corrosion resistance of Ti6Al4V, Mater. Sci. Eng. C 59 (2016) 677–689, https://doi.org/10.1016/j.msec.2015.10.056.
[63] K. U. Savitha, H. Gurumallesh Prabu, One-pot synthesis of PANI–TiO2 (anatase) hybrid of low electrical resistance using TiCl4 as precursor, Mater. Chem. Phys. 130 (2011) 275-279. https://doi.org/10.1016/j.matchemphys.2011.06.037.
[64] M. Łukaszewski, M. Soszko, A. Czerwiński, Electrochemical methods of real surface area determination of noble metal electrodes – an overview, Int. J. Electrochem. Sci. 11 (2016) 4442–4469 https://doi.org/10.20964/2016.06.71.
[65] N. Mayet, K. Servat, K.B. Kokoh, T.W. Napporn, Probing the surface of noble metals electrochemically by underpotential deposition of transition metals, Surfaces 2 (2019) 257–276, https://doi.org/10.3390/surfaces2020020.
[66] F. Finger, K. Welter, F. Urbain, V. Smirnov, B. Kaiser, W. Jaegermann, Photoelectrochemical water splitting using adapted silicon based multi-junction solar cell structures: development of solar cells and catalysts, upscaling of combined photovoltaic-electrochemical devices and performance stability, Z. Phys. Chem. (2019), https://doi.org/10.1515/zpch-2019-1453.
[67] S. Jia, X. Li, B. Zhang, J. Yang, S. Zhang, S. Li, Z. Zhang, TiO_2/CuS heterostructure nanowire array photoanodes toward water oxidation: the role of CuS, Appl. Surf. Sci. 463 (2019) 829–837, https://doi.org/10.1016/j.apsusc.2018.09.003.
[68] M. Morozova, P. Kluson, J. Krysa, P. Dzik, M. Vesely, O. Solcova, Thin TiO_2 films prepared by inkjet printing of the reverse micelles sol–gel composition, Sens. Actuat. B Chem. 160 (2011) 371–378, https://doi.org/10.1016/j.snb.2011.07.063.
[69] H. Krysova, M. Zlamalova, H. Tarabkova, J. Jirkovsky, O. Frank, M. Kohout, L. Kavan, Rutile TiO_2 thin film electrodes with excellent blocking function and optical transparency, Electrochim. Acta 321 (2019) 134685, , https://doi.org/10.1016/j.electacta.2019.134685.
[70] S.M. Pawar, B.S. Pawar, B. Hou, J. Kim, A.T. Aqueel Ahmed, H.S. Chavan, Y. Jo, S. Cho, A.I. Inamdar, J.L. Gunjakar, H. Kim, S.N. Cha, H. Im, Self-assembled two-dimensional copper oxide nanosheet bundles as an efficient oxygen evolution reaction (OER) electrocatalyst for water splitting applications, J. Mater. Chem. A 5 (2017) 12747–12751, https://doi.org/10.1039/C7TA02835K.
[71] S.Z. Oener, S.A. Mann, B. Sciacca, C. Sfiligoj, J. Hoang, E.C. Garnett, Au-Cu_2O core-shell nanowire photovoltaics, Appl. Phys. Lett. 106 (2015) 023501, , https://doi.org/10.1063/1.4905652.
[72] S.Y. Tee, E. Ye, P.H. Pan, C.J.J. Lee, H.K. Hui, S.Y. Zhang, L.D. Koh, Z. Dong, M.Y. Han, Fabrication of bimetallic Cu/Au nanotubes and their sensitive, selective, reproducible and reusable electrochemical sensing of glucose, Nanoscale 7 (2015)

11190–11198, https://doi.org/10.1039/C5NR02399H.
[73] Y. Tang, Q. Liu, X. Liu, X. Yang, M. Wei, M. Zhnag, Copper oxide coated gold Nanorods like a film: a facile route to nanocomposites for electrochemical application, J. Electroanal. Chem. 806 (2017) 814, https://doi.org/10.1016/j.jelechem.2017.10.032.
[74] A.S. Rajpurohit, N.S. Punde, A.K. Srivastava, An electrochemical sensor with a copper oxide/gold nanoparticle-modified electrode for thesimultaneous detection of the potential diabeticbiomarkers methylglyoxal and its detoxificationenzyme glyoxalase, New J. Chem. 43 (2019) 16572–16582, https://doi.org/10.1039/C9NJ03553B.
[75] I. Nadjovski, P.R. Selvakannan, S.K. Bhargava, A.P. O'Mullane, Formation of nanostructured porous Cu–Au surfaces: the influence of cationic sites on (electro)-catalysis, Nanoscale 4 (2012) 6298–6306, https://doi.org/10.1039/C2NR31409F.
[76] R.A. Ismail, R.S. Abdul-Hamed, Laser ablation of Au–CuO core–shell nanocomposite in water for optoelectronic devices, Mater. Res. Express 4 (2017) 125020, , https://doi.org/10.1088/2053-1591/aa9e14.
[77] A.B. Ghosh, N. Saha, A. Sarkar, A.K. Dutta, S.K. Maji, B. Adhikary, Observation of enhanced photocurrent response in M-$CuInS_2$ (M = Au, Ag) heteronanostructures: phase selective synthesis and application, New J. Chem. 41 (2017) 692–701, https://doi.org/10.1039/C6NJ02439D.
[78] J.S. Yoon, J.W. Lee, Y.M. Sung, Enhanced photoelectrochemical properties of Z-scheme ZnO/p-n Cu_2O PV-PEC cells, J. Alloys Compd. 771 (2019) 869–876, https://doi.org/10.1016/j.jallcom.2018.09.021.
[79] L.J. Minggu, K.H. Ng, H.A. Kadir, M. Bin Kassim, Bilayer n-WO_3/p-Cu_2O photoelectrode with photocurrent enhancement in aqueous electrolyte photoelectrochemical reaction, Ceramic Intern. 40 (2014) 16015–16021, https://doi.org/10.1016/j.ceramint.2014.07.135.
[80] L. Liu, X. Gu, C. Sun, H. Li, Y. Deng, F. Gao, L. Dong, In situ loading of ultra-small Cu_2O particles on TiO_2nanosheets to enhance the visible-light photoactivity, Nanoscale 4 (2012) 6351–6359, https://doi.org/10.1039/C2NR31859H.
[81] Y. Sugano, Y. Shiraishi, D. Tsukamoto, S. Ichikawa, S. Tanaka, T. Hirai, Supported Au–Cu bimetallic alloy nanoparticles: an aerobic oxidation catalyst with regenerable activity by visible-light irradiation, Angew. Chem. 125 (2013) 5403–5407, https://doi.org/10.1002/ange.201301669.
[82] M. Liu, W. Zhou, T. Wang, D. Wang, L. Liu, J. Ye, High performance Au-Cu alloy for enhanced visible-light water splitting driven by coinage metals, Chem. Commun. 52 (2016) 4694–4697, https://doi.org/10.1039/C6CC00717A.
[83] B. Kumar, S. Saha, M. Basu, A.K. Ganguli, Enhanced hydrogen/oxygen evolution and stability of nanocrystalline (4–6 nm) copper particles, J. Mater. Chem. A 1 (2013) 4728–4735, https://doi.org/10.1039/C3TA01194A.
[84] H. Yoo, S. Kahng, K.J. Hyeun, Z-scheme assisted ZnO/Cu_2O-CuO photocatalysts to increase photoactive electrons in hydrogen evolution by water splitting, Sol. Energy Mater. Sol. Cells 204 (2020) 110211, , https://doi.org/10.1016/j.solmat.2019.110211.
[85] H. Hou, M. Shang, F. Gao, L. Wang, Q. Liu, J. Zheng, Z. Yang, W. Yang, Highly efficient photocatalytic hydrogen evolution in ternary hybrid TiO_2/CuO/Cu thoroughly mesoporous nanofibers, ACS Appl. Mater. Interfaces 8 (2016) 20128–20137, https://doi.org/10.1021/acsami.6b06644.
[86] D. Zeng, L. Yang, P. Zhou, D. Hu, Y. Xie, S. Li, L. Jiang, Y. Ling, J. Zhao, Au-Cu alloys deposited on titanium dioxide nanosheets for efficient photocatalytic hydrogen evolution, Int. J. Hydrog. Energy 43 (2018) 15155–15163, https://doi.org/10.1016/j.ijhydene.2018.06.078.
[87] S. Fu, J. Chen, H. Han, W. Wang, H. Shi, J. Fu, Y. Jia, ZnO@Au@Cu_2O nanotube arrays as efficient visible-light-driven photoelectrod, J. Alloys Compd. 799 (2019) 183–192, https://doi.org/10.1016/j.jallcom.2019.05.340.
[88] J. Xue, D. Jing, H. Xie, W. Ni, X. Li, Exponential dependence of photocatalytic activity on linker chain length of Au-linker-Cu_2O plasmonic photocatalysts with sub-nanometer precision, Catal. Lett. 148 (2018) 363–3369, https://doi.org/10.1007/s10562-018-2560-8.
[89] A.J. Bard, L.R. Faulkner, Electrochemical Methods, Fundamentals and Applications, Second edition, Department of Chemistry and Biochemistry University of Texas at Austin, John Wiley & Sons, 2001.

Supporting information to the article A1

Thermally tuneable optical and electrochemical properties of Au-Cu nanomosaic formed over the host titanium dimples

Wiktoria Lipińska[1], Katarzyna Grochowska[1], Jakub Karczewski[2], Jacek Ryl[3], Adam Cenian[1] and Katarzyna Siuzdak[1]

[1]Centre for Plasma and Laser Engineering, The Szewalski Institute of Fluid-Flow Machinery Polish Academy of Sciences, Fiszera 14 St., 80-231 Gdańsk, Poland

[2]Faculty of Applied Physics and Mathematics, Gdańsk University of Technology, Narutowicza 11/12 St., 80-233 Gdańsk, Poland

[3]Faculty of Chemistry, Gdańsk University of Technology, Narutowicza 11/12 St., 80-233 Gdańsk, Poland

TABLE OF CONTENTS

S1. Experimental

X-ray diffraction (XRD) spectra were registered, using Bruker D2PHASER diffractometer. It operated with Cu Kα radiation at 30 kV and 10 mA. The XRD patterns were collected at 2θ angle within the range of 10° - 90°, while scanning step was 0.02° and counting time was 0.4 s per step.

S2. XRD measurements

XRD analysis indicated mostly Ti in the case of all samples, see Fig. S1, since titanium foil acts here as a Cu/Au support. The peaks at 35.1°, 38.4°, 40.2°, 52.9°, 62.9°, 70.7° and 76.2° correspond to the following crystal orientations of Ti: (100), (002), (101), (102), (110), (103) and (200), respectively. For 10Au, 10Cu, 5Au/5Cu, 5Cu/5Au and TiND annealed at 600°C a small diffraction peak found at 27.6° can be indexed to the rutile phase[1]. The weak diffraction peak found at 44.3° for XRD patterns recorded for 10Au(450°C), 5Au/5Cu(450°C), 5Cu/5Au(450°C), 10Au(600°C), 5Au/5Cu(600°C) and 5Cu/5Au(600°C) corresponds to Au(200)[2]. Another diffraction signal which is observed at 29.2° is related to $Cu_2O(110)$[3]. Nevertheless, its presence is hardly distinguishable. Summarizing, all patters are very similar for Au/Cu based materials and when only Au and Cu species are present onto TiND irrespectively on the applied temperature, while the signals attributed to the Ti substrates are the most intensive among others.

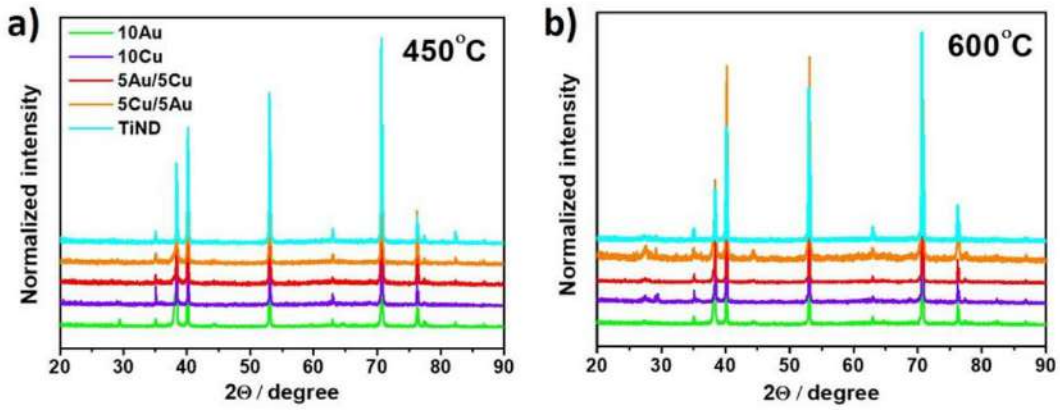

Fig. S1. XRD patterns for 10Au, 10Cu, 5Au/5Cu, 5Cu/5Au, TiND samples annealed at a) 450°C and b) 600°C.

S3. The Auger spectra

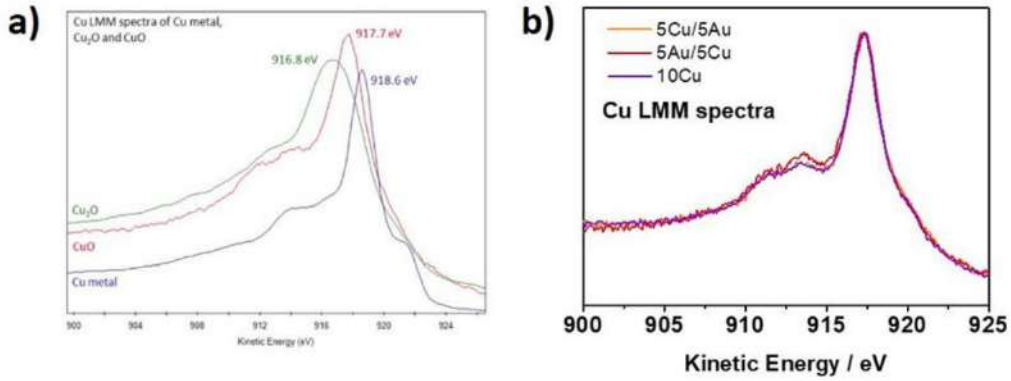

Fig. S2. The Auger spectra recorded for CuLMM a) literature[4] and b) experimental data for 5Au/5Cu, 5Cu/5Au, 10Cu samples annealed at 450°C.

S4. Active surface area determination

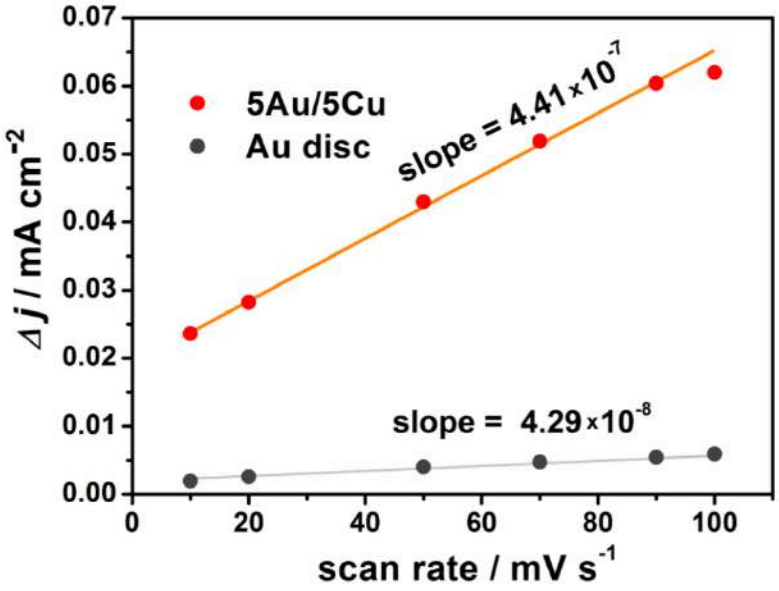

Fig. S3. Dependence of double layer charging current at potential of -0.68 V vs. Ag/AgCl/0.1M KCl on scan rate for 5Au/5Cu and Au disc electrode in 0.1 M NaOH.

S5. Stability test

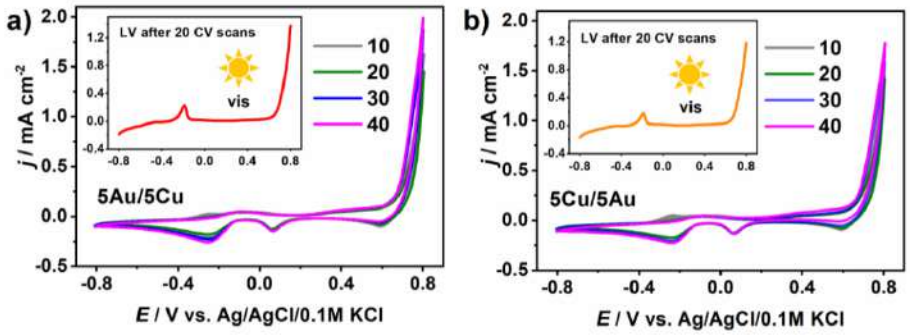

Fig. S4. Cyclic voltammetry (50 mV/s) and linear voltammetry curves (10 mV/s) registered in 0.1 M NaOH for a) 5Au/5Cu and b) 5Cu/5Au samples annealed at 450°C.

References

[1] Y.Y. Lu, Y.Y. Zhang, Y. Shi, Z. Li, Z.C. Feng, C. Li, In situ loading of CuS nanoflowers on rutile TiO_2 surface and their improved photocatalytic performance, Appl. Surf. Sci. 370 (2016) 312-319. https://doi.org/10.1016/j.apsusc.2016.02.170.

[2] Y. Yoshida, K. Uto, M. Hattori, M. Tsuji, Synthesis and growth mechanism of Au@Cu core–shell nanorods having excellent antioxidative properties, CrystEngComm 16 (2014) 5672-5680. https://doi.org/10.1039/C4CE00672K.

[3] Q. He, Y. Tian, Y. Wu, J. Liu, G. Li, P. Deng, D. Chen, Electrochemical sensor for rapid and sensitive detection of tryptophan by a Cu_2O nanoparticles-coated reduced graphene oxide nanocomposite, Biomolecules 9 (2019) 176. https://doi.org/10.3390/biom9050176.

[4] https://xpssimplified.com/elements/copper.php (accessed 20.05.2020)

7.2 Photoresponse depending on the various temperatures during rapid thermal annealing of AuCu on Ti nanodimples

Brief overview of the article A2

Introduction

In order to explore photoelectrochemical activity of AuCu bimetallic nanostructures, electrodes can be thermally treated in the rapid thermal annealing furnace. So far, Schmuki group has reported articles concerning TiO_2 NTs thermally annealed in rapid thermal annealing furnace. Cu-doped TiO_2 NTs were annealed using RTA and used as efficient photoanodes for methanol oxidation[207] and photocatalytic H_2 production[208]. Furthermore, it was proved that rapid ramping rate during annealing of TiO_2 NTs changes fabricated material and significantly increases photocurrents and IPCE[104].

First of all, I decided to perform preliminary tests for AuCu electrode annealed in MF or RTA. Figure 45 presents comparison of the photoelectrochemical activity for the 5Au5Cu/TiND electrode thermally annealed in MF and RTA at the same annealing temperatures (450 °C) and time (10 min). Taking into account the 5Au5Cu/TiND electrode annealed in muffle furnace the photoelectrochemical activity under vis and UV-vis light was registered in cathodic regime from ca. -0.5 V to -0.8 V and -0.17 V, and +0.8 V (see Figure 45). The photoelectrochemical activity under UV-vis behaves similarly to the one under visible light illumination (see Figure 45). As was described in the article A1 AuCu material annealed in MF exhibits significant activity towards oxygen evolution reaction. This process was only supported by light which means that thermal treatment in the MF influences more significantly on material activity toward OER than on photocurrent generation in the wide potential range.

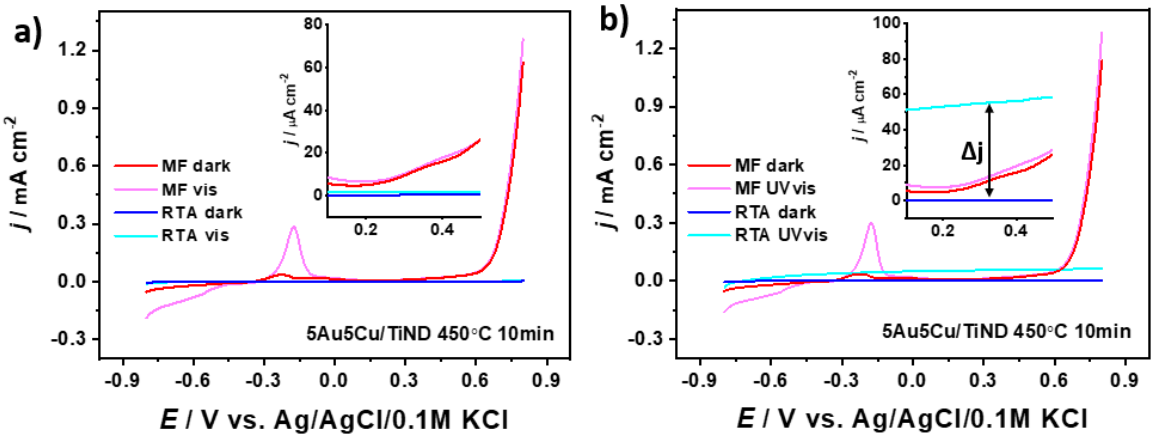

Figure 45. Linear voltammetry for 5Au5Cu/TiND electrodes thermally treated in MF (muffle furnace) or RTA (rapid thermal annealing) registered in 0.1 M NaOH in dark and under vis and UV-vis light illumination.

However, in the case of the 5Au5Cu/TiND electrode annealed in RTA the photoelectrochemical activity under UV-vis light with photocurrent of ca. 50 μA cm^{-2} at +0.3 V can be observed in the wide potential range (see Figure 45b). Unfortunately, as can be seen in Figure 45a the 5Au5Cu/TiND electrodes thermally treated in the RTA are not active under vis light illumination. Therefore, in depth studies concerning optimization of fabrication procedure towards AuCu materials active in vis light will be presented in next articles.

Article A2 regards the influence of temperature changes from 100 °C to 600 °C during rapid thermal treatment (heating rate of 45 °C/s) of 10AuCu alloy, 5Au/5Cu and 5Cu/5Au thin layers deposited on Ti nanodimples platform on their properties. Morphology, optical and structural properties as well as photoelectrochemical activity were fully described. The hypothesis was that the deposition of various sequences of Au and Cu layers or bimetallic AuCu alloy layer as well as usage of different annealing temperatures will allow to tune the composition and distribution of Au and Cu in nanoparticle which further will manifest on the photocurrent values. In previous article A1 nanomaterials were annealed in preheated muffle furnace at two different temperatures: 450 °C and 600 °C, whereas, in article A2 materials were annealed in RTA from 100 to 600 °C providing wider overview about properties of bimetallic AuCu nanostructures.

Nanomaterial synthesis

Bimetallic AuCu electrodes were fabricated in four steps such as anodization of Ti foil, chemical etching, magnetron sputtering and thermal treatment in rapid thermal annealing furnace. The schematic of fabrication process is presented in Figure 46. The TiND were fabricated same as described in the article A1. In the next step, Ti nanodimples were covered by thin 10 nm layer of AuCu alloy or 5 nm gold and 5 nm copper layers in various sequences (5Au/5Cu and 5Cu/5Au). The deposition was realized using magnetron sputtering machine. Afterwards, materials were annealed in RTA furnace in air atmosphere at 100 °C, 200 °C, 300 °C, 400 °C, 500 °C or 600 °C for 30 minutes with the annealing rate of 40 °C/s.

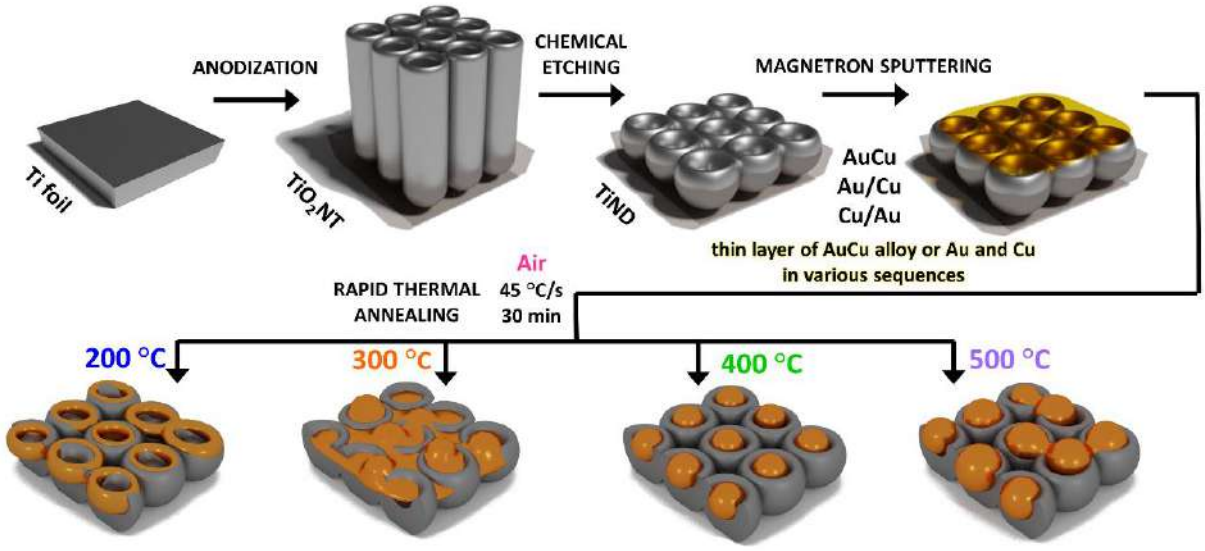

Figure 46. Schematic of fabrication process of AuCu-decorated nanostructured Ti platform thermally treated in the rapid thermal annealer at different temperatures.

Optical and structural properties

The optical properties of fabricated bimetallic AuCu materials were examined by UV-vis spectroscopy measurements (see article A2, Figure 3). The results gathered during such measurements allow to understand how material interacts with light as well as support highly the analysis of the photoelectrochemical activity. The values of position of reflectance minimum for electrodes annealed at 200 °C, 300 °C and 400 °C are listed in Table 7. The non-annealed and annealed at 100 °C and 200 °C AuCu-decorated nanostructured Ti electrodes are characterized by similar shape of the reflectance spectra as TiND which may be caused by the geometry of bimetallic AuCu samples where characteristic Ti nanodimples are still visible (see Figure 3a in article A2). The reflectance band minima for 10AuCu, 5Au5Cu and 5Cu5Au annealed at 300 °C are located at 405 nm, 475 nm 420 nm, respectively. According to literature the peak position shifts toward higher wavelengths with increase of Cu amount in AuCu nanoparticles[209]. In here, shift can be correlated with higher amount of Cu on the top of the electrode surface. In the case of 10AuCu, 5Au5Cu and 5Cu5Au electrodes annealed at 400 °C their reflectance minima are at 530 nm, 520 nm and 540 nm, respectively. The red shift in the reflectance minimum from ca. 405 nm (for 300 °C) to ca. 530 nm (for 400 °C) for 10AuCu electrode was caused by significant changes in morphology after increasing the temperature. Bimetallic AuCu films thermally treated at 300 °C form islands of irregular shapes, whereas, at 400 °C we can observe irregular nanoparticles with an average diameter of 70 ± 34 nm. Similar red shift caused by the increase of annealing temperature was observed for 5Au/5Cu

and 5Cu/5Au electrodes annealed in muffle furnace according to article A1. Furthermore, annealing of AuCu electrodes at 600 °C resulted in wide absorbance band from 300 to 1000 nm.

Table 7. The reflectance minimum for materials annealed at 200 °C, 300 °C and 400 °C.

Electrode	Position of the reflectance minimum depending on the temperature treatment / nm		
	200 °C	300 °C	400 °C
10AuCu	390	405	530
5Au5Cu	390	475	520
5Cu5Au	400	420	540

The XPS measurements were performed for 10AuCu electrode annealed at 200 °C, 300 °C, 400 °C and 500 °C (article A2 Figure 6). The Au4f peak appears at ca. 84.0 eV for all samples and is ascribed to metallic Au[154]. The content of metallic Au increases with temperature and reaches maximum at 400 °C. Such phenomenon can be correlated with the reflectance minimum of 530 nm for 10AuCu sample annealed at 400 °C which is related to literature maximum of absorbance for gold nanoparticles[19]. For the samples annealed at 200, 300 and 400 °C three Cu2p 3/2 chemical states at 935.2 eV, 933.8 eV and 932.6 eV were assigned to $Cu(OH)_2$ or $CuCO_3$, CuO and AuCu alloy[210]. Moreover, the highest At% of Cu(II) was registered for AuCu-decorated Ti platform annealed at 300 °C. In the case of material thermally treated at 500 °C one more peak located at 931.2 eV was associated with CuAuTi alloy. The TiO_2 was present for sample thermally treated at 300, 400 and 500 °C and its atomic content increases with the increasing temperature. As atomic content of TiO_2 increases, photocurrent increases reaching 16.4 μA cm^{-2}, 47.7 μA cm^{-2} and 75.7 μA cm^{-2} for 10AuCu electrodes annealed at 300, 400 and 500 °C, respectively (see Table 7).

Photoelectrochemical properties

According to preliminary research described in *introduction* (page 89), where the 5Au5Cu/TiND electrode annealed in RTA showed activity under UV-vis light in wide potential range (Figure 45b), insightful studies concerning bimetallic AuCu materials in various configurations were developed. The photoactivity was determined by linear voltammetry measurements under chopped light and each single dark and UV-vis light period lasts for 5 second (see Figure 47a). As can be observed in Figure 10 presented in article A2, the shape of linear voltammetry curves for 10AuCu, 5Au5Cu, 5Cu5Au annealed at 200 °C and 300 °C (article A2) is similar to the LV curve for 5Au/5Cu, 5Cu/5Au electrodes annealed at 450 °C in MF (article A1). Nevertheless, for electrodes annealed in RTA no gas bubbles and no oxygen evolution reaction was registered. Therefore, it can be assumed that oxidation of Cu^{2+} to Cu^{3+}

can occur at potential of +0.8 V[211]. The photocurrent response with efficient electron hole pair generation characterized by square shape profile for the consecutive on-off cycles was registered for bimetallic AuCu materials annealed at 500°C and 600°C. The values of photocurrent density registered under UV-vis light illumination are listed in Table 8. The highest value of photocurrent was achieved for the 5Au/5Cu electrode annealed at 600 °C. Whereas, the lowest photocurrent was obtained for the 5Cu/5Au electrode. Therefore, it can be assumed that more efficient e-h pair generation and electron transfer is when gold is closer to titanium dioxide while copper oxides are at the top of the sample (TiO_2/AuCu/Cu_2O/CuO).

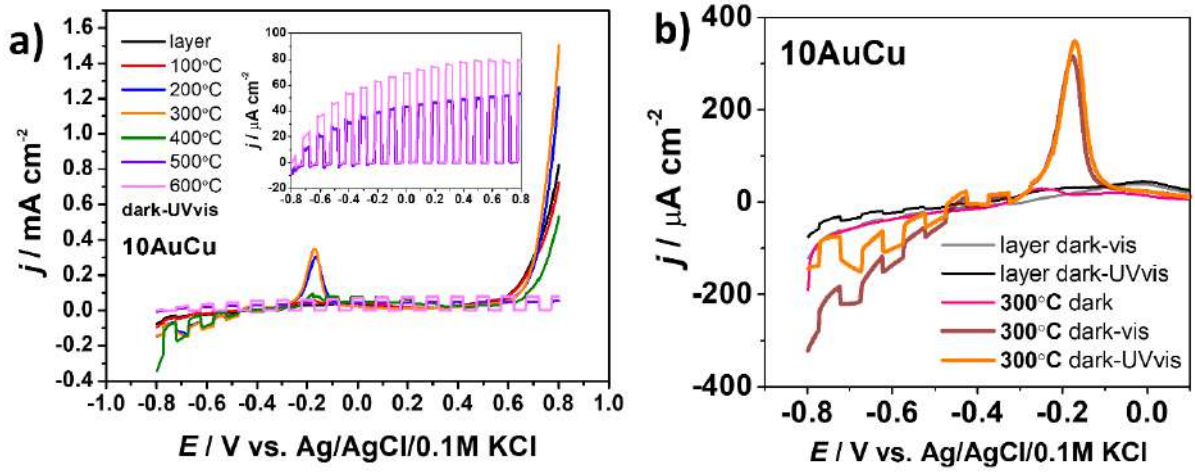

Figure 47. Linear voltammetry curves for 10AuCu electrodes thermally treated at different temperatures registered in 0.1 M NaOH under UV-vis illumination.

Table 8. Values of photocurrent density registered under UV-vis light illumination for materials thermally treated at 400 °C, 500 °C and 600 °C (E= +0.3 V vs. Ag/AgCl/0.1 M KCl).

Electrode	Temperature / °C	j / µA cm^{-2}
10AuCu	400	16.4
	500	47.7
	600	75.7
5Au5Cu	400	16.3
	500	49.4
	600	91.4
5Cu5Au	400	18.3
	500	50.9
	600	64.3

The unique oxidation process enhanced by UV-vis or visible light illumination took place at -0.17 V vs. Ag/AgCl/0.1M KCl. This photoelectrochemical activity can occur due to the synergetic effect between gold and copper metals. As was observed, values of the photocurrent density at -0.17 V for 10AuCu, 5Au5Cu and 5Cu5Au electrodes annealed at 300 °C differ significantly. Therefore, it can be assumed that the arrangement of Au and Cu

plays crucial role in the photocurrent increase. The highest photocurrent under UV-vis and vis light of ca. 320 μA cm^{-2} and 300 μA cm^{-2} was obtained for the 10AuCu electrode annealed in RTA at 300 °C (Figure 47b). In the case of 10AuCu electrode, AuCu alloy target was used for the magnetron sputtering process which might ensure uniform mixture of metals. This intriguing phenomenon is preserved when the material is continuously illuminated by light (article A1) as well as when the chopped light is used (article A2). Therefore, two types of light interaction with material such as e-h pair generation (Figure 47b from -0.8 to -0.3 V) and photogenerated charge accumulation (Figure 47b from -0.3 to +0.1 V) can be distinguished.

Photoelectrochemical activity for 5Au/5Cu electrode annealed at 700 and 800 °C

After measurements presented in articles A1 and A2, I decided to study the characteristic of AuCu nanoparticles formed on Ti nanodimples in the wider annealing temperature range. Therefore, I performed some additional photoelectrochemical measurements. In order to characterize AuCu-decorated substrates in the full range of temperatures selected for thermal treatment, 5Au/5Cu electrodes were annealed in RTA and MF furnace at 600, 700 and 800 °C. The 5Au/5Cu electrode was chosen due to the highest photocurrent recorded at +0.3 V vs. Ag/AgCl/0.1M KCl when it was annealed at 600 °C. The linear voltammetry curves were registered under UV-vis light illumination in 0.1 M NaOH solution (Figure 48). The values of photocurrent density are listed in Table 9. As the temperature increases, the photocurrent value for samples fabricated in RTA decreases. In the case of electrodes annealed in muffle furnace, the photocurrent increases with increasing temperature. Nonetheless taking the reached values into account, it can be assumed that thermal treatment in RTA improves photoelectrochemical activity as the highest value was achieved for the 5Au5Cu electrode annealed at 600 °C.

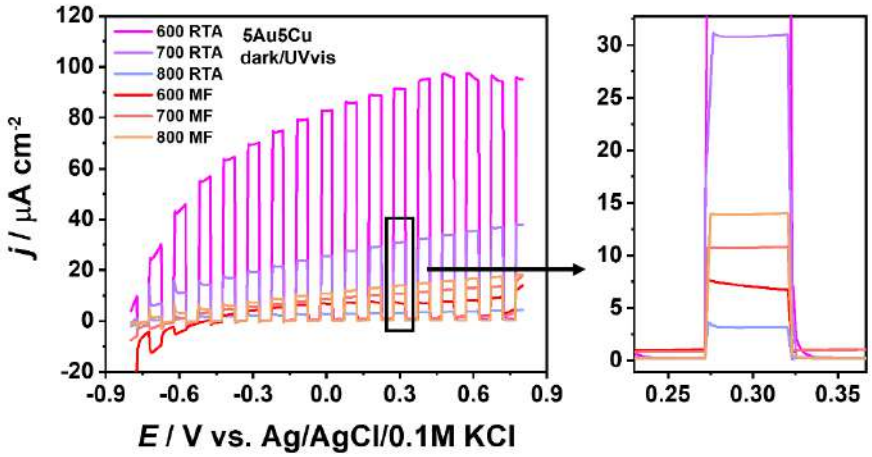

Figure 48. Linear voltammetry curves for 5Au5Cu electrodes thermally treated at 600, 700 and 800 °C in RTA or MF registered in 0.1 M NaOH under UV-vis illumination.

Table 9. Values of photocurrent density registered under UV-vis light illumination for materials thermally treated at 600, 700 and 800 °C in RTA or MF (E= +0.3 V vs. Ag/AgCl/0.1 M KCl).

Electrode	Temperature / °C	j / μA cm^{-2}
5Au5Cu (RTA)	600	91.4
	700	30.6
	800	2.9
5Au5Cu (MF)	600	6.2
	700	9.9
	800	13.7

Conclusions

In here, it was proved that the rapid thermal treatment has a positive effect on photocurrent generation in wide potential range. According to XPS measurements the highest atomic content of copper oxides was obtained for samples annealed at 300 °C. Furthermore, nanostructured AuCu electrodes fabricated at this temperature were characterized by unique oxidation peak at -0.17 V vs. Ag/AgCl/0.1M KCl during visible and UV-vis illumination. The 10AuCu electrode annealed at 300 °C obtained ca. 11 times higher current density than non-annealed one at -0.17 V. AuCu nanoparticles formed on Ti platform thermally treated at 600 °C manifest the wide absorption band from 300 nm to 1000 nm. Moreover, samples annealed at 600 °C were characterized by the highest photocurrent under UV-vis light with efficient e-h pair generation.

A2) W. Lipińska, K. Grochowska, J. Karczewski, J. Ryl, K. Siuzdak, ***Temperature-controlled nanomosaics of AuCu bimetallic structure towards smart light management***, Journal of Materials Science: Materials in Electronics 33 (2022) 19385, IF = 2.8 / 70 points mechanical engineering

J Mater Sci: Mater Electron (2022) 33:19385–19404

Temperature-controlled nanomosaics of AuCu bimetallic structure towards smart light management

Wiktoria Lipińska[1,*], Katarzyna Grochowska[1], Jakub Karczewski[2,3], Jacek Ryl[2,3], and Katarzyna Siuzdak[1]

[1] *Centre for Plasma and Laser Engineering, The Szewalski Institute of Fluid-Flow Machinery Polish Academy of Sciences, Fiszera 14 St., 80-231 Gdańsk, Poland*

[2] *Institute of Nanotechnology and Materials Engineering, Faculty of Applied Physics and Mathematics, Gdańsk University of Technology, Narutowicza 11/12 St., 80-233 Gdańsk, Poland*

[3] *Advanced Materials Center, Gdańsk University of Technology, Narutowicza 11/12 St., 80-233 Gdańsk, Poland*

Received: 19 February 2022
Accepted: 13 July 2022
Published online: 6 August 2022

ABSTRACT

Gold–copper nanostructures are promising in solar-driven processes because of their optical, photocatalytic and photoelectrochemical properties, especially those which result from the synergy between the two metals. Increasing interest in their internal structure, such as the composition or distribution of the Au and Cu as well as the size and shape of the nanoparticles, have developed to define their physicochemical properties.

In this work, we present the influence of thermal treatment in temperature ranges from 100 to 600 °C on the formation process of bimetallic AuCu structures and their properties. AuCu materials were placed on nanostructured titanium foil substrates that were fabricated using electrochemical anodisation and chemical etching. Thin layers of AuCu mixture, as well as Au and Cu, were sputtered on the obtained Ti nanodimples. The materials were then annealed in a rapid thermal annealing furnace in an air atmosphere. Thermal treatment strongly affected the morphology and optical properties of the fabricated materials. AuCu NPs formed at 400 °C in titanium dimples. The material exhibits absorption of visible light in the range from c.a. 400 to 700 nm. The characterisation of the chemical nature of the samples was determined using X-ray photoelectron spectroscopy. In addition, X-ray diffraction and Raman spectroscopy defined composition and crystallinity. Based on photoelectrochemical studies carried out with the use of linear voltammetry in 0.1 M NaOH, it is possible to distinguish two types of interactions of light with the materials such as photogenerated charge accumulation and electron–hole pair separation. A 10AuCu electrode annealed at 300 °C achieved the highest current registered under illumination at − 0.17 V vs. Ag/AgCl/0.1 M KCl. The value was 11 times higher than for a non-annealed structure.

Address correspondence to E-mail: wlipinska@imp.gda.pl

https://doi.org/10.1007/s10854-022-08775-9

1 Introduction

Nowadays, a lot of effort has been directed to the control of the fine morphology of materials such as their size, shape, and homogeneity since at the nanoscale, the quantum confinement effect determines the overall performance. However, not only the material appearance but also its internal structure is of high importance and can make it suitable for a multitude of applications e.g. in catalytic reactions, photo-induced processes or the formation of hydrophobic surfaces [1]. The ability to control the properties of a nanomaterial and perform a comprehensive analysis are critically important tools in a scientist's hands in order to find applications in novel, highly efficient solar cells, water splitting devices, fuel cells, batteries, pollutant degradation devices, and sensors. Metals of dimensions limited by several or tens of nanometers are considered to be a very interesting objects due to a variety of unique properties such as electrical conductivity, catalytic, and optical activity [2] which are completely different from their bulk counterparts. Following that, research was focussed on pure metal nanoparticles (NPs) formed by noble metals (Au, Pt) [3, 4] and non-noble ones, typically in the form of oxides (Fe_2O_3, TiO_2) [5, 6]. Next, combinations of both noble and non-noble element were proposed [7] and it was found that the chemical and physical properties of such structures were atypical compared to their pure elements, this being caused by the so-called synergetic effect. Among others, AuCu bimetallic structures have been extensively explored, where gold ensures higher resistance to the oxidation process than Cu, while copper oxide is a popular semiconducting oxide for photocatalytic applications [8]. As can be expected, various shapes of colloidal AuCu forms can be obtained, namely nanostars [9], nanocubes [10], and nanorods [11], this process being controlled by added surfactants, the concentration of the metal precursor, and the reaction temperature during the synthesis process. Moreover, such bimetallic species have been used for the decoration of other nanomaterials exhibiting semiconducting or quasi-metallic characters, such as SiO_2 [12], TiO_2 [13], TiO_2/MoS_2 [14], TiSi [15], CeO_2 [16], rGO [8], and g-C_3N_4 [17], providing improved photoresponse or catalytic properties, e.g. towards methanol oxidation or the reduction of dioxygen and hydrogen peroxide [18]. Nevertheless, in spite of the various synthesis methods and modifications based on wet-chemistry routes [19], all of the procedures lead to the formation of colloid that after some time can aggregate because of the high surface energy of the NPs. Following that, activity can be lost as further usage as an electrode material requires immobilisation onto the conductive support. Thus, for electrocatalytic and photoelectrochemical reactions, a uniform distribution of nanoparticles onto the substrate should be achieved. Typically, transparent metal oxide (FTO, ITO), glassy carbon [20], or carbon paper [21] as a charge collector have been proposed, while optimised spin-coating, dip-coating, or electrochemical deposition were utilised for the preparation of the complete electrode material. Another way to form an electrode with an already-anchored bimetallic nanostructure on a stable surface is via rapid thermal annealing of sputtered thin metallic films [22]. Thin metal film dewetting is a simple route for the formation of nanoparticles. Their size can be tuned by changing the annealing temperature, atmosphere, or initial film thickness. The annealing process can be divided into conventional furnace annealing (CFA), and rapid thermal annealing (RTA). RTA has many advantages over CFA such as lower dewetting temperatures of thin metal films with an increase of heating rate, lower crystallisation temperature, minimised film substrate interface reactions, shorter annealing time, better electrical properties, and reduced thermal costs [23]. According to Bergum et al. [24], rapid thermal annealing of thin layers of Cu_2O prepared using magnetron sputtering improves their carrier transport, while Kumar et al. [25] reported that RTA, owing to the faster heating rates, shorter time, and lower temperatures, promotes the formation of a smaller grain size of Cu and Ag–Cu materials. Moreover, Khaoo et al. [26] achieved an increase in photovoltaic performance and external quantum efficiency for ZnO/Cu_2O by rapid thermal annealing. The number of grain boundaries decreased while the number of pores increased simultaneously with the temperature growth. In such a case, a more porous structure with carrier recombination sites is formed due to the higher temperature. Films can be formed on a flat or textured substrate exhibiting a developed surface area that can also limit the size of the formed nanoparticles and ensure a high degree of spatial ordering. In that case, the thermal conditions play a crucial role since the temperature stress is applied

both to the metallic film and the substrate, affecting its possible oxidation, and a change in the resistance of the whole material. Taking into account the increased available surface area, and the higher catalytic and electrocatalytic response, a semiconducting interlayer or matrix for further hosting of AuCu is frequently selected, such as titania [27], zinc oxide [28], carbon paste with nano P zeolite [29], or carbon nanofibre [30]. However, achieving a uniform distribution of NPs is especially challenging and therefore the reproducibility is poor. Focussing on photoresponsive electrode materials containing small metal species, the selection of TiO_2 is commonly recommended due to its semiconducting character ensuring efficient e–h pair separation, low-cost, non-toxicity, and corrosion resistance. However, its wide bandgap energy limits activity in the visible light spectrum, but further decoration by metal nanostructures can shift the absorbance of the material towards longer wavelengths, thereby improving the photoelectrochemical activity. Similar to the case where a wide bandgap semiconductor is modified by monometallic nanoparticles, surface plasmon resonance (SPR) [31] and the formation of a Schottky heterojunction are mainly responsible for the improved light-driven harvesting of electrochemical response, and the simultaneous suppression the recombination of photogenerated carriers [32, 33]. The mechanism of the photon-harvesting abilities exhibits a complex nature since it depends on the illumination side of the material, first titania and then AuCu nanoparticles, and vice versa [34] for a structure deposited onto a semitransparent substrate. When both a wide bandgap semiconductor and a bimetallic nanostructure are exposed to radiation at the same time, several phenomena occur. In such a case, the overall performance depends on the reaction dynamics, and smart but simple control of the morphology and internal structure can result in highly effective nanocatalytic platforms for organic transformations [35], CO_2-to-CH_4 conversion [21], as well as light-driven current generation [32].

In this paper, we focus onto the precisely temperature-managed synthesis of nanomosaic material created by bimetallic AuCu nanostructures directly on a textured Ti substrate. The Ti substrate was produced by electrochemical anodisation resulting in the growth of ordered titania nanotubes (TiO_2NTs). After selective etching of titania, a platform composed of highly ordered titanium nanodimples (TiNDs) remains. In order to obtain a AuCu nanomosaic, gold and copper layers in various sequences as well as a AuCu mixture were sputtered onto the Ti substrate. Finally, the samples were annealed at 100, 200, 300, 400, 500, and 600 °C in a rapid thermal annealing furnace (RTA) under an air atmosphere in contrast to the procedure where substrates are simply introduced into a preheated muffle furnace and removed after a certain period [36]. In our previous report, we showed only the behaviour of the material in two temperature regimes and the given results were just an announcement for further studies providing a wider overview regarding the outstanding features and perspective applications of AuCu bimetallic nanostructures. Thus, complex characterisation of the temperature-controlled morphology is carried out while the structural and optical features were examined using scanning electron microscopy and different spectroscopic techniques: X-ray diffraction, Raman, X-ray photoelectron, and UV–vis absorption spectroscopies. Moreover, the study shows the strong influence of the thermal annealing conditions on the electrochemical and photoelectrochemical performance of AuCu structures formed over a titanium support covered with a thin passivation TiO_2 layer.

2 Experimental

2.1 Reagents

Titanium foil (99.7%, thickness: 0.127 mm, Strem), acetone (Chempur), ethanol (96%, Chempur), ammonium fluoride (98%, Chempur), ethylene glycol (99%, Chempur), oxalic acid dihydrate (99.5%, Sigma-Aldrich), gold target (99.99%, Quorum Technologies), copper target (99.99%, Quorum Technologies), and gold/copper alloy target (Au50/Cu50 At%, Goodfellow).

2.2 AuCu electrode fabrication

The Ti foil was cut into 2 × 3 cm^2 plates and ultrasonically cleaned in acetone, ethanol, and water for 10 min. Then Ti was used for the electrochemical anodisation process. Anodisation was conducted in the two-electrode system, where the Ti was used as the anode, and a Pt mesh as the cathode. The electrodes were placed against at a distance of 2 cm from

each other in a cylindrical glass cell filled with electrolyte. The synthesis was based on two subsequent anodisations followed by chemical etching processes. The electrolyte contained 0.27 M NH_4F dissolved in a mixture composed of 1% vol. deionised water and 99% vol. ethylene glycol. The anodisation process was carried out in glass cells with a thermostated jacket at a voltage of 40 V, and a temperature of 23 °C for 2 h for the first stage, and 6 h for the second stage. After each anodisation stage, the formed TiO_2 nanotubes were chemically etched overnight in 0.5% oxalic acid solution in glass beakers, and afterwards the samples were rinsed with deionised water. A complete description of the applied procedures can be found elsewhere [37, 38]. As a result, a honeycomb structure composed of closely packed dimples of a diameter corresponding to the external diameter of the nanotubes was formed, and labelled as TiND. The obtained platform was used during magnetron sputtering (Q150T S system, Quorum Technologies) of 10 nm of AuCu alloy (in the manuscript, assigned as 10AuCu) as well as 5 nm layers of Au and Cu in both sequences (assigned as 5AuCu and 5CuAu, respectively). The non-annealed samples were labelled as NA. Afterwards, the electrodes were thermally treated in a Rapid Thermal Annealing furnace (MILA 5000 P-N) for 30 min in air with a heating rate of 45 °C/s. The modifications of different samples were carried out at 100, 200, 300, 400, 500, and 600 °C.

2.3 Sample characterisation

The morphology of the prepared samples was investigated by a field emission scanning electron microscope (FEI Quanta FEG250) equipped with a secondary ET detector and with the beam accelerating voltage kept at 10 kV. The optical properties of the nanostructures were inspected using a UV–vis spectrophotometer (Lambda 35, Perkin-Elmer) equipped with a diffuse reflectance accessory. The spectra were registered in the range of 300–1000 nm with a scanning speed of 60 nm/min. The crystal structure of the 10AuCu sample was verified by X-ray diffraction over the range of 20–80 degrees using a Bruker 2D Phaser diffractometer with CuKα radiation and an XE-T detector. The Raman spectra were recorded by means of a confocal micro-Raman spectrometer (InVia, Renishaw) with sample excitation by an argon ion laser emitting at 514 nm and operating at 50% of its total power. The chemical nature of the samples was studied by an X-ray photoelectron spectroscope (Escalab 250Xi, ThermoFisher Scientific) with a monochromatic AlKα source. The high resolution spectra of *Au4f*, *Cu2p*, *Ti2p*, and *O1s* for the 10AuCu electrode were captured. The electrochemical and photoelectrochemical properties were measured using an AutoLab PGStat 302 N potentiostat–galvanostat in the three-electrode assembly, where the titanium substrate modified by gold–copper structures was the working electrode (WE), Ag/AgCl/0.1 M KCl served as the reference electrode (RE), and a Pt mesh was the counter electrode (CE). Cyclic voltammetry and linear voltammetry measurements were carried out in deaerated 0.1 M NaOH electrolyte. The cyclic voltammetry (CV) curves were registered within the range from − 0.5 towards + 0.5 V with a scan rate of 50 mV/s, while the linear voltammetry (LV) scans were performed across a wider potential range from − 0.8 to + 0.8 V with a scan rate of 10 mV/s. The LV curves were recorded in the dark and under illumination with a xenon lamp (LOT-QuantumDesign GmbH) as a light source. The chronoamperometry measurements (CA) under chopped light were performed at + 0.3 V during 200 s. The 3D map of the photocurrent density was registered by photoelectric spectrometer (Instytut Fotonowy) equipped with Xe lamp 150 W. The curves were recorded at the potential range from − 0.8 to + 0.8 V and wavelengths from 300 to 700 nm. The measurement was carried out in 0.1 M NaOH solution in three-electrode system where 10AuCu electrode was the WE, Ag/Ag/AgCl/0.1 M KCl was the RE, and Pt wire served as the CE.

3 Results and discussion

3.1 Morphology

SEM images of the fabricated samples composed of gold–copper structures on a nanotextured titanium substrate are shown in Fig. 1. Of all of the prepared samples, the 10AuCu alloy was selected for detailed analysis, due to it having the best electrochemical results, which will be discussed further on. As can be observed, thermal annealing strongly affected the morphology of the electrodes. For electrodes without thermal treatment (Fig. 1a) or annealed at 100 °C (Fig. 1b) or 200 °C (Fig. 1c), the characteristic dimples

are clearly visible. The diameter of the dimples for the 10AuCu layer was estimated to be 76 ± 8 nm. Whereas, in our previous work, the diameter of closely packed Ti dimples without the AuCu layer and thermal treatment was reported to be 85 ± 3 nm [38]. With the temperature increase to 200 °C, the diameter of the nanodimples did not change significantly, however, further growth of the temperature caused the gradual disappearance of the cavities (Fig. 1d). Similar to Grochowska et al. [34], the layer fragmentation started at the grain boundaries. At a temperature of 300 °C, islands of irregular shapes were created [39], while at 400 °C, AuCu nanoparticles formed. The resulting AuCu NPs were irregular in

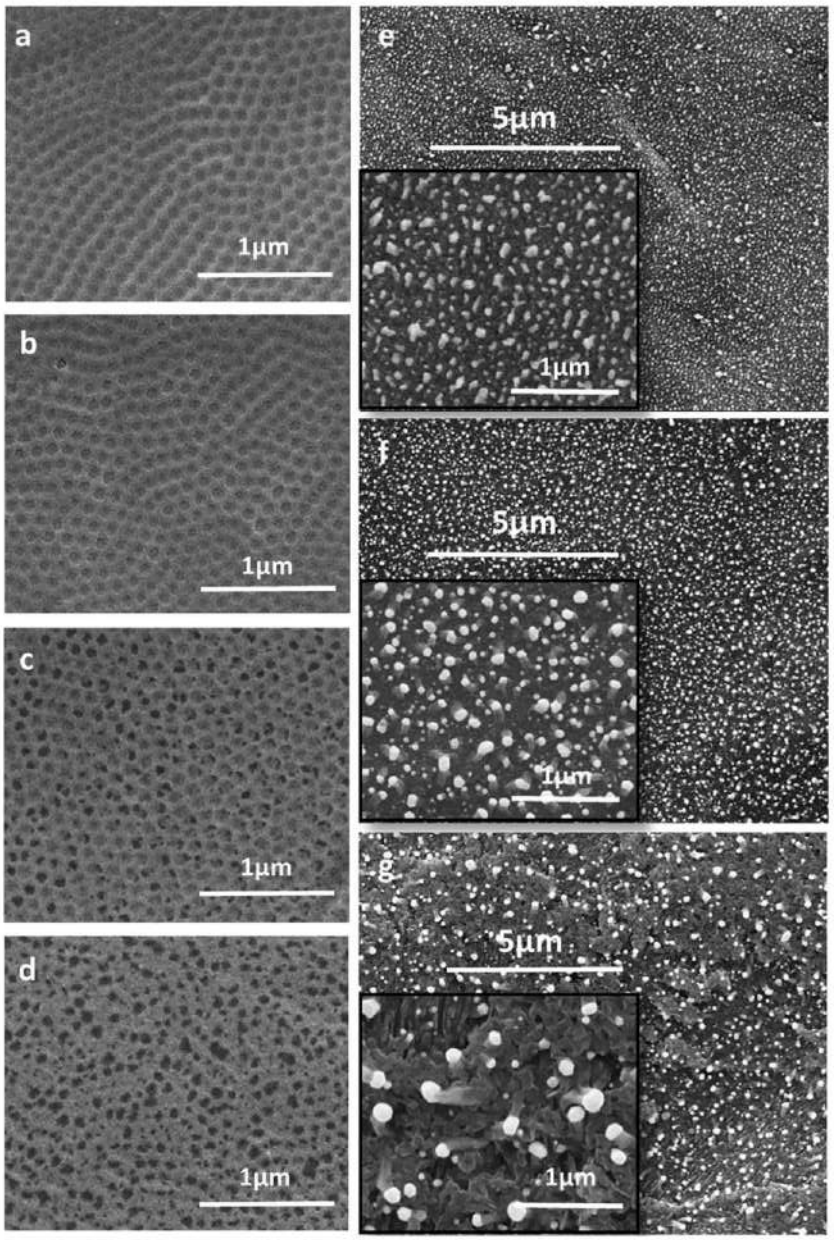

Fig. 1 SEM images of 10AuCu electrode **a** without thermal treatment, and after thermal annealing at **b** 100 °C, **c** 200 °C, **d** 300 °C, **e** 400 °C, **f** 500 °C, **g** 600 °C

shape and the average size equalled 70 ± 34 nm. At the temperatures of 500 °C (Fig. 1e) and 600 °C (Fig. 1f), the fabricated nanoparticles became more spherical and the Ti nanodimples were no longer distinguished. The diameter of the AuCu NPs formed at 500 °C was 74 ± 28 nm, while those annealed at 600 °C were 123 ± 49 nm. As can be observed, the size of the nanoparticles as well as the standard deviation increased with the temperature. This may be related to the disappearance of the nanodimples as it is known that the presence of cavities in Ti foil ensures the formation of nanoparticles that are regularly distributed and quite regular in shape and size [40].

3.2 Optical properties

The differences in the annealing temperature of the AuCu nanostructures influenced colour changes of the electrode surface which can be observed by the naked eye (Fig. 2). A variety of colours from pearl (100 °C), gold brown (200, 300 °C), and violet (400 °C) to grey (600 °C) were obtained. According to Fredj et al., the temperature during the fabrication process is associated with changes in the colour of copper oxides films [41]. Moreover, the dependence between the appearance of the surface and the thickness of the created oxide was also evaluated. Additionally, the colour impression depending on the thickness of the Ti and TiO_2 layers was reported by L. Skowroński et al. [42]. Nevertheless, in our case, it was most likely the presence of copper, and titanium and titanium dioxide that influenced the colour of the samples.

The reflectance spectra were recorded to reveal the optical properties of the 10AuCu, 5Au5Cu, and 5Cu5Au electrodes (Fig. 3). As can be observed, the shape of the spectrum changed because of the differences in the morphology caused by thermal dewetting, and the presence of the resulting gold–copper structure. From the SEM images, it can be observed that the AuCu nanostructures annealed below 200 °C preserved the periodic arrangement of Ti nanocavities, and possibly their geometry influenced the shape of the spectrum in the range from 300 to 600 nm [43]. The reflectance band minima for the 10AuCu, 5Au5Cu, and 5Cu5Au annealed at 200 °C were located at 390, 390, and 400 nm, respectively (Fig. 3d), while for 300 and 400 °C, they were shifted to c.a. 405, 475, and 420 nm, and 530, 520, and 540 nm, respectively (Fig. 3e). According to Guo et al. [44], the peak intensity and position are component-dependent for $Au_xCu@TiO_2$ structures, and are located at 430, 470, and 550 nm for Au_3Cu, AuCu, and $AuCu_3$ nanoparticles. In our previous studies, a shift in the absorbance maxima for gold–copper materials from 470 to 900 nm was revealed, and caused by changes in morphology after increasing the annealing temperature from 450 to 600 °C [36]. In that work, the temperature increase resulted in the formation of AuCu NPs on the surface of the substrate at 600 °C. The same phenomenon took place here, however, at a much lower temperature,

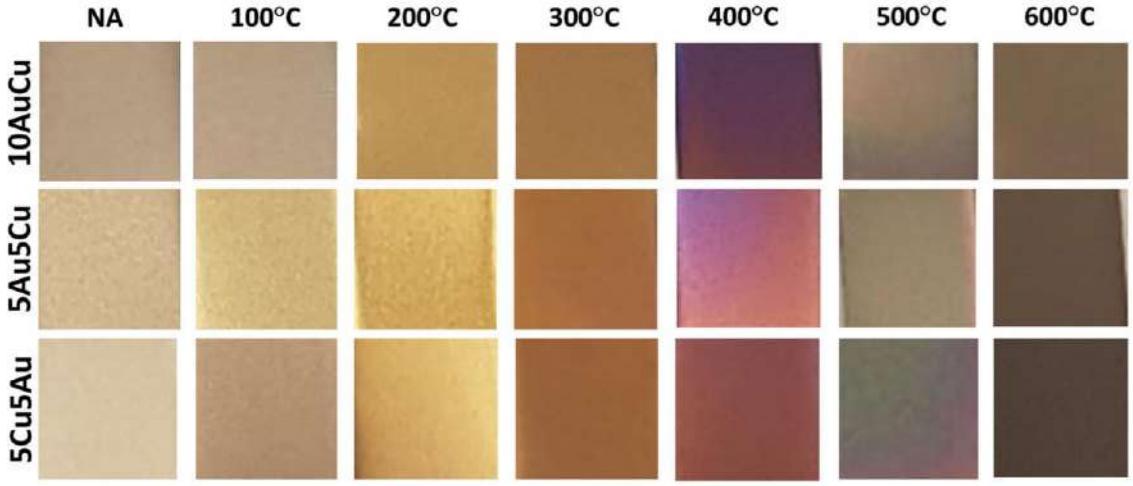

Fig. 2 Dependence of colour of the prepared samples on the annealing temperature

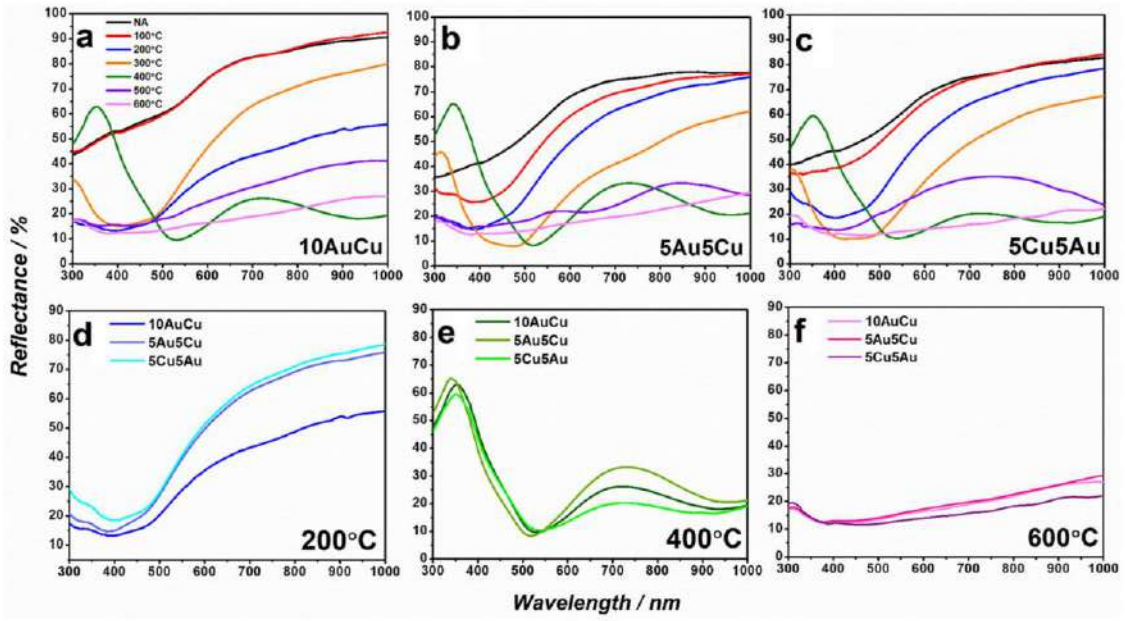

Fig. 3 Reflectance spectra of **a** 10AuCu, **b** 5Au5Cu, **c** 5Cu5Au and selected results for electrodes annealed at **d** 300 °C, **e** 400 °C, **f** 600 °C

namely 400 °C. Above this temperature, AuCu nanoparticles were formed on the surface, and broadband absorbance from c.a. 400 to 1000 nm was observed. According to Scaiano et al. [45], CuNPs show a surface plasmon absorption band between 575 and 580 nm. Nguyen et al. reported that AuNPs/TiO_2 nanostructures exhibited increased absorbance in the UV region below 380 nm, corresponding to the bandgap of anatase TiO_2, and in the visible light region from 490 to 650 nm, attributed to the SPR effect of AuNPs [46]. In our case, no anatase phase presence was demonstrated, however, the rutile phase for the materials fabricated at 500 and 600 °C was established from the Raman spectroscopy measurements. Even though the substrate was titanium on its surface, a passivation layer of TiO_2 was formed. The rutile was confirmed by XRD patterns not only for 500 and 600 °C, but also a small amount for 400 °C. With increasing the annealing temperature from 400 to 600 °C, a thicker layer of TiO_2 was formed on the surface. Therefore, a decrease in reflectance in the range from 300 to 400 nm above 400 °C may be found [47]. As can be observed, the annealing of the 10AuCu, 5Au5Cu, and 5Cu5Au samples at 600 °C resulted in wide absorbance from 300 to 1000 nm (Fig. 3f).

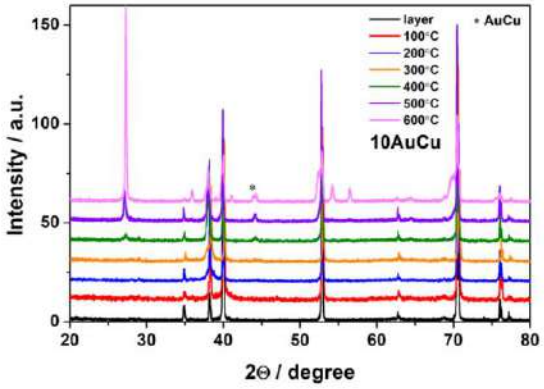

Fig. 4 XRD pattern of 10AuCu electrode annealed at different temperatures

3.3 Composition and crystallinity

The XRD diffraction patterns of the 10AuCu electrodes annealed at different temperatures are shown in Fig. 4. The peaks located at 34.9, 38.3, 39.9, 52.8, 62.7, 70.4, 76.1, and 77.2 degrees can be associated with the (100), (002), (101), (102), (110), (103), (112), and (201) planes of Ti [48], and only those peaks are present in the case of the electrode without annealing

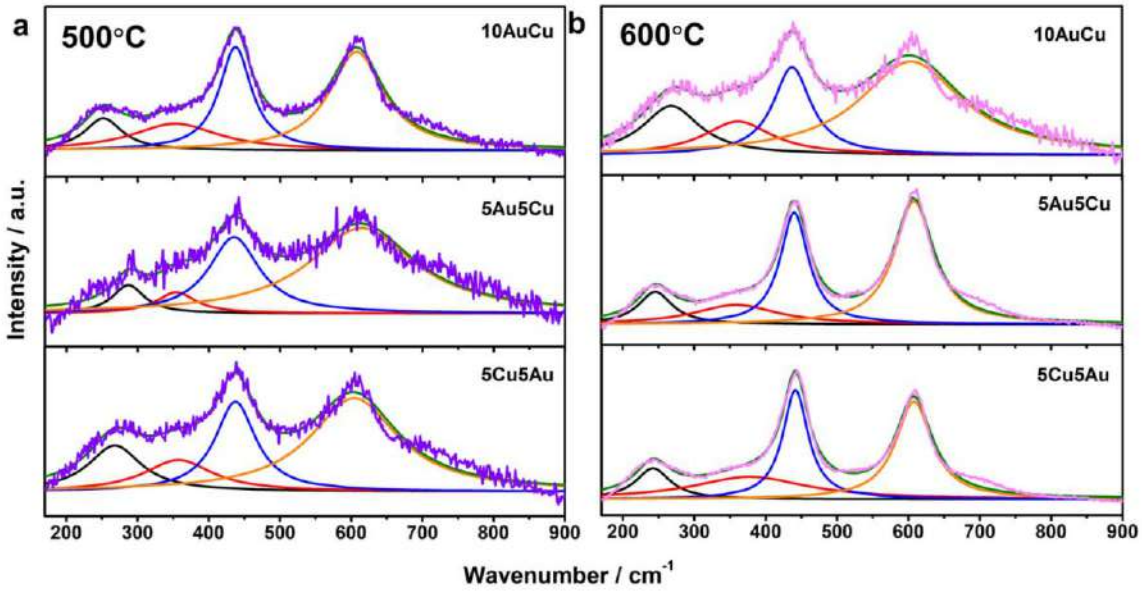

Fig. 5 Raman spectra of the samples annealed at **a** 500 °C and **b** 600 °C

and the ones treated up to 300 °C. When the temperature exceeded 400 °C, peaks at 27.3, and 44.2 degrees appeared, and they can be ascribed to the (110), and (210) planes of rutile. Moreover, the peaks already assigned to titanium foil are broadened, as the (002), and (301) rutile planes can be registered at 62.5, and 69.8 degrees. With the sample heated up to 600 °C, peaks related to the (101), (111), (211), (220), and (310) rutile planes arose, and the corresponding positions are 35.9, 41.1, 54.2, 56.5, and 64.5 degrees, respectively [49]. Additionally, with the increase of the rutile phase in the samples, pronounced broadening of the Ti peak located at 70.4 degrees is observed, as the 69.8 degrees peak of rutile is more intense. The increment of the rutile signal with the temperature growth from 400 to 600 °C is in agreement with the work of Qian et al. [50]. The SEM images show the formation of AuCu NPs at these temperatures, and the subsequent exposure of the substrate may be related to the increase in the intensity of the rutile peak. It should also be mentioned that rutile is formed out of the amorphous TiO_2 passivation layer and growth of the thickness of the oxide layer is expected at higher temperatures. Moreover, for the 10AuCu samples annealed at 600 °C, a peak from AuCu can be observed [51].

More detailed characterisation of the structure of the samples was conducted based on Raman measurements. The Raman spectra of the gold–copper structures on the Ti substrate annealed at 500, and 600 °C are shown in Fig. 5. These temperatures were selected based on the XRD measurements. It can be observed that not only the increase in temperature affects the Raman spectra but also the configuration of the gold and copper. Raman bands associated with AuCu can be found from 240 to 270 cm^{-1} [52]. The location of CuO bands is calculated to occur in the 350–370 cm^{-1} region [53]. According to Kalaivani and Anilkumar[54], bands located at c.a. 230, 440, and 605 cm^{-1} can be ascribed to rutile. Nevertheless, based on the values collected in Table 1, determined using deconvolution, it can be observed that the band corresponding to AuCu for the 5Au5Cu and 5Cu5Au samples is redshifted after the increase of the temperature from 500 to 600 °C. Moreover, the largest shift of c.a. 40 cm^{-1} was observed for the 5Au5Cu electrode. This phenomenon may occur because of the higher ratio between rutile and AuCu at 600 °C for this sample. The rutile bands can be found not only at 440 and 605 cm^{-1}, but are also probably hidden in the spectrum at 230 cm^{-1}. However, for the 10AuCu electrode, a shift for the AuCu compound from 252 to 268 cm^{-1} can be observed. The blue shift may be caused by the formation of a higher amount of CuO species from gold–copper alloy after increasing the temperature from 500 to 600 °C. This

Table 1 Location of Raman bands derived from Fig. 5

Compound	Temperature/°C	Raman shifts/cm^{-1}			References
		10AuCu	5Au5Cu	5Cu5Au	
AuCu	500	252	287	268	[47]
	600	268	246	242	
CuO	500	353	354	357	[48]
	600	361	359	378	
Rutile	500	437	435	437	[49]
		607	615	603	
	600	437	440	442	
		604	608	608	

phenomenon can dominate over rutile formation. The blueshift of the band associated with CuO after thermal treatment at 600 °C can be ascribed to the enhancement of interactions between the CuO and rutile phases. In Mosquera et al. [55], the shift of the Raman band was observed for rutile from 235 to 245 cm^{-1} during temperature changes.

3.4 Characterisation of the chemical nature of the samples

XPS measurements were conducted to track the chemical character of the 10AuCu electrode. Figure 6 presents the XPS spectra for the electrodes annealed at 200, 300, 400, and 500 °C. The obtained results are summarised in Table 2. Moreover, the changes in the proportion of the elements/compounds in the studied materials depending on the temperature are shown in Fig. 7. The spectrum for *Au4f* appears as a peak doublet (Fig. 6a) located at − 84.0 and − 87.5 eV, and confirmed the presence of metallic Au [56]. The Au At% increases with the increase in temperature, reaching the maximum at 400 °C (Fig. 7). In the case of copper, the *Cu2p* chemical states were analysed (Fig. 6b). For the electrodes annealed at 200, 300, and 400 °C, three chemical states were designated. The first, located at 932.6 eV is ascribed as Cu (AuCu)[57]. The second component, shifted by − 1.2 eV, is assigned to CuO. Finally, the component located at 935.2 eV is associated with $Cu(OH)_2$*-$CuCO_3$. For the 10AuCu electrode annealed at 500 °C, the presence of CuAuTi alloy is confirmed by the peak situated at 931.2 eV. The *Ti2p3/2* chemical state was not found for the sample annealed at 200 °C, which may be caused by the substrate being covered with a tight layer of AuCu. Above 300 °C, the TiO_2 (458.6 eV) At% increases with increasing temperature (Fig. 7) caused by the subsequent exposure of the substrate. Last but not least, the analysis of the *O1s* spectrum is shown in Fig. 6d. The most notable component at − 529.7 eV should be related to the O^{2-} present in the 10AuCu electrode in the form of metal oxides. In addition, the peaks at 531.5 eV are linked to surface-adsorbed OH^- and $Cu(OH)_2$ [58].

To define the changes in the thickness of the passivation layer resulting from the formation of bimetallic 10AuCu structures (after thermal treatment at 400 °C), we carried out another XPS experiment, this time using Ar^+ ions to provide a depth profile study. The results of this study are shown in Fig. S1. The 10AuCu electrode thermally treated at 400 °C was selected for detailed analysis, due to the presence of both AuCuNPs and TiNDs (Fig. 1e). Comparing the Ti foil and the 10AuCu electrode depth profiles allows us to draw some conclusions on the thickness of the passivation TiO_2 layer. The naturally grown oxides on the Ti foil are formed primarily of TiO_2 but also of some Ti_2O_3. Their share at the surface is over four times higher when compared with the 10AuCu sample, but the TiO_2 was present in both cases (see Fig. S1b). The surface $Ti2p_{3/2}$ spectrum recorded for the Ti foil is also composed of the metallic Ti component at 453.8 eV. This result testifies that the thickness of the native film is below 5 nm thick, considering the depth of photoelectron acquisition in XPS. The native oxide layer is removed from the Ti foil after − 40 s of argon ion bombardment, suggesting an approx. 0.12 nm/s etching rate in our case. From the changes in the depth profile at Fig. S1a, it should be concluded that for the 10AuCu sample, the TiO_2 oxide layer is dominant after roughly 100–440 s of ion bombardment, leading to the assumption that the passive layer is a few times thicker than the Ti foil. These changes should be explained by the calcination process modifying the

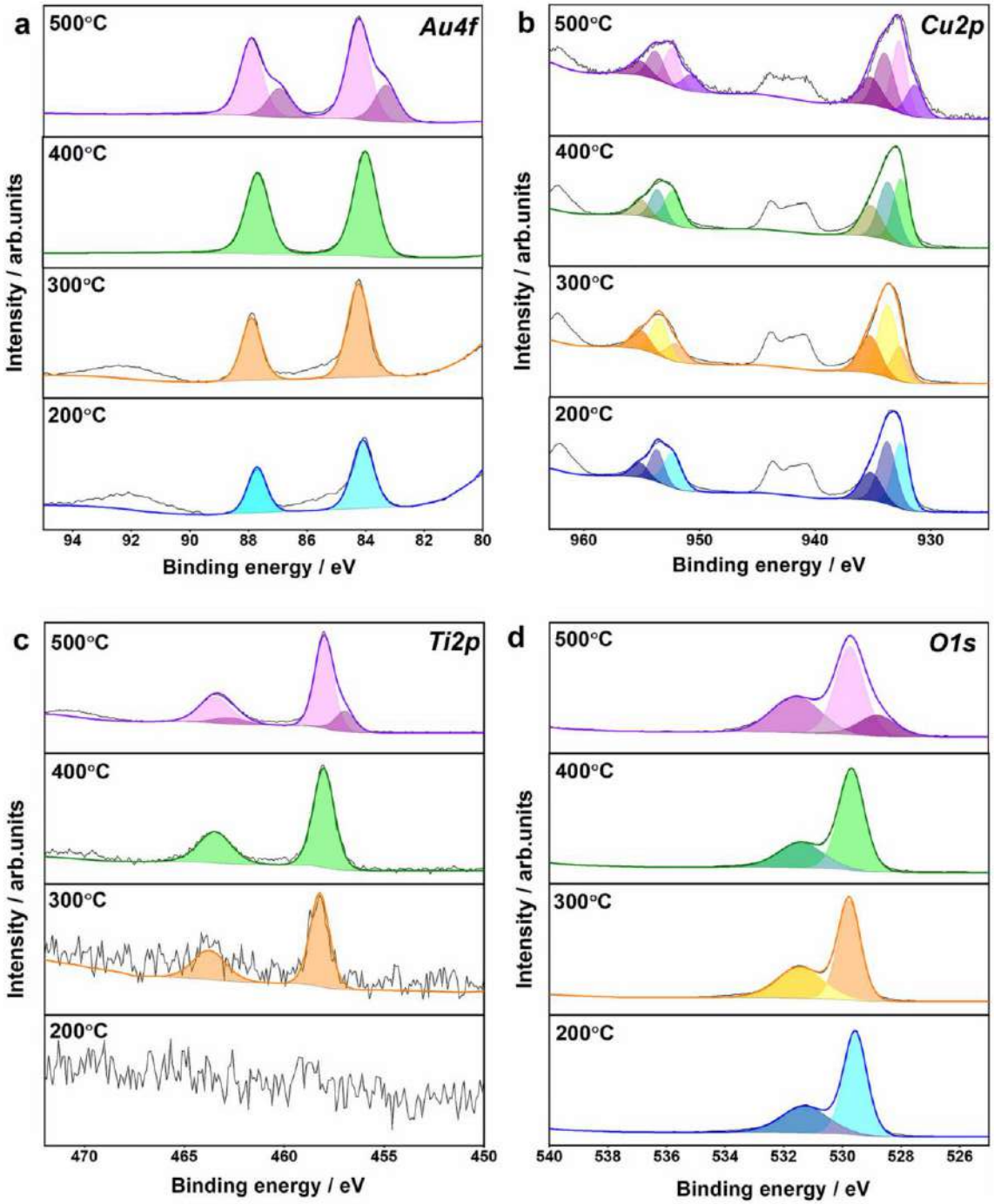

Fig. 6 XPS high-resolution spectra registered for 10AuCu electrode annealed at 200 °C, 300 °C, 400 °C, 500 °C: **a** *Au4f*, **b** *Cu2p*, **c** *Ti2p*, and **d** *O1s*

Table 2 Binding energies (BE) of 10AuCu electrodes: annealed at 200 °C, 300 °C, 400 °C, 500 °C

Peak	Component	BE/eV	At.%	Peak	Component	BE/eV	At.%
200 °C				200 °C			
Au4f 7/2	Au	84.1	0.83	Ti2p 3/2	–	–	
300 °C				300 °C			
Au4f 7/2	Au	84.2	1.4	Ti2p 3/2	TiO_2	458.6	0.6
400 °C				400 °C			
Au4f 7/2	Au	84.0	12.4	Ti2p 3/2	TiO_2	458.4	4.4
500 °C				500 °C			
Au4f 7/2	Au (CuAuTi)	83.3	1.4	Ti2p 3/2	Ti (CuAuTi)	457.3	3.7
Au4f 7/2	Au	84.2	3.7	Ti2p 3/2	TiO_2	458.4	15.6
200 °C				200 °C			
Cu2p 3/2	Cu (AuCu)	932.6	13.6	O1s	O^{2-}	529.5	44.6
Cu2p 3/2	CuO	933.8	14.6	O1s	OH^-	531.3	27.7
Cu2p 3/2	$Cu(OH)_2$*$CuCO_3$	935.2	7.9				
300 °C				300 °C			
Cu2p 3/2	Cu (AuCu)	932.6	6.7	O1s	O^{2-}	529.8	41.1
Cu2p 3/2	CuO	933.6	16.7	O1s	OH^-	531.5	22.0
Cu2p 3/2	$Cu(OH)_2$*$CuCO_3$	935.2	9.7				
400 °C				400 °C			
Cu2p 3/2	Cu (AuCu)	932.6	10.7	O1s	O^{2-}	529.7	37.8
Cu2p 3/2	CuO	933.8	11.1	O1s	OH^-	531.4	16.9
Cu2p 3/2	$Cu(OH)_2$*$CuCO_3$	935.2	6.8				
500 °C				500 °C			
Cu2p 3/2	Cu (CuAuTi)	931.2	1.2	O1s	O^{2-}	528.8	10.9
Cu2p 3/2	Cu (AuCu)	932.5	2.2	O1s	O^{2-}	529.7	34.4
Cu2p 3/2	CuO	933.8	2.1	O1s	OH^-	531.6	23.6
Cu2p 3/2	$Cu(OH)_2$*$CuCO_3$	935.0	1.3				

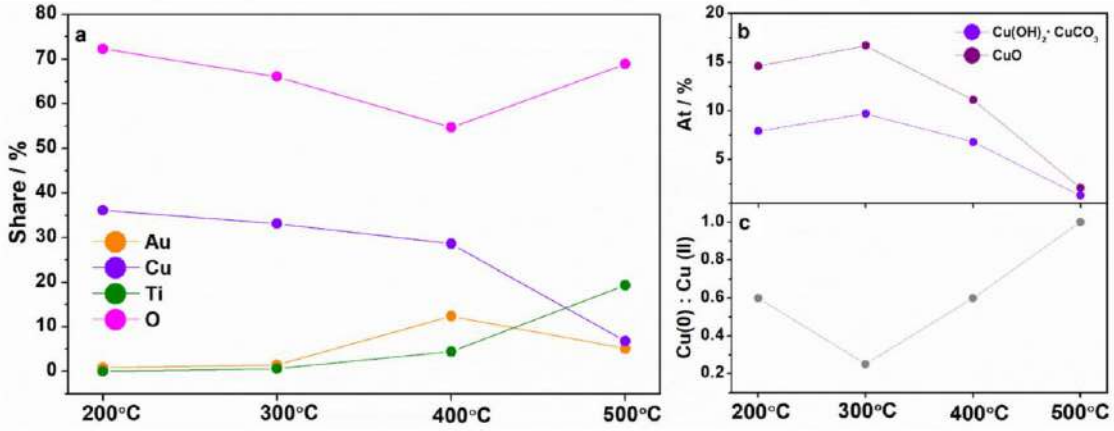

Fig. 7 Surface chemistry changes based on XPS analysis: **a** proportion of Au, Cu, Ti, and O elements as a result of annealing at different temperatures, **b** contribution of various Cu(II) species, **c** metallic Cu share

structure of the TiO_2 layer combined with some chemical changes within the layer. These are best observed in Fig. S1c, where the primary $Ti2p_{3/2}$ spectral component is shifted from 458.7 eV, characteristic of TiO_2, to 459.3 eV due to the formation of mixed (CuTi)O compounds.

It should be kept in mind that depth profiling with XPS is subject to some level of uncertainty,

originating primarily from three factors. First, the etching rate for the pure TiO_2 of the Ti foil and the AuCu nanostructures is most certainly different. Thus the direct etch time comparison is flawed. Next, the titanium oxides tend to be reduced under the influence of the Ar^+ ion gun leading to surface chemistry changes. For this reason, the share of both TiO_2 and Ti_2O_3 was summarised to present the depth profile in Fig. S1a. Finally, the ion gun is known to hammer some of the sample's atoms deeper into its structure rather than etching them, leading to the presence of some residual oxides even deep underneath the surface. For this reason, we subjectively recognised the limiting $Ti2p_{3/2}$ TiO_2 share in the passive film to be − 15 at.%.

The XPS for 10AuCu electrode annealed at 500 °C after photoelectrochemical measurements together with the data analysis was added to Electronic Supporting Information (Fig. S2).

3.5 Electrochemical performance

The electrochemical activity of gold–copper structures with and without rapid thermal annealing was tested firstly using cyclic voltammetry in 0.1 M NaOH. The results obtained for bimetallic 10AuCu, 5Au5Cu, and 5Cu5Au electrodes are shown in Fig. 8. During the anodic potential scan, the oxidation of Cu (1) and Cu_2O (2) occurs, while during the reverse, cathodic scan, the reduction of copper oxides (3), (4) takes place [59]:

$$2Cu + 2OH^- \rightarrow Cu_2O + 2e^- + H_2O \quad (1)$$

$$Cu_2O + 2OH^- \rightarrow 2CuO + 2e^- + H_2O \quad (2)$$

$$CuO + 2e^- + H_2O \rightarrow Cu_2O + 2OH^- \quad (3)$$

$$Cu_2O + 2e^- + H_2O \rightarrow 2Cu + 2OH^- \quad (4)$$

Regarding the 10AuCu sample before and after annealing at 100 °C, 200 °C, the visible oxidation peak (2) is present at ca. 0 V vs. Ag/AgCl/0.1 M KCl, and corresponds to the oxidation of Cu(I) to Cu(II). In addition, the peak observed at ca. − 0.1 V can be interpreted as the reduction of Cu(II) to Cu(I), and is labelled as (3). For the electrodes annealed at 300 °C and 400 °C, the abovementioned peaks are less intense, however, an additional reduction peak at + 0.1 V can also be found (5). This cathodic peak was ascribed by N. Shen et al. [60] to the reduction of Au_2O_3. For the electrodes annealed at 500 °C and 600 °C, no faradaic peaks were noticed. Moreover, the recorded currents were much lower than those for the electrodes treated at temperatures equal to and lower than 400 °C, which may be caused by the increased resistivity of Ti at higher temperatures [61]. It should be noted that the 10AuCu samples annealed at 500 and 600 °C exhibit a very poor capacitive character. The CV recorded for the 5Au5Cu layer demonstrates two oxidation peaks, first at ca. − 0.15 V corresponding to the oxidation of Cu(0) to Cu (I) (1), and second at + 0.05 V established as the oxidation of Cu(I) to Cu (II) (2). The cathodic peaks observed at ca. − 0.1 and at − 0.4 V can be interpreted as a transformation of Cu(II) into Cu(I) (3), and Cu(I) into Cu(0) (4), respectively. The electrodes annealed at 100 and 200 °C behave similarly to the 10AuCu electrodes fabricated at this temperature. The 5Au5Cu electrode treated at 300 °C behaves differently than the 10AuCu and 5Cu5Au. Also, this phenomenon will be further observed in the case of the linear voltammetry scans shown in Fig. 10. From the temperature of 400 °C, no Faraday peaks are noticeable. In addition, the capacitive current increases when 600 °C is applied, which is related to the increase in the rutile content on the electrode surface, as indicated by XRD [62]. According to Salari et al. [63], the CV curves demonstrate the increase in capacitance with the increasing annealing temperature of TiO_2 NTs up to 600 °C because of the gradual growth of the share of rutile. Regarding the 5Cu5Au sample, for the non-annealed and those annealed at 100 and 200 °C, two anodic peaks can be observed at − 0.2 and at + 0.05 V vs. Ag/AgCl/0.1 M KCl, which can be assigned to the oxidation of Cu(0) to Cu(I) (1), and Cu(I) to Cu(II) (2), respectively. Furthermore, the cathodic signals at − 0.1 and − 0.45 V correspond to a reduction of Cu(II) to Cu(I) (3), and Cu(I) to Cu(0) (4), respectively. The 5Cu5Au electrode treated at 300 °C has the same electrochemical character of oxidation and reduction processes as the 10AuCu sample at this temperature. Similarly, to the 5Au5Cu, above 400 °C there are no Faraday peaks, and there is a rather poor capacitive character with low currents exhibited for the material treated at 500 and 600 °C. It should be noted that the electrochemical properties of each electrode, i.e. 10AuCu, 5Au5Cu, and 5Cu5Au, are related to the titanium substrate which is heated at the same time. The voltammetric curves for TiND annealed at different temperatures are shown in Fig. 8h. Within the investigated potential range, any Faradaic reaction

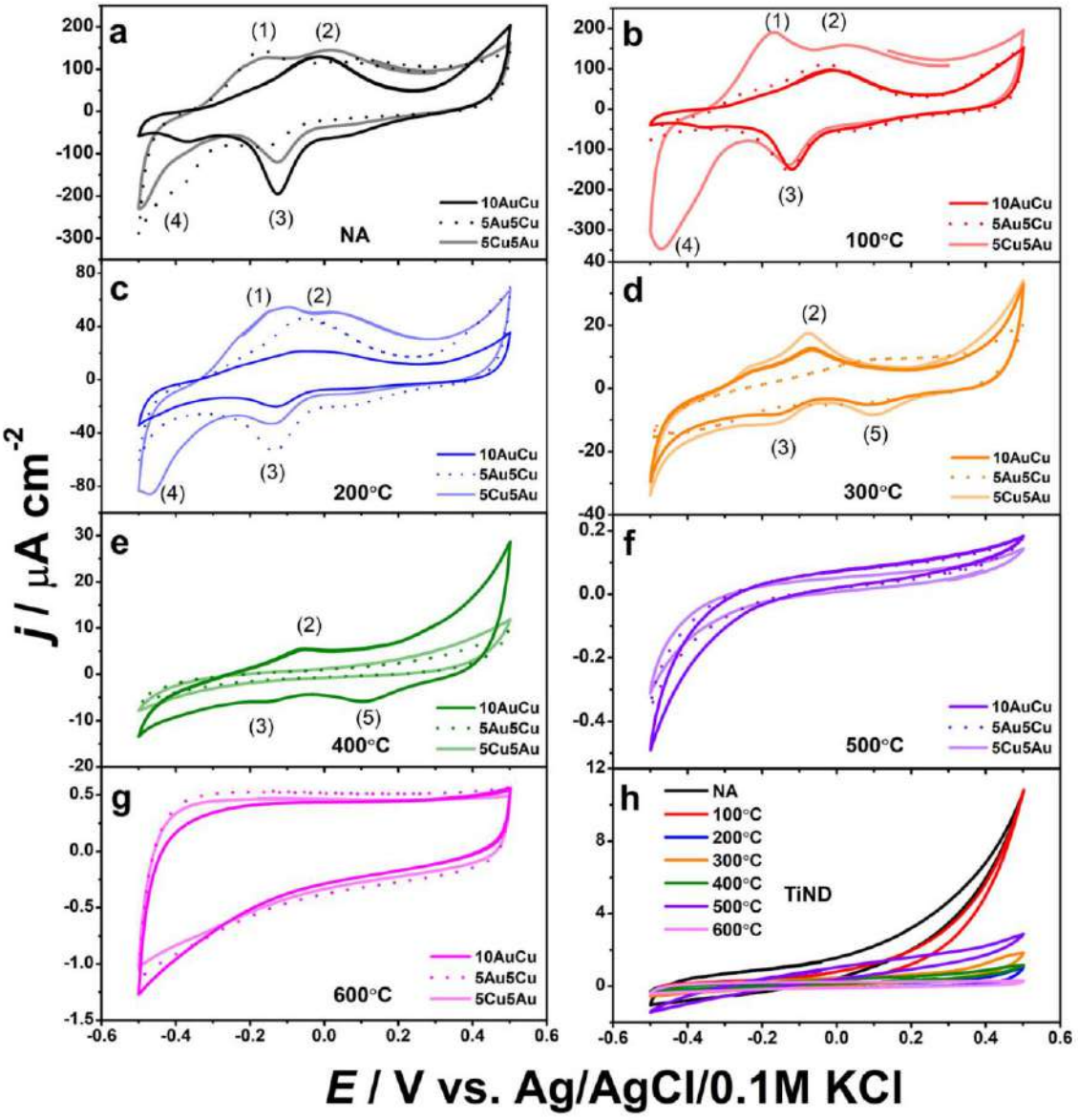

Fig. 8 Cyclic voltammetry curves registered in 0.1 M NaOH for 10AuCu, 5Au5Cu, 5Cu5Au electrodes **a** without annealing and thermally treated at **b** 100 °C, **c** 200 °C, **d**) 300 °C, **e**) 400 °C, **f** 500 °C, **g** 600 °C, and for **h** TiND substrate

was not recorded and only quite poor capacitive behaviour can be observed. Following that, up to 400 °C, the TiND as a supporting platform does not affect the electrochemical characteristics of bimetallic gold–copper structures. However, above this temperature, the titanium substrate significantly influences the material response. It can be observed in the SEM images that at 500 °C and above, nanoparticles integrate with the titanium surface and the ordered Ti platform morphology is no longer seen. Such phenomena may be explained with the formation of $TiCu_3$ and Ti_3Cu_4 intermetallic phases, as was reported by Li et al. [64]. In our case, CuAuTi alloy was obtained.

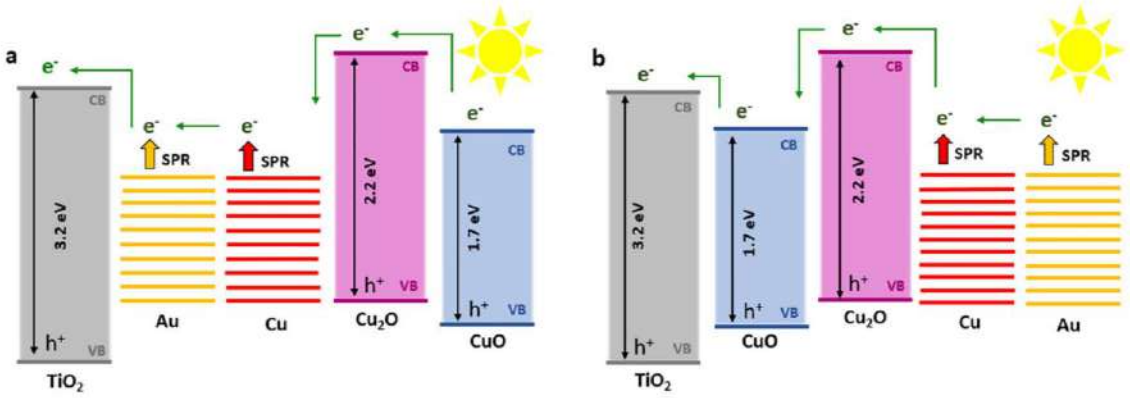

Fig. 9 Energy band diagrams in AuCu NPs on TiNDs when **a** gold is closer to TiO_2, **b** copper oxides are closer to TiO_2

In order to examine the photoactivity of the fabricated nanostructures, linear voltammetry measurements in the dark, under UV–vis, and under visible illumination were performed. The temperature changes applied during thermal processing obviously influence the current density and the overall photoresponse of gold–copper nanomaterials. The signal in the cathodic potential regime when the electrodes were polarised at − 0.8 V, and in the anodic regime at + 0.8 V vs. Ag/AgCl/0.1 M KCl reached the maximum value at the particular temperature treatment. The comparison of the current densities recorded at − 0.8 and + 0.8 V under UV–vis illumination is given in Table 3. The maximum current density values recorded in the dark for each electrode material were obtained for temperatures in the range from 200 to 400 °C, which can be caused by the formation of the most catalytically active sites on gold–copper nanostructures. According to Tachikawa et al. [65], areal OER activity decreases as the annealing temperature increases from 300 to 450 °C due to the reduction in the number of catalytically active sites. The 5Au5Cu electrode annealed at 300 °C exhibits the highest value of current density at − 0.8 V. However, at the potential of + 0.8 V, the best result of 1.5 mA cm^{-2} was recorded for the 10AuCu sample also annealed at 300 °C. It should be mentioned that in the established anodic limit, any gas bubbles were not noticed at the electrode surface. According to our previous article [36], AuCu nanostructures annealed in a muffle furnace at 450 °C exhibit a high response towards OER with the intense evolution of gas bubbles. In that work, the current density for 5Au/5Cu and 5Cu/5Au electrodes at + 0.8 V vs. Ag/AgCl/0.1 M KCl under visible light illumination reached 1.32 and 1.26 mA cm^{-2}, respectively. For a more precise analysis, an additional measurement in the potential range from − 0.8 to + 1.5 V was performed for the 10AuCu electrode annealed in the RTA furnace at 300 °C (Fig. S3). The evolution of weak gas bubbles could be observed at + 1.2 V. Therefore, two processes such as OER or oxidation of Cu^{2+} to Cu^{3+} [66] may take place at this potential.

In addition, the oxidation process enhanced by light took place at the potential of − 0.17 V vs. Ag/AgCl/0.1 M KCl. The current densities are summarised in Table 4. This phenomenon occurs for a bimetallic gold–copper structure because of the synergistic effect [67]. It is possible that the increase in activity is related to the presence of copper oxides on top of the gold. This may be confirmed by the highest current value for the non-annealed 5Au5Cu electrode in which the topmost layer is copper. The greatest increase in the current recorded under UV–vis illumination between non-annealed and the thermally treated sample at − 0.17 V was achieved by the 10AuCu electrode annealed at 300 °C (see Fig. 11a). The value increases from 31.2 to 349.1 μA cm^{-2} which results in a current density 11 times higher than for a non-annealed nanostructure.

In order to analyse the changes caused by light, it is important to underline that when Cu_2O and TiO_2 semiconductors are connected, a p–n heterojunction can be formed [68]. The character of this junction is exhibited at the potential of ca. − 0.3 V for electrodes

Table 3 Values of current density at − 0.8 V and + 0.8 V vs. Ag/AgCl/0.1 M KCl under UV–vis illumination for bimetallic nanostructures

	Current density at − 0.8 V/mA cm^{-2}			Current density at + 0.8 V/mA cm^{-2}		
	10AuCu	5Au5Cu	5Cu5Au	10AuCu	5Au5Cu	5Cu5Au
NA	− 0.08	− 0.15	− 0.1	0.83	0.88	1.22
100 °C	− 0.09	− 0.16	− 0.02	0.73	0.92	1.21
200 °C	− 0.15	− 0.16	**− 0.15**	1.27	**1.37**	1.38
300 °C	− 0.14	**− 0.38**	− 0.02	**1.5**	0.11	**1.49**
400 °C	**− 0.34**	− 0.09	− 0.1	0.53	0.03	0.03
500 °C	− 0.009	− 0.006	− 0.007	0.05	0.06	0.06
600 °C	− 0.00003	0.004	− 0.0004	0.08	0.1	0.07

Bold values indicate the highest current density obtained for the specific electrode (10AuCu, 5Au5Cu, 5Cu5Au) at the particular potential

Table 4 Values of current density at − 0.17 V vs. Ag/AgCl/0.1 M KCl under UV–vis illumination for bimetallic nanostructures

	j at − 0.17 V/μA cm^{-2}						
	NA	100 °C	200 °C	300 °C	400 °C	500 °C	600 °C
10AuCu	31.2	54.5	299.8	**349.1**	77.8	− 0.5	0.1
5Au5Cu	**233.8**	141.4	152.5	30.4	1.9	− 0.3	0.3
5Cu5Au	119.2	192.2	182.5	**370.0**	1.8	− 0.3	0.1

Bold values indicate the highest current density obtained for the specific electrode 10AuCu, 5Au5Cu and 5Cu5Au at − 0.17 V

annealed at 400 °C, and also for the 5Au5Cu sample thermally treated at 300 °C. A noticeable photocurrent response with efficient e–h pair separation [69] at 500 and 600 °C can be observed in Fig. 9. It can be assigned to the formation of a TiO_2 crystalline phase on the surface of the electrodes, as confirmed by the XRD and Raman measurements, in contrast to the materials annealed below 400 °C, where no rapid current increase and decrease is observed. The change in the current does not track the change in the light, and charge is accumulated at a potential of − 0.17 V. The current densities recorded at + 0.3 V vs. Ag/AgCl/0.1 M KCl for the 10AuCu, 5Au5Cu, and 5Cu5Au electrodes without and with thermal annealing at 500 and 600 °C are listed in Table 5. In our case, the highest value of photocurrent (91.4 μA cm^{-2}) was achieved for the 5Au5Cu sample annealed at 600 °C. The stability tests using CA for 10AuCu, 5Au5Cu, and 5Cu5Au electrodes annealed at 600 °C at + 0.3 V are shown in Figure S4. The run of photocurrent indicates high photostability of the material under intermitted lighting. Due to UV–vis light irradiation, photogenerated electron–hole pairs are created in the TiO_2, Cu_2O, and CuO [67, 70]. At the same time, the Au and Cu generate hot electrons. It is possible that a more efficient electron transfer

Table 5 Values of current density at + 0.3 V vs. Ag/AgCl/0.1 M KCl under UV–vis illumination for bimetallic nanostructures

Sample	Temperature/°C	j/μA cm^{-2}
10AuCu	NA	14.3
	500	47.7
	600	75.7
5Au5Cu	NA	17.6
	500	49.4
	600	**91.4**
5Cu5Au	NA	39.3
	500	50.9
	600	64.3

Bold value indicates the highest current density of all electrodes annealed at 500 and 600 °C obtained at + 0.3 V

process can be found when the gold is closer to the TiO_2, and the copper oxides are on the surface $CuO \rightarrow Cu_2O \rightarrow AuCu \rightarrow TiO_2$ (Fig. 10). In our case, in one nanoparticle, a mixture of the abovementioned components is present, however, for the 5Au5Cu electrode configuration $CuO/Cu_2O/AuCu/TiO_2$ can dominate. According to Oh et al. [13], Au/Cu_2O core–shell NPs on TiO_2 nanorods, in which Au nanoparticles are the core while Cu_2O is the shell, can enhance photocatalytic activity. This may indicate

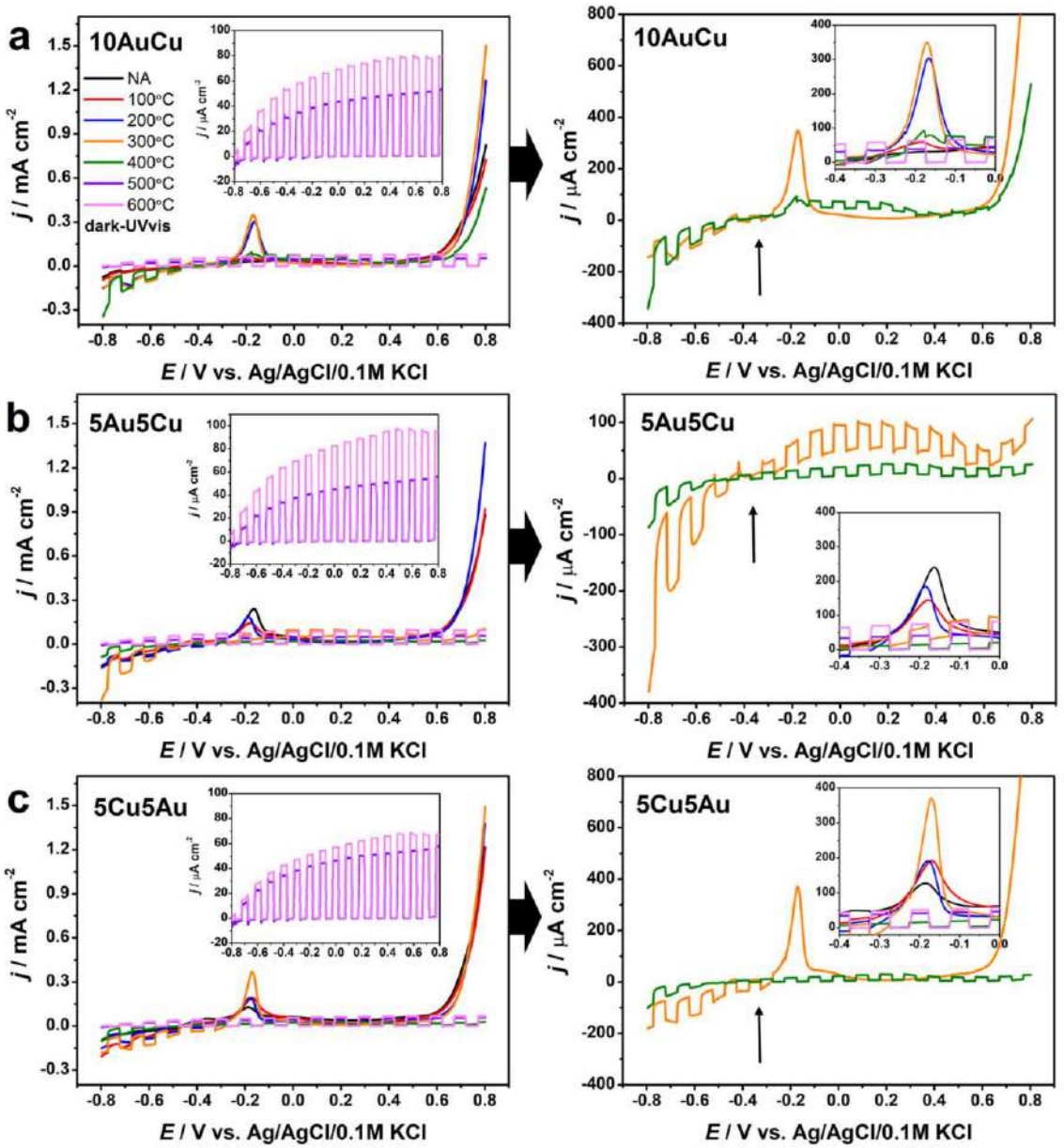

Fig. 10 Linear voltammetry curves registered in 0.1 M NaOH under UV-vis illumination for **a** 10AuCu, **b** 5Au5Cu, **c** 5Cu5Au electrodes annealed at different temperatures

that photocurrent enhancement is in favour of samples that contain copper species on the top.

The comparison of photocurrent density values for fabricated electrodes and for various materials containing Au and copper oxides are listed in Table 6. The photocurrent density of the 5Au5Cu electrode is higher than for Au@TiO_2/Cu_2O and AR-10AuCu/TiO_2NTs samples. In the case of the 5Au5Cu electrode, there is only a thin layer of TiO_2 which comes from naturally grown oxide onto the patterned Ti foil, whereas Au@TiO_2/Cu_2O and AR-10AuCu/TiO_2NTs are based on TiO_2 nanorods or TiO_2 nanotubes. The

Table6 Values of photocurrent density for materials containing Au and copper oxides

Electrode material	Photocurrent density/μA cm^{-2}	Potential/V vs. Ag/AgCl/0.1 M KCl	Electrolyte	References
Au@TiO_2/Cu_2O	17	+ 0.5	0.1 M PBS	[68]
AR-10AuCu/TiO_2NTs	64	− 0.2	0.1 M NaOH	[71]
Au_ZnO:Cu NRs	750	− 0.1	0.5 M Na_2SO_4	[28]
10AuCu	76	+ 0.3	0.1 M NaOH	This work
5Au5Cu	91	+ 0.3	0.1 M NaOH	This work
5Cu5Au	64	+ 0.3	0.1 M NaOH	This work

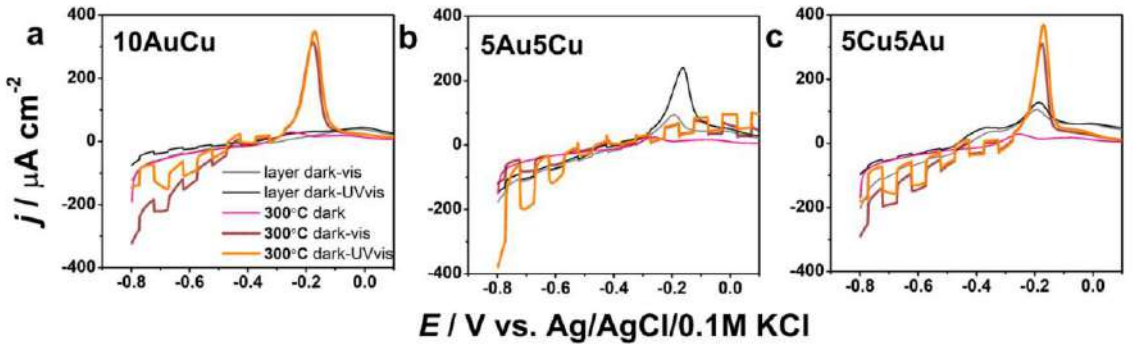

Fig. 11 Linear voltammetry curves registered in 0.1 M NaOH under visible and UV–vis illumination for **a** 10AuCu, **b** 5Au5Cu, **c** 5Cu5Au without and with thermal treatment at 300 °C

highest value of photocurrent density which equals to 750 μA cm^{-2} was obtained for Au_ZnO:Cu NRs, however, copper is not in the form of nanoparticles but as a dopant introduced into the structure of ZnO nanorods.

The 3D map of the photocurrent density was registered for the 10AuCu electrode annealed at 600 °C at the potential range from − 0.8 to + 0.8 V and wavelengths between 300 and 700 nm (Fig. S5a). As can be observed in the 3D curve the photocurrent grows when electrode is polarised towards anodic direction in the region of wavelengths between ca. 300 and 400 nm. The graph presented in Fig. S5b shows both absorbance spectra and the photocurrent spectra recorded at + 0.3 V vs. Ag/AgCl/0.1 M KCl. As can be observed within the range between 300 and 430 nm, electrons are effectively converted into photocurrent. Within this region, the maximum of the photocurrent value was obtained when the light of 370 nm irradiates the electrode material.

Activity could be observed at the potential of − 0.17 V vs. Ag/AgCl/0.1 M KCl for the bimetallic nanostructures not only under UV–vis illumination, but also when the electrode surface was exposed to visible light (Fig. 11). As was mentioned before, the highest current value was achieved by the 10AuCu electrode. The sample is also active under visible light illumination, and this is equal to 0.3 mA cm^{-2}. This phenomenon can be related to the presence of Cu_2O, and CuO, which are p-type visible-active-light materials, and their stabilisation by Au after thermal annealing.

4 Conclusion

In this work, we proposed a fabrication procedure of a nanomosaic material composed of AuCu nanostructures located on a Ti nanotextured substrate. The TiND platform was fabricated via the electrochemical anodisation and chemical etching processes. The substrate was then covered by thin metal layers of AuCu mixture as well as Au and Cu in various sequences. The nanomaterials were modified in a RTA furnace heated to a temperature of 100, 200, 300, 400, 500, and 600 °C, and compared with the non-

annealed substrate. The different temperatures of thermal treatment had a significant impact on the morphology, optical, structural, and electrochemical properties. At a temperature of 400 °C, AuCu NPs are formed on the surface, and the size of these nanoparticles increases with the temperature. XRD and Raman spectroscopy measurements confirmed the formation of a rutile phase from the amorphous TiO_2 passivation layer on the electrodes annealed at 500 and 600 °C. For the samples thermally treated at 600 °C, wide absorbance from 300 to 1000 nm was obtained. The electrochemical and photoelectrochemical activity of all samples were measured using cyclic and linear voltammetry techniques in 0.1 M NaOH. The peaks of the oxidation of Cu(0) to Cu(I), and Cu(I) to Cu(II), as well as the reduction of Cu(II) to Cu(I), and Cu(I) to Cu(0) were visible for the samples annealed below 400 °C. An oxidation process enhanced by light caused by a synergistic effect of the combination of AuCu took place at − 0.17 V vs. Ag/AgCl/0.1 M KCl. The 10AuCu electrode annealed at 300 °C achieved a current density 11 times higher than that recorded for the non-annealed nanostructure. We believe that the proposed approach can be extended to other platforms exhibiting a high degree of ordering, and therefore provides new opportunities in designing advanced photoactive materials.

Acknowledgements

The research is financed by the National Science Centre (Poland): Grant No. 2019/35/N/ST5/02604.

Author contribution

WL: Investigation, Validation, Conceptualisation, Writing—original draft, Writing—review & editing, Visualisation, and Funding acquisition. KG: Writing—original draft, Writing—review & editing, and Supervision. JK: Investigation, Validation, and Writing—review & editing. JR: Investigation, Validation, and Writing—review & editing. KS: Conceptualisation, Writing—original draft, Writing—review & editing, Supervision, and Funding acquisition.

Data availability

The datasets generated during and/or analysed during the current study are available from the corresponding author on reasonable request.

Declarations

Conflict of interest The authors declare that there is no conflict of interest.

Supplementary Information: The online version contains supplementary material available at https://doi.org/10.1007/s10854-022-08775-9.

Supplementary Information: The online version contains supplementary material available at https://doi.org/10.1007/s10854-022-08775-9.

References

1. A.K. Sra, R.E. Schaak, J. Am. Chem. Soc. **126**, 6667–6672 (2004)
2. S. Thota, Y. Wang, J. Zhao, Mater. Chem. Front. **2**, 1074–1089 (2018)
3. P. Suchomel, L. Kvitek, R. Prucek, A. Panacek, A. Halder, S. Vajda, R. Zboril, Sci. Rep. **8**, 4589–4600 (2018)
4. S. Hussain, N. Kongi, H. Erikson, M. Rähn, M. Merisalu, L. Matisen, N. Alonso-Vante, Electrochim. Acta **316**, 162–172 (2019)
5. P. Kupracz, E. Coy, K. Grochowska, J. Karczewski, J. Rysz, K. Siuzdak, Appl. Surf. Sci. **530**, 147097–147107 (2020)

6. R. Singh, S. Dutta, Adv. Powder Technol. **29**, 211–219 (2018)
7. Y. Liu, Y. Liu, R. Yan, Y. Gao, P. Wang, Electrochim. Acta **331**, 135370 (2019)
8. L. Rout, A. Kumar, R.S. Dhaka, G.N. Reddy, S. Giri, P. Dash, Appl. Catal. A **538**, 107–122 (2017)
9. Q.Y. Liu, Y. Zhong, Z.Z. Jiang, K. Chen, S. Ma, P.F. Wang, Q. Wang, J. Mater. Chem. C. **8**, 4869–4875 (2020)
10. R. Mendoza-Cruz, L. Bazán-Diaz, J.J. Velázquez-Salazar, J.E. Samaniego-Benitez, F.M. Ascencio-Aguirre, R. Herrera-Becerra, M. Jose-Yacaman, G. Guisbiers, Nanoscale **9**, 9267–9274 (2017)
11. J. Wang, X. Wu, W. Ma, C. Xu, Adv. Func. Mater. **30**, 2000670–2000680 (2020)
12. S. Schünemann, G. Dodekatos, H. Tüysüz, Chem. Mater. **27**, 7743–7750 (2015)
13. J.T. Oh, S.R. Chowdhury, T. Lee, M. Misra, Dyes Pigm. **160**, 936–943 (2019)
14. Y. Liu, Ch. Xu, Y. Xie, L. Yang, Y. Ling, L. Chen, J. Alloy. Compd. **820**, 153440–153448 (2020)
15. I. Barroso-Martín, E. Moretti, A. Talon, L. Storaro, E. Rodríguez-Castellón, A. Infantes-Molina, Materials. **11**, 890–907 (2018)
16. T.E.R. Fiuza, D.S. Gonçalves, I.F. Gomes, D. Zanchet, Catal. Today **381**, 171–180 (2020)
17. P. Li, L. Liu, W. An, H. Wang, H. Guo, Y. Liang, W. Cui, Appl. Catal. B **266**, 118618–118632 (2020)
18. N.S.K. Gowthaman, S. Shankar, S. Abraham John, J. Electroanal. Chem. **812**, 37–44 (2018)
19. W. Xu, J. Jia, T. Wang, C. Li, B. He, J. Zong, Y. Wang, H.J. Fan, H. Xu, Y. Feng, H. Chen, Angew. Chem. Int. Ed. **59**, 22246–22251 (2020)
20. M. Tominaga, Y. Taema, I. Taniguchi, J. Electroanal. Chem. **624**, 1–8 (2008)
21. D. Kim, C. Xie, N. Becknell, Y. Yu, M. Karamad, K. Chan, P. Yang, J. Am. Chem. Soc. **139**, 8329–8336 (2017)
22. D. Chocyk, A. Proszynski, G. Gladyszewski, J. Nanosci. Nanotechnol. **12**, 8647–8650 (2012)
23. K.U. Joshi, D. Kabiraj, A.M. Narsale, D.K. Avasthi, T.K. Gundurao, T.N. Warang, D.C. Kothari, Surf. Coat. Technol. **203**, 2497–2500 (2009)
24. K. Bergum, H.N. Riise, S. Gorantla, P.F. Lindberg, I.J.T. Jensen, A.E. Gunnæs, A. Galeckas, S. Diplas, B.G. Svenssak, E. Monakhov, J. Phys.: Condens. Matter **30**, 075702–075724 (2018)
25. K. Kumar, P. Swaminathan, Thin Solid Films **642**, 364–369 (2017)
26. P.L. Khoo, Y. Kikkawa, K. Satou, T. Shinagawa, M. Izaki, Thin Solid Films **653**, 158–164 (2018)
27. Y. Sato, S. Naya, H. Tada, APL Mater. **3**, 104502–114510 (2015)
28. H.Q. Huynh, K.N. Pham, B.T. Phan, C.K. Tran, H. Lee, V.Q. Dang, J. Photochem. Photobiol., A **399**, 112639–112676 (2020)
29. F. Amiripour, S.N. Azizi, S. Ghasemi, Int. J. Hydrogen Energy **44**, 605–617 (2019)
30. J. Wang, H. Zhu, D. Yu, J. Chen, J. Chen, M. Zhang, L. Wang, M. Du, ACS Applied Mater Interfaces. **9**, 19756–19765 (2017)
31. L. Van Turnhout, Y. Hattori, J. Meng, K. Zheng, J. Sá, Nano Lett. **20**, 8220–8228 (2020)
32. H. Wen, Y. Long, W. Han, W. Wu, Y. Yang, J. Ma, Appl. Catal. A **549**, 237–244 (2018)
33. Y. Liu, C. Xu, Y. Xie, L. Yang, Y. Ling, L. Chen, J. Alloy. Compd. **820**, 153440–153448 (2019)
34. D. Zeng, L. Yang, P. Zhou, D. Hu, Y. Xie, S. Li, J. Zhao, Int. J. Hydrogen Energy **43**, 15155–15163 (2018)
35. A. Gellé, T. Jin, L. de la Garza, G.D. Price, L.V. Besteiro, A. Moores, Chem. Rev. **120**, 986–1041 (2020)
36. W. Lipińska, K. Grochowska, J. Karczewski, J. Ryl, K. Siuzdak, Chem. Eng. J. **399**, 125673–125685 (2020)
37. J. Wawrzyniak, J. Karczewski, P. Kupracz, K. Grochowska, K. Załęski, O. Pshyk, E. Coy, M. Barmański, M. Szkodo, K. Siuzdak, Appl. Surf. Sci. **508**, 145143–1451153 (2019)
38. W. Lipińska, K. Siuzdak, J. Ryl, P. Barski, G. Śliwiński, K. Grochowska, Mater. Res. Express. **6**, 1150e3 (2019)
39. K. Grochowska, K. Siuzdak, J. Karczewski, M. Szkoda, G. Śliwiński, Plasmonics **12**, 1939–1946 (2016)
40. K. Grochowska, K. Siuzdak, Ł Macewicz, F. Skiba, M. Szkoda, J. Karczewski, G. Śliwiński, Appl. Surf. Sci. **418**, 472–480 (2017)
41. N. Fredj, T.D. Burleigh, J. Electrochem. Soc. **158**, C104 (2011)
42. L. Skowronski, A.A. Wachowiak, A. Grabowski, Appl. Surf. Sci. **388**, 731–740 (2016)
43. H.N. Umh, S. Yu, Y.H. Kim, S.Y. Lee, J. Yi, ACS Appl. Mater. Interfaces. **8**, 15802–15808 (2016)
44. L. Guo, Q. Sun, K. Marcus, Y. Hao, J. Deng, K. Bi, Y. Yang, J. Mater. Chem. A. **6**, 22005–22012 (2013)
45. J.C. Scaiano, K.G. Stamplecoskie, G.L. Hallett-Tapley, Chem. Commun. **48**, 4798–4808 (2012)
46. V.N. Nguyen, M.V. Nguyen, T.H.T. Nguyen, M.T. Doan, L.L.T. Ngoc, E. Janssens, A. Yadav, P. Lin, M.S. Nguyen, N.H. Hoang, Catalysts **10**, 261–272 (2020)
47. M. Lai, H. Yong, K. Zhong, W. Wang, J. Huang, S. Yao, X. Wang, Surf. Rev. Lett. **26**, 1950040–1950048 (2019)
48. S.B. Patel, A. Hamlekhan, D. Royhman, A. Butt, J. Yuan, T. Shokuhfar, C.G. Takoudis, J. Mater. Chem. B. **2**, 3597–3608 (2014)
49. O. Fesenko, L. Yatsenko, Springer Proc. Phys. **167**, 1–489 (2015)

50. L. Qian, R. Li, L. Zhou, Y. Liu, M. Yu, F. Xiong, X. Hao, BioResources **10**, 4391–4402 (2015)
51. C.L. Bracey, P.R. Ellis, G.J. Hutchings, Chem. Soc. Rev. **38**, 2231–2243 (2009)
52. O. Rocha-Rocha, M. Cortez-Valadez, G. Calderón-Ayala, C.E. Martínez-Nuñez, M. Pedroza-Montero, M. Flores-Acosta, Phys. Lett. A **383**, 125985–125992 (2019)
53. Y. Deng, A.D. Handoko, Y. Du, S. Xi, B.S. Yeo, ACS Catal. **6**, 2473–2481 (2016)
54. T. Kalaivani, P. Anilkumar, SILICON **10**, 1679–1686 (2018)
55. A.A. Mosquera, J.M. Albella, V. Navarro, D. Bhattacharyya, J.L. Endrino, Sci. Rep. **6**, 32171–32184 (2016)
56. W. Lipińska, J. Ryl, P. Slepski, K. Siuzdak, K. Grochowska, Measurement **174**, 109015 (2021)
57. W. Zhan, J. Wang, H. Wang, J. Zhang, X. Liu, P. Zhang, H. Zhu, J. Am. Chem. Soc. **139**, 8846–8854 (2017)
58. H. Park, S.E. Kim, IEEE Trans. Components Packag. Manuf. Technol. **1**, 332–338 (2019)
59. A. Bohme, F. Sterl, E. Kath, M. Ubl, V. Manninen, H. Giessen, ACS Photonics **6**, 1863–1868 (2019)
60. N. Shen, H. Xu, W. Zhao, Y. Zhao, X. Zhang, Sensors. **19**, 1203–1213 (2019)
61. B. Sundqvist, V.K. Tolpygo, J. Phys. Chem. Solids **122**, 41–50 (2018)
62. W. Tan, T. Gao, Y. Wang, Langmuir **36**, 3836–3842 (2020)
63. M. Salari, S.H. Aboutalebi, A.T. Chidembo, I.P. Nevirkovets, K. Konstantinov, H.K. Liu, Phys. Chem. Chem. Phys. **14**, 4770–4779 (2012)
64. J. Li, N. Yu, H. Jiang, J. Leng, H. Geng, Corros. Sci. **91**, 95–100 (2015)
65. T. Tachikawa, A. Beniya, K. Shigetoh, S. Higashi, Catal. Lett. **150**, 1976–1984 (2020)
66. X. Gong, Y. Gu, F. Zhang, Z. Liu, Y. Li, G. Chen, B. Wang, Front. Mater. **6**, 1–9 (2019)
67. P. Basnet, E.C. Anderson, Y. Zhao, ACS Appl. Nano Mater. **2**, 2446–2455 (2019)
68. L. Luo, T. Zhang, X. Zhang, R. Yun, Y. Lin, B. Zhang, X. Xiang, Catalysts **10**, 539–557 (2020)
69. M. Szkoda, A. Lisowska-Oleksiak, K. Siuzdak, J. Solid State Electrochem. **20**, 1765–1774 (2016)
70. G.Y. Yao, Z.Y. Zhao, J. Mater. Chem. C. **8**, 8567–8578 (2020)
71. W. Lipińska, K. Grochowska, J. Ryl, J. Karczewski, K. Siuzdak, ACS Appl. Mater. Interface. **13**, 52967–52977 (2021)

Supporting information to the article A2

Temperature-controlled nanomosaics of AuCu bimetallic structure towards smart light management

Wiktoria Lipińska*[1], Katarzyna Grochowska[1], Jakub Karczewski[2,3], Jacek Ryl[2,3] and Katarzyna Siuzdak[1]

[1]Centre for Plasma and Laser Engineering, The Szewalski Institute of Fluid-Flow Machinery Polish Academy of Sciences, Fiszera 14 St., 80-231 Gdańsk, Poland

[2]Institute of Nanotechnology and Materials Engineering, Faculty of Applied Physics and Mathematics, Gdańsk University of Technology, Narutowicza 11/12 St., 80-233 Gdańsk, Poland

[3]Advanced Materials Center, Gdańsk University of Technology, Narutowicza 11/12 St., 80-233 Gdańsk

Corresponding author
*Email wlipinska@imp.gda.pl

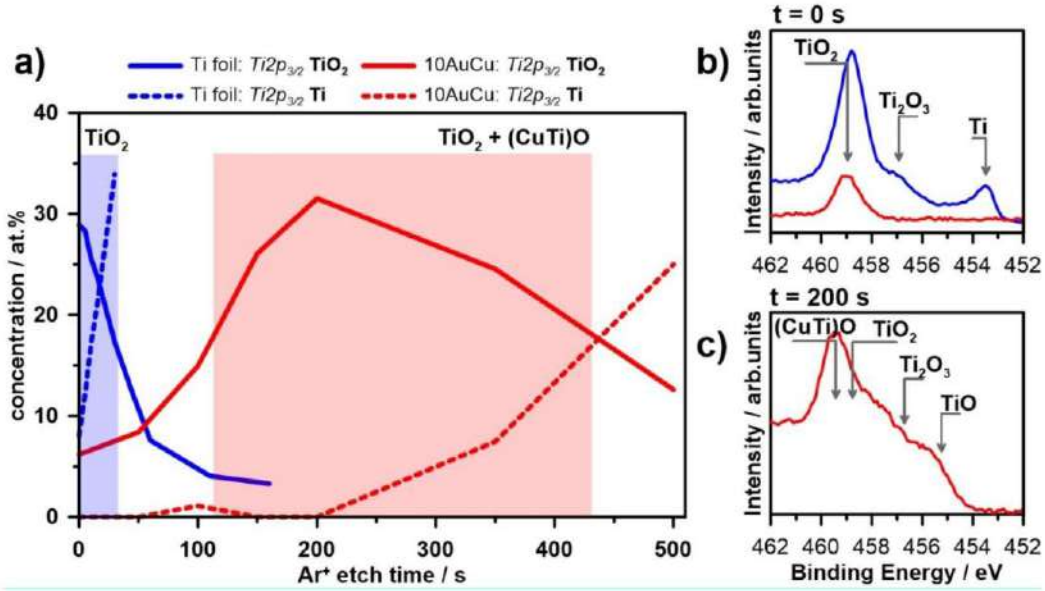

Fig. S1 – a) depth profile through the Ti foil and 10AuCu sample formed at 400 °C considering the share of $Ti2p_{3/2}$ spectral components TiO_2 and metallic Ti, b) $Ti2p_{3/2}$ spectra of the studied samples b) at the surface and c) after 200 s Ar^+ bombardment.

XPS measurements were conducted for the 10AuCu electrode annealed at 500°C after photoelectrochemical measurements. The curves are presented in Fig.S2 and results are summarized in Tab.S1. The spectrum of copper appears as an overlapping four peaks located at 931.2 eV, 932.6 eV, 933 eV, and 935.0 eV same as for the sample before electrochemical measurements. The same peaks after and before electrochemical measurements can be observed for Ti2p and O1s spectra. The most prominent change occurring due to the performed measurements was noted for Au4f spectrum as a new third peak Au_2O_3 located at 86.3 eV [1, 2]. The Au_2O_3 oxide was formed during cyclic voltammetry measurements, however, its amount was too small to observe an anodic peak on the CV curve. Additionally, the increase of Atomic% of metallic Au were confirmed.

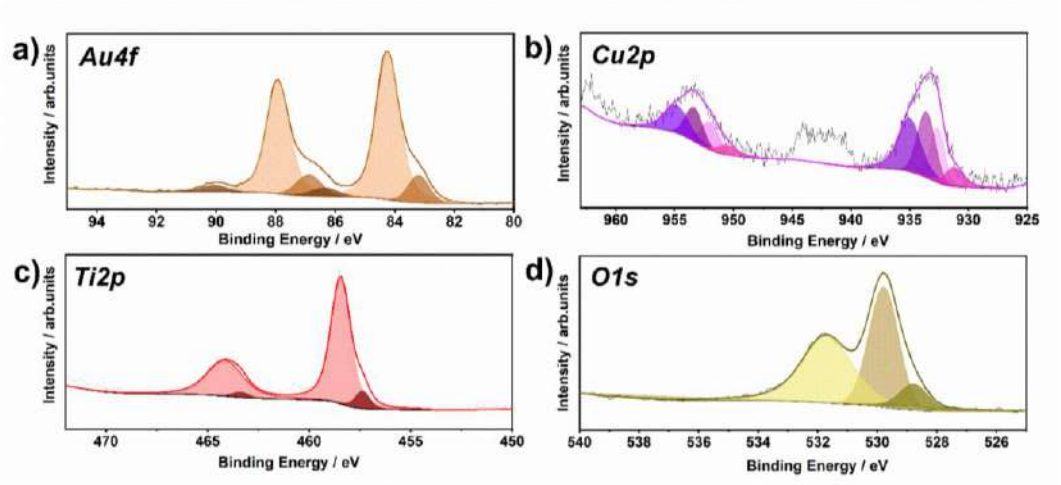

Fig.S2 XPS high resolution spectra registered for 10AuCu electrode annealed at 500°C after photoelectrochemical measurements

Table.S1 Binding energies (BE) of 10AuCu electrodes annealed at 500°C after photoelectrochemical measurements.

Peak	Component	BE / eV	At.%	Peak	Component	BE / eV	At.%
Au4f 7/2	Au (CuAuTi)	83.2	1.16	Cu2p 3/2	Cu (CuAuTi)	931.2	0.48
Au4f 7/2	Au	84.2	8.26	Cu2p 3/2	Cu (Au-Cu)	932.6	0.93
Au4f 7/2	Au_2O_3	86.3	0.51	Cu2p 3/2	CuO	933.6	1.4
				Cu2p 3/2	$Cu(OH)_2$*$CuCO_3$	935.0	1.7
O1s	O^{2-}	528.8	7.02				
O1s	O^{2-}	529.8	29.2	Ti2p 3/2	Ti (CuAuTi)	457.4	1.5
O1s	OH^-	531.7	32.8	Ti2p 3/2	TiO_2	458.5	15.0

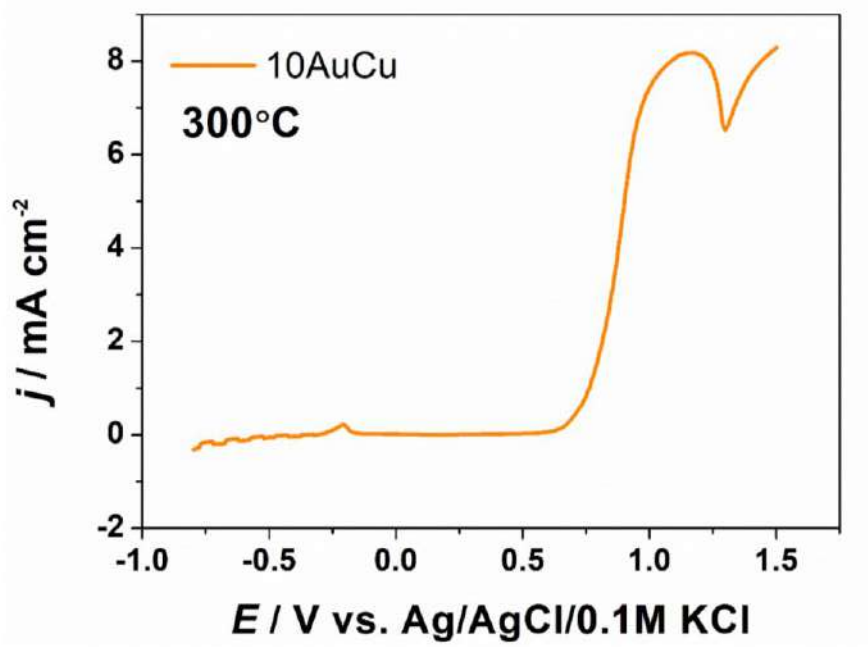

Fig.S3 Linear voltammetry curve registered in 0.1 M NaOH
under UV-vis illumination for 10AuCu electrode annealed at 300°C.

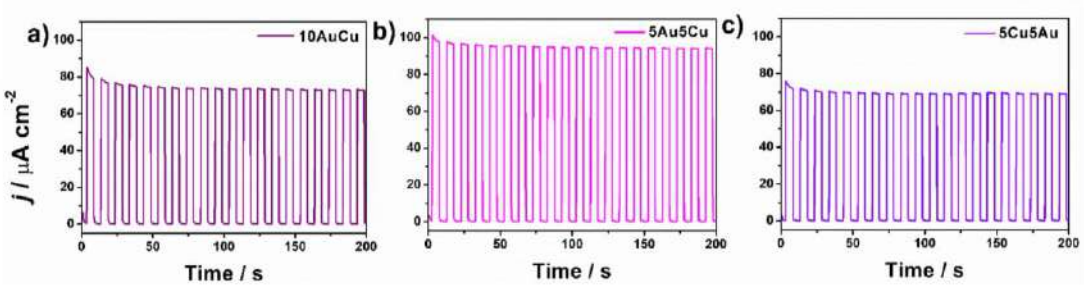

Fig. S4 Chronoamperometry curves registered in 0.1M NaOH under UV-vis illumination for
a) 10AuCu, b) 5Au5Cu, c) 5Cu5Au electrode.

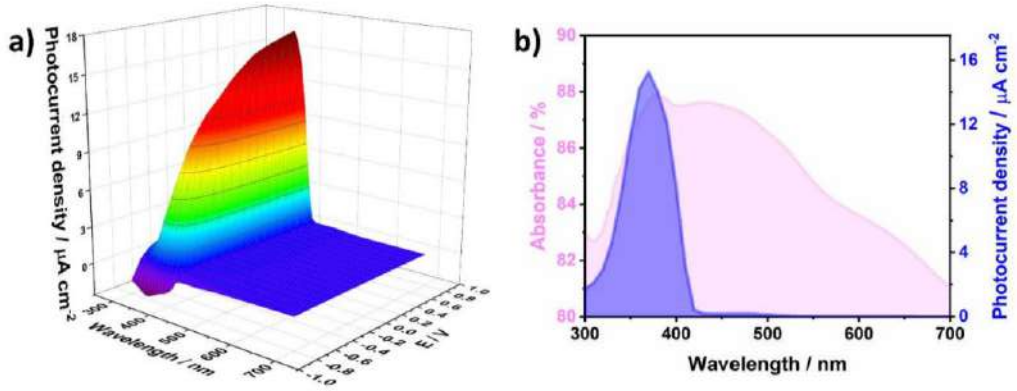

Fig. S5 a) 3D map for the photocurrent density and b) the relationship between absorbance, photocurrent density at +0.3 V and wavelength registered for 10AuCu electrode annealed at 600°C.

References

1. J.P. Sylvestre, S. Poulin, A.V. Kabashin, E. Sacher, M. Meunier, J.H.T. Luong, J. Phys. Chem. B. **108**, 16864-16869 (2018)
2. M. Gougis, A. Pereira, D. Ma, M. Mohamedi, RSC Adv. **4**, 39955-39961 (2014)

7.3 Effect of various annealing rate and time on AuCu-decorated Ti nanodimples towards photoelectrochemical activity

Brief overview of the article A3

Introduction

Changing the nanomaterials synthesis procedure effects on materials properties and among others the efficiency of photocurrent generation. As it was previously described, TiO_2 is characterized by wide band gap of 3.2 eV[212]. Therefore, modifications with Au nanoparticles and semiconductors such as CuO and Cu_2O capable of absorbing visible light are frequently exploited. Huang et al.[213] demonstrated that optical properties of Au-Cu_2O core-shell nanocrystals are facet-dependent (colloid suspension of nanoparticles). Tuning the copper oxide morphology and crystallography from rhombic, octahedral to cubic structure effects on gold surface plasmon resonance band position. On the other hand Xu et al.[214] showed that differences in the Au-Cu_2O Janus nanostructure where Au nanoparticle is engulfed in various degree by Cu_2O cube strongly influence on charge separation and photocurrent generation (Au-Cu_2O nanostructures on FTO).

AuCu nanoparticles described in the article A2 were active in the vis light at -0.17 V and in the UV-vis light from ca. -0.8 V to +0.8 V. Therefore, the next goal was to obtain AuCu nanoparticles active in the visible light not only at -0.17 V (A1, A2) but in the wider potential window. The wider potential window means that photoanodes can generate photocurrents at a larger range of applied potential without being limited to oxidation and reduction processes. This approach allows to increase the efficiency of e^- h^+ pair generation and stability of the photoanodes[215]. Based on already gathered results (given in article A2) the highest At% of copper oxides was registered for bimetallic AuCu electrode annealed at 300 °C. AuCu materials thermally treated at 400 °C had the reflectance band minima at ca. 530 nm while SPR band for Au or Cu NP can be observed approximately in that region[19]. Therefore, in order to obtain structure active in the visible light spectrum, where materials active under visible light are placed on the top of the electrode, the sputtering process was divided into two stages.

The preliminary results are presented in Figure 49. Firstly, Ti nanodimples were sputtered with thin 5 nm layer of Au and thermally treated at 600 °C. Secondly, those materials were sputtered with 5 nm layer of Cu and finally annealed at 300 °C or 400 °C. All annealing processes were conducted for 1 min and with the heating rate of 30 °C/s. The schematic fabrication route is presented in Figure 50 This approach allows to fabricate AuCu core-shell nanoparticles where Au plays as a core and Cu/copper oxides are assigned as a shell. According to Table 10

the highest photocurrent of 14.0 μA cm^{-2} for 5Au/TiND 600 °C + 5Cu 300 °C material was ca. 9 times higher than for 5Au5Cu/TiND 600 °C electrode.

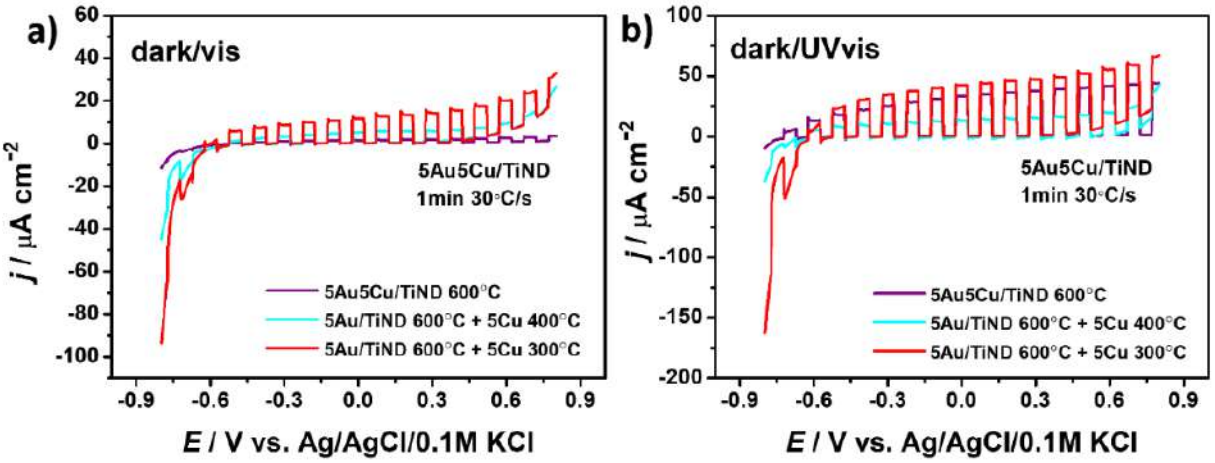

Figure 49. Linear voltammetry curves recorded for 5Au5Cu/TiND electrodes in 0.1 M NaOH under chopped dark/vis and dark/UV-vis radiation.

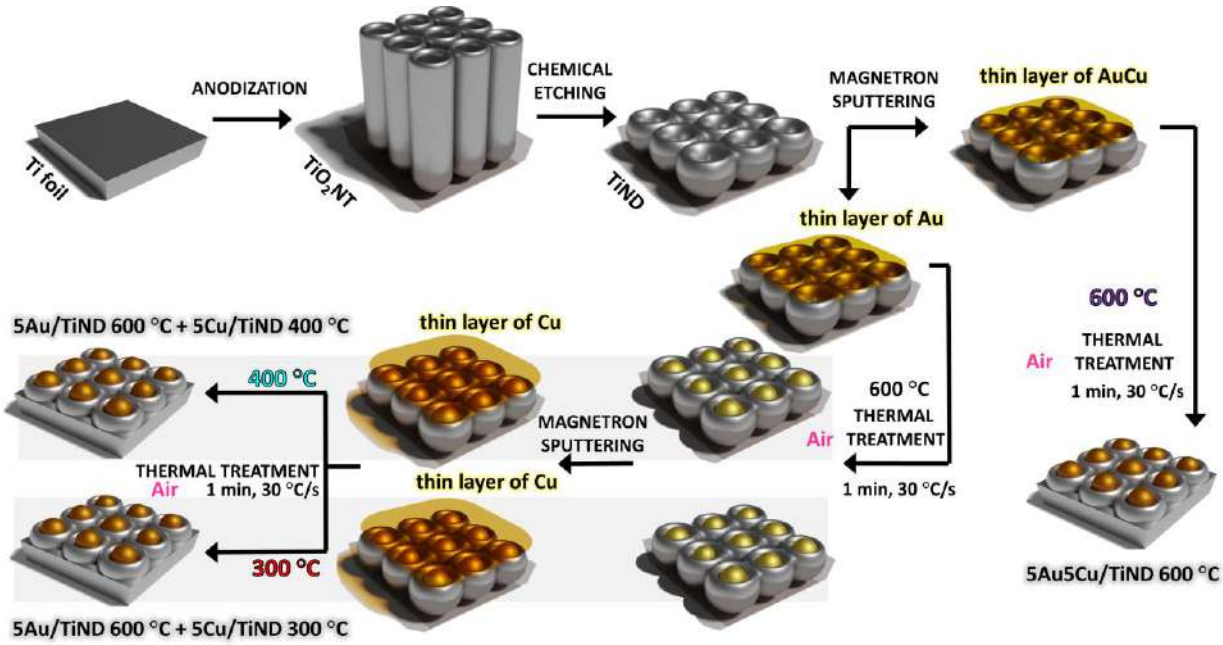

Figure 50. Schematic fabrication route of AuCu nanoparticles formed on Ti nanodimples.

Table 10. Values of photocurrent density registered under vis and UV-vis light illumination at +0.3 V for 5Au5Cu electrodes fabricated by one and two stages sputtering process.

Electrode	$j_{(vis)}$ / μA cm^{-2}	$j_{(UV-vis)}$ / μA cm^{-2}
5Au5Cu/TiND 600 °C	1.6	37.4
5Au/TiND 600 °C + 5Cu 400 °C	5.1	14.2
5Au/TiND 600 °C + 5Cu 300 °C	14.0	46.7

In article A3, the core-shell AuCu nanoparticles formed on Ti nanodimples were fabricated by thermal treatment with various annealing rates (fast or slow) and different annealing times (short or long) in rapid thermal annealing furnace and then exploit as photoanodes. Taking above into account the magnetron sputtering and thermal annealing process were divided into two stages. Firstly, Au layer sputtering and annealing in 600 °C, then Cu layer deposition and thermal treatment in 300 °C. Such procedure was chosen to verify if copper oxides are more preferred on the top layer of nanoparticle and gold should be located between copper oxides and TiO_2/Ti platform. Furthermore, studies regarding the influence of various rates and times of thermal treatment on morphology, optical properties and photoactivity of the nanomaterials are justified.

Nanomaterials synthesis

Ti nanodimples were fabricated using the same procedure as given in article A1. As was mentioned in the *introduction* (page 121) the sputtering process was divided into two stages. TiNDs were sputtered by 5 nm Au layer and thermally treated at 600 °C during 1 minute (short thermal treatment – 1) or 4 hours (long thermal treatment – 4) and with annealing rate of 30 °C/s (fast – F) or 0.67 °C/s (slow – S). Then materials were again sputtered with 5 nm Cu layer and annealed at 300 °C during 30 min with annealing rate of 30 °C/s (fast) or 0.67 °C/s (slow). The schematic –abrication process is p–esented in Figure 51.

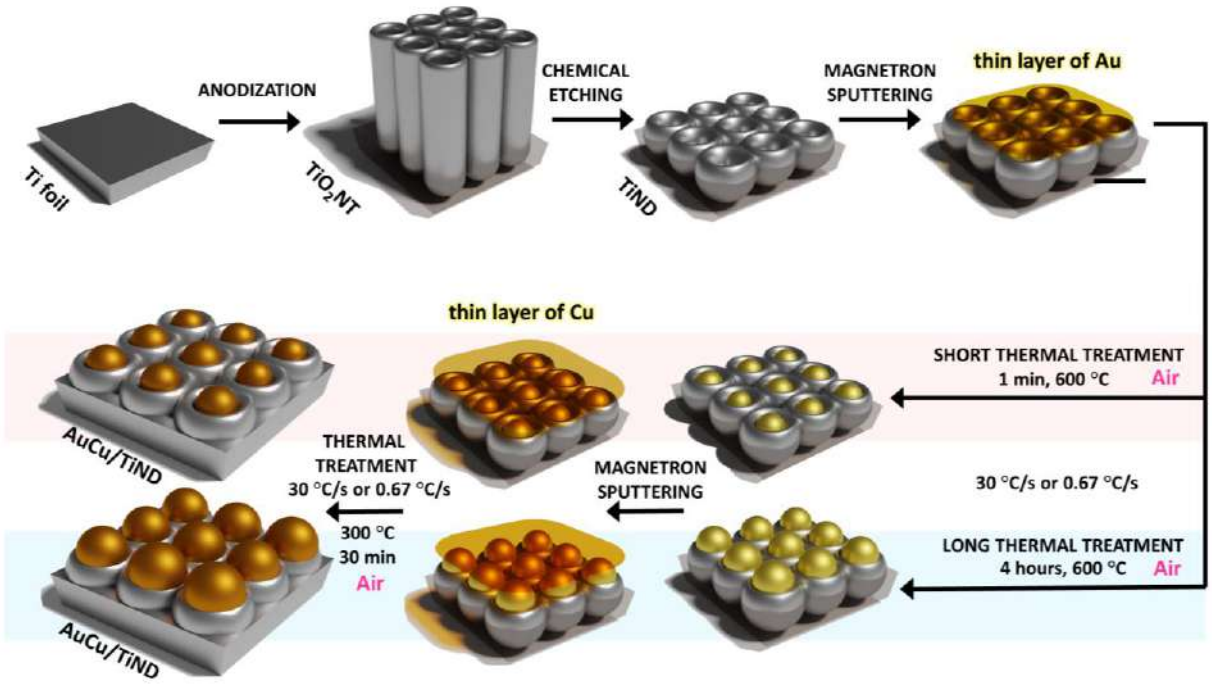

Figure 51. Schematic fabrication process of AuCu-decorated nanostructured Ti platform thermally treated in the rapid thermal annealer with various annealing times and rates.

Optical properties

Analysing the reflectance spectra (see in article A3, Figure 2a) enables to indicate that AuCu-decorated materials which were thermally treated during 1 minute in the first stage are characterized by well-defined absorption bands, whereas, electrodes annealed during 4 hours by flat line of reflectance. The reflectance minima for the 1F-AuCu/TiND and 1S-AuCu/TiND are placed at 550 nm and 600 nm, respectively. Based on the DFT calculations the reasons behind various positions of reflectance minima for materials thermally treated with different annealing rates (30 °C/s or 0.67 °C/s) were changes in the local crystallographic structure of Cu_2O/CuO junction, surface states and the crystallographic orientation of Cu_2O.

Electrochemical and photoelectrochemical properties

The photoelectrochemical activity was tested by means of linear voltammetry measurements under chopped light (dark/vis and dark/UV-vis) in 0.1 M NaOH solution (article A3, Figure 3). The values of photocurrent density are listed in Table 11. The LV curves for TiND, Cu/TiND, AuCu/TiND annealed with different times and annealing rates registered only under visible light illumination are presented in Figure 52. The Cu/TiND sample acts as reference electrode in order to highlighted synergetic effect of Au and Cu composition. As can be seen, bimetallic AuCu electrode annealed in the first stage for 1 minute and with the annealing rate of 30 °C/s (fast heated) labelled as 1F-AuCu/TiND obtained 24 times higher photocurrent (14.1 μA cm^{-2}) than pure 1F-TiND (see Figure 52a). In the case of AuCu/TiND electrode thermally treated in the first stage for 4 hours and with annealing rate of 30 °C/s no significant changes in photoresponse were registered (see Figure 52b). Similar behaviour was observed for electrodes thermally treated with annealing rate reduced by ca. 45 times (0.67 °C/s). AuCu-decorated substrate after short thermal treatment (Figure 52c) was active toward visible light illumination in contrast to platform after long annealing process (Figure 52d). It should be highlighted that decrease of annealing rate leads to 3 times higher photocurrent (47.2 μA cm^{-2}) in comparison to 1F-AuCu/TiND electrode. According to DFT calculations loss of the symmetry in crystallographic structure of Cu_2O/CuO junction, additional surface states and different crystallographic orientation are responsible for photocurrent changes between slow and fast heated electrodes. Furthermore, Au nanoparticles have significant influence on activity under visible light illumination in terms of transferring absorbed energy from copper oxides to nanostructured Ti platform and increasing tunnelling across the copper oxide junction.

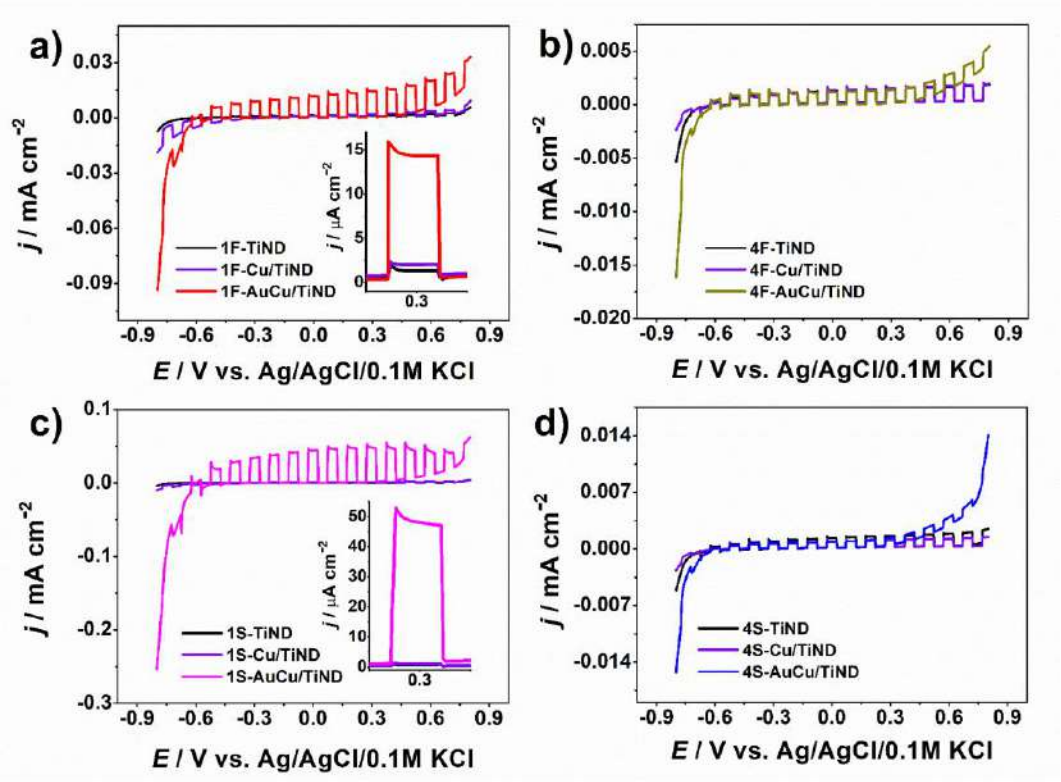

Figure 52. Linear voltammetry curves for TiND, Cu/TiND and AuCu/TiND electrodes thermally treated with various annealing rates (30 °C/s or 0.67 °C/s) and times (1 minute or 4 hours) registered in 0.1 M NaOH under vis illumination.

Table 11. Values of photocurrent density registered under vis and UV-vis light illumination for materials thermally treated with various annealing rates (30 °C/s or 0.67 °C/s) and times (1 minute or 4 hours) (E = +0.3 V vs. Ag/AgCl/0.1 M KCl).

Electrode	$j_{(vis)}$ / μA cm^{-2}	$j_{(UV-vis)}$ / μA cm^{-2}
1F-TiND	0.6	40.9
1F-Cu/TiND	1.3	14.1
1F-AuCu/TiND	14.1	46.8
4F-TiND	1.3	139.7
4F-Cu/TiND	1.3	66.7
4F-AuCu/TiND	1.3	73.1
1S-TiND	0.3	22.3
1S-Cu/TiND	0.5	13.8
1S-AuCu/TiND	47.2	63.0
4S-TiND	1.4	136.6
4S-Cu/TiND	0.9	60.5
4S-AuCu/TiND	0.9	65.8

Electrochemical impedance spectroscopy was carried out in order to determine differences between charge transfer resistance of AuCu-decorated Ti nanodimples thermally treated during 1 minute or 4 hours with fast (30 °C/s) or slow (0.67 °C/s) annealing rate

(see Figure 6 in article A3). EIS spectra for the 1F-AuCu/TiND and 1S-AuCu/TiND electrode as the most photoactive nanomaterials are presented below (Figure 53). The highest value ratio of R_{CT} recorded in dark and under visible light illumination was obtained for the 1S-AuCu/TiND and the 1F-AuCu/TiND electrodes, and was equal to 5.0 and 2.8, respectively. As can be seen, obtained results are in accordance with linear voltammetry measurements presented above registered under vis light (47.2 μA cm^{-2} and 14.1 μA cm^{-2}).

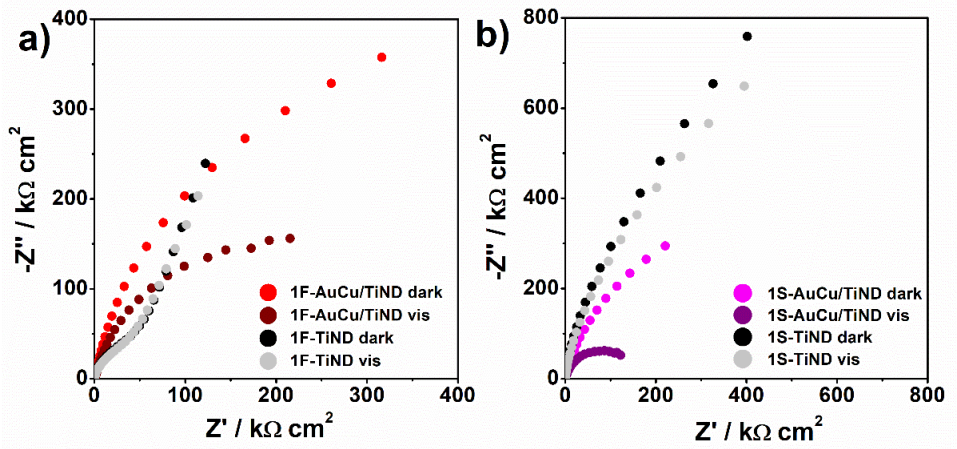

Figure 53. Electrochemical impedance spectra registered in dark and under visible light for a) 1F-AuCu/TiND, 1F-TiND and b) 1S-AuCu/TiND, 1S-TiND electrodes.

Conclusions

In this work, AuCu nanoparticles on Ti nanodimples fabricated via anodization, chemical etching, two steps sputtering process (first Au and then Cu layer), and short thermal treatment during 1 minute manifested significant photoelectrochemical activity under visible light illumination. Bimetallic AuCu electrodes annealed during 1 minute were characterized by well-defined reflectance band in contrast to materials annealed during 4 hours. The reflectance band minimum was shifted from 550 nm to 600 nm for fast and slow heated electrode. As was mentioned, 1F- AuCu/TiND (14.1 μA cm^{-2}) and 1S-AuCu/TiND (47.2 μA cm^{-2}) electrodes were active under visible light illumination, however, slow heated material exhibited ca. 3 times higher photocurrent than fast heated. Furthermore, the 1S-AuCu/TiND sample manifested ca. 80 and 3 times higher photocurrent under visible and UV-vis light than the pure nanostructured Ti platform, respectively.

A3) W. Lipińska, A. Olejnik, J. Karczewski, K. Grochowska, K. Siuzdak, ***Annealing Rate as a Crucial Parameter Controlling the Photoelectrochemical Properties of AuCu Mosaic Core-Shell Nanoparticles***, Energy Technology 11 (2023) 2201021 IF= 4.1 / 100 points mechanical engineering

RESEARCH ARTICLE

Energy Technology
Generation, Conversion, Storage, Distribution
www.entechnol.de

Annealing Rate as a Crucial Parameter Controlling the Photoelectrochemical Properties of AuCu Mosaic Core–Shell Nanoparticles

Wiktoria Lipińska, Adrian Olejnik, Jakub Karczewski, Katarzyna Grochowska, and Katarzyna Siuzdak*

Thermal processing is an essential step during the synthesis of various metal nanostructures and for tailoring their morphology, optical, and electrochemical properties. Herein, a profound impact of the annealing rate and time on photoactivity of gold–copper nanostructures by changes in the position and alignment of energy levels and surface states is reported. AuCu nanoparticles (NPs) are fabricated by sputtering of thin metal layers on the Ti nanopatterned foil followed by slow (0.67 °C s^{-1}) or fast (30 °C s^{-1}) treatment in the rapid thermal annealing furnace and then utilized as photoanodes. Photocurrent in the visible range of the slow-heated AuCu materials is 77 times higher, whereas for the fast heated 24 times higher than for pure Ti platform. On the other hand, the fast-heated material exhibits higher photon-to-current efficiency, longer recombination rate which reaches 10s, and higher carrier transport rate of 150 µs. Based on the simulated projected local density of states analysis and the characteristics of intensity-modulated spectra, this phenomenon is attributed to the presence of deeper midgap states in the electronic band structure for the fast-heated samples. Furthermore, photocurrent is enhanced by the presence of Au inside NPs, which increases tunneling across copper oxides junction.

1. Introduction

Considering the increasing worldwide energy demand and climate changes induced by fossil fuel consumption, a necessity for renewable, green energy is urgent. Therefore, a lot of scientific interest is focused nowadays on leveraging efficient, inexpensive strategies for solar energy harvesting and storage.[1] These typically include photovoltaics and photoelectrochemical water splitting for hydrogen production.[2,3]

Among the huge variety of available semiconductors suited for those purposes, copper oxides exhibit a very high photoactivity in the visible light spectrum and thus a huge potency toward listed applications.[4,5] Moreover, a synergy between copper oxides and noble metals such as Au has been reported. While Cu_2O and CuO cause the visible light absorption and electron–hole pair generation, Au facilitates charge transport between semiconductors and electrode contacts.[6] Moreover, gold and copper are interesting due to the surface plasmon resonance (SPR) effect resulting in the enhancement of the electromagnetic field, leading to the improvement of charge separation and hot electron generation. TiO_2 is an n-type semiconductor which has a wide bandgap of 3.2 eV[5] and it absorbs mostly ultraviolet light which is only 5% of solar spectrum light.[7] While TiO_2 solely has poor photoactivity, modifications of this semiconductor with narrower bandgap materials such as CuO (1.2–1.6 eV) and Cu_2O (2.1–2.6 eV) are predicted to enhance its photoactivity in visible light.[8]

The enhancement of solar energy utilization can be realized by different nanomaterials synthesis procedures. According to Xu et al.[9] the distal separation of the Au–Cu_2O domains in Janus structure increases charge separation and photocurrents. The photocurrent of Au–Cu_2O Janus structure is 5 and 10 times higher than that of Au–Cu_2O core–shell and Cu_2O nanocubes. Transformation of the Au–CuO Janus structure into core–shell was controlled by $CuCl_2$ precursor concentration. Yang et al.[3] reported that the composition of Cu_2O/CuO exhibits significant improvement of photocurrent compared to pure Cu_2O or CuO film. The UV–vis reflectance spectrum of Cu_2O shows

W. Lipińska, A. Olejnik, K. Grochowska, K. Siuzdak
Centre for Plasma and Laser Engineering
The Szewalski Institute of Fluid–Flow Machinery
Polish Academy of Sciences
80-231 Gdańsk, Poland
E-mail: wlipinska@imp.gda.pl

A. Olejnik
Department of Metrology and Optoelectronics
Faculty of Electronics, Telecommunications and Informatics
Gdańsk University of Technology
80-233 Gdańsk, Poland

J. Karczewski
Faculty of Applied Physics and Mathematics
Institute of Nanotechnology and Materials Engineering
Gdańsk University of Technology
80-233 Gdańsk, Poland

The ORCID identification number(s) for the author(s) of this article can be found under https://doi.org/10.1002/ente.202201021.

DOI: 10.1002/ente.202201021

absorption maximum at 450 nm while for Cu_2O/CuO it is shifted to 600 nm. Moreover, the Cu_2O-to-CuO thickness ratio was controlled by the electrodeposition and thermal oxidation time which influenced the photoelectrochemical properties. Furthermore, it was also outlined that thermal treatment of TiO_2 nanotubes modified by AuCu the magnetron-sputtered layer in air, vacuum, argon, or hydrogen atmosphere has a great impact on the chemical structure and electrochemical activity of AuCu-modified electrodes.[10] Thermal processing under argon leads to the formation of AuCuTi alloy, having increased donor concentration, defects as well as electron mobility, and improves the photocurrent in contrast to materials fabricated in air, vacuum, or hydrogen. Reports on the AuCu/nanopatterned Ti bimetallic structures indicate a synergetic effect compared to pure gold or copper oxides.[11] Au and Cu metals sputtered in sequence on the nanostructured Ti platform and annealed at 450 °C exhibit ≈9 and 5 times higher photocurrent in visible light illumination compared to electrodes thermally treated at 600 °C. Therefore, control of nanoparticles (NPs) synthesis parameters results in changes of materials properties which can be used for efficient solar light management. A combination of experimental approaches with theoretical simulations opens a new door to the deeper exploration of the nanomaterials world. The development of a huge variety of ab initio and semi-empirical computational approaches in recent years allows detailed, in-depth modeling of materials and grounding the experimentally observed phenomena into the first principles of quantum mechanics. Among those techniques, density functional theory (DFT) coupled with nonequilibrium Green's function (NEGF) gathers significant attention in deciphering the electron transport mechanisms in molecular and solid-state junctions.[12,13] Projected local density of states (PLDOS) analysis is particularly useful for examining intermolecular interactions between the constituents of the junction, energy-level alignment along the length of the junction, and construction of the energy band diagrams of heterojunctions on the level of several nanometers. This paradigm was successfully applied for explaining complex interactions in van der Waals heterostructures,[14] polyoxometalates molecular heterojunctions,[15] and the carbon nanotube | graphene interface.[16]

In this work, we present the fabrication method of AuCu NPs located on Ti-nanostructured platform and explore the effect of the heating rate (30 °C s^{-1} or 0.67 °C s^{-1}) and annealing time (1 min or 4 h)on their optical and photoelectrochemical properties. The titanium platform was produced by anodization and chemical etching process. Sequentially, a thin gold layer was sputtered on the Ti substrate and thermal annealing ensured formation of AuNPs. The magnetron sputtering and heat treatment process were repeated; however the second time the copper layer was sputtered on the previously modified electrode material and annealed at 300 °C in order to prevent mixing of Au and Cu and obtain AuCu core–shell NPs.[17] The impact of heating rate on AuCu NP properties was particularly examined using UV–vis absorption spectroscopy and DFT calculations of the optical spectra. We utilize computational approaches to investigate the interactions between Cu_2O and CuO and their photoelectrical properties. The photoelectrochemical activity of electrodes was characterized in the dark and under visible as well as UV–vis illumination in alkaline solution by linear voltammetry (LV) and electrochemical impedance spectroscopy. Moreover, an effect of various AuCu heating rates on photoactivity was analyzed using incident photon-to-current efficiency (IPCE) and intensity-modulated photocurrent/photovoltage spectroscopy (IMPS/IMVS). The results showed longer photocarrier lifetime and faster transport in fast-heated AuCu samples, but higher photocurrent magnitudes for slow-heated AuCu. Interestingly, analyses at different potentials suggested the presence of deep electronic traps in fast-heated AuCu NPs and shallow traps in slow-heated AuCu NPs. Furthermore, for the first time we reported computational investigations of the gold–copper oxides triple junction supporting explanation of the experimentally observed trends in photoactivity of AuCu core–shell NPs. In particular, we showed that Au greatly facilitates electronic transport from copper oxides to the electrode contacts.

2. Results and Discussion

2.1. Morphology and Crystallinity

scanning electron microscopy (SEM) images of TiNDs and AuCu/TiNDs electrodes are presented in **Figure 1** and S1, Supporting Information. As shown, thermal treatment conditions strongly affect the morphology of titanium platform as well as AuCu-modified samples. The characteristic morphology of titanium nanodimples can be observed for TiNDs electrodes annealed for 1 min (Figure 1a, S1a, Supporting Information), whereas for materials thermally treated for 4 h, TiO_2 nanosheets are visible on the surface, which is confirmed by X-ray diffraction (XRD) (Figure 1b, S1c, Supporting Information). Regarding the case of AuCu structures, annealing of the Au layer at 600 °C leads to the formation of spherical NPs which are sequentially covered by thin Cu. It can be assumed that core–shell NPs, where gold is a core and copper oxides constitute a shell, are formed on the surface. According to our previous results,[11] gold NPs can be obtained during annealing of Au layer at 600 °C, whereas it cannot be possible for the copper one. The average size of NPs for the 1F-AuCu/TiND and the 1S-AuCu/TiND is equal to 42 ± 15 and 48 ± 18 nm, respectively (Figure 1c, S1b, Supporting Information). Longer annealing time affects the growth of NP size and the average diameter reaches 78 ± 25 and 75 ± 21 nm for the 4F-AuCu/TiND and the 4S-AuCu/TiND electrodes (Figure 1d, Figure S1d, Supporting Information).

The XRD diffraction patterns for TiND and AuCu/TiND electrodes are shown in Figure 1e,f. The peaks located at 34.9°, 38.2°, 40.0°, 52.8°, 62.8°, 70.5°, 76.1°, and 77.1° correspond to the following Ti crystal planes: (100), (002), (101), (102), (110), (103), (112), and (201), respectively. For samples annealed for 1 min, peak at 27.3° appeared and can be ascribed to TiO_2 rutile (110) (Figure 1e). When the annealing time increased to 4 h, additional rutile peaks located at 36.0°, 41.2°, 43.9°, 54.3°, 56.6°, 62.7°, 64.4°, and 69.8° are observed and correspond to (001), (111), (120), (121), (220), (002), (130), and (112) planes (Figure 1f).

2.2. Optical Properties

Figure 2a shows the reflectance spectra of thermally treated TiND and AuCu/TiND electrodes. For bimetallic AuCu materials

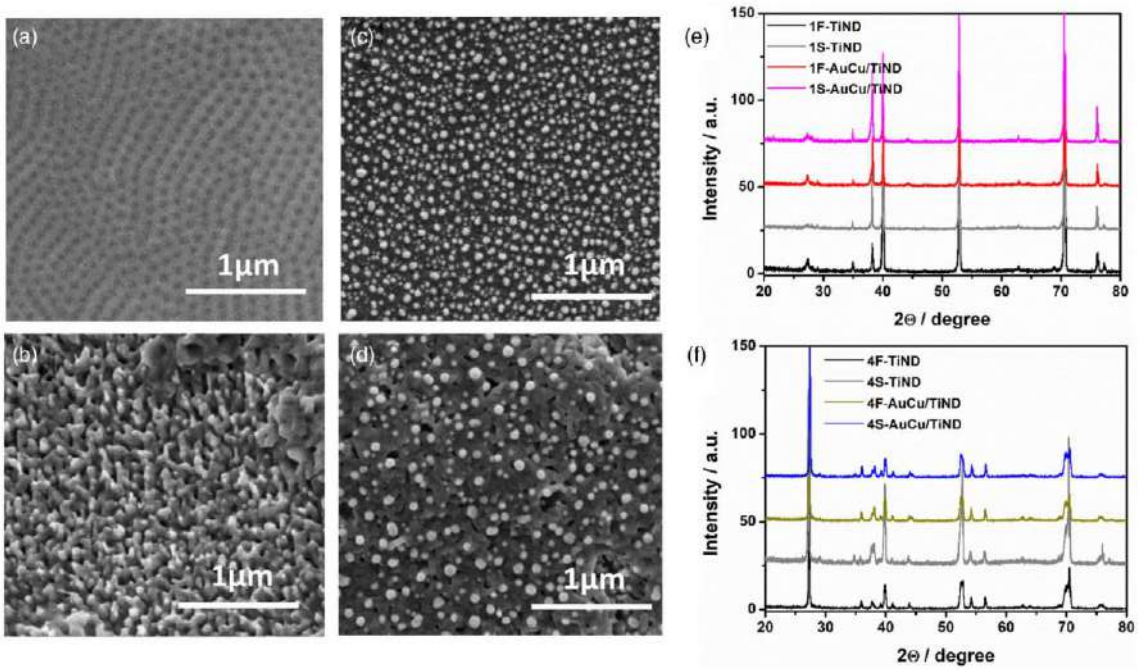

Figure 1. SEM images of a) 1S- TiND, b) 4S- TiND, c) 1S-AuCu/TiND, and d) 4S-AuCu/TiND and XRD pattern of electrodes annealed for e) 1 min and f) 4 h.

with Au annealed for 1 min (1F-AuCu/TiND or 1S-AuCu/TiND), several well-defined absorption bands can be visible. In the case of the 1F-AuCu/TiND electrode, two ranges from 200 to 320 nm and 420 to 680 nm with the maximum of absorption band at 550 nm can be distinguished. While for the 1S-AuCu/TiND electrode, three ranges from 200 to 300 nm, 310 to 400 nm, and 500 to 680 nm with the maximum of absorption at 600 nm are detectable. The differences are caused by different heating rates of Au and Cu layers. In the case of 1F electrodes, a very fast heating rate equal to 30 °C s^{-1} was used during thermal treatment, whereas for 1S electrodes, the heating rate was reduced by ≈45 times.

According to Guo et al.,[18] the absorption band was modulated by Cu content in Au_xCu alloy. The AuCu NPs with the size of 20–30 nm were synthesized by e-beam deposition and thermal dewetting and dispersed in TiO_2 nanocavities. The maxima of absorption were located at 430, 470, and 550 nm for Au_3Cu, AuCu, and $AuCu_3$, respectively. In the beginning, content of copper and gold as well as thickness of the metal layer in our experiments was the same for each sample. According to Wang et al.,[19] the shell thickness of Cu_2O on Au core can be responsible for the shift of gold plasmon resonance peak beyond 600 nm. The blueshift of 68 nm was observed when copper oxide shell thickness decreased from 159 to 53 nm. The difference between the smallest and the largest NP is ≈100 nm. In our case, SEM analysis indicates the difference between the NP size of the 1F-AuCu/TiND and the 1S-AuCu/TiND electrodes that equals only ≈5 nm and because of that, the shift cannot be directly connected just with NP size. Similar electrodes with the same Au and Cu film thicknesses were annealed also for 4 h to verify the influence of the prolonged conditioning on the UV–vis response. The markedly different morphology and chemical structure of the AuCu NPs on the surface lead to the nearly flat line of the diffuse reflectance with no clear peak on the reflectance spectra.

For further in-depth explanation of the observed relations between annealing rate and optical characteristics and to build the bridge between the molecular and macroscopic properties of the AuCu systems DFT calculations of the optical spectra and band structures were employed. First, the Cu_2O (100) | CuO (100) junction consisting of two unit cells was built and optimized with cell parameters allowed to relax. Several frames were withdrawn from the optimization procedure (initial, 10th, 30th, and final 140th step) and are presented in Figure 2d.

Those frames were then used for calculation of the reflectivity and absorption spectra (Figure 2b,c respectively). This methodology was adopted to model the difference between atomic configurations of the Cu_2O | CuO junction, resulting from different heating rates attempting to reflect experimental conditions.

The initial configuration 0th step is the one with highest total energy and higher atomic stresses. Therefore, it is assumed to correspond to the experimental situation with no annealing: two unit cells are aligned on top of each other without changing the positions of atoms.

The last, fully optimized step is the one with lowest total energy and lowest atomic stresses. Therefore, it is assumed to correspond to the ideal situation with an infinitesimally slow heating rate (adiabatic in the quantum mechanical sense

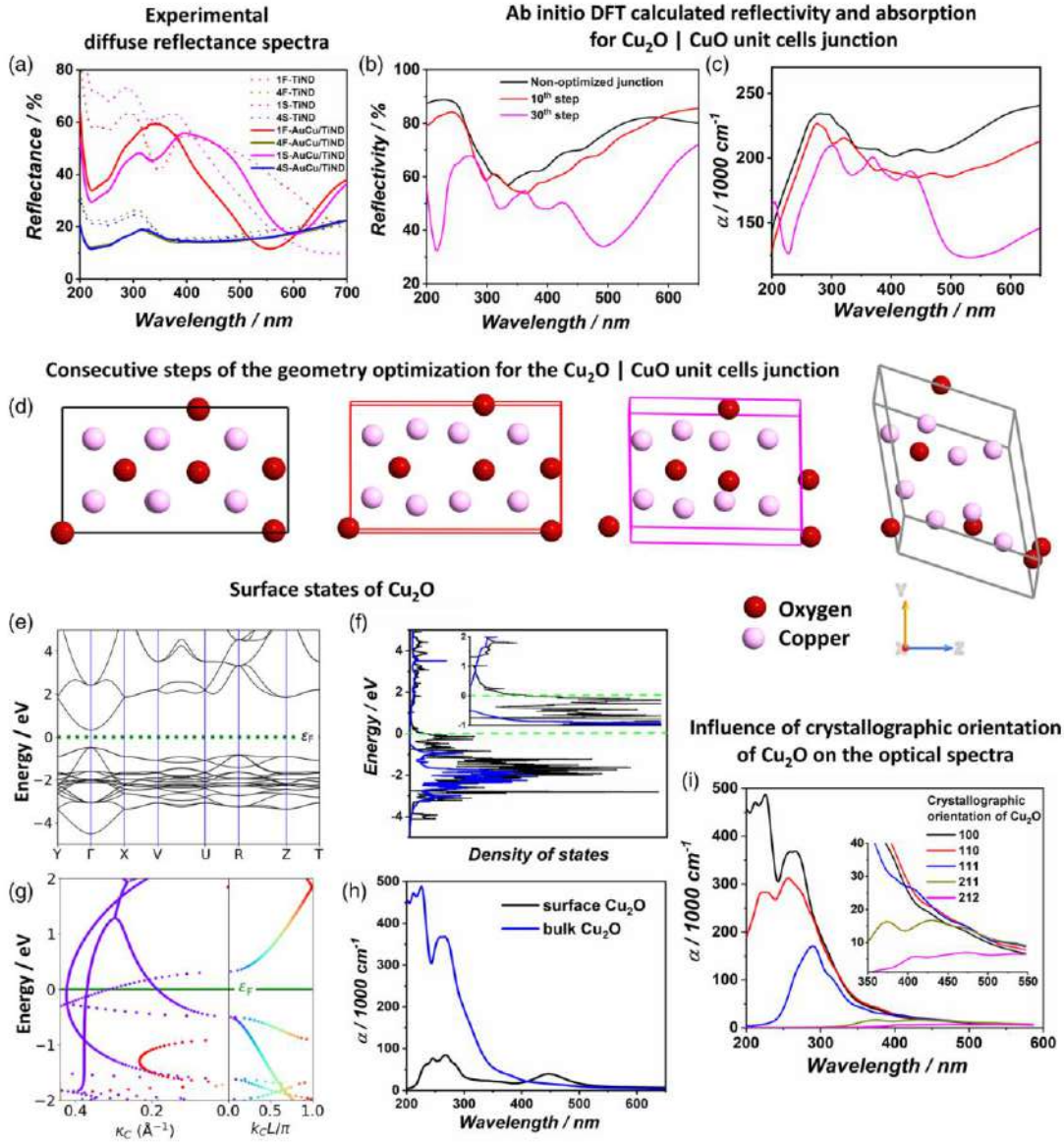

Figure 2. a) Experimental reflectance spectra of 1F-TiND, 4F-TiND, 1S-TiND, 4S-TiND, 1F-AuCu/TiND, 4F-AuCu/TiND, 1S-AuCu/TiND, 4S-AuCu/TiND. b,c) DFT-calculated reflectivity and absorption spectra for Cu_2O | CuO junction for different optimization steps. d) Corresponding frames for geometry optimization steps (from left to right panels: 0th, 10th, 30th, and the last 140th step). e) Band structure and f) density of states spectra for surface and bulk states of Cu_2O oriented along (100) plane, g) complex band structure analysis of evanescent states on the Cu_2O surface projected onto [001] direction, and comparison of DFT-calculated absorption spectra for h) bulk and surface states of Cu_2O and i) for different crystallographic orientation of bulk Cu_2O unit cells.

introduced by Max Born in 1927[20]—this structure is in a thermodynamic minimum. Considering that the fully optimized structure is obtained adiabatically and with removed symmetry constraints, it might not be manifested in the experiment, because in real conditions the heating rate is always finite and the atomic system is not fully stress relaxed. An evidence for this in the studied system can be inferred from the XRD spectra showing peaks of copper oxides from the cubic system.[21]

Finally, in the proposed model, the two middle configurations (10th and 30th steps of optimization, red and pink curves, respectively) are partially relaxed and they are assumed to correspond to the experimental results with fast and slow heating rates,

respectively. Heuristic justification of this choice is because as the heating rate is slower, the obtained structure has smaller mechanical stress (connected with smaller atomic stresses) and is less defected and therefore closer to its thermodynamical minimum.[22]

In general, the calculated optical spectra contain an absorption band centered at ≈280 nm, which is redshifted with consecutive steps. Moreover, several small absorption peaks are present in the range between 300 and 500 nm and magnified with subsequent optimization steps. In addition, the corresponding dips on the reflectivity plot are also redshifted. These changes originate from the fact that during optimization, the simulation box is distorted and stretched, accompanied with the loss of symmetry. If the optimization is performed further (toward thermodynamical minimum and lowest atomic stresses), deformation of the cell is even higher and the corresponding optical spectrum has a markedly different shape (see Figure S2, Supporting Information). In the framework of the proposed model, the fully optimized cell corresponds to the thermodynamical atomic configuration obtained during infinitesimally slow heating. The computationally reported redshifts stay in parallel to the ones observed in the experiment and support the argument that the changes in the local crystallographic structure induced by the variation in heating rates are responsible for the shape of the registered reflectance spectra.

Another contribution to the optical properties of AuCu/TiND structures can be associated to the surface states of the copper oxides. Figure 2e shows the bulk band structure of Cu_2O calculated on the DFT −½ level of theory and density of states spectra for both bulk and surface states, cleaved along (100) plane. Bulk Cu_2O exhibits a well-defined direct bandgap of ≈1 eV at the gamma point and the Fermi level inside the gap. However, in the surface spectrum, several additional midgap states are manifested in the whole gap, reducing the apparent bandgap to zero (inset in the Figure 2f). Interestingly, the majority of the introduced electronic levels lie in the vicinity of the valence band just below the Fermi energy. While they are not present in the normal band structure, the complex band structure (CBS) plot reveals them as evanescent states with nonzero imaginary part of the wavevector (Figure 2g).

In the CBS procedure, the wavevector is assumed to contain both the real and imaginary part. While the real part corresponds to the Bloch, bulk, propagating states, and is plotted on the classic band structure diagrams, the imaginary part is interpreted as evanescent or tunneling states.[23,24] Therefore, this technique is perfectly suited to study surface states and its results for the investigated system show undoubtedly that they are present in the case of Cu_2O. When the cell is not periodically extended to infinity, previously dormant evanescent states are manifested as additional peaks in the density of states spectrum. Moreover, a well-defined branching point can be observed at ≈−1.2 eV, which connects filled electronic bands. Based on this, the tunneling length of the evanescent state can be estimated to ≈4.5 Ang. Those surface evanescent states of Cu_2O can also contribute to the changes in the optical spectra, as the additional absorption band is reported at ≈480 nm (Figure 2h).

Finally, the crystallographic orientation of the pristine bulk Cu_2O is also a factor determining the presence and position of absorption bands. In general, higher Miller indices lead to smaller values of absorption coefficients, redshift of the main absorption bands, and emergence of several small bands in the range between 350 and 600 nm (Figure 2i).

Summing up, three effects, variable heating rate, leading to different local structures of the Cu_2O (100) | CuO (100) junction, surface states and crystallographic orientation of the Cu_2O, were proposed to determine the shape of the optical spectra. Those phenomena are anticipated to have a profound influence on the photoelectrochemical response of the AuCu/TiND structures and their quantum efficiency explored in the further section of the paper, underlining the importance of the synthesis parameters on the properties of materials on the molecular level.

2.3. Photoelectrochemical Properties

The LV measurements were performed under chopped dark–visible light illumination of electrodes. The tests were carried out in 0.1 M NaOH electrolyte. **Figure 3** shows the LV curves for TiND, Cu/TiND, and AuCu/TiND annealed at different time and heating rates. The values of photocurrent density recorded at +0.3 V versus Ag/AgCl/0.1 M KCl are listed in **Table 1.** In Figure 3a, the photocurrent responses are given for electrode materials thermally treated for 1 min with a heating rate of 30 °C s^{-1} (label with prefix 1F): fast heated. The photocurrent of the 1F-AuCu/TiND electrode was 24 times higher than for 1F-TiND and was equal to 14.1 μA cm^{-2}. In the case of samples annealed for 4 h with a heating rate of 30 °C s^{-1} (prefix 4F) (Figure 3c), any significant photocurrent can be observed. Figure 3b shows the LV curves registered for electrodes thermally treated for 1 min with a heating rate of 0.67 °C s^{-1} (prefix 1S): slow heated. The decrease of the rate value leads to formation of the material named 1S-AuCu/TiND which is characterized by higher photocurrent compared to 1F-AuCu/TiND. The increase of the photocurrent can be correlated with loss of the symmetry of Cu_2O | CuO junction (Figure 2d), additional surface states, or different crystallographic orientations discussed previously. The difference between current density in the dark and under visible light illumination at +0.3 V for the 1S-TiND is equal to 0.6 μA cm^{-2} whereas for 1S-AuCu/TiND reaches 47.2 μA cm^{-2} which is 77 times higher than that for material without AuCu NP. However, samples annealed for 4 h and with a heating rate of 0.67 °C s^{-1} (label with prefix 4S) almost do not produce photocurrents (Figure 3c,d). Despite very low reflectance, these structures presumably are not capable of forming photocarriers. Therefore, the photoactivity of AuCu NPs is strongly dependent on the conditions of thermal treatment including time and heating rate. It should be highlighted that the significant increase of photocurrents under visible light irradiation after annealing is caused by the formation of AuNPs. According to literature, gold enables efficient conversion of solar energy due to the light-trapping effect, hot electron injection, and transferring absorbed energy from metal to semiconductors.[6,25] Moreover, Cu_2O and CuO absorb energy what can lead to photoexcited electron flow to Au.[9]

Because of the significant increase of photocurrents under visible light for the 1F-AuCu/TiND and the 1S-AuCu/TiND electrodes, more detailed electrochemical measurements were carried out. The photoelectrochemical activity under UV–vis light

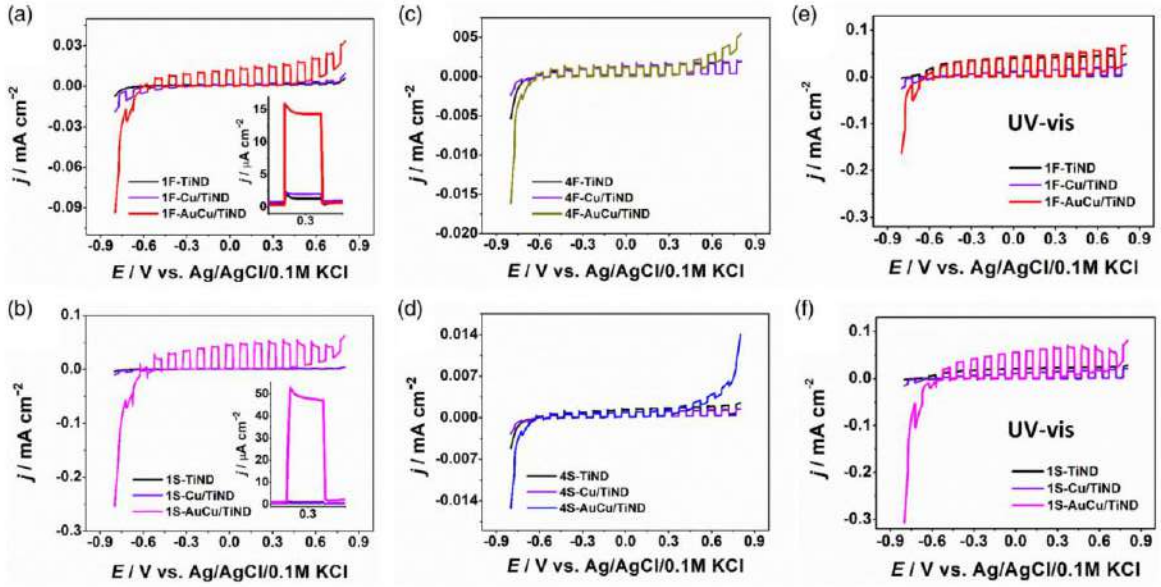

Figure 3. LV curves registered in 0.1 M NaOH under Vis illumination for a) 1F-TiND, 1F-Cu/TiND, 1F-AuCu/TiND, b) 1S-TiND, 1S-Cu/TiND, 1S-AuCu/TiND, c) 4F-TiND, 4F-Cu/TiND, 4F-AuCu/TiND, d) 4S-TiND, 4S-Cu/TiND, 4S-AuCu/TiND, and LV curves registered under UV–vis illumination for electrodes annealed with heating rate of e) 30 °C s^{-1} and f) 0.67 °C s^{-1}.

Table 1. Values of current density at +0.3 V versus Ag/AgCl/0.1 M KCl under Vis illumination (j μA^{-1} cm^{-2}).

	1F (1 min fast)	4F (4 h fast)	1S (1 min slow)	4S (4 h slow)
TiND	0.6	1.3	0.6	1.4
Cu/TiND	1.3	1.4	0.5	0.9
AuCu/TiND	**14.1**	1.3	**47.2**	1.0

illumination for short annealed samples is shown in Figure 3e,f. Gold- and copper-based electrodes reached higher photocurrents than pure TiND and only copper-modified TiND. A high heating rate equal to 30 °C s^{-1} during thermal treatment is supposed to be beneficial for TiO_2 photoactivity due to the highly defected crystal structure of rutile. The 1F-TiND electrode reaches 2 times higher photocurrents (41.1 $\mu A\,cm^{-2}$) than the 1S-TiND in contrast to AuCu/TiND samples where the 1S-AuCu/TiND electrode has ≈3 times higher photocurrent than the 1F-AuCu/TiND electrode (**Table 2**). It should be taken into account that the 1S-AuCu/TiND sample exhibits additional absorption maximum at 335 nm on the UV–vis reflectance spectra which can correlate with better

Table 2. Values of current density at +0.3 V versus Ag/AgCl/0.1 M KCl under UV–vis illumination (j μA^{-1} cm^{-2}).

	1 F (1 min fast)	1S (1 min slow)
TiND	41.1	22.3
Cu/TiND	14.2	13.9
AuCu/TiND	**46.8**	**62.6**

light absorption in the range of 310–400 nm and higher photocurrents. The highest photocurrent of 62.6 $\mu A\,cm^{-2}$ was obtained for the 1S-AuCu/TiND electrode. Therefore, the photoactivity of AuCu not only increases under visible light but also under UV–vis.

Figure 4 shows IPCE curves registered for the 1F-AuCu/TiND and the 1S-AuCu/TiND electrodes. As shown, the AuCu sample annealed with heating rate of 30 °C s^{-1} has higher photon-to-current efficiency with maximum equal to 2.3% than material annealed with rate of 0.67 °C s^{-1}. Three ranges of wavelengths such as 320–420, 420–540, and 540–680 nm can be detailed on the 3D map. The most significant for the 1F-AuCu/TiND sample are values from 320 to 540 nm; however, in the case of the 1S-AuCu/TiND electrode, the third region is also detectable. The percentage ratio of maximum values of IPCE at 600 and 380 nm is equal to 12.8% in contrast to the 1F-AuCu/TiND electrode where it reaches 2.6%. Results indicate that the heating rate has a significant effect on photon-to-electron efficiency exhibited by the obtained material. It should be highlighted that in comparison to AuCu/TiND electrodes, the pure TiND samples do not have any detectable IPCE (Figure S3, Supporting Information). Such behavior originates from almost the lack of the semiconducting layer present in the Ti surface. For AuCu/TiND electrodes, we can distinguish two important phenomena such as light absorption and charge transfer. In the range of 320–420 nm, copper oxides located on the top of the electrode surface absorb light and generate electron–hole pairs sequentially transferring electrons to Ti where efficient charge transfer takes place. According to reflectance spectra (Figure 2a), the minima of absorption for 1F-AuCu/TiND and the 1S-AuCu/TiND are located at ≈350 and 390 nm, respectively. However, according

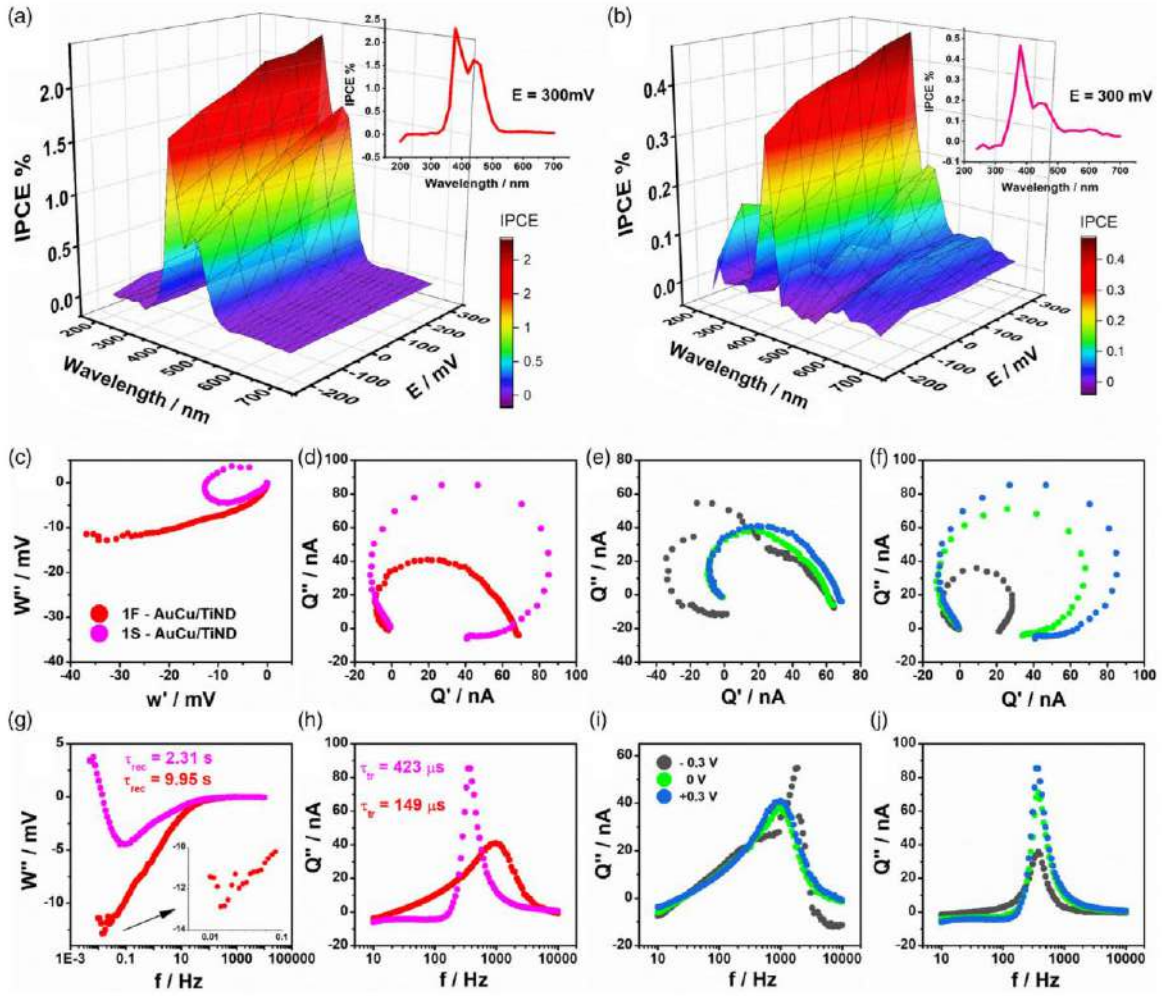

Figure 4. IPCE of a) 1F-AuCu/TiND, b) 1S-AuCu/TiND, c–f) Nyquist diagrams in orthogonal projections of c) IMVS, d) IMPS, e) comparison of IMPS spectra for 1F-AuCu/TiND for three polarizations, f) comparison of IMPS spectra for 1S-AuCu/TiND for three polarizations, and g–j) corresponding imaginary part versus frequency plots.

to the literature, absorption bands for pure CuO oxides can be found from 250 to 800 nm.[26] In the case of the second range on IPCE between 420 and 540 nm, the absorption process is more significant. CuO oxide absorbs light and generates electron–hole pairs. In Figure 2a, significant increase of the absorption from ≈400 to 600 nm can be observed. It should be highlighted that for the 1F-AuCu/TiND sample, the maximum is located at 550 nm; however, for 1S-AuCu/TiND, it is shifted toward higher values and reaches 600 nm. The maxima of the absorption band might be enhanced by localized SPR (LSPR) effect. According to Bharati et al.,[27] the maximum of absorption with the SPR peak for AuCu NPs is located at 566 nm. The SPR peak for pure Cu NPs was observed at 616 nm,[28] whereas for Au NPs at 550 nm.[29] Moreover, the LSPR absorption band of the Au cores can be dependent on the surface faces of copper oxide shell.[25] The free carriers injected by AuNPs enhance conductivity as well due to the SPR improving the photoactivity of semiconductors such as TiO_2, CuO, and Cu_2O.[30]

Further investigations of the AuCu/TiND photoelectrochemistry were conducted using IMVS and IMPS techniques (Figure 4c–j). In the IMVS, a Nyquist plot representing W-function plane is shown. Real (W') and imaginary (W'') parts of the W-function are defined as the following integrals.

$$Re(W) = W(\omega)' = \frac{\int_0^T E(t)\cos(\omega t)dt}{T} \quad (1)$$

$$\mathrm{Im}(W) = W(\omega)'' = \frac{\int_0^T E(t)\sin(\omega t)dt}{T} \quad (2)$$

where T is a period of the light intensity stimulus and $E(t)$ is a time-dependent potential recorded by the potentiostat. In the

linear approximation, *W* function can be viewed as the Laplace transform of the potential divided by the Laplace transform of the modulated light flux. In the case of 1S-AuCu/TiND, *W*-function exhibits almost full circle, which is a straightforward indication of the charge recombination.[31] However, 1F-AuCu/TiND displays a partial circle at high frequencies (100 Hz–10 kHz), transforming to the almost straight line at low frequencies (5 mHz–100 Hz). This behavior strongly suggests competition between charge recombination and diffusion followed by the chemisorption process, as the straight line on the Nyquist resembles the response of Warburg impedance.[32] In the corresponding plot (Figure 4g) of the imaginary part of the W function, it is easy to find the minimum for the 1S-AuCu/TiND, which corresponds to the characteristic recombination time equal to 2.31 s. However, due to the unique shape of the 1F-AuCu/TiND, the peak is not well defined, but the small minimum can be noted at the lowest frequencies (Figure 4g) and recombination time was equal to 9.95 s. Those values are superior compared to other semiconductor structures (≈0.2 ms[33]), indicating a relatively long time of the photogenerated charge carriers in the AuCu/TiND NPs. Furthermore, IMVS measurements confirmed a longer charge recombination rate for the 1F-AuCu/TiND than for 1S-AuCu/TiND (Figure 4c), which strongly suggest that deeper trap states are present in the electronic band structure of the fast-heated AuCu structures. IMPS Nyquist plots represent Q function on the complex plane. It is defined analogously as the W function for IMVS, yet the time-dependent potential is replaced by the time-dependent current. Figure 4d shows a well-defined semicircle of the Q function for the 1S-AuCu/TiND sample again and the distorted semicircle for 1F-AuCu/TiND. Distortion is especially seen at low frequencies, which also supports the hypothesis of the chemisorption process. It should be highlighted that magnitudes of the *Q* function are higher for the slow-heated structure (Figure 4h) in high and moderate frequencies (100 Hz and higher), which are in good correspondence with higher photocurrents in Figure 3. However, at the low-frequency limit, the relation is opposite, and real part of the red curve is higher than the pink one. These limiting values are directly linked to the observed higher IPCE value for the fast-annealed sample, because the low-frequency limit is known to correspond to the external quantum efficiency.[34] The characteristic time of the transport of the majority carriers (electrons) is higher for 1F-AuCu/TiND and is equal to 149 µs, compared to 423 µs for 1S-AuCu/TiND. Additional insights into the photodriven phenomena were obtained by comparing the IMPS spectra of the AuCu/TiND structures in different applied potentials (Figure 4e,f,i,j). In case of the 1F-AuCu/TiND, similar semicircles are observed at +300 and 0 mV, but at the negative potential of −300 mV, the semicircle is significantly distorted at moderately high frequencies (few kHz). This distortion could not be removed by manipulating of the DC and AC components of the light stimulus; therefore, it is interpreted as an intrinsic feature of the material. Presumably, the discrete character of the change in the Nyquist plots originates from the presence of the deep electronic traps.[34] As the potential is swept toward the more negative potentials, at some point, the Fermi level hits the deep trap level and the *Q* function (and thus photocurrent) is changed. Because it is a deep trap which cannot conduct electrons, the Nyquist semicircle is markedly shifted in the direction of negative values of the real part of the *Q* function. The observed phenomenon might be also related with photocurrent polarity switch at lower potentials, which is typically associated with the shift of the Nyquist plot to the II and III quadrants.[34] It was also observed in $BiVO_4$ electrodes.[35] Consequently, it is difficult to estimate the transport time for this sample at −300 mV potential. On the other hand, the 1S-AuCu/TiND sample does not have such discrete changes of the IMPS spectra at negative potentials. *Q* function values at the moderate- and low-frequency range increase monotonously with potential (also at the low-frequency limit) which stay in a good correspondence with the IPCE spectra in Figure 4b where with higher-potentials IPCE is also greater. These observations suggest that the slow-heated AuCu/TiND is mostly shallow or no electronic traps; therefore, no distortions in the IMPS are registered. Finally, despite change in the value of the photocurrents, the characteristic times do not change with the potential (Figure 4j).

For clear demonstration, the comparison of optical and photoelectrochemical properties for deeply analyzed fast- and slow-annealed electrodes (1F-AuCu/TiND, 1S-AuCu/TiND) is presented in **Table 3**.

For further explanation of the IMVS/IMPS results and gaining in-depth knowledge of the heterojunctions present in the AuCu core–shell structures, a set of computations involving DFT-NEGF formalism was applied (**Figure 5**). PLDOS plots for Cu_2O | CuO semiconductor heterojunctions in the unoptimized (as-drawn) and optimized configuration are given in Figure 5a,b, respectively. Similarly to the concepts given in Figure 2, the unoptimized configuration is a model for fast-heated sample (30 °C s^{-1}) and the optimized state is a model for slow-heated sample (0.67 °C s^{-1}).

In general, three areas can be distinguished: pristine Cu_2O with ≈1.2 eV bandgap, interface between Cu_2O and CuO with midgap states, and pristine CuO with ≈3 eV bandgap. Bandgap value of Cu_2O is in good correspondence with experiments[36] and slightly higher than that typically computed from DFT calculations,[37] because of the application of DFT −1/2 correction. Assuming that the more oxidized copper oxide CuO is an external layer of the AuCu NPs,[11] band alignment facilitates electron transfer from CuO toward Cu_2O due to the potential gradient formed at the Cu_2O | CuO interface. On the other hand, holes will tend to be accumulated on the CuO with potential use for photoelectrochemical reactions. In the unoptimized

Table 3. The comparison of optical and photoelectrochemical properties of the 1F-AuCu/TiND and the 1S-AuCu/TiND electrodes.

Parameter	1F-AuCu/TiND	1S-AuCu/TiND
Position of the reflectance minimum	550 nm	600 nm
Position of reflectance maximum	350 nm	400 nm
Photocurrent density under visible light illumination	14.1 µA cm^{-2}	47.2 µA cm^{-2}
Photocurrent density under UV–vis light illumination	46.8 µA cm^{-2}	62.6 µA cm^{-2}
Maximum IPCE	2.3%	0.5%
Recombination time	9.95 s	2.31 s
Electrons diffusion time	149 µs	423 µs

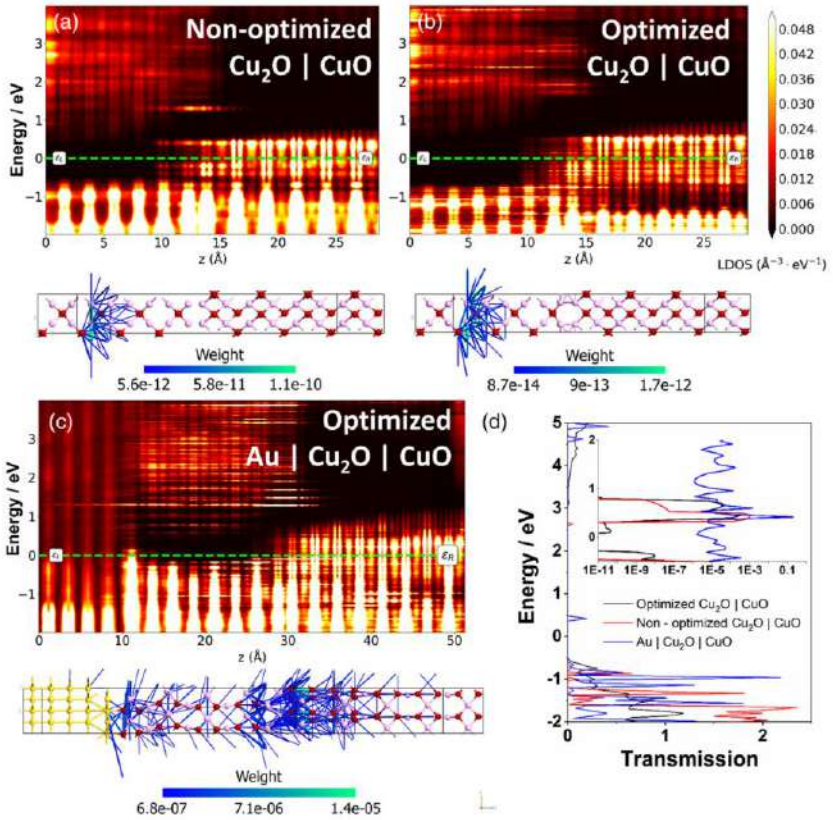

Figure 5. PLDOS spectra and transmission pathways maps at zero bias for a) unoptimized (as assembled) Cu_2O | CuO, b) fully optimized Cu_2O | CuO, and c) fully optimized Au | Cu_2O | CuO heterojunctions. d) Comparison of electronic transmission spectra for three configurations.

configuration, highly populated midgap electronic states are located deeply (1.3 eV). However, optimization shifts them upward on the energy scale up to 1.8 eV, making them more shallow. These results stay in perfect correspondence with the concept of shallow traps in slow-heated AuCu and deep traps in fast-heated AuCu anticipated from IMVS results. Moreover, electron transmission pathways plots of both structures strongly evidence that transmission through the Cu_2O | CuO junction solely is negligible regardless of whether the optimization and midgap states do not contribute to the conduction of photocurrent.

Therefore, for a more realistic model of the experimental results, a triple heterojunction including Au | Cu_2O | CuO was constructed and given in Figure 5c along with PLDOS and transmission pathways analyses. Surprisingly, due to the coupling of Cu_2O with gold, a series of additional electronic energy levels appear in just below the conduction band of Cu_2O, reducing its apparent bandgap from 1.5 eV to less than 1 eV. Moreover, the overall Fermi level of the system is shifted downward, indicating a more *p* character of the Cu_2O. Another effect of the coupling with Au is the creation of densely populated midgap states on the CuO side induced by changes in the atomistic geometry. As a result of those changes, electron transmission is greatly facilitated at the zero bias and many pathways in the real space are formed. This phenomenon is also reflected on the transmission spectra in Figure 5d, as the probability of the off-resonant transport near zero energy is increased from 10^{-13} to 10^{-4}. In addition, gold increases the magnitude of a small transmission mode at +0.5 eV by 4 orders of magnitude, from 3×10^{-5} of the bare Cu_2O | CuO to 0.2 for triple unction (see inset in Figure 5d). This enhancement originates from the partial overlap of the Au-mediated states of Cu_2O, just below the Cu_2O conduction band, and the electronic states of the CuO valence band at the interface with Cu_2O.

Summing up, as the junctions between copper oxides serve as a site for the generation of charge carriers, gold is a facilitator of electron transport toward the contacts. On the other hand, holes are most probably accumulated on the electrode | electrolyte interface in the CuO layer. The depth of the midgap states is highly dependent on the atomic alignment on the interface which can be controlled by the heating rate.

Finally, the electrochemical impedance spectroscopy was used to determine the charge transfer resistance of the thin oxide electrode composed of AuCu NPs and the titanium nanostructured platform (**Figure 6**). The impedance spectra were recorded in the dark and under visible light illumination in 0.1 M NaOH solution at +0.3 V versus Ag/AgCl/0.1 M KCl. In order to analyze spectra,

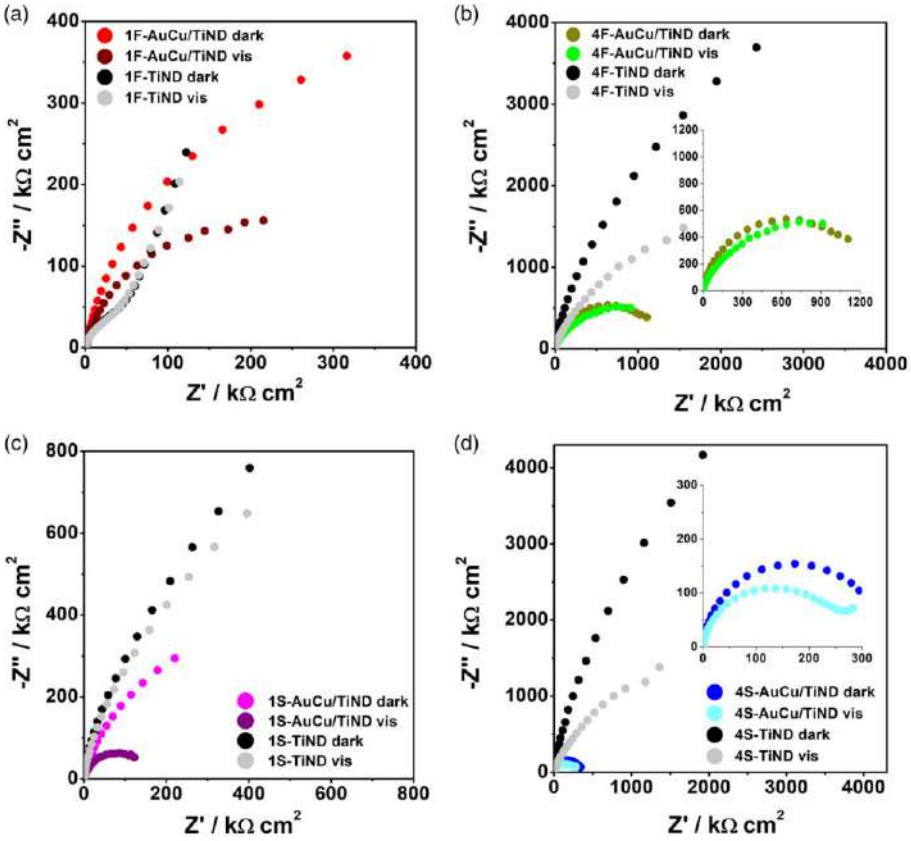

Figure 6. Electrochemical impedance spectra registered in the dark and under Vis illumination for a) 1F, b) 4F, c) 1S, and d) 4S AuCu/TiND and TiND electrodes.

the $R_E(R_{CT}CPE)$ equivalent circuit was used for all electrodes (R_{CT} and constant-phase element (CPE) are connected parallel). The R_E element corresponds to electrolyte resistance, R_{CT} is charge transfer resistance of electrode, and CPE is attributed to constant-phase element which takes into account not only capacity but also the homogeneity of sample. The detailed analysis was conducted for electrodes annealed for 1 min, such as 1F-TiND, 1F-AuCu/TiND, 1S-TiND, and 1S-AuCu/TiND. The results are summarized in **Table 4 and 5**. The highest value ratio of resistance recorded in the dark to the value obtained under light illumination was reached for 1S-AuCu/TiND and 1F-AuCu/TiND and was equal to 5.0 and 2.8, respectively. In the case of 1S-TiND and 1F-TiND, ratio equals 1.2 and 1.0, respectively. These results can be correlated with the LV scans where the most significant photocurrent was measured for short thermal-treated bimetallic NPs. According to Oh et al.,[38] the charge transfer resistance for the $Au/Cu_2O/TiO_2$ nanorods (NRs) under light illumination is lower than that for Au/TiO_2 and TiO_2 NRs, confirming efficient transfer of electrons from Cu_2O shell and Au NPs to TiO_2 semiconductor. The homogeneity of electrodes produced with a heating rate of 0.67 °C s^{-1} such as 1S-AuCu/TiND and 1S-TiND is higher than that for materials fabricated with the heating rate of 30 °C s^{-1}. The CPE component describes the homogeneity and its increase corresponds to increase of homogeneity.[39] It can be assumed that various

Table 4. Electrochemical impedance data for AuCu/TiND.

	Units	1F-AuCu/TiND dark	1F-AuCu/TiND vis	1S-AuCu/TiND dark	1S-AuCu/TiND vis
R_E	Ω cm^{-2}	19.68	18.00	23.50	23.36
R_{CT}	Ω cm^{-2}	125.08×10^4	44.25×10^4	77.81×10^4	15.55×10^4
Q	F cm^{-2}	0.25×10^{-5}	0.32×10^{-5}	0.30×10^{-5}	0.36×10^{-5}
n		0.82	0.80	0.87	0.86

Table 5. Electrochemical impedance data for TiND.

	Units	1F-TiND dark	1F-TiND vis	1S-TiND dark	1S-TiND vis
R_E	Ω cm^{-2}	25.00	25.00	33.43	32.89
R_{CT}	Ω cm^{-2}	24.53×10^4	23.50×10^4	174.73×10^4	143.91×10^4
Q	F cm^{-2}	0.25×10^{-5}	0.30×10^{-5}	0.13×10^{-5}	0.14×10^{-5}
n		0.83	0.82	0.93	0.93

heating rates have a significant impact on the crystallization behavior of the Cu_2O and CuO shell. According to the literature, Cu_2O as well as CuO which are formed on the top of the NP can be present in different crystal planes such as (111), (110) for Cu_2O,[4] and (111), (002) for CuO.[5,17,40] Moreover, not only planes but also grain size can change during various thermal treatment conditions.[41] The electrochemical impedance spectra highly support the already-discussed photoelectrochemical activity (Figure 3).

3. Conclusion

In this work, we presented a fabrication procedure of AuCu mosaic core–shell NPs directly formed onto the nanopatterned Ti foil. The electrodes were fabricated by anodization of Ti foil, chemical etching, magnetron sputtering of thin Au, Cu layers, and thermal treatment in the rapid thermal annealing furnace. The different annealing times and heating rates had a significant impact on morphology, optical, and photoelectrochemical properties. The samples thermally treated for 1 min (short) had the average size of AuCu NP of ≈45 nm, whereas for 4 h (long), the average size was equal to ≈77 nm. In the case of short annealed samples, a clear absorption peak in the reflectance spectra with maximum at 550 and 600 nm for 1F-AuCu/TiND and 1S-AuCu/TiND is detectable, respectively. The shift can be correlated not only with NP size but also with various local structures of the Cu_2O | CuO junction, surface states, and crystallographic orientation of copper oxides. However, long annealing of materials led to the formation of the flat reflectance spectra. The highest photocurrent under visible light illumination was obtained for the short annealed electrode at the slow heating rate (1S-AuCu/TiND) and reached 47.2 μA cm^{-2}, which is 77 times higher value than for pure TiND. Increasing the heating rate 45 times resulted in triple decrease in current density. However, in contrast to photocurrent, the photon-to-current efficiency was higher for fast-heated AuCu bimetallic electrode which can be correlated with deeper midgap states in the electronic band surface controlled by different heating rates.

4. Experimental Section

Reagents: Titanium foil (99.7%, thickness: 0.127 mm, Strem), acetone, ethanol, ammonium fluoride, ethylene glycol (99%, Chempur), and oxalic acid dihydrate were used for the electrochemical anodization process. The gold target (99.99%, Quorum Technologies) and copper target (99.99%, Quorum Technologies) were used for magnetron sputtering.

Sample Preparation: First, the Ti foil was cut into 2 × 3 cm^2 plates and ultrasonically cleaned in acetone, ethanol, and deionized water for 10 min. Then such samples were used for the anodization process. That process was conducted out in the two-electrode system, where Ti plate was an anode and Pt mesh was a cathode. Electrodes were immersed in electrolyte that contained 0.27 M NH_4F dissolved in a mixture composed of 1% vol. deionized water and 99% vol. ethylene glycol. The anodization was carried out in a cylindrical glass cell with thermostatic jacked with constant temperature of 23 °C and consisted of two stages. The first one took 2 h and the second one 6 h. At each stage, voltage of 40 V was applied between electrodes. After the anodization processes, samples were rinsed with water and immersed in 0.5% oxalic acid solution overnight to form Ti nanodimples (TiND) by removing the top layer of TiO_2 nanotubes. Then, TiNDs were covered by thin 5 nm Au or Cu layer using magnetron sputtering (Q150T S system, Quorum Technologies). Next, materials were annealed in the rapid thermal annealing furnace (MILA 5000P-N). TiNDs, Cu/TiNDs, and Au/TiNDs electrodes were thermally treated in four variants: 1F-heating rate of 30 °C s^{-1} for 1 min at 600 °C, 4F-heating rate of 30 °C s^{-1} for 4 h at 600 °C, 1S-heating rate of 0.67 °C s^{-1} for 1 min at 600 °C, 4S-heating rate of 0.67 °C s^{-1} for 4 h at 600 °C. Finally, Au/TiND samples were covered by 5 nm Cu layer and annealed at 300 °C for 30 min with heating rate of 30 °C s^{-1} or 0.67 °C s^{-1} (AuCu/TiNDs) in the rapid thermal annealing furnace. In the manuscript, electrodes were assigned as 1F-TiND (30 °C s^{-1}, 1 minute), 4F-TiND (30 °C s^{-1}, 4 h), 1S-TiND (0.67 °C s^{-1}, 1 min), 4S-TiND (0.67 °C s^{-1}, 4 hours), 1F-AuCu/TiND (30 °C s^{-1}, 1 min, AuCu), 4F-AuCu/TiND (30 °C s^{-1}, 4 h, AuCu), 1S-AuCu/TiND (0.67 °C s^{-1}, 1 min, AuCu), 4S-AuCu/TiND (0.67 °C s^{-1}, 4 h, AuCu).

Computational Modeling: Atomic structures of Cu_2O, CuO, Au, and their heterojunctions were designed using a builder tool provided by Atomistic ToolKit Quantumwise (ATK, Synopsys, USA) as reported in ref. [42] DFT on the generalized gradient approximation (GGA) level of theory with the Perdew–Burke–Ernzerhof (PBE) functional was applied as implemented in the package. The linear combination of atomic oOrbitals (LCAO) method[43] with medium ATK basis set and Pseudo–Dojo norm-conserving pseudopotentials were applied.[44] Density mesh cutoff for most of the calculations was either 125 Ha or 140 Ha depending on the system capability of the SCF convergence. The *k*-point mesh for geometry optimizations was 4 × 4 × 4 and for optical spectra calculations it was increased to 7 × 7 × 7. DFT −½ bandgap correction procedure was implemented for calculating band structures and optical spectra.[36] Reflectivity and absorption spectra were computed based on the susceptibility tensor calculated from DFT orbitals using Kubo–Greenwood formula[45] and periodic boundary conditions unless stated otherwise. The first set of optical calculations involved pristine Cu_2O with different crystallographic orientations (100), (110), (111), (211), and (212). The second set involved building small Cu_2O | CuO junctions consisting of two adjacent unit cells with different orientations of Cu_2O, keeping CuO orientation fixed at (100). These junctions were optimized with the threshold of 0.05 eV Ang^{-1}. The third set involved withdrawing several frames from optimization of Cu_2O (100) | CuO (100) junction and computing optical spectra for the resulting geometries. Finally, surface states of Cu_2O (100) were modeled as the slab consisting of two unit cells separated with the 20 Ang vacuum. Periodic boundary conditions were kept in the *X* and *Y* directions, while the *Z* direction in the electrode end was set as Dirichlet boundary conditions and on the vacuum end as von Neumann boundary conditions. CBS of Cu_2O was calculated according to the procedure[46] and the bands were projected onto [001] direction (*Z*). Branching point detected in the imaginary part of the plot was used to calculate the tunneling distance of the evanescent state according to the works.[23,24]

Prior to the PLDOS analysis and the photocurrent calculations, semiconductor Cu_2O | CuO heterojunctions as well as triple Au | Cu_2O | CuO junctions were built and optimized according to the procedure provided in the ATK documentation.[42] Briefly, two electrodes consisting of a series of unit cells were built and connected with each other through the scattering region in between. The system was periodic in *X* and *Y* directions, but Dirichlet boundary conditions were applied in the *Z* direction, which was direction of the junction. In case of the double junction, bulk Cu_2O and CuO were electrode extensions and the interface between them was the scattering region. The structure obtained for the double junction was used as a starting point for the optimization of the triple junction. In case of the triple heterojunctions, bulk Au was the left electrode extension and the bulk CuO was the right electrode extension. The scattering region consisted of the interface between Au and Cu_2O, followed by 3 nm layer of the preoptimized Cu_2O, finished by Cu_2O | CuO interface. Optimization of the assembled devices was performed in the several steps. First, electrodes and scattering region were relaxed separately and then relaxed again after assembly. PLDOS analysis was performed using nonequilibrium Green's function (NEGF) methodology[12,13] in the Landauer–Buttiker regime,[47] with PBE–GGA-calculated orbitals as an input. The *k*-point mesh was set to 4 × 4 × 150 for the DFT orbitals calculations and 7 × 7 × 150 for the PLDOS and photocurrents with 125 Ha density mesh cutoff. Photocurrent was calculated for the every *k*-point and then averaged to obtain a single value on the energy scale with 0.05 eV resolution.

Sample Characterization: The morphology of the prepared samples was investigated by a field-emission scanning electron microscope (FEI Quanta FEG250) equipped with a secondary ET detector and with the beam accelerating voltage kept at 10 kV. The crystallinity was studied by means of the XRD technique over the range of 20°–80° using Bruker 2D Phaser diffractometer with CuKα radiation and XE-T detector. The optical properties of the nanostructures were inspected using a UV–vis spectrophotometer (Lambda 35, Perkin-Elmer) equipped with a diffuse reflectance accessory. The photoelectrochemical properties were measured using an AutoLab PGStat 302N potentiostat-galvanostat in the three-electrode assembly, where the modified electrode was the working electrode, Ag/AgCl/0.1 M KCl served as the reference electrode, and a Pt mesh was the counter electrode. The LV scans were performed from −0.8 to +0.8 V with a scan rate of 10 mV s^{-1} in 0.1 M NaOH. The LV curves were recorded in the dark and under illumination with a xenon lamp (LOT-QuantumDesign GmbH) as a light source. The 3D map of the photocurrent density was registered by a photoelectric spectrometer (Instytut Fotonowy) equipped with Xe lamp 150 W. The IMVS (Instytut Fotonowy) measurements were registered from 5 mHz to 10 kHz under 455 nm light illumination. IMPS (Instytut Fotonowy) measurements were performed from 10 to 1000 Hz at +0.3, 0 and −0.3 V versus Ag/AgCl/0.1 M KCl under 455 nm light illumination. Electrochemical impedance spectroscopy measurements were conducted at +0.3 V with frequency from 10 kHz to 0.1 Hz covering 20 points per decade with 0.01 V amplitude.

Supporting Information

Supporting Information is available from the Wiley Online Library or from the author.

Acknowledgements

Research was financed by National Science Centre (Poland): grant no. 2019/35/N/ST5/02604.

Conflict of Interest

The authors declare no conflict of interest.

Data Availability Statement

The data that support the findings of this study are available from the corresponding author upon reasonable request.

Keywords

annealing rates, AuCu nanostructures, midgap states, photoactivity

Received: September 2, 2022
Revised: November 10, 2022
Published online: November 22, 2022

[1] A. Rani, R. Reddy, U. Sharma, P. Mukherjee, P. Mishra, A. Kuila, P. Saravanan, *J. Nanostruct. Chem.* **2018**, *8*, 255.
[2] R. P. Wijesundera, L. K. A. D. D. S. Gunawardhana, W. Siripala, *Sol. Energy Mater. Sol. Cells* **2016**, *157*, 881.
[3] Y. Yang, D. Xu, Q. Wu, P. Diao, *Sci. Rep.* **2016**, *6*, 35158.
[4] M. Sun, Y. Yao, Z. Zhang, B. Gao, W. Ding, *Int. J. Hydrogen Energy* **2020**, *45*, 21493.
[5] S. Jabeen, T. A. Sherazi, R. Ullah, S. A. R. Naqvi, M. A. Rasheed, G. Ali, Y. Khan, *Appl. Nanoscience* **2020**, *MA2020-02*, 1426.
[6] J. Li, S. K. Cushing, F. Meng, T. R. Senty, A. D. Bristow, N. Wu, *Nat. Photonics* **2015**, *9*, 601.
[7] L. Yanbiao, Z. Haibin, L. Jinhua, Ch. Hongchong, L. Di, Z. Baoxue, C. Weimin, *Nano-Micro Lett.* **2010**, *2*, 277.
[8] S. Masudy-Panah, M. R. Siavash, C. S. Chua, A. Kushwaha, T. I. Wong, G. K. Dalapati, *RSC Adv.* **2016**, *6*, 29383.
[9] W. Xu, J. Jia, T. Wang, Ch. Li, B. He, J. Zong, Y. Wang, H. J. Fan, H. Xu, Y. Feng, H. Chen, *Angew. Chem.* **2020**, *59*, 22246.
[10] W. Lipinska, K. Grochowska, J. Ryl, J. Karczewski, K. Siuzdak, *ACS Appl. Mater. Interfaces* **2021**, *13*, 52967.
[11] W. Lipińska, K. Grochowska, J. Karczewski, J. Ryl, A. Cenian, K. Siuzdak, *Chem. Eng. J.* **2020**, *399*, 125673.
[12] H. Rahman, U. Kleinekathöfer, *J. Chem. Phys.* **2018**, *149*, 234108.
[13] M. Thoss, F. Evers, *J. Chem. Phys.* **2018**, *148*, 030901.
[14] F. Ning, S. Z. Chen, Y. Zhang, G. H. Liao, P. Y. Tang, Z. L. Li, L. M. Tang, *Appl. Surf. Sci.* **2019**, *496*, 143629.
[15] P. Lapham, L. Vilà-Nadal, L. Cronin, V. P. Georgiev, *J. Phys. Chem. C* **2021**, *125*, 3599.
[16] Y. Zhu, C. Chen, S. Wu, R. Cheng, L. Cheng, W. L. Zhou, *J. Appl. Phys.* **2020**, *128*, 064302.
[17] S. Masudy-Panah, K. Radhakrishnan, H. R. Tan, R. Yi, T. I. Wong, G. K. Dalapati, *Sol. Energy Mater. Sol. Cells* **2015**, *140*, 266.
[18] L. Guo, Q. Sun, K. Marcus, Y. Hao, J. Deng, K. Bi, Y. Yang, *J. Mater. Chem. A* **2018**, *6*, 22005.
[19] Y. Wang, M. Zheng, S. Liu, Z. Wang, *Nanoscale Res. Lett.* **2016**, *11*, 390.
[20] M. Born, *Nature* **1927**, *119*, 354.
[21] R. Betancourt-Galindo, P. Y. Reyes-Rodriguez, B. A. Puente-Urbina, C. A. Avila-Orta, O. S. Rodríguez-Fernández, G. Cadenas-Pliego, R. H. Lira-Saldivar, L. A. García-Cerda, *J. Nanomater.* **2014**, *2014*, article no: 980545.
[22] M. Ashby, H. Shercliff, D. Cebon, *Materials: Engineering, Science, Processing and Design*, Butterworth-Heinemann, Oxford **2018**.
[23] M. G. Reuter, *J. Phys. Condens. Matter* **2016**, *29*, 053001.
[24] S. Clima, B. Kaczer, B. Govoreanu, M. Popovici, J. Swerts, A. S. Verhulst, G. Pourtois, *IEEE Electron Device Lett.* **2013**, *34*, 402.
[25] Y. C. Yang, H. J. Wang, J. Whang, J. S. Huang, L. M. Lyu, P. H. Lin, M. H. Huang, *Nanoscale* **2014**, *6*, 4316.
[26] B. Li, Y. Wang, *Superlattices Microstruct.* **2010**, *47*, 615.
[27] M. S. Satya Bharati, C. Byram, V. R. Soma, *Front. Phys.* **2018**, *6*.
[28] M. S. Satya Bharati, B. Chandu, S. V. Rao, *RSC Adv.* **2019**, *9*, 1517.
[29] S. N. Meysam, S. B. G. Hosein, K. Naimeh, *Nanomed. J.* **2015**, *2*, 153.
[30] S. Fu, J. Chen, H. Han, W. Wang, H. Shi, J. Fu, Y. Jia, *J. Alloys Compd.* **2019**, *799*, 183.
[31] S. Ravishankar, A. Riquelme, S. K. Sarkar, M. Garcia-Batlle, G. Garcia-Belmonte, *J. Phys. Chem. C* **2019**, *123*, 24995.
[32] A. Lasia, *Electrochemical Impedance Spectroscopy and its Applications*, Springer, Berlin **2014**.
[33] C. J. Pereyra, Y. Di Iorio, M. Berruet, M. Vazquez, R. Marotti, *Phys. Chem. Chem. Phys.* **2019**, *21*, 20360.
[34] M. Antuch, *Curr. Opin. Electrochem.* **2022**, *35*, 101043.
[35] M. Antuch, P. Millet, A. Iwase, A. Kudo, *Appl. Catal., B* **2018**, *237*, 401.
[36] L. G. Ferreira, M. Marques, L. K. Teles, *AIP Adv.* **2011**, *1*, 032119.
[37] M. French, R. Schwartz, H. Stolz, R. Redmer, *J. Phys. Condens. Matter* **2008**, *21*, 015502.
[38] J. T. Oh, S. R. Chowdhury, T. Lee, M. Misra, *Dyes Pigm.* **2018**, *116*, 936.
[39] W. Lipińska, J. Ryl, P. Slepski, K. Siuzdak, K. Grochowska, *Measurement* **2021**, *174*, 109015.
[40] A. D. Faisal, W. K. Khalef, H. T. Hussein, *Eng. Technol. J.* **2016**, *34*, 797.
[41] C. C. Vidyasagar, Y. Arthoba Naik, T. G. Venkatesha, R. Viswanatha, *Nano-Micro Lett.* **2012**, *4*, 73.

[42] S. Smidstrup, T. Markussen, P. Vancraeyveld, J. Wellendorff, J. Schneider, T. Gunst, K. Stokbro, *J. Phys. Condens. Matter.* **2019**, *32*, 015901.
[43] J. M. Soler, E. Artacho, J. D. Gale, A. García, J. Junquera, P. Ordejón, D. Sánchez-Portal, , *J. Phys. Condens. Matter* **2002**, *14*, 2745.
[44] M. J. Van Setten, M. Giantomassi, E. Bousquet, M. J. Verstraete, D. R. Hamann, X. Gonze, G. M. Rignanese, *Comput. Phys. Commun.* **2018**, *226*, 39.
[45] J. E. Sipe, E. Ghahramani, *Phys. Rev. B* **1993**, *48*, 11705.
[46] Y. C. Chang, J. N. Schulman, *Phys. Rev. B* **1982**, *25*, 3975.
[47] U. Wulf, *Micromachines* **2020**, *11*, 359.

Supporting information to the article A3

Annealing Rate as a Crucial Parameter Controlling the Photoelectrochemical Properties of AuCu Mosaic Core-Shell Nanoparticles

Wiktoria Lipińska, Adrian Olejnik, Jakub Karczewski, Katarzyna Grochowska, Katarzyna Siuzdak*

W. Lipińska, A. Olejnik, K. Grochowska, K. Siuzdak

Centre for Plasma and Laser Engineering, The Szewalski Institute of Fluid–Flow Machinery, Polish Academy of Sciences, Fiszera 14 Street, 80-231 Gdańsk, Poland

A. Olejnik

Department of Metrology and Optoelectronics, Faculty of Electronics, Telecommunications and Informatics, Gdańsk University of Technology, Narutowicza 11/12 Street, 80-233 Gdańsk, Poland

J. Karczewski

Faculty of Applied Physics and Mathematics, Institute of Nanotechnology and Materials Engineering, Gdańsk University of Technology, Narutowicza 11/12 Street, 80-233 Gdańsk, Poland

*Corresponding author email: wlipinska@imp.gda.pl

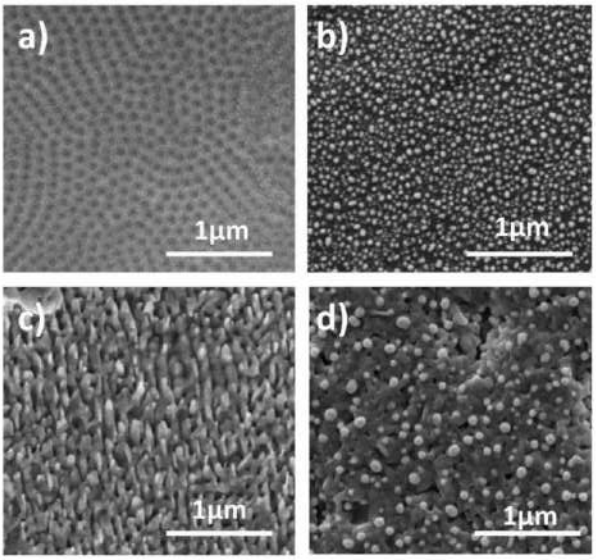

Fig. S1 SEM images of a) 1F- TiND b) 1F-AuCu/TiND, c) 4F- TiND d) 4F-AuCu/TiND

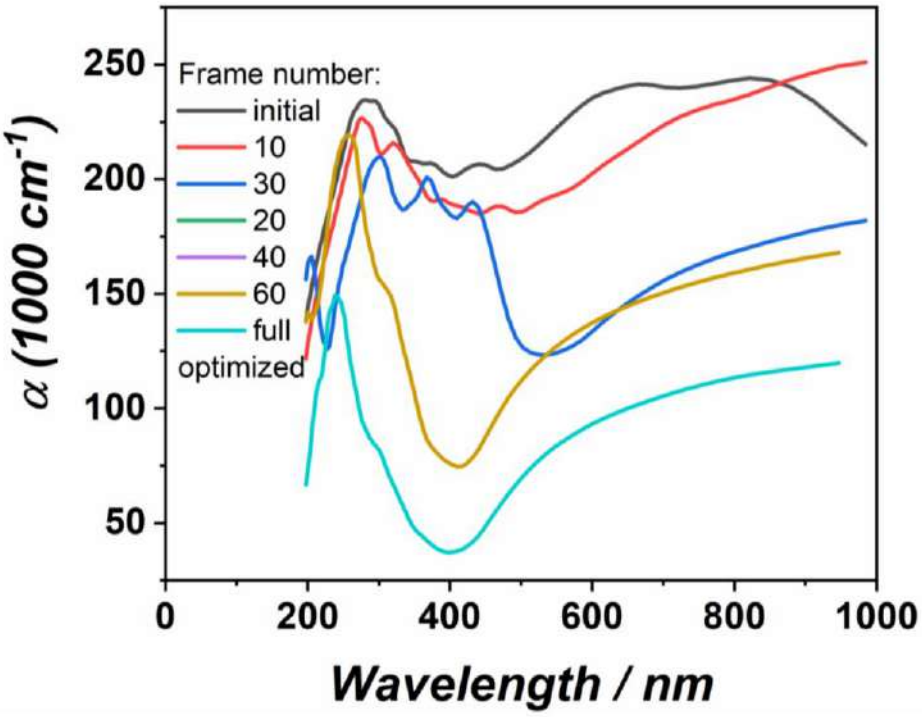

Fig.S2 DFT calculated absorption spectra for Cu_2O | CuO junction

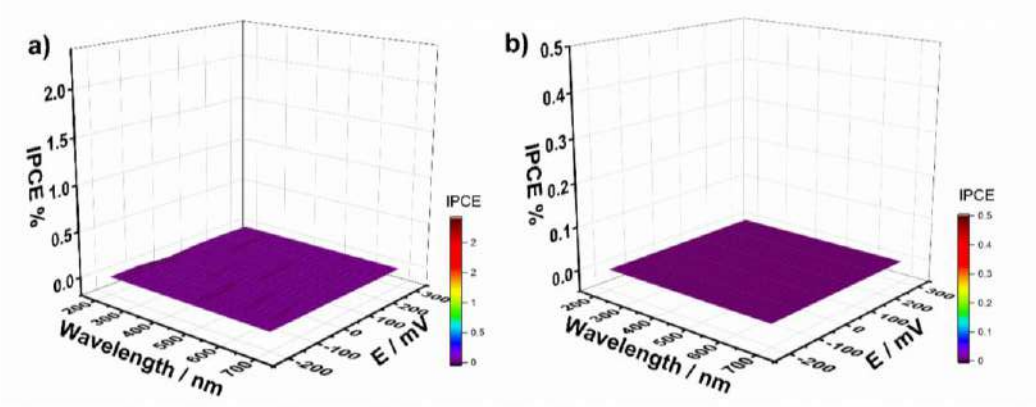

Fig.S3 IPCE of a) 1F- TiND b) 1S- TiND

7.4 Impact of annealing atmosphere during rapid thermal annealing of AuCu nanostructures deposited on Ti platform on photoelectrochemical activity

Brief overview of the article A4

Introduction

The atmosphere used during thermal treatment can strongly effect on properties of fabricated nanomaterials. Hydrogeneration of TiO_2, which can be performed by thermal treatment in hydrogen atmosphere, introduces disorders into nanostructure and causes enhancement of material photoactivity[216]. Furthermore, Wang et al.[103] compared conventional hydrogen annealing with hydrogeneration of TiO_2/FTO system in rapid thermal annealer and showed that annealing in RTA provides better performance towards solar energy conversion and water splitting process. In the case of copper oxides, post annealing of Cu_2O in hydrogen atmosphere and H^+ implantation can effect on the hole carrier density and acceptor level[217].

Similar as in the previous experiments (article A3, pages 127-141) the aim was to obtain AuCu nanoparticles active in the visible range not only at -0.17 V (article A1 and A2) but in wider potential window. However, not only temperature (article A1 and A2), time and annealing rates (article A3) but also atmosphere used during thermal treatment can impact onto photoelectrochemical activity under visible light illumination. According to article A2 the highest photocurrent under UV-vis light illumination was obtained when material was annealed at 600 °C, during 30 minutes with annealing rate of 45 °C/s. Therefore, in the case of article A4 I decided to choose the same temperature, time and similar heating rate (40 °C/s).

In the article A4, AuCu nanostructures were deposited on nanostructured Ti platform and rapidly annealed in various atmospheres such as air, vacuum, argon and hydrogen (named A-AuCu/TiND, V-AuCu/TiND, AR-AuCu/TiND, H-AuCu/TiND, respectively). Further, materials were investigated in terms of their morphology, optical and structural properties using synchrotron radiation (X-ray absorption spectroscopy and X-ray photoelectron spectroscopy) as well as photoelectrochemical activity.

Nanomaterials synthesis

Ti nanodimples were fabricated using the same procedure as in article A1. Subsequently, Ti nanodimples were covered by thin 10 nm layer of AuCu alloy by magnetron sputtering and annealed in the rapid thermal annealer in various atmospheres (air, vacuum, argon, hydrogen) at 600 °C during 30 minutes with annealing rate of 40 °C/s. The schematic fabrication process is presented in Figure 54.

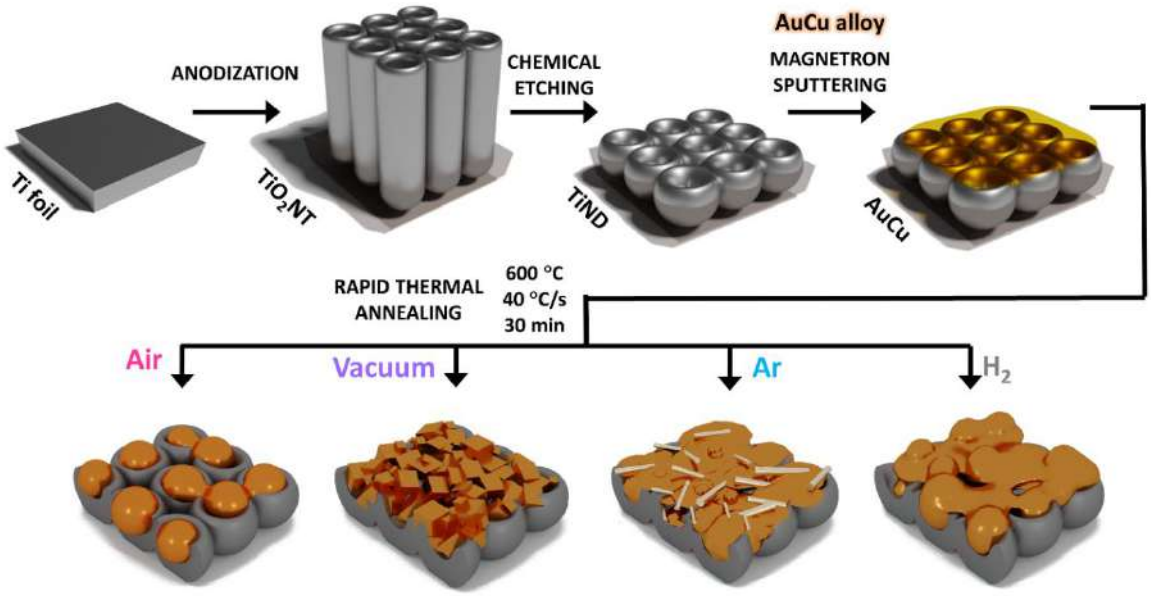

Figure 54. Schematic fabrication process of AuCu nanostructures deposited on Ti nanodimpled platform thermally treated in the rapid thermal annealer in various atmospheres.

Optical properties

The UV-vis spectra differ significantly between TiND electrodes annealed in various atmospheres not only in the UV region which is associated with the presence of TiO_2 passivation layer but also in the visible range (see article A4 Figure 6a). After AuCu-decoration of Ti platform and rapid thermal treatment the decrease of reflectance in the whole range was registered for all samples (see article A4 Figure 6b). The reflectance spectra for AuCu nanostructures are presented in Figure 55. The lowest reflectance with minimum at 750 nm was registered for AuCu nanostructure annealed in hydrogen atmosphere.

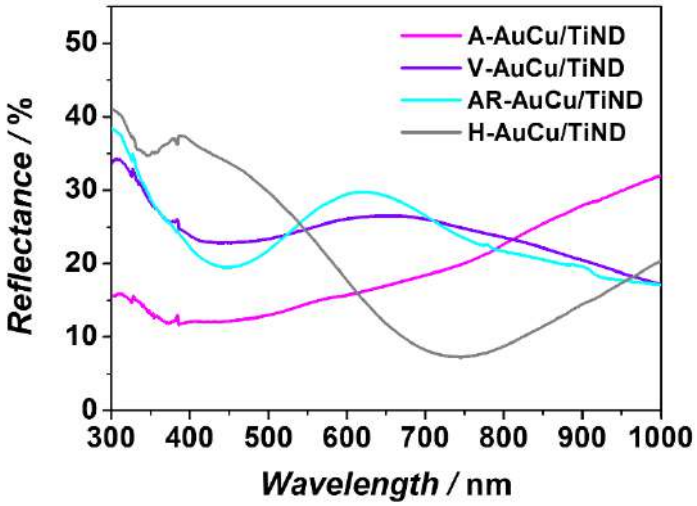

Figure 55. Reflectance spectra for AuCu-decorated Ti platform annealed in various atmospheres.

The thermal treatment in high temperatures changes morphology and crystalline phase of AuCu/TiND samples. According to article A2 annealing above 400 °C resulted in the broadband absorbance from 400 nm to 1000 nm. Despite the fact that AuCu NPs were still on the electrode surface no SPR peaks were seen. It should be added that the absorbance spectra strongly depend on the platform where NPs are deposited. In the case of article A4 the shape of UV-vis spectra was influenced by titanium dioxide which was present in various phases after thermal treatment in different atmospheres. According to XRD (see article A4, Figure 4), for the AuCu/TiND electrode annealed in air atmosphere only peaks from anatase and rutile crystal plane were registered. Whereas, for the AuCu-decorated materials annealed in vacuum and argon peak signals confirmed presence of not only TiO_2 but also Ti_2O_3 and non-stoichiometric titanium oxide as Ti_4O_7[218]. Furthermore, especially during annealing in air copper oxidation takes place which also effects on SPR peak disappearing. Additionally, only in the case of AuCu samples annealed in hydrogen Cu^{1+} was present on the electrode surface which could be responsible for the lowest reflectance from all of samples.

Electrochemical and photoelectrochemical properties

The electrochemical activity of Ti and AuCu decorated Ti electrodes was tested using cyclic voltammetry measurements in the range from -0.8 V to +0.8 V in 0.1 M NaOH. Annealing in oxygen free atmosphere resulted in increase of molecular diffusion of oxygen and therefore higher current density at +0.8 V in contrast to electrodes annealed in air (see article A4 Figure S2). Moreover, oxygen free atmosphere enhanced capacitive current because of higher density of hydroxyl groups on TiO_2 surface[219]. The thermal treatment in vacuum leads to formation of defects which can play important role in catalytic processes and in this case decreased electrochemical overpotential characteristic for oxygen evolution reaction[220]. Taking into account photoelectrochemical activity under visible and UV-vis light the highest photocurrent was obtained for sample annealed in hydrogen and air atmosphere, respectively. As was mentioned above the lowest reflectance with minimum at 750 nm was obtained for the H-AuCu/TiND electrode (Figure 55) supporting the best photoactivity of hydrogenated sample under visible light illumination (Figure 56). The values of photocurrent density for Ti and AuCu modified Ti are presented in Table 12.

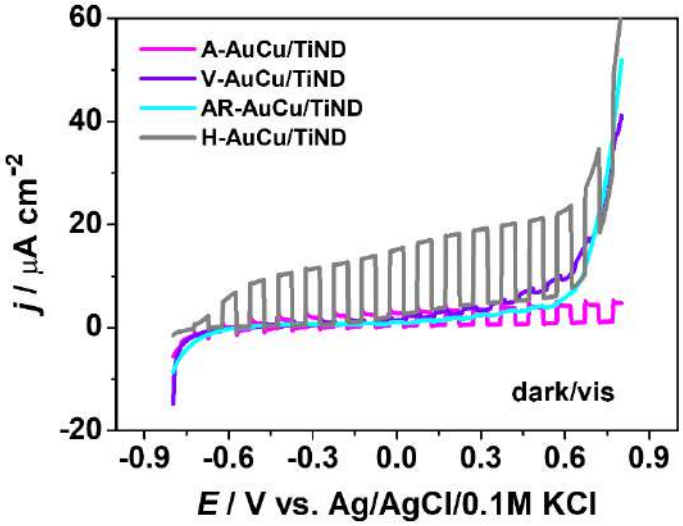

Figure 56. Linear voltammetry curves registered under visible light for AuCu-decorated Ti platform annealed in various atmospheres.

Table 12. Values of photocurrent density registered under vis and UV-vis light illumination for materials thermally treated in various atmospheres (E = +0.3 V vs. Ag/AgCl/0.1 M KCl).

Electrode	Atmosphere	$j_{(vis)}$ / μA cm^{-2}	$j_{(UV-vis)}$ / μA cm^{-2}
AuCu/TiND	Air	2.9	76.3
	Vacuum	0.5	22.3
	Argon	0.4	34.4
	Hydrogen	16.1	14.7
TiND	Air	1.7	139.6
	Vacuum	0.3	20.7
	Argon	0.4	18.3
	Hydrogen	0.6	36.4

Structural properties

Structural properties of pure TiND and AuCu modified TiND electrodes annealed under various atmospheres in rapid thermal annealer were investigated by X-ray absorption spectroscopy and X-ray photoelectron spectroscopy using synchrotron radiation. Based on XAS analysis for the AuCu/TiND electrode annealed in air copper was recognized in the form of CuO, whereas, for the AuCu/TiND sample thermally treated in hydrogen - Cu_2O or metallic Cu[167] (Figure 57). Combination of XAS and XPS analysis suggested that for the A-AuCu/TiND CuO was recognised in the upper layer (2-3 nm) while going deeper into surface layer to bulk zone more and more Cu_2O or metallic Cu was present. However, in the case of the H-AuCu/TiND electrode no Cu_2O or Cu appeared in the bulk zone. It can be claimed that, the lowest reflectance and the best photoelectrochemical activity in the visible light range for hydrogenated AuCu nanostructures are the result of presence of Cu_2O in the upper surface layer. XPS measurements of the Ti2p chemical states found TiO_2 and Ti_2O_3 at 458.8 eV and 457 eV, respectively.

Furthermore, in the case of the AuCu/TiND thermally treated in vacuum bands are shifted towards higher values which can be assigned to oxygen vacancy.

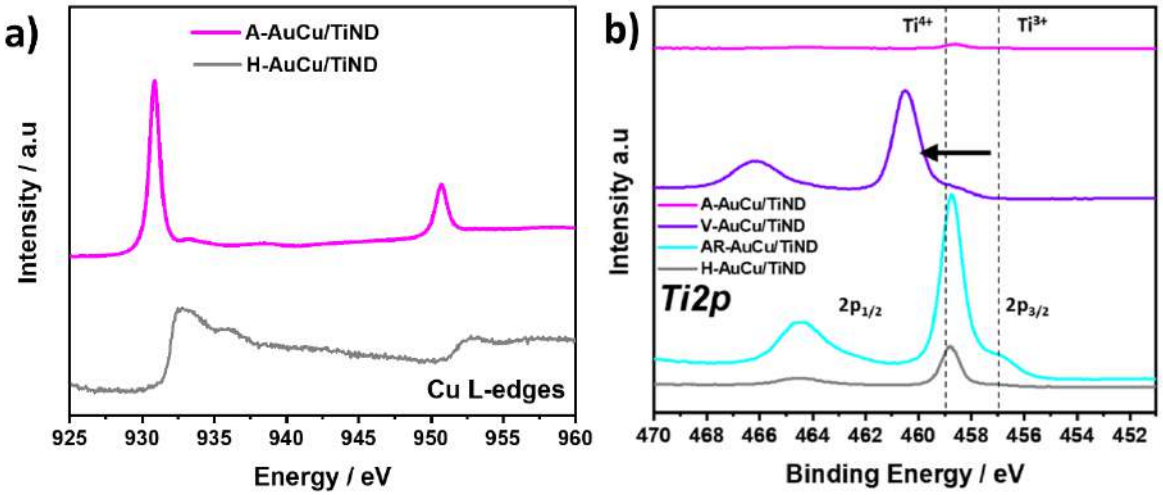

Figure 57. a) XAS spectra for Cu L-edges collected in TEY (total electron-yield) mode for AuCu-decorated TiND annealed in air and hydrogen atmosphere (2-3 nm depth), b) XPS for Ti2p of AuCu/TiND electrodes thermally treated in air, vacuum, argon and hydrogen atmosphere.

Conclusions

The best photoelectrochemical activity in the visible light range was obtained for the AuCu hydrogenated electrode (16 μA cm^{-2}). The photocurrent was ca. 27 times higher than for hydrogenated Ti nanodimpled platform. The H-AuCu/TiND electrode showed the lowest reflectance with minimum at 750 nm. Synchrotron radiation studies allowed to distinguish three zones such as upper surface layer (2-3 nm), deeper surface layer (5-7 nm) and bulk (12-15 nm). In the case of hydrogenated AuCu nanostructures copper and copper oxides were confirmed in the upper and deeper layer where the amount of Cu_2O was ca. 2 times higher in the upper layer than in deeper layer. Hydrogenation has positive effect on photoelectrochemical activity under visible light of AuCu nanostructures on TiND due to the efficient acceptor-donor configuration of AuCu doped TiO_2/Ti platform material.

A4) W. Lipińska, Z. Bielan, A. Witkowska, J. Karczewski, K. Grochowska, E. Partyka-Jankowska, T. Sobol, M. Szczepanik, K. Siuzdak, ***Insightful studies of AuCu nanostructures deposited on Ti platform: Effect of rapid thermal annealing on photoelectrochemical activity supported by synchrotron radiation studies***, Applied Surface Science 638 (2023) 158048, IF = 6.7 / 140 points mechanical engineering

Applied Surface Science 638 (2023) 158048

Contents lists available at ScienceDirect

Applied Surface Science

journal homepage: www.elsevier.com/locate/apsusc

Full Length Article

Insightful studies of AuCu nanostructures deposited on Ti platform: Effect of rapid thermal annealing on photoelectrochemical activity supported by synchrotron radiation studies

Wiktoria Lipińska [a,*], Zuzanna Bielan [a], Agnieszka Witkowska [b], Jakub Karczewski [b,c], Katarzyna Grochowska [a], Ewa Partyka-Jankowska [d], Tomasz Sobol [d], Magdalena Szczepanik [d], Katarzyna Siuzdak [a]

[a] Centre for Plasma and Laser Engineering, Institute of Fluid-Flow Machinery, Polish Academy of Sciences, Fiszera 14 St., 80-231 Gdańsk, Poland
[b] Institute of Nanotechnology and Materials Engineering, Faculty of Applied Physics and Mathematics, Gdańsk University of Technology, Narutowicza 11/12 St., 80-233 Gdańsk, Poland
[c] Advanced Materials Center, Gdańsk University of Technology, Narutowicza 11/12 St., 80-233 Gdańsk, Poland
[d] National Synchrotron Radiation Centre SOLARIS, Jagiellonian University, Czerwone Maki 98 St., 30-392 Kraków, Poland

ARTICLE INFO

Keywords:
AuCu nanostructures
Hydrogenation
Synchrotron radiation
Depth-profile
Photoactivity

ABSTRACT

In this work, we present the influence of annealing atmospheres during rapid thermal annealing (40 °C/s) on nanostructured Ti platforms modified by 10 nm layer of AuCu alloy obtained via magnetron sputtering. The AuCu/Ti platform annealed under hydrogen atmosphere exhibits the best photoelectrochemical activity under visible light, i.e. 27 times higher photocurrent than for pure Ti dimpled platform, and the lowest reflectance with minimum at ca. 750 nm. Synchrotron radiation studies allow for inspection in three zones, such as the upper (2–3 nm) and deeper (5–7 nm) surface layers as well as the bulk structure (12–15 nm). Taking into account hydrogenated AuCu/Ti platforms gold presence was confirmed in the upper and deeper surface layers as well as in bulk whereas Au_xCu_y nanoalloy only in the deeper layer. In the case of copper, Cu_2O or Cu were distinguished in the upper and deeper surface layers, where Cu^{+1}/Cu_{tot} ratio reaches 70 % in the upper layer and drops to about 40 % at a depth of 5–7 nm. Hydrogenation has a positive effect on photovoltaic performance by efficient acceptor–donor configuration of AuCu doping on/into TiO_2 semiconductor showing its potential ability as photoanode in solar cells.

1. Introduction

Since the work of Haruta [1] in 1997, summarizing the dependency of gold reactivity on the size of its particles, this material is continuously used in electronics [2], sensors [3], diagnostics and medicine [4] as well as catalysis [5]. Nanosized gold was also proved to reveal outstanding absorption of light in broad wavelength range due to the presence of a localized surface plasmon resonance (LSPR) [6]. However, availability of this material is limited, thus, its price, among noble metals, is almost the highest. Therefore, several solutions have been proposed in order to decrease the amount of used gold (or even eliminate it from the material) without loss in activity.

One of the most frequently used method is combining Au with other metals (M), both noble [7–9] and transition [10–12], creating active bimetallic structures. Au-M nanoparticles' (NPs) distribution, size as well as oxidation states are subjected to changes with the synthesis parameters differing. In the work of Gołąbiewska et al. [13], dependency of calcination temperature and type of used reducing agent on AuPt nanoparticles' size and AuPt-TiO_2's visible light activity was described. When sodium borohydride was used as a reducing agent, obtained nanoparticles were rather small (~7.3 nm) with the gold in $Au^{\delta-}$ form, which had positive impact on the efficiency of phenol photodegradation. Moreover, it was determined that the size of modifying nanoparticles increased with elevating the calcination temperature. Similar studies have been carried out by Cybula et al. [14]. They discovered that changes of annealing temperature cause redistribution of Au and Pd nanoparticles, going from the gold core palladium shell structure at 300 °C, through AuPd alloyed islands with different compositions, until

* Corresponding author.
E-mail address: wlipinska@imp.gda.pl (W. Lipińska).

https://doi.org/10.1016/j.apsusc.2023.158048
Received 22 March 2023; Received in revised form 7 June 2023; Accepted 13 July 2023
Available online 16 July 2023
0169-4332/

full alloy at 700 °C. However, such reorganization leads to decrease of material's photoactivity for $\lambda > 420$ nm over 5 times. In turn, Nazemi et al. [15] proved, that the use of femtosecond laser at 808 nm allows for analogous changes of metal domains in AuPd bimetallic nanorods, enhancing their optical and electronic properties. Taking into account photoelectrochemical activity, the Au-, Pd- and AuPd-decorated TiO_2 photoanodes obtained higher photocurrents under visible light illumination and photoconversion efficiency than the pure TiO_2 [16]. Furthermore, such composition of bimetallic noble metals resulted in higher photocurrent values in comparison to monometallic counterparts (2 and 1.5 times higher than for Pd and Au, respectivetly). According to Manchala et al. [17] the bimetallic AgAu plasmonic nanoparticles deposited on graphene enhance photocatalytic water reduction process. The AgAu-graphene material exhibits ca. 2 times higher photocatalytic H_2 production than Ag-graphene electrode and 1.4 times higher than Au-graphene one. Haider et al. [18] reported that the photocatalytic oxygen evolution reaction differs as a function of the ratio of Ag and Au in Ag_xAu_{1-x}/TiO_2 electrode. The $Ag_{0.6}Au_{0.4}/TiO_2$ composition exhibited the best photocatalytic water oxidation performance, namely ca. 3 times higher than for the monometallic counterparts. Among Au-M bimetallic junction, the one with copper is often described in the literature as promising due to the fact, that both materials reveal LSPR effect at similar wavelength region [19]. Moreover, high activity of gold together with high selectivity of copper lead to their efficient catalytic performance in various reactions, e.g., CO_2 electroreduction [20], alcohol oxidation [21,22] electrochemical sensing [23] or water splitting [24]. However, as it was written by Sha et al. [25], the arrangement between Au and Cu metal atoms is the most important factor for establishing material which is as active as possible. In this regard, researchers concentrated on developing fabrication routes of AuCu bimetal nanostructures, together with their detailed structural examination.

Suzuki et al. [26] described AuCu bimetallic alloy synthesis by using metals' magnetron sputtering directly onto ionic liquid. Further, using heating in the temperature range of 323–573 K resulted in the alloy transformation to $L1_0$ structure (tetragonal distortion of the fcc structure), which is described as the most stable one. In turn, in the work of Sakamoto et al. [27] AuCu bimetallic NPs, characterized by different shapes and sizes were synthetized in continuous polymer film with the use of 355 nm laser as an irradiation source. Due to the laser matter interaction the reduction of the oxidation species can occur. Authors found, that NPs dimensions are changing with their position in relation to the centre of laser spot. In the most outer area from the spot centre, characterized by lower irradiation intensity, the AuCu particles are almost three times larger in size, comparing to those from the middle of the laser spot. Certainly, this affects their physicochemical and optical properties, together with their future applications. Moreover, changes in AuCu structure could have appeared during the course of the catalytic reaction. Liu et al. [28] carried out CO oxidation reaction where AuCu NPs were used as catalysts. The in situ techniques including X-ray diffraction (XRD), electron paramagnetic resonance (EPR), diffuse reflectance infrared Fourier transform (DRIFT), and X-ray absorption near edge structure (XANES) revealed changes in copper oxidation states with process parameters (mostly temperature increasing) changes while gold remained in 0 valent metal form. To the best of our knowledge results related to synchrotron radiation studies of gold-copper structures onto dimpled titanium foil and influence of structure as well as atomic arrangement on photoelectrochemical activity have not been reported before. Such studies allow for a better understanding of prepared electrode material and confirm the assumption concerning the mechanisms responsible for the enhanced photoelectrochemical activity. As conventional approaches are often inadequate to thoroughly describe such materials behaviour under incident light illumination, more sophisticated techniques are of key importance to understand their physicochemical properties. Such knowledge is of great importance in interpretation of material's behaviour when illuminated with light.

According to our previous works [29,30] we can compare the effect of two types of annealing procedures on electrochemical and photoelectrochemical properties of AuCu-decorated dimpled surface (AuCu/TiND). Despite the fact, that described samples were treated in similar temperatures and annealing time their photoresponse differed significantly. In the case of the preheated muffle furnace AuCu nanoparticles could have experienced the thermal shock. Thermal treatment in muffle furnace at 450 °C in air atmosphere resulted in high activity towards oxygen evolution reaction (OER) at +0.8 V vs. Ag/AgCl/0.1 M KCl assisted by visible light illumination. On the contrary, the AuCu/TiND electrodes treated in rapid thermal annealing (RTA) furnace at 400 °C or 500 °C in air atmosphere with heating rate of 40 °C/s resulted in efficient electron-hole pair generation under UV–vis light illumination. The photocurrent was recorded in the wide potential range from −0.8 V to +0.8 V vs. Ag/AgCl/0.1 M KCl.

In this work we used rapid thermal annealing furnance (40 °C/s). However, in contrast to our previous work where annealing was performed only in air, here we tested four different annealing atmospheres: air (A), vacuum (V), argon (AR) and hydrogen (H). The study showed that annealing atmosphere strongly influences on photoelectrochemical activity of AuCu nanostructures deposited on Ti dimpled platform. Obtained AuCu-decorated dimpled surface were, for the first time, characterized by X-ray absorption spectroscopy (XAS) with the use of total electron-yield (TEY) and total fluorescence-yield (TFY) detectors. Moreover, distribution and oxidation states changes of Au and Cu were verified using X-ray photoelectron spectroscopy (XPS) with different X-ray energies, allowing for chemical composition's depth profile determination. The X-ray spectroscopy measurements were performed at the PHELIX beamline at the National Synchrotron Radiation Centre SOLARIS in Cracow (Poland). Detailed knowledge of nanostructure allows to propose the energy diagram of the whole material and indicating the charge transfer supporting the improved photoconversion. The understanding of the structure details supports elaboration of synthesis procedure towards more efficient materials used for advanced solar cells of the future.

2. Experimental

2.1. AuCu electrode fabrication

The Ti foil was cut into 2×3 cm^2 pieces and ultrasonically cleaned in acetone, ethanol and water, for 10 min in each. Then the electrochemical anodization process was carried out in two-electrode system where Ti plate was the anode and Pt mesh was the cathode. The electrolyte contained 0.27 M NH_4F dissolved in a mixture composed of 1 % vol. deionised water and 99 % vol. ethylene glycol. The process was carried out in the thermostated glass cell with a temperature of 23 °C and at a voltage of 40 V. The anodization process was repeated twice and after each of anodization TiO_2 nanotubes were chemically etched in the oxalic acid solution in order to form Ti nanodimples (TiND). Subsequently, titanium nanodimples were covered by 10 nm AuCu layer using magnetron sputtering machine (Q150T S system, Quorum Technologies). The thickness was controlled by quartz microbalance weight. For this purpose the AuCu target was used with the composition of Au50/Cu50 At % (Goodfellow). Afterwards, electrodes were thermally treated in the Rapid Thermal Annealing furnace (MILA 5000P-N) at 600 °C with heating rate of 40 °C/s for 30 min in different atmospheres (air, vacuum, argon and hydrogen). Labels assigned to the obtained electrodes are gathered in.

Table 1. Moreover, the schematic diagram of the electrode preparation is presented in Fig. 1 (NTs – nanotubes, L – layer).

2.2. Samples characterization techniques

The morphology of the electrodes was investigated using a field emission scanning microscope (SEM) (FEI Quanta FEG250) equipped with an ET secondary detector while the beam accelerating voltage was

Table 1
Description of obtained samples.

Sample	Annealing atmosphere	Thickness of sputtered AuCu film [nm]
A-TiND	Air	–
A-AuCu/TiND	Air	10
V-TiND	Vacuum	–
V-AuCu/TiND	Vacuum	10
AR-TiND	Argon	–
AR-AuCu/TiND	Argon	10
H-TiND	Hydrogen	–
H-AuCu/TiND	Hydrogen	10

kept at 10 kV.

The UV–vis reflectance spectra of nanostructured titanium platform (TiND) and AuCu modified titanium (AuCu/TiND) were measured with spectrophotometer (Lambda 35, Perkin-Elmer) equipped with an accessory for reflectance spectra registration.

The crystal structure was measured by X-ray diffraction (XRD) technique over the range of 20–80° using Bruker 2D Phaser diffractometer with CuKα radiation and XE-T detector.

NEXAFS (Near Edge X-ray Absorption Fine Structure) and XPS (X-ray Photoelectron Spectroscopy) measurements were performed at the PHELIX beamline of the SOLARIS synchrotron in Cracow (Poland) [31]. The source of soft X-rays (available photon energy range 50–1500 eV) is an elliptically polarizing undulator APPLE II type with permanent magnets. All experiments were performed under UHV conditions. NEXAFS spectra at the Au N-edges (340–360 eV), Cu L-edges (925–960 eV), Ti L-edges (450–475 eV) and O K-edge (525–555 eV) were collected in total electron yield (TEY) and total fluorescence yield (TFY) modes, thus obtaining information from different sampling depths. Before the analysis, spectra were normalized to the incident beam intensity. XPS measurements were performed with an electrostatic hemispherical analyser manufactured by SPECS GmbH, PHOIBOS 225, characterized by energy resolution better than 2 meV. The Au4f, Cu2p, Ti2p and O1s spectra were measured using monochromatic radiation chosen from the range between 600 eV and 1300 eV. By tuning the energy of the X-rays one can further adjust the penetration depth. Thus, in the case of the studied materials registering photoelectrons with 100–1000 eV of kinetic energy, we were able to obtain depth profiles of the bond chemistry and sample composition reaching up to around 15 nm into the sample. The schematic representation of nanomaterial zones is shown in Fig. 2. For quantitative analysis the following atomic sensitivity factors were applied [28]: ASF($Au4f_{7/2}$) = 1.9; ASF($Cu2p_{3/2}$) = 4.3; ASF($Ti2p_{3/2}$) = 1.1; ASF(O1s) = 0.63.

The electrochemical and photoelectrochemical measurements of TiND and AuCu/TiND samples, such as cyclic voltammetry (CV) and linear voltammetry (LV) were conducted using AutoLab PGStat 302 N potentiostat–galvanostat. The measurements were carried out in 3 electrode arrangement where reference electrode was Ag/AgCl/0.1 M KCl, Pt mesh acted as counter electrode while investigated materials took the role of the working electrode. This set of electrodes were introduced into the special electrochemical cell equipped with quartz window transparent for the UV light. The photoelectrochemical measurements were conducted using xenon lamp (LOT-QuantumDesign GmbH) equipped with AM1.5 filter. The irradiation intensity was set to 100 $mWcm^{-2}$ and calibrated using Si reference cell (Rera). For obtaining only visible light region, the cut-off filter (Schott, 420 nm) was used. The CV and LV curves were registered form −0.8 V to +0.8 V vs. Ag/AgCl/0.1 M KCl in deaerated 0.1 M NaOH solution. The CV scans were recorded with 50 mV/s scan rate while LV from cathodic towards anodic direction with 10 mV/s.

3. Results and discussion

3.1. Crystal structure

Crystal phase composition of samples was checked using X-ray diffractometry and obtained results are presented in Figs. 3 and 4. For unmodified TiND, the dominant TiO_2 phase was rutile, with the main

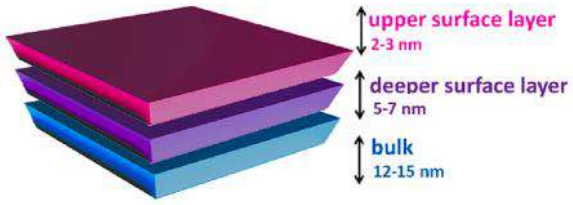

Fig. 2. Schematic representation of nanomaterial zones that were considered during synchrotron studies.

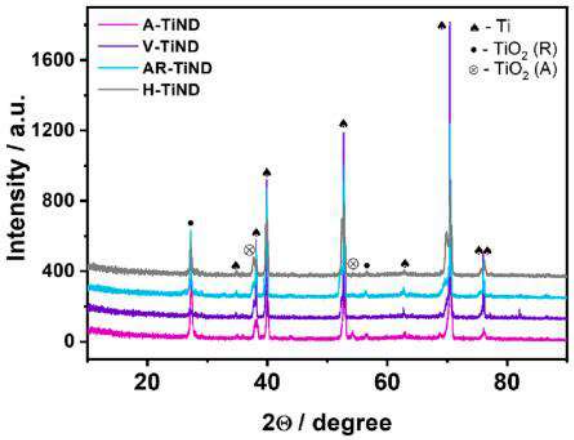

Fig. 3. XRD patterns of the titanium nanodimples (TiND) electrodes annealed in four different atmospheres (air, vacuum, argon, hydrogen).

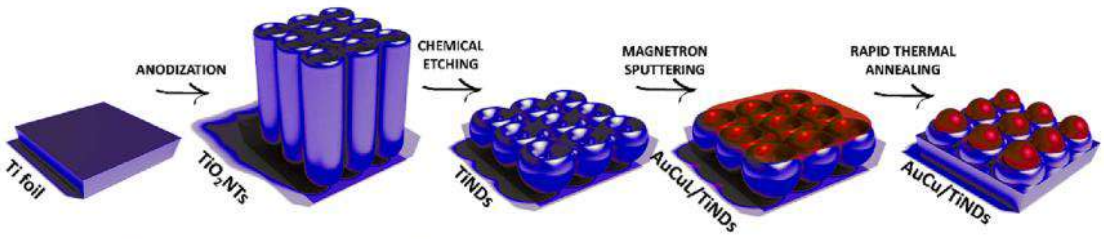

Fig. 1. The diagram of the preparation of Ti nanodimples modified with AuCu showing all steps from anodization, chemical etching, magnetron sputtering to rapid thermal annealing in different atmospheres.

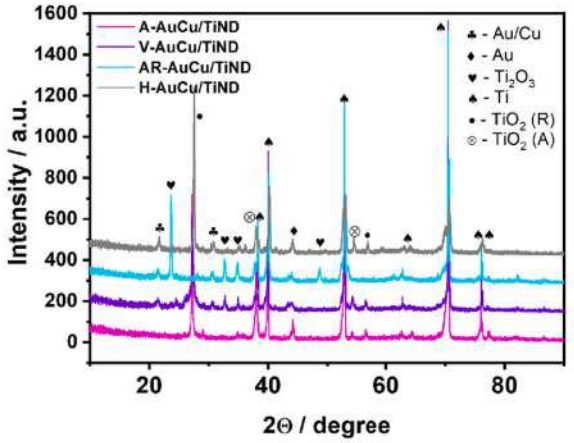

Fig. 4. XRD patterns of the AuCu-decorated dimpled platforms (AuCu/TiND) annealed in four different atmospheres (air, vacuum, argon, hydrogen).

peak at 27.2°, corresponding to (110) crystalline plane. Low intensity anatase peaks at 37.8° (004) and 52.5° (105) are also visible. What is important, the annealing atmosphere had significant impact on the titania crystalline phase. While in the sample prepared in air the rutile and anatase peaks are sharp and intense, for V-TiND material their presence is almost negligible. This could be related to lack of oxygen in the RTA furnace during annealing process and, as a consequence, stoichiometric titanium dioxide is not formed. Remaining peaks, located at 34.9°, 38.1°, 39.9°, 52.7°, 62.8°, 70.3°, 75.9° and 76.2° could be attributed to (100), (002), (101), (102), (110), (103), (112) and (201) Ti substrate's planes, respectively. After magnetron sputtering of AuCu layers and annealing of samples under given atmospheres, meaningful changes could be seen (Fig. 4). First of all, for the set of AuCu/TiND samples, a single signal originating from gold at 44.1° is visible, confirming its presence in the material [32]. Moreover, for AuCu/TiND annealed in hydrogen an AuCu NPs alloy was formed, which is confirmed by two peaks at 21.6° (001) and 30.8° (110), similarly to the work by Wang et al. [33]. Whereas, the same peaks for AuCu/TiND material annealed in vacuum and argon might correspond to non-stoichiometric titanium oxide Ti_4O_7 and brookite phase [34,35]. Interestingly, the change in the oxidation state of titanium could be observed for V-AuCu/TiND and AR-AuCu/TiND. After annealing of AuCu/TiND in argon gas, the TiO_2 phase was almost completely reduced to Ti_2O_3 in comparison to AR-TiND sample where TiO_2 was present. In turn, after vacuum treatment both TiO_2 (rutile and anatase) as well as Ti_2O_3 were created, while none of those phases occurred before. Presented in Fig. 4, Ti_2O_3 peaks at 23.6°, 32.7°, 34.9° and 48.7°, attributed to (012), (104), (110) and (024), respectively, are in agreement with

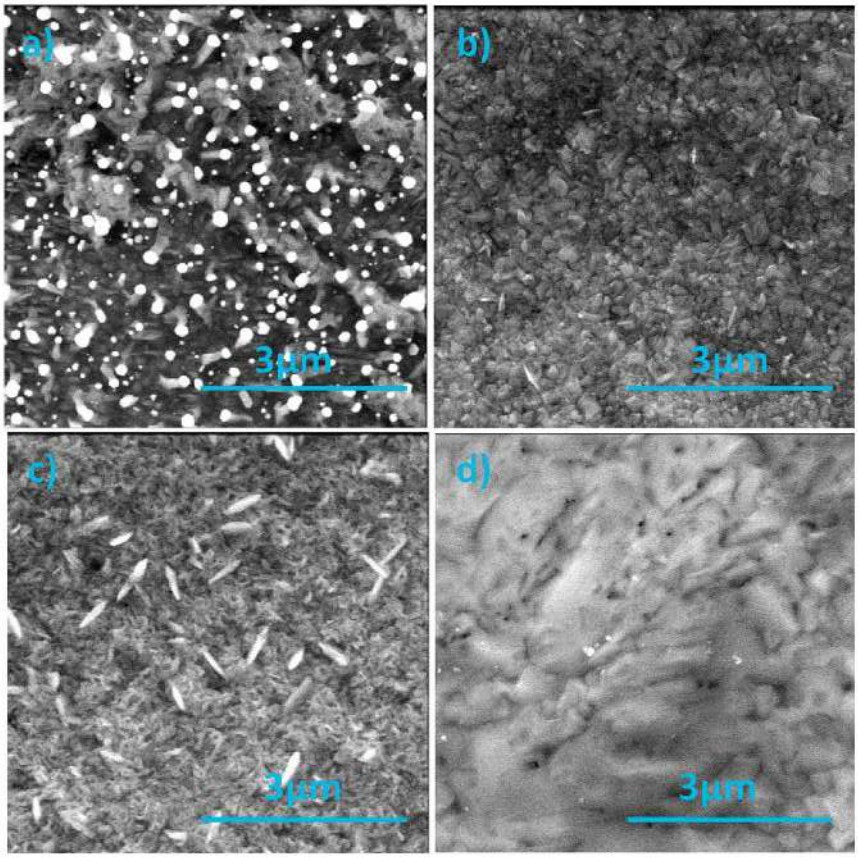

Fig. 5. SEM images of AuCu-decorated dimpled surface annealed in a) air (A-AuCu/TiND), b) vacuum (V-AuCu/TiND), c) argon (AR-AuCu/TiND) and d) hydrogen (H-AuCu/TiND).

the literature [36,37]. Finally, for A-AuCu/TiND sample no phase changes are observed, although the intensity of TiO_2 peaks increased, which proves the increment of material's crystallinity.

3.2. Morphology

The series of the fabrication steps led to the electrode material. Due to the anodization well-ordered titania nanotubes are formed (Fig. S1a), and as expected after their selective removal, the titanium substrate exhibiting dimple like structure (Fig. S1b). According to the final steps of the procedure the AuCu thin film was sputtered and rapid thermal treatment was carried out that significantly changes both morphology and electrochemical properties.

Following that, morphology shown in Fig. 5 does not really provide the initial geometry of structured titanium foil. TiND is characterized by the cavities of 85 ± 3 nm in diameter and 7 ± 1 nm in depth. The details regarding substrate material are reported in [3]. After deposition of AuCu layer and subsequent annealing at 600 °C in different atmospheres, the characteristic dimples are not visible. In the case of RTA-treatment in air, the spherical AuCu particles are obtained while for argon some spindle-shaped particles are formed (Fig. 5 a and c). For vacuum and hydrogen atmospheres, there are no distinct particles (Fig. 5 b and d). In the case of both Au and Cu, the dewetting of thin layers is strongly dependent on film thickness, substrates and the conditions in which the process occurs. It was already proven that the annealing atmosphere can influence the dewetting process by changing the anisotropy of the deposited film [38]. Moreover, the oxidation, i.e. thermal treatment in oxidizing atmosphere, can induce the inhibition of dewetting process [39]. While in the case of gold annealed in the air we obtained nanoparticles filling the whole interior of each nanodimple, the gold-copper nanoparticles seem to be more randomly distributed over the entire sample area [29]. This can lead to the conclusion that indeed, in our case the thermal process is slowed down. In the literature, it was also reported that thermal treatment of copper in oxidizing environment results in more spherical shapes while in reducing one in more flatten ones [40]. Whereas the dewetting of the gold thin films seems to lead to spherical nanoparticles independently on the applied atmosphere [41]. Taking those findings into account, we believe that atmosphere is of key importance in controlling dewetting process.

3.3. Optical properties

The UV–vis spectra of obtained materials are shown in Fig. 6. First of all, the change in reflectance spectra is already easily observed for the substrates thermally treated in various atmospheres (see Fig. 6 a). According to our previous work [42] structured titanium foil (see Fig. S1b) absorbs mainly in the UV region while for wavelengths above 400 nm the absorption drops significantly. The absorption in the UV region is caused by the presence of thin passive TiO_2 oxide layer on the TiND electrode surface. Moreover, thermal treatment of TiND at 450 °C and 600 °C can shift the absorbance maxima from 340 to 460 nm, respectively, due to the changes of the dimple dimension [29]. In this work all materials were annealed at the same temperature that equals 600 °C, however, annealing atmosphere was changed. Rapid thermal treatment of prepared TiND platforms in various atmospheres changed the shape of the spectra indicating either changes in nanodimples geometry as well as crystalline phase of oxide layer (Fig. 6 a). After the deposition of AuCu film and dewetting, the reflectance for all the samples decreases in the whole wavelength range (Fig. 6 b). Moreover, no distinct peaks that could be related to plasmon resonance of gold-copper nanoparticles are seen for obtained samples while at least for air-annealed one could expect their appearing. According to literature the SPR band for Au and Cu can be located at ca. 510 and 580 nm, however, it should be highlighted that the absorbance spectra significantly depend on the platform where NPs are immobilized [29]. Similar shape of spectra as seen in Fig. 4b, although with some small plasmon resonance band, was also reported by Petrovic et al. [43] for AgCu nanoparticles. The lack of plasmon band for Au and Cu can be attributed to heating at high temperatures and oxidation of copper [44].

3.4. Photoelectrochemical activity

The electrochemical and photoelectrochemical properties were taken as a main criterion for the sample selection. At the beginning, the electrochemical activity of the materials was tested using cyclic voltammetry (see Fig. S2). The measurements were carried out in the range from −0.8 to +0.8 V in 0.1 M NaOH (pH = 13), knowing about the significant effect of the annealing atmosphere in the anodic range (Fig. S2). This effect can be observed even for bare substrates. After annealing in vacuum, the samples show rapid increase of current and lowering of the electrochemical overpotential in the anodic regime that is typical for the improved water splitting process [45]. According to Pei et al. [46], the presence of defects plays important role in the catalytic activity. They also indicated that apart from the higher carrier density, the presence of coordination-unsaturated titanium sites affects the facilitated molecular diffusion of oxygen along the conducting crystal channels of non-stoichiometric oxide structure. The highest current density at +0.8 V was recorded for the bare nanodimples annealed in argon suggesting, that available titania surface area is crucial in this process rather than AuCu species. Additionally, due to the annealing in the oxygen free atmosphere, obtained Ti dimpled samples exhibit larger capacitive current attributed to the enhanced carrier density and increased density of hydroxyl group on TiO_2 surface [47]. Here, such a phenomenon is also present, however due to the very low Ti dimpled

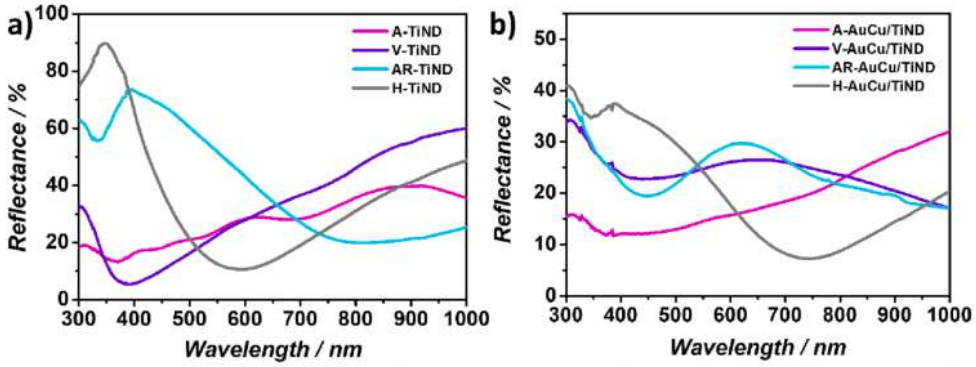

Fig. 6. Reflectance spectra of a) titanium nanodimples (TiND) and b) titanium nanodimples modified by AuCu (AuCu/TiND) rapidly annealed in different atmospheres (air, vacuum, argon, hydrogen).

surface area (TiND do not exhibit as large developed surface area as nanotubes), this increase is not prominent.

The electrochemical characterization of materials exposed to the solar radiation provides results, where much more features of materials should be considered and photoactivity is not only determined by its light absorption. Considering visible light range (Fig. 7 a), the photocurrent recorded for AuCu/TiND annealed under hydrogen atmosphere (H-AuCu/TiND) is outstanding. When the sample was irradiated with light >420 nm, the current density at +0.3 V vs. Ag/AgCl/0.1 M KCl was equal to 16 μA/cm^2. It is ca. 27 times higher than photocurrent density for the bare TiND sample thermally treated in hydrogen (Fig. 7 b). In the case of photocurrent recorded under UV–vis illumination the highest photoactivity was obtained for both bare and AuCu decorated dimpled surface annealed in air atmosphere (Fig. 7 c,d) reaching 140 and 76 μA/cm^2, respectively. In order to carry on insightful analysis of the observed photoactivity, detailed structural studies were carried out with the support of the synchrotron radiation.

3.5. Chemical nature of samples

Structural investigation of the samples prepared in various atmospheres was performed by soft X-ray absorption spectroscopy (XAS). Oxidation state of elements, their local environment, valence and conduction bands nature are given in Fig. 8, providing analysis and understanding of the NEXAFS Au N-edges, Cu L-edges, Ti L-edges and O K-edge spectra.

Fig. 8 a presents Au N-edges measured in TEY and TFY modes. The spectra recorded in TEY mode confirmed the presence of gold in the upper surface layer, i.e. in the depth of 2–3 nm, in all AuCu/TiND electrodes. These results are in accordance with XRD measurements where gold was visible for all AuCu/TiND materials (Fig. 4). However, using bulk sensitive measurement mode (TFY) gold can be observed only for air- and hydrogen-annealed AuCu/TiND samples. Furthermore, in Cu L-edges spectra, shown in Fig. 8 b, for A-AuCu/TiND electrode copper was detected in the form of CuO on the surface (TEY mode) and Cu_2O or metallic Cu in bulk (TFY mode). In the case of H-AuCu/TiND sample on the surface Cu_2O or metallic Cu was found. For the other types of the samples any XAS signals at the Cu L-edges range neither in the surface nor in the bulk were distinguished.

In the case of titanium(IV) oxide, the conduction band (probed by the XAS experiment) is formed by Ti3d, 4s, 4p and O2p orbitals. Octahedral symmetry of surrounding oxygen atoms induces the crystal field interaction to split Ti3d orbitals into two sub-bands, namely t_{2g} and e_g. Due to the specific orientation of Ti3d orbitals toward 2p orbitals of surrounding oxygen atoms the relative intensity of the proper e_g and t_{2g} transition lines (viewed in both O K-edge and Ti L-edges spectra) is highly sensitive to the local structure and coordination. Thus, in Fig. 8c, a comparison of O K-edge spectra of all studied samples is shown. The spectra are characterized by two relatively sharp features in the pre-edge region, i.e., lines at 530.5 eV and 533.3 eV (labelled as t_{2g} and e_g, respectively), related to the electron transition from O1s to the hybridized orbitals of the O2p and Ti3d states sensitive to the short-range order (as mentioned above) and three features at higher energy range, i.e., lines at 539.4 eV, 542.4 eV and 545 eV, attributed to the transition from O1s state to O2p state with partial contribution of Ti4s and 4p states, sensitive to the long-range order. All the spectra compared in Fig. 8c are very similar, indicating that the electronic structures of all samples are alike. Detailed analysis of the line presence, position and lines relative intensity between t_{2g} and e_g features leads to the conclusion that on the surface of all electrodes titanium(IV) oxide exists in a form of rutile TiO_2 [48,49]. Moreover, small but still visible difference in a peak broadening between samples prepared in various atmospheres can be noted. The

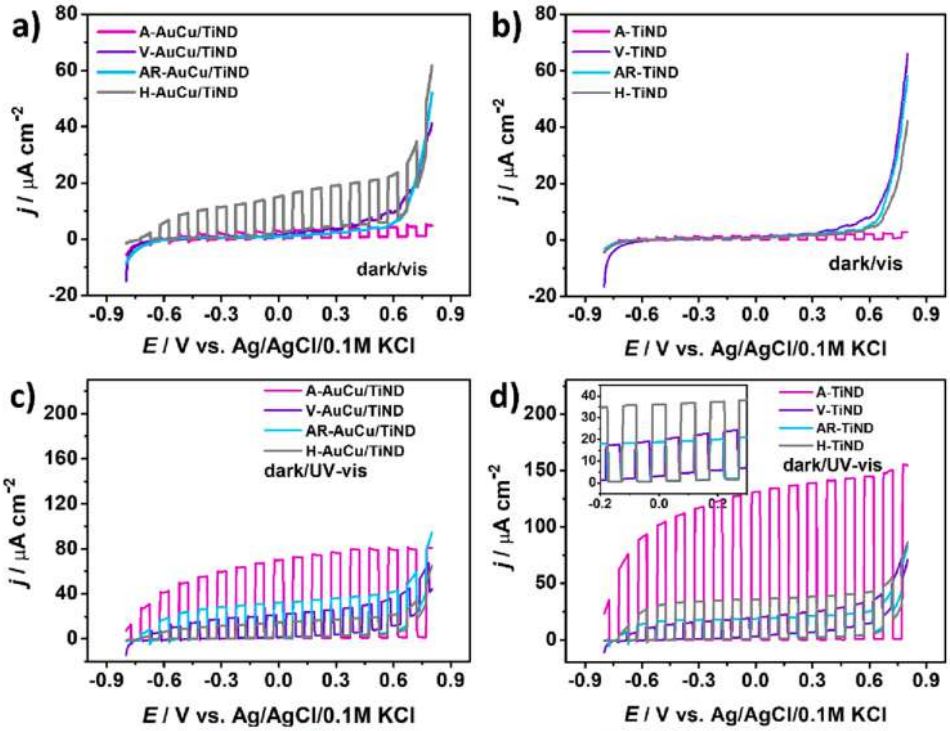

Fig. 7. Linear voltammetry curves for pure (TiND) and AuCu-decorated titanium nanodimples (AuCu/TiND) annealed in various atmospheres (air, vacuum, argon, hydrogen) registered in deaerated 0.1 M NaOH (10 mV/s).

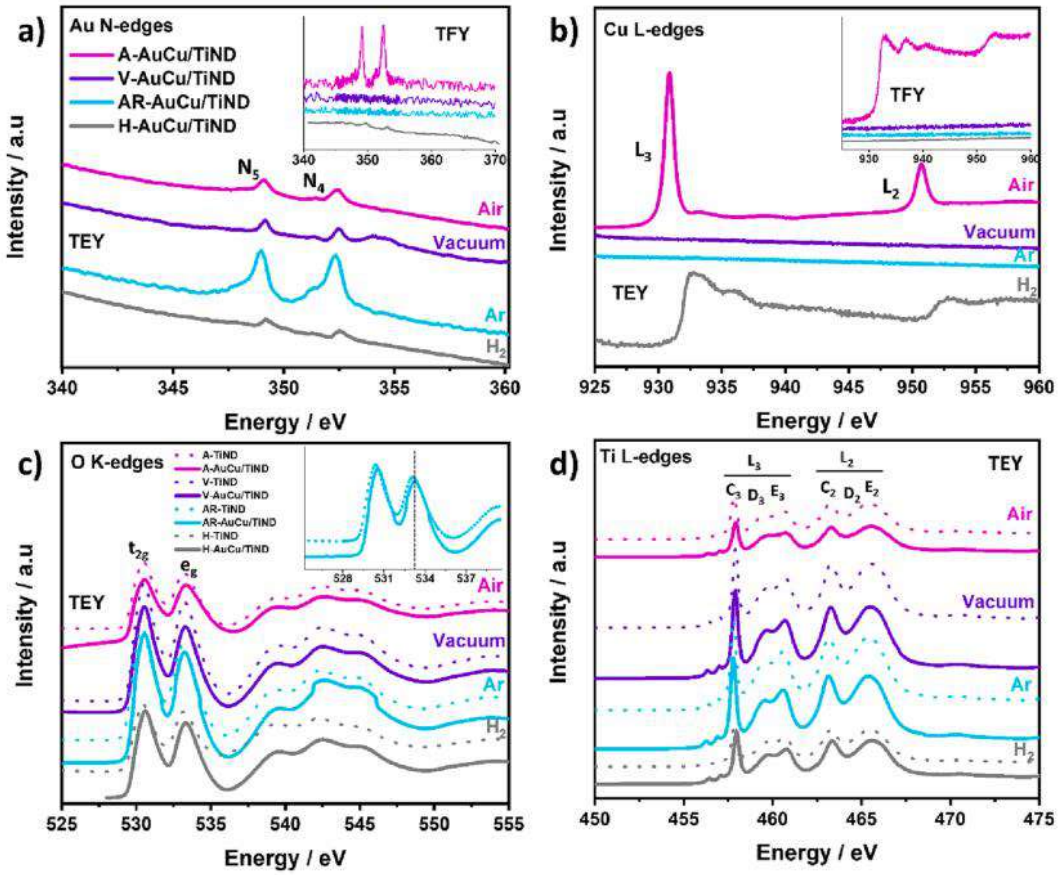

Fig. 8. XAS spectra collected in TEY mode for all studied pure and AuCu-decorated titanium nanodimples (AuCu/TiND): a) Au N-edges, b) Cu L-edges, c) O K-edges, d) Ti L-edges. Insets in panels a) and b) show results of TFY measurements, whereas inset in panel c) shows magnification of pre-edge region for argon annealed electrodes.

broadening effect is related to the local structure ordering, where the higher broadening means the lower ordering in bond length and angle distributions. The bond length, defined as the shortest distance to a neighbouring atom, can be disordered as the average distance from two atoms increases or decreases, resulting in metastable positions. The analogous situation, whereas, with the change of angle between two atoms, takes place for angle distribution. For AuCu electrode modified in both argon and hydrogen atmospheres, the local structural order increases compared to pure TiND electrodes obtained in these atmospheres. At the same time the photoactivity of these materials increases in UV–Vis and Vis, respectively. Additionally, a slight shift of t_{2g} and e_g features position can be noted in the case of electrodes annealed in argon atmosphere. The shift in the range of 0.2–0.3 eV towards higher energy was noted for AuCu modified sample. This can be attributed to slightly larger band gap than in pure TiND. Such phenomena might be responsible for higher photoelectrochemical activity of AR-AuCu/TiND electrode than AR-TiND sample in UV–vis light illumination.

In Fig. 8 d Ti L-edges spectra collected in TEY mode are presented. Six absorption lines can be distinguished in the spectra (marked C_3, D_3, E_3, C_2, D_2 and E_2 in the figure) which are the result of the spin–orbit splitting mentioned above ($2p_{3/2}$ and $2p_{1/2}$ orbitals, L_3 and L_2-edge region, respectively), crystal field splitting into e_g and t_{2g} orbital and additional e_g states splitting due to distorted octahedral symmetry. Detailed inspection and analysis of all these spectra features clearly confirm the formation of TiO_2 rutile phase on the electrodes surface [48,49]. Furthermore, the visible splitting phenomenom of e_g state in L_3-edge region indicates that titanium octahedral environment is distorted. Energy separation between both e_g components (D_3 and E_3 lines) can be interpreted in terms of distortion from ideal O_h symmetry [48,49]. In the case of pure rutile this splitting is equal to 1.2 eV [46], however for studied samples it reaches 0.9–1 eV. This indicates that Ti atoms in TiND and AuCu/TiND are slightly more ordered than in bulk pure TiO_2 rutile.

Fig. 9 shows the XPS spectra for AuCu/TiND samples prepared in various atmospheres by collecting photoelectrons with a kinetic energy of 320–370 eV, which gives depth sensitivity to 7 nm under the surface layer. It is widely known that line related to 4f electrons of metallic gold have a binding energy equals to 84 eV. However, when the gold forms alloys with copper this binding energy shifts towards higher value with the copper content increment. Thus, according to Fig. 8 a it can be noted that metallic gold or Au_xCu_y alloy with dominant content of gold is present in A-AuCu/TiND electrode. On the other hand, for H-AuCu/TiND sample Au4f lines shift towards more positive energy values indicating a higher Cu content in investigated nanoalloy. However, in both cases AuCu phase can be considered as a gold-rich phase. Due to the fact, that the XPS signal comes from the deeper surface layer (ca. 7 nm) in contrast to XAS measurements (ca. 2–3 nm) the Au component is not detected for V-AuCu/TiND and AR-AuCu/TiND electrodes. Regarding Cu2p spectra for A-AuCu/TiND and H-AuCu/TiND electrodes, Cu_2O as well as metallic Cu signals, located at 932.6 eV and 932 eV, respectively, were registered. Additionally, in A-AuCu/TiND electrode small

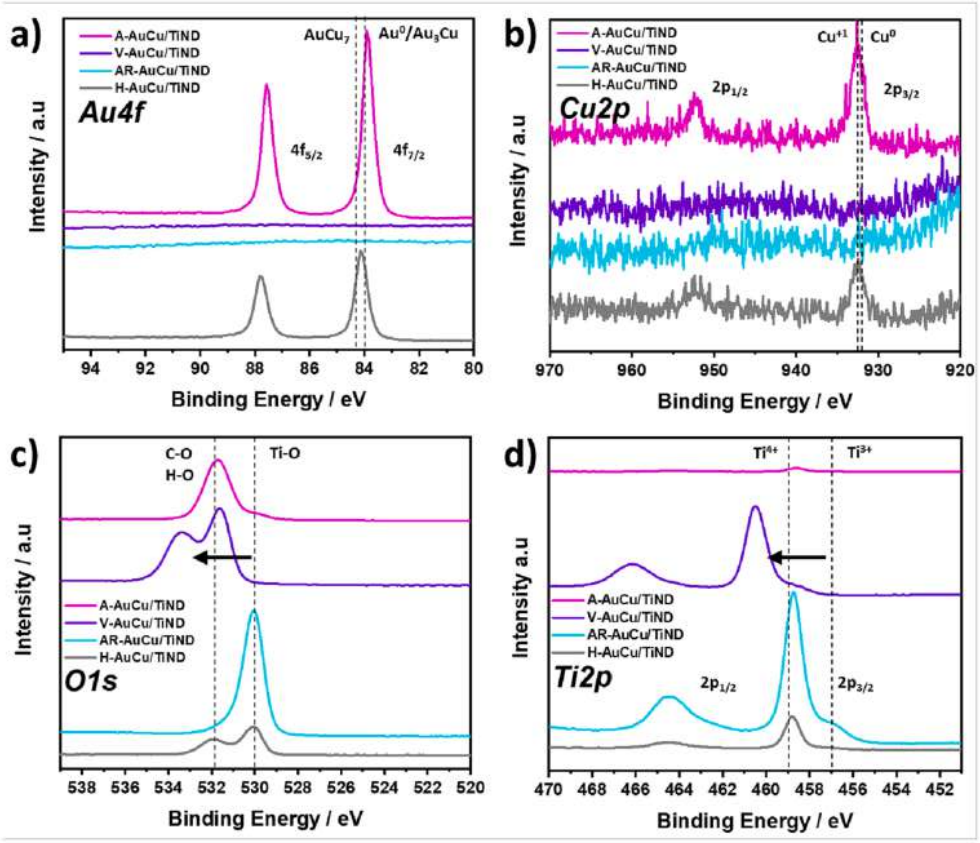

Fig. 9. XPS spectra of AuCu-decorated dimpled platforms (AuCu/TiND) prepared in various atmospheres for a) Au4f, b) Cu2p, c) O1s, d) Ti2p, obtained by collecting photoelectrons with 320–370 eV of kinetic energy (studied sample depth – 7 nm).

contribution of CuO phase is still visible at this depth. Combining XAS observation (see Fig. 8b) and quantitative XPS spectra analysis, it can be suggested that for air annealed AuCu material in its upper surface layer only CuO phase exists. Going deeper into the surface layer, the content drops to about 20 %, with Cu^{+1}/Cu_{tot} ratio reaching about 70 %, while only Cu_2O and metallic Cu are present in the bulk. In the case of H-AuCu/TiND samples, Cu_2O and metallic Cu phases are present in the upper and deeper surface layers, but not in a bulk (see Fig. 7b, TFY XAS measurement). In the O1s spectrum lines located at 532 eV and 530 eV confirmed the presence of O—H and O—Ti interactions, respectively (Fig. 9 c). In the case of titanium, two Ti2p chemical states were distinguished (Fig. 9 d). The line located at 458.8 eV confirmed the presence of TiO_2, whereas line located at 457 eV indicates Ti_2O_3 oxide. For the V-AuCu/TiND electrode both bands related to O1s and Ti2p photoelectrons are shifted toward higher values which proves the presence of oxygen vacancies [46].

Due to the fact that AuCu hydrogenated electrode showed the best photoelectrochemical activity (see Fig. 7 a) the detailed depth-profile XPS data analysis was performed for this sample and obtained results are shown (Fig. 10) and discussed in details below. The depth profiles of A-AuCu/TiND, V-AuCu/TiND and AR-AuCu/TiND samples for Ti2p spectra are also presented in Fig. S3.

The inspection and quantitative analysis of Au4f and Cu2p lines for H-AuCu/TiND sample indicate that two Au-based components, such as metallic gold and gold-rich AuCu alloy can be distinguished in AuCu phase. Moreover, it can be assumed that this phase has layered structure. In the topmost layer (up to about 5–7 nm, top two spectra in Fig. 10 a) AuCu gold-rich alloy dominates among Au-based components. This conclusion is supported by the shift of Au4f line towards higher binding energy value. On the other hand, metallic Au is dominant in the bulk part, which is confirmed by XAS measurements (see Fig. 8 a and b, TEY and TFY results). Moreover, additional phenomena that arise as a red shift of photoelectron lines in Au4f spectra in bulk part (collected for higher beam energy) can be explained as an effect of hydrogen treatment and interaction between gold and supporting titanium dioxide [50]. Summing up, it is possible to observe two competitive processes responsible for Au4f spectrum structure such as blue shift caused by AuCu presence in the sample and the red shift caused by interaction between gold and hydrogen atmosphere and/or TiO_2. As it was mentioned previously, the Cu2p spectra decomposition indicates that up to about 5–7 nm metallic Cu and Cu^{+1} are still present in the sample. Furthermore, the Cu^{+1}/Cu_{tot} ratio reaches 70 ± 5 % at the surface and drops to about 40 % at a depth of about 7 nm.

Deconvolution of Ti2p region shows presence of TiO_2 and Ti_2O_3 located at 458.8 eV and 457 eV, respectively (Fig. 10 d). However, that components are not the only ones that could describe properly the spectra structure like high energy tail of $2p_{3/2}$ line and broaden $2p_{1/2}$ line. In order to obtain good fit, the interaction between titanium oxides with gold (TiO_x/Au) should be taken into account as well as the influence of hydrogen atmosphere (Ti-OH). Furthermore, the O1s lines located at 532 eV and 530 eV describe O–H and O-Ti interactions, respectively (Fig. 10 c). Thus, these spectra confirm various titanium oxides presence in the sample and decreased influence of hydrogen on the deeper material layers, up to 15 nm depth (limit of XPS depth

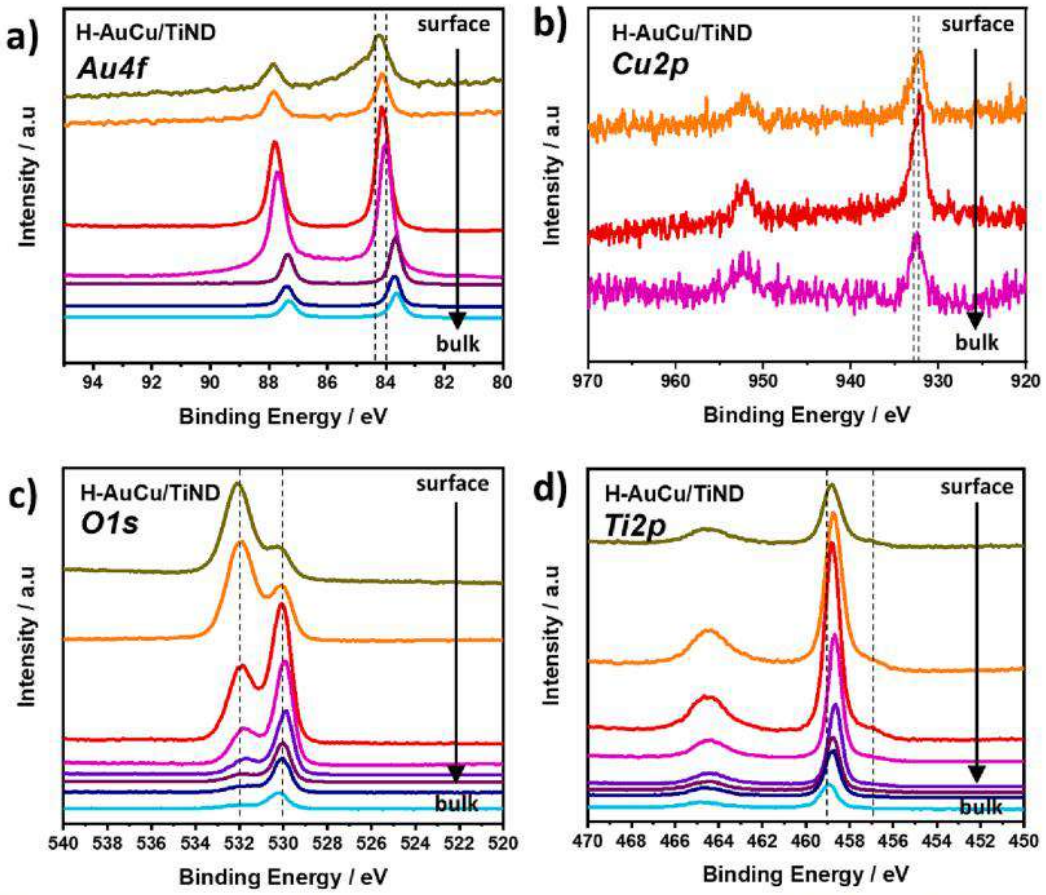

Fig. 10. XPS spectra presenting depth-profile of AuCu-decorated titanium nanodimples annealed in hydrogen (H-AuCu/TiND) for a) Au4f, b) Cu2p, c) O1s, d) Ti2p (spectra shown from top to bottom correspond to increasingly higher X-ray beam energy).

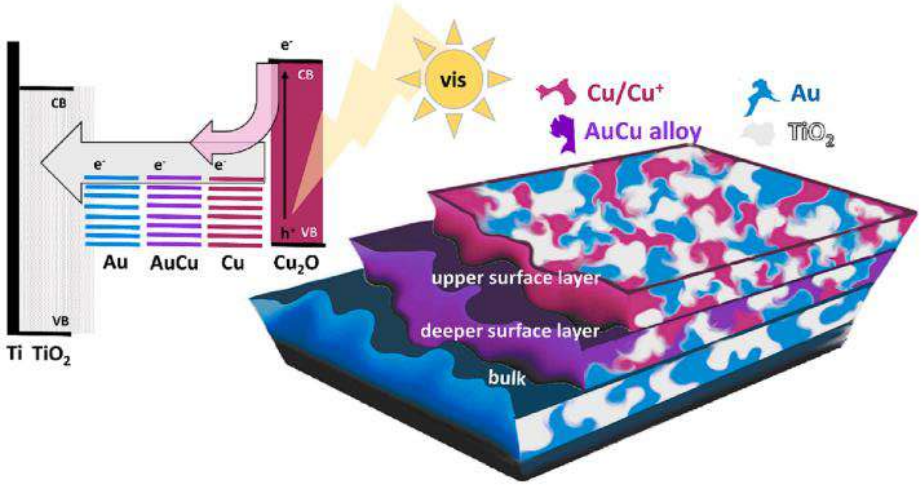

Fig. 11. Schematic energy band diagram and the visualisation of cross-section for AuCu-decorated Ti nanodimples annealed in hydrogen atmosphere.

profiling used in this work).

According to Fig. 7a the best photoelectrochemical activity for H-AuCu/TiND electrode under visible light mostly can be correlated with the presence of Cu_2O in the upper surface layer (Fig. 8b). Furthermore, presence of gold in upper, deeper surface layers and in the bulk also can lead to increase of photocurrent response. According to literature [51] localized surface plasmon resonance of Au can facilitate charge carrier generation for Cu_2O on the Au/Cu_2O nanostructures. Furthermore, the tunnelling of electrons through the Schottky barrier in Au/TiO_2 interface affects the photoactivity [52]. It should be noted that the injection of tunnelling electrons is strongly influenced by Au dimensions where 3–4 nm NPs show the highest activity as well as the number of Ti^{4+} atoms located at the Au/TiO_2 interface. Regarding the morphology, there were no distinct particles on the H-AuCu/TiND electrode surface, however, synchrotron radiation studies confirmed the presence of gold on the electrode surface. It might happen that due to the very small size of Au nanoparticles they are hard to be distinguished during SEM inspection. However, according to Fig. 10a the red shift of photoelectron lines in Au4f curve indicates the interaction between gold and titanium dioxide which was not recorded for other materials. This can be one of the manifestations how they can take part in tunnelling process.

For better understanding of this material the schematic energy band diagram and the visualisation of cross-section for AuCu-decorated Ti nanodimples annealed in hydrogen atmosphere are presented in Fig. 11. When the H-AuCu/TiND electrode is illuminated by visible light the electrons from valence band of Cu_2O are excited to the conduction one. The photo-generated electrons from Cu_2O are transferred to Cu, AuCu and Cu materials. Firstly, it should be noted that, metallic nanoparticles have discrete valence band states in contrast to bulk metals and because of that Au, AuCu and Cu nanoparticles are also responsible for electron-hole pair generation. Secondly, noble metal nanoparticles exhibit surface plasmon resonance and in consequence generation of hot electrons explained by Landau damping phenomena or plasmon induced resonant energy transfer occurs [53]. Thirdly, small Au nanoparticles can take part in tunneling process through titanium dioxide. In the end, all photo-generated electrons are transferred to TiO_2 and finally Ti platform acting here as current collector [54].

In the case of UV–vis illumination, the bimetallic AuCu electrode annealed under argon atmosphere obtained higher photocurrent than TiND sample thermally treated in the same conditions (Fig. 7 c,d). The photocurrent for the AR-AuCu/TiND sample reaches 34 $\mu A/cm^2$, whereas for the AR-TiND is equal to 18 $\mu A/cm^2$. According to our previous article [50] TiO_2 NTs modified by AuCu nanoparticles annealed in argon atmosphere exhibits higher photocurrent under UV–vis illumination than pure TiO_2NTs annealed in the same atmosphere which was explained as the influence of increment of donor density in AuCu modified sample. The higher photocurrent of the H-AuCu/TiND and the Ar-AuCu/TiND electrodes than for the TiND, under vis and UV–vis illumination, can be associated with the increase in the local structural order of AuCu modified samples (Fig. 8 c) due to the positive effect of the nanostructural order on electron transport in crystalline lattice [55]. However, the highest photocurrent tracked under UV–vis light among all electrodes, including both bare and AuCu decorated Ti nanodimples, was obtained for samples annealed in air. According to XRD measurements, the most intense TiO_2 peaks, providing information about the degree of material's crystallinity, were obtained for materials annealed in air atmosphere. Furthermore, for the A-AuCu/TiND electrode the presence of gold in upper, deeper surface layer and in bulk, as well as CuO, Cu_2O and Cu can influence photocurrent values. Analysing those data we should therefore distinguish two light conditions and take into account the shape of the reflectance spectra. Hydrogenated AuCu/TiND exhibits the lowest reflectance at ca. 750 nm that supports its outstanding performance, while TiND treated in air exhibits the lowest value of reflectance in UV range. Taking into account the results presented in this work it was explained that annealing atmosphere used during fabrication of bimetallic AuCu nanostructures strongly affects their chemical composition and photoelectrochemical activity.

4. Conclusion

In this work we presented the influence of various atmospheres such as air, vacuum, argon and hydrogen during rapid thermal annealing (40 °C/s) on morphology, chemical composition as well as photoelectrochemical activity of AuCu modified nanostructured Ti platforms. The highest photocurrent density under visible light illumination was obtained for AuCu hydrogenated material (16 $\mu A/cm^2$) which is 27 times higher than for nanostructured Ti platform covered by thin TiO_2 passivation layer. The reflectance minimum for the H-AuCu/TiND sample was located at 750 nm. However, AuCu/TiND and TiND electrodes thermally treated in air atmosphere showed the highest photocurrent under UV–vis illumination, reaching 76 and 140 $\mu A/cm^2$, respectively. It should be noted, that reflectance minimum for the A-AuCu/TiND sample was located at 370 nm supporting the photoelectrochemical activity under UV–vis light. Synchrotron radiation studies allow to distinguish three components' layers, such as upper (2–3 nm) and deeper (5–7 nm) surface layers as well as bulk (12–15 nm). These areas are located at different depths from which the signal was collected. For the AuCu-decorated Ti nanodimples annealed in hydrogen atmosphere, gold in different arrangement was detected in upper and deeper surface layers as well as in the bulk. In the deeper surface layer the Au_xCu_y nanoalloy was present. Furthermore, Cu_2O or Cu were found in upper and deeper layers. However, the copper/copper oxide was not detected in the bulk. In the case of the AuCu/TiND electrode thermally treated in air atmosphere gold also was present in upper and deeper surface layers as well as in bulk. Regarding copper, CuO was distinguished in the surface layers, whereas Cu_2O or Cu in bulk. Summing up, studies of materials with techniques based on the synchrotron radiation provided a massive amount of information about material composition at the nanoscale that was valuable in interpretation of behaviour of material exposed to light.

CRediT authorship contribution statement

Wiktoria Lipińska: Investigation, Validation, Visualization, Conceptualization, Writing – original draft, Writing – review & editing, Visualization, Funding acquisition. **Zuzanna Bielan:** Investigation, Writing – original draft. **Agnieszka Witkowska:** Investigation, Conceptualization, Writing – original draft. **Jakub Karczewski:** Investigation, Validation, Writing – review & editing. **Katarzyna Grochowska:** Writing – original draft, Writing – review & editing. **Ewa Partyka-Jankowska:** Methodology, Writing – review & editing. **Tomasz Sobol:** Methodology, Writing – review & editing. **Magdalena Szczepanik:** Methodology, Writing – review & editing. **Katarzyna Siuzdak:** Conceptualization, Visualization, Writing – original draft, Writing – review & editing, Supervision, Funding acquisition.

Declaration of Competing Interest

The authors declare that they have no known competing financial interests or personal relationships that could have appeared to influence the work reported in this paper.

Data availability

Data will be made available on request.

Acknowledgments

Research is financed by National Science Centre (Poland): Grant No. 2019/35/N/ST5/02604.

This publication was developed under the provision of the Polish Ministry of Education and Science project: "*Support for research and*

development with the use of research infrastructure of the National Synchrotron Radiation Centre SOLARIS" under contract nr 1/SOL/2021/2.

We acknowledge SOLARIS Centre for the access to the PHELIX Beamline where the measurements were performed.

Appendix A. Supplementary material

Supplementary data to this article can be found online at https://doi.org/10.1016/j.apsusc.2023.158048.

References

[1] M. Haruta, Size- and support-dependency in the catalysis of gold, Catal. Today 36 (1997) 153–166, https://doi.org/10.1016/S0920-5861(96)00208-8.
[2] M. Takakuwa, K. Fukuda, T. Yokota, D. Inoue, D. Hashizume, S. Umezu, T. Someya, Direct gold bonding for flexible integrated electronics, Sci. Adv. 7 (2021), eabl6228, https://doi.org/10.1126/sciadv.abl6228.
[3] W. Lipińska, K. Siuzdak, J. Ryl, P. Barski, G. Śliwiński, K. Grochowska, The optimization of enzyme immobilization at Au-Ti nanotextured platform and its impact onto the response towards glucose in neutral media, Mater. Res. Express 6 (2019), 1150e3, https://doi.org/10.1088/2053-1591/ab4fab.
[4] A. Casini, S.R. Thomas, The beauty of gold: knowledge of mechanisms leads to different applications of organogold compounds in medicine and catalysis, Chem. Lett. 50 (2021) 1516–1522, https://doi.org/10.1246/cl.210238.
[5] T.R. Mogan, A. Lehoux, M. Takashima, E. Kowalska, B. Ohtani, Slow photon-induced enhancement of photocatalytic activity of gold nanoparticle-incorporated titania inverse opal, Chem. Lett. (2021), https://doi.org/10.1246/cl.200804.
[6] E. Kowalska, R. Abe, B. Ohtani, Visible light-induced photocatalytic reaction of gold-modified titanium(IV) oxide particles: action spectrum analysis, Chem. Commun. 2 (2009) 241–243, https://doi.org/10.1039/b815679d.
[7] A. Zielińska-Jurek, E. Kowalska, J.W. Sobczak, W. Lisowski, B. Ohtani, A. Zaleska, Preparation and characterization of monometallic (Au) and bimetallic (Ag/Au) modified-titania photocatalysts activated by visible light, Appl. Catal. B: Environ. 101 (2011) 504–514, https://doi.org/10.1016/j.apcatb.2010.10.022.
[8] H. Wang, H. Hao, Y. Li, Size-dependent electrochemistry and electrocatalysis at single Au@Pt bimetallic nanoparticles, J. Phys. Chem. C 124 (2020) 24740–24746, https://doi.org/10.1021/acs.jpcc.0c06520.
[9] S. Yeon, S.J. Lee, D. Chinnadurai, Y. Yu, Y.W. Lee, M.Y. Choi, Rapid alloying of Au–Pd nanospheres by a facile pulsed laser technique: insights into a molar-dependent electrocatalytic methanol oxidation reaction, J. Alloy. Compd. 891 (2021), 162011, https://doi.org/10.1016/j.jallcom.2021.162011.
[10] N. Todoroki, H. Tei, T. Miyakawa, H. Tsurumaki, T. Wadayama, Electrochemical CO2 reduction on bimetallic surface alloys: enhanced selectivity to CO for Co/Au (110) and to H2 for Sn/Au(110), ChemElectroChem 6 (2019) 3101–3107, https://doi.org/10.1002/celc.201900725.
[11] M.A. Bratescu, O. Takai, N. Saito, One-step synthesis of gold bimetallic nanoparticles with various metal-compositions, J. Alloy. Compd. 562 (2013) 74–83, https://doi.org/10.1016/j.jallcom.2013.02.033.
[12] K. Radinović, J. Milikić, A. Balčiūnaitė, Z. Sukackienė, M. Bošković, Tamašauskaitė-Tamašiūnaitė, Š. Biljana, Low Au-content CoAu electrodes for environmental applications, RSC Adv. 12 (2022), 26134, https://doi.org/10.1039/d2ra04828k.
[13] A. Gołąbiewska, W. Lisowski, M. Jarek, G. Nowaczyk, A. Zielińska-Jurek, A. Zaleska, Visible light photoactivity of TiO_2 loaded with monometallic (Au or Pt) and bimetallic (Au/Pt) nanoparticles, Appl. Surf. Sci. 317 (2014) 1131–1142, https://doi.org/10.1016/j.apsusc.2014.09.039.
[14] A. Cybula, J.B. Priebe, M.-M. Pohl, J.W. Sobczak, M. Schneider, A. Zielińska-Jurek, A. Brückner, A. Zaleska, The effect of calcination temperature on structure and photocatalytic properties of Au/Pd nanoparticles supported on TiO_2, Appl. Catal. B: Environ. 152–153 (2014) 202–211, https://doi.org/10.1016/j.apcatb.2014.01.042.
[15] M. Nazemi, S.R. Panikkanvalappil, C.-K. Liao, M.A. Mahmoud, M.A. El-Sayed, Role of femtosecond pulsed laser-induced atomic redistribution in bimetallic Au-Pd nanorods on optoelectronic and catalytic properties, ACS Nano 15 (2021) 10241–10252, https://doi.org/10.1021/acsnano.1c02347.
[16] R.S. Moakhar, M. Jalali, A. Kushwaha, G.K.L. Goh, N. Riahi-Noori, A. Dolati, M. Ghorbani, AuPd bimetallic nanoparticle decorated TiO_2 rutile nanorod arrays for enhanced photoelectrochemical water splitting, J. Appl. Electrochem. 48 (2018) 995–1007, https://doi.org/10.1007/s10800-018-1231-1.
[17] S. Manchala, L.R. Nagappagari, S.M. Venkatakrishnan, V. Shanker, Solar-light harvesting bimetallic Ag/Au decorated graphene plasmonic system with efficient photoelectrochemical performance for the enhanced water reduction process, ACS Appl. Nano Mater. 2 (2019) 4782, https://doi.org/10.1021/acsanm.9b00684.
[18] R.S. Hider, S. Wang, Y. Gao, A.S. Malik, N. Ta, H. Li, B. Zheng, M. Dupuis, F. Fan, C. Li, Boosting photocatalytic water oxidation by surface plasmon resonance of Ag_xAu_{1-x} alloy nanoparticles, Nano Energy 87 (2021), 106189, https://doi.org/10.1016/j.nanoen.2021.106189.
[19] D. Manikandan, S. Mohan, K.G.M. Nair, Synthesize of embedded gold and AgAu & CuAu alloynanoclusters in soda-lime glass by ion-exchange - a novel route, J. Solid State Sci. Technol. Lett. 12 (2005) 353–359.
[20] H. Mistry, R. Reske, P. Strasser, B. Roldan Cuenya, Size-dependent reactivity of gold-copper bimetallic nanoparticles during CO_2 electroreduction, Catal. Today 288 (2017) 30–36, https://doi.org/10.1016/j.cattod.2016.09.017.
[21] W. Lipińska, K. Grochowska, J. Karczewski, E. Coy, K. Siuzdak, et al., Electrocatalytic oxidation of methanol, ethylene glycol and glycerine in alkaline media on TiO_2 nanotubes decorated with AuCu nanoparticles for an application in fuel cells, J. Mater. Sci. 57 (2022) 13345–13361, https://doi.org/10.1007/s10853-022-07471-7.
[22] R. Biswas, S. Singh, I. Ahmed, R.A. Patil, Y.-R. Ma, K.K. Haldar, Rational design of bimetallic Au/Cu nanostructure: an efficient catalyst for methanol oxidation, ChemNanoMat 7 (2021) 158–164, https://doi.org/10.1002/cnma.202000578.
[23] X. Liang, W. Li, H. Han, Z. Ma, Non-enzymatic electrochemical sensor based on Cu_2O/AuCu/Cu composite for hydrogen peroxide detection, J. Electroanal. Chem. 834 (2019) 43–48, https://doi.org/10.1016/j.jelechem.2018.12.045.
[24] D. Zeng, L. Yang, P. Zhou, D. Hu, Y. Xie, S. Li, L. Jiang, Y. Ling, J. Zhao, Au–Cu alloys deposited on titanium dioxide nanosheets for efficient photocatalytic hydrogen evolution, Int. J. Hydrogen Energy 43 (2018) 15155–15163, https://doi.org/10.1016/j.ijhydene.2018.06.078.
[25] J. Sha, S. Paul, F. Dumeignil, R. Wojcieszak, Au-based bimetallic catalysts: How the synergy between two metals affects their catalytic activity, RSC Adv. 9 (2019), 29888, https://doi.org/10.1039/c9ra06001d.
[26] S. Suzuki, Y. Tomita, S. Kuwabata, T. Torimoto, Synthesis of alloy AuCu nanoparticles with the L10 structure in an ionic liquid using sputter deposition, Dalt. Trans. 44 (2015) 4186–4194, https://doi.org/10.1039/c4dt03557g.
[27] M. Sakamoto, T. Tachikawa, M. Fujitsuka, T. Majima, Photochemical formation of Au/Cu bimetallic nanoparticles with different shapes and sizes in a poly(vinyl alcohol) film, Adv. Funct. Mater. 17 (2007) 857–862, https://doi.org/10.1002/adfm.200600700.
[28] X. Liu, A. Wang, L. Li, T. Zhang, C.-Y. Mou, J.-F. Lee, Structural changes of Au-Cu bimetallic catalysts in CO oxidation: in situ XRD, EPR, XANES, and FT-IR characterizations, J. Catal. 278 (2011) 288–296, https://doi.org/10.1016/j.jcat.2010.12.016.
[29] W. Lipińska, K. Grochowska, J. Karczewski, J. Ryl, A. Cenian, K. Siuzdak, Thermally tuneable optical and electrochemical properties of Au-Cu nanomosaic formed over the host titanium dimples, Chem. Eng. J. 399 (2020), 125673, https://doi.org/10.1016/j.cej.2020.125673.
[30] W. Lipińska, K. Grochowska, J. Karczewski, J. Ryl, K. Siuzdak, Temperature-controlled nanomosaics of AuCu bimetallic structure towards smart light management, J. Mater. Sci. Mater. Electron. 33 (2022) 19385–19404, https://doi.org/10.1007/s10854-022-08775-9.
[31] M. Szczepanik-Ciba, T. Sobol, J. Szade, PHELIX – a new soft X-ray spectroscopy beamline at SOLARIS synchrotron, Nucl. Instrum. Methods Phys. Res., Sect. B 492 (2021) 49–55, https://doi.org/10.1016/j.nimb.2021.01.021.
[32] E. Kowalska, S. Juodkazis, P. Henkiel, D. Kowalski, Site-selective Au+ electroreduction in titania nanotubes for electrochemical and plasmonic applications, ACS Appl. Nano Mater. 5 (2022) 7696–7703, https://doi.org/10.1021/acsanm.2c00044.
[33] G. Wang, L. Xiao, B. Huang, Z. Ren, X. Tang, L. Zhuang, J. Lu, AuCu intermetallic nanoparticles: surfactant-free synthesis and novel electrochemistry, J. Mater. Chem. 22 (2012) 15769–15774, https://doi.org/10.1039/c2jm32264a.
[34] M. M. A. Sinthiya, N. Kumeresan, K. Ramamurthi, K. Sethuraman, Development of pure rutile TiO_2 and Magneli titanium sub-oxide microstructures over titanium oxide-seeded glass substrates using surfactant-free hydrothermal process, doi: 10.1007/s12034-019-1791-7.
[35] B. Bulut, S. Duman, Effects of calcination temperature on hydrothermal synthesized titanium dioxide submicron powders, 9 (2021) 676, doi: 10.36306/konjes.915062.
[36] Y. Li, Y. Yang, X. Shu, D. Wan, N. Wei, X. Yu, M.B.H. Breese, T. Venkatesan, J. M. Xue, Y. Liu, S. Li, T. Wu, J. Chen, From titanium sesquioxide to titanium dioxide: oxidation-induced structural, phase, and property evolution, Chem. Mater. 30 (2018) 4383–4392, https://doi.org/10.1021/acs.chemmater.8b01739.
[37] R. Sasikumar, P. Ranganathan, S.-M. Chen, P. Sireesha, T.-W. Chen, P. Veerakumar, S.-P. Rwei, T. Kavitha, Economically applicable Ti_2O_3 decorated m-aminophenol-formaldehyde resin microspheres for dye-sensitized solar cells (DSSCs), J. Colloid Interface Sci. 494 (2017) 82–91, https://doi.org/10.1016/j.jcis.2017.01.061.
[38] A. Kosinova, O. Kovalenko, L. Klinger, E. Rabkin, Mechanisms of solid-state dewetting of thin Au films in different annealing atmospheres, Acta Mater. 83 (2015) 91–101, https://doi.org/10.1016/j.actamat.2014.09.049.
[39] F. Leroy, Ł. Borowik, F. Cheynis, Y. Almadori, S. Curiotto, M. Trautmann, P. Müller, How to control solid state dewetting: a short review, Surf. Sci. Rep. 71 (2016) 391–409, https://doi.org/10.1016/j.surfrep.2016.03.002.
[40] O. Boeva, A. Antonov, K. Zhavoronkova, Influence of the nature of IB group metals on catalytic activity in reactions of homomolecular hydrogen exchange on Cu, Ag, Au nanoparticles, Catal. Commun. 148 (2021), 106173, https://doi.org/10.1016/j.catcom.2020.106173.
[41] M. Bechelany, X. Maeder, J. Riesterer, J. Hankache, D. Lerose, S. Christiansen, L. Philippe, Synthesis mechanisms of organized gold nanoparticles: influence of annealing temperature and atmosphere, Cryst. Growth Des. 10 (2010) 587–596, https://doi.org/10.1021/cg900981q.
[42] K. Siuzdak, D. Döhler, J. Bachmann, J. Karczewski, K. Grochowska, Light-improved glucose sensing on ordered Au-Ti heterostructure, Optik (2020), 164166, https://doi.org/10.1016/j.ijleo.2019.164166.
[43] S. Petrović, B. Salatić, D. Milovanović, V. Lazović, L. Živković, M. Trtica, B. Jelenković, Agglomeration in core-shell structure of CuAg nanoparticles synthesized by the laser ablation of Cu target in aqueous solutions, J. Opt. 17 (2015) (2015), 025402, https://doi.org/10.1088/2040-8978/17/2/025402.

[44] J. Hu, P. Liu, L. Chen, Comparison of surface plasmon resonance responses to dry/wet air for Ag, Cu, and Au/SiO_2, Appl. Opt. 51 (2012) 1357, https://doi.org/10.1364/ao.51.001357.
[45] Y. Yan, X. Cheng, W. Zhang, G. Chen, H. Li, A. Konkin, P. Schaaf, Plasma hydrogenated TiO_2/nickel foam as an efficient bifunctional electrocatalyst for overall water splitting, ACS Sustain. Chem. Eng. 7 (2018) (2018) 885, https://doi.org/10.1021/acssuschemeng.8b04496.
[46] D.N. Pei, L. Gong, A.Y. Zhang, X. Zhang, J.J. Chen, Y. Mu, H.O. Yu, Defective titanium dioxide single crystals exposed by high-energy 001 facets for efficient oxygen reduction, Nat. Commun. 6 (2015) 8696, https://doi.org/10.1038/ncomms9696.
[47] X. Lu, G. Wang, T. Zhai, M. Yu, J. Gan, Y. Tong, Y. Li, Hydrogenated TiO_2 nanotube arrays for supercapacitors, Nano Lett. 12 (2012) 1690–1696, https://doi.org/10.1021/nl300173j.
[48] V. Prusakova, C. Collini, M. Nardi, R. Tatti, L. Lunelli, L. Vanzetti, L. Lorenzelli, G. Baldi, A. Chiappini, A. Chiasera, D. Ristic, R. Verucchi, M. Bortolotti, S. Dir'e, The development of sol–gel derived TiO2thin films and corresponding memristor architectures, RSC Adv. 7 (2017), 1654, https://doi.org/10.1039/c6ra25618j.
[49] R. Ramanathan, D.E. Weibel, NEXAFS and FTIR-ATR investigation of the static and dynamic superhydrophobicity of functionalized titanium dioxide nanoparticle coatings, J. Braz. Chem. Soc. 6 (2013) 1041–1048, https://doi.org/10.5935/0103-5053.20130134.
[50] J. Radnik, C. Mohr, P. Claus, J. Radnik, C. Mohr, P. Claus, On the origin of binding energy shifts of core levels of supported gold nanoparticles and dependence of pretreatment and material synthesis, Chem. Chem. Phys. 5 (2003) 172, https://doi.org/10.1039/B207290D.
[51] T.H. Lai, C.W. Tsao, M.J. Fang, J.Y. Wu, Y.-P. Chang, Y.H. Chiu, P.-Y. Hsieh, M.-Y. Kuo, K.-D. Chang, Y.-J. Hsu, Au@Cu_2O core–shell and Au@Cu_2Se yolk–shell nanocrystals as promising photocatalysts in photoelectrochemical water splitting and photocatalytic hydrogen production, 14 (2022) 40771, doi: 10.1021/acsami.2c07145.
[52] W. Lipinska, K. Grochowska, J. Ryl, J. Karczewski, K. Siuzdak, Influence of annealing atmospheres on photoelectrochemical activity of TiO_2 nanotubes modified with AuCu nanoparticles, 13 (2021) 52967, doi: 10.1021/acsami.1c16271.
[53] W. Xu, J. Jia, T. Wang, C. Li, B. He, J. Zong, Y. Wang, H.J. Fan, H. Xu, Y. Feng, H. Chen, Continuous tuning of the Au-Cu_2O Janus nanostructures for efficient charge separation, Angew. Chem. 59 (2020), 22246, https://doi.org/10.1039/C6RA25618J.
[54] Y. Shiraishi, N. Yasumoto, J. Imai, H. Sakamoto, S. Tanaka, S. Ichikawa, B. Ohtani, T. Hirai, Quantum tunneling injection of hot electrons in Au/TiO_2 plasmonic photocatalysts, Nanoscale 9 (2017), 8349, https://doi.org/10.1039/C7NR02310C.
[55] P.M. Beaujuge, J.M.J. Fréchet, Molecular design and ordering effects in π-functional materials for transistor and solar cell applications, J. Am. Chem. Soc. 133 (2011) 20009–20029, https://doi.org/10.1021/ja2073643.

Supporting information to the article A4

Insightful studies of AuCu nanostructures deposited on Ti platform: effect of rapid thermal annealing on photoelectrochemical activity supported by synchrotron radiation studies

Wiktoria Lipińska[1], Zuzanna Bielan[1], Agnieszka Witkowska[2], Jakub Karczewski[2,3], Katarzyna Grochowska[1], Ewa Partyka-Jankowska[4], Tomasz Sobol[4], Magdalena Szczepanik[4], Katarzyna Siuzdak[1]

[1]Centre for Plasma and Laser Engineering, Institute of Fluid-Flow Machinery, Polish Academy of Sciences, Fiszera 14 St., 80-231 Gdańsk, Poland

[2]Institute of Nanotechnology and Materials Engineering, Faculty of Applied Physics and Mathematics, Gdańsk University of Technology, Narutowicza 11/12 St., 80-233 Gdańsk, Poland

[3]Advanced Materials Center, Gdańsk University of Technology, Narutowicza 11/12 St., 80-233 Gdańsk, Poland

[4]National Synchrotron Radiation Centre SOLARIS, Jagiellonian University, Czerwone Maki 98 St., 30-392 Kraków, Poland

Address correspondence to email: wlipinska@imp.gda.pl

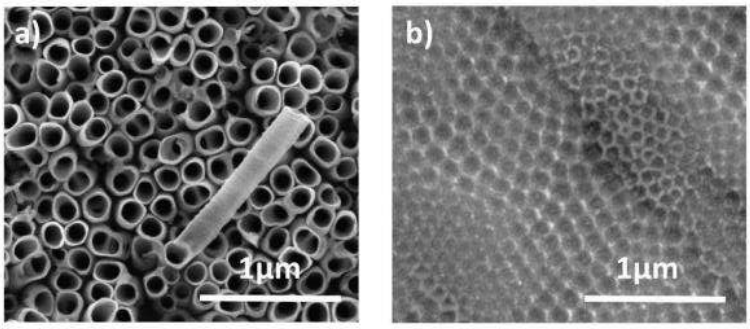

Fig.S1 SEM images of a) TiO_2 nanotubes, b) TiND samples.

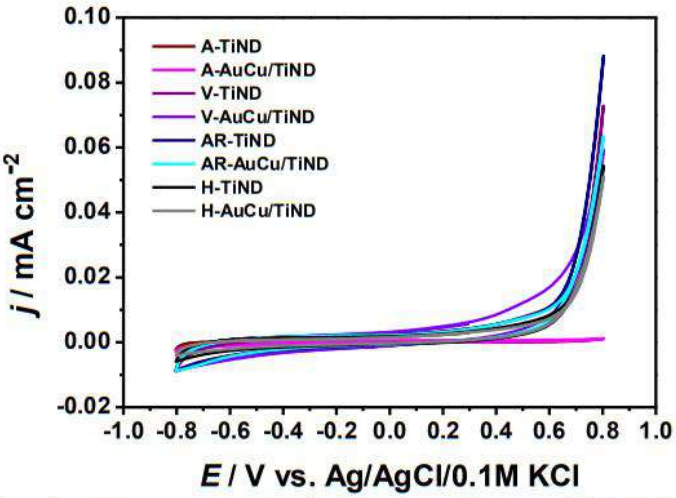

Fig. S2 Cyclic voltammetry curves recorded for electrode materials in 0.1 M NaOH, 50 mV/s.

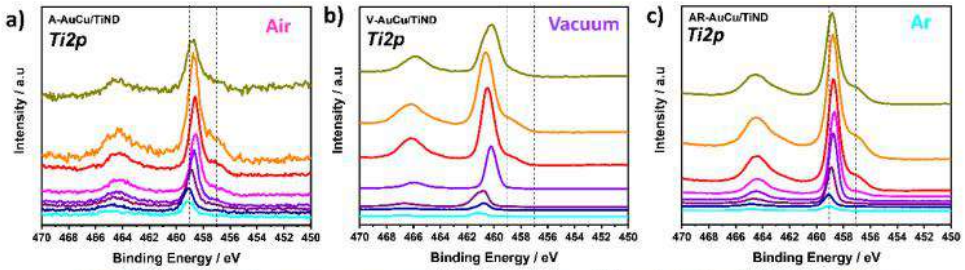

Fig.S3 XPS Ti2p spectra presenting depth-profile of AuCu/TiND samples prepared in various atmospheres: a) air, b) vacuum, c) argon.

7.5 Impact of various atmospheres during rapid thermal treatment of TiO_2 nanotubes modified by AuCu nanoparticles on photoelectrochemical activity

Brief overview of the article A5

Introduction

Efficient electron-hole pair separation is important in material used for solar driven processes because it can significantly improve its photoelectrochemical activity. Material absorbs light and it generates electron-hole pairs which then slowly or quickly recombine. In the case of quick recombination process the energy of absorbed light is lost and material photoactivity is reduced. In order to prevent fast electron-hole recombination TiO_2 can be fabricated in a form of ordered structures as nanotubes or nanowires[221]. The highly ordered structure promotes faster charge transport than porous structure or randomly distributed NPs. Furthermore, when n-type and p-type semiconductors are combined, higher position of the valence and conduction band of p-type than n-type semiconductor favours faster charge transport and decreases recombination processes[222].

Taking above into account photoelectrochemical activity of materials can be characterized based on shape profiles of LV or CA measurements which help choosing electrode characterized by efficient e-h separation. In Figure 58a,b,c three various shape profiles are distinguished. All curves present cut-out of linear voltammetry measurement registered under chopped visible light illumination in 0.1 M NaOH solution. As can be seen in Figure 58a, despite chopped light illumination electrode changes of the current are continuous. Such a curve shape was observed in article A1 and A2 and was assigned to photogenerated charge accumulation. In the case of Figure 58c square shape profile for the consecutive on-off cycles is associated with efficient e-h pair generation (see article A3 pages 126-140 and A4 146-159). Whereas, in Figure 58b it is possible to observe two mechanisms in the same curve.

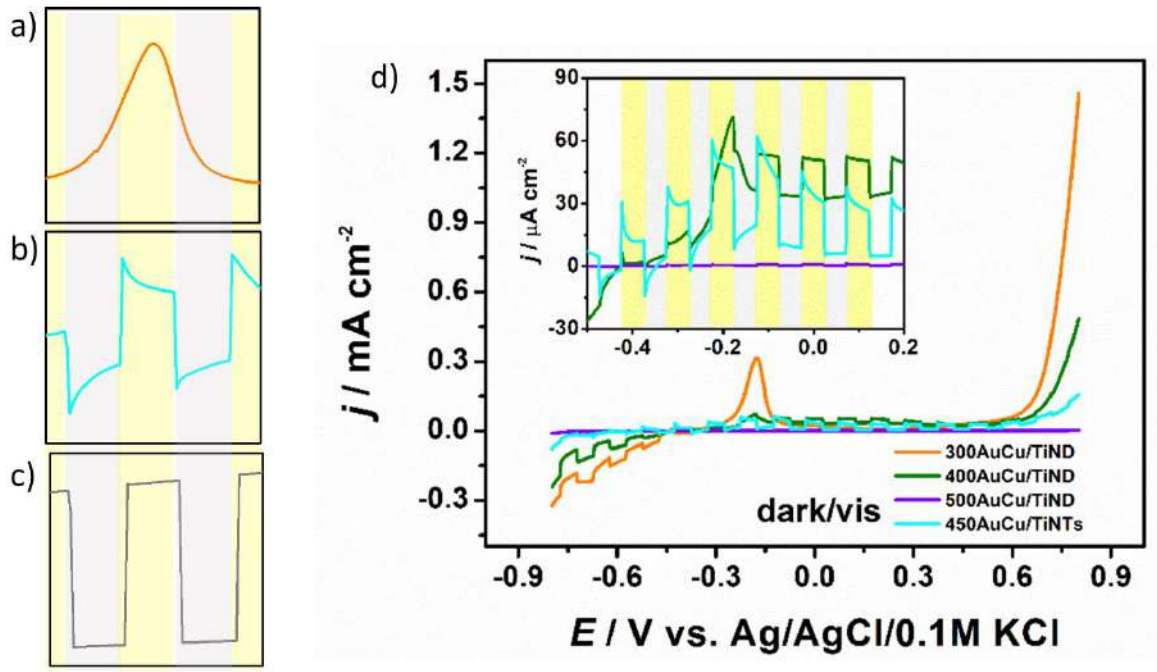

Figure 58. Various shape profiles of LV curve registered under light illumination assigned to different mechanisms of charge generation a) charge accumulation b) charge accumulation and efficient e-h pair generation, c) efficient e-h pair generation, d) linear voltammetry curves for 10AuCu/TiND and 10AuCu/TiO_2NTs in 0.1M NaOH under visible light illumination.

The brief comparison of chosen results from article A2 and A5 presented in the Figure 58d is intended to highlight an observation regarding various types of charge generation. The AuCu bimetallic nanostructures were fabricated on different nanotextured platform than Ti nanodimples in order to study the phenomenon which occurs under light illumination at -0.17 V vs. Ag/AgCl/0.1 M KCl (see Figure 58d). TiO_2NTs were chosen because of the highly ordered structure and higher geometrical surface area for further AuCu modification than TiNDs. It should be added that titanium nanodimple platform which was utilize in article A1-A4 is composed of thin passivation layer of TiO_2 present on the electrode surface, whereas, nanotubes are all made of titanium dioxide. According to Xiao et al.[223] with an increase of semiconductor amount the photocurrents increases. However, this process takes place to the point where saturation of light absorption is reached.

In the article A5 thin AuCu layers deposited on TiO_2 nanotubes were rapidly thermal annealed at 450 °C with heating rate of 40 °C/s in various atmospheres such as air, vacuum, argon and hydrogen. In the article A5 the same variety of annealing atmospheres (air, vacuum, argon, hydrogen) as well as the heating rate of 40 °C/s as in article A4 were chosen. However, the temperature was changed to 450 °C because thermal treatment at this temperature allows to

obtain TiO_2 in the form of anatase phase as well as leads to formation of such crystallite size and surface area of TiO_2 which can increase their photon utilization and photocatalytic activity[224,225]. The question was if different annealing atmospheres (air, vacuum, argon, hydrogen) will allow to obtain photoactive bimetallic AuCu nanoparticles on TiO_2NTs and how their chemical structure will change.

Nanomaterials synthesis

Firstly, Ti plate was cleaned in acetone, ethanol and deionized water. Then, TiO_2NTs were fabricated by electrochemical anodization of Ti in two-electrode system where Ti was an anode and Pt cathode. The process was carried out with temperature of 40 °C, voltage of 30 V, during 2 hours and with electrolyte contained 0.09 M NH_4F dissolved in 1.3 % vol. HF, 6.2 % vol. H_2O and 92.5 % vol. diethylene glycol. Then, TiO_2NTs were covered by 5 nm and 10 nm AuCu alloy layer by magnetron sputtering and rapid thermal annealed at 450 °C during 1 hour with a heating rate of 40 °C/s in different atmospheres such as air, vacuum, argon and hydrogen. The schematic fabrication process is presented in Figure 59.

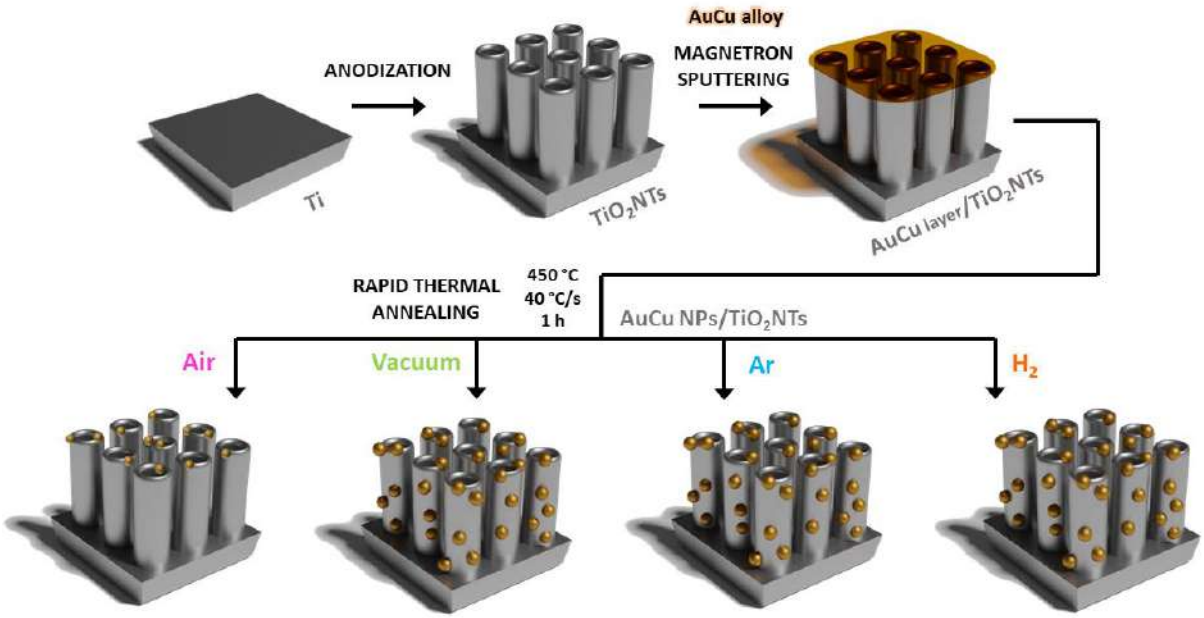

Figure 59. Schematic fabrication process of bimetallic AuCu-decorated TiO_2 nanotubes thermally treated in the rapid thermal annealer in various atmospheres.

Optical and structural properties

The shape of reflectance spectrum for the AR-TiO_2NTs is characterized by strong absorption in UV region. After formation of AuCu nanoparticles the shape of the spectrum differs significantly especially in the range from 400 to 650 nm which is assigned to enhanced absorption in visible light (Figure 60a). The XPS allows to confirm the presence of AuCuTi alloy[141],

AuCu alloy[226], CuO and $Cu(OH)_2 \cdot CuCO_3$[197] on the AR-10AuCu/TiO_2NTs electrode surface, with peaks at 931.4 eV, 932.5 eV, 933.7 eV and 935.0 eV, respectively (Figure 60b). It should be highlighted that unique CuAuTi alloy was fabricated only for annealing in argon atmosphere. Therefore, it can be assumed that this alloy has positive impact on increase of photoactivity in the visible light range which will be described below in electrochemical and photoelectrochemical properties section.

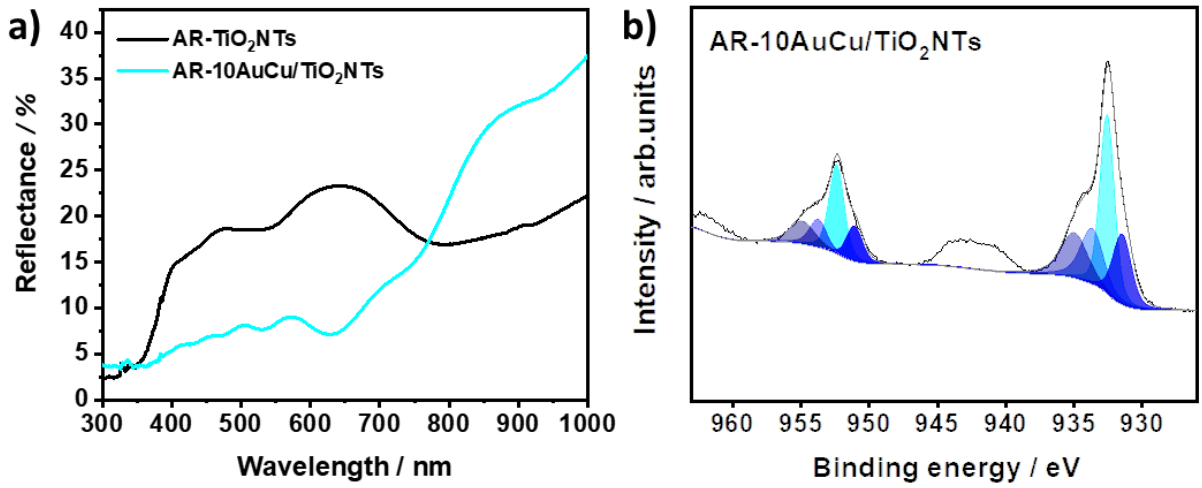

Figure 60. a) Reflectance spectra for pure TiO_2NTs and AuCu decorated TiO_2NTs annealed in argon, b) XPS high resolution spectra of AR-10AuCu/TiO_2NTs for Cu2p.

Electrochemical and photoelectrochemical properties

The photoelectrochemical activity of pure TiO_2NTs and AuCu decorated TiO_2NTs annealed in argon was tested by linear voltammetry measurements under chopped light from -0.8 V to +0.8 V in 0.1 M NaOH solution. The highest difference between the current density recorded in dark and under light illumination was registered at -0.2 V vs. Ag/AgCl/0.1M KCl. As can be seen, under UV-vis light illumination the AR-10AuCu/TiO_2 electrode has higher photocurrent than the AR-TiO_2NTs only around -0.2 V (Figure. 61a). However, when the AR-10AuCu/TiO_2NTs electrode is illuminated by visible light strong enhancement can be seen in the whole potential range (Figure. 61b). Enhanced photocurrent in the visible light is in accordance with UV-vis spectroscopy measurement where AuCu modified electrode exhibited wide absorption band from 400 to 650 nm. The photocurrent recorded for TiO_2NTs decorated by AuCu nanoparticles thermally annealed in argon atmosphere reached 37 $\mu A\ cm^{-2}$ under visible light at the potential of -0.2 V. It should be noticed that pure TiO_2NTs present square shape profile for the consecutive on-off cycles while AuCu-modified nanotubes manifest cathodic and anodic spikes which are assigned to hole accumulation in the space charge layer[227]. The shape of LV is similar under UV-vis and vis light therefore it can be claimed that

the presence of AuCu species is responsible for the unique character of this curves. The oxidation peak at -0.2 V vs. Ag/AgCl/0.1M KCl can be interpreted as oxidation of Cu to Cu_2O which came from CuAuTi or AuCu alloys. The photocurrent generation under vis light takes place on AuCu alloys species while TiO_2NTs are regarded as the support material. The optimal pathway for electron transport is ensured by the vertical tubular geometry of TiO_2 nanotubes.

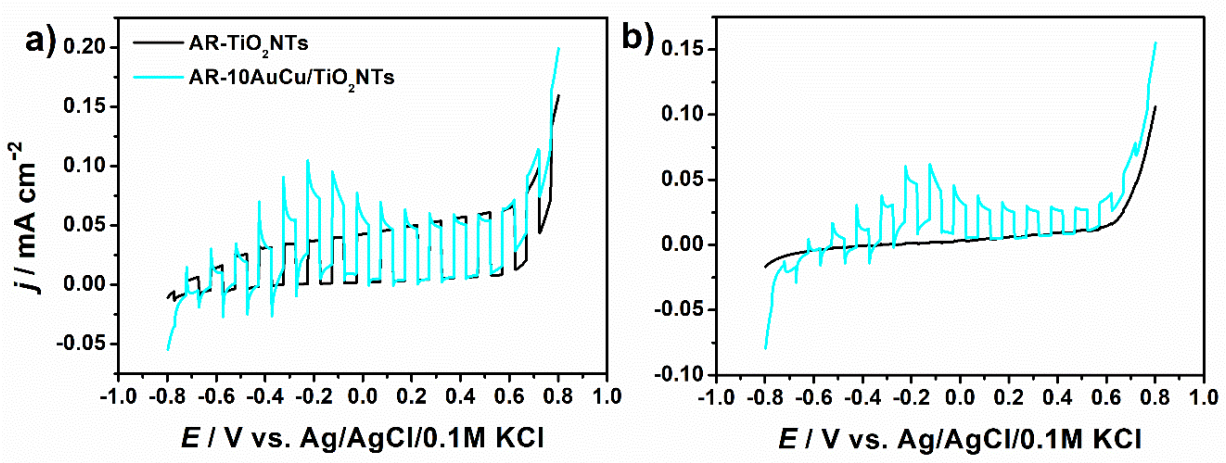

Figure 61. Linear voltammetry curves for AR-TiO_2NTs and AR-10AuCu/TiO_2NTs registered under a) UV-vis and b) visible light illumination.

Conclusions

In this work, AuCu NPs formed onto TiO_2 nanotubes rapid thermal treated in argon atmosphere exhibited the highest photocurrent under UV-vis and visible light illumination. The photocurrent reached 64 µA cm^{-2} and 37 µA cm^{-2} under UV-vis and vis light at -0.17 V. Based on UV-vis spectrometry measurements AuCu decorated nanotubes manifested the shift in absorbance band and stronger absorption in the range from 400 nm to 650 nm. XPS analysis confirmed the unique CuAuTi alloy for electrode annealed in argon. The AR-10AuCu/TiO_2NTs electrode is an n-type semiconductor where small amount of copper oxides in the form of NPs can form additional p-n heterojunction increasing photoactivity under visible light. Furthermore, SPR effect from AuCu NPs enhances ability of light absorption.

A5) W. Lipińska, K. Grochowska, J. Ryl, J. Karczewski, K. Siuzdak, ***Influence of Annealing Atmospheres on Photoelectrochemical Activity of TiO_2 Nanotubes Modified with AuCu Nanoparticles,*** ACS Applied Materials and Interfaces 13 (2021) 52967, IF = 10.4 / 200 points mechanical engineering

ACS APPLIED MATERIALS & INTERFACES

www.acsami.org Research Article

Influence of Annealing Atmospheres on Photoelectrochemical Activity of TiO_2 Nanotubes Modified with AuCu Nanoparticles

Wiktoria Lipińska,* Katarzyna Grochowska, Jacek Ryl, Jakub Karczewski, and Katarzyna Siuzdak

Cite This: https://doi.org/10.1021/acsami.1c16271 Read Online

ACCESS | Metrics & More | Article Recommendations | Supporting Information

ABSTRACT: In this article, we studied the annealing process of AuCu layers deposited on TiO_2 nanotubes (NTs) conducted in various atmospheres such as air, vacuum, argon, and hydrogen in order to obtain materials active in both visible and UV−vis ranges. The material fabrication route covers the electrochemical anodization of a Ti plate, followed by thin AuCu film magnetron sputtering and further thermal treatment. Scanning electron microscopy images confirmed the presence of spherical nanoparticles (NPs) formed on the external and internal walls of NTs. The optical and structural properties were characterized using UV−vis, X-ray diffraction, and X-ray photoelectron spectroscopies. It was proved that thermal processing under the argon atmosphere leads to the formation of a CuAuTi alloy in contrast to materials fabricated in air, vacuum, and hydrogen. The electrochemical measurements were carried out in NaOH using cyclic voltammetry, linear voltammetry, and chronoamperometry. The highest photoactivity was achieved for materials thermally treated in the argon atmosphere. In addition, the Mott−Schottky analysis was performed for bare TiO_2 NTs and TiO_2 NTs modified or covered with gold copper NPs indicating a shift in the flatband potential. Overall, thermal processing resulted in changes in optical and structural properties as well as electrochemical and photoelectrochemical activities.

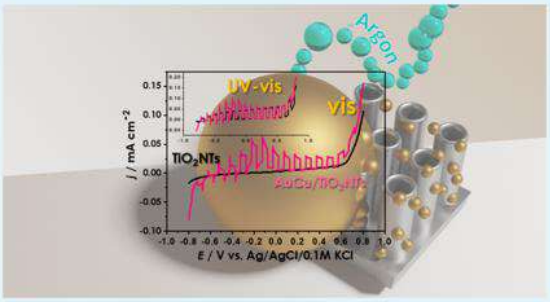

KEYWORDS: *nanostructures, AuCu nanoparticles, titania nanotubes, annealing atmospheres, photoelectrochemical activity*

INTRODUCTION

It is well known that metallic nanoparticles (NPs) attracted a lot of attention due to their unique properties, both chemical and physical ones.[1] As they exhibit extraordinary magnetic, optical, electronic, and catalytic features, they can be applied in many fields of nanotechnology.[2−4] However, combination of two different metals forming bimetallic NPs can show a superior performance. Namely, the functionality of nanometals can be enhanced by joining different metallic components.[5] So far, different kinds of bimetallic NPs have been reported, such as platinum-,[6] nickel-,[7] iron-,[8] palladium-,[9] and gold[10]-based ones. When it comes to the fabrication of bimetallic NPs, there are basically two different routes. Similar to typical monometallic particles, also in this case bottom-up and top-down methods are being used. The most popular methods applied for the synthesis of such NPs are: (i) electrochemical reduction, (ii) chemical reduction, (iii) sputtering, (iv) the sol−gel method, (v) the chemical precipitation method, (vi) the microemulsion method, and (vii) the hydrothermal method.[11] It should be kept in mind that the final arrangement of bimetallic NPs depends on the parameters of the fabrication methods as well as on the thermodynamics. Bimetallic NPs can be synthesized as core−shell, Janus, or chemically ordered and disordered structures.[12]

Despite as mentioned above, many different kinds of bimetallic nanostructures can be produced, and Au-based NPs showed promising results in catalytic reactions. Especially, combination of Au with Cu is being considered as the most interesting one. This is due to the fact that both types of metals exhibit a plasmonic behavior. Au NPs are regarded chemically inert, stable, and biocompatible, while Cu ones can be used in, for example, oxidation of CO or benzyl alcohol or reduction of CO_2.[13] It should be taken into account that copper easily oxidizes when exposed to air. The solution to overcome this problem is to combine copper and gold (or other stable metals) in order to obtain alloy.[14] The synergistic effect between Au and Cu affects the properties of composed materials, namely improves stability, allows for optical property modulation, and influences catalytic activity. Moreover, when the Au−Cu alloy is in the form of NPs, its high surface area enables its further use in electrolytic applications.

Received: August 25, 2021
Accepted: October 14, 2021

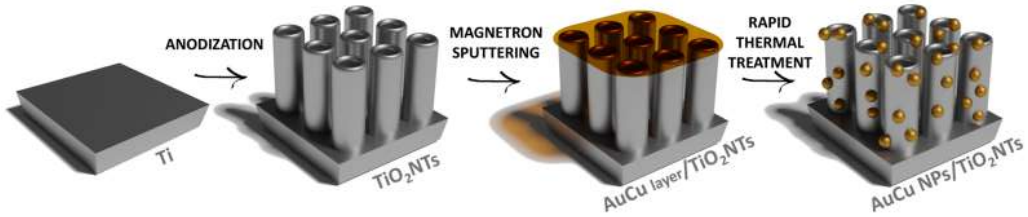

Figure 1. Diagram depicting the preparation of TiO_2 NTs modified with AuCu NPs.

The easiest way to form NPs out of an alloy is its thermal treatment. In such a case, a phase transition diagram should be taken into account. From theoretical predictions, it is known that at high temperatures gold and copper form a random solid solution, while at low temperatures ordered ones: $AuCu_3$, Au_3Cu, and AuCu. Moreover, the melting temperature is size- and shape-dependent.[15] Also, the atmosphere ensured during thermal processing has a great impact on the final structure and composition of NPs. The presence of different gases as well as their pressure can lead to surface segregation,[16] dealloying of the alloy parts,[17] and selective oxidation of one of the components.[18] All these abovementioned factors can result in surface defect (structure) formation that in consequence enhances catalytic performance. Additionally, the NP support, that is, a substrate on which AuCu NPs are located, is a key factor in the Cu alloying/dealloying process. It also influences the stabilization of different species under various atmospheres.[19]

To the best of our knowledge, AuCu NPs have been studied in a reactive environment at elevated temperature in the case when they were deposited on SiO_2 or Al_2O_3. In our case, we chose titania nanotubes (TiO_2 NTs) due to their chemical stability, ordered architecture, high specific surface area, and photocatalytic properties.[20,21] No detailed discussion can be found in the literature regarding the influence of an atmosphere on fabrication, structural, and electrochemical/photoelectrochemical properties of thermally formed AuCu NPs supported on TiO_2 NTs.

TiO_2 NTs are widely used as materials for photoelectrochemical water splitting and photocatalytic reactions. TiO_2NTs provide great electron mobility, and therefore, a decrease of recombination and scattering processes. However, pure TiO_2 owing to its wide band gap and low activity in the visible light region should be modified by metal or non-metal dopants. For example, TiO_2 NTs can be enriched during the electrochemical anodization process by the addition of $Cu(NO_3)_2$ to the electrolyte resulting in copper and copper oxide doping.[22] Such a $CuTiO_2$NT electrode exhibited five times higher photocatalytic H_2 evolution in comparison to pure NTs.[22] Moreover, the synergistic effect was a consequence of tungsten's benefit to copper. The Cu−WO_3−TiO_2NT sample showed a photocurrent density at +0.6 V Ag/AgCl equal to 2.3 mA/cm^2, which was ca. five times higher than that of the Cu−TiO_2NTs.[23] Furthermore, for a copper-decorated WO_3−TiO_2 NT (Cu/WTN) electrode, a synergistic effect was detected with a 2.5 times higher methylene blue photodegradation rate than for WTNs.[24] Instead of copper, gold NPs have been added as other dopants for TiO_2−WO_3 NTs.[25] The H_2 evolution on the Au/WO_3TiO_2NT material was three times higher than that on the WO_3TiO_2NTs and even nine times higher than that on pure TiO_2NTs. Furthermore, the enhanced absorbance in visible light attributed to the SPR effect as well as a higher photocatalytic water-splitting activity have been observed for the Au/$CrTiO_2$NT and the Ag/$CrTiO_2$NT nanomaterials fabricated via a photodeposition process of noble metals on the NTs.[26] However, it should also be taken into account that not only TiO_2 but also CuO are increasingly used as support materials for solar-driven processes.[27,28]

In this work, we addressed this issue and highlighted the importance of the annealing atmosphere. The TiO_2 NTss were prepared via electrochemical anodization, and as a result highly ordered tubular arrays were obtained. Afterward, the substrate was covered by thin AuCu films by means of magnetron sputtering. In the next step, the thermal annealing at 450 °C was performed under different atmospheres, that is, air, vacuum, argon, and hydrogen. The morphology of the prepared materials was studied by scanning electron microscopy (SEM), while structure and chemical properties were characterized by X-ray diffraction (XRD) and X-ray photoelectron spectroscopies (XPS). Optical properties were determined using a UV−vis spectrophotometer. Finally, electrochemical activity of materials was characterized in the dark and upon exposing the electrodes to solar and visible light. As it was expected, the atmosphere strongly affects the overall performance of electrode materials. We believe that such structures can be used in solar-driven processes.

EXPERIMENTAL SECTION

Materials. Titanium foil (99.7%, Stream), acetone (99.5%, Chempur), ethanol (96%, Chempur), diethylene glycol (99.5% Chempur), hydrofluoric acid (Chempur), and ammonium fluoride (Chempur) were used for the electrochemical anodization process. The pure target of AuCu (Au50/Cu50 at. %, Goodfellow) was exploited for metal layer deposition.

Electrode Fabrication. The fabrication route of electrodes is shown in Figure 1. First, the Ti foil was cut into 2 × 3 cm^2 plates and ultrasonically cleaned in acetone, ethanol, and deionized water for 10 min. Then, substrates were used for the electrochemical anodization process. The anodization was conducted in a two-electrode system, where Ti was used as an anode and Pt as a cathode. Electrodes were placed in a cell with a thermostatic jacket for preservation at 40 °C for the whole process. The electrolyte contained 0.09 M NH_4F/1.3% vol HF/6.2% vol H_2O/92.5% vol diethylene glycol. During the anodization, a voltage of 30 V was applied between electrodes for 2 h. As a result, highly ordered TiO_2 NTs were obtained over the entire surface of the electrode. Second, NTs were covered by 5 and 10 nm thick AuCu layers, denoted as 5AuCu and 10AuCu, using a magnetron sputtering machine (Q150T S system, Quorum Technologies). Third, the samples were thermally treated using a rapid thermal annealing furnace (MILA 5000 P-N) at 450 °C for 1 h. Electrodes were annealed in various atmospheres such as air, vacuum, hydrogen, and argon. In this article, the electrodes were assigned the following names: NA-TiO_2NTs (TiO_2NTs non-annealed), A-TiO_2NT_S (TiO_2NTs annealed in air), V-TiO_2NTs (TiO_2NTs annealed in vacuum), AR-TiO_2NTs (TiO_2NTs annealed in argon),

https://doi.org/10.1021/acsami.1c16271
ACS Appl. Mater. Interfaces XXXX, XXX, XXX−XXX

H-TiO_2NTs (TiO_2NTs annealed in hydrogen), NA-10AuCu/TiO_2NTs (10AuCu/TiO_2NTs non-annealed), A-10AuCu/TiO_2NTs (10AuCu/TiO_2NTs annealed in air), V-10AuCu/TiO_2NTs (10AuCu/TiO_2NTs annealed in vacuum), AR-10AuCu/TiO_2NTs (10AuCu/TiO_2NTs annealed in argon), and H-10AuCu/TiO_2NTs (10AuCu/TiO_2NTs hydrogen).

Sample Characterization. The morphology and cross section of the electrodes were investigated using a field-emission scanning microscope (FEI Quanta FEG250) equipped with an ET secondary detector, and with the beam accelerating voltage kept at 10 kV. The EDX mapping was carried out using an EDAX Genesis APEX 2i with an Apollo X SDD spectrometer. The UV−vis reflectance spectra of bare TiO_2 NTs and TiO_2 NTs modified with gold copper NPs (AuCu/TiO_2NTs) were measured with a spectrophotometer (Lambda 35, PerkinElmer) equipped with an accessory for recording the reflectance spectra. The spectra were recorded in the range of 300−1000 nm, with a scanning speed of 60 nm/min. Band gap energy values were determined as the intercept of the relationship between the transformation of the Kubelka−Munk function $(F(R)^{0.5}\ E_{ph}^{0.5})$ versus E_{ph} (photon energy), where $F(R) = (1 - R)^2/2R$ and R—reflectance. The photoluminescence spectra (PL) were measured at room temperature using a SHAMROCK—SR-303I-A Spectrograph equipped with a 450 mW light-emitting diode as an excitation light source and an ICCD camera as a detector. The spectra were recorded from 390 to 800 nm. The crystallinity was studied by means of the XRD technique over the range of 20−80° using a Bruker 2D Phaser diffractometer with CuKα radiation and a XE-T detector. The samples were characterized using an X-ray photoelectron spectrometer (Escalab 250Xi, ThermoFisher Scientific) with a monochromatic AlKα source in order to determine the chemical structure. The electrochemical and photoelectrochemical studies on electrodes such as cyclic voltammetry (CV), linear voltammetry (LV), chronoamperometry (CA), and electrochemical impedance spectroscopy (EIS) were conducted using an AutoLab PGStat 302N potentiostat−galvanostat, where TiO_2NTs and AuCu/TiO_2NTs electrodes served as working electrodes, a Pt mesh was used as a counter electrode, and Ag/AgCl/0.1 M KCl was used as a reference electrode. The CV and LV curves were registered from −0.8 V to +0.8 V versus Ag/AgCl/0.1 M KCl. The CA measurements under chopped light were performed at −0.2 V for 200 s, while a single dark and light period lasts for 5 s. The electrochemical tests were carried out in deaerated 0.1 M NaOH. EIS measurements were conducted at a frequency of 1000 Hz, in the range from 0 to −1.2 V versus Ag/AgCl/0.1 M KCl, covering 25 points with a 50 mV amplitude. The chronopotentiometry curves at OCP were registered in the dark and under UV−vis and visible light illumination (ESI). Those measurements were carried out for the selected materials for 35 min. The photoelectrochemical measurements were conducted using a xenon lamp (LOT-QuantumDesign GmbH). The radiation intensity was calibrated using a Si cell (Rera) and established at 100 mW/cm^2.

Morphology. SEM images of TiO_2 NTs and TiO_2 NTs modified with AuCu NPs annealed in different atmospheres are shown in Figure 2. The 10AuCu electrodes were chosen for the morphology analysis because of the best photoelectrochemical activity. The ordered surface is composed of NTs with 101 ± 13 nm in diameter and a length of 709 ± 53 nm. It can be clearly seen that thermal treatment with a thin AuCu layer in vacuum, argon, and hydrogen resulted in the formation of spherical bimetallic NPs deposited both on the surface and inside TiO_2 NTs. For materials fabricated in the air, NPs are visible on the surface but are hardly visible in the TiO_2 interior. Depending on the atmosphere, various dimensions of NPs were obtained. The diameter of AuCu NPs for the sample thermally treated in air was estimated to be 25 ± 7 nm, while those of electrodes annealed in vacuum, argon, and hydrogen were equal to 38 ± 15, 38 ± 12, and 39 ± 12 nm, respectively. The EDX map of the AN-10AuCu/TiO_2NT electrode is shown in Figure S1. The EDX data show atomic percentages of 99.4, 0.33, and 0.28 of Ti, Cu, and Au, respectively, on the sample and confirm the homogenous distribution of AuCu NPs on the titanium dioxide NTs. According to Bechelany et al.,[29] the morphology of Au deposited on the Si substrate highly depends on the atmosphere ensured during annealing of the sputtered gold layers. Thermal treatment at 1000 °C for 1 h in the air atmosphere tends to the formation of Au nanodots with a size of ca. 100 nm, whereas in the vacuum atmosphere Au nanowires are created. The NiO NPs synthesized via the sol−gel method subsequently annealed in air and O_2 atmospheres had approximately the same average particle size at lower temperatures (400−500 °C). However, at higher temperatures, especially at 800 °C, the size was different and equal to 75.6 nm in air and 65.2 nm in O_2 atmospheres.[30] According to Boeva et al.,[31] during the reaction of homomolecular hydrogen exchange on Cu, a change in the surface structure of the particles was observed. In an oxidizing atmosphere, NPs become more spherical, whereas the reducing agents cause surface flattening. This phenomenon is attributed to the change in the number of faces exposed on the surface. Moreover, the influence of a reactive atmosphere on the formation of Ag, Ti, and Al NPs during the rapid thermal annealing realized with the use of nanosecond pulsed irradiation was investigated by Girualt et al.[32] For experiments conducted at the lowest concentration of O_2 (only 1 vol % of O_2), the size of Al NPs and Ti NPs was equal to ca. 5 nm, whereas in the O_2− N_2 gas mixture (15 vol % of O_2) decreases to 1.9 and 3.4 nm, respectively. Therefore, it is possible that a higher oxygen concentration is related to a smaller size for NPs fabricated in the air.

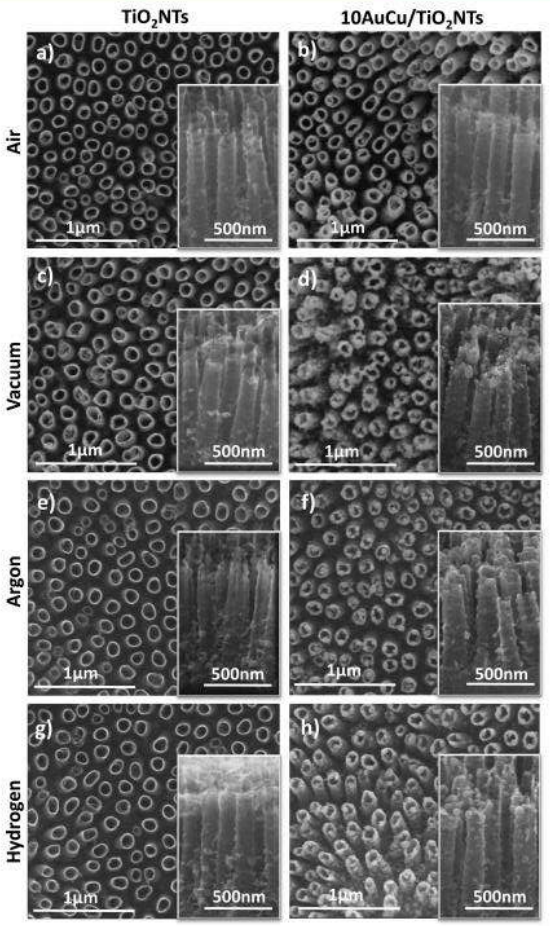

Figure 2. SEM images of the TiO_2NT and 10AuCu/TiO_2NT electrodes annealed in (a,b) air, (c,d) vacuum, (e,f) argon, and (g,h) hydrogen.

https://doi.org/10.1021/acsami.1c16271
ACS Appl. Mater. Interfaces XXXX, XXX, XXX−XXX

Optical Properties. To characterize the optical properties of the prepared nanomaterials, first the appearance of the samples was studied—see Figure 3. The as-anodized TiO_2 NTs appear yellow in

Figure 3. Appearance of TiO_2NTs and 10AuCu/TiO_2NTs before and after calcination under different atmospheres.

color, which is consistent with previous reports.[33] It is a well-known fact that after heating of TiO_2, the phase transformation occurs, from amorphous to crystalline one. After calcination in the air, the plate covered by NTs changes its color to white, which is expected for TiO_2 as the electronic configuration of Ti^{2+} is $4s^03d^2$, and therefore there are no unpaired electrons. However, due to the presence of the metallic substrate below, they seem to be blue as a series of constructive and destructive interferences can arise. Thermal processing in argon leads to a color change to gray, which can be attributed to the increased concentration of oxygen vacancies known also as defects.[34] Finally, when TiO_2 NTs are processed under vacuum or in hydrogen, i.e., in a reducing atmosphere, TiO_2 can turn to yellow, gray, or black. This is due to the Ti^{3+} or/and oxygen vacancy formation.[35] As can be seen, our observations are in agreement with the other literature data. Nevertheless, it should be kept in mind that the final color of the TiO_2 samples strongly depends not only on the processing atmosphere but also on detailed parameters such as temperature values or gas pressure.

The AuCu-alloyed film should have a rosegold color.[36] Taking into account this information as well as the initial color of the TiO_2 support, the observed brownish color of the 10AuCu/TiO_2NTs before calcination is reasonable. Changing of the material appearance after thermal treatment can be related to the modification of (i) the morphology because NPs are formed and (ii) the chemical composition because copper and copper oxide under various atmospheres can be oxidized or reduced. We believe that in our case, all phenomena can be responsible for the final appearance of the material.

A more detailed characterization of optical properties was conducted by means of UV−vis spectroscopy, and the registered spectra are shown in Figure 4. First of all, the shape of the spectrum with the strong absorption in the deep UV region for TiO_2 NTs before annealing is typical for an amorphous material.[37] Calcination in air causes the redshift of the absorption edge and the occurrence of a new absorbance band in the infrared part of the spectrum. The redshift can be associated with the change in the structural phase, while the additional absorbance band can be associated with the modification of the surface morphology.[38] Altering the processing atmosphere leads to reshaping of the UV−vis spectra. This may be explained by the varied crystalline size, phase transformation, or the presence of the oxygen/Ti^{3+} vacancies.[39]

After deposition of AuCu, one may clearly observe the fringes. Thermal processing of the samples causes a shift of their position or a change of their intensity. This phenomenon can be explained by the light-scattering effect, i.e., pronounced when the surface is more rough, by constructive and destructive interference of reflected light, by surface plasmon resonance as NPs are formed and both gold and copper exhibit plasmonic behavior,[40] and finally by the presence of the Ti^{3+} and/or vacancies in the Supporting Information.

Based on the reflectance spectra and Kubelka−Munk relation (Figure S2), the optical energy band gap (E_{bg}) values for all investigated materials were estimated—see Table 1. The value of E_{bg}

Table 1. Values of Optical Energy Band gaps of the Prepared Materials

electrode material	optical energy band gap/eV
NA-TiO_2NTs	3.36
A-TiO_2NTs	3.14
V-TiO_2NTs	3.16
AR-TiO_2NTs	2.93
H-TiO_2NTs	2.87
NA-10AuCu/TiO_2NTs	3.02
A-10AuCu/TiO_2NTs	2.77
V-10AuCu/TiO_2NTs	
AR-10AuCu/TiO_2NTs	
H-10AuCu/TiO_2NTs	

for amorphous TiO_2 NTs is 3.36 eV and it drops after crystallization. This result is consistent with theoretical simulations.[41] Treatment in different atmospheres leads to a reduction of the band gap, and this can be attributed to the localized states induced by oxygen vacancies or disordered surface layers.[42] Annealing in vacuum, argon, and hydrogen causes the removal of oxygen atoms and generates oxygen vacancies surrounded by Ti cations in the Ti^{3+} or Ti^{2+} valence state.[43,44] Moreover, the vacuum treatment decreases the structural order of TiO_2.[43] After deposition of the bimetallic layer, the E_{bg} value decreases in comparison to that of the non-annealed TiO_2 material, and this value is further reduced owing to air processing at the elevated temperature. For electrodes thermally treated in vacuum, argon, and hydrogen, it was impossible to estimate the value of the optical energy band gap as the materials absorb at nearly the same level for the whole wavelength range.

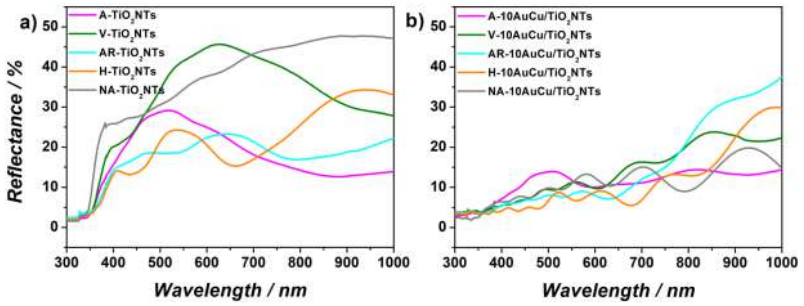

Figure 4. Reflectance spectra of (a) bare TiO_2 NTs and (b) TiO_2 NTs covered with the AuCu layer before and after thermal treatment under different atmospheres.

https://doi.org/10.1021/acsami.1c16271
ACS Appl. Mater. Interfaces XXXX, XXX, XXX−XXX

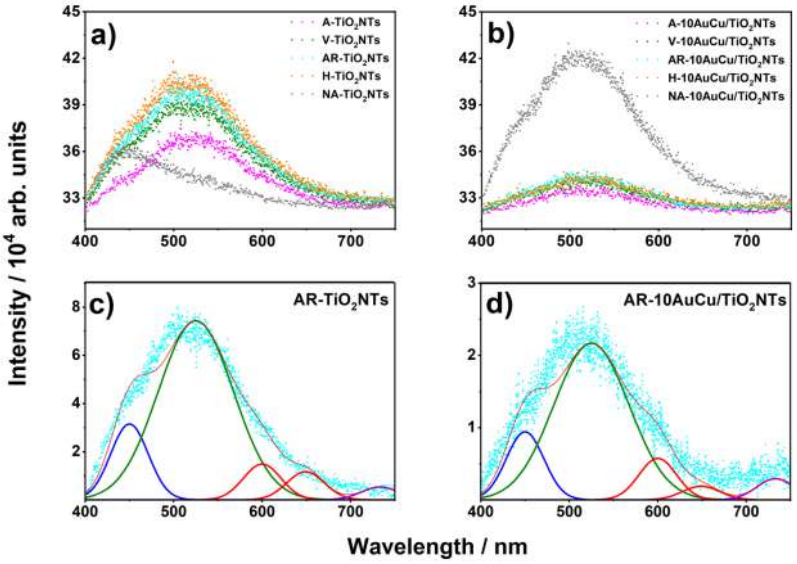

Figure 5. Photoluminescence spectra of (a) TiO_2NTs and (b) 10AuCu/TiO_2NTs annealed in various atmospheres and the deconvoluted photoluminescence spectra of (c) AR-TiO $_2$NT and (d) AR-10AuCu/TiO_2NT electrodes.

All in all, thermal treatment of TiO_2NTs in argon and hydrogen atmospheres reduces the energy band gap. Moreover, the reduction of the band gap is also achieved by the deposition of the AuCu alloy on the TiO_2 platform. Furthermore, the sputtering of the AuCu alloy on the titanium surface results in the wide absorbance from 300 to 700 nm.

The photoluminescence spectra of the TiO_2NT and 10AuCu/TiO_2NT samples are presented in Figure 5. Bimetallic AuCu samples thermally treated in air, vacuum, argon, and hydrogen are characterized by a lower PL intensity compared to non-modified TiO_2 NTs. In general, the decrease of intensity can be correlated with a reduced recombination rate of electrons and holes.[45] Figure 5c,d presents the deconvoluted photoluminescence spectra of the AR-TiO_2NT and the AR-10AuCu/TiO_2NT electrodes. One may distinguish four light emission ranges, namely: blue (400−480 nm), green (500−540 nm), red (570−700 nm), and infrared (from 700 nm). Each of them is responsible for different recombination processes.[46] The blue emission can be associated with electrons trapped in oxygen vacancies,[47] whereas green emission with holes trapped on Ti^{3+} ions.[48] The strongest difference between the AN-TiO_2NTs (Figure 5c) and the AN-10AuCu/TiO_2NTs (Figure 5d) can be observed for red emission associated with electrons trapped with valence band holes.[49] Such a change supports the enhanced photoactivity of the samples annealed in argon.

Crystallinity. The XRD patterns of TiO_2NT and 10AuCu/TiO_2NT electrodes annealed in various atmospheres (air, vacuum, argon, and hydrogen) indicate the formation of anatase and rutile phases as well as the presence of titanium (Figure 6). Seven peaks are located at 34.9, 38.3, 40.0, 52.9, 62.7, 70.6, and 76.0°, and are assigned to the (100), (002), (101), (102), (110), (103), and (200) planes of Ti, respectively.[50] The diffraction peaks at 25.1 and 47.7° prove that pure TiO_2NTs as well as modified TiO_2NTs annealed in each atmosphere are present in the form of anatase.[51] Moreover, not only the anatase but also rutile phase is present, and the peak is located at 27.3°.[52]

Chemical Nature of Samples. The X-ray photoelectron spectroscopy allows investigating the chemical nature of the sample. Figure 7 shows high-resolution XPS spectra of gold Au 4f (Figure 7a) and copper Cu 2p (Figure 7b). The chemical states of titanium Ti 2p (Figure S3a) and oxygen O 1s (Figure S3b) are given in the Supporting Information file. The positions of each maxima are

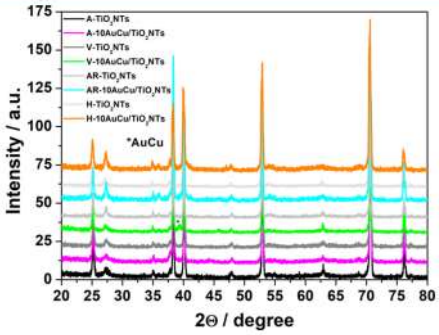

Figure 6. XRD patterns of TiO_2NT and 10AuCu/TiO_2NT electrodes annealed in various atmospheres.

summarized in Table 2. The XPS spectra of Au 4f located at 84.2 and 84.7 eV confirm the presence of Au[53] and Au_2O,[54] respectively, on the electrode surface. However, the peak at 83.9 eV for the 10AuCu/TiO_2NT electrode annealed in the argon atmosphere corresponded to the CuAuTi alloy. It is shifted toward a more negative value of 0.3 eV compared to pure Au. The AuCu[55] alloy was detected in the Cu 2p spectra for each atmosphere and the appropriate peak appears at 932.5 eV. The 10AuCu/TiO_2NT electrode thermally treated in air possesses an additional chemical state with copper (II) oxides apart from the alloy. Cu(II) is present in two forms, that is, CuO and $Cu(OH)_2{\cdot}CuCO_3$, and the corresponding peaks are located at 933.8 and 935.0 eV, respectively. For the electrode thermally treated in vacuum, the Cu 2p peak at 933.6 eV is assigned to CuO. In the case of electrodes annealed in vacuum and hydrogen, the ratios of metallic copper to copper oxide equal to 9:1 and 6:1 were obtained. Regarding the 10AuCu/TiO_2NT electrode thermally treated in argon, four separate chemical states are identified. The unique peak at 931.4 eV corresponds to the CuAuTi alloy. Furthermore, the AuCu alloy (932.5 eV), CuO (933.7 eV), and $Cu(OH)_2{\cdot}CuCO_3$ (935.0 eV) are present on the electrode surface. The atomic ratio within the CuAuTi alloy is equal to 3.18/4.48/3.00. In the case of titanium (Figure S3), the strong peak at ca. 459.0 eV visible for each electrode is ascribed to

https://doi.org/10.1021/acsami.1c16271
ACS Appl. Mater. Interfaces XXXX, XXX, XXX−XXX

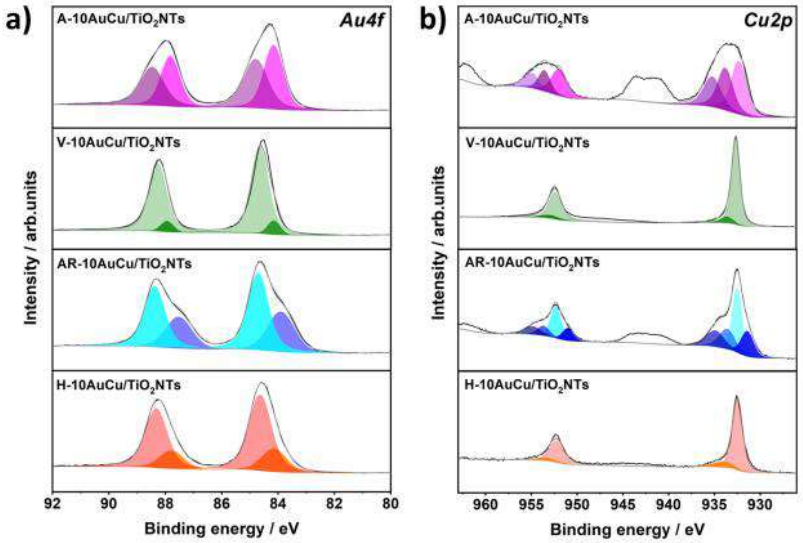

Figure 7. High-resolution XPS spectra for 10AuCu/TiO_2NT samples annealed in air, vacuum, argon, and hydrogen: (a) Au 4f; (b) Cu 2p.

Table 2. Binding Energies of 10AuCu/TiO_2NT Electrodes Annealed in Various Atmospheres

peak	component	BE/eV	at. %	peak	component	BE/eV	at. %
	A-10AuCu/TiO_2NTs				A-10AuCu/TiO_2NTs		
Au $4f_{7/2}$	Au	84.2	9.45	Cu $2p_{3/2}$	Cu (AuCu)	932.5	6.91
Au $4f_{7/2}$	Au_2O	84.8	9.6	Cu $2p_{3/2}$	CuO	933.8	5.82
	V-10AuCu/TiO_2NTs			Cu $2p_{3/2}$	$Cu(OH)_2$·CuCO3	935.0	4.81
Au $4f_{7/2}$	Au	84.2	1.59		V-10AuCu/TiO_2NTs		
Au $4f_{7/2}$	Au_2O	84.6	16.71	Cu $2p_{3/2}$	Cu (AuCu)	932.6	29.45
	AR-10AuCu/TiO_2NTs			Cu $2p_{3/2}$	CuO	933.6	3.33
Au $4f_{7/2}$	Au (CuAuTi)	83.9	4.48		AR-10AuCu/TiO_2NTs		
Au $4f_{7/2}$	Au_2O	84.7	7.6	Cu $2p_{3/2}$	Cu (CuAuTi)	931.4	3.18
	H-10AuCu/TiO_2NTs			Cu $2p_{3/2}$	Cu (AuCu)	932.5	6.21
Au $4f_{7/2}$	Au	84.2	4.36	Cu $2p_{3/2}$	CuO	933.7	3.32
Au $4f_{7/2}$	Au_2O	84.6	14.58	Cu $2p_{3/2}$	$Cu(OH)_2$·CuCO3	935.0	3.11
					H-10AuCu/TiO_2NTs		
				Cu $2p_{3/2}$	Cu (AuCu)	932.5	17.09
				Cu $2p_{3/2}$	CuO and $Cu(OH)_2$·CuCO3	934.2	2.71

TiO_2. Peak ranges for Ti $2p_{3/2}$ and Ti $2p_{1/2}$ are labeled in Figure S3b. As for the O1s spectra (Figure 3a), peaks at ca. 530 and 532 eV confirm the presence of lattice oxygen and surface-adsorbed OH^-.[56] The detailed positions of the maxima and particular components for the titanium and oxygen chemical states are given in Table S1. To sum up, annealing in the air atmosphere results in the formation of a great amount of copper oxides such as CuO and $Cu(OH)_2$·$CuCO_3$ in contrast to vacuum and hydrogen. Therefore, it can be claimed that copper oxides are under the control of the annealing atmosphere. Besides, the unique CuAuTi alloy was created during thermal treatment in argon, which may be related to the enhancement of photocurrent in both the UV–vis and vis light range.

Electrochemical Properties. CV was performed to characterize materials thermally treated in various atmospheres. The tests were performed in contact with an alkaline electrolyte, because copper is stable in this environment. Curves plotted for pure TiO_2NTs as well as TiO_2NTs modified with AuCu NPs are shown in Figure 8. Comparing all materials containing AuCu, intense faradaic peaks are observed when electrodes were annealed in vacuum, argon, and hydrogen in comparison to electrodes that were processed in the air. The AuCu/TiO_2NT samples annealed in a vacuum and argon exhibit a similar electrochemical activity (Figure 8b,c). During the anodic potential scan, the oxidation of Cu to Cu_2O occurs at −0.2 V versus Ag/AgCl/0.1 M KCl. The highest value of current density (407 μA cm^{-2}) is observed for the 5AuCu/TiO_2 NTs electrode treated in a vacuum, which is ca. 80 times higher than for this material fabricated in the air. On the other hand, during the cathodic scan, the reduction of Cu_2O to Cu occurs at −0.5 V versus Ag/AgCl/0.1 M KCl. In this case, the V-5AuCu/TiO_2NT electrode shows 60 times higher current density (−430 μA cm^{-2}) than the A-5AuCu/TiO_2 NT electrode. It should be underlined that electrodes produced when the RTA chamber was fully filled with hydrogen exhibit completely different characters with additional redox peaks (Figure 8d). The oxidation process at 0 V vs Ag/AgCl/0.1 M KCl as well as the reduction at −0.2 V vs Ag/AgCl/0.1 M KCl can be interpreted in two ways. First, it seems clear that Cu_2O is oxidized to CuO, and subsequently CuO is reduced to Cu_2O. However, it can be stated that multiple redox reactions, and thereby oxidation and reduction waves are registered.[57] Other interpretation indicates a two stage oxidation process of Cu to CuO, and a reduction of CuO to Cu at the same potential can be observed.[46] The current density at −0.2 V vs Ag/AgCl/0.1 M KCl for the 10AuCu/TiO_2NT electrode annealed in hydrogen was −0.65 mA cm^{-2}, and is ca. 330 times higher than that for the sample thermally treated in the air. Moreover, the CV curves clearly show a reduction

https://doi.org/10.1021/acsami.1c16271
ACS Appl. Mater. Interfaces XXXX, XXX, XXX−XXX

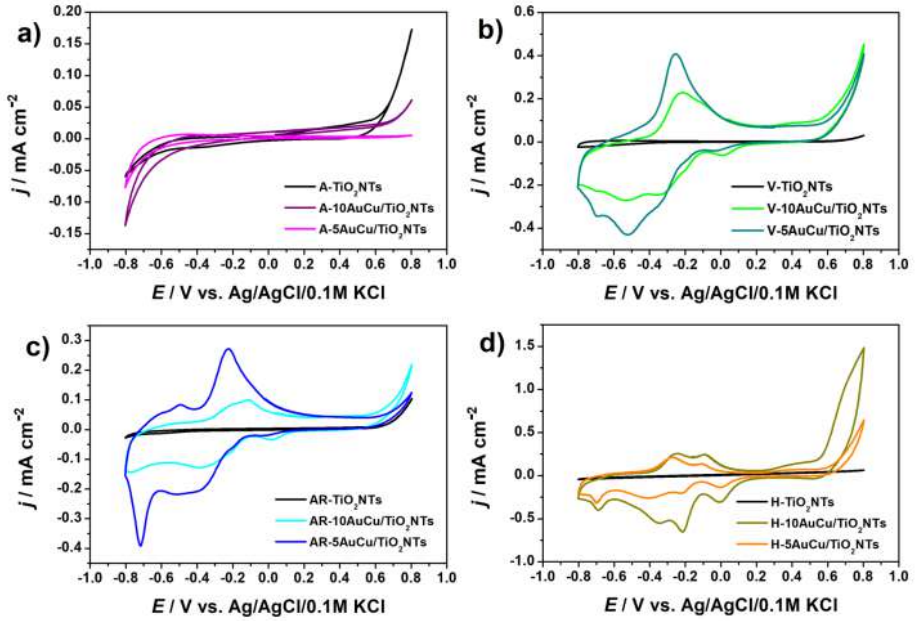

Figure 8. CV curves registered in 0.1 M NaOH for electrodes: TiO_2NTs, 10AuCu/TiO_2NTs, and 5AuCu/TiO_2NTs annealed in (a) air, (b) vacuum, (c) argon, and (d) hydrogen.

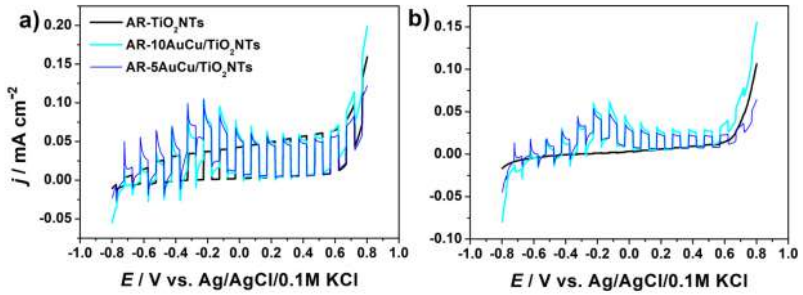

Figure 9. LV scan registered in 0.1 M NaOH for the bare and AuCu-modified TiO_2 NTs treated in the argon atmosphere: (a) UV−vis; (b) vis.

peak located at ca. 0 V Ag/AgCl/0.1 M KCl, which may correspond to the reduction of gold oxides.[58]

The LV curves for all the materials were recorded not only in the dark but also when the material was exposed to the whole solar spectrum and only visible radiation. In Figure 9, the LV for the material treated in the argon atmosphere is provided, while the photoresponse of the remaining samples is given in the electronic supporting Information file (Figure S5). 10AuCu/TiO_2NT samples annealed in argon are distinguished here because of the highest and complex photoactivity, and they are worth for a detailed analysis. However, as far as the pure TiO_2NTs are concerned, the highest photocurrent measured by the LV under UV−vis light illumination was for TiO_2NTs thermally treated in the hydrogen atmosphere, which can be correlated with the lowest band gap of the H-TiO_2NT electrode out of pure NTs. The sudden changes in current correspond to the successive periods when the light was switched on and off every 5 s.

Regarding the response of materials to the incident light, the difference between the current recorded under UV−vis irradiation and in the dark above +0.2 V versus Ag/AgCl/0.1 M KCl is slight for modified and unmodified TiO_2. However, the difference between the current density recorded in the dark and under UV−vis illumination at −0.2 V for the AR-10AuCu/TiO_2NTs electrode reaches 64 μA/cm^2, whereas for the AR-TiO_2NTs electrode is equal to 32 μA/cm^2. As for the AR-10AuCu/TiO_2NTs sample, AuCu NPs enhanced the light absorption in the UV−vis light region resulting in a light enhancement of the photocurrent density compared to the non-modified electrode. The CA curves registered at −0.2 V are given in the Supporting Information (Figure S4). The strongest enhancement for those materials is observed when only visible irradiation was applied during LV measurements. Comparing the profile of LV scan for bare and modified TiO_2, one may observe for TiO_2 an almost ideal square shape for the consecutive on−off cycles, while for structures containing AuCu, the cathodic and anodic spikes can be found. Those positive photocurrent spikes are related to the accumulation of holes in the electrode space charge layer during sample irradiation. The negative ones, when the access to light is denied, are observed in the range from −0.8 to −0.2 V vs Ag/AgCl/0.1 M KCl, and correspond to the situation when the holes are accumulated in the space charge layer during irradiation and recombined with the bulk electrons.[59] In such case, the back flow of electrons toward the photoanode occurs. It should be noted that the intensity of those spikes changes depending on the electrode polarization. In the range from −0.8 to −0.2 V vs Ag/AgCl/0.1 M KCl, the intensities of positive and negative spikes

https://doi.org/10.1021/acsami.1c16271
ACS Appl. Mater. Interfaces XXXX, XXX, XXX−XXX

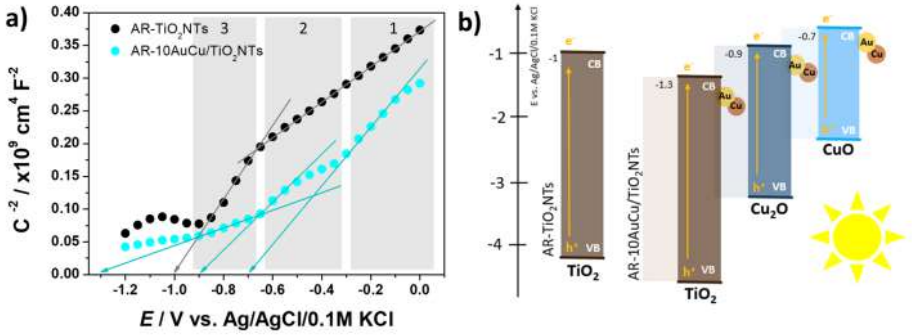

Figure 10. (a) Mott−Schottky plots and (b) schematic energy band diagrams of AR-TiO_2NT and AR-10AuCu/TiO_2NT electrodes.

are similar, whereas above −0.2 V the negative ones almost disappear, while the positive ones systematically diminish upon further polarization toward the anodic direction. Between −0.1 and +0.6 V, still positive spikes are present, and therefore still some holes occupy the surface states. Then, above ca. +0.6 V an almost well squared shape is present indicating a low e−h recombination rate and the lack of holes accumulated at the electrode/electrolyte interface.

We would like also to indicate the unique current behavior identified in the range of −0.4 and −0.2 V that is very similar to the TiO_2 modified with $[Fe(CN)_6]^{4-}$,[60] selenide, or metal selenide.[61] Following the previous reports, this change within the current−potential profile results from the different nature of elements forming our material. According to Rajeshwar et al.,[62] the investigated junction contains parts exhibiting p-and n-type conductivity, and the electrode polarization enables to track the conditions, where both p and n elements contribute in the similar degree (below −0.4 V) or n-type prevails, that is above −0.1 V. Taking into account the electrode composition, TiO_2 NTs act here as n-type while AuCu-based species as p-type species.

When the 10AuCu/TiO_2NT materials annealed in the argon atmosphere were exposed to visible irradiation, their activity is significantly higher than those of bare TiO_2 and other AuCu-containing structures that have been annealed in vacuum, ambient air, or hydrogen. Knowing that TiO_2 is not active under visible irradiation, even after annealing in the argon atmosphere, this response when only irradiation above 420 nm is applied is due to the presence of AuCu species Au_2O, AuCu, CuO, $Cu(OH)_2{\cdot}CuCO_3$, and even AuCuTi. The photocurrent value that can be read from graph (b) is lower than that in part (a) but the overall shape is very similar. Thus, it can be concluded that AuCu species are responsible for the unique behavior of LV, while TiO_2 NTs enhance light capture due to the activity in the UV range.

Furthermore, the $E-t$ measurements for AR-TiO_2NTs, AR-5AuCu/TiO_2NTs, and AR-10AuCu/TiO_2NTs in the dark and under visible and UV−vis light illumination are shown in Figure S6. In general, for one type of electrode material, the changes recorded in the open circuit potential provide information about charge transfer recombination kinetics.[63] ΔOCP for AR-TiO_2NTs between the dark and UV−vis light is equal to ca. 300 mV, whereas for AR-10AuCu/TiO2NTs, it is equals to ca. 100 mV. However, in our case, AR-5AuCu/TiO_2NT and AR-10AuCu/TiO_2NT electrodes contain two type of semiconductors such as the n-type and p-type. Therefore, the p-type activity reduces the negative drop of OCP of TiO_2.

Figure 10a shows the Mott−Schottky plot of TiO_2NT and 10AuCu/TiO_2NT samples thermally treated in argon. To determine the flat band potential for electrodes, linear regions were investigated. Such a segmental profile of the Mott−Schottky plot is typical for this kind of nanostructures as shown by Muñoz et al.[64] indicating the impact of the porosity and ordering on the position of the flat band potential. With reference to Lee and Pyun,[65] the linear analysis of the Mott−Schottky plot can be made in the case of a TiO_2 single-crystal semiconductor at the single-donor level. However, multiple donor levels result in the non-linear behavior of the Mott−Schottky plot. Additionally, non-linearity can be attributed to the non-homogeneous donor contribution in the depletion layer.[66] According to the intersection of the tangent to the plot with the potential axis, the position of flat band potential was determined. For bare TiO_2, it equals to ca. −1.0 V versus Ag/AgCl/0.1 M KCl. According to Grochowska et al.,[67] the flat band potential for pure TiO_2 NTs calcined in a tube furnace at 450 °C in the air atmosphere was equal to −0.67 V versus Ag/AgCl/0.1 M KCl. Therefore, annealing in the argon atmosphere shifts the potential toward more negative values, and causes an increase in the concentration of defects. Furthermore, the second region covering both 1 and 2 segments exhibits a decrease of the slope (2.72×10^8 cm^4 F^{-2}/V) compared to segment 3 (5.65×10^8 cm^4 F^{-2}/V) that may be caused by (1) multiple donor levels[65] or (2) a larger space charge layer built at the base of TiO_2NTs.[64] The concentration of donors for the AR-TiO_2NTs equals 3.84×10^{33} cm^3. In the case of the AR-10AuCu/TiO_2NTs, the dependence of the Mott−Schottky plot shows a complex shape because the material includes a greater amount of conductive oxide nanostructures. Determination of the donor concentration will be here significantly burdened with an error because of the dielectric constant that is used in the calculations will be different for those materials. Assuming that titanium dioxide included in the 10AuCu/TiO_2NTs makes the larger share, comparing both slopes in section 3 indicates the higher concentration of donors in the modified electrode. The concentration of donors for the 10AuCu/TiO_2NTs electrode is equal to ca. 1.52×10^{34} cm^3 assuming that the dielectric constant for the TiO_2 semiconductor is 65 F/m.[68] According to Radecka et al.,[68] the flat band potential as well as donor density were counted for the Cr-doped TiO_2 electrode despite the non-linear behavior of the Mott−Schottky plot. Similar to Xu et al.'s[69] report concerning the $Ca_2Nb_3O_{11}$/FTO electrode, three regions of the different slopes were observed. In our case, this phenomenon results not only from the presence of three types of semiconductors such as TiO_2, Cu_2O, and CuO but is also affected by the nature of their conductivity. According to Ding et al.,[70] TiO_2 is a n-type, whereas Cu_2O and CuO are p-type semiconductors. As a result of the combination of these oxides, a p−n heterojunction can be formed. The slope obtained from the Mott−Schottky curve can define the type of semiconductor: n-type, the positive slope; p-type, the negative slope.[71] Although, TiO_2 NTs are covered by AuCu NPs containing Cu_2O as well as CuO oxides, it should be kept in mind that TiO_2 NTs take the greater part of the electrode. For this reason, no negative slope is visible indicating that the obtained material as a whole is an n-type semiconductor.[72] To gain a better understanding of this material, the schematic energy band diagrams of electrodes are presented in Figure 10b. When the AR-10AuCu/TiO_2NT electrode is illuminated with light, the electrons on the valence band of CuO, Cu_2O, and TiO_2 are excited to the conduction band. The photo-generated electrons from CuO and Cu_2O can be transferred to TiO_2 owing to their higher flat band potential. In addition, a synergetic effect between SPR of AuCuNPs and their light adsorption ability enhances the photoactivity. The

https://doi.org/10.1021/acsami.1c16271
ACS Appl. Mater. Interfaces XXXX, XXX, XXX−XXX

linear fit of region 1 defined as the potential range between +0.1 and −0.3 V provides a flat band potential of ca. −0.7 V versus Ag/AgCl/0.1 M KCl. It is possible that this change is related to the space charge layer capacitance of CuO. When the electrode is more cathodically polarized and reaches the range of −0.6−−0.3 V, the second slope has been determined while the flat band potential equals to ca. −0.9 V. This segment of the Mott−Schottky plot can result from Cu_2O. As it was shown on the CV curves, the reduction process of Cu_2O takes place at −0.5 V versus Ag/AgCl/0.1 M KCl, which can be interpreted as a faradaic reaction on the Mott−Schottky plot. The third region, placed in the most cathodic limit, is characterized by the lowest slope of a linear relationship of C^{-2} versus E than others. The flat band potential determined in this range for the 10AuCu/TiO_2NT electrode equals ca. −1.3 V. The modified electrode flat band potential is cathodically shifted in comparison to pure TiO_2 (from −1 to −1.3 V).[73] The shift toward more negative values can result in more defects. Additionally, the shift of the potential indicates the shift of the Fermi level. Therefore, the Fermi level of the TiO_2-modified AuCu electrode is lower compared to that of pure TiO_2NTs. The Fermi energy of the electrode after immersion into the electrolyte tends to achieve equilibrium with the Fermi level of the redox pair in the electrolyte. It means that it affects the charge transfer and the efficiency of reactions.[74] In summary, the formation of AuCu NPs on TiO_2NTs leads to the increase of the donor concentration, the formation of more defects on the electrode surface, and an enhanced electron mobility.

CONCLUSIONS

In this work, we presented the influence of various annealing atmospheres such as air, vacuum, argon, and hydrogen on properties of bimetallic NPs formed over TiO_2 NTs. The materials were fabricated via the electrochemical anodization process of Ti, AuCu layer magnetron sputtering, and thermal treatment at 450 °C. The different atmospheres have a great impact especially on the chemical structure and electrochemical and photoelectrochemical activities. The XPS spectra confirmed the changes in the ratio of metallic copper to copper oxide. The highest at. % of metallic copper in the form of an AuCu alloy was detected in the electrodes annealed in vacuum and hydrogen. Furthermore, thermal treatment in the argon atmosphere leads to the formation of the CuAuTi alloy on the electrode surface. The CV measurements carried out in 0.1 M NaOH showed intense faradaic peaks for 5AuCu/TiO_2NT and 10AuCu/TiO_2NT electrodes annealed in vacuum, argon, and hydrogen in comparison to the samples fabricated in the air atmosphere. Moreover, TiO_2 NTs modified with AuCu NPs thermally treated in argon exhibited the highest photocurrent in both the visible and UV−vis light range. Furthermore, an investigation using EIS and the Mott−Schottky analysis for doped and pure TiO_2 NTs confirmed the increase of the donor concentration for the AuCu-modified electrode. To sum up, the results reported in this article showed an efficient method for enhancing the photoresponse through annealing in an argon atmosphere.

ASSOCIATED CONTENT

Supporting Information

The Supporting Information is available free of charge at https://pubs.acs.org/doi/10.1021/acsami.1c16271.

EDX map for the AR-10AuCu/TiO_2NTs; Tauc plot for the TiO_2NTs and AuCuNPs/TiO_2NTs; high-resolution XPS spectra of O 1s and Ti 2p for TiO_2NTs and AuCu/TiO_2NTs; CA curves for TiO_2NTs and AuCu/TiO_2NTs registered at −0.2 V versus Ag/AgCl/0.1 M KCl; LV scans for TiO_2NTs and AuCu/TiO_2NTs annealed in air, vacuum, and hydrogen; and $E-t$ scans for AR-TiO_2NTs, AR-5AuCu/TiO_2NTs, and AR-10AuCu/TiO_2NTs (PDF)

AUTHOR INFORMATION

Corresponding Author

Wiktoria Lipińska − *Centre for Plasma and Laser Engineering, The Szewalski Institute of Fluid-Flow Machinery Polish Academy of Sciences, 80-231 Gdańsk, Poland;* orcid.org/0000-0002-4738-2507; Phone: 662240618; Email: wlipinska@imp.gda.pl

Authors

Katarzyna Grochowska − *Centre for Plasma and Laser Engineering, The Szewalski Institute of Fluid-Flow Machinery Polish Academy of Sciences, 80-231 Gdańsk, Poland;* orcid.org/0000-0001-7577-3399

Jacek Ryl − *Institute of Nanotechnology and Materials Engineering, Faculty of Applied Physics and Mathematics and Advanced Materials Center, Gdańsk University of Technology, 80-233 Gdańsk, Poland*

Jakub Karczewski − *Institute of Nanotechnology and Materials Engineering, Faculty of Applied Physics and Mathematics and Advanced Materials Center, Gdańsk University of Technology, 80-233 Gdańsk, Poland*

Katarzyna Siuzdak − *Centre for Plasma and Laser Engineering, The Szewalski Institute of Fluid-Flow Machinery Polish Academy of Sciences, 80-231 Gdańsk, Poland;* orcid.org/0000-0001-7434-6408

Complete contact information is available at: https://pubs.acs.org/10.1021/acsami.1c16271

Notes

The authors declare no competing financial interest.

ACKNOWLEDGMENTS

This research was financially supported by the National Science Centre (Poland): Grant no. 2019/35/N/ST5/02604. K.S. and K.G. acknowledge the financial support of National Science Centre via grant no 2017/26/E/ST5/00416. The authors are very thankful to Prof. M. Sawczak for the help with the photoluminescence spectra measurements.

REFERENCES

(1) Khan, I.; Saeed, K.; Khan, I. Nanoparticles: Properties, Applications and Toxicities. *Arabian J. Chem.* **2019**, *12*, 908−931.

(2) Chen, P.-C.; Liu, X.; Hedrick, J. L.; Xie, Z.; Wang, S.; Lin, Q.-Y.; Hersam, M. C.; Dravid, V. P.; Mirkin, C. A. Polyelemental Nanoparticle Libraries. *Science* **2016**, *352*, 1565−1569.

(3) Yao, Y.; Huang, Z.; Xie, P.; Lacey, S. D.; Jacob, R. J.; Xie, H.; Chen, F.; Nie, A.; Pu, T.; Rehwoldt, M.; Yu, D.; Zachariah, M. R.; Wang, C.; Shahbazian-Yassar, R.; Li, J.; Hu, L. Carbothermal Shock Synthesis of High-entropy-alloy Nanoparticles. *Science* **2018**, *359*, 1489−1494.

(4) Cortie, M. B.; McDonagh, A. M. Synthesis and Optical Properties of Hybrid and Alloy Plasmonic Nanoparticles. *Chem. Rev.* **2011**, *111*, 3713−3735.

(5) Zhang, H.; Pan, J.; Zhou, Q.; Xia, F. Nanometal Thermocatalysts: Transformations, Deactivation, and Mitigation. *Small* **2021**, *17*, 2005771−3005796.

(6) Karthikeyan, B.; Murugavelu, M. Nano bimetallic Ag/Pt system as efficient opto and electrochemical sensing platform towards adenine. *Sens. Actuators, B* **2012**, *163*, 216−223.

(7) Shah, M.; Guo, Q.-X.; Fu, Y. The colloidal synthesis of unsupported nickel-tin bimetallic nanoparticles with tunable composition that have high activity for the reduction of nitroarenes. *Catal. Commun.* **2015**, *65*, 85−90.
(8) Kumar, A.; Guo, C.; Sharma, G.; Pathania, D.; Naushad, M.; Kalia, S.; Dhiman, P. Magnetically recoverable ZrO2/Fe3O4/chitosan nanomaterials for enhanced sunlight driven photoreduction of carcinogenic Cr(vi) and dechlorination & mineralization of 4-chlorophenol from simulated waste water. *RSC Adv.* **2016**, *6*, 13251−13263.
(9) Nasrollahzadeh, M.; Azarian, A.; Maham, M.; Ehsani, A. Synthesis of Au/Pd bimetallic nanoparticles and their application in the Suzuki coupling reaction. *J. Ind. Eng. Chem.* **2015**, *21*, 746−748.
(10) Yu, H.; He, Y. Seed-assisted synthesis of dendritic Au-Ag bimetallic nanoparticles with chemiluminescence activity and their application in glucose detection. *Sens. Actuators, B* **2015**, *209*, 877−882.
(11) Sharma, G.; Kumar, A.; Sharma, S.; Naushad, M.; Prakash Dwivedi, R.; Alothman, Z. A.; Mola, G. T. Novel Development of Nanoparticles to Bimetallic Nanoparticles and their Composites: A Review. *J. King Saud Univ., Sci.* **2019**, *31*, 257−269.
(12) Fiuza, T. E. R.; Zanchet, D. Supported AuCu Alloy Nanoparticles for the Preferential Oxidation of CO (CO-PROX). *ACS Appl. Nano Mater.* **2020**, *3*, 932−934.
(13) Gawande, M. B.; Goswami, A.; Felpin, F.-X.; Asefa, T.; Huang, X.; Silva, R.; Zou, X.; Zboril, R.; Varma, R. S. Cu and Cu-Based Nanoparticles: Synthesis and Applications in Catalysis. *Chem. Rev.* **2016**, *116*, 3722−3811.
(14) Xu, Z.; Lai, E.; Shao-Horn, Y.; Hamad-Schifferli, K. Compositional Dependence of the Stability of AuCu Alloy Nanoparticles. *Chem. Commun.* **2012**, *48*, 5626−5628.
(15) Thota, S.; Wang, Y.; Zhao, J. Colloidal Au-Cu alloy nanoparticles: synthesis, optical properties and applications. *Mater. Chem. Front.* **2018**, *2*, 1074−1089.
(16) Dai, S.; You, Y.; Zhang, S.; Cai, W.; Xu, M.; Xie, L.; Wu, R.; Graham, G. W.; Pan, X. In Situ Atomic-scale Observation of Oxygen-driven Core-shell Formation in Pt3Co Nanoparticles. *Nat. Commun.* **2017**, *8*, 204.
(17) Zhan, W.; Wang, J.; Wang, H.; Zhang, J.; Liu, X.; Zhang, P.; Chi, M.; Guo, Y.; Guo, Y.; Lu, G.; Sun, S.; Dai, S.; Zhu, H. Crystal Structural Effect of AuCu Alloy Nanoparticles on Catalytic CO Oxidation. *J. Am. Chem. Soc.* **2017**, *139*, 8846−8854.
(18) Yin, J.; Shan, S.; Yang, L.; Mott, D.; Malis, O.; Petkov, V.; Cai, F.; Shan Ng, M.; Luo, J.; Chen, B. H.; Engelhard, M.; Zhong, C.-J. Gold-Copper Nanoparticles: Nanostructural Evolution and Bifunctional Catalytic Sites. *Chem. Mater.* **2012**, *24*, 4662−4674.
(19) Destro, P.; Kokumai, T. M.; Scarpellini, A.; Pasquale, L.; Manna, L.; Colombo, M.; Zanchet, D. The Crucial Role of the Support in the Transformations of Bimetallic Nanoparticles and Catalytic Performance. *ACS Catal.* **2018**, *8*, 1031−1037.
(20) Haryński, Ł.; Karczewski, J.; Ryl, J.; Grochowska, K.; Siuzdak, K. Rapid Development of the Photoresponse and Oxygen Evolution of TiO_2 Nanotubes Sputtered with Cr Thin Films Realized via Laser Annealing. *J. Alloys Compd.* **2021**, *877*, 160316−160325.
(21) Song, H.; Cheng, K.; Guo, H.; Wang, F.; Wang, J.; Zhu, N.; Bai, M.; Wang, X. Effect of ethylene glycol concentration on the morphology and catalytic properties of TiO2 nanotubes. *Catal. Commun.* **2017**, *97*, 23−26.
(22) Momeni, M. M.; Ghayeb, Y.; Ghonchegi, Z. Fabrication and characterization of copper doped TiO2 nanotube arrays by in situ electrochemical method as efficient visible-light photocatalyst. *Ceram. Int.* **2015**, *41*, 8735−8741.
(23) Momeni, M. M.; Ghayeb, Y.; Ezati, F. Fabrication, characterization and photoelectrochemical activity of tungsten-copper co-sensitized TiO2 nanotube composite photoanodes. *J. Colloid Interface Sci.* **2018**, *514*, 70−82.
(24) Momeni, M. M. Fabrication of copper decorated tungsten oxide-titanium oxide nanotubes by photochemical deposition technique and their photocatalytic application under visible light. *Appl. Surf. Sci.* **2015**, *357*, 160−166.
(25) Momeni, M. M.; Ghayeb, Y. Photoinduced deposition of gold nanoparticles on TiO_2−WO_3 nanotube films as efficient photoanodes for solar water splitting. *Appl. Phys. A: Mater. Sci. Process.* **2016**, *122*, 620.
(26) Sharifi, T.; Ghayeb, Y.; Mohammadi, T.; Momeni, M. M. Enhanced photoelectrochemical water splitting of CrTiO2 nanotube photoanodes by the decoration of their surface via the photodeposition of Ag and Au. *Dalton Trans.* **2018**, *47*, 11593−11604.
(27) Momeni, M. M.; Mohammadi, N.; Mirhosseini, M. Photo catalytic property of Pt-CuO nanostructure films prepared by wet-chemical route and photochemical deposition method. *J. Mater. Sci.: Mater. Electron.* **2016**, *27*, 10147−10156.
(28) Momeni, M. M.; Ghayeb, Y.; Menati, M. Fabrication, characterization and photoelectrochemical properties of cuprous oxide-reduced graphene oxide photocatalysts for hydrogen generation. *J. Mater. Sci.: Mater. Electron.* **2017**, *29*, 4136−4146.
(29) Bechelany, M.; Maeder, X.; Riesterer, J.; Hankache, J.; Lerose, D.; Christiansen, S.; Michler, J.; Philippe, L. Synthesis Mechanisms of Organized Gold Nanoparticles: Influence of Annealing Temperature and Atmosphere. *Cryst. Growth Des.* **2010**, *10*, 587−596.
(30) Jafari, A.; Jahromi, S. P.; Boustani, K.; Goh, B. T.; Huang, N. M. Evolution of Structural and Magnetic Properties of Nickel Oxide Nanoparticles: Influence of Annealing Ambient and Temperature. *J. Magn. Magn. Mater.* **2019**, *469*, 383−390.
(31) Boeva, O.; Antonov, A.; Zhavoronkova, K. Influence of the Nature of IB Group Metals on Catalytic Activity in Reactions of Homomolecular Hydrogen Exchange on Cu, Ag, Au Nanoparticles. *Catal. Commun.* **2021**, *148*, 106173−106179.
(32) Girault, M.; Le Garrec, J.-L.; Mitchell, J. B. A.; Jouvard, J.-M.; Carvou, E.; Menneveux, J.; Yu, J.; Ouf, F.-X.; Carles, S.; Potin, V.; Pillon, G.; Bourgeois, S.; Perez, J.; Marco de Lucas, M. C.; Lavisse, L. Influence of the Reactive Atmosphere on the Formation of Nanoparticles in the Plasma Plume Induced by Nanosecond Pulsed Laser Irradiation of Metallic Targets at Atmospheric Pressure and High Repetition Rate. *Appl. Surf. Sci.* **2016**, *374*, 132−137.
(33) Wang, D.; Liu, L.; Zhang, F.; Tao, K.; Pippel, E.; Domen, K. Spontaneous Phase and Morphology Transformations of Anodized Titania Nanotubes Induced by Water at Room Temperature. *Nano Lett.* **2011**, *11*, 3649−3655.
(34) Wang, X. W.; Gao, X. P.; Li, G. R.; Gao, L.; Yan, T. Y.; Zhu, H. Y. Ferromagnetism of Co-doped TiO2(B) nanotubes. *Appl. Phys. Lett.* **2007**, *91*, 143102−143106.
(35) Chen, X.; Liu, L.; Huang, F. Black titanium dioxide (TiO2) nanomaterials. *Chem. Soc. Rev.* **2015**, *44*, 1861−1885.
(36) Ramanandan, G. K. P.; Adam, A. J. L.; Ramakrishnan, G.; Petrik, P.; Hendrikx, R.; Planken, P. C. M. Optical Characterization of Gold-cuprous Oxide Interfaces for Terahertz Emission Applications. *Appl. Opt.* **2014**, *53*, 1994−2000.
(37) Cheng, C.; Amini, A.; Zhu, C.; Xu, Z.; Song, H.; Wang, N. Enhanced photocatalytic performance of TiO2-ZnO hybrid nanostructures. *Sci. Rep.* **2014**, *4*, 4181−4186.
(38) Ali, S. M.; Khan, M. A. M. Annealing effects on structural, optical and electrical properties of TiO2/FTO heterojunction. *Appl. Phys. A: Mater. Sci. Process.* **2020**, *126*, 468−475.
(39) Gonçalves, M.; Pereira, J.; Matos, J.; Vasconcelos, H. Photonic Band Gap and Bactericide Performance of Amorphous Sol-Gel Titania: An Alternative to Crystalline TiO2. *Molecules* **2018**, *23*, 1677−1697.
(40) Grochowska, K.; Molenda, Z.; Karczewski, J.; Bachmann, J.; Darowicki, K.; Ryl, J.; Siuzdak, K. Laser induced formation of copper species over TiO2 nanotubes towards enhanced water splitting performance. *Int. J. Hydrogen Energy* **2020**, *45*, 19192−19205.
(41) Prasai, B.; Cai, B.; Underwood, M. K.; Lewis, J. P.; Drabold, D. A. Properties of Amorphous and Crystalline Titanium Dioxide from First Principles. *J. Mater. Sci.* **2012**, *47*, 7515−7521.
(42) Meng, M.; Zhou, S.; Yang, L.; Gan, Z.; Liu, K.; Tian, F.; Zhu, Y.; Li, C.; Liu, W.; Yuan, H.; Zhang, Y. Hydrogenated TiO2 nanotube

https://doi.org/10.1021/acsami.1c16271
ACS Appl. Mater. Interfaces XXXX, XXX, XXX−XXX

photonic crystals for enhanced photoelectrochemical water splitting. *Nanotechnology* **2018**, *29*, 155401−155426.
(43) Hannula, M.; Ali-Löytty, H.; Lahtonen, K.; Sarlin, E.; Saari, J.; Valden, M. Improved Stability of Atomic Layer Deposited Amorphous TiO2 Photoelectrode Coatings by Thermally Induced Oxygen Defects. *Chem. Mater.* **2018**, *30*, 1199−1208.
(44) Nycz, M.; Paradowska, E.; Arkusz, K.; Pijanowska, D. G. Influence of geometry and annealing temperature in argon atmosphere of TiO2 nanotubes on their electrochemical properties. *Acta Bioeng. Biomech.* **2020**, *22*, 165−177.
(45) Vasilaki, E.; Vernardou, D.; Kenanakis, G.; Vamvakaki, M.; Katsarakis, N. TiO2/WO3 photoactive bilayers in the UV-Vis light region. *Appl. Phys. A: Mater. Sci. Process.* **2017**, *123*, 231−240.
(46) Wawrzyniak, J.; Karczewski, J.; Kupracz, P.; Grochowska, K.; Załęski, K.; Pshyk, O.; Coy, E.; Bartmański, M.; Szkodo, M.; Siuzdak, K. Laser-assisted modification of titanium dioxide nanotubes in a tilted mode as surface modification and patterning strategy. *Appl. Surf. Sci.* **2020**, *508*, 145143−145153.
(47) Abazović, N. D.; Comor, M. I.; Dramićanin, M. D.; Jovanović, D. J.; Ahrenkiel, S. P.; Nedeljković, J. M. Photoluminescence of anatase and rutile TiO2 particles. *J. Phys. Chem. B* **2006**, *110*, 25366−25370.
(48) Pallotti, D. K.; Passoni, L.; Maddalena, P.; Di Fonzo, F.; Lettieri, S. Photoluminescence Mechanisms in Anatase and Rutile TiO2. *J. Phys. Chem. C* **2017**, *121*, 9011−9021.
(49) Mercado, C.; Seeley, Z.; Bandyopadhyay, A.; Bose, S.; McHale, J. L. Photoluminescence of Dense Nanocrystalline Titanium Dioxide Thin Films: Effect of Doping and Thickness and Relation to Gas Sensing. *ACS Appl. Mater. Interfaces* **2011**, *3*, 2281−2288.
(50) Patel, S. B.; Hamlekhan, A.; Royhman, D.; Butt, A.; Yuan, J.; Shokuhfar, T.; Sukotjo, C.; Mathew, M. T.; Jursich, G.; Takoudis, C. G. Enhancing surface characteristics of Ti-6Al-4V for bio-implants using integrated anodization and thermal oxidation. *J. Mater. Chem. B* **2014**, *2*, 3597−3608.
(51) Gao, Q.; Wu, X.; Fan, Y. The effect of iron ions on the anatase-rutile phase transformation of titania (TiO2) in mica-titania pigments. *Dyes Pigm.* **2012**, *95*, 96−101.
(52) Fesenko, O.; Yatsenko, L. *Nanoplasmonics, Nano-Optics, Nanocomposites and Surface Studies*; Springer Proceedings in Physics; Springer, 2015; Vol. *167*, pp 1−489.
(53) Lipińska, W.; Ryl, J.; Slepski, P.; Siuzdak, K.; Grochowska, K. Exploring Multi-step Glucose Oxidation Kinetics at GOx-functionalized Nanotextured Gold Surfaces with Differential Impedimetric Technique. *Measurement* **2021**, *174*, 109015−109026.
(54) Li, L.; Li, Z.; Zhang, H.; Zhang, S.; Majeed, I.; Tan, B. Effect of Polymer Ligand Structures on Fluorescence of Gold Clusters Prepared by Photoreduction. *Nanoscale* **2013**, *5*, 1986−1993.
(55) Lipińska, W.; Grochowska, K.; Karczewski, J.; Ryl, J.; Cenian, A.; Siuzdak, K. Thermally Tuneable Optical and Electrochemical Properties of Au-Cu Nanomosaic Formed over the Host Titanium Dimples. *Chem. Eng. J.* **2020**, *399*, 125673−125685.
(56) Yao, G.; Wu, L.; Lv, T.; Li, J.; Huang, Y.; Dong, K.; Li, X. The effect of CuO modification for a TiO2 nanotube confined CeO2 catalyst on the catalytic combustion of butane. *Open Chem.* **2018**, *16*, 1−8.
(57) Giri, S. D.; Sarkar, A. Electrochemical Study of Bulk and Monolayer Copper in Alkaline Solution. *J. Electrochem. Soc.* **2016**, *163*, H252−H259.
(58) Shen, N.; Xu, H.; Zhao, W.; Zhao, Y.; Zhang, X. Highly Responsive and Ultrasensitive Non-Enzymatic Electrochemical Glucose Sensor Based on Au Foam. *Sensors* **2019**, *19*, 1203−1213.
(59) Tamirat, A. G.; Dubale, A. A.; Su, W.-N.; Chen, H.-M.; Hwang, B.-J. Sequentially Surface Modified Hematite Enables Lower Applied Bias Photoelectrochemical Water Splitting. *Phys. Chem. Chem. Phys.* **2017**, *19*, 20881−20890.
(60) Pilarczyk, K.; Kwolek, P.; Podborska, A.; Gawęda, S.; Oszajca, M.; Szaciłowski, K. Unconventional Computing Realized with Hybrid Materials Exhibiting the PhotoElectrochemical Photocurrent Switching (PEPS) Effect. *Advances in Unconventional Computing*; Springer, 2017; Vol. *23*, pp 429−467.
(61) Somasundaram, S.; Chenthamarakshan, C. R.; de Tacconi, N. R.; Ming, Y.; Rajeshwar, K. Photoassisted Deposition of Chalcogenide Semiconductors on the Titanium Dioxide Surface: Mechanistic and Other Aspects. *Chem. Mater.* **2004**, *16*, 3846−3852.
(62) Rajeshwar, K.; de Tacconi, N. R.; Chenthamarakshan, C. R. Spatially Directed Electrosynthesis of Semiconductors for Photoelectrochemical Applications. *Curr. Opin. Solid State Mater. Sci.* **2004**, *8*, 173−182.
(63) Asha, K.; Satsangi, V. R.; Shrivastav, R.; Kant, R.; Dass, S. Effect of morphology and impact of the electrode/electrolyte interface on the PEC response of Fe2O3 based systems - comparison of two preparation techniques. *RSC Adv.* **2020**, *10*, 42256−42266.
(64) Muñoz, A. G.; Chen, Q.; Schmuki, P. Interfacial properties of self-organized TiO2 nanotubes studied by impedance spectroscopy. *J. Solid State Electrochem.* **2006**, *11*, 1077−1084.
(65) Lee, E.-J.; Pyun, S.-I. Analysis of nonlinear Mott-Schottky plots obtained from anodically passivating amorphous and polycrystalline TiO2 films. *J. Appl. Electrochem.* **1992**, *22*, 156−160.
(66) Schoonman, J.; Vos, K.; Blasse, G. Donor Densities in TiO2 Photoelectrodes. *J. Electrochem. Soc.* **1981**, *128*, 1154−1157.
(67) Grochowska, K.; Nedyalkov, N.; Karczewski, J.; Haryński, Ł.; Śliwiński, G.; Siuzdak, K. Anodic Titania Nanotubes Decorated with Gold Nanoparticles Produced by Laser-induced Dewetting of Thin Metallic Films. *Sci. Rep.* **2020**, *10*, 20506−20522.
(68) Radecka, M.; Wierzbicka, M.; Komornicki, S.; Rekas, M. Influence of Cr on photoelectrochemical properties of TiO2 thin films. *Phys. B* **2004**, *348*, 160−168.
(69) Xu, P.; Milstein, T. J.; Mallouk, T. E. Flat-Band Potentials of Molecularly Thin Metal Oxide Nanosheets. *ACS Appl. Mater. Interfaces* **2016**, *8*, 11539−11547.
(70) Ding, R. C.; Fan, Y. Z.; Wang, G. S. High Efficient Cu2O/TiO2Nanocomposite Photocatalyst to Degrade Organic Polluant under Visible Light Irradiation. *ChemistrySelect* **2018**, *3*, 1682−1687.
(71) Chandran, R.; C.K.Behera, C. K.; Mallik, A. Electrochemical Impedance (EIS) Behavior of CuInSe 2 (CIS) Thin Films on High Resistance ITO/PET Flexible Substrates. *Mater. Today: Proc.* **2017**, *4*, 12473−12479.
(72) Fu, S.; Chen, J.; Han, H.; Wang, W.; Shi, H.; Fu, J.; Jia, Y. ZnO@Au@Cu2O nanotube arrays as efficient visible-light-driven photoelectrod. *J. Alloys Compd.* **2019**, *799*, 183−192.
(73) Gu, F.; Huang, W.; Wang, S.; Cheng, X.; Hu, Y.; Lee, P. S. Open-circuit voltage improvement in tantalum-doped TiO2 nanocrystals. *Phys. Chem. Chem. Phys.* **2014**, *16*, 25679−25683.
(74) Radecka, M.; Rekas, M.; Trenczek-Zajac, A.; Zakrzewska, K. Importance of the band gap energy and flat band potential for application of modified TiO2 photoanodes in water photolysis. *J. Power Sources* **2008**, *181*, 46−55.

https://doi.org/10.1021/acsami.1c16271
ACS Appl. Mater. Interfaces XXXX, XXX, XXX−XXX

Supporting information to the article A5

Electronic Supplementary Information

Influence of Annealing Atmospheres on Photoelectrochemical Activity of TiO_2 Nanotubes Modified with AuCu Nanoparticles

Wiktoria Lipińska*[1], Katarzyna Grochowska[1], Jacek Ryl[2,3]
Jakub Karczewski[2,3] and Katarzyna Siuzdak[1]

[1]Centre for Plasma and Laser Engineering, The Szewalski Institute of Fluid-Flow Machinery Polish Academy of Sciences, Fiszera 14 St., 80-231 Gdańsk, Poland

[2]Institute of Nanotechnology and Materials Engineering, Faculty of Applied Physics and Mathematics, Gdańsk University of Technology, Narutowicza 11/12 St., 80-233 Gdańsk, Poland

[3]Advanced Materials Center, Gdańsk University of Technology, Narutowicza 11/12 St., 80-233 Gdańsk

***Corresponding author**: e-mail wlipinska@imp.gda.pl

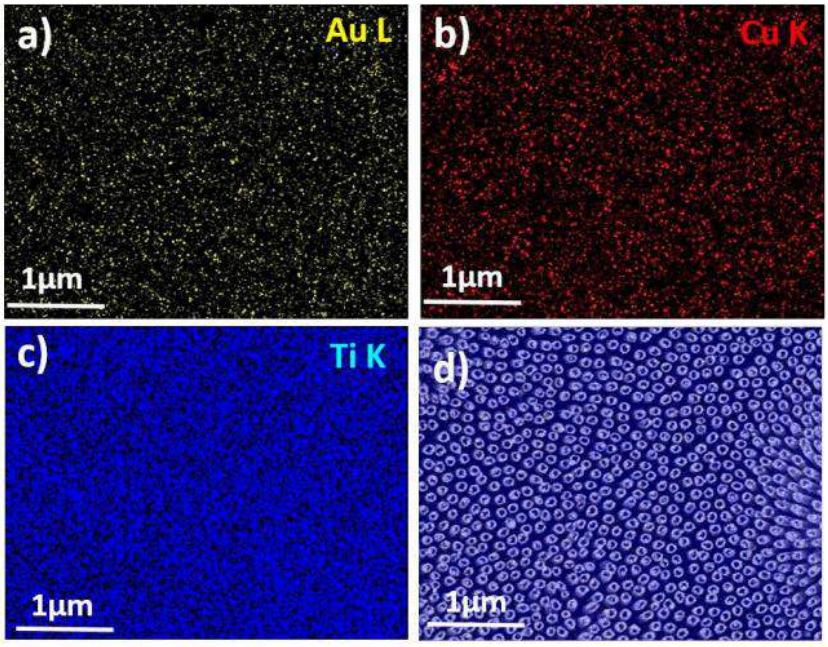

Fig.S1 EDX mapping of a) Au, b) Cu, c) Ti and d) EDX map overlay in SEM images for the AR-10AuCu/TiO_2NTs electrode.

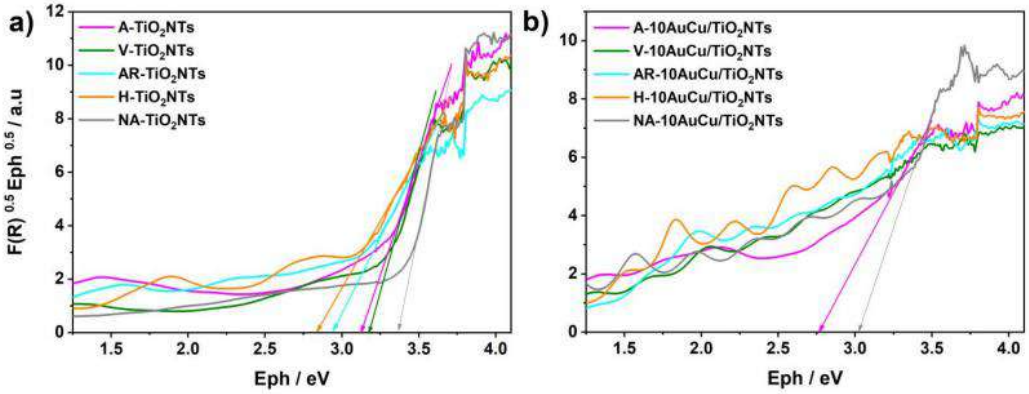

Fig. S2 The Tauc plot for a) titania nanotubes, b) titania nanotubes modified with AuCu NPs.

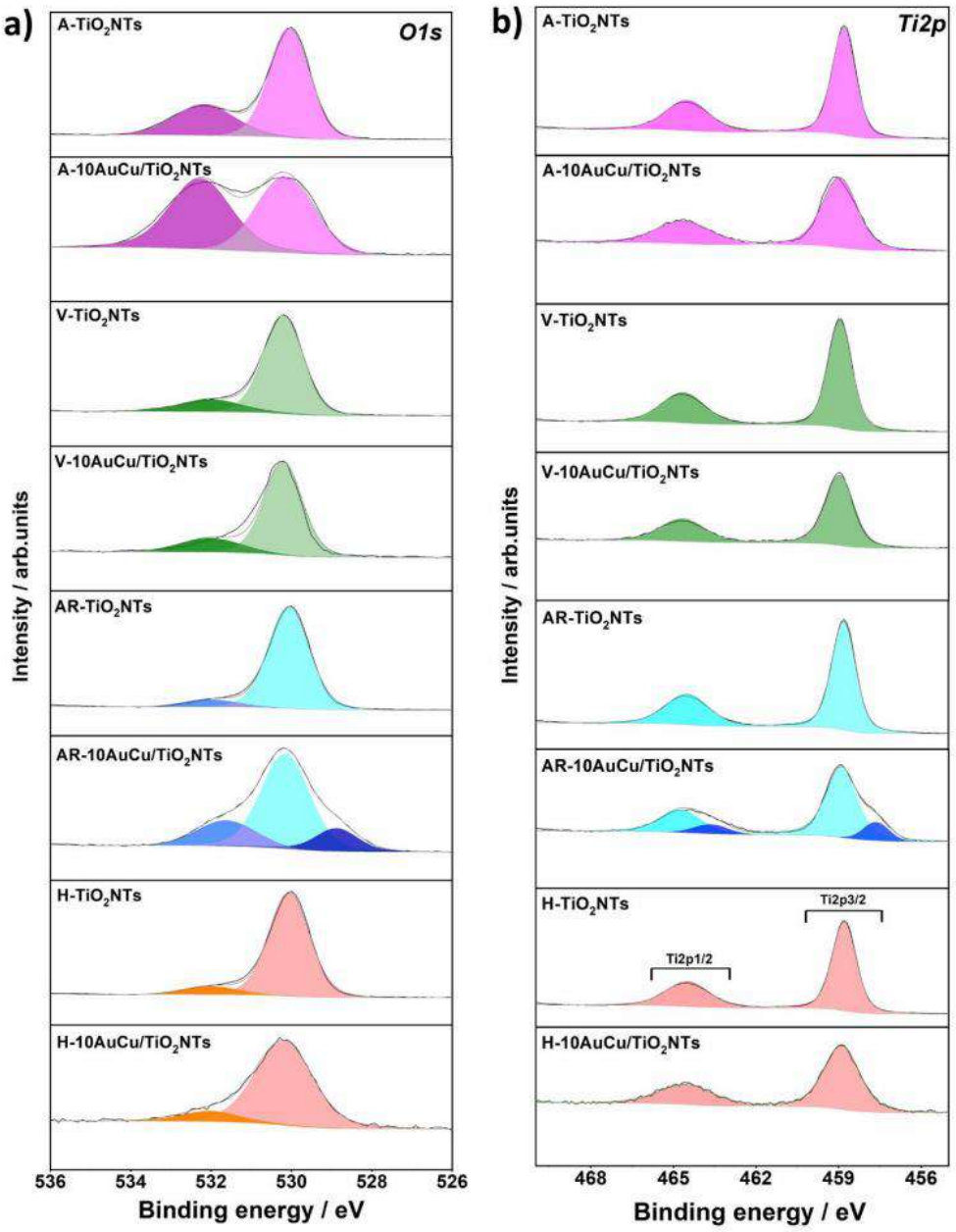

Fig.S3 XPS high resolution spectra registered for TiO_2NTs and 10AuCu/TiO_2NTs samples annealed in air, vacuum, argon and hydrogen a) *O1s*, b) *Ti2p*

Table S1 The binding energies of TiO_2NTs and 10AuCu/TiO_2NTs electrodes annealed in various atmospheres

Peak	Component	BE / eV	At. %
A-TiO_2NTs			
Ti2p 3/2	TiO_2	458.9	34.05
A-10AuCu/TiO_2NTs			
Ti2p 3/2	TiO_2	459.0	14.72
V-TiO_2NTs			
Ti2p 3/2	TiO_2	459.0	34.69
V-10AuCu/TiO_2NTs			
Ti2p 3/2	TiO_2	459.0	17.16
AR-TiO_2NTs			
Ti2p 3/2	TiO_2	458.8	34.25
AR-10AuCu/TiO_2NTs			
Ti2p 3/2	**Ti (CuAuTi)**	**457.6**	**3.00**
Ti2p 3/2	TiO_2	458.9	15.91
H-TiO_2NTs			
Ti2p 3/2	TiO_2	458.8	34.42
H-10AuCu/TiO_2NTs			
Ti2p 3/2	TiO_2	458.9	19.11

Peak	Component	BE / eV	At. %
A-TiO_2NTs			
O1s	O^{2-}	530.0	65.95
O1s	OH^-	532.2	-
A-10AuCu/TiO_2NTs			
O1s	O^{2-}	530.2	48.68
O1s	OH^-	532.3	-
V-TiO_2NTs			
O1s	O^{2-}	530.2	65.31
O1s	OH^-	532.1	-
V-10AuCu/TiO_2NTs			
O1s	O^{2-}	530.2	31.76
O1s	OH^-	532.2	-
AR-TiO_2NTs			
O1s	O^{2-}	530.1	65.75
O1s	OH^-	532.1	-
AR-10AuCu/TiO_2NTs			
O1s	O^{2-}	528.9	8.27
O1s	O^{2-}	530.2	36.7
O1s	OH^-	531.7	-
H-TiO_2NTs			
O1s	O^{2-}	530.1	65.58
O1s	OH^-	532.1	-
H-10AuCu/TiO_2NTs			
O1s	O^{2-}	530.2	42.15
O1s	OH^-	532.1	-

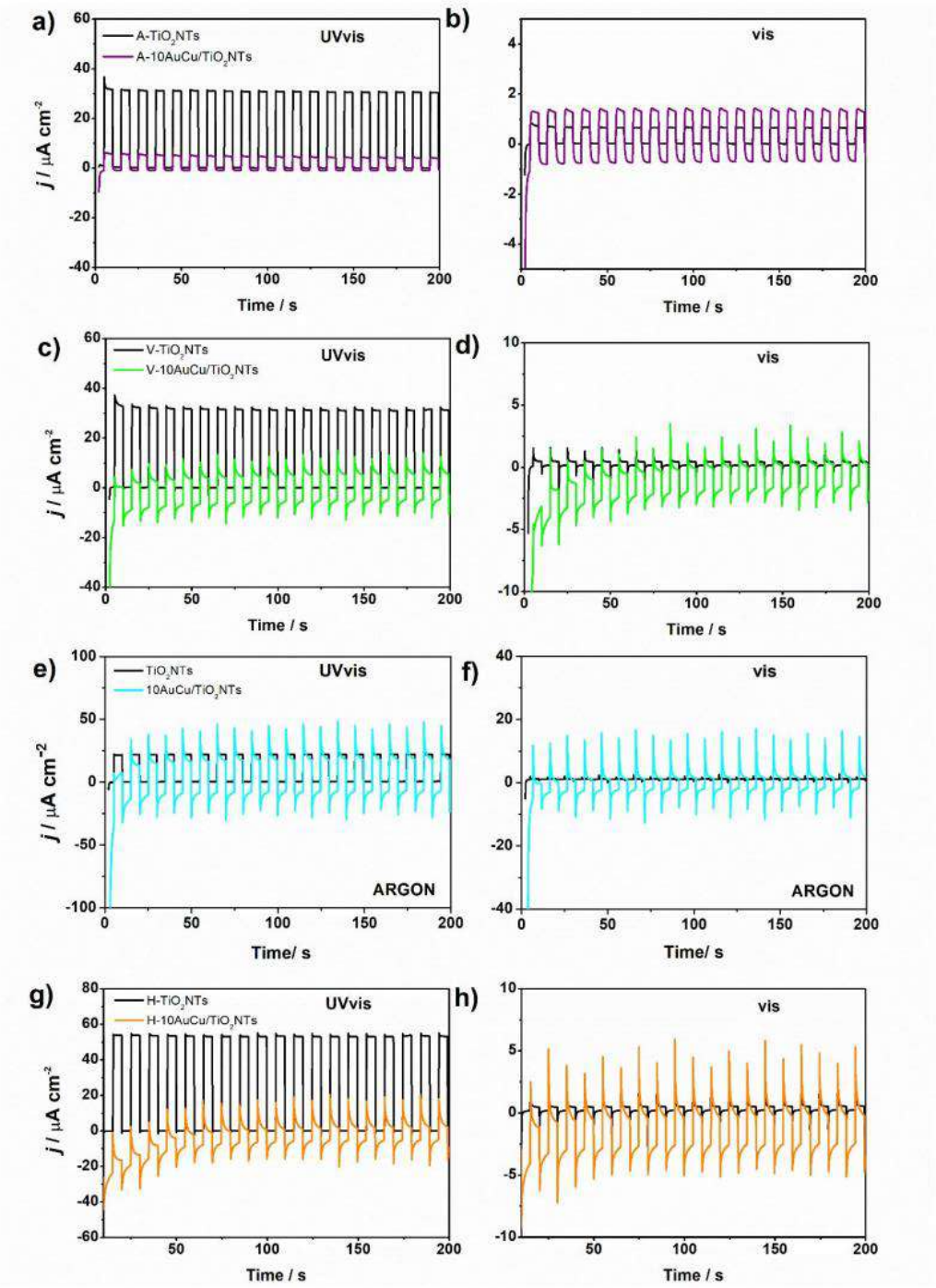

Fig.S4 The chronoamperometry curves registered in 0.1M NaOH for TiO_2NTs and 10AuCu/TiO_2NTs annealed in air, vacuum, argon and hydrogen at -0.2V under a, c, e, g) UV-vis and b, d, f, h) vis illumination.

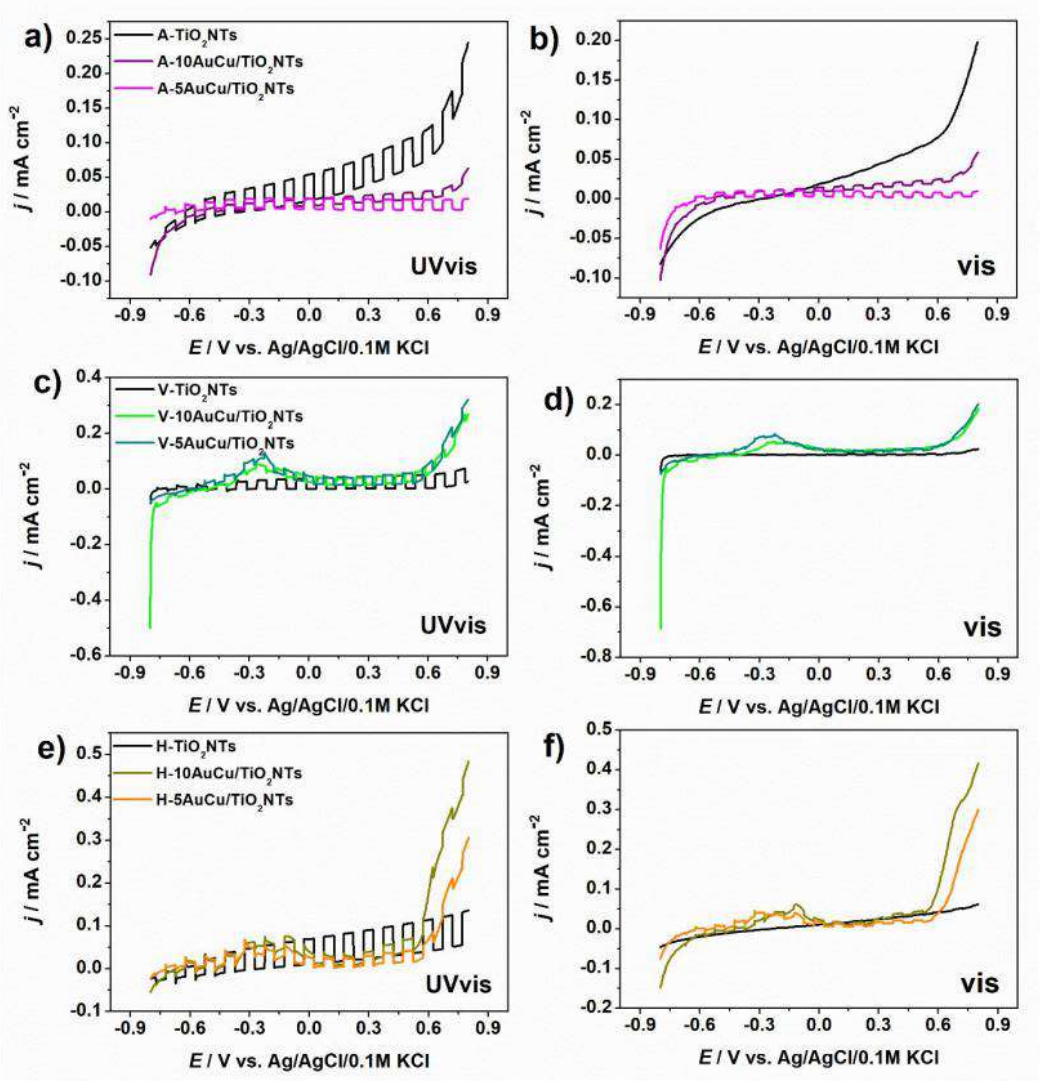

Fig. S5 The linear voltammetry scan registered in 0.1M NaOH for TiO_2NTs, 10AuCu/TiO_2NTs, 5AuCu/TiO_2NTs annealed in a-b) air, c-d) vacuum, e-f) hydrogen.

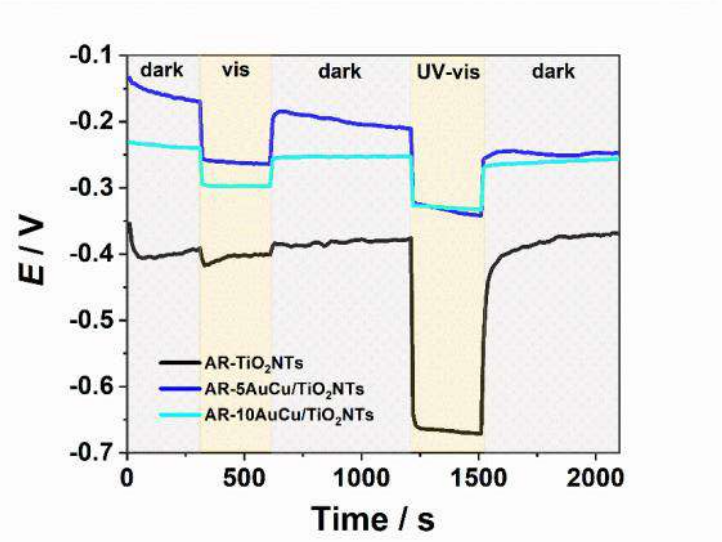

Fig. S6 Chronopotentiometry curves under chopping illumination of AR-TiO_2NTs, AR-5AuCu/TiO_2NTs and AR-10AuCu/TiO_2NTs at OCP conditions.

7.6 Importance of thermal treatment on catalytic and photocatalytic activity of AuCu-modified TiO_2 nanotubes toward alcohol oxidation

Brief overview of the article A6

Introduction

AuCu nanoparticles have many catalytic applications where one of them is methanol[228], glycerol[229] as well as benzyl alcohol oxidation[230]. Therefore, I wanted to find the answer if AuCu bimetallic structures deposited on TiO_2NTs will indicate activity toward alcohol oxidation as well as oxidation assisted by light illumination. As can be find in the literature, upon illumination when the light is periodically switched on and off the transient photocurrent can be registered[231,232]. The life-time of photo-generated charges for the transient photocurrent is shorter than in the case of the state photocurrent. The positive photocurrent spike assigned to capacitance charging of the space charge layer can be registered for anodic photocurrents. In here, positive spikes assigned to hole accumulation were registered for the AR-10AuCu/TiO_2NTs electrode (described in article A5 pages 165-182) (see Figure 62). Therefore, it suggested the possible application of accumulated charges to alcohol oxidation.

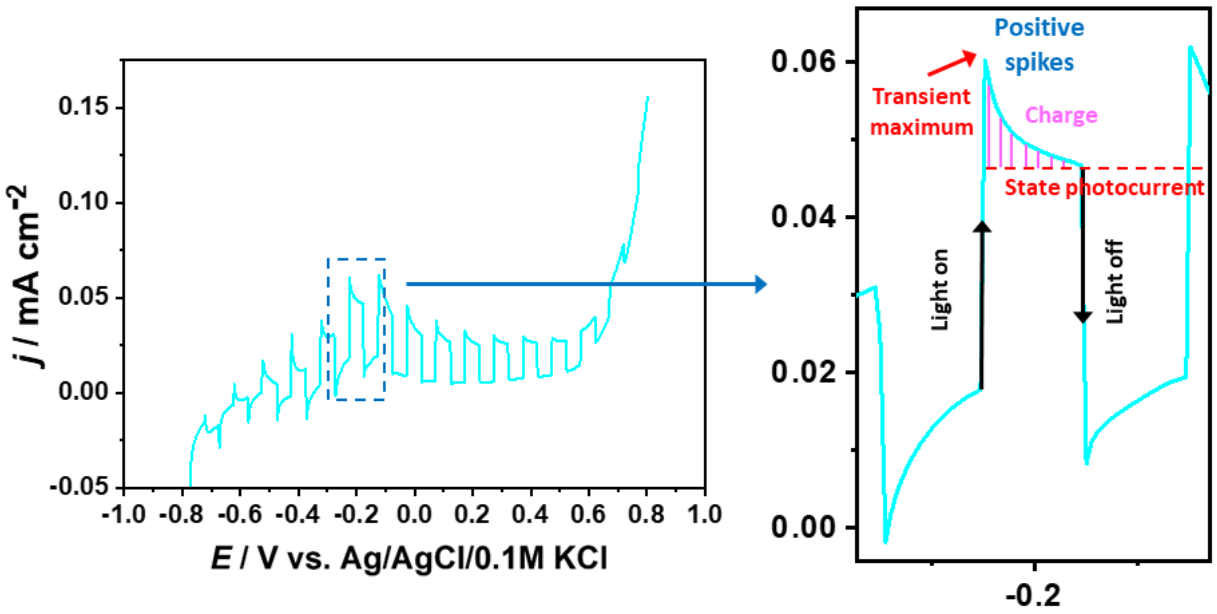

Figure 62. Linear voltammetry curve for the 10AuCu/TiO_2NTs electrode under visible light illumination carried out in 0.1 M NaOH.

In the article A6 bimetallic AuCu nanoparticles formed on TiO_2 nanotubes during annealing in argon atmosphere were measured toward alcohol oxidation. Such alcohols as methanol, ethylene glycol and glycerine were examined. The sample annealed in argon was chosen based on article A5 where it exhibited the highest photocurrent activity under visible light illumination. In here, the question was if AuCu nanoparticles will be electrocatalytically active

as well as photogenerated holes will take part in photocatalytic alcohol oxidation. Furthermore, the activity of non-annealed AuCu layers deposited on TiO_2NTs (n-ACT) were compared with thermally treated bimetallic AuCu electrodes (an-ACT).

Nanomaterials synthesis

AuCu-decorated TiO_2 nanotubes thermally treated in argon were fabricated using the same procedure as in article A5. Due to the fact that, in article A6 no changes in fabrication route were done, the synthesis is not fully described.

Electrochemical and photoelectrochemical properties

The electrochemical activity of non-annealed and annealed AuCu-modified electrodes was characterized by cyclic voltammetry measurements in 0.1 M NaOH solution containing alcohols such as methanol, glycol or glycerine with concentration of 0.5 M. In the case of methanol no oxidation peaks were registered. The oxidation process of ethylene glycol (GE) and glycerine (GLY) takes place both for non-annealed AuCu electrode as well as annealed one (see Figure 63). In the case of annealed ACT electrodes two anodic peaks from $C_2H_4(OH)_2$ and $C_3H_6(OH)_3$ oxidation are located at +0.3 V and +1 V[233]. Values of current density registered at +0.3 and +1 V in 0.1 M NaOH with 0.5 M alcohol are listed in Table 13. The highest enhancement of current density from 38 μA cm^{-2} to 3.6 mA cm^{-2} was obtained for the an-ACT electrode at +0.3 V after glycerine addition. The catalytic process of alcohol oxidation takes place on metallic Au and Cu counterparts. Furthermore, electrocatalytic activity is improved by rapid thermal treatment in argon atmosphere due to electrochemical active surface area extension and much more active sites at their surface[234].

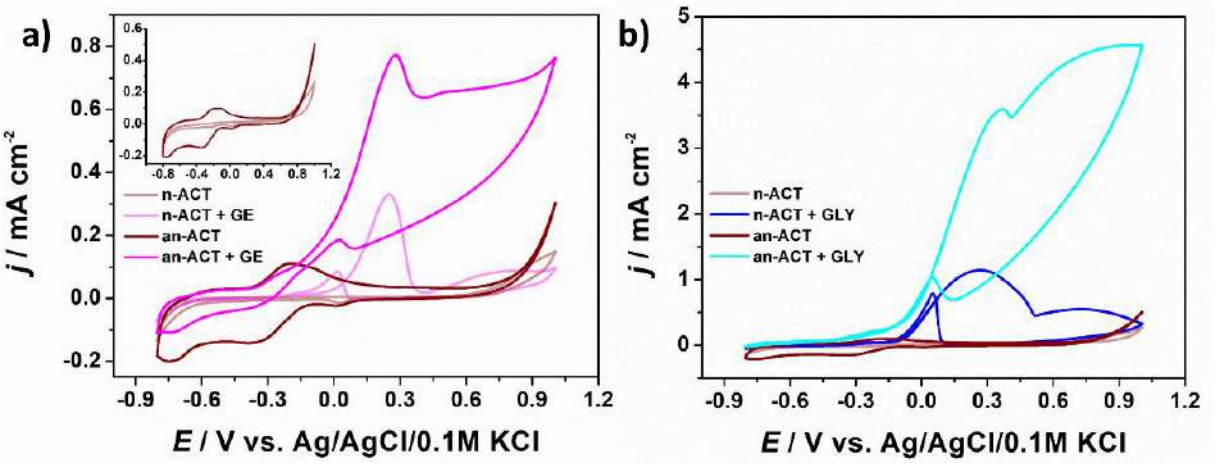

Figure 63. Cyclic voltammetry curves for n-ACT and an-ACT electrodes in 0.1 M NaOH solution without and with 0.5 M a) ethylene glycol and b) glycerine.

Table 13. Values of current density registered at +0.3 and +1 V in 0.1 M NaOH with 0.5 M ethylene glycol and glycerine.

applied potential	+0.3 V vs. Ag/AgCl/0.1 M KCl		+1.0 V vs. Ag/AgCl/0.1 M KCl	
electrolyte	0.1 M NaOH	0.1 M NaOH + 0.5 M ethylene glycol	0.1 M NaOH	0.1 M NaOH + 0.5 M ethylene glycol
	j / μA cm^{-2}		j / μA cm^{-2}	
n-ACT	4	330	149	97
an-ACT	40	800	300	800

electrolyte	0.1 M NaOH	0.1 M NaOH + 0.5 M glycerine	0.1 M NaOH	0.1 M NaOH + 0.5 M glycerine
	j / μA cm^{-2}		j / μA cm^{-2}	
n-ACT	19	1.4 mA cm^{-2}	267	326
an-ACT	38	3.6 mA cm^{-2}	505	4.6 mA cm^{-2}

Further investigation concerning photoelectrochemical activity of n-ACT and an-ACT electrodes was conducted by means of linear voltammetry measurements under continuous visible light illumination in 0.1 M NaOH with alcohol solution. The an-ACT electrode obtained the highest photocurrent in 0.1 M NaOH after glycerine addition at +1 V (Figure 64). The photocurrent was equal to 120 and 360 μA cm^{-2} at +0.3 and +1 V vs. Ag/AgCl/0.1 M KCl. The reaction steps of glycerine oxidation during light illumination are presented in Scheme 2 in article A6. Firstly, when visible light is illuminating the sample, the e-h pairs are generated on titanium dioxide and copper oxides species. Then, holes which are accumulated in the space charge region of Cu_2O and CuO are consumed for glycerine photocatalytic oxidation reaction. Similar as in the case of alcohol oxidation in dark conditions electrodes which were thermally treated in argon are characterized by higher current density values under visible light illumination (see Figure 5 in article A6).

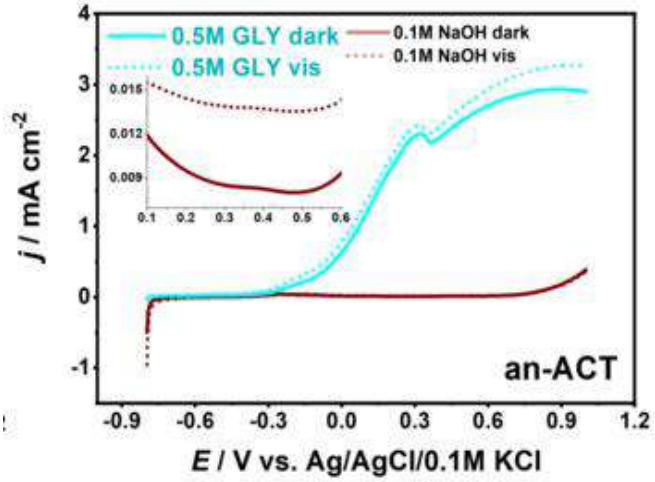

Figure 64. Linear voltammetry curves for an-ACT in dark and under visible light illumination.

Conclusions

In here, AuCu-nanostructures in the form of thin layers (n-ACT) or nanoparticles (an-ACT) on TiO_2 nanotubes were enveloped toward electrochemical and photoelectrochemical alcohol oxidation. Fabricated AuCu electrodes were electrocatalytically active both toward ethylene glycol and glycerine. Rapid thermal annealing in argon enhances activity toward alcohol oxidation therefore an-ACT electrodes are more promoted ones. The highest current density was obtained for the an-ACT electrode after glycerine addition at +0.3 V vs. Ag/AgCl/0.1 M KCl. The value increased ca. 90 times from 38 μA cm^{-2} to 3.6 mA cm^{-2}. Moreover, the highest photocurrent under visible light illumination was also registered for the an-ACT electrode in glycerine solution.

A6) W. Lipińska, K. Grochowska, J. Karczewski, E. Coy, K. Siuzdak, ***Electrocatalytic oxidation of methanol, ethylene glycol and glycerine in alkaline media on TiO_2 nanotubes decorated with AuCu nanoparticles for an application in fuel cells,*** Journal of Materials Science 57 (2022) 13345, IF = 4.7 / 100 points mechanical engineering

J Mater Sci (2022) 57:13345–13361

Chemical routes to materials

Electrocatalytic oxidation of methanol, ethylene glycol and glycerine in alkaline media on TiO_2 nanotubes decorated with AuCu nanoparticles for an application in fuel cells

Wiktoria Lipińska[1,*], Katarzyna Grochowska[1], Jakub Karczewski[2,3], Emerson Coy[4], and Katarzyna Siuzdak[1]

[1] Centre for Plasma and Laser Engineering, The Szewalski Institute of Fluid-Flow Machinery Polish Academy of Sciences, Fiszera 14 St, 80-231 Gdańsk, Poland
[2] Institute of Nanotechnology and Materials Engineering, Faculty of Applied Physics and Mathematics, Gdańsk University of Technology, Narutowicza 11/12 St, 80-233 Gdańsk, Poland
[3] Advanced Materials Center, Gdańsk University of Technology, Narutowicza 11/12 St, 80-233 Gdańsk, Poland
[4] NanoBioMedical Centre, Adam Mickiewicz University, Wszechnicy Piastowskiej 3, 61-614 Poznań, Poland

Received: 31 January 2022
Accepted: 22 June 2022
Published online: 14 July 2022

ABSTRACT

In this work, we present the catalytic and photocatalytic activity of AuCu nanostructures obtained on TiO_2 nanotubes toward methanol, ethylene glycol and glycerine oxidation. The electrode material is prepared by anodization of Ti foil, thin AuCu layer sputtering and rapid thermal treatment under argon atmosphere. Scanning electron microscopy images confirmed the presence of ordered tubular architecture of TiO_2 as well as nanoparticles formed on the surface of the nanotubes. The electrodes were measured using cyclic voltammetry, linear voltammetry and electrochemical impedance spectroscopy in dark and under illumination. Obtained results show a significant current increase: 20 and 90 times higher current density at + 0.3 V versus Ag/AgCl/0.1 M KCl after glycol and glycerine addition, respectively. Moreover, a higher current toward alcohol oxidation was registered for thermally annealed samples than for non-annealed ones. Reported studies demonstrate deep insight into the electrical properties of AuCu-modified titania materials.

Handling Editor: Christopher Blanford.

Address correspondence to E-mail: wlipinska@imp.gda.pl

https://doi.org/10.1007/s10853-022-07471-7

GRAPHICAL ABSTRACT

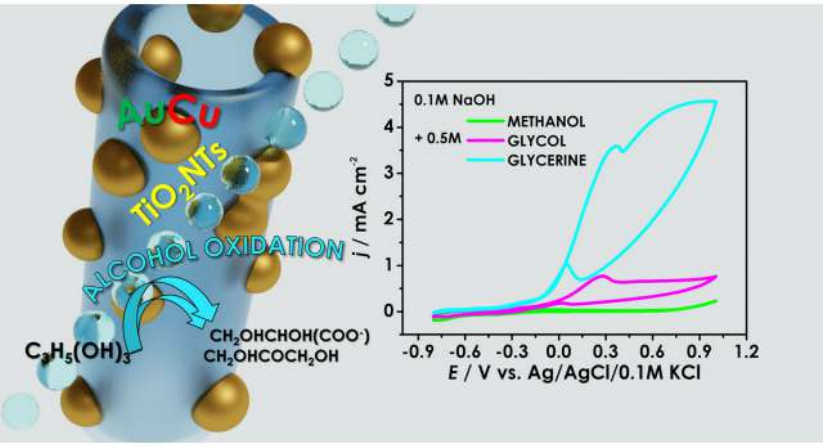

Introduction

Non-renewable energy fuels represent most of the contribution to the world energy production. Raw materials have a limited amount; their extraction and exploitation result in the Earth balance disability and its destruction. It can be seen as climate changes and ecosystem disturbance.

Therefore, nowadays novel energy conversion devices are extremely significant. First fuel cell was discovered 180 years ago and has become extensively studied since that days because of its more environmentally friendly properties than conventional energy sources such as coil or gas [1]. Such devices allow to convert chemical energy into electrical one without pollutant gasses emission [2]. As a fuel, one can distinguish hydrogen [3], methane [4] or alcohol such as methanol, ethanol, glycol and glycerine.

The study of alcohol electrooxidation is of major importance for fuel and electrolytic cells used as a power generation source. Furthermore, the alkaline electrolyte used in those devices can offer a number of advantages comparing to acidic media, such as improved kinetics at both anode and cathode for alcohol oxidation, reduced adsorption of spectator ions as well as lower corrosion rate [5]. The commercial electrodes used in cells are based on Pt plate [6], and therefore, the alternative and economic electrocatalytic materials for alcohol oxidation are of increasing urgency. The Pt catalyst can be replaced with bimetallic gold–copper metallic nanoparticles (NPs) or AuCu NPs supported on platform material which improves their catalytic activity, stability as well as influences on dispersion and size distribution of NPs [7, 8].

In recent years, bimetallic NPs have attracted increasing attention in view of synergistic effect which triggers unique chemical and physical properties of nanoparticles. The bimetallic NPs can be produced by many advanced synthetic methods which allow to control their size, shape, crystal structure and composition [9]. Various morphologies and compositions can enhance catalytic activity of nanoparticles. As far as copper is concerned, it plays a prominent part in improvement of catalytic activity for noble metal such as Au, Pt and Pd owing to weaker strength of metal–CO bonds and better regeneration of active sites [10]. Especially, AuCu NPs are widely used for alcohol oxidation [10, 11] such as methanol, ethanol, glycol, glycerine, benzyl alcohol as well as CO [12] or H_2O_2 [13] oxidation. According to Sobczak and Wolski [14], the AuCu system based on Nb_2O_5 was active toward methanol and glycerol oxidation processes. The addition of copper to Au–Nb_2O_3 increases the activity in contrast

to monometallic gold electrode. Copper which was present in the form of CuO, oligonuclear $[Cu^{\delta+}\cdots O^{\delta-}\cdots Cu^{\delta+}]_n$ clusters and isolated cations, led to changes in the chemical nature of gold resulting in increase in metallic gold content. Moreover, Biswas et al. [15] investigated more efficient methanol oxidation reaction on the AuCu bimetallic nanostructures than on their monometallic counterparts. Furthermore, Palacio et al. [16] converted glycerol in aqueous media at high reaction temperature of 200 °C on the $AuCu/CeO_2$ catalyst and showed that copper improved gold activity owing to higher selectivity and longer catalytic lifetime. Apart from pure catalytic processes, also photocatalytic oxidation of alcohols is strongly developed field [17] since the process can be supported by the solar radiation. Then photons are responsible for initiation of the chemical reaction on metal/semiconductor interface [17] in contrast to electrocatalysis where metal active sites are responsible for it. Higher photocatalytic activity resulting from light harvesting in visible light and promotion of charge separation is facilitated by surface plasmon resonance of Au and Cu NPs [18]. According to Chen et al. [18], $AuCu@CeO_2$ bimetallic-core CeO_2 shell nanocomposite exhibits high activity toward benzyl alcohol photocatalytic oxidation. Furthermore, the Cu species improve the catalytic oxidation via AuCu alloy and oxygen vacancy formation. The AuCu NPs can be fabricated using bottom-up or top-down methods. The synthesis of such nanoparticles by bottom-up technique can be performed using $HAuCl_4{\cdot}H_2O$ and $Cu(CH_3COO)_2{\cdot}H_2O$ liquid solutions with heating at the temperatures in the range of 80–300 °C [19]. As an example of top-down method, Au and Cu magnetron sputtering with further heating up to ca. 300 °C in Ar or N_2 atmosphere can be performed [20].

In our work, we present the properties of gold–copper-modified titania nanotubes (TiO_2NTs) fabricated via electrochemical anodization of Ti foil, thin AuCu layers magnetron sputtering and rapid thermal annealing (RTA) in argon atmosphere. Nanomaterials morphology was characterized using scanning and transmission electron microscopy (SEM, TEM) techniques. The electrocatalytic and photocatalytic activities were tested toward methanol, ethylene glycol and glycerine oxidation. The electrochemical measurements were carried out in 0.1 M NaOH solution containing alcohol using cyclic voltammetry (CV), linear voltammetry (LV) and electrochemical impedance spectroscopy (EIS) in dark and under visible light electrode illumination. It should be highlighted that, attention has been also paid to the comparison between catalytic efficiency of non-annealed and annealed bimetallic electrodes. Thermally treated materials have larger active surface and more active sites used for alcohol oxidation. As it was expected, thermal treatment strongly influences on stability and activity of fabricated materials.

Experimental

Materials

Titanium foil (99.7%, Strem), acetone (99.5%, Chempur), ethanol (96%, Chempur), ammonium fluoride (Chempur), diethylene glycol (99.5% Chempur), hydrofluoric acid (Chempur) were used for the electrochemical anodization process. The AuCu target (Au50/Cu50 At%, Goodfellow) and targets of gold (99.99%, Quorum Technologies) and copper (99.99%, Quorum Technologies) were exploited for metal layer deposition. The Ar gas (Air Liquide Polska Sp. z o o.) was used for thermal annealing as well as electrolyte deaeration. NaOH (P.P.H "STANLAB" Sp. J), methanol (ME, 99.8%, POCH), ethylene glycol (GE, 99.5%, Chempur), glycerine (GLY, POCH) were used for electrochemical measurements.

Electrode fabrication

Firstly, the Ti foil was cut into 2 × 3 cm^2 plates and ultrasonically cleaned in acetone, ethanol and water for 10 min. Titania nanotubes were fabricated via electrochemical anodization process in a two-electrode system, where Ti was an anode and Pt mesh was used as a cathode. The electrolyte contained 0.09 M NH_4F/1.3% vol. HF/6.2% vol. H_2O/92.5% vol. diethylene glycol. The anodization was carried out in thermostated glass cell at the temperature of 40 °C and the voltage of 30 V for 2 h. After anodization TiO_2 nanotubes were rinsed with ethanol and dried in cold air. Secondly, nanotubes were covered by thin 10 nm thick AuCu alloy layer by magnetron sputtering (Q150T S system, Quorum Technologies). Samples which were fabricated up to this step are labeled as n-ACT. Next electrodes were thermally treated in a Rapid Thermal Annealing

furnace (MILA 5000 P-N) at 450 °C for 1 h in argon atmosphere. TiO_2 nanotubes modified by AuCu alloy and annealed in RTA are assigned as an-ACT. Moreover, as a reference sample pure TiO_2 nanotubes were thermally treated also in the same conditions and an-ACT was used as their label. The applied fabrication procedure for monometallic electrodes consisted of electrochemical anodization of Ti plate, magnetron sputtering of thin 5 nm Au or Cu layers and thermal treatment also (assigned as an-AT and an-CT, respectively).

Samples characterization

The morphology and cross section of the samples were investigated by the field emission scanning electron microscope (FEI Quanta FEG250) equipped with an ET secondary detector and with the beam accelerating voltage kept at 10 kV. The nanotubes and nanoparticles size was analyzed by Gwyddion. The an-ACT sample was measured in aberration-corrected high-resolution transmission electron microscope (JEOL ARM 200F) equipped with an EDX (energy-dispersive X-ray) detector. Measurements were performed at an accelerating voltage of 200 eV. The electrochemical and photoelectrochemical measurements of pure and modified nanotubes were conducted using potentiostat–galvanostat system (AutoLab PGStat 302 N) in three-electrode arrangement, where TiO_2NTs, n-ACT and an-ACT served as working electrodes (WE), Pt mesh as counter electrode (CE) and Ag/AgCl/0.1 M KCl as a reference electrode (RE). All electrochemical measurements were carried out in deaerated 0.1 M NaOH solution and 0.1 M NaOH with 0.5 M methanol, 0.5 M ethylene glycol or 0.5 M glycerine. Cyclic and linear voltammetry curves were registered from -0.8 V to + 1 V with a scan rate of 50 mV/s and 10 mV/s, respectively. LV scans under visible light illumination were measured using xenon lamp (LOT-QuantumDesign GmbH). Electrochemical impedance spectroscopy measurements were conducted for an-ACT sample at frequency from 20 kHz to 0.1 Hz covering 20 points per decade and with 0.01 V amplitude at the open circuit potential (OCP) in dark and during electrode illumination. The impedance data were analyzed on the basis of an electrical equivalent circuit (EEQC) via EIS Spectrum Analyser.

Results and discussion

Morphology

Figure 1 shows the morphology of the pure titania nanotubes and nanotubes modified by gold–copper nanoparticles. The diameter of TiO_2NTs is equal to 101 ± 13 nm and the wall thickness to 13 ± 3 nm. Moreover, cross section image of nanotubes allows the determination of length: 709 ± 53 nm. Nanotubes were covered by thin AuCu layer using magnetron sputtering resulting in increase in wall thickness up to 20 ± 4 nm. After thermal treatment spherical gold–copper nanoparticles with a diameter of 38 ± 5 nm were formed on the NTs surface. The AuCu NPs are present in the crown position [21] as well as on nanotubes walls. The TEM images showed that particles are consistently bigger at the top of the TiO_2 nanotubes (Fig. 2). The diameter changes from ca. 60 to ca. 5 nm. EDX images allow to confirm the presence of AuCu nanoparticles and their distribution mostly in the upper part of nanotubes. The thorough studies of other physicochemical properties of prepared material can be found in our previous work [22].

Electrochemical performance

The electrochemical activity toward alcohol electrooxidation of non-annealed and annealed ACT as well as TiO_2NTs electrodes was characterized using cyclic voltammetry. In this work, the measurements were carried out in 0.1 M NaOH solution containing methanol, ethylene glycol or glycerine with a concentration of 0.5 M. The results are shown in Fig. 3. The reactions of alcohol electrooxidation in alkaline media (1–3) consume OH^- depending on the number of hydroxyl groups per molecule. The number of electrons captured can be different:

$$CH_3OH + 8OH^- \rightarrow CO_3^{2-} + 6H_2O + 6e^- \quad (1)$$

$$C_2H_4(OH)_2 + 14OH^- \rightarrow 2CO_3^{2-} + 10H_2O + 10e^- \quad (2)$$

$$C_3H_5(OH)_3 + 20OH^- \rightarrow 3CO_3^{2-} + 14H_2O + 14e^- \quad (3)$$

The number of electrons indicates the available amount of energy accumulated in particular alcohol [23] for further utilization toward energy conversion and storage. After the addition of methanol, no intense peaks related to the alcohol oxidation were observed (Fig. 3a). Moreover, capacitance currents

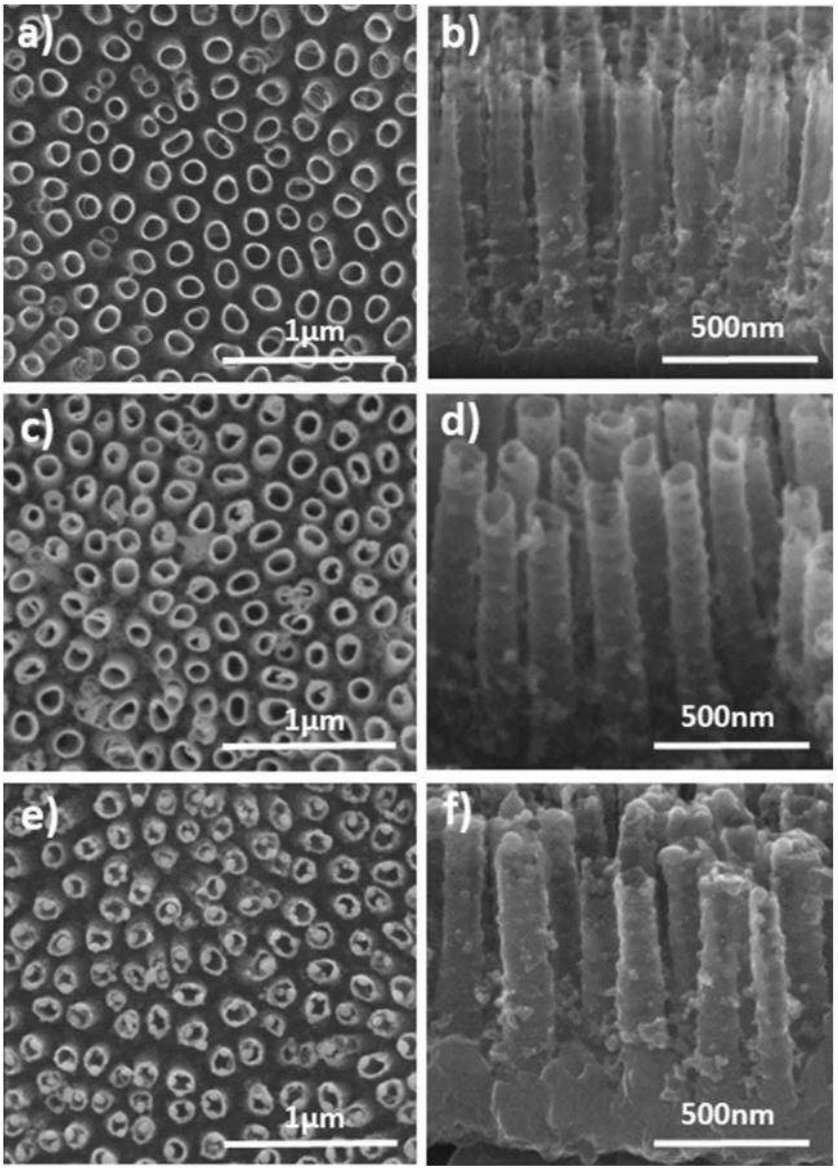

Figure 1 SEM images of **a** TiO_2NTs, **b** cross section of TiO_2NTs, **c** n-ACT, **d** cross section of n-ACT, **e** an-ACT and **f** cross section of an-ACT [22].

densities from − 0.8 V to + 0.1 V were lower in the 0.5 M methanol solution comparing to 0.1 M NaOH, especially for the an-ACT electrode for the reduction peaks at − 0.8 V and − 0.5 V as well as the oxidation peaks at − 0.2 V and + 1 V versus Ag/AgCl/0.1 M KCl. Therefore, the TiO_2NTs, n-ACT and an-ACT materials do not enable electrocatalytic methanol oxidation. According to Biswas et al. [15] pure Cu, Au or Au/Cu nanoparticles exhibited activity for the methanol oxidation at the potential of + 0.55 V, + 0.52 V and + 0.46 V versus Ag/AgCl in 0.5 M methanol solution. The X-ray photoelectron spectroscopy measurements confirmed metallic states of Au located at 83.67 eV and Cu at 932.77 eV in the Au/Cu nanostructure and absence of oxide species [22]. However, in our case, for the an-ACT electrode thermally treated in argon four copper and two gold separate chemical states were identified [22].

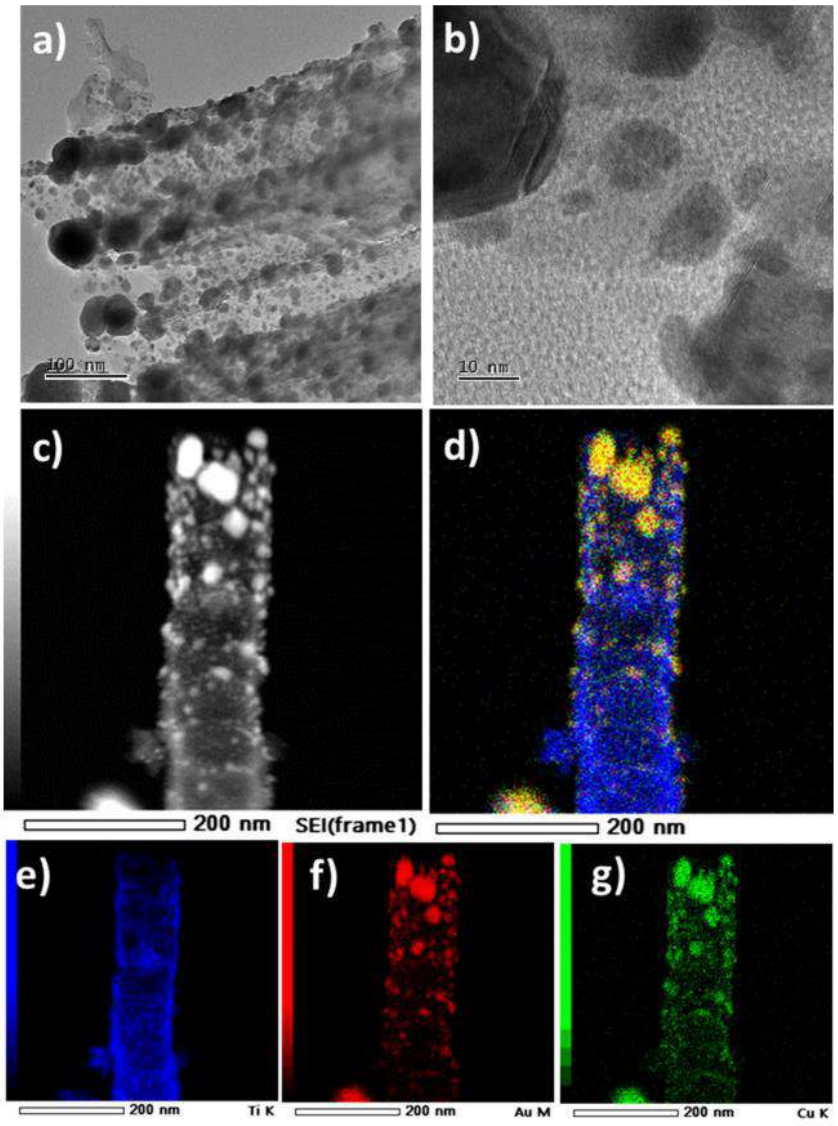

Figure 2 **a**, **b** TEM and **c**–**g** EDX images of an-ACT electrode.

Additionally, CuAuTi, AuCu, CuO, $Cu(OH)_2$. $\times$ $CuCO_3$ and Au_2O were present on the electrode surface. It can indicate that formation of oxides decreases materials activity toward methanol oxidation due to the less-exposed surface atoms of Au and Cu. In the case of ethylene glycol, the oxidation process takes place both for non-annealed AuCu electrode as well as annealed AuCu sample (Fig. 3b). The proposed oxidation mechanism of $C_2H_4(OH)_2$ can be found in the literature [24–27]. The ethylene glycol can be oxidase to oxalate $(COO^-)_2$, formate ($HCOO^-$) or carbonate (CO_3^{2-}). Two intense anodic peaks located at + 0.3 V and + 1 V versus Ag/AgCl/0.1 M KCl can be found for the an-ACT electrode, whereas for the n-ACT sample the second peak is shifted by − 0.25 V. The anodic current density registered at + 0.3 V for the annealed AuCu material increases from ca. 40 μA cm^{-2} to 800 μA cm^{-2} after the ethylene glycol addition while at + 1 V the value enhances from ca. 300 μA cm^{-2} to 800 μA cm^{-2}. The current density due to the glycol oxidation registered at + 0.3 V is 2 times higher for thermally treated

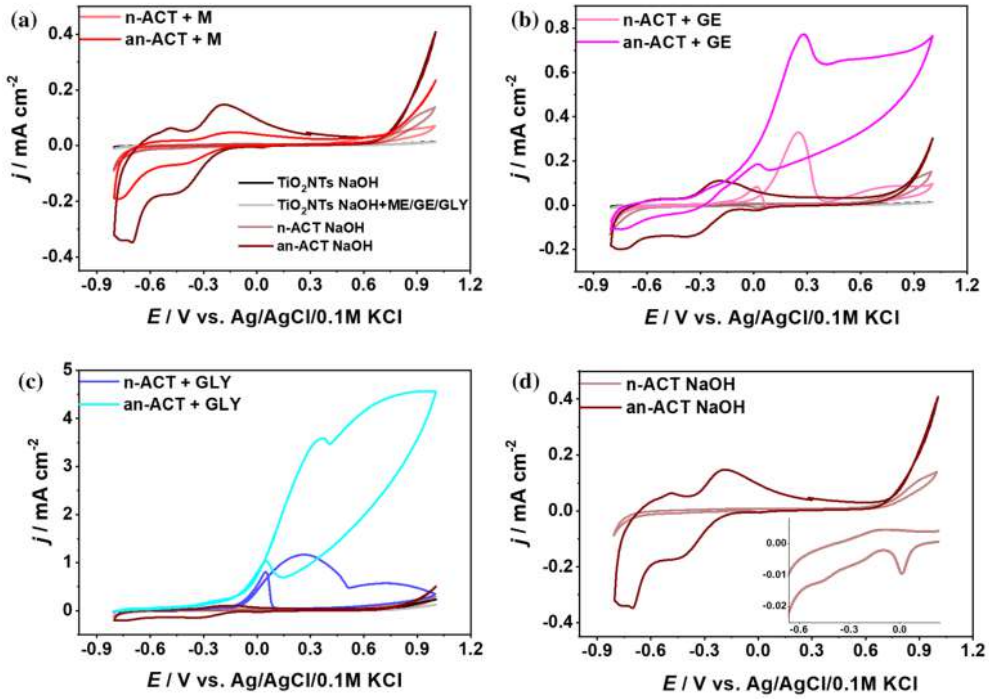

Figure 3 Cyclic voltammetry curves for TiO_2NTs, n-ACT and an-ACT electrodes in 0.1 M NaOH with or without 0.5 M: **a** methanol, **b** ethylene glycol, **c** glycerine and **d** 0.1 M NaOH.

bimetallic electrode than for the non-annealed one. Moreover, the value of current density at + 1 V is about 8 times higher for the an-ACT electrode than for the n-ACT sample. As for the ACT sample fabricated using the RTA furnace, the electrocatalytic activity toward glycol oxidation is much more intensive than for materials without the thermal treatment which is caused by the larger electrochemical active surface area and a greater amount of active sites [28]. Besides, it should be evoked here that TiO_2NTs alone are not sensitive to glycol. According to Marelli et al. [9], the highest activity toward benzyl alcohol oxidation with respect to Au monometallic electrode was achieved for sample containing low amount of CuO oxide which partially covers the Au-rich core of the NPs that indicated that the synergistic effect occurs. Whereas, when the CuO completely covers the AuNPs, the reaction is inhibited. It should be highlighted that the catalysis process takes place on Au and Cu metallic components while Cu_2O, CuO or TiO_2 semiconductors are regarded here only as the catalyst support [29]. According to Fashedemi et al. [30], the FeCo@Fe@Pd/C electrode has shown activity in the electrooxidation of ethylene, ethylene glycol and glycerol. The current densities of ca. 4 mA cm^{-2}, 5 mA cm^{-2}, 4.8 mA cm^{-2} at 0 V versus Ag/AgCl/KCl were registered in 0.5 M KOH with 0.5 M ethanol, GE and GLY, respectively. Therefore, the palladium-based material exhibits the best electrocatalytic performance toward ethylene glycol. In our work, the AuCu electrodes are electrocatalytically active both toward glycol and glycerine. The CV scans recorded in alkaline solution with 0.5 M glycerine are shown in Fig. 3c. The peaks located at + 0.3 V and + 1 V correspond to $C_3H_5(OH)_3$ oxidation process [31]. The proposed mechanism can be found in the literature [24, 26, 27], where two various intermediates are possible to be formed during reaction such as glyceric acid $CH_2OHCHOH(COO^-)$ and dihydroxyacetone $CH_2OHCOCH_2OH$. Similarly as for ethylene glycol reaction oxalate, formate and carbonate might be the final products. The significant enhancement of the current density from 38 μA cm^{-2} to 3.6 mA cm^{-2} is recorded for the an-ACT sample at + 0.3 V versus Ag/AgCl/0.1 M KCl after glycerine addition to the

electrolyte. When the electrode is polarized toward more anodic direction the current increase from 505 μA cm^{-2} to even 4.56 mA cm^{-2} at + 1 V is observed. The materials annealed at the RTA furnace exhibit improved activity toward glycerine oxidation than non-annealed ones. The current density of alcohol oxidation was 3 or even 11 times higher at + 0.3 V and + 1 V, respectively. Such improvement was reported by Houache et al., [32] for Ni electrode that was electrochemically treated in the solution of 0.1 M Na_2SO_4 with 30 mM ascorbic acid and 4 times higher current density for glycerol electrooxidation was noted than for the untreated sample. Such behavior was justified by the formation of active sites of nickel oxyhydroxide where catalytic reaction takes place. In the case of our material, we regard that similar phenomena take place. Moreover, we should take into account the CuAuTi alloy which is present only at the an-ACT material [22]. As far as the TiO_2NTs electrode is concerned, no electrocatalytic activity toward glycerine was registered.

Figure 3d presents electrochemical response for n-ACT and an-ACT electrodes registered in 0.1 M NaOH solution. The intense faradic peaks can be observed for the thermally treated sample in contrast to non-annealed material with only one reduction peak located at ca. 0 V which may correspond to reduction of gold oxides [33]. According to Liu et al. [34], unidirectional diffusion from the Au shell to Cu core was explored via thermal alloying. The core–shell samples were heated up to 260 °C finally forming AuCu intermetallic compound. Therefore, various shapes of CVs curves are observed resulting from different internal structures of bimetallic AuCu compounds that underwent change during thermal treatment. For the an-ACT electrode, two anodic and two cathodic peaks associated with copper oxides redox reactions can be distinguished [35]. It can be claimed that two-stage oxidation process of Cu to CuO and reduction of CuO to Cu can be observed for this material [36]. The CV scans correlate with the XPS data for an-ACT electrode where copper was detected in two forms such as metallic Cu (CuAuTi, AuCu) as well as copper (II) oxides [22].

The cyclic voltammetry curves for Au and Cu deposited on TiO_2NTs registered in alkaline solution without and with 0.5 M methanol, ethylene glycol or glycerine are shown in Fig. 4. In the case of methanol, after its addition to the solution no oxidation peak can be observed (Fig. 4a). For ethylene glycol, the oxidation takes place only on gold-modified electrode (Fig. 4b). One oxidation peak at + 1 V versus Ag/AgCl/0.1 M KCl can be distinguished for the an-AT electrode, whereas for the bimetallic AuCu electrodes two anodic peaks located at + 0.3 V and + 1 V were observed. The addition of copper to gold nanoparticles is responsible for synergistic effect and formation of second oxidation peak at lower potentials. Taking into account current density at + 0.3 V for the an-AT electrode its value increased from 23 to 408 μA/cm^2 which is two times lower than for bimetallic an-ACT electrode at the same potential. This behavior confirmed the positive effect of the alloy on the catalytic activity toward ethylene glycol oxidation providing reduction of oxidation potential as well as increase in current density. In the case of glycerine, the activity was also obtained only for gold-modified electrode (Fig. 4c). Here, also only one oxidation peak can be found for the an-AT electrode at + 0.6 V. However, current density recorded at + 0.3 V for the an-AT electrode is 2.5 times higher than for AuCu bimetallic samples.

In order to evaluate the photoactivity of the fabricated nanomaterials, the linear voltammetry measurements in dark and under vis illumination were carried out (Fig. 5). The LV scans were recorded in 0.1 M NaOH and in 0.1 M NaOH with 0.5 M methanol, ethylene glycol or glycerine solution. The n-ACT electrode measured in 0.1 M NaOH as well as with methanol does not show any photocurrent growth, moreover the decrease in current density during illumination can be seen above + 0.75 V versus Ag/AgCl/0.1 M KCl (Fig. 5a). This activity can result from the presence of amorphous TiO_2 in contrast to thermally treated samples. As far as the an-ACT sample is concerned, where TiO_2NTs are present in the crystalline form [22], the addition of methanol caused the increase in photoactivity in the range from − 0.5 V to + 0.8 V (Fig. 5b). It should be highlighted that the presence of bimetallic AuCu structures has got significant effect on LVs results obtained in methanol solution. As it was described above, materials which contain gold and copper are electroactive, namely the oxidation of ethylene glycol and glycerine occurs at their surface. Not only above presented reactions take place but also radical-catalyzed alcohol oxidation by photogenerated holes (photocatalytic activity). According to our earlier work [22], the positive photocurrent spikes for the structures containing AuCu were observed from

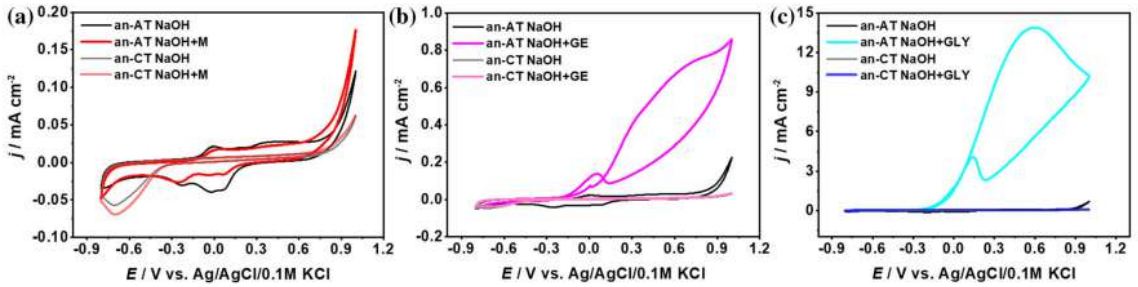

Figure 4 Cyclic voltammetry curves for an-AT and an-CT electrodes in 0.1 M NaOH with or without 0.5 M: **a** methanol, **b** ethylene glycol and **c** glycerine.

− 0.8 to + 0.6 V when the electrode is exposed to light. The mechanism of ethylene glycol oxidation by photogenerated holes is shown in Scheme 1 [37–39].

The electron–hole pairs are generated on TiO_2, Cu_2O and CuO, sequentially holes which come from copper oxides are consumed in the photocatalytic alcohol oxidation. For the n-ACT electrode, the enhancement of current density from 67 μA cm^{-2} to 277 μA cm^{-2} at ca. + 0.3 V in ethylene glycol solution was achieved during light illumination (Fig. 5c). The increase in photocurrent above − 0.3 V versus Ag/AgCl/0.1 M KCl was registered for the an-ACT sample immersed in 0.1 M NaOH with 0.5 M $C_2H_4(OH)$ (Fig. 5d) due to the activity of AuCu annealed at 450 °C in argon atmosphere. Besides, the current grows from 0.5 mA cm^{-2} to 0.73 mA cm^{-2} at the potential of ca. + 0.3 V. The values of photocurrent density defined as the difference between current recorded under illumination and in dark obtained for the non-annealed electrode and the annealed one are quite similar and are equal to 210 μA cm^{-2} and 230 μA cm^{-2} at + 0.3 V, respectively (Table 1). Therefore, it may be related to synergistic effect of copper oxides active under visible light and AuCu presence [40]. Moreover, the photocurrent enhancement for the an-ACT electrode at + 1 V equals to 223 μA cm^{-2}. Furthermore, the photopromoted catalysis of glycerine leads to the increase in current density for the n-ACT and the an-ACT materials. The proposed mechanism is shown in Scheme 2[37, 38, 41].

The n-ACT electrode exhibits the photocurrent increase of 200 μA cm^{-2} registered in 0.1 M NaOH with 0.5 M glycerine at + 0.3 V versus Ag/AgCl/0.1 M KCl, whereas the an-ACT sample—120 μA cm^{-2} (Table 1). However, higher photocurrent of 360 μA cm^{-2} was obtained at + 1 V for the AuCu annealed nanomaterial and the current density at this potential was equal to ca. 3.3 mA cm^{-2}.

Figures 6 and 7 show the CV curves recorded in the solution of ethylene glycol and glycerine, respectively, and clearly the alcohol oxidation at the an-ACT electrode is observed. As it can be seen, in Figs. 6a and 7a with the increase in the scan rate the oxidation peak current density also grows up. A linear relationship between the peak current density and the square root of the scan rate was found up to 90 mV s^{-1} and 120 mV s^{-1} for GE and GLY, respectively (see Figs. 6b and 7b). The results indicate that the oxidation of GE and GLY is diffusion-controlled process [42]. However, it can be also stated that it is not a fully diffusion-controlled process due to the nonzero intercept of the equation [43]. According to Shahrokhian et al. [44], trimetallic Pt–Pd–Co/rGO nanomaterial exhibited dual linear region for the dependency of the anodic peak current density of ethylene oxidation versus scan rate with slopes equal to 812 mA cm^{-2} and 210 mA cm^{-2}. Dual behavior was ascribed to the decreasing rate of GE diffusion to electrode at higher scan rates. The measurements were performed from 0.2 mV/s to 600 mV/s [44]. According to Etesami et al. [43], the effect of scan rate on glycerol electrooxidation on the AuNPs/PG electrode showed increase in anodic peak with increasing scan rate up to 1000 mV/s with a slope of 2.1 mA/cm^2. In the case of ethylene glycol for our materials, two peaks located at + 0.3 V and + 1 V show the same slope equals to 17 μA cm^{-2} mV^{-1} s in contrast to glycerine where 51 and 81 μA cm^{-2} mV^{-1} s were determined. The higher value of slope of a Randles–Sevcik (RDS) plot for glycerine in contrast to ethylene glycol can be correlated with the amount of hydroxyl groups—more hydroxyl groups the greater slope value. According to Khouchaf et al. [45], the peak

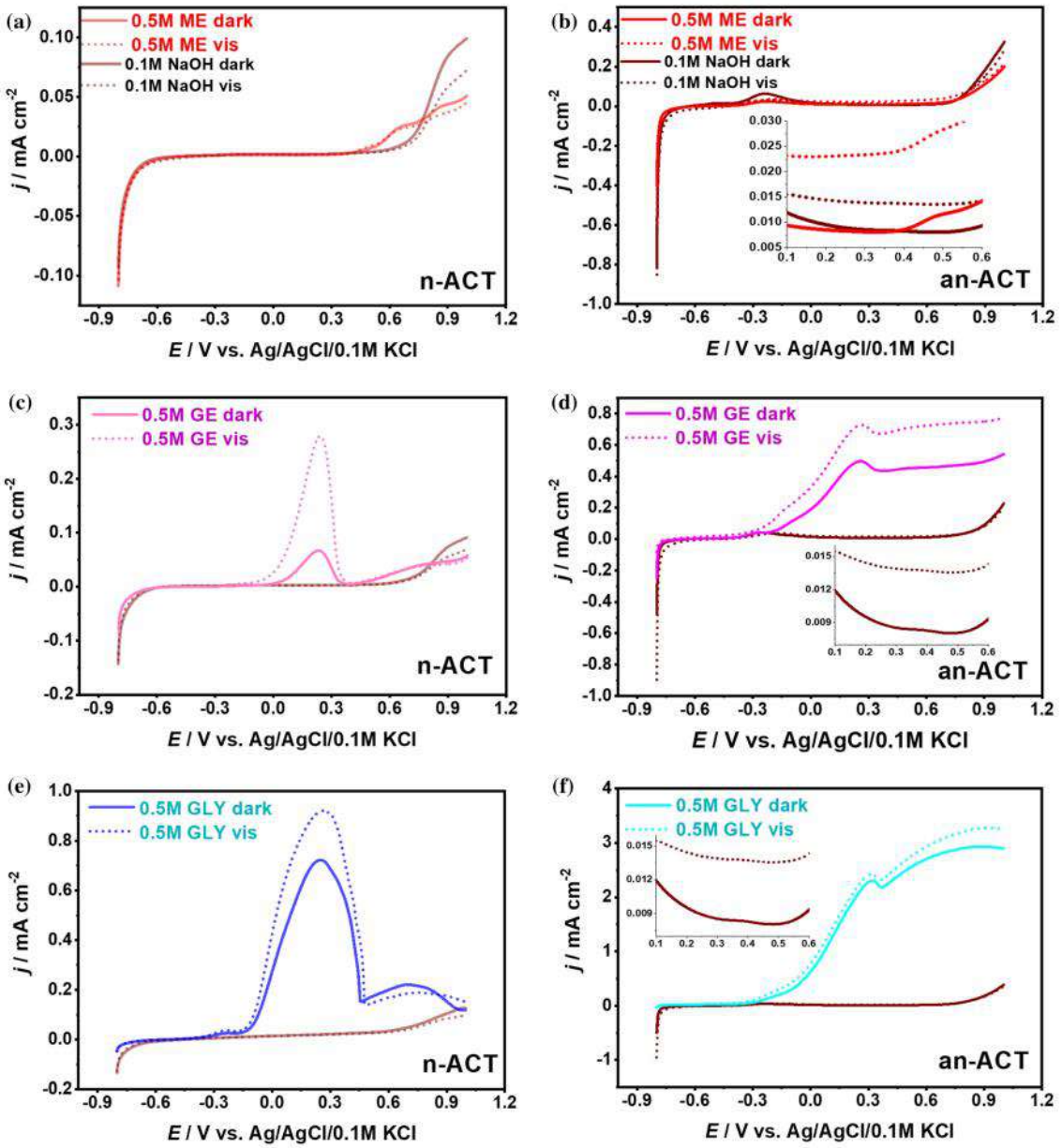

Figure 5 Linear voltammetry curves registered in 0.1 M NaOH without and with 0.5 M **a**, **b** methanol, **c**, **d** ethylene glycol and **e**, **f** glycerine for n-ACT and an-ACT electrodes in dark and under vis illumination. (solid red—n-ACT 0.1 M NaOH dark, dotted red—n-ACT 0.1 M NaOH vis).

located at c.a. 0.0 V versus Ag/AgCl was attributed to Cu/Cu(II) and Cu(I)/Cu(II) oxidation process in alkaline solution, and also it was the potential of methanol oxidation. However, at the potential of + 0.57 V, where Cu(III) was formed in NaOH solution, higher anodic peak resulting from methanol oxidation was obtained. In our case, considering the glycerol containing electrolyte, one may assume that

redox reaction involving high oxidation states of copper is replaced by GLY oxidation and the alcohol oxidation reaction is more promoted at + 1 V than at lower potentials (+ 0.3 V). Difference between $C_2H_4(OH)_2$ and $C_3H_5(OH)_3$ oxidation can be also caused by the interaction strength between the substrate and the adsorbate intermediates [30]. The interaction between the metal d states and the adsorbate states can be measured by density functional (DFT) calculations. As the scan rate exceeded 90 mV/s and 120 mV/s for glycol and glycerine, the current density approaches a plateau due to the reduction of the diffusion barrier resulting in the same concentration of alcohols in the solution and at the electrode surface.

Electrochemical impedance spectroscopy measurements were performed to obtain deeper insight into the electrical performance of the an-ACT electrode immersed in the solutions of different alcohols. The reaction not only depends on the applied potential but also on the availability of the charge carriers, therefore the experiments were carried out at the open circuit potential. Thus, the mechanism of reaction concerned charge transfer between solution and semiconductor as well as chemical bounds and compounds formed at the surface [46]. The Nyquist plots are shown in Fig. 8 while the equivalent electrical circuit used for fitting procedure (R_E(CPER$_{CT}$-W_O)) is presented in Fig. 9.

The R_E element corresponds to the electrolyte resistance, the R_{CT} is the charge transfer resistance, the W_O is the Warburg open element and the CPE corresponds to the constant phase element. The impedance data obtained from Fig. 8 are listed in Tables 2 and 3. After immersion of the electrodes into the electrolyte their potentials have to compensate [47]. In the case of the semiconductor, it is Fermi level, whereas for the electrolyte—the chemical potential. If the Fermi level and the electrolyte potential are not equal, the electron transfer between them occurs. Schematic representation of energy levels and the possible charge transfer at the an-ACT

$$AuCu/TiO_2NTs + hv \longrightarrow e^- + h^+$$
$$C_2H_4(OH)_2 + h^+ \longrightarrow C_2H_3(OH)_2^{\bullet} + H^+$$

Scheme. 1 Oxidation reaction steps of ethylene glycol during material illumination.

Table 1 The photocurrent values for n-ACT and an-ACT electrode at + 0.3 V and + 1 V

	0.1 M NaOH + GE		0.1 M NaOH + GLY	
	Δj/μA cm^{-2}	E/V	Δj/μA cm^{-2}	E/V
n-ACT	210	+ 0.3	200	+ 0.3
an-ACT	230	+ 0.3	120	+ 0.3
	233	+ 1	360	+ 1

$$AuCu/TiO_2NTs + hv \longrightarrow e^- + h^+$$
$$C_3H_5(OH)_3 + h^+ \longrightarrow C_3H_4(OH)_3^{\bullet} + H^+$$

Scheme. 2 Oxidation reaction steps of glycerine during material illumination.

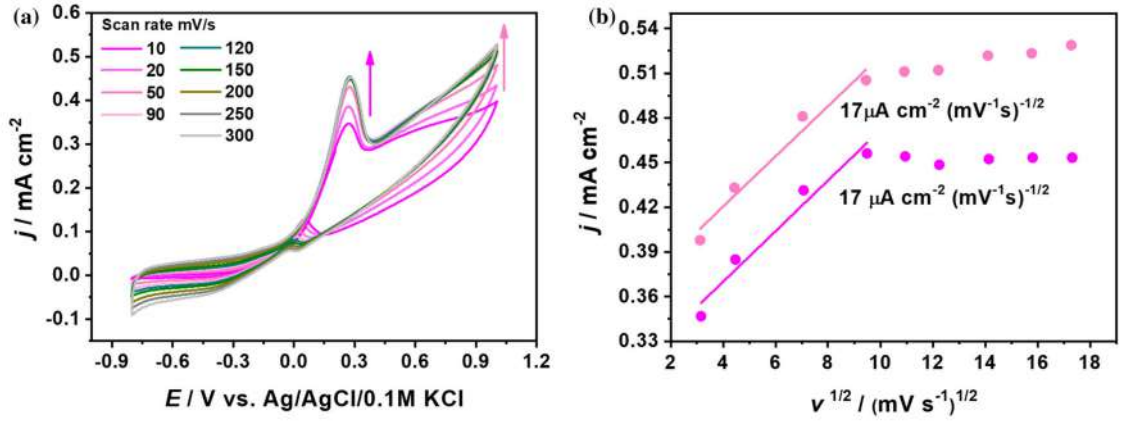

Figure 6 **a** CV curves of ethylene glycol oxidation at the an-ACT electrode at different scan rates in 0.1 M NaOH with 0.5 M GE solution and **b** corresponding calibration curves.

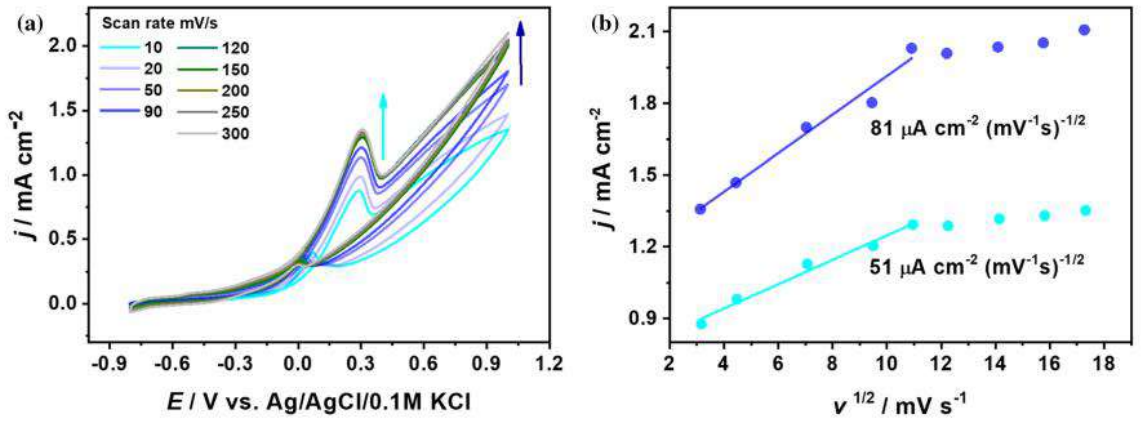

Figure 7 **a** CV curves of glycerine oxidation at the an-ACT electrode at different scan rates in 0.1 M NaOH with 0.5 M GLY solution and **b** corresponding calibration curves.

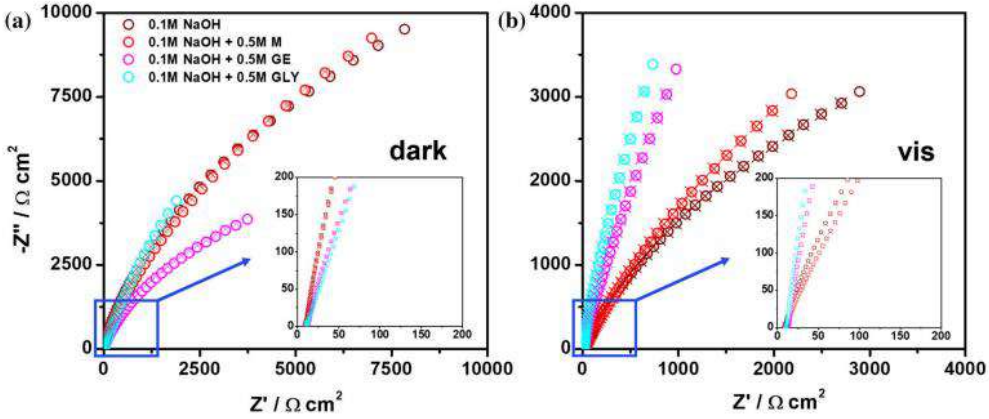

Figure 8 Impedance plots of the an-ACT electrode in methanol, ethylene glycol and glycerine solutions **a** in dark and **b** under vis light illumination.

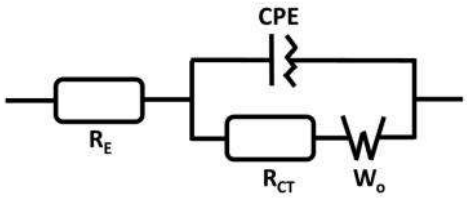

Figure 9 Model of the equivalent electrical circuit.

electrode/electrolyte interface is presented in Fig. 10. The values of potential presented in Fig. 10 above pink and blue bubbles correspond to the maximum of first alcohol oxidation peak on CV curves (Fig. 2).

Taking into account values of the ΔR_{CT} between samples resistance measured in the alkaline solution without and with methanol, ethylene glycol or glycerine was equal to 200, 1000 and 1790 Ω cm^{-2}, respectively. However, the lowest value of R_{CT} equaled to ca. 10 Ωcm^{-2} was measured for electrode immersed in glycerine solution. Such a small value of charge transfer resistance for GLY confirms the highly facilitated electron transfer between glycerine compound and electrode. These results can be correlated with the cyclic voltammetry scans where the highest current density was obtained for the glycerine oxidation. The decrease in the R_{CT} for all the electrodes under their illumination indicates their photoactivity, shift of the energy bands at the boundary of the electrode/electrolyte and a high mobility of carriers in TiO_2 [48]. Moreover, the

Table 2 Electrochemical impedance data for the an-ACT electrode carried out in methanol, ethylene glycol and glycerine solution in dark

Element	Unit	0.1 M NaOH	0.1 M NaOH + ME	0.1 M NaOH + GE	0.1 M NaOH + GLY
R_E	Ωcm^2	9.3	9.3	11.3	9.7
R_{CT}	Ωcm^2	1.8×10^4	1.6×10^4	0.8×10^4	10.2
Q	Fcm^{-2}	7.5×10^{-5}	7.9×10^{-5}	1.67×10^{-4}	2.92×10^{-4}
n		0.886	0.882	0.835	0.767
W_{or}	$\Omega cm^2\ s^{-1/2}$	41.7	305.6	13.5	288.3
W_{oc}	$\Omega cm^2\ s^{-1/2}$	0.0102	0.0594	0.0105	0.0112
χ^2		1.45×10^{-3}	1.84×10^{-3}	1.26×10^{-3}	7.34×10^{-4}

Table 3 Electrochemical impedance data for the an-ACT electrode carried out in methanol, ethylene glycol and glycerine solution under visible light illumination

Element	Unit	0.1 M NaOH	0.1 M NaOH + ME	0.1 M NaOH + GE	0.1 M NaOH + GLY
R_E	Ωcm^2	8.3	8.0	10.1	9.5
R_{CT}	Ωcm^2	0.6×10^4	5.6	1.2	0.5
Q	Fcm^{-2}	1.97×10^{-4}	3.53×10^{-4}	2.45×10^{-4}	2.54×10^{-4}
n		0.796	0.674	0.695	0.805
W_{or}	$\Omega cm^2\ s^{-1/2}$	6.2	10.4	149.9	124.2
W_{oc}	$\Omega cm^2\ s^{-1/2}$	0.0037	0.0003	0.0414	0.0337
χ^2		1.76×10^{-3}	1.24×10^{-3}	7.34×10^{-4}	7.36×10^{-4}

carriers' mobility is enhanced by the addition of alcohol to the electrolyte. As far as the constant phase element is concerned, it can be described by equation: $Z_{CPE} = 1/Q(j\omega)^n$ where Q is CPE parameter and n is CPE exponent with a value of $0 < n < 1$ [49]. In the case when the $n = 1$ the impedance corresponds to the pure capacitor, while for $n = 0$ the CPE is assigned to the resistor. The exponent n determines the surface heterogeneity, whereas Q is a quasi-capacitance of the electrode described as a double layer capacitance or a functionalized layer capacitance [50]. In our case the quasi-capacitance results from the absorbed hydroxyl groups of NaOH, methanol, ethylene glycol and glycerine on nanoparticles, while the heterogeneity originates from the alloy structure and the adsorption sites of alcohols and its coverage. For solid electrodes immersed in the electrolyte typical n value is in the range from 0.7 to 0.9 [51]. The influence of the position of hydroxyl groups of the dihydroxybenzene isomers on the adsorption mechanism was reported by Ryl et al. [52] Resorcinol, the compound containing two hydroxyl groups linked to the benzene ring, was characterized by impedance measurements and the best inhibitor efficiency at the high concentration equals to 100 mM in contrast to the ligand exchange model of adsorption for catechol and quinol at lower concentrations (1 and 10 mM). According to Wysocka et al. [51] when the carboxylic acids corrosion inhibitors fully covered the electrode surface in the form of monolayer, the value of the homogeneity increased and resulted in increase in n values. Therefore, in our case there is a visible decrease in homogeneity along with the growing number of OH groups with simultaneous increase in a quasi-capacitance for experiments carried out in dark. The Warburg open element is attributed to the finite-length diffusion with refractive boundary ascribed by the equation:

$$Z_{W_O}(\omega) = \frac{W_{Or}}{\sqrt{\omega}}(1-j)coth\left[W_{Oc}\sqrt{j\omega}\right] \quad (4)$$

where W_{Or} is equal to Warburg coefficient and $W_{Oc} = d/D^{0.5}$ where d is the thickness of modified layer and D is the diffusion coefficient. The W_{Or} increases after methanol addition to the 0.1 M NaOH solution in dark as well as in light illumination. In the case of electrode immersed in the pure alkaline solution $Cu(OH)_{ads}$ [53] and $Au(OH)_{ads}$ [54] are formed on the surface. For the an-ACT sample in methanol solution, additional alcohol adsorption layer causes increase in the Warburg impedance. Furthermore, after light illumination in both cases, with and without methanol, decrease in W_{Or} and

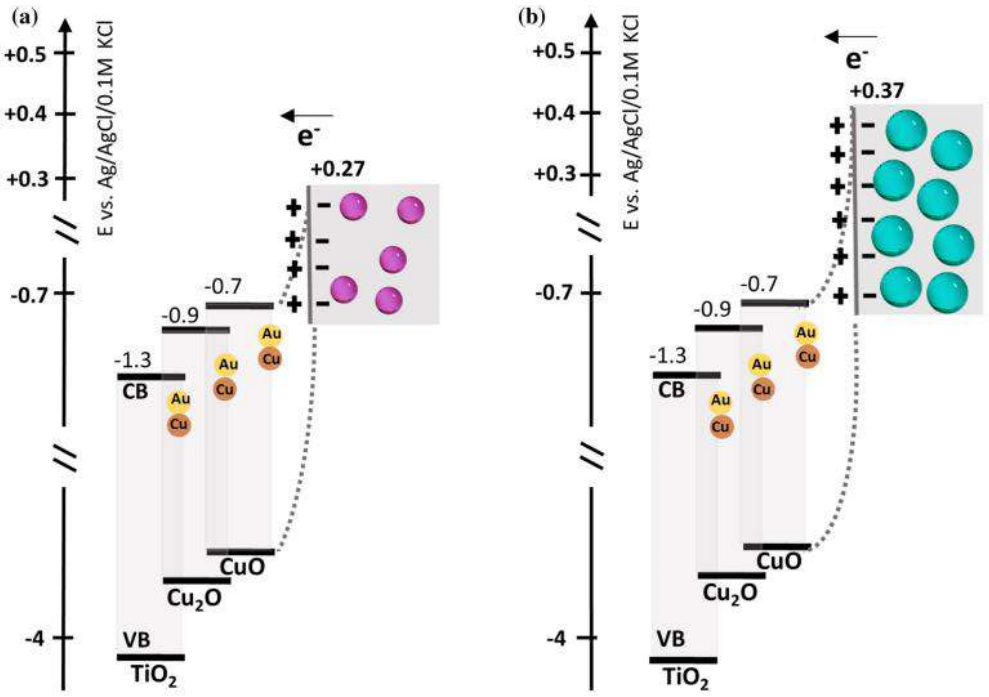

Figure 10 Schematic representation of energy levels and charge transfer for an-ACT electrode in dark in the solution of **a** ethylene glycol and **b** glycerine in 0.1 M NaOH.

W_{Oc} impedance takes place which can be attributed to the photoconductivity of material [55]. Other phenomena can be observed for samples measured in ethylene glycol and glycerine solution where not only alcohol adsorption layer and charge transfer under light illumination but also alcohol oxidation processes are taken into account. According to CV scans, at the OCP potential the beginning of glycol as well as glycerine oxidation, observed as current increase, can be seen, and therefore, not only $Cu(OH)_{ads}$ and alcohol adsorption layer but also intermediates can be present at the electrode/electrolyte interface. The glycol oxidation process is slower than glycerine oxidation. The diffusion coefficient [56] of OH^- is higher for electrode immersed in ethylene glycol than in glycerine which can result in sparser layer at the electrode surface.

Conclusion

In this work, we presented detailed electrochemical results of catalytic active AuCu-modified TiO_2 nanotubes toward ethylene glycol and glycerine oxidation. The electrodes were fabricated via anodization of Ti, AuCu layer sputtering and rapid thermal treatment in an argon atmosphere which resulted in ordered TiO_2 nanostructure with spherical bimetallic nanoparticles. The prepared electrode material exhibited at + 0.3 V versus Ag/AgCl/0.1 M KCl ca. 20 times higher current density after glycol addition and 90 times after glycerine addition to the alkaline electrolyte. It should be highlighted that, annealed bimetallic structures are more catalytically active toward alcohol oxidation than non-annealed ones because of the increased number of Au and Cu active sites. Furthermore, AuCu-modified nanotubes exhibit enhancement of photocurrent under visible light illumination from photocatalytic alcohol oxidation caused by Cu_2O and CuO oxides presence. Moreover, pure titania nanotubes are not sensitive to ethylene glycol and glycerine. Additionally, rapid thermal

annealing in Ar atmosphere of bimetallic electrodes enhanced materials activity toward alcohol oxidation.

Acknowledgements

Research is financed by National Science Centre (Poland): Grant No. 2019/35/N/ST5/02604. KS and KG acknowledge the financial support of National Science Centre (Poland) via Grant No. 2017/26/E/ST5/00416.

Declarations

Conflict of interest The authors declare no competing financial interest.

References

[1] Guaitolini SVM, Yahyaoui I, Fardin JF, Encarnacao LF, Tadeo F (2018) A review of fuel cell and energy cogeneration technologies. 2018 9th International Renewable Energy Congress https://doi.org/10.1109/irec.2018.8362573

[2] Cassir M, Jones D, Ringuedé A, Lair V (2013) Electrochemical devices for energy: fuel cells and electrolytic cells. Handbook of Membrane Reactors 553–606. https://doi.org/10.1533/9780857097347.3.553

[3] Malik FR, Tieqing Z, Kim YB (2020) Temperature and hydrogen flow rate controls of diesel autothermal reformer for 3.6 kW PEM fuel cell system with autoignition delay time analysis. Int J Hydrogen Energy 45:29345–29355. https://doi.org/10.1016/j.ijhydene.2020.07.20

[4] Tu B, Yin Y, Zhang F, Su X, Lyu X, Cheng M (2020) High performance of direct methane-fuelled solid oxide fuel cell with samarium modified nickel-based anode. Int J Hydrogen Energy 45:27587–27596. https://doi.org/10.1016/j.ijhydene.2020.07.07

[5] Bambagioni V, Bevilacqua M, Bianchini C, Filippi J, Marchionni A, Vizza F, Wang LQ, Shen PK (2010) Ethylene glycol electrooxidation on smooth and nanostructured pd electrodes in alkaline media. Fuel Cells 10:582–590. https://doi.org/10.1002/fuce.200900120

[6] Peera SG, Lee TG, Sahu AK (2019) Pt-rare earth metal alloy/metal oxide catalysts for oxygen reduction and alcohol oxidation reactions: an Overview. Sustain Energy Fuels 3:1866–1891. https://doi.org/10.1039/c9se00082h

[7] Kannan R, Kim AR, Yoo DJ (2014) Enhanced electrooxidation of methanol, ethylene glycol, glycerol, and xylitol over a polypyrrole/manganese oxyhydroxide/palladium nanocomposite electrode. J Appl Electrochem 44:893–902. https://doi.org/10.1007/s10800-014-0706-y

[8] Kaur A, Kaur G, Singh PP, Kaushal S (2021) Supported bimetallic nanoparticles as anode catalysts for direct methanol fuel cells: a review. Int J Hydrogen Energy 46:15820–15849. https://doi.org/10.1016/j.ijhydene.2021.02.037

[9] Marelli M, Jouve A, Villa A, Psaro R, Balerna A, Prati L, Evangelisti C (2019) Hybrid Au-CuO nanoparticles: effect of structural features for selective benzyl alcohol oxidation. J Phys Chem C 123:2861–2871. https://doi.org/10.1021/acs.jpcc.8b09449

[10] Xu H, Yan B, Wang J, Zhang K, Li S, Xiong Z, Yang P (2017) Self-supported porous 2D AuCu triangular nanoprisms as model electrocatalysts for ethylene glycol and glycerol oxidation. J Mater Chem A 5:15932–15939. https://doi.org/10.1039/c7ta04598k

[11] Guo W, Yao X, Peng L, Lin B, Kang Y, Gan L (2020) Platinum monolayers stabilized on dealloyed AuCu core-shell nanoparticles for improved activity and stability on methanol oxidation reaction. Chin Chem Lett 31:836–840. https://doi.org/10.1016/j.cclet.2019.06.018

[12] Zhan W, Wang J, Wang H, Zhang J, Liu X, Zhang P, Chi M, Guo Y, Lu G, Sun S, Dan S, Zhu H (2017) Crystal structural effect of aucu alloy nanoparticles on catalytic CO oxidation. J Am Chem Soc 139:8846–8854. https://doi.org/10.1021/jacs.7b01784

[13] Wang N, Han Y, Xu Y, Gao C, Cao X (2014) Detection of H_2O_2 at the nanomolar level by electrode modified with ultrathin AuCu nanowires. Anal Chem 87:457–463. https://doi.org/10.1021/ac502682n

[14] Sobczak I, Wolski Ł (2015) Au–Cu on Nb_2O_5 and Nb/MCF supports – Surface properties and catalytic activity in glycerol and methanol oxidation. Catal Today 254:72–82. https://doi.org/10.1016/j.cattod.2014.10.051

[15] Biswas R, Singh S, Ahmed I, Patil RA, Ma YR, Haldar KK (2021) Rational design of Bimetallic Au/Cu nanostructure: an efficient catalyst for methanol oxidation. ChemNanoMat 7:158–164. https://doi.org/10.1002/cnma.202000578

[16] Palacio R, López D, Hernández D (2019) Bimetallic AuCu nanoparticles supported on CeO_2 as selective catalysts for glycerol conversion to lactic acid in aqueous basic medium. J Nanopart Res 21(7):1–3. https://doi.org/10.1007/s11051-019-4594-2

[17] Schünemann S, Dodekatos G, Tüysüz H (2015) Mesoporous silica supported Au and AuCu nanoparticles for surface plasmon driven glycerol oxidation. Chem Mater 27:7743–7750. https://doi.org/10.1021/acs.chemmater.5b03520

[18] Chen B, Li X, Zheng R, Chen R, Sun X (2017) Bimetallic (Au–Cu core)@(ceria shell) nanotubes for photocatalytic oxidation of benzyl alcohol: improved reactivity by Cu. J Mater Chem A 5:13382–13391. https://doi.org/10.1039/c7ta02047c

[19] Kim D, Xie C, Becknell N, Yu Y, Karamad M, Chan K, Crumlin EJ, Norskov JK, Yang P (2017) Electrochemical activation of CO_2 through atomic ordering transformations of AuCu nanoparticles. J Am Chem Soc 139:8329–8336. https://doi.org/10.1021/jacs.7b03516

[20] Suzuki S, Tomita Y, Kuwabata S, Torimoto T (2015) Synthesis of alloy AuCu nanoparticles with the L10 structure in an ionic liquid using sputter deposition. Dalton Trans 44:4186–4194. https://doi.org/10.1039/c4dt03557g

[21] Nguyen NT, Altomare M, Yoo J, Schmuki P (2015) Efficient photocatalytic H_2 evolution: controlled dewetting-dealloying to fabricate site-selective high-activity nanoporous Au particles on highly ordered TiO_2Nanotube arrays. Adv Mater 27:3208–3215. https://doi.org/10.1002/adma.201500742

[22] Lipińska W, Grochowska K, Ryl J, Karczewski J, Siuzdak K (2021) Influence of annealing atmosphere on photoelectrochemical activity of TiO_2 nanotubes modified with AuCu nanoparticles. ACS Appl Mater Interfaces 13:52967–52977. https://doi.org/10.1021/acsami.1c16271

[23] Martins CA, Ibrahim OA, Pei P, Kjeang E (2018) Towards a fuel-flexible direct alcohol microfluidic fuel cell with flow-through porous electrodes: assessment of methanol, ethylene glycol and glycerol fuels. Electrochim Acta 271:537–543. https://doi.org/10.1016/j.electacta.2018.03.197

[24] Bhunia K, Khilari S, Pradhan D (2018) Monodispersed PtPdNi trimetallic nanoparticles-integrated reduced graphene oxide hybrid platform for direct alcohol fuel cell. ACS Sustain Chem Eng 6:7769–7778. https://doi.org/10.1021/acssuschemeng.8b00721

[25] Xu H, Yan B, Zhang K, Wang J, Li S, Wang C, Shiraishi Y, Du Y, Yang P (2017) Ultrasonic-assisted synthesis of N-doped graphene-supported binary PdAu nanoflowers for enhanced electro-oxidation of ethylene glycol and glycerol. Electrochim Acta 245:227–236. https://doi.org/10.1016/j.electacta.2017.05.146

[26] Fashedemi OO, Miller HA, Marchionni A, Vizza F, Ozoemena KI (2015) Electro-oxidation of ethylene glycol and glycerol at palladium-decorated FeCo@Fe core–shell nanocatalysts for alkaline direct alcohol fuel cells: functionalized MWCNT supports and impact on product selectivity. J Mater Chem A 3:7145–7156. https://doi.org/10.1039/c5ta00076a

[27] Ozoemena KI (2016) Nanostructured platinum-free electrocatalysts in alkaline direct alcohol fuel cells: catalyst design, principles and applications. RSC Adv 6:89523–89550. https://doi.org/10.1039/c6ra15057h

[28] Bao Y, Liu H, Liu Z, Wang F, Feng L (2020) Pd/FeP catalyst engineering via thermal annealing for improved formic acid electrochemical oxidation. Appl Catal B 274:119106. https://doi.org/10.1016/j.apcatb.2020.119106

[29] Bagheri S, Muhd Julkapli N, Bee Abd Hamid S (2014) Titanium dioxide as a catalyst support in heterogeneous catalysis. Sci World J 2014:1–21. https://doi.org/10.1155/2014/727496

[30] Fashedemi OO, Ozoemena KI (2014) Comparative electrocatalytic oxidation of ethanol, ethylene glycol and glycerol in alkaline medium at Pd-decorated FeCo@Fe/C core-shell nanocatalysts. Electrochim Acta 128:279–286. https://doi.org/10.1016/j.electacta.2013.10.194

[31] Panjiara D, Pramanik H (2019) Electrooxidation study of glycerol on synthesized anode electrocatalysts Pd/C and Pd-Pt/C in a Y-shaped membraneless air-breathing microfluidic fuel cell for power generation. Ionics 26:2435–2452. https://doi.org/10.1007/s11581-019-03385-8

[32] Houache MSE, Cossar E, Ntais S, Baranova EA (2018) Electrochemical modification of nickel surfaces for efficient glycerol electrooxidation. J Power Sources 375:310–319. https://doi.org/10.1016/j.jpowsour.2017.08.089

[33] Lipińska W, Grochowska K, Karczewski J, Ryl J, Cenian A, Siuzdak K (2020) Thermally tuneable optical and electrochemical properties of Au-Cu nanomosaic formed over the host titanium dimples. Chem Eng J 399:125673–125685. https://doi.org/10.1016/j.cej.2020.125673

[34] Liu S, Sun Z, Liu Q, Wu L, Huang Y, Yao T, Zhang J, Hu T, Ge M, Hu F, Xie Z, Pan G, Wei S (2014) Unidirectional thermal diffusion in bimetallic Cu@Au nanoparticles. ACS Nano 8:1886–1892. https://doi.org/10.1021/nn4063825

[35] Böhme A, Sterl F, Kath E, Ubl M, Manninen V, Giessen H (2019) Electrochemistry on inverse copper nanoantennas: active plasmonic devices with extraordinarily large resonance shift. ACS Photonics 6:1863–1868. https://doi.org/10.1021/acsphotonics.9b00716

[36] Giri SD, Sarkar A (2016) Electrochemical study of bulk and monolayer copper in alkaline solution. J Electrochem Soc 163:H252–H259

[37] Rajeshwar K (2007) Fundamentals of semiconductor electrochemistry and photoelectrochemistry. In: Bard AJ, Stratmann M, Licht S (eds) Semiconductor electrodes and photoelectrochemistry

[38] Liu J, Fan C, Xie X, Jiang L (2021) Recent progress on photo-promoted alcohol electro-oxidation for fuel cells. Energ Technol 9:2000842–2000873. https://doi.org/10.1002/ente.202000842

[39] Xu H, Song P, Fernandez C, Wang J, Zhu M, Shiraishi Y, Du Y (2018) Sophisticated construction of binary PdPb alloy nanocubes as robust electrocatalysts toward ethylene glycol and glycerol oxidation. ACS Appl Mater Interfaces 10:12659–12665. https://doi.org/10.1021/acsami.8b00532

[40] Song P, Xu H, Wang J, Shiraishi Y, Du Y (2018) Construct 3D networked Au-Cu nanowires for enhanced plasmon-driven catalytic ethylene glycol oxidation through visible light irradiation. J Power Sources 399:59–65. https://doi.org/10.1016/j.jpowsour.2018.07.0

[41] Wang H, Gao H, Zhai Ch, He Z, Yuan Ch, Zhu M (2020) Newly found photoactivated pt anchored on three-dimensional layered WS_2/Carbon cloth for highly efficient ethylene glycol electro-oxidation. Ind Eng Chem Res 59:19252–19259. https://doi.org/10.1021/acs.iecr.0c03436

[42] Campton RG, Batchelor-McAuley Ch, Dickinson EJF (2019) Understanding voltammetry: problems and solutions, vol 7. Imperial College Press, pp 128–129

[43] Etesami M, Mohamed N (2011) Catalytic application of gold nanoparticles electrodeposited by fast scan cyclic voltammetry to glycerol electrooxidation in alkaline electrolyte. Int J Electrochem Sci 6:4676–4689

[44] Shahrokhian S, Rezaee S (2017) Fabrication of trimetallic Pt−Pd−Co porous nanostructures on reduced graphene oxide by galvanic replacement: application to electrocatalytic oxidation of ethylene glycol. Electroanalysis 29:2591–2601. https://doi.org/10.1002/elan.201700355

[45] Khouchaf A, Takky D, El Mahi CM, Benmokhtar S (2016) Electrocatalytic oxidation of methanol on glassy carbon electrode modified by metal ions (Copper and Nickel) dispersed into polyaniline film. J Mater Sci Chem Eng 4:97–105. https://doi.org/10.4236/msce.2016.42011

[46] Lebedev MV (2020) Modification of the atomic and electronic structure of III–V semiconductor surfaces at interfaces with electrolyte solutions (Review). Semiconductors 54(7):699–741. https://doi.org/10.1134/S1063782620070064

[47] Gerischer H, Ekardt W (1983) Fermi levels in electrolytes and the absolute scale of redox potentials. Appl Phys Lett 43:393–395. https://doi.org/10.1063/1.94356

[48] Coy E, Siuzdak K, Pavlenko M, Załęski K, Graniel O, Ziółek M, Balme S, Miele P, Weber M, Bechelany M, Iatsunskyi I (2020) Enhancing photocatalytic performance and solar absorption by schottky nanodiodes heterojunctions in mechanically resilient palladium coated TiO_2/Si nanopillars by atomic layer deposition. Chem Eng J 392:123702–123723. https://doi.org/10.1016/j.cej.2019.123702

[49] Córdoba-Torres P (2017) Relationship between constant-phase element (CPE) parameters and physical properties of films with a distributed resistivity. Electrochim Acta 225:592–604. https://doi.org/10.1016/j.electacta.2016.12.087

[50] Lipińska W, Ryl J, Slepski P, Siuzdak K, Grochowska K (2021) Exploring multi-step glucose oxidation kinetics at GOx-functionalized nanotextured gold surfaces with differential impedimetric technique. Measurement 174:109015–109026. https://doi.org/10.1016/j.measurement.2021.109015

[51] Wysocka J, Cieslik M, Krakowiak S, Ryl J (2018) Carboxylic acids as efficient corrosion inhibitors of aluminium alloys in alkaline media. Electrochim Acta 289:175–192. https://doi.org/10.1016/j.electacta.2018.08.070

[52] Ryl J, Brodowski M, Kowalski M, Lipinska W, Niedzialkowski P, Wysocka J (2019) Corrosion inhibition mechanism and efficiency differentiation of dihydroxybenzene isomers towards aluminum alloy 5754 in alkaline media. Materials 12:3067–3087. https://doi.org/10.3390/ma12193067

[53] Kunze J, Maurice V, Klein LH, Strehblow HH, Marcus P (2003) In situ STM study of the effect of chlorides on the initial stages of anodic oxidation of Cu(111) in alkaline solutions. Electrochim Acta 48:1157–1167. https://doi.org/10.1016/s0013-4686(02)00826-5

[54] Liu Z, Huang L, Zhang L, Ma H, Ding Y (2009) Electrocatalytic oxidation of d-glucose at nanoporous Au and Au–Ag alloy electrodes in alkaline aqueous solutions. Electrochim Acta 54:7286–7293. https://doi.org/10.1016/j.electacta.2009.07.0

[55] Liu Z, Pesic B, Raja KS, Rangaraju RR, Misra M (2009) Hydrogen generation under sunlight by self ordered TiO_2 nanotube arrays. Int J Hydrog Energy 34:3250–3257. https://doi.org/10.1016/j.ijhydene.2009.02.044

[56] Olejnik A, Karczewski J, Dołęga A, Siuzdak K, Grochowska K (2020) Novel approach to interference analysis of glucose sensing materials coated with Nafion. Bioelectrochemistry 135:107575–107586. https://doi.org/10.1016/j.bioelechem.2020.107575

8. Conclusions

The presented dissertation consists of a theoretical part including an introduction and methods section, and an experimental part in the form of a series of six articles. The introduction presents a brief overview of functional nanomaterials, their applications, synthesis methods, nanoparticles especially gold nanoparticles as well as p-type and n-type semiconductors such as copper oxides and titanium dioxide. Further, processes used for material fabrication as electrochemical anodization of Ti leading to TiO_2 nanotubes formation, chemical etching, magnetron sputtering and thermal treatment among other rapid thermal annealing were precisely explained. The methods applied for morphology analysis as SEM, AFM, TEM, optical and structural properties investigation with literature review regarding peak positions, binding energy and absorption edges of Au, Cu, Ti and oxides measured via XRD, Raman, XPS and XAS techniques were described. The last part of the methods section was dedicated to electrochemical measurements such as CV, LV and EIS. Furthermore, photoelectrochemical measurements where the solar simulator was turned on and material was tested under light illumination as well as IPCE measurements were elaborated. These parts of the dissertation were intended to introduce materials that are developed in the result section containing the series of six articles.

Bimetallic AuCu nanostructures exhibit unique optical, electrochemical and photoelectrochemical properties in comparison to their monometallic counterparts. This metal combination can result in enhanced catalytic activity, increase in absorption and photocurrent generation under visible light illumination. In here the fabrication process of AuCu nanoparticles on TiNDs and TiO_2NTs via anodization of Ti foil, chemical etching, thin Au, Cu, AuCu alloy layers magnetron sputtering and annealing in various temperatures, rates, time and atmosphere was developed and elaborated. It should be highlighted that nanomaterials were fabricated using cost-effective and easily scalable methods. Furthermore, nanostructured Ti and TiO_2 are highly ordered platforms and ensure higher surface area for surface modifications than flat materials. The proposed electrode is characterized by flexibility which allows to avoid breakage or destruction which is highly important during its future applications.

First article A1 describes the fabrication process of thin Au, Cu and Au/Cu layers on TiNDs thermally treated in a muffle furnace in 450 °C or 600 °C. AuCu-nanomosaic on TiNDs annealed at 450 °C exhibited significant activity towards OER with ca. 30 times higher current density at +0.8 V than monometallic 10Au electrode. Furthermore, oxidation evolution reaction was enhanced by visible light illumination.

Further, in the article A2 Au/Cu layers in different sequences and AuCu alloy layer on TiNDs were rapidly thermal annealed in a wide range of temperatures from 100 °C to 600 °C. Rapid thermal annealing in RTA furnace allowed to obtain nanostructures characterized by higher photoelectrochemical activity in contrast to materials annealed in MF. Depending on the annealing temperature two types of light interaction with AuCu/TiNDs structures were distinguished as photogenerated charge accumulation and efficient electron-hole separation for 200-300 °C and 400-600 °C, respectively. AuCu nanostructures annealed at 600 °C were characterized by wide absorbance from 300-1000 nm. Furthermore, the highest photocurrent under UV-vis light illumination was obtained for 5Au5Cu electrode with copper on the top during the sputtering process and annealed at 600 °C.

Therefore, moving on to the next article A3, magnetron sputtering and annealing processes were divided into two stages in order to obtain AuCu core-shell nanoparticles with Au as a core and Cu as a shell on TiNDs. In this system, Cu_2O and CuO play as visible light absorbers where generate e-h pairs are generated, and then generate electrons are transported by Au to TiO_2 platform finally reaching electrode contact. Moreover, nanomaterials were thermally treated with various annealing rates (30 °C/s and 0.67 °C/s) and times (1 minute and 4 hours). Materials annealed during a short time as 1 minute were characterized by the reflectance band with minima at 550-600 nm and higher photocurrent under vis light than materials annealed during a longer time (4 hours). This result indicated that short annealing time has a positive effect on photoelectrochemical activity under vis light of AuCu bimetallic structures on TiNDs. AuCu/TiNDs electrode annealed during 1 minute and with a slower annealing rate of 0.67 °C/s obtained the highest photocurrent at +0.3 V under vis and UV-vis light ca. 80 and 3 times higher than TiNDs.

Fourth article A4 describes the fabrication of AuCu/TiNDs electrodes rapidly thermal treated at 600 °C at various atmospheres such as air, vacuum, argon and hydrogen. Thermal treatment of thin AuCu alloy layer deposited on Ti nanodimples in hydrogen atmosphere allowed to obtain AuCu nanostructure active under visible light illumination with photocurrent at +0.3 V ca. 27 times higher than for hydrogenated TiNDs. In the case of hydrogenated materials the presence of Cu_2O or Cu in the upper (2-3 nm) and deeper (5-7 nm) surface layer leads to enhancement of photocurrent in the visible light.

Article A5 is focused on AuCu nanoparticles fabricated during rapid thermal treatment of thin AuCu alloy layers deposited on TiO_2 nanotubes at 450 °C in various atmospheres (air, vacuum, argon and hydrogen). AuCu-modified TiO_2NTs annealed in argon atmosphere exhibited the highest photocurrent at -0.2 V under visible and UV-vis light ca. 37 and 2 times

higher than TiO_2NTs. The AuCu/TiO_2NTs electrode was characterized by an intense oxidation peak and anodic spikes registered under light illumination with maximum current at ca. -0.2 V.

Therefore, in article A6 the AuCu/TiO_2NTs electrode annealed at 450 °C in argon was applied as material active towards alcohol electrochemical oxidation enhanced by vis light illumination. The highest current density was registered for glycerine oxidation. The material exhibited at +0.3 V ca. 90 times higher current after glycerine addition to the electrolyte.

Summing up, the presented series of articles provide a comprehensive study of the fabrication process of AuCu nanostructures on Ti nanodimples and TiO_2 nanotubes and their characteristics of morphology, optical and structural properties as well as electrochemical and photoelectrochemical activity. AuCu-modified Ti and TiO_2 nanostructured electrodes are characterized by increased absorbance in visible light and significant enhancement of photoelectrochemical activity under visible light illumination. Complex study of nanomaterials composition allowed to interpretate light-matter interactions. The obtained results show that fabricated electrodes are active toward water splitting process as well as alcohol oxidation supported by visible light illumination. Therefore, such bimetallic AuCu materials can be used for future solar cells, fuel cells and green energy production.

9. Scientific achievements

Articles in JCR Journals

1. **W. Lipińska**, V. Saska, K. Siuzdak, J. Karczewski, K. Załęski, E. Coy, A. de Poulpiquet, I. Mazurenko, E. Lojou, ***"Interaction between bilirubin oxidase and Au nanoparticles distributed over dimpled titanium foil towards oxygen reduction reaction"***, Electrochimica Acta (2024) DOI:10.1016/j.electacta.2023.143535 (100 points, mechanical engineering, IF=7.3)

2. **W. Lipińska**, Z. Bielan, A. Witkowska, J. Karczewski, K. Grochowska, E. Partyka-Jankowska, T. Sobol, M. Szczepanik, K. Siuzdak, ***Synchrotron radiation studies of AuCu nanostructures deposited on Ti platform: effect of rapid thermal annealing on photoelectrochemical activity***, Applied Surface Science (2023) DOI:10.1016/j.apsusc.2023.158048 (140 points, mechanical engineering, IF=6.7)

3. **W. Lipińska**, A. Olejnik, M. Janik, M. Brodowski, K. Sapiega, M. Pierpaoli, K. Siuzdak, R. Bogdanowicz, J. Ryl, ***„Texture or Linker? Competitive Modulation of Receptor Assembly Toward Impedimetric Detection of Viral Species at Gold-Nanotextured Surfaces",*** The Journal of Physical Chemistry C (2023) DOI:10.1021/acs.jpcc.3c00697 (140 points, IF =4.2)

4. **W. Lipińska**, A. Olejnik, J. Karczewski, K. Grochowska, K. Siuzdak, ***"Annealing Rate as a Crucial Parameter Controlling the Photoelectrochemical Properties of AuCu Mosaic Core–Shell Nanoparticles"*** Energy Technology (2023) DOI: 10.1002/ente.202201021 (100 points, mechanical engineering, IF=4.1)

5. **W. Lipińska**, K. Grochowska, J. Karczewski, J. Ryl, K. Siuzdak, ***"Temperature controlled nanomosaics of AuCu bimetallic structure towards smart light management",*** Journal of Materials Science: Materials in Electronics (2022) DOI:10.1007/s10854-022-08775-9 (70 points, mechanical engineering, IF=2.8)

6. **W. Lipińska**, K. Grochowska, J. Karczewski, E. Coy, K. Siuzdak**, "*Electrocatalytic oxidation of methanol, ethylene glycol and glycerine in alkaline media on TiO_2 nanotubes decorated with AuCu nanoparticles for an application in fuel cells,*** Journal of Materials Science (2022) DOI: 10.1007/s10853-022-07471-7 (100 points, mechanical engineering, IF=4.7)

7. **W. Lipińska**, K. Grochowska, J. Ryl, J. Karczewski, K. Siuzdak, "***Influence of annealing atmosphere on photoelectrochemical activity of TiO_2 nanotubes modified with AuCu nanoparticles",*** ACS Applied Materials and Interfaces (2021) DOI:10.1021/acsami.1c16271 (200 points, mechanical engineering, IF = 10.4)

8. **W. Lipińska**, J. Ryl, P. Ślepski, K. Siuzdak, K. Grochowska, "***Exploring Multi-step Glucose Oxidation Kinetics at GOx functionalized Nanotextured Gold Surface with Differential Impedimetric Technique"***, Measurement (2021) DOI:10.1016/j.measurement.2021.109015 (200 points, mechanical engineering, IF = 5.1)

9. **W. Lipińska**, K. Grochowska, K. Siuzdak, ***"Enzyme Immobilization on Gold Nanoparticles for Electrochemical Glucose Biosensor"*** (2021) Nanomaterials DOI: 10.3390/nano11051156 (70 points, mechanical engineering, IF = 5.7)

10. **W. Lipińska**, K. Siuzdak, J. Karczewski, A. Dołęga, K. Grochowska "***Electrochemical glucose sensor based on the glucose oxidase entrapped in chitosan immobilized onto laser-processed Au-Ti electrode"***, Sensors and Actuators B (2021) DOI: 10.1016/j.snb.2020.129409 (140 points, mechanical engineering, IF = 9.2)

11. **W. Lipińska**, K. Grochowska, J. Karczewski, J. Ryl, A. Cenian, K. Siuzdak, "***Thermally tuneable optical and electrochemical properties of Au-Cu nanomosaic formed over the host titanium dimples"***, Chemical Engineering Journal (2020) DOI: 10.1016/j.cej.2020.125673 (200 points, mechanical engineering, IF =13.0)

12. **W. Lipińska**, K. Siuzdak, J. Ryl, P. Barski, G. Śliwiński, K. Grochowska, **"*The optimization of enzyme immobilization at Au-Ti nanotextured platform and its impact onto the response towards glucose in neutral media"***, Materials Research Express (2019) DOI: 10.1088/2053-1591/ab4fab (70 points, mechanical engineering, IF = 2.0)

13. J. Ryl, M. Brodowski, M. Kowalski, **W. Lipińska**, P. Niedziałkowski, J. Wysocka, "***Corrosion Inhibition Mechanism and Efficiency Differentiation of Dihydroxybenzene Isomers Towards Aluminum Alloy 5754 in Alkaline Media"*** Materials (2019) DOI: 10.3390/ma12193067 (140 points, mechanical engineering, IF=3.7)

articles under review:

14. **W. Lipińska**, K. Grochowska, J. Ryl, J. Karczewski, M. Sawczak, V. Mauritz, R. Crisp, K. Siuzdak, **"*Fusion between the photoactivity and CO_2 adsorption on rapidly thermal hydrogenated vs. conventionally annealed copper oxides deposited on TiO_2 nanotubes"***, article number: JMSC-D-23-05052, Journal of Materials Science

15. V. Myndrul, A. Tamashewski, **W. Lipińska**, K. Siuzdak, I. Iatsunskyi, ***"Highly Sensitive Electrochemical Immunosensor for a Cluster of Differentiation 5 (CD5) Detection in Human Blood Serum Based on Laser-Processed Ti/Au Electrodes"*** article number: am-2023-17242p, ACS Applied Materials & Interfaces

Conferences

1. **W. Lipińska**, K. Grochowska, J. Karczewski, E. Coy, K. Siuzdak, ***"Catalytic Activity of Au-Cu Alloy on TiO_2 Nanotubes for Alcohol Oxidation"*** poster, 244st ECS Meeting (stationary, Gothenburg, Sweden, 8-12.10.2023)

2**. W. Lipińska**, M. Shinnur, K. Grochowska, R. Crisp, K. Siuzdak, ***"Formation of the Heterojunction Based on Titania Modified with Ni and Ag Sulfide Via SILAR Method - Electrochemical and Photoelectrochemical Activity"*** poster, 244st ECS Meeting (stationary, Gothenburg, Sweden, 8-12.10.2023)

3. **W. Lipińska**, K. Grochowska, J. Karczewski, K. Siuzdak, ***„AuCu Nanostructures Active in the Visible Light – Optical and Photoelectrochemical Properties"*** poster, 241st ECS Meeting (stationary, Vancouver, Canada, 29.05-02.06.2022)

4. **W. Lipińska**, K. Grochowska, J. Karczewski, J. Ryl, K. Siuzdak, 72nd Annual Meeting of the International Society of Electrochemistry, ***"Fabrication of gold-copper nanostructures by means of rapid thermal annealing - morphology, optical and photoelectrochemical properties"*** poster, 72nd Annual ISE Meeting hybrid, (online, 29-3.09.2021)

5. **W. Lipińska**, K. Grochowska, J. Karczewski, J. Ryl, K. Siuzdak, ***"Effect of annealing atmosphere on the TiO_2 nanotubes modified with AuCu nanoparticles"*** poster, NanoTech Poland 2021, (online, 9-11.06.2021)

6. **W. Lipińska**, K. Siuzdak, J. Ryl, J. Karczewski, K. Grochowska, ***„Enzyme functionalized AuNPs-TiND electrode towards glucose sensing"*** poster, 71st Annual ISE Online Meeting, (online, 31-04.09.2020)

7. **W Lipińska**, K. Grochowska, J. Ryl, J. Karczewski, K. Siuzdak, ***"Electrocatalytic activity of Au-Cu nanomosaic towards CO_2 reduction"*** poster, 71st Annual ISE Online Meeting (online, 31-04.09.2020)

8. **W. Lipińska**, K. Grochowska, J. Karczewski, J. Ryl, K. Siuzdak, ***"The synergistic effect of the bimetallic Au-Cu nanostructures onto the optical and photoelectrochemical performance"*** poster, Symposium on Advanced Technologies and Materials ATAM 2020 (online, 13-15.10.2020)

9. **W. Lipińska**, K. Siuzdak, J. Karczewski, A. Dołęga, K. Grochowska, ***"Electrochemical glucose sensor based on glucose oxidase immobilized by chitosan-matrix on laser-processed Au-Ti electrode"*** poster, The 1st International Electronic Conference on Biosensor 2020 (online, 02-17. 11. 2020)

10. **W. Lipińska**, K. Siuzdak, J. Ryl, P. Ślepski, K. Grochowska, ***"Studies of the charge transfer kinetics and surface inhomogeneities of enzyme-functionalized Au-Ti electrode"*** poster, 9th SMCBS (stationary, Żelechów, Poland, 8-12.11.2019)

11. **W. Lipińska**, K. Siuzdak, P. Barski, A. Lindstaedt, K. Grochowska, ***„Modyfikacja nanostrukturyzowanej powierzchni Au-Ti oksydazą glukozową przy użyciu samoorganizującej się monowarstwy organicznej"*** (Au-Ti platform modified by glucose oxidase using self-assembled monolayers) poster, Nano&BioMateriały (stationary, Toruń, Poland, 6-7.06.2019)

12. K. Siuzdak, Z. Molenda, **W. Lipińska**, A. Cenian, G. Śliwiński, K. Grochowska, ***„Enzymatic glucose sensor based on Au-Ti heterostructure"*** poster, 13th NANOSMAT (stationary, Gdańsk, Poland, 11-14.09.2018)

Scientific internship

1. **CNRS French National Centre for Scientific Research**, Bioenergetic and Protein Engineering Laboratory, Marseille, France, 03.2022, internship

Aim of study: bioelectrochemistry, enzymatic bioelectrocatalysis, surface and interface modifications, functional immobilization of redox enzymes on nanostructured electrodes, charge transfer between redox enzymes and electrode in enzymatic fuel cells

2. **Prochimia Surfaces Sp. z o.o.**, Laboratory of Organic Synthesis, Gdynia, Poland, 03.2019 – 05.2019, internship

Aim of study: Organic Synthesis of sulfur-containing compounds dedicated to self-assembled monolayers (distillation, vacuum distillation, extraction, crystallization, thin-layer chromatography, column chromatography, rotary evaporation).

Science projects

1. **OPUS-LAP (2020/39/I/ST5/01781)** *"*Solar Reduction of CO_2 at Nano-Architectured Photoelectrodes Featuring Advanced Photon Management (SOLAFAME)*"* financed by National Science Centre in Poland, executor, 07.2022 - present

2. **Preludium (2019/35/N/ST5/02604)** *"Ordered mosaic of the bimetallic Au-Cu nanoparticles onto the conductive substrate – fabrication and properties"* financed by National Science Centre in Poland, principal investigator, 10.2020 - present

3. **SOLARIS Centre (1/SOL/2021/2)** *„The effect of atmosphere on AuCu structure properties during rapid thermal treatment"* Polish Ministry of Education and Science, PHELIX, executor, 17-22.05.2022

4. **Lider (2/0003/L8/16/NCBR/2017)** *„Innovative biocompatible sensor for noninvasive determination of glucose level"* The National Centre for Research and Development, executor, 06.2018 - 08.2020

Patent

Co-author of the invention entitled: *„**Sposób wytwarzania enzymatycznych elektrod”** (Fabrication method for enzymatic electrodes)*, (nr. **P.435033**), submission 20.08.2020, Warszawa, Poland, **W. Lipińska**, K. Grochowska, K. Siuzdak

Science popularization

1. **Festiwal Nauki w Jabłonnie – Nauka z Pałacem w tle** (Science Festival with the Palace) (23.09.2023 and 24-25.09.2022, Jabłonna, Poland)

Aim of work: Chemical and physical experiments. Preparation of promotional materials and experimental station.

2. **E(x)plory** (20-22.10.2021, Gdynia, Poland)

Webinar with young female scientists regarding behind-the-scene work at the university and implementation of innovative scientific projects.

„Wygrywać w nowoczesnych technologiach – spotkanie z laureatkami Konkursu im. R. Szczęsnego oraz o Projekcie InnovaBio Pomorze i warsztatach w Bio Laboratorium dla uczniów szkół ponadpodstawowych”

Courses

1. Artificial intelligence and ChatGPT in Academic Writing, 2023
2. Agile Project Management – fundaments, theory and practise, 2023
3. Project Management by International Project Management Association NCB 4.0, 2023
4. Legal aspects in the R+D project management, 2023
5. Blender 3D Modelling and Graphic Design, 2020
6. MBLC Mindfulness Based Living Course, 2019
7. Coating inspector in accordance with the IMO SOLAS convention, 2018
8. Cathodic protection level 1 in accordance with the PN-EN ISO 15257 standard, 2018

Additional activities

1. Construction of the research station for the rapid thermal annealing in the Laboratory of Functional Materials, Centre for Plasma and Laser Engineering, Institute of Fluid-Flow Machinery Polish Academy of Science, 2020

2. Cosmos Lem Jewellery organized by the Eugeniusz Geppert Academy of Art and Design in Wroclaw. The project of jewellery which presented idea of the Universe and the literary output of Stanislaw Lem, the great Polish artist (see Figure 8d).

Awards

1. Award for the presentation of scientific results on 72nd Annual Meeting of the International Society of Electrochemistry conference, ***"Fabrication of gold-copper nanostructures by means of rapid thermal annealing - morphology, optical and photoelectrochemical properties"*** (09.2021)
2. The Professor Romuald Szczesny Award for the best master thesis in the field of modern technologies (12.2020)
3. Diploma of the year 2019 Award for the best master thesis on the Faculty of Chemistry Gdańsk University of Technology (10.2020)
4. Polish Chemical Society Award for the best master thesis on the Faculty of Chemistry Gdańsk University of Technology 2018/2019 (12.2019)
5. Award for the presentation of scientific results on Surface Modification for Chemical and Biochemical Sensing SCMBS 2019 conference organized by The Institute of Physical Chemistry and University of Warsaw, ***"Studies of the charge transfer kinetics and surface inhomogeneities of enzyme-functionalized Au-Ti electrode"*** (11.2019)
6. Gdańsk University of Technology Gold Badge for the graduate with honors (08.2019)
7. Gdańsk University of Technology Rector's scholarship for the best students (2015, 2016, 2017, 2018, 2019)

Societies

1. The Electrochemical Society ECS Member, ECS ID: 532626, 07.2023 – present
2. RedOx student research club on Gdańsk University of Technology, 07.2023 - present

Scientific activity in numbers

Name	MSc Eng Wiktoria Lipińska
h-index	7
Citations	164
Number of articles (JCR)	13
Participation in conferences	12
Participation in science projects	4

10.Authors contribution statement

A1) W. Lipińska, K. Grochowska, J. Karczewski, J. Ryl, A. Cenian, K. Siuzdak, ***Thermally tuneable optical and electrochemical properties of Au-Cu nanomosaic formed over the host titanium dimples***, Chemical Engineering Journal 399 (2020) 125673 IF=16.7 / 200 points mechanical engineering

Wiktoria Lipińska

I have fabricated AuCu-modified TiNDs electrodes, performed UV-vis spectroscopy measurements and characterized electrochemical and photoelectrochemical activity (CV, LV). I have analysed morphology, optical and structural properties as well as electrochemical and photoelectrochemical activity. I have written the original draft and response to reviewers comments.

Katarzyna Grochowska

I took part in the analysis of optical measurements. I have revised the manuscript and response to reviewers comments.

Jakub Karczewski

I have performed SEM, AFM and XRD measurements. I have revised the manuscript.

Jacek Ryl

I have performed the XPS measurements. I have revised the manuscript.

Adam Cenian

I have revised the manuscript.

Katarzyna Siuzdak

I have initiated the research topic. I have planned experiments. I took part in the analysis of electrochemical and photoelectrochemical measurements. I have revised the manuscript and response to reviewers comments. I have provided funding and guidance.

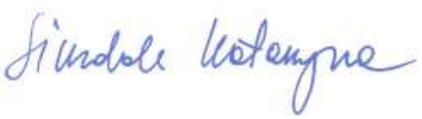

A2) W. Lipińska, K. Grochowska, J. Karczewski, J. Ryl, K. Siuzdak, ***Temperature-controlled nanomosaics of AuCu bimetallic structure towards smart light management***, Journal of Materials Science: Materials in Electronics 33 (2022) 19385, IF = 2.8 / 70 points mechanical engineering

Wiktoria Lipińska

I have initiated the research topic. I have planned experiments. I have fabricated AuCu-modified TiNDs electrodes, performed UV-vis spectroscopy and Raman measurements and characterized electrochemical and photoelectrochemical activity (CV, LV, IPCE). I have analysed morphology, optical and structural properties as well as electrochemical and photoelectrochemical activity. I have proposed mechanism for observed effects. I have written the original draft and response to reviewers comments. Part of funding has been provided from my Preludium project no 2019/35/N/ST5/02604.

Katarzyna Grochowska

I have revised the manuscript and response to reviewers comments.

Jakub Karczewski

I have performed SEM and XRD measurements. I have revised the manuscript.

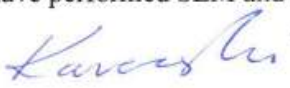

Jacek Ryl

I have performed the XPS measurements. I took part in the analysis of structural properties. I have revised the manuscript and response to reviewers comments.

Katarzyna Siuzdak

I have revised the manuscript and response to reviewers comments. I have provided funding and guidance.

A3) W. Lipińska, A. Olejnik, J. Karczewski, K. Grochowska, K. Siuzdak, ***Annealing Rate as a Crucial Parameter Controlling the Photoelectrochemical Properties of AuCu Mosaic Core-Shell Nanoparticles***, Energy Technology 11 (2023) 2201021 IF= 3.8 / 100 points mechanical engineering

Wiktoria Lipińska

I have initiated the research topic. I have planned experiments. I have fabricated AuCu-modified TiNDs electrodes, performed UV-vis spectroscopy measurements and characterized electrochemical and photoelectrochemical activity (LV, EIS, IPCE, IMPS, IMVS). I have analysed morphology, optical and structural properties as well as photoelectrochemical activity. I have written the original draft and response to reviewers comments. Part of funding has been provided from my Preludium project no 2019/35/N/ST5/02604.

Adrian Olejnik

I have performed DFT calculations. I wrote part of the original draft regarding DFT and IMPS/IMVS results. I have revised the manuscript.

Jakub Karczewski

I have performed SEM and XRD measurements. I have revised the manuscript.

Katarzyna Grochowska

I have revised the manuscript and response to reviewers comments.

Katarzyna Siuzdak

I have revised the manuscript and response to reviewers comments. I have provided funding and guidance.

A4) W. Lipińska, Z. Bielan, A. Witkowska, J. Karczewski, K. Grochowska, E. Partyka-Jankowska, T. Sobol, M. Szczepanik, K. Siuzdak, ***Insightful studies of AuCu nanostructures deposited on Ti platform: Effect of rapid thermal annealing on photoelectrochemical activity supported by synchrotron radiation studies***, Applied Surface Science 638 (2023) 158048, IF = 6.7 / 140 points mechanical engineering

Wiktoria Lipińska

I have initiated the research topic. I took part in planning experiments. I have fabricated AuCu-modified TiNDs electrodes, performed UV-vis spectroscopy measurements, XPS and XAS measurements, and characterized electrochemical and photoelectrochemical activity (CV, LV). I have analysed morphology, optical and structural properties (especially XPS and XAS) as well as electrochemical and photoelectrochemical activity. I have proposed mechanism for observed effects. I have written the original draft and response to reviewers comments. Part of funding has been provided from my Preludium project no 2019/35/N/ST5/02604.

Zuzanna Bielan

I have performed XPS and XAS measurements. I wrote part of the original draft regarding XRD results. I have revised the manuscript.

Agnieszka Witkowska

I took part in planning experiments. I wrote part of the original draft regarding XPS and XAS results. I have revised the manuscript.

Jakub Karczewski

I have performed SEM and XRD measurements. I have revised the manuscript.

Katarzyna Grochowska

I took part in the analysis of optical measurements. I wrote part of the original draft regarding optical properties. I have revised the manuscript and response to reviewers comments.

Ewa Partyka-Jankowska

I took part in performing XPS and XAS measurements. I have revised the manuscript.

Tomasz Sobol

I took part in performing XPS and XAS measurements. I have revised the manuscript.

Magdalena Szczepanik

I have revised the manuscript.

Katarzyna Siuzdak

I took part in planning experiments. I took part in the analysis of electrochemical and photoelectrochemical measurements. I wrote part of the original draft regarding photoelectrochemistry. I have revised the manuscript and response to reviewers comments. I have provided funding and guidance.

A5) W. Lipińska, K. Grochowska, J. Ryl, J. Karczewski, K. Siuzdak, ***Influence of Annealing Atmospheres on Photoelectrochemical Activity of TiO_2 Nanotubes Modified with AuCu Nanoparticles,*** ACS Applied Materials and Interfaces 13 (2021) 52967, IF = 9.5 / 200 points mechanical engineering

Wiktoria Lipińska

I took part in initiating the research topic. I took part in planning experiments. I have fabricated AuCu-modified TiO_2NTs electrodes, performed UV-vis spectroscopy measurements and characterized electrochemical and photoelectrochemical activity (CV, LV, CA, CP). I have analysed morphology, optical and structural properties as well as electrochemical and photoelectrochemical activity. I have proposed mechanism for observed effects. I have written the original draft and response to reviewers comments. Part of funding has been provided from my Preludium project no 2019/35/N/ST5/02604.

Katarzyna Grochowska

I took part in the analysis of optical measurements. I wrote part of the original draft regarding optical properties. I have revised the manuscript and response to reviewers comments.

Jacek Ryl

I have performed the XPS measurements. I have revised the manuscript.

Jakub Karczewski

I have performed SEM and XRD measurements. I have revised the manuscript.

Katarzyna Siuzdak

I took part in initiating the research topic. I took part in planning experiments. I took part in the analysis of electrochemical and photoelectrochemical measurements. I wrote part of the original draft regarding photoelectrochemical activity. I have revised the manuscript and response to reviewers comments. I have provided funding and guidance.

A6) W. Lipińska, K. Grochowska, J. Karczewski, E. Coy, K. Siuzdak, ***Electrocatalytic Oxidation of methanol, ethylene glycol and glycerine in alkaline media on TiO_2 nanotubes decorated with AuCu nanoparticles for an application in fuel cells,*** Journal of Materials Science 57 (2022) 13345, IF = 4.5 / 100 points mechanical engineering

Wiktoria Lipińska

I took part in planning experiments. I have fabricated AuCu-modified TiO_2NTs electrodes, characterized electrochemical and photoelectrochemical activity (CV, LV, EIS). I have analysed morphology as well as electrochemical and photoelectrochemical activity. I have written the original draft and response to reviewers comments. Part of funding has been provided from my Preludium project no 2019/35/N/ST5/02604.

Katarzyna Grochowska

I have revised the manuscript and response to reviewers comments.

Jakub Karczewski

I have performed SEM measurements. I have revised the manuscript.

Emerson Coy

I have performed TEM measurements.

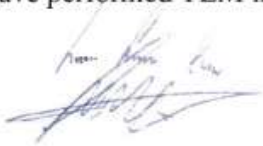

Katarzyna Siuzdak

I have initiated the research topic. I took part in planning experiments. I have revised the manuscript and response to reviewers comments. I have provided funding and guidance.

11. Bibliography

(1) Sen, M. Nanocomposite Materials. In *Nanotechnology and the Environment*; Sen, M., Ed.; IntechOpen, **2020**. https://doi.org/10.5772/intechopen.93047.

(2) Bhattacharya, S.; John, S. Beyond 30% Conversion Efficiency in Silicon Solar Cells: A Numerical Demonstration. *Sci. Rep.* **2019**, *9* (1), 12482. https://doi.org/10.1038/s41598-019-48981-w.

(3) Li, Z.; Klein, T. R.; Kim, D. H.; Yang, M.; Berry, J. J.; Van Hest, M. F. A. M.; Zhu, K. Scalable Fabrication of Perovskite Solar Cells. *Nat. Rev. Mater.* **2018**, *3* (4), 18017. https://doi.org/10.1038/natrevmats.2018.17.

(4) Liu, B.; Sun, G.; Sun, Q.; Lv, Y.; Huang, M.; Qi, B. Low-Temperature Fabrication of Perovskite Solar Cells Using Modified TiO_2 Electron Transport Layer. *Mater. Sci. Semicond. Process.* **2022**, *138*, 106303. https://doi.org/10.1016/j.mssp.2021.106303.

(5) Pei, J.; Mao, J.; Liang, X.; Chen, C.; Peng, Q.; Wang, D.; Li, Y. Ir–Cu Nanoframes: One-Pot Synthesis and Efficient Electrocatalysts for Oxygen Evolution Reaction. *Chem. Commun.* **2016**, *52* (19), 3793–3796. https://doi.org/10.1039/C6CC00552G.

(6) Tuo, Y.; Lu, Q.; Chen, C.; Liu, T.; Pan, Y.; Zhou, Y.; Zhang, J. The Facile Synthesis of Core–Shell PtCu Nanoparticles with Superior Electrocatalytic Activity and Stability in the Hydrogen Evolution Reaction. *RSC Adv.* **2021**, *11* (42), 26326–26335. https://doi.org/10.1039/D1RA04001D.

(7) Li, W.; Chu, X.; Wang, F.; Dang, Y.; Liu, X.; Wang, X.; Wang, C. Enhanced Cocatalyst-Support Interaction and Promoted Electron Transfer of 3D Porous g-C_3N_4/GO-M (Au, Pd, Pt) Composite Catalysts for Hydrogen Evolution. *Appl. Catal. B Environ.* **2021**, *288*, 120034. https://doi.org/10.1016/j.apcatb.2021.120034.

(8) Anitha, V. C.; Zazpe, R.; Krbal, M.; Yoo, J.; Sopha, H.; Prikryl, J.; Cha, G.; Slang, S.; Schmuki, P.; Macak, J. M. Anodic TiO_2 Nanotubes Decorated by Pt Nanoparticles Using ALD: An Efficient Electrocatalyst for Methanol Oxidation. *J. Catal.* **2018**, *365*, 86–93. https://doi.org/10.1016/j.jcat.2018.06.017.

(9) Maya-Cornejo, J.; Carrera-Cerritos, R.; Sebastián, D.; Ledesma-García, J.; Arriaga, L. G.; Aricò, A. S.; Baglio, V. PtCu Catalyst for the Electro-Oxidation of Ethanol in an Alkaline Direct Alcohol Fuel Cell. *Int. J. Hydrog. Energy* **2017**, *42* (46), 27919–27928. https://doi.org/10.1016/j.ijhydene.2017.07.226.

(10) Mohindar Seehra, Alan Bristow. Noble and Precious Metals - Properties, Nanoscale Effects and Applications. **2018**. https://doi.org/10.5772/intechopen.69142.

(11) *Introduction to Nano: Basics to Nanoscience and Nanotechnology*; Sengupta, A., Sarkar, C. K., Eds.; Engineering Materials; Springer Berlin Heidelberg: Berlin, Heidelberg, 2015. https://doi.org/10.1007/978-3-662-47314-6.

(12) Berends, A. C.; De Mello Donega, C. Ultrathin One- and Two-Dimensional Colloidal Semiconductor Nanocrystals: Pushing Quantum Confinement to the Limit. *J. Phys. Chem. Lett.* **2017**, *8* (17), 4077–4090. https://doi.org/10.1021/acs.jpclett.7b01640.

(13) Abid, N.; Khan, A. M.; Shujait, S.; Chaudhary, K.; Ikram, M.; Imran, M.; Haider, J.; Khan, M.; Khan, Q.; Maqbool, M. Synthesis of Nanomaterials Using Various Top-down and Bottom-up Approaches, Influencing Factors, Advantages, and Disadvantages: A Review. *Adv. Colloid Interface Sci.* **2022**, *300*, 102597. https://doi.org/10.1016/j.cis.2021.102597.

(14) Paradowska, E.; Arkusz, K.; Pijanowska, D. G. Comparison of Gold Nanoparticles Deposition Methods and Their Influence on Electrochemical and Adsorption Properties of Titanium Dioxide Nanotubes. *Materials* **2020**, *13* (19), 4269. https://doi.org/10.3390/ma13194269.

(15) Lipińska, W.; Grochowska, K.; Siuzdak, K. Enzyme Immobilization on Gold Nanoparticles for Electrochemical Glucose Biosensors. *Nanomaterials* **2021**, *11* (5), 1156. https://doi.org/10.3390/nano11051156.
(16) Viñes, F. Simulating Heterogeneous Catalysis on Metallic Nanoparticles: From under-Coordinated Sites to Extended Facets. In *Frontiers of Nanoscience*; Elsevier, 2018; Vol. 12, pp 101–128. https://doi.org/10.1016/B978-0-08-102232-0.00002-6.
(17) Thota, S.; Wang, Y.; Zhao, J. Colloidal Au–Cu Alloy Nanoparticles: Synthesis, Optical Properties and Applications. *Mater. Chem. Front.* **2018**, *2* (6), 1074–1089. https://doi.org/10.1039/C7QM00538E.
(18) Moon, C. W.; Choi, M.-J.; Hyun, J. K.; Jang, H. W. Enhancing Photoelectrochemical Water Splitting with Plasmonic Au Nanoparticles. *Nanoscale Adv.* **2021**, *3* (21), 5981–6006. https://doi.org/10.1039/D1NA00500F.
(19) Peiris, S.; McMurtrie, J.; Zhu, H.-Y. Metal Nanoparticle Photocatalysts: Emerging Processes for Green Organic Synthesis. *Catal. Sci. Technol.* **2016**, *6* (2), 320–338. https://doi.org/10.1039/C5CY02048D.
(20) Jeon, H. B.; Tsalu, P. V.; Ha, J. W. Shape Effect on the Refractive Index Sensitivity at Localized Surface Plasmon Resonance Inflection Points of Single Gold Nanocubes with Vertices. *Sci. Rep.* **2019**, *9* (1), 13635. https://doi.org/10.1038/s41598-019-50032-3.
(21) Ahlawat, M.; Mittal, D.; Govind Rao, V. Plasmon-Induced Hot-Hole Generation and Extraction at Nano-Heterointerfaces for Photocatalysis. *Commun. Mater.* **2021**, *2* (1), 114. https://doi.org/10.1038/s43246-021-00220-4.
(22) Kreibig, U.; Vollmer, M. *Optical Properties of Metal Clusters*; Toennies, J. P., Gonser, U., Osgood, R. M., Panish, M. B., Sakaki, H., Lotsch, H. K. V., Series Eds.; Springer Series in Materials Science; Springer Berlin Heidelberg: Berlin, Heidelberg, 1995; Vol. 25. https://doi.org/10.1007/978-3-662-09109-8.
(23) Gołąbiewska, A.; Malankowska, A.; Jarek, M.; Lisowski, W.; Nowaczyk, G.; Jurga, S.; Zaleska-Medynska, A. The Effect of Gold Shape and Size on the Properties and Visible Light-Induced Photoactivity of Au-TiO_2. *Appl. Catal. B Environ.* **2016**, *196*, 27–40. https://doi.org/10.1016/j.apcatb.2016.05.013.
(24) Cheng, X.; Tian, X.; Wu, A.; Li, J.; Tian, J.; Chong, Y.; Chai, Z.; Zhao, Y.; Chen, C.; Ge, C. Protein Corona Influences Cellular Uptake of Gold Nanoparticles by Phagocytic and Nonphagocytic Cells in a Size-Dependent Manner. *ACS Appl. Mater. Interfaces* **2015**, *7* (37), 20568–20575. https://doi.org/10.1021/acsami.5b04290.
(25) Woźniak, A.; Malankowska, A.; Nowaczyk, G.; Grześkowiak, B. F.; Tuśnio, K.; Słomski, R.; Zaleska-Medynska, A.; Jurga, S. Size and Shape-Dependent Cytotoxicity Profile of Gold Nanoparticles for Biomedical Applications. *J. Mater. Sci. Mater. Med.* **2017**, *28* (6), 92. https://doi.org/10.1007/s10856-017-5902-y.
(26) Sigitas Tamulevicius, D. P. Shape Influence on the Ultrafast Plasmonic Properties of Gold Nanoparticles. *Opt. Express* **2022**. https://doi.org/10.1364/OE.463961.
(27) P. S. Kumar, A. D. Plasmonic Applications of Gold Copper Bimetallic Alloy Nanoparticles. **2022**, *17*, 2173–2186. https://doi.org/10.1007/s11468-022-01704-w.
(28) K. Singh, M. B. Review—Multifunctional Copper Nanoparticles: Synthesis and Applications. *ECS J. Solid State Sci. Technol.* **2021**, *10*, 063011. https://doi.org/10.1149/2162-8777/ac07f8.
(29) Xu, V. W.; Nizami, M. Z. I.; Yin, I. X.; Yu, O. Y.; Lung, C. Y. K.; Chu, C. H. Application of Copper Nanoparticles in Dentistry. *Nanomaterials* **2022**, *12* (5), 805. https://doi.org/10.3390/nano12050805.
(30) Guo, X.; Hao, C.; Jin, G.; Zhu, H.; Guo, X. Copper Nanoparticles on Graphene Support: An Efficient Photocatalyst for Coupling of Nitroaromatics in Visible Light. *Angew. Chem. Int. Ed.* **2014**, *53* (7), 1973–1977. https://doi.org/10.1002/anie.201309482.

(31) Khalifeh, S. Optimization of Electrical, Electrical, Electronic and Optical Properties of Organic Electronic Structures. In *Polymers in Organic Electronics*; Elsevier, 2020; pp 185–202. https://doi.org/10.1016/B978-1-927885-67-3.50009-2.
(32) Brus, L. E. Electron–Electron and Electron-Hole Interactions in Small Semiconductor Crystallites: The Size Dependence of the Lowest Excited Electronic State. *J. Chem. Phys.* **1984**, *80* (9), 4403–4409. https://doi.org/10.1063/1.447218.
(33) Kisch, H. Semiconductor Photocatalysis.
(34) Ishida, T.; Murayama, T.; Taketoshi, A.; Haruta, M. Importance of Size and Contact Structure of Gold Nanoparticles for the Genesis of Unique Catalytic Processes. *Chem. Rev.* **2020**, *120* (2), 464–525. https://doi.org/10.1021/acs.chemrev.9b00551.
(35) Al-Hakkani, M. F. Biogenic Copper Nanoparticles and Their Applications: A Review. *SN Appl. Sci.* **2020**, *2* (3), 505. https://doi.org/10.1007/s42452-020-2279-1.
(36) Taketoshi, A.; Haruta, M. Size- and Structure-Specificity in Catalysis by Gold Clusters. *Chem. Lett.* **2014**, *43* (4), 380–387. https://doi.org/10.1246/cl.131232.
(37) Krishnan Rajeshwar. Fundamentals of Semiconductor Electrochemistry and Photoelectrochemistry. In *Encyclopedia of Electrochemistry*; Bard, A. J., Stratmann, M., Gileadi, E., Urbakh, M., Calvo, E. J., Unwin, P. R., Frankel, G. S., Macdonald, D., Licht, S., Sch¿fer, H. J., Wilson, G. S., Rubinstein, I., Fujihira, M., Schmuki, P., Scholz, F., Pickett, C. J., Rusling, J. F., Eds.; Wiley, 2002. https://doi.org/10.1002/9783527610426.bard060001.
(38) Shen, S.; Chen, J.; Wang, M.; Sheng, X.; Chen, X.; Feng, X.; Mao, S. S. Titanium Dioxide Nanostructures for Photoelectrochemical Applications. *Prog. Mater. Sci.* **2018**, *98*, 299–385. https://doi.org/10.1016/j.pmatsci.2018.07.006.
(39) Górska, P.; Zaleska, A.; Kowalska, E.; Klimczuk, T.; Sobczak, J. W.; Skwarek, E.; Janusz, W.; Hupka, J. TiO_2 Photoactivity in Vis and UV Light: The Influence of Calcination Temperature and Surface Properties. *Appl. Catal. B Environ.* **2008**, *84* (3–4), 440–447. https://doi.org/10.1016/j.apcatb.2008.04.028.
(40) Al Zoubi, W.; Salih Al-Hamdani, A. A.; Sunghun, B.; Ko, Y. G. A Review on TiO_2 - Based Composites for Superior Photocatalytic Activity. *Rev. Inorg. Chem.* **2021**, *41* (4), 213–222. https://doi.org/10.1515/revic-2020-0025.
(41) Shi, Q.; Ping, G.; Wang, X.; Xu, H.; Li, J.; Cui, J.; Abroshan, H.; Ding, H.; Li, G. CuO/TiO_2 Heterojunction Composites: An Efficient Photocatalyst for Selective Oxidation of Methanol to Methyl Formate. *J. Mater. Chem. A* **2019**, *7* (5), 2253–2260. https://doi.org/10.1039/C8TA09439J.
(42) Hanaor, D. A. H.; Sorrell, C. C. Review of the Anatase to Rutile Phase Transformation. *J. Mater. Sci.* **2011**, *46* (4), 855–874. https://doi.org/10.1007/s10853-010-5113-0.
(43) Van De Krol, R. Principles of Photoelectrochemical Cells. In *Photoelectrochemical Hydrogen Production*; Van De Krol, R., Grätzel, M., Eds.; Electronic Materials: Science & Technology; Springer US: Boston, MA, 2012; Vol. 102, pp 13–67. https://doi.org/10.1007/978-1-4614-1380-6_2.
(44) Khlyustova, A.; Sirotkin, N.; Kusova, T.; Kraev, A.; Titov, V.; Agafonov, A. Doped TiO_2 : The Effect of Doping Elements on Photocatalytic Activity. *Mater. Adv.* **2020**, *1* (5), 1193–1201. https://doi.org/10.1039/D0MA00171F.
(45) Watcharapasorn A., J. P. The Effects of Donor (Nb^{5+}) and Acceptor (Cu^{2+}, Zn^{2+}, Mn^{2+}, Mg^{2+}) Doping at B-Site on Crystal Structure, Microstructure, and Electrical Properties of $(Ba_{0.85}Ca_{0.15})Zr_{0.1}Ti_{0.9}O_3$ Ceramics. *J. Alloys Compd.* **2022**, *899*, 162909. https://doi.org/10.1016/j.jallcom.2021.162909.
(46) Masudy-Panah, S.; Moakhar, R. S.; Chua, C. S.; Kushwaha, A.; Wong, T. I.; Dalapati, G. K. Rapid Thermal Annealing Assisted Stability and Efficiency Enhancement in a Sputter

Deposited CuO Photocathode. *RSC Adv.* **2016**, *6* (35), 29383–29390. https://doi.org/10.1039/C6RA03383K.
(47) Weller1967.Pdf.
(48) R. Davlen. Introduction to Applied Solid State Physic. **1990**. https://doi.org/10.1007/978-1-4684-1330-4.
(49) Shao G., W. L. 3D CuO Network Supported TiO_2 Nanosheets with Applications for Energy Storage and Water Splitting. *Sci. Adv. Mater. 8*, 1256–1262. https://doi.org/10.1166/sam.2016.2714.
(50) Bharthuar, S. Reproducibility Tests for Measurements with CV-IV and TCT Setups.
(51) Synthesis, Characterization, and Photovoltaic Applications of Mesoscopic Phthalocyanine Structures, 2011.
(52) Tan, C. F.; Su Su Zin, A. K.; Chen, Z.; Liow, C. H.; Phan, H. T.; Tan, H. R.; Xu, Q.-H.; Ho, G. W. Inverse Stellation of CuAu-ZnO Multimetallic-Semiconductor Nanostartube for Plasmon-Enhanced Photocatalysis. *ACS Nano* **2018**, *12* (5), 4512–4520. https://doi.org/10.1021/acsnano.8b00770.
(53) Feng, T.; Ding, L.; Chen, L.; Di, J. Deposition of Gold Nanoparticles upon Bare and Indium Tin Oxide Film Coated Glass Based on Annealing Process. *J. Exp. Nanosci.* **2019**, *14* (1), 13–22. https://doi.org/10.1080/17458080.2018.1520399.
(54) Yadav, A.; Gerislioglu, B.; Ahmadivand, A.; Kaushik, A.; Cheng, G. J.; Ouyang, Z.; Wang, Q.; Yadav, V. S.; Mishra, Y. K.; Wu, Y.; Liu, Y.; RamaKrishna, S. Controlled Self-Assembly of Plasmon-Based Photonic Nanocrystals for High Performance Photonic Technologies. *Nano Today* **2021**, *37*, 101072. https://doi.org/10.1016/j.nantod.2020.101072.
(55) David, T. M.; Dev, P. R.; Wilson, P.; Sagayaraj, P.; Mathews, T. A Critical Review on the Variations in Anodization Parameters toward Microstructural Formation of TiO_2 Nanotubes. *Electrochem. Sci. Adv.* **2022**, *2* (4), e202100083. https://doi.org/10.1002/elsa.202100083.
(56) Masuda, H.; Fukuda, K. Ordered Metal Nanohole Arrays Made by a Two-Step Replication of Honeycomb Structures of Anodic Alumina. *Science* **1995**, *268* (5216), 1466–1468. https://doi.org/10.1126/science.268.5216.1466.
(57) Https://Spottingit.Com/Technology-News/What-Is-the-Anodizing-Process/.
(58) Https://Www.Genesis-Ai.Com/Es/Capabilities/Aluminium-Anodising/.
(59) Https://Cosmoslemjewellery.Com/.
(60) Oxide Morphology and Adhesive Bonding on Titanium Surfaces.
(61) Allam, N. K.; Grimes, C. A. Effect of Cathode Material on the Morphology and Photoelectrochemical Properties of Vertically Oriented TiO_2 Nanotube Arrays. *Sol. Energy Mater. Sol. Cells* **2008**, *92* (11), 1468–1475. https://doi.org/10.1016/j.solmat.2008.06.007.
(62) Suwanchawalit Ch., A. M. Curcumin Modified Titanium Dioxide Nanotubes with Enhanced Visible Light Photocatalytic Performance. *Int J Electrochem Sci* **2019**, *14*, 1954–1967. https://doi.org/10.20964/2019.02.28.
(63) Yoo, H.; Kim, M.; Kim, Y.-T.; Lee, K.; Choi, J. Catalyst-Doped Anodic TiO_2 Nanotubes: Binder-Free Electrodes for (Photo)Electrochemical Reactions. *Catalysts* **2018**, *8* (11), 555. https://doi.org/10.3390/catal8110555.
(64) *Electrochemistry at the Nanoscale*; Schmuki, P., Virtanen, S., Eds.; Nanostructure Science and Technology; Springer New York: New York, NY, 2009. https://doi.org/10.1007/978-0-387-73582-5.
(65) Shin, Y.; Lee, S. Self-Organized Regular Arrays of Anodic TiO_2 Nanotubes. *Nano Lett.* **2008**, *8* (10), 3171–3173. https://doi.org/10.1021/nl801422w.

(66) Kowalski, D.; Kim, D.; Schmuki, P. TiO_2 Nanotubes, Nanochannels and Mesosponge: Self-Organized Formation and Applications. *Nano Today* **2013**, *8* (3), 235–264. https://doi.org/10.1016/j.nantod.2013.04.010.
(67) Ozkan, S.; Nguyen, N. T.; Mazare, A.; Cerri, I.; Schmuki, P. Controlled Spacing of Self-Organized Anodic TiO_2 Nanotubes. *Electrochem. Commun.* **2016**, *69*, 76–79. https://doi.org/10.1016/j.elecom.2016.06.004.
(68) Díaz-Real, J. A.; Dubed-Bandomo, G. C.; Galindo-de-la-Rosa, J.; Arriaga, L. G.; Ledesma-García, J.; Alonso-Vante, N. Impact of the Anodization Time on the Photocatalytic Activity of TiO_2 Nanotubes. *Beilstein J. Nanotechnol.* **2018**, *9*, 2628–2643. https://doi.org/10.3762/bjnano.9.244.
(69) Song, J.; Zheng, M.; Zhang, B.; Li, Q.; Wang, F.; Ma, L.; Li, Y.; Zhu, C.; Ma, L.; Shen, W. Fast Growth of Highly Ordered TiO_2 Nanotube Arrays on Si Substrate under High-Field Anodization. *Nano-Micro Lett.* **2017**, *9* (2), 13. https://doi.org/10.1007/s40820-016-0114-4.
(70) Regonini, D.; Clemens, F. J. Anodized TiO_2 Nanotubes: Effect of Anodizing Time on Film Length, Morphology and Photoelectrochemical Properties. *Mater. Lett.* **2015**, *142*, 97–101. https://doi.org/10.1016/j.matlet.2014.11.145.
(71) Macak, J. M.; Schmuki, P. Anodic Growth of Self-Organized Anodic TiO_2 Nanotubes in Viscous Electrolytes. *Electrochimica Acta* **2006**, *52* (3), 1258–1264. https://doi.org/10.1016/j.electacta.2006.07.021.
(72) Sun, Y.; Zhao, Q.; Wang, G.; Yan, K. Influence of Water Content on the Formation of TiO_2 Nanotubes and Photoelectrochemical Hydrogen Generation. *J. Alloys Compd.* **2017**, *711*, 514–520. https://doi.org/10.1016/j.jallcom.2017.03.007.
(73) Roy, P.; Berger, S.; Schmuki, P. TiO_2 Nanotubes: Synthesis and Applications. *Angew. Chem. Int. Ed.* **2011**, *50* (13), 2904–2939. https://doi.org/10.1002/anie.201001374.
(74) Xiang, C.; Sun, L.; Wang, Y.; Wang, G.; Zhao, X.; Zhang, S. Large-Scale, Uniform and Superhydrophobic Titania Nanotubes at the Inner Surface of 1000-Mm-Long Titanium Tubes. *J. Phys. Chem.*
(75) Escobedo, C. On-Chip Nanohole Array Based Sensing: A Review. *Lab. Chip* **2013**, *13* (13), 2445. https://doi.org/10.1039/c3lc50107h.
(76) Najiminaini, M.; Vasefi, F.; Kaminska, B.; Carson, J. J. L. Optical Resonance Transmission Properties of Nano-Hole Arrays in a Gold Film: Effect of Adhesion Layer. *Opt. Express* **2011**, *19* (27), 26186. https://doi.org/10.1364/OE.19.026186.
(77) Karabiyik M., P. N. Electron Beam Lithography (EBL). *Encycl. Nanotechnol. Springer* **2016**, 1033–1057. https://doi.org/10.1007/978-94-017-9780-1_344.
(78) Kotera H., W. K. *Handbook of Sputter Deposition Technology. Fundamentals and Applications for Functional Thin Films*; Nano-Materials and MEMS, 2012.
(79) Grove W. R. On the Electro-Chemical Polarity of Gases. *Philos. Trans. R. Soc. Lond.* **1852**, *142*, 87–101. https://doi.org/10.1098/rstl.1852.0008.
(80) Bräuer, G.; Szyszka, B.; Vergöhl, M.; Bandorf, R. Magnetron Sputtering – Milestones of 30 Years. *Vacuum* **2010**, *84* (12), 1354–1359. https://doi.org/10.1016/j.vacuum.2009.12.014.
(81) Bogaerts, A. The Glow Discharge: An Exciting Plasma!† Invited Lecture.
(82) *Reactive Sputter Deposition*; Depla, D., Mahieu, S., Eds.; Springer series in materials science; Springer: Berlin Heidelberg, 2008.
(83) Fornari, C. I.; Fornari, G.; Rappl, P. H. D. O.; Abramof, E.; Travelho, J. D. S. Monte Carlo Simulation of Epitaxial Growth. In *Epitaxy*; Zhong, M., Ed.; InTech, 2018. https://doi.org/10.5772/intechopen.70220.
(84) Entikaria Rachmanita, R.; Suweni Muntini, M.; Thawankaew, S.; Chao-Moo, W.; Vora-Ud, A.; Seetawan, T. Fabrication and Characterization of Interdigital Capacitors Thin

Film by DC Magnetron Sputtering for Measuring the Permittivity of Crude Oil. *Mater. Today Proc.* **2018**, *5* (7), 15192–15197. https://doi.org/10.1016/j.matpr.2018.04.081.
(85) Lipińska, W.; Siuzdak, K.; Karczewski, J.; Dołęga, A.; Grochowska, K. Electrochemical Glucose Sensor Based on the Glucose Oxidase Entrapped in Chitosan Immobilized onto Laser-Processed Au-Ti Electrode. *Sens. Actuators B Chem.* **2021**, *330*, 129409. https://doi.org/10.1016/j.snb.2020.129409.
(86) Hu N., M. X., Wei Q. ,. Long H. ,. Yu Z. ,. Deng Z. ,. Meng L. Long-Term Stability of Au Nanoparticle-Anchored Porous Boron-Doped Diamond Hybrid Electrode for Enhanced Dopamine Detection. **2018**, *271*, 84–91. https://doi.org/10.1016/j.electacta.2018.03.1.
(87) Díez-Sierra J., Martínez A., Etxarri I., Azpitarte I., Pozo B., Quintana I. Manufacturing Smart Surfaces with Embedded Sensors via Magnetron Sputtering and Laser Scribing,. **2022**, *606*, 154844. https://doi.org/10.1016/j.apsusc.2022.154844.
(88) Nanotechnology Coatings for Erosion Protection of Turbine Components. *J. Eng. Gas Turbines Power*.
(89) Crespo-Villegas, J.;, Cavarroc, M.;, Knittel, S.;, Martinu, L.;, Klemberg-Sapieha, J.E.;. Self-Organized Multilayer Structure in Magnetron Sputtered Si-Pt Reservoirs on TiAl Alloy Induced by High Temperature Annealing and Oxidation. **2022**, *447*, 128865. https://doi.org/10.1016/j.surfcoat.2022.128865.
(90) Krylova, G.; Na, C. Photoinduced Crystallization and Activation of Amorphous Titanium Dioxide. *J. Phys. Chem. C* **2015**, *119* (22), 12400–12407. https://doi.org/10.1021/acs.jpcc.5b02048.
(91) Shufian, A.; Mahin, Md. S. R.; Islam, R. Electronics and Waste Material Recycler Energy-Efficient Electric Furnace System. *Clean. Eng. Technol.* **2022**, *6*, 100407. https://doi.org/10.1016/j.clet.2022.100407.
(92) Stansfield A. *The Electric Furnace: Its Construction, Operation and Uses*; McGraw-Hill Book Company Inc, 1914.
(93) Downey, D. F.; Falk, S. W.; Bertuch, A. F.; Marcus, S. D. Effects of "Fast" Rapid Thermal Anneals on Sub-keV Boron and BF2 Ion Implants. *J. Electron. Mater.* **1999**, *28* (12), 1340–1344. https://doi.org/10.1007/s11664-999-0119-6.
(94) Kubacka D., Eggeler Y.M., Volz N., Neumeier S., Spiecker E. Using Rapid Thermal Annealing for Studying Early Stages of High-Temperature Oxidation of Superalloys. *Springer Int. Publ.* **2020**. https://doi.org/10.1007/978-3-030-51834-9_74.
(95) 10th IEEE International Conference on Advanced Thermal Processing of Semiconductors - RTP 2002 (Cat. No.02EX574). In *10th IEEE International Conference of Advanced Thermal Processing of Semiconductors*; IEEE: Vancouver, BC, Canada, 2002; p 1039431. https://doi.org/10.1109/RTP.2002.1039431.
(96) Fair R. B. *Rapid Thermal Processing Science and Technology*; Academic Press, 1993.
(97) Roozeboom F., Ozturk M.C., Gusev E.P., Kwong D.L., Chen L.J., Timans P.J. Advanced Short-Time Thermal Processing for Si-Based CMOS Devices : Proceedings of the International Symposium. *Electrochem. Soc.* **2003**.
(98) Jain, S. C.; Schoenmaker, W.; Lindsay, R.; Stolk, P. A.; Decoutere, S.; Willander, M.; Maes, H. E. Transient Enhanced Diffusion of Boron in Si. *J. Appl. Phys.* **2002**, *91* (11), 8919–8941. https://doi.org/10.1063/1.1471941.
(99) Nishi Y., Doering R. *Handbook of Semiconductor Manufacturing Technology*; CRC Press, 2007.
(100) Sharangpani, R.; Singh, R.; Drews, M.; Ivey, K. Chemical Vapor Deposition and Characterization of Amorphous Teflon Fluoropolymerthin Films. *J. Electron. Mater.* **1997**, *26* (4), 402–409. https://doi.org/10.1007/s11664-997-0110-z.
(101) Stalmans, L.; Poortmans, J.; Bender, H.; Caymax, M.; Said, K.; Vazsonyi, E.; Nijs, J.; Mertens, R. Porous Silicon in Crystalline Silicon Solar Cells: A Review and the Effect on

the Internal Quantum Efficiency. *Prog. Photovolt. Res. Appl.* **1998**, *6* (4), 233–246. https://doi.org/10.1002/(SICI)1099-159X(199807/08)6:4<233::AID-PIP207>3.0.CO;2-D.
(102) Wan, Z.; Huang, S.; Green, M. A.; Conibeer, G. Rapid Thermal Annealing and Crystallization Mechanisms Study of Silicon Nanocrystal in Silicon Carbide Matrix. *Nanoscale Res. Lett.* **2011**, *6* (1), 129. https://doi.org/10.1186/1556-276X-6-129.
(103) Wang, X.; Estradé, S.; Lin, Y.; Yu, F.; Lopez-Conesa, L.; Zhou, H.; Gurram, S. K.; Peiró, F.; Fan, Z.; Shen, H.; Schaefer, L.; Braeuer, G.; Waag, A. Enhanced Photoelectrochemical Behavior of H-TiO_2 Nanorods Hydrogenated by Controlled and Local Rapid Thermal Annealing. *Nanoscale Res. Lett.* **2017**, *12* (1), 336. https://doi.org/10.1186/s11671-017-2105-x.
(104) Raza, W.; Hwang, I.; Denisov, N.; Schmuki, P. Thermal Ramping Rate during Annealing of TiO_2 Nanotubes Greatly Affects Performance of Photoanodes. *Phys. Status Solidi A* **2021**, *218* (12), 2100040. https://doi.org/10.1002/pssa.202100040.
(105) Xie, Z.; Shuang, S.; Ma, L.; Zhu, F.; Liu, X.; Zhang, Z. Annealing Effect on the Photoelectrochemical and Photocatalytic Performance of TiO_2 Nanorod Arrays. *RSC Adv.* **2017**, *7* (81), 51382–51390. https://doi.org/10.1039/C7RA09801D.
(106) Jiang, X.; Zhang, Y.; Jiang, J.; Rong, Y.; Wang, Y.; Wu, Y.; Pan, C. Characterization of Oxygen Vacancy Associates within Hydrogenated TiO_2 : A Positron Annihilation Study. *J. Phys. Chem. C* **2012**, *116* (42), 22619–22624. https://doi.org/10.1021/jp307573c.
(107) Mohajernia, S.; Hejazi, S.; Mazare, A.; Nguyen, N. T.; Schmuki, P. Photoelectrochemical H_2 Generation from Suboxide TiO_2 Nanotubes: Visible-Light Absorption versus Conductivity. *Chem. – Eur. J.* **2017**, *23* (50), 12406–12411. https://doi.org/10.1002/chem.201702245.
(108) Bogner, A.; Jouneau, P.-H.; Thollet, G.; Basset, D.; Gauthier, C. A History of Scanning Electron Microscopy Developments: Towards "Wet-STEM" Imaging. *Micron* **2007**, *38* (4), 390–401. https://doi.org/10.1016/j.micron.2006.06.008.
(109) Goldstein, J. I.; Newbury, D. E.; Michael, J. R.; Ritchie, N. W. M.; Scott, J. H. J.; Joy, D. C. *Scanning Electron Microscopy and X-Ray Microanalysis*; Springer New York: New York, NY, 2018. https://doi.org/10.1007/978-1-4939-6676-9.
(110) Eaton P., West P. *Atomic Force Microscopy*; Oxford University Press, 2010.
(111) Asmatulu, R.; Khan, W. S. Characterization of Electrospun Nanofibers. In *Synthesis and Applications of Electrospun Nanofibers*; Elsevier, 2019; pp 257–281. https://doi.org/10.1016/B978-0-12-813914-1.00013-4.
(112) Barber, D. J. Transmission Electron Microscopy. Physics of Image Formation and Microanalysis. *Opt. Acta Int. J. Opt.* **1984**, *31* (8), 848–848. https://doi.org/10.1080/713821585.
(113) Ebnesajjad, S. Surface and Material Characterization Techniques. In *Surface Treatment of Materials for Adhesive Bonding*; Elsevier, 2014; pp 39–75. https://doi.org/10.1016/B978-0-323-26435-8.00004-6.
(114) Tissue B.M. Ultraviolet and Visible Absorption Spectroscopy. *Charact. Mater.* **2012**, *2*, 688–698. https://doi.org/10.1002/0471266965.com059.pub2.
(115) L.C. Passos, M.; M.F.S. Saraiva, M. L. Detection in UV-Visible Spectrophotometry: Detectors, Detection Systems, and Detection Strategies. *Measurement* **2019**, *135*, 896–904. https://doi.org/10.1016/j.measurement.2018.12.045.
(116) Airaksinen, V.-M. Silicon Wafer and Thin Film Measurements. In *Handbook of Silicon Based MEMS Materials and Technologies*; Elsevier, 2015; pp 381–390. https://doi.org/10.1016/B978-0-323-29965-7.00015-4.
(117) Okitsu, K. UV-Vis Spectroscopy for Characterization of Metal Nanoparticles Formed from Reduction of Metal Ions During Ultrasonic Irradiation. In *UV-VIS and Photoluminescence Spectroscopy for Nanomaterials Characterization*; Kumar, C., Ed.;

Springer Berlin Heidelberg: Berlin, Heidelberg, 2013; pp 151–177. https://doi.org/10.1007/978-3-642-27594-4_4.
(118) Harris N., Blaber M.G.,Schatz G.C. Optical Properties of Metal Nanoparticles. *Encycl. Nanotechnol.* **2016**, 3027–3048. https://doi.org/10.1007/978-94-017-9780-1_22.
(119) Acharya R. Interaction of Waves with Medium. In *Satellite Signal Propagation, Impairments and Mitigation*; Academic Press, 2017; pp 57–86.
(120) Https://Www.Nobelprize.Org/Prizes/Physics/1914/Laue/Facts/. 2023.
(121) Moffat, K. Laue Diffraction and Time-Resolved Crystallography: A Personal History. *Philos. Trans. R. Soc. Math. Phys. Eng. Sci.* **2019**, *377* (2147), 20180243. https://doi.org/10.1098/rsta.2018.0243.
(122) Https://Www.Britannica.Com/Science/X-Ray-Diffraction/.
(123) Pandey, A.; Dalal, S.; Dutta, S.; Dixit, A. Structural Characterization of Polycrystalline Thin Films by X-Ray Diffraction Techniques. *J. Mater. Sci. Mater. Electron.* **2021**, *32* (2), 1341–1368. https://doi.org/10.1007/s10854-020-04998-w.
(124) Zielinski, E. M.; Vinci, R. P.; Bravman, J. C. The Influence of Strain Energy on Abnormal Grain Growth in Copper Thin Films. *Appl. Phys. Lett.* **1995**, *67* (8), 1078–1080. https://doi.org/10.1063/1.114455.
(125) Yang, J. H.; Kim, K. H.; Bark, C. W.; Choi, H. W. The Effect of Dye-Sensitized Solar Cell Based on the Composite Layer by Anodic TiO_2 Nanotubes. *Nanoscale Res. Lett.* **2014**, *9* (1), 671. https://doi.org/10.1186/1556-276X-9-671.
(126) Han, M.-K.; Im, J.-B.; Hwang, M.-J.; Kim, B.-J.; Kim, H.-Y.; Park, Y.-J. Effect of Indium Content on the Microstructure, Mechanical Properties and Corrosion Behavior of Titanium Alloys. *Metals* **2015**, *5* (2), 850–862. https://doi.org/10.3390/met5020850.
(127) El-Desoky, M. M.; Morad, I.; Wasfy, M. H.; Mansour, A. F. Synthesis, Structural and Electrical Properties of PVA/TiO_2 Nanocomposite Films with Different TiO_2 Phases Prepared by Sol–Gel Technique. *J. Mater. Sci. Mater. Electron.* **2020**, *31* (20), 17574–17584. https://doi.org/10.1007/s10854-020-04313-7.
(128) Peng, X.; Wang, Z.; Huang, P.; Chen, X.; Fu, X.; Dai, W. Comparative Study of Two Different TiO_2 Film Sensors on Response to H2 under UV Light and Room Temperature. *Sensors* **2016**, *16* (8), 1249. https://doi.org/10.3390/s16081249.
(129) Wu, M.; Zhang, Z.; Xu, X.; Zhang, Z.; Duan, Y.; Dong, J.; Qiao, R.; You, S.; Wang, L.; Qi, J.; Zou, D.; Shang, N.; Yang, Y.; Li, H.; Zhu, L.; Sun, J.; Yu, H.; Gao, P.; Bai, X.; Jiang, Y.; Wang, Z.J.; Ding, F.; Yu, D.; Wang, E.; Liu, K. Seeded Growth of Large Single-Crystal Copper Foils with High-Index Facets. *Nature* **2020**, *581* (7809), 406–410. https://doi.org/10.1038/s41586-020-2298-5.
(130) Mardiansyah, D.; Badloe, T.; Triyana, K.; Mehmood, M. Q.; Raeis-Hosseini, N.; Lee, Y.; Sabarman, H.; Kim, K.; Rho, J. Effect of Temperature on the Oxidation of Cu Nanowires and Development of an Easy to Produce, Oxidation-Resistant Transparent Conducting Electrode Using a PEDOT:PSS Coating. *Sci. Rep.* **2018**, *8* (1), 10639. https://doi.org/10.1038/s41598-018-28744-9.
(131) Wang, X.; Zhang, Y.; Wang, Q.; Dong, B.; Wang, Y.; Feng, W. Photocatalytic Activity of Cu_2O/ZnO Nanocomposite for the Decomposition of Methyl Orange under Visible Light Irradiation. *Sci. Eng. Compos. Mater.* **2019**, *26* (1), 104–113. https://doi.org/10.1515/secm-2018-0170.
(132) Zhu, D.; Wang, L.; Yu, W.; Xie, H. Intriguingly High Thermal Conductivity Increment for CuO Nanowires Contained Nanofluids with Low Viscosity. *Sci. Rep.* **2018**, *8* (1), 5282. https://doi.org/10.1038/s41598-018-23174-z.
(133) Ulas B., Caglar A., Kivrak A., Aktas N., Kivrak H. Tailoring the Metallic Composition of Pd, Pt, and Au Containing Novel Trimetallic Catalysts to Achieve Enhanced Formic

Acid Electrooxidation Activity. *Ionics* **2020**, *26*, 3109–3121. https://doi.org/10.1007/s11581-020-03444-5.
(134) Li, J.; Heng, H.; Lv, J.; Jiang, T.; Wang, Z.; Dai, Z. Graphene Oxide-Assisted and DNA-Modulated SERS of AuCu Alloy for the Fabrication of Apurinic/Apyrimidinic Endonuclease 1 Biosensor. *Small* **2019**, *15* (48), 1901506. https://doi.org/10.1002/smll.201901506.
(135) Mosca, S.; Conti, C.; Stone, N.; Matousek, P. Spatially Offset Raman Spectroscopy. *Nat. Rev. Methods Primer* **2021**, *1* (1), 21. https://doi.org/10.1038/s43586-021-00019-0.
(136) Vázquez-López, A.; Maestre, D.; Martínez-Casado, R.; Ramírez-Castellanos, J.; Píš, I.; Nappini, S.; Cremades, A. Unravelling the Role of Lithium and Nickel Doping on the Defect Structure and Phase Transition of Anatase TiO2 Nanoparticles. *J. Mater. Sci.* **2022**, *57* (14), 7191–7207. https://doi.org/10.1007/s10853-022-07122-x.
(137) Debbichi, L.; Marco De Lucas, M. C.; Pierson, J. F.; Krüger, P. Vibrational Properties of CuO and Cu_4O_3 from First-Principles Calculations, and Raman and Infrared Spectroscopy. *J. Phys. Chem. C* **2012**, *116* (18), 10232–10237. https://doi.org/10.1021/jp303096m.
(138) Pan, X.; Yang, M.-Q.; Fu, X.; Zhang, N.; Xu, Y.-J. Defective TiO_2 with Oxygen Vacancies: Synthesis, Properties and Photocatalytic Applications. *Nanoscale* **2013**, *5* (9), 3601. https://doi.org/10.1039/c3nr00476g.
(139) Paidi V.K, Lee B.H., Ahn D., Kim K.J., Kim Y., Hyeon T., Lee K.S. Oxygen-Vacancy-Driven Orbital Reconstruction at the Surface of TiO_2 Core–Shell Nanostructures. **2021**, *21*, 7953–7959.
(140) Cao, G.; Yi, N. Quantitative Analysis of Anatase-Rutile Mixtures by Raman Spectroscopy. *ChemistrySelect* **2020**, *5* (37), 11530–11533. https://doi.org/10.1002/slct.202002931.
(141) Lipińska, W.; Grochowska, K.; Karczewski, J.; Ryl, J.; Siuzdak, K. Temperature-Controlled Nanomosaics of AuCu Bimetallic Structure towards Smart Light Management. *J. Mater. Sci. Mater. Electron.* **2022**, *33* (24), 19385–19404. https://doi.org/10.1007/s10854-022-08775-9.
(142) Deng, Y.; Handoko, A. D.; Du, Y.; Xi, S.; Yeo, B. S. *In Situ* Raman Spectroscopy of Copper and Copper Oxide Surfaces during Electrochemical Oxygen Evolution Reaction: Identification of Cu^{III} Oxides as Catalytically Active Species. *ACS Catal.* **2016**, *6* (4), 2473–2481. https://doi.org/10.1021/acscatal.6b00205.
(143) Purusottam-Reddy, B.; Sivajee-Ganesh, K.; Jayanth-Babu, K.; Hussain, O. M.; Julien, C. M. Microstructure and Supercapacitive Properties of Rf-Sputtered Copper Oxide Thin Films: Influence of O_2/Ar Ratio. *Ionics* **2015**, *21* (8), 2319–2328. https://doi.org/10.1007/s11581-015-1403-5.
(144) Kar, P.; El-Tahlawy, M. K.; Zhang, Y.; Yassin, M.; Mahdi, N.; Kisslinger, R.; Thakur, U. K.; Askar, A. M.; Fedosejevs, R.; Shankar, K. Anodic Copper Oxide Nanowire and Nanopore Arrays with Mixed Phase Content: Synthesis, Characterization and Optical Limiting Response. *J. Phys. Commun.* **2017**, *1* (4), 045012. https://doi.org/10.1088/2399-6528/aa93a4.
(145) Rocha-Rocha O., Cortez-Valadez M., Calderón-Ayala G., Martínez-Nuñez C.E., Pedroza-Montero M., Flores-Acosta M. Confined Clustering of AuCu Nanoparticles under Ambient Conditions. *Phys. Lett. A* **2019**, *383*, 125985–125992. https://doi.org/10.1016/j.physleta.2019.125985.
(146) Mather, R. R. Surface Modification of Textiles by Plasma Treatments. In *Surface Modification of Textiles*; Elsevier, 2009; pp 296–317. https://doi.org/10.1533/9781845696689.296.

(147) Urquart A.J., Alexander M.R. Characterisation Using X-Ray Photoelectron Spectroscopy (XPS) and Secondary Ion Mass Spectrometry (SIMS). In *Tissue Engineering Using Ceramics and Polymers*; Woodhead Publishing, 2007; pp 175–203.
(148) Stevie, F. A.; Donley, C. L. Introduction to X-Ray Photoelectron Spectroscopy. *J. Vac. Sci. Technol. Vac. Surf. Films* **2020**, *38* (6), 063204. https://doi.org/10.1116/6.0000412.
(149) Sambalova, O.; Billeter, E.; Mann, J.; Miyayama, T.; Burnat, D.; Heel, A.; Bleiner, D.; Borgschulte, A. Hard and Soft X-ray Photoelectron Spectroscopy for Selective Probing of Surface and Bulk Chemical Compositions in a Perovskite-type Ni Catalyst. *Surf. Interface Anal.* **2020**, *52* (12), 811–817. https://doi.org/10.1002/sia.6843.
(150) Biesinger, M. C.; Lau, L. W. M.; Gerson, A. R.; Smart, R. St. C. Resolving Surface Chemical States in XPS Analysis of First Row Transition Metals, Oxides and Hydroxides: Sc, Ti, V, Cu and Zn. *Appl. Surf. Sci.* **2010**, *257* (3), 887–898. https://doi.org/10.1016/j.apsusc.2010.07.086.
(151) Iatsunskyi, I.; Gottardi, G.; Micheli, V.; Canteri, R.; Coy, E.; Bechelany, M. Atomic Layer Deposition of Palladium Coated TiO_2/Si Nanopillars: ToF-SIMS, AES and XPS Characterization Study. *Appl. Surf. Sci.* **2021**, *542*, 148603. https://doi.org/10.1016/j.apsusc.2020.148603.
(152) Zhidkov, I. S.; Kurmaev, E. Z.; Cholakh, S. O.; Fazio, E.; D'Urso, L. XPS Study of Interactions between Linear Carbon Chains and Colloidal Au Nanoparticles. *Mendeleev Commun.* **2020**, *30* (3), 285–287. https://doi.org/10.1016/j.mencom.2020.05.007.
(153) Grochowska K., Ryl J., Karczewski J., Śliwiński G., Cenian A., Siuzdak K. Non-Enzymatic Flexible Glucose Sensing Platform Based on Nanostructured TiO_2 – Au Composite. *J. Electroanal. Chem.* **2019**, *837*, 230–239. https://doi.org/10.1016/j.jelechem.2019.02.04.
(154) Lipińska W., Ryl J., Slepski P., Siuzdak K., Grochowska K. Exploring Multi-Step Glucose Oxidation Kinetics at GOx-Functionalized Nanotextured Gold Surfaces with Differential Impedimetric Technique. *Measurement* **2021**, *174*, 109015. https://doi.org/10.1016/j.measurement.2021.10.
(155) Ashok, J.; Kostrzewa, M.; Srinivasa Reddy, M.; Ravi Kumar, V.; Venkatramiah, N.; Piasecki, M.; Veeraiah, N. Structural and Physical Characteristics of Au_2O_3 -doped Sodium Antimonate Glasses – Part I. *J. Am. Ceram. Soc.* **2019**, *102* (4), 1628–1641. https://doi.org/10.1111/jace.16013.
(156) Liang, B.; Ma, J.; Su, X.; Yang, C.; Duan, H.; Zhou, H.; Deng, S.; Li, L.; Huang, Y. Investigation on Deactivation of Cu/ZnO/Al_2O_3 Catalyst for CO_2 Hydrogenation to Methanol. *Ind. Eng. Chem. Res.* **2019**, *58* (21), 9030–9037. https://doi.org/10.1021/acs.iecr.9b01546.
(157) Lee, K.; Lee, S.; Cho, H.; Jeong, S.; Kim, W. D.; Lee, S.; Lee, D. C. Cu^+ Incorporated TiO_2 Overlayer on Cu_2O Nanowire Photocathodes for Enhanced Photoelectrochemical Conversion of CO_2 to Methanol. *J. Energy Chem.* **2018**, *27* (1), 264–270. https://doi.org/10.1016/j.jechem.2017.04.019.
(158) Liu, Y.L.; Zhu, Y.C.; Qu, L.B.; Yang, R.; Yu, X.D.; Zhao, W.W. Unique Redox Reaction between CuO Photocathode and Cysteine: Insight into the Mechanism for Cathodic Photoelectrochemical Bioanalysis. *ACS Appl. Bio Mater.* **2019**, *2* (7), 2703–2707. https://doi.org/10.1021/acsabm.9b00428.
(159) Zimmermann, P.; Peredkov, S.; Abdala, P. M.; DeBeer, S.; Tromp, M.; Müller, C.; Van Bokhoven, J. A. Modern X-Ray Spectroscopy: XAS and XES in the Laboratory. *Coord. Chem. Rev.* **2020**, *423*, 213466. https://doi.org/10.1016/j.ccr.2020.213466.
(160) Liu, X.; Weng, T.C. Synchrotron-Based x-Ray Absorption Spectroscopy for Energy Materials. *MRS Bull.* **2016**, *41* (6), 466–472. https://doi.org/10.1557/mrs.2016.113.
(161) Penner-Hahn, J. E. 2.13 X-Ray Absorption Spectroscopy.

(162) Yano, J.; Yachandra, V. K. X-Ray Absorption Spectroscopy. *Photosynth. Res.* **2009**, *102* (2–3), 241–254. https://doi.org/10.1007/s11120-009-9473-8.
(163) Liu, L.; Sham, T.K. Luminescence from TiO_2 Nanotubes and Related Nanostructures Investigated Using Synchrotron X-Ray Absorption Near-Edge Structure and X-Ray Excited Optical Luminescence. In *Titanium Dioxide - Material for a Sustainable Environment*; Yang, D., Ed.; InTech, 2018. https://doi.org/10.5772/intechopen.72856.
(164) Mo, L.-B.; Bai, Y.; Xiang, Q.-Y.; Li, Q.; Wang, J.-O.; Ibrahim, K.; Cao, J.-L. Band Gap Engineering of TiO_2 through Hydrogenation. *Appl. Phys. Lett.* **2014**, *105* (20), 202114. https://doi.org/10.1063/1.4902445.
(165) Mosquera, A. A.; Endrino, J. L.; Albella, J. M. XANES Observations of the Inhibition and Promotion of Anatase and Rutile Phases in Silver Containing Films. *J. Anal. At. Spectrom.* **2014**, *29* (4), 736. https://doi.org/10.1039/c3ja50354b.
(166) Mao, S. S.; Shen, S.; Guo, L. Nanomaterials for Renewable Hydrogen Production, Storage and Utilization. *Prog. Nat. Sci. Mater. Int.* **2012**, *22* (6), 522–534. https://doi.org/10.1016/j.pnsc.2012.12.003.
(167) Jiang, P.; Prendergast, D.; Borondics, F.; Porsgaard, S.; Giovanetti, L.; Pach, E.; Newberg, J.; Bluhm, H.; Besenbacher, F.; Salmeron, M. Experimental and Theoretical Investigation of the Electronic Structure of Cu_2O and CuO Thin Films on Cu(110) Using x-Ray Photoelectron and Absorption Spectroscopy. *J. Chem. Phys.* **2013**, *138* (2), 024704. https://doi.org/10.1063/1.4773583.
(168) Bard A.J., Faulkner L.R., White H.S. *Electrochemical Methods: Fundamentals and Applications*; Wiley, 2001.
(169) Tyagi A., Gupta R.K. Carbon Nanostructures from Biomass Waste for Supercapacitor Applications. In *Nanomaterials*; CRC Press, 2016; p 22.
(170) Nnamchi, P. S.; Obayi, C. S. Electrochemical Characterization of Nanomaterials. In *Characterization of Nanomaterials*; Elsevier, 2018; pp 103–127. https://doi.org/10.1016/B978-0-08-101973-3.00004-3.
(171) Wang, H.; Sayed, S. Y.; Luber, E. J.; Olsen, B. C.; Shirurkar, S. M.; Venkatakrishnan, S.; Tefashe, U. M.; Farquhar, A. K.; Smotkin, E. S.; McCreery, R. L.; Buriak, J. M. Redox Flow Batteries: How to Determine Electrochemical Kinetic Parameters. *ACS Nano* **2020**, *14* (3), 2575–2584. https://doi.org/10.1021/acsnano.0c01281.
(172) Brownson D.A.C., Banks C.E. Interpreting Electrochemistry. In *The Handbook of Graphene Electrochemistry*; Springer, 2014; pp 23–77.
(173) Srejić, I.; Smiljanić, M.; Rakočević, Z.; Štrbac, S. Oxygen Reduction on Au(100)-like Polycrystalline Gold Electrode in Alkaline Solution. *Int. J. Electrochem. Sci.* **2016**, *11* (12), 10436–10448. https://doi.org/10.20964/2016.12.51.
(174) Doyle, R. L.; Lyons, M. E. G. The Mechanism of Oxygen Evolution at Superactivated Gold Electrodes in Aqueous Alkaline Solution. *J. Solid State Electrochem.* **2014**, *18* (12), 3271–3286. https://doi.org/10.1007/s10008-014-2665-y.
(175) Jankulovska, M.; Berger, T.; Wong, S. S.; Gómez, R.; Lana-Villarreal, T. Trap States in TiO_2 Films Made of Nanowires, Nanotubes or Nanoparticles: An Electrochemical Study. *ChemPhysChem* **2012**, *13* (12), 3008–3017. https://doi.org/10.1002/cphc.201200072.
(176) Bogdanowicz, R.; Ryl, J.; Darowicki, K.; Kosmowski, B. B. Ellipsometric Study of Oxide Formation on Cu Electrode in 0.1 M NaOH. *J. Solid State Electrochem.* **2009**, *13* (11), 1639–1644. https://doi.org/10.1007/s10008-008-0650-z.
(177) Celante, V. G.; Freitas, M. B. J. G. Electrodeposition of Copper from Spent Li-Ion Batteries by Electrochemical Quartz Crystal Microbalance and Impedance Spectroscopy Techniques. *J. Appl. Electrochem.* **2010**, *40* (2), 233–239. https://doi.org/10.1007/s10800-009-9996-x.

(178) Wei, C.; Xu, Z. J. The Comprehensive Understanding of as an Evaluation Parameter for Electrochemical Water Splitting. *Small Methods* **2018**, *2* (11), 1800168. https://doi.org/10.1002/smtd.201800168.
(179) Berger, T.; Monllor-Satoca, D.; Jankulovska, M.; Lana-Villarreal, T.; Gómez, R. The Electrochemistry of Nanostructured Titanium Dioxide Electrodes. *ChemPhysChem* **2012**, *13* (12), 2824–2875. https://doi.org/10.1002/cphc.201200073.
(180) Shaislamov U., Kim H., Yang B.L. CuO/ZnO/TiO_2 Photocathodes for a Self-Sustaining Photocell: Efficient Solar Energy Conversion without External Bias and under Visible Light. *Int. J. Hydrog. Energy* **2020**, *45*, 6148–6158. https://doi.org/10.1016/j.ijhydene.2019.12.05.
(181) Maljusch, A.; Ventosa, E.; Rincón, R. A.; Bandarenka, A. S.; Schuhmann, W. Revealing Onset Potentials Using Electrochemical Microscopy to Assess the Catalytic Activity of Gas-Evolving Electrodes. *Electrochem. Commun.* **2014**, *38*, 142–145. https://doi.org/10.1016/j.elecom.2013.11.024.
(182) Bott A.W. Electrochemistry of Semiconductors. *Curr. Sep.* **1998**, *17*, 87–91.
(183) Wang, S.; Zhang, J.; Gharbi, O.; Vivier, V.; Gao, M.; Orazem, M. E. Electrochemical Impedance Spectroscopy. *Nat. Rev. Methods Primer* **2021**, *1* (1), 41. https://doi.org/10.1038/s43586-021-00039-w.
(184) Park, J.Y.; Park, S.M. DNA Hybridization Sensors Based on Electrochemical Impedance Spectroscopy as a Detection Tool. *Sensors* **2009**, *9* (12), 9513–9532. https://doi.org/10.3390/s91209513.
(185) Park, S.M.; Yoo, J.S.; Chang, B.Y.; Ahn, E.S. Novel Instrumentation in Electrochemical Impedance Spectroscopy and a Full Description of an Electrochemical System. *Pure Appl. Chem.* **2006**, *78* (5), 1069–1080. https://doi.org/10.1351/pac200678051069.
(186) Bredar A.R.C., Chown A.L., Burton A.R., Farnum B.H. Electrochemical Impedance Spectroscopy of Metal Oxide Electrodes for Energy Applications. *ACS Appl. Energy Mater.* **2020**, *3*, 66–98. https://doi.org/10.1021/acsaem.9b01965.
(187) Wu, C. H.; Weatherup, R. S.; Salmeron, M. B. Probing Electrode/Electrolyte Interfaces in Situ by X-Ray Spectroscopies: Old Methods, New Tricks. *Phys. Chem. Chem. Phys.* **2015**, *17* (45), 30229–30239. https://doi.org/10.1039/C5CP04058B.
(188) Chiu, Y.-H.; Lai, T.-H.; Chen, C.-Y.; Hsieh, P.-Y.; Ozasa, K.; Niinomi, M.; Okada, K.; Chang, T.-F. M.; Matsushita, N.; Sone, M.; Hsu, Y.-J. Fully Depleted Ti–Nb–Ta–Zr–O Nanotubes: Interfacial Charge Dynamics and Solar Hydrogen Production. *ACS Appl. Mater. Interfaces* **2018**, *10* (27), 22997–23008. https://doi.org/10.1021/acsami.8b00727.
(189) Chen Z., Deutsch T.G., Dinh H.N., Domen K., Emery K., Forman A.J., Turner J. Incident Photon-to-Current Efficiency and Photocurrent Spectroscopy. **2013**, 87–97. https://doi.org/10.1007/978-1-4614-8298-7_7.
(190) Tang, M.; Sun, B.; Zhou, D.; Gu, Z.; Chen, K.; Guo, J.; Feng, L.; Zhou, Y. Broad-Band Plasmonic Cu-Au Bimetallic Nanoparticles for Organic Bulk Heterojunction Solar Cells. *Org. Electron.* **2016**, *38*, 213–221. https://doi.org/10.1016/j.orgel.2016.08.023.
(191) Gong, H.; Zhang, W.; Li, F.; Yang, R. Enhanced Electrocatalytic Performance of Self-Supported AuCuCo for Oxygen Reduction and Evolution Reactions. *Electrochimica Acta* **2017**, *252*, 261–267. https://doi.org/10.1016/j.electacta.2017.08.194.
(192) Zhang A., Wu J., Xuea L., Lia C., Zeng S., Caracciolob D., Wang S., Zhong Ch.J. Engineering Active Sites of Gold-Cuprous Oxide Catalysts for Electrocatalytic Oxygen Reduction Reaction. *ACS Appl Mater Interfaces* **2021**, *13*, 46577–46587. https://doi.org/10.1021/acsami.1c11730.
(193) Dai, S.; Huang, T.H.;, Liu, W.I.;, Hsu, Ch.W.; Lee S.W.; Chen T.Y.; Wang Y.Ch.; Wang J.H.; Wang K.W.; Enhanced CO_2 Electrochemical Reduction Performance over

Cu@AuCu Catalysts at High Noble Metal Utilization Efficiency. *Nano Lett.* **2021**, *21*, 9293–9300. https://doi.org/10.1021/acs.nanolett.1c03483.
(194) Marelli, M.; Jouve, A.; Villa, A.; Psaro, R.; Balerna, A.; Prati, L.; Evangelisti, C. Hybrid Au/CuO Nanoparticles: Effect of Structural Features for Selective Benzyl Alcohol Oxidation. *J. Phys. Chem. C* **2019**, *123* (5), 2864–2871. https://doi.org/10.1021/acs.jpcc.8b09449.
(195) Su, Y.H.; Wang, W.L. Surface Plasmon Resonance of Au-Cu Bimetallic Nanoparticles Predicted by a Quasi-Chemical Model. *Nanoscale Res. Lett.* **2013**, *8* (1), 408. https://doi.org/10.1186/1556-276X-8-408.
(196) Hossain, M. Z.; Shimizu, N. Covalent Immobilization of Gold Nanoparticles on Graphene. *J. Phys. Chem. C* **2019**, *123* (6), 3512–3516. https://doi.org/10.1021/acs.jpcc.8b09619.
(197) Yan, X.; Sun, J.; Meng, Y. Experimental Insight into the Chemical Corrosion Mechanism of Copper with an Oil-in-Water Emulsion Solution. *RSC Adv.* **2018**, *8* (18), 9833–9840. https://doi.org/10.1039/C8RA00432C.
(198) Shi, Y.; Zhang, Y.; Zhang, X.; Cai, J.; Lin, S. A Non-Noble Metal Oxide Ti_2O_3/rGO Composite as Efficient and Highly Stable Electrocatalyst for Oxygen Reduction. *Int. J. Hydrog. Energy* **2019**, *44* (52), 28134–28142. https://doi.org/10.1016/j.ijhydene.2019.09.079.
(199) Shen, N.; Xu, H.; Zhao, W.; Zhao, Y.; Zhang, X. Highly Responsive and Ultrasensitive Non-Enzymatic Electrochemical Glucose Sensor Based on Au Foam. *Sensors* **2019**, *19* (5), 1203. https://doi.org/10.3390/s19051203.
(200) Liu, K.; Ma, M.; Wu, L.; Valenti, M.; Cardenas-Morcoso, D.; Hofmann, J. P.; Bisquert, J.; Gimenez, S.; Smith, W. A. Electronic Effects Determine the Selectivity of Planar Au–Cu Bimetallic Thin Films for Electrochemical CO_2 Reduction. *ACS Appl. Mater. Interfaces* **2019**, *11* (18), 16546–16555. https://doi.org/10.1021/acsami.9b01553.
(201) Giri, S. D.; Sarkar, A. Electrochemical Study of Bulk and Monolayer Copper in Alkaline Solution. *J. Electrochem. Soc.* **2016**, *163* (3), H252–H259. https://doi.org/10.1149/2.0071605jes.
(202) Zhao, Y.; Wang, C.; Liu, Y.; MacFarlane, D. R.; Wallace, G. G. Engineering Surface Amine Modifiers of Ultrasmall Gold Nanoparticles Supported on Reduced Graphene Oxide for Improved Electrochemical CO_2 Reduction. *Adv. Energy Mater.* **2018**, *8* (25), 1801400. https://doi.org/10.1002/aenm.201801400.
(203) Bhargava, S. S.; Proietto, F.; Azmoodeh, D.; Cofell, E. R.; Henckel, D. A.; Verma, S.; Brooks, C. J.; Gewirth, A. A.; Kenis, P. J. A. System Design Rules for Intensifying the Electrochemical Reduction of CO_2 to CO on Ag Nanoparticles. *ChemElectroChem* **2020**, *7* (9), 2001–2011. https://doi.org/10.1002/celc.202000089.
(204) Umeda, M.; Niitsuma, Y.; Horikawa, T.; Matsuda, S.; Osawa, M. Electrochemical Reduction of CO_2 to Methane on Platinum Catalysts without Overpotentials: Strategies for Improving Conversion Efficiency. *ACS Appl. Energy Mater.* **2020**, *3* (1), 1119–1127. https://doi.org/10.1021/acsaem.9b02178.
(205) Ma X., Shen Y., Yao S., An C., Zhang W., Zhu J., Si R., Guo Ch. Core–Shell Nanoporous $AuCu_3$@Au Monolithic Electrode for Efficient Electrochemical CO_2 Reduction. *J Mater Chem A* **2020**, *8*, 3344–3350. https://doi.org/10.1039/C9TA09471G.
(206) Morales-Guio, C. G.; Cave, E. R.; Nitopi, S. A.; Feaster, J. T.; Wang, L.; Kuhl, K. P.; Jackson, A.; Johnson, N. C.; Abram, D. N.; Hatsukade, T.; Hahn, C.; Jaramillo, T. F. Improved CO_2 Reduction Activity towards C^{2+} Alcohols on a Tandem Gold on Copper Electrocatalyst. *Nat. Catal.* **2018**, *1* (10), 764–771. https://doi.org/10.1038/s41929-018-0139-9.

(207) Mohajernia, S.; Hejazi, S.; Andryskova, P.; Zoppellaro, G.; Tomanec, O.; Zboril, R.; Schmuki, P. Conductive Cu-Doped TiO_2 Nanotubes for Enhanced Photoelectrochemical Methanol Oxidation and Concomitant Hydrogen Generation. *ChemElectroChem* **2019**, *6* (4), 1244–1249. https://doi.org/10.1002/celc.201900076.
(208) Hejazi, S.; Mohajernia, S.; Wu, Y.; Andryskova, P.; Zoppellaro, G.; Hwang, I.; Tomanec, O.; Zboril, R.; Schmuki, P. Intrinsic Cu Nanoparticle Decoration of TiO_2 Nanotubes: A Platform for Efficient Noble Metal Free Photocatalytic H2 Production. *Electrochem. Commun.* **2019**, *98*, 82–86. https://doi.org/10.1016/j.elecom.2018.11.020.
(209) Guo L., Sun Q., Marcus K., Hao Y., Deng J., Bi K., Yang Y. Photocatalytic Glycerol Oxidation on Au_xCu–CuS@TiO_2 Plasmonic Heterostructures. *J Mater Chem A* **2018**, *6*, 22005–22012. https://doi.org/10.1039/C8TA02170H.
(210) Zhan, W.; Wang, J.; Wang, H.; Zhang, J.; Liu, X.; Zhang, P.; Chi, M.; Guo, Y.; Guo, Y.; Lu, G.; Sun, S.; Dai, S.; Zhu, H. Crystal Structural Effect of AuCu Alloy Nanoparticles on Catalytic CO Oxidation. *J. Am. Chem. Soc.* **2017**, *139* (26), 8846–8854. https://doi.org/10.1021/jacs.7b01784.
(211) Gong, X.; Gu, Y.; Zhang, F.; Liu, Z.; Li, Y.; Chen, G.; Wang, B. High-Performance Non-Enzymatic Glucose Sensors Based on CoNiCu Alloy Nanotubes Arrays Prepared by Electrodeposition. *Front. Mater.* **2019**, *6*, 3. https://doi.org/10.3389/fmats.2019.00003.
(212) Jabeen, S.; Sherazi, T. A.; Ullah, R.; Naqvi, S. A. R.; Rasheed, M. A.; Ali, G.; Shah, A. U.; Khan, Y. Electrodeposition-Assisted Formation of Anodized TiO_2–CuO Heterojunctions for Solar Water Splitting. *Appl. Nanosci.* **2021**, *11* (1), 79–90. https://doi.org/10.1007/s13204-020-01557-x.
(213) Huang, M. H.; Rej, S.; Chiu, C. Facet-Dependent Optical Properties Revealed through Investigation of Polyhedral Au–Cu_2O and Bimetallic Core–Shell Nanocrystals. *Small* **2015**, *11* (23), 2716–2726. https://doi.org/10.1002/smll.201403542.
(214) Xu, W.; Jia, J.; Wang, T.; Li, C.; He, B.; Zong, J.; Wang, Y.; Fan, H. J.; Xu, H.; Feng, Y.; Chen, H. Continuous Tuning of Au–Cu_2O Janus Nanostructures for Efficient Charge Separation. *Angew. Chem.* **2020**, *132* (49), 22430–22435. https://doi.org/10.1002/ange.202010613.
(215) Xue M., Chu Z., Jiang D., Dong H., Wang P., Sun G., Yao Y., Luo W., Zou Z. Bipolarized Intrinsic Faradaic Layer on a Semiconductor Surface under Illumination. *Natl. Sci. Rev.* **2023**, *10*. https://doi.org/10.1093/nsr/nwac249.
(216) Chen, X.; Liu, L.; Yu, P. Y.; Mao, S. S. Increasing Solar Absorption for Photocatalysis with Black Hydrogenated Titanium Dioxide Nanocrystals. *Science* **2011**, *331* (6018), 746–750. https://doi.org/10.1126/science.1200448.
(217) Kumar, R.; Bergum, K.; Riise, H. N.; Monakhov, E.; Galeckas, A.; Svensson, B. G. Impact of Post Annealing and Hydrogen Implantation on Functional Properties of Cu_2O Thin Films for Photovoltaic Applications. *J. Alloys Compd.* **2020**, *825*, 153982. https://doi.org/10.1016/j.jallcom.2020.153982.
(218) Sinthiya, M. M. A.; Kumaresan, N.; Ramamurthi, K.; Sethuraman, K. Development of Pure Rutile TiO_2 and Magneli Titanium Sub-Oxide Microstructures over Titanium Oxide-Seeded Glass Substrates Using Surfactant-Free Hydrothermal Process. *Bull. Mater. Sci.* **2019**, *42* (3), 127. https://doi.org/10.1007/s12034-019-1791-7.
(219) Lu, X.; Wang, G.; Zhai, T.; Yu, M.; Gan, J.; Tong, Y.; Li, Y. Hydrogenated TiO_2 Nanotube Arrays for Supercapacitors. *Nano Lett.* **2012**, *12* (3), 1690–1696. https://doi.org/10.1021/nl300173j.
(220) Yan, Y.; Cheng, X.; Zhang, W.; Chen, G.; Li, H.; Konkin, A.; Sun, Z.; Sun, S.; Wang, D.; Schaaf, P. Plasma Hydrogenated TiO_2/Nickel Foam as an Efficient Bifunctional Electrocatalyst for Overall Water Splitting. *ACS Sustain. Chem. Eng.* **2019**, *7* (1), 885–894. https://doi.org/10.1021/acssuschemeng.8b04496.

(221) Zhu, K.; Neale, N. R.; Miedaner, A.; Frank, A. J. Enhanced Charge-Collection Efficiencies and Light Scattering in Dye-Sensitized Solar Cells Using Oriented TiO_2 Nanotubes Arrays. *Nano Lett.* **2007**, *7* (1), 69–74. https://doi.org/10.1021/nl062000o.
(222) Bhaumik, A.; Haque, A.; Karnati, P.; Taufique, M. F. N.; Patel, R.; Ghosh, K. Copper Oxide Based Nanostructures for Improved Solar Cell Efficiency. *Thin Solid Films* **2014**, *572*, 126–133. https://doi.org/10.1016/j.tsf.2014.09.056.
(223) Xiao, J.; Peng, L.; Gao, L.; Zhong, J.; Huang, Z.; Yuan, E.; Srinivasapriyan, V.; Zhou, S.-F.; Zhan, G. Improving Light Absorption and Photoelectrochemical Performance of Thin-Film Photoelectrode with a Reflective Substrate. *RSC Adv.* **2021**, *11* (27), 16600–16607. https://doi.org/10.1039/D1RA02826J.
(224) Li Y., Sun J., Chen Y., Ma H., Zhu J., Chen Z., Meng L., Liu T. Fabrication of an in Situ-Grown TiO_2 Nanowire Thin Film and Its Enhanced Photocatalytic Activity. *Env. Sci Pollut Res Int* **2023**, *30*, 82560–82574. https://doi.org/10.1007/s11356-023-28229-x.
(225) Chen, S.; Li, C.; Hou, Z. The Novel Behavior of Photoelectrochemical Property of Annealing TiO_2 Nanorod Arrays. *J. Mater. Sci.* **2020**, *55* (14), 5969–5981. https://doi.org/10.1007/s10853-020-04379-y.
(226) Lipińska, W.; Grochowska, K.; Karczewski, J.; Ryl, J.; Cenian, A.; Siuzdak, K. Thermally Tuneable Optical and Electrochemical Properties of Au-Cu Nanomosaic Formed over the Host Titanium Dimples. *Chem. Eng. J.* **2020**, *399*, 125673. https://doi.org/10.1016/j.cej.2020.125673.
(227) Tamirat, A. G.; Dubale, A. A.; Su, W.N.; Chen, H.M.; Hwang, B.J. Sequentially Surface Modified Hematite Enables Lower Applied Bias Photoelectrochemical Water Splitting. *Phys. Chem. Chem. Phys.* **2017**, *19* (31), 20881–20890. https://doi.org/10.1039/C7CP02890C.
(228) Sobczak, I.; Wolski, Ł. Au–Cu on Nb_2O_5 and Nb/MCF Supports – Surface Properties and Catalytic Activity in Glycerol and Methanol Oxidation. *Catal. Today* **2015**, *254*, 72–82. https://doi.org/10.1016/j.cattod.2014.10.051.
(229) Schünemann, S.; Dodekatos, G.; Tüysüz, H. Mesoporous Silica Supported Au and AuCu Nanoparticles for Surface Plasmon Driven Glycerol Oxidation. *Chem. Mater.* **2015**, *27* (22), 7743–7750. https://doi.org/10.1021/acs.chemmater.5b03520.
(230) Brindle J., Sufyan S.A., Nigra M.M. Support, Composition, and Ligand Effects in Partial Oxidation of Benzyl Alcohol Using Gold–Copper Clusters. *Catal Sci Technol* **2022**, *12*, 3846–3855. https://doi.org/10.1039/D2CY00137C.
(231) Hankin, A.; Bedoya-Lora, F. E.; Alexander, J. C.; Regoutz, A.; Kelsall, G. H. Flat Band Potential Determination: Avoiding the Pitfalls. *J. Mater. Chem. A* **2019**, *7* (45), 26162–26176. https://doi.org/10.1039/C9TA09569A.
(232) Le Formal, F.; Sivula, K.; Grätzel, M. The Transient Photocurrent and Photovoltage Behavior of a Hematite Photoanode under Working Conditions and the Influence of Surface Treatments. *J. Phys. Chem. C* **2012**, *116* (51), 26707–26720. https://doi.org/10.1021/jp308591k.
(233) Panjiara, D.; Pramanik, H. Electrooxidation Study of Glycerol on Synthesized Anode Electrocatalysts Pd/C and Pd-Pt/C in a Y-Shaped Membraneless Air-Breathing Microfluidic Fuel Cell for Power Generation. *Ionics* **2020**, *26* (5), 2435–2452. https://doi.org/10.1007/s11581-019-03385-8.
(234) Bao, Y.; Liu, H.; Liu, Z.; Wang, F.; Feng, L. Pd/FeP Catalyst Engineering via Thermal Annealing for Improved Formic Acid Electrochemical Oxidation. *Appl. Catal. B Environ.* **2020**, *274*, 119106. https://doi.org/10.1016/j.apcatb.2020.119106.